

Alma Mater Studiorum - Università di Bologna

**DOTTORATO DI RICERCA IN
ASTROFISICA**

Ciclo XXXVI

Settore Concorsuale: 02/C1 - ASTRONOMIA, ASTROFISICA, FISICA DELLA TERRA E DEI PIANETI

Settore Scientifico Disciplinare: FIS/05 - ASTRONOMIA E ASTROFISICA

**A COMPREHENSIVE STUDY OF THE AGN FEEDBACK CYCLE IN GALAXY
CLUSTERS FROM HIGH RESOLUTION X-RAY AND RADIO
OBSERVATIONS**

Presentata da: Francesco Ubertosi

Coordinatore Dottorato

Prof. Andrea Miglio

Supervisore

Prof. Myriam Gitti

Co-supervisore

Prof. Fabrizio Brighenti

Esame finale anno 2024

*"I've heard it said
That people come into our lives for a reason
Bringing something we must learn and we are led
to those who help us most to grow
if we let them and we help them in return
Well, I don't know if I believe that's true
But I know I'm who I am today
Because I knew you"*

– Wicked

Abstract

Doctor of Philosophy

A comprehensive study of the AGN feedback cycle in galaxy clusters from high resolution X-ray and radio observations

by FRANCESCO UBERTOSI

Located at the apex of massive structures, galaxy groups and galaxy clusters are complex cosmic laboratories. Beside gravity, a number of physical mechanisms – such as radiative cooling, heating, conduction and transport processes – shape the formation and evolution of these systems. Among the constituents of galaxy clusters ($\sim 80\%$ Dark Matter, $\sim 20\%$ baryons), the diffuse, hot gas phase – referred to as Intracluster Medium (ICM), and accounting for $\sim 85\%$ of the baryons – is the most visibly affected by these phenomena. In particular, feedback from active supermassive black holes (SMBH) is currently the favored mechanism to regulate the star formation activity in massive galaxies, and to influence the fraction of baryons in the halo of such galaxies.

The cores of galaxy clusters (the innermost ~ 100 kpc) represent the region where such feedback interplay between different actors - namely the ICM, the brightest cluster galaxy (BCG) and the SMBH in the active galactic nucleus (AGN) - is violently manifested. The footprints of AGN feedback are evident from X-ray observations of galaxy groups and clusters, where X-ray-deficient cavities in the gas spatially coincide with energetic AGN outbursts traced by their lobe radio emission. Jet activity also drives shock fronts that expand and distribute heat in the surrounding environment. At the same time, cooling of the ICM can lead to cold gas reservoirs around the BCG that may fuel both star-formation and AGN activity. The energy required to carve X-ray cavities is in the range $10^{55} - 10^{62}$ erg, corresponding to an average power of $10^{42} - 10^{45}$ erg/s. This matches the radiative cooling rate of the hot gas, suggesting that cluster- and group-central AGN can regulate cooling of the same gas that fuels them. This finely-tuned balance is usually referred to as AGN feeding and feedback cycle.

Understanding AGN feedback in massive structures has key outcomes on two main fields. First, the physics of relativistic jets, and specifically accretion, ejection and termination can be investigated from parsec to hundreds of kiloparsec scales, thanks to the joint efforts of multi-wavelength observations. Second, jet feedback in groups and clusters bears the information on the co-evolution of SMBHs and their host massive structures, since it links the central galactic engine to its large scale environment. The derived observables are crucial to investigate the evolution of galaxies, the physics of the diffuse baryonic component, and the thermodynamics of large scale structures.

The above picture is the result of tremendous advances on these topics over the last three decades. Yet, a deeper understanding of how the heating – cooling regulation of hot atmospheres is achieved and maintained is needed to complete such picture. Several works have shed lights on the thermodynamics of systems where feedback is evidently ongoing; on the contrary, the conditions that lead to the *onset* of the feedback cycle are virtually unexplored. Additionally, theoretical and numerical predictions have long indicated that shocks, besides X-ray cavities, are an essential ingredient of jet feedback. Observationally, it is still unclear which of the two mechanisms (shock or cavity heating) dominates, and if this has any dependence on the mechanical jet power. Ultimately, there is growing interest in bridging the physics of the active engine in the dominant galaxy to the thermal structure of its environment on larger scales. Understanding how the micro AGN scales (parsec) are connected to the macro environment (tens of kpc) is essential to draw a conclusive picture of the hot atmospheres of galaxy clusters and groups.

In this Thesis we delve into the above key aspects of AGN feedback in galaxy clusters and groups. The broad aim of the Thesis is to investigate the connection between cluster- or group- central jetted AGN and the surrounding gaseous medium. To this end, we combine the information from multi-frequency observations (mainly X-ray and radio) of several top-level facilities. First, we address the question of which conditions determine the emergence of a feedback response to gas cooling. Then, we turn our focus to the details of how the AGN – ICM interaction progresses. We select the galaxy cluster RBS 797 as an exemplary system where we can examine cavity and shock heating with multi-frequency, deep observations. Moreover, while individual, well studied systems can reveal the details of how feedback operates, we also wish to look at the larger picture. Using selected samples of clusters, groups, and elliptical galaxies, we consider how distinct feedback and jet power regimes couple to the environment. Ultimately, as heating models rely on the connection between the direct evidence (the radio jet) and the smoking gun (the X-ray cavities) of feedback, we investigate the cases in which these two seem disconnected.

In this Thesis, the above goals are presented as follows:

- In [Chapter 1](#) we provide an overview of the physics of relaxed galaxy clusters, focusing on the role of central radio galaxies in regulating the thermodynamics of the surrounding hot gas. We summarize the current understanding of this interplay and the questions yet unanswered.
- In [Chapter 2](#) we present our pilot study on how the feedback cycle is onset in galaxy clusters, investigating two galaxy clusters with a newly-born central radio galaxy (younger than $\sim 10^4$ yr). This study allows us to probe for the first time the properties of the ICM *before* feedback emerges. Interestingly, we find evidence for an as-yet unheated cluster gas.
- In [Chapter 3](#) we analyze deep *Chandra* observations of RBS 797, a strong cool core cluster that offers a perfect opportunity to investigate extreme AGN feedback in action. We discuss the discovery of perpendicular pairs of X-ray cavities and of three nested shock fronts in the gas, and we reconstruct the AGN – ICM interplay over time. We present evidence that repetitive shock heating is able to offset radiative losses due to ICM cooling in this cluster, and that the mechanical jet power can remain stable for ~ 80 Myr.
- In [Chapter 4](#) we use a wealth of radio observations (JVLA, LOFAR, eMERLIN, VLBA and EVN) to reveal the morphological and spectral properties of the central radio galaxy in RBS 797. By modeling the synchrotron spectrum we derive the radiative ages of radio lobes and jets. The dynamical, morphological and spectral properties of the jets are all consistent with geodesic precession. We find compelling evidence that the multi-faceted radio galaxy hosts (or hosted) binary SMBHs in its core.
- In [Chapter 5](#) we discuss how different classes of radio galaxies can provide different feedback to their environments, when they are located within clusters. First, we extend the study of shock heating in RBS 797 by investigating the heating – cooling balance in a sample of 15 galaxy clusters, galaxy groups and elliptical galaxies with cavities and shocks. Our results indicate that high jet-power AGN (FR II-like) are usually overpowered with respect to their environment, but this does not cause any overheating of the gas. Then, we present the first investigation of feedback from a radio compact “FR 0” in the cluster Abell 795.
- In [Chapter 6](#) we present our investigation of the jet reorientation mechanism in a sample of 16 galaxy clusters and groups. We evaluate the occurrence of misalignments between the radio jets on the parsec scale and large scale feedback imprints (i.e. the cavities) on the kpc scale. We exclude that environmental or projection effects can explain the misaligned cases. Based on this sample, we suggest that reorientation events favor large changes in jet direction.
- In [Chapter 7](#) we outline the most relevant results presented in this Thesis.

Throughout this Thesis we adopt a Λ CDM cosmological model with $\Omega_\Lambda = 0.7$, $\Omega_m = 0.3$, and $H_0 = 70 \text{ km s}^{-1} \text{ Mpc}^{-1}$. We also adopt the convention $S_\nu \propto \nu^{-\alpha}$ for the synchrotron spectrum, where S_ν is the flux density at frequency ν and α is the spectral index. Unless otherwise stated, uncertainties are reported at 1σ confidence.

Part of the results obtained during the Ph.D. and presented in this Thesis are reported in the following publications:

1. *The deepest Chandra view of RBS 797: evidence for two pairs of equidistant X-ray cavities*
Ubertosi, F., Gitti, M., Brighenti, F., Brunetti, G., McDonald, M., Nulsen, P., McNamara, B., Randall, S., Forman, W., Donahue, M., Ignesti, A., Gaspari, M., Ettori, S., Feretti, L., Blanton, E. & Jones-Forman, C. (2021), *The Astrophysical Journal Letters*, Volume 923, Issue 2, id.L25.
2. *A Chandra study of Abell 795 – a sloshing cluster with a FR0 radio galaxy at its center*
Ubertosi, F., Gitti, M., Torresi, E., Brighenti, F., & Grandi, P. (2021), *Monthly Notices of the Royal Astronomical Society*, 503(3), 4627-4645.
3. *The central FR0 in the sloshing cluster Abell 795: indications of mechanical feedback from Chandra data*
Ubertosi, F., Gitti, M., Torresi, E., Brighenti, F., & Grandi, P. (2021), *Astronomische Nachrichten*, Volume 342, Issue 1207, pp. 1207-1211.
4. *Multiple shock fronts in RBS 797: the Chandra window on shock heating in galaxy clusters*
Ubertosi, F., Gitti, M., Brighenti, F., McDonald, M., Nulsen, P., Donahue, M., Brunetti, G., Randall, S., Gaspari, M., Ettori, S., Calzadilla, M., Ignesti, A., Feretti, L., & Blanton, E. L. (2023), *The Astrophysical Journal*, Volume 944, Issue 2, id.216, 25 pp.
5. *Waking the monster: the onset of AGN feedback in galaxy clusters hosting young central radio galaxies*
Ubertosi, F., Gitti, M., Brighenti, F., Olivares, V., O’Sullivan, E., & Schellenberger, G. (2023), *Astronomy & Astrophysics*, Volume 673, id.A52, 8 pp.
6. *A JVLA, LOFAR, e-Merlin, VLBA and EVN study of RBS 797: can binary SMBHs explain the outburst history of the central radio galaxy?*
Ubertosi, F., Giroletti, M., Gitti, M., et al., submitted to *Astronomy & Astrophysics*.
7. *Jet reorientation in clusters and groups central galaxies: insights from VLBA and Chandra data*
Ubertosi, F., Schellenberger, G., O’Sullivan, E., Vrtilik, J., Giacintucci, S., David, L. P., Forman, W., Gitti, M., Venturi, T., Jones, C., & Brighenti, F. (2024), *The Astrophysical Journal*, Volume 961, Issue 1, id.134, 19 pp.

The following publications are the result of work conducted during the PhD, but not presented in this Thesis:

1. *Chasing ICM cooling and AGN feedback from the macro to the meso scales in the galaxy cluster ZwCl 235*
Ubertosi F., Gitti, M., & Brighenti, F. (2023), *Astronomy & Astrophysics*, Volume 670, id.A23, 23 pp.
2. *Testing the Limits of AGN Feedback and the Onset of Thermal Instability in the Most Rapidly Star-forming Brightest Cluster Galaxies*
Calzadilla, M. S., McDonald, M., Donahue, M., McNamara, B. R., Fogarty, K., Gaspari, M., Gitti, M., Russell, Helen R., Tremblay, G. R., Voit, G. M., & **Ubertosi, F.** (2022), *The Astrophysical Journal*, Volume 940, Issue 2, id.140, 18 pp.

3. *Shock imprints on the radio mini halo in RBS 797*
Bonafede, A., Gitti, M., La Bella, N., Biava, N., **Ubertosi, F.**, Brunetti, G., Lusetti, G., Brienza, M., Riseley, C. J., Stuardi, C., Botteon, A., Ignesti, A., Röttgering, H., & van Weeren, R. J. (2023), *Astronomy & Astrophysics*, Volume 680, id.A5, 13 pp.
4. *Deep Chandra observations of Abell 2495: a possible sloshing-regulated feedback cycle in a triple-offset galaxy cluster*
Rosignoli, L., **Ubertosi, F.**, Gitti, M., Brighenti, F., Pasini, T., O'Sullivan, E., Gastaldello, F., Gaspari, M., & Temi, P. (2024), *The Astrophysical Journal*, arXiv:2312.12855.

Contents

Abstract	iv
1 Introduction	1
1.1 Galaxy clusters	1
1.1.1 The intracluster medium: thermodynamic properties and metal content	2
1.1.2 Cooling of hot atmospheres: from cooling flows to cool cores	6
1.2 AGN feeding & feedback in galaxy clusters	13
1.2.1 Evidence of AGN feedback: X-ray cavities and shock fronts	15
1.2.2 Evidence of AGN feeding: the multiphase atmospheres of BCGs	25
1.3 Properties and life-cycle of jetted AGN	32
1.3.1 Different classes of radio galaxies: FR I, FR II and FR 0	32
1.3.2 The life-cycle of radio galaxies: transitory, repetitive, and directional activity	35
2 How AGN feedback is onset: young radio galaxies in cool core clusters	41
2.1 Motivation	41
2.2 Selection of objects and data reduction	42
2.2.1 A list of “pre-feedback” galaxy clusters	42
2.2.2 Data reduction	43
2.3 Results	44
2.3.1 ICM morphology and warm gas kinematics	44
2.3.2 ICM entropy and cooling time profiles	45
2.4 Discussion	47
2.5 Conclusions	48
3 AGN feedback at play in the galaxy cluster RBS 797	51
3.1 Motivation: the cluster RBS 797 and its multi-faceted radio galaxy	51
3.2 Data and Methods	52
3.2.1 X-ray - Chandra	52
3.2.2 Radio - VLA	54
3.3 Equidistant and perpendicular pairs of X-ray cavities in the core of RBS 797	55
3.3.1 Detection of two additional X-ray cavities in the deep <i>Chandra</i> data	56
3.3.2 Interpretation of the perpendicular X-ray cavities: rapid jet reorientation or binary SMBHs?	59
3.4 Multiple AGN-driven shock fronts in the ICM of RBS 797	61
3.4.1 The detection and analysis of shocks	61
3.4.2 Interpretation: reconstructing the history of feedback in RBS 797	67
3.5 Global ICM properties and X-ray emission from the AGN in RBS 797	70
3.5.1 Results	70
3.5.2 The central X-ray point source	75
3.5.3 Discussion	77
3.6 Summary and Conclusions	78

4	A JVLA, LOFAR, e-Merlin, VLBA and EVN study of RBS 797: can binary SMBHs explain the outburst history of the central radio galaxy?	81
4.1	Context: the variations in jet orientation over time	81
4.2	Radio observations of RBS 797: data reduction	82
4.2.1	VLBA, EVN and e-Merlin data reduction	82
	VLBA and EVN data	82
	e-Merlin data	84
4.2.2	JVLA observations and data reduction	84
4.2.3	LOFAR long-baseline observations	84
4.2.4	Complementary archival data	86
4.3	Results: multi-scale morphological and spectral properties of the radio galaxy	87
4.3.1	The kpc scale	88
	Radio galaxy morphology	88
	Spectral properties of the inner jets	88
	Spectral properties of the perpendicular lobes	91
4.3.2	From the kpc to the pc scale	93
4.3.3	The pc scale	95
	Does the radio core of RBS 797 show time variability?	96
4.4	Discussion: which mechanism caused the complex radio morphology of the central AGN?	97
4.4.1	Deciphering the morphology of the radio galaxy in RBS 797	97
	Modelling jet precession	97
	The connection between the inner jets and the outer lobes: single or multiple precession modes?	99
	The connection between the inner jets and the outer lobes: injection index and jet power	100
4.4.2	Is the central AGN powered by binary SMBHs?	101
4.5	Summary and Conclusions	104
5	Feedback from FR 0, FR I, and FR II radio galaxies in galaxy clusters and groups	107
5.1	Motivation	107
5.2	Shock and cavity heating of hot atmospheres: differences between FR I and FR II radio galaxies	108
5.2.1	The sample	108
5.2.2	Results	108
5.3	A first look at feedback from FR 0 radio galaxies: the case of Abell 795	113
5.3.1	<i>Chandra</i> observation and data reduction	113
5.3.2	X-ray morphology and spectral properties of the ICM in A795	114
5.3.3	The heating cooling balance in a galaxy cluster with a central FR 0	120
5.4	Summary and conclusions	122
6	Jet reorientation in the central galaxies of clusters and groups	125
6.1	Motivation	125
6.2	Sample selection	126
6.3	Data and Methods	126
6.3.1	VLBA radio data	126
6.3.2	<i>Chandra</i> X-ray data	128
6.4	Measurement of position angles	128
6.5	Results	133
6.5.1	Jet-cavity misalignments in the plane of the sky	133
6.5.2	Jet inclination angle with respect to the line of sight	135

6.6	Discussion	135
6.6.1	Projection effects	136
6.6.2	The environment	137
6.6.3	The likelihood of jet reorientation	138
6.6.4	The timescales and mechanism of jet reorientation	139
6.7	Conclusions	141
7	Thesis Conclusions	143
A	Methods to derive entropy and cooling time profiles of pre-feedback galaxy clusters	147
B	Alternative methods to detect the N-S cavities in RBS 797	149
C	Details on the morphological and spectral analysis of shocks fronts in RBS 797	151
D	VLBI observations of RBS 797: notes on the previous EVN – RSG05 observation	153
E	Alternative methods to measure jets position angles on VLBA scales	155
F	Insights on the jet position and inclination angles from VLBA data at other frequencies	157
G	RXC J1558.3-1410: X-ray morphological analysis	159
H	Results of fitting in DIFMAP the VLBA data of the 16 galaxy groups and clusters	161
I	Comments on individual galaxy clusters from the aligned/misaligned sample	163
	Acknowledgements	167
	Bibliography	169

List of Figures

1.1	Composite X-ray and optical images of four relaxed galaxy clusters.	3
1.2	Spectral models for ICM at different temperatures.	4
1.3	Image and surface brightness profile of Abell 1689, fitted with a double β -model.	6
1.4	Median abundance profile from the sample of Lovisari and Reiprich (2019).	7
1.5	Efficiency of star formation versus cooling rate, from McDonald et al. (2018).	9
1.6	RGS spectrum of Abell 1835, fitted with a cooling flow model	10
1.7	Density and entropy profiles of the clusters in the sample of Sanderson et al. (2009).	11
1.8	Sloshing in the Centaurus galaxy cluster.	12
1.9	Composite X-ray, optical, and radio image of the Phoenix cluster, from McDonald et al. (2019).	14
1.10	Deviation of the entropy profiles from the cosmological prediction, from McDonald et al. (2014).	15
1.11	Schematic representation of a jet inflating an X-ray cavity, from Bourne and Yang (2023).	16
1.12	Cavity power versus cooling luminosity for groups and clusters, from Eckert et al. (2021).	18
1.13	Uplift of metal-rich gas from cluster-central AGN jets, from Kirkpatrick and McNamara (2015).	20
1.14	Example of shock fronts in galaxy clusters.	22
1.15	Shock energy versus cavity energy from Liu et al. (2019b).	24
1.16	Warm gas filaments in Perseus and connection with ICM cooling.	25
1.17	Connection between cold molecular filaments and warm filaments in cool core clusters, from Olivares et al. (2019).	27
1.18	Different diagnostics of efficient ICM condensation.	28
1.19	Cavity power versus central molecular gas mass, from Russell et al. (2019) and Fujita et al. (2023).	29
1.20	Molecular emission and absorption in Hydra A, from Rose et al. (2020).	30
1.21	Categories and evolution of AGN.	34
1.22	Examples of changes in jet axis orientation.	36
1.23	Simulations of jet precession from Nolting et al. (2023).	37
2.1	<i>Chandra</i> and MUSE images of the two pre-feedback clusters.	43
2.2	Comparison between the entropy and the cooling time profiles of pre-feedback and mature-feedback galaxy clusters.	45
3.1	Exposure-corrected, background-subtracted mosaiced <i>Chandra</i> images of RBS 797 showing the perpendicular X-ray cavities.	55
3.2	Significance of the X-ray cavities in RBS 797	56
3.3	Outburst interval of the X-ray cavities in RBS 797 from the X-ray <i>Chandra</i> data.	60
3.4	Original and filtered <i>Chandra</i> images of RBS 797 showing the nested shock fronts in the ICM.	62
3.5	Surface brightness profiles across the weak shocks in RBS 797.	64

3.6	Combined X-ray and radio data of RBS 797, showing the interaction between the central radio galaxy, the hot ICM, and the diffuse radio emission.	68
3.7	Radial profiles of ICM thermodynamic quantities in RBS 797.	71
3.8	Temperature, pressure, and entropy maps of RBS 797.	72
3.9	Spectral maps in sectors of RBS 797.	73
3.10	Metallicity map and radial profile in RBS 797.	76
4.1	Composite optical (HST, red), <i>Chandra</i> (X-ray, blue), 3 GHz (JVLA, green), 144 MHz (LOFAR-International, pink) image of RBS 797	83
4.2	Final JVLA and LOFAR maps of RBS 797.	87
4.3	Spectral index maps of the jets in RBS 797 from JVLA and LOFAR data.	89
4.4	Radio spectrum and radiative age maps of the jets in RBS 797	90
4.5	Study of radiative age of the perpendicular radio lobes in RBS 797.	91
4.6	e-Merlin images at 1.6 GHz and 5 GHz of RBS 797.	93
4.7	VLBA and EVN maps of RBS 797 at different frequencies.	94
4.8	Jet precession model fitted to the radio images of the kpc-scale jets in RBS 797.	98
4.9	Schematic representation of the three scenarios involving binary SMBHs at the center of the radio galaxy in RBS 797	102
5.1	Mechanical cavity power, shock power, and total heating power versus cooling luminosity for 15 systems with detection of X-ray cavities and shocks.	110
5.2	Feedback ratio versus central entropy excess for 15 systems with detection of X-ray cavities and shocks.	111
5.3	Large scale <i>Chandra</i> image, best-fit β -model, residual image, and temperature map of A795.	115
5.4	Radial profiles of thermodynamic quantities of A795.	116
5.5	Zoom-in in the central regions of A795: original <i>Chandra</i> image and unsharp-masked image.	119
5.6	Comparison between cavity power and cooling luminosity in A795.	121
6.1	Schematic representation of how we measured the jet and cavity angles.	130
6.2	VLBA images at 5 GHz of the systems in our sample.	131
6.3	Residual <i>Chandra</i> images of the systems in our sample	132
6.4	Comparison between the position angle of jets and the position angle of cavities for the systems in our sample.	134
6.5	Diagnostic plot of misaligned jets and X-ray cavities.	136
6.6	<i>Left panel:</i> Jet – cavity position angle difference $\Delta\Psi$ versus cavity age t_{cav} for the cavities in the systems of Tab. 6.2 with an available estimate of the age from the literature. <i>Right panel:</i> Largest jet – cavity position angle difference $\Delta\Psi$ for each system in our sample versus the Eddington ratio of the central AGN (see Sect. 6.6.4 for details). In the right panel, only the 14/16 systems with available measurements of L_{bol} and L_{Edd} are plotted.	139
A.1	Comparison between different methods of deriving density, entropy, and cooling time profiles of the two pre-feedback clusters.	148
B.1	Alternative tests on the significance of the N-S cavities in RBS 797.	150
D.1	Alternative test on the EVN-RSG05 observations of RBS 797.	153
E.1	Comparison between the three methods used to measure the jet position angle.	156
F.1	The effect of observing frequency on the measurement of position angles.	158

G.1 *Chandra* images of RXC J1558.3-1410. 160

List of Tables

2.1	List of galaxy clusters hosting a young central radio galaxy.	44
3.1	Summary of the 15 <i>Chandra</i> observations of the galaxy cluster RBS 797.	53
3.2	Properties of the four X-ray cavities in RBS 797.	59
3.3	Properties of the AGN-driven, nested shock fronts in RBS 797	66
3.4	Energetics of the four X-ray cavities in RBS 797.	69
4.1	Summary of the EVN, VLBA, e-Merlin, JVLA and LOFAR data presented in this work.	85
4.2	Image parameters of the EVN, VLBA, e-Merlin, JVLA and LOFAR data used in this work.	86
4.3	CI-off best-fit to the perpendicular radio lobes of RBS 797.	92
4.4	DIFMAP results for the EVN and VLBA data of RBS 797.	95
5.1	Galaxy clusters, galaxy groups and elliptical galaxies with X-ray cavities and weak shocks.	109
5.2	Spectral analysis of the ICM around the FR 0 J092405.30+14.	117
5.3	Properties of the putative X-ray cavities in the cluster A795	120
6.1	Sample of galaxy clusters and groups used to study jet-cavity misalignments.	127
6.2	Position and inclination angle of the jets and position angle of the X-ray cavities for the systems in the sample.	129
C.1	Analysis of the surface brightness profile of the shock fronts in RBS 797.	151
C.2	Spectral analysis of three pairs of surface brightness edges in RBS 797	151
H.1	Properties of VLBA images and DIFMAP results for the systems in our sample.	162

List of Abbreviations

ADAF	Advection Dominated Accretion Flow
AGN	Active Galactic Nucleus
AIPS	Astronomical Image Processing System
ALMA	Atacama Large Millimeter Array
AXIS	Advanced X-ray Imaging Satellite
BCG	Brightest Cluster Galaxy
BRATS	Broadband Radio Astronomy ToolS
CCA	Chaotic Cold Accretion
CIAO	Chandra Interactive Analysis of Observations
CSO	Caltech Submillimeter Observatory
CSO	Compact Symmetric Objects
CSS	Compact Steep Spectrum
EI	Excitation Index
e-MERLIN	enhanced Multi Element Remotely Linked Interferometer Network
EVN	European VLBI Network
FIRST	Faint Images of the Radio Sky at Twenty-Centimeters
FR 0	Fanaroff-Riley Type 0
FR I	Fanaroff-Riley Type I
FR II	Fanaroff-Riley Type II
GPS	Gigahertz Peak Spectrum
HERG	High Excitation Radio Galaxy
HST	Hubble Space Telescope
ICM	Intra Cluster Medium
LOFAR	LOW Frequency ARray
JCMT	James Clerk Maxwell Telescope
JVLA	Jansky Very Large Array
LERG	Low Excitation Radio Galaxy
LINER	Low-Ionization Nuclear Emission-line Region
NVSS	NRAO VLA Sky Survey
RGS	Reflection Grating Spectrometer
RQQ	Radio Quiet Quasars
SDSS	Sloan Digital Sky Survey
SMBH	Super Massive Black Hole
SSS	Solid State Spectrometer
VLA	Very Large Array
VLASS	Very Large Array Sky Survey
VLBA	Very Long Baseline Array
VLBI	Very Long Baseline Interferometry

Physical Constants

Speed of Light	c	$2.998 \times 10^{10} \text{ cm s}^{-1}$
Boltzmann's constant	k	$1.381 \times 10^{-16} \text{ cm}^2 \text{ g s}^{-1} \text{ K}^{-1}$
Planck's constant	h	$6.626 \times 10^{-27} \text{ cm}^2 \text{ g s}^{-1}$
Proton mass	m_p	$1.673 \times 10^{-24} \text{ g}$
Gravitational constant	G	$6.674 \times 10^{-8} \text{ cm}^3 \text{ g}^{-1} \text{ s}^{-2}$

Chapter 1

Introduction

Abstract

In this Chapter, we present the main background information regarding the subject of this Thesis. In the first section (§1.1), we describe the physical parameters, composition and global properties of galaxy clusters. In particular, we describe the properties of the intracluster medium and the historical understanding of the *cooling flow* problem in relaxed systems. Then, in the second section (§1.2) we summarize the current evidence for the AGN *feeding and feedback loop* in cool core galaxy clusters, focusing on the imprints of AGN activity on the surrounding hot medium (X-ray cavities and shock fronts), and on the signature of multiphase cooling of hot gas that lead to SMBH feeding. Lastly, we outline in the third section (§1.3) the different classes of jetted AGN and the typical life-cycle of radio galaxies.

1.1 Galaxy clusters

A complete definition of galaxy clusters is difficult to enunciate, since these structures are composed of different types of matter (baryonic and non-baryonic), in very different states (gas, galaxies and stars). In addition to that, even single components (such as the hot gas filling the cluster volume) show peculiar behaviors from one cluster to another. Nevertheless, clusters possess a unique feature: they represent the apex of massive structures, being the largest gravitationally collapsed concentrations of matter in the Universe. They have sizes that range from a few to several Mpc, and typical masses of $10^{13-15} M_{\odot}$. Clusters typically contain 10 – 1000 galaxies, which represent 2-5% of the total mass (visible and dark matter) of the galaxy cluster. The dominant galaxy (referred to as “brightest cluster galaxy”, BCG) is the most massive galaxy in the cluster (with a total mass of up to $10^{13} M_{\odot}$), and if no strong dynamical perturbations are present, it is usually located near the geometric and kinematic center of the host cluster (see Fig. 1.1). A supermassive black hole (SMBH) is located at the center of BCGs. When a SMBH accretes gas and drives powerful outflows, it is referred to as an Active Galactic Nucleus (AGN).

The majority of a cluster’s mass is accounted for by dark matter, with a mass fraction of ~ 0.8 . This component is responsible for the formation and growth of these structures: clusters form by subsequent mergers of smaller over-densities of matter; the deep potential well of dark matter guides the process of merging and evolution of clusters of galaxies. The remaining component is the hot (with temperatures as high as 10^8 K) and tenuous (with typical electron densities $n_e \approx 10^{-3} \text{cm}^{-3}$) gas which fills the cluster’s space: the intra cluster medium (ICM), with a mass fraction of $\sim 0.15-0.20$ (e.g., for reviews Bahcall 1999; Voit 2005; Kravtsov and Borgani 2012; Bykov et al. 2015).

Since catalogs of galaxy clusters and groups began to be available in the early 1950’s and 1960’s, it became clear that these massive structures come in two flavors. In particular, Abell (1958) already divided galaxy clusters in two populations: while some systems display a regular and spheroidal form, others show evidence of dynamical activity, due to the presence of substructures and irregularities in the spatial distribution of galaxies. In the last decades, this dichotomy identifies *cool core*

and *non-cool core* clusters (see e.g., Molendi and Pizzolato 2001; Chen et al. 2007; Sanderson et al. 2009; Hudson et al. 2010; Rossetti et al. 2011; Zhang et al. 2016). At first approximation, while the first category is composed of relaxed clusters, the second one contains systems that display evidences of recent or on-going merging processes. In practice, it is non-trivial to define a one-to-one correspondence between relaxed (unrelaxed) systems and cool core (non cool core) clusters, as we will discuss further in §1.1.2.

In the first subsection, we present the main morphological, thermal, and dynamical properties of the ICM. In the following subsections, given the subject of this Thesis, we restrict our focus to the physics of cool core galaxy clusters. We also note that this Thesis is focused on low-redshift ($z < 1$) galaxy clusters. As such, we do not discuss either high-redshift galaxy clusters, or the over-dense structures at high-redshift (the so-called protoclusters), that are expected to evolve into virialized clusters of galaxies. We refer the reader to the following non-exhaustive list of works on high-redshift galaxy clusters and protoclusters: Steidel et al. (2000), Venemans et al. (2007), Daddi et al. (2009), Capak et al. (2011), Chiang et al. (2013), Overzier (2016), Dannerbauer et al. (2017), Cucciati et al. (2018), Tozzi et al. (2022), and Di Mascolo et al. (2023).

1.1.1 The intracluster medium: thermodynamic properties and metal content

While the total mass of clusters is dominated by dark matter, there is a significant baryonic contribution of $\sim 20\%$; the processes that involve baryons are indeed particularly significant for the dynamical and chemical evolution of galaxy clusters. The ICM comprises the majority of these baryons, and consists in a hot gas (at temperatures of 10^7 - 10^8 K in rich clusters, corresponding to 1 – 10 keV) embedding cluster's galaxies. The high temperature of the ICM is set by the virialization process in the cluster's deep potential well: in the process of cluster formation, a large fraction of the released gravitational energy is transformed into thermal energy that heats the ICM through shocks and adiabatic compression (e.g., for reviews Sarazin 1986; Biviano 2000; Molendi 2004; Donahue and Voit 2022).

The ICM is best visible by observing galaxy clusters in the X-ray band. Three fundamental emission processes contribute to the X-ray radiation: bremsstrahlung (or “free-free”) radiation caused by the deflection of an electron due to the fly-by of an ion, recombination radiation (“bound-free”), and de-excitation radiation (“bound-bound”) of an electron changing the quantum level in an ion. All these radiative processes depend on the collision (i.e. close encounter) of an electron and a ion. Due to the very low density of ICM ($10^{-3} - 10^{-4} \text{ cm}^{-3}$) all the ions excited by collisions have sufficient time for radiative de-excitation before de-exciting collisions occur (e.g., Sarazin 1986).

Since the collision rates of the different ions are function of temperature, the shape of the resulting spectrum is both a function of plasma temperature and of chemical composition (e.g., Böhringer and Werner 2010; Sanders 2023; see Fig. 1.2). For rich clusters with an average ICM temperature higher than 2 keV, the gas emits X-ray photons primarily through thermal bremsstrahlung, for which the specific emissivity per unit frequency ν has the following dependencies:

$$\epsilon_\nu \propto n_e^2 T^{-1/2} e^{-h\nu/kT} \quad (1.1)$$

where n_e is the gas electron density, T is the gas temperature, h is the Planck constant and k is the Boltzmann constant.

Eq. 1.1 shows that the X-ray emission is proportional to the square of the plasma density (e.g., Sarazin 1986; Biviano 2000; Donahue and Voit 2022). Therefore, the density and temperature of the plasma can be derived from X-ray observations of galaxy clusters. In turn, these observed quantities define useful properties of the ICM, such as the gas pressure (p), and the entropy parameter (S , or K , usually simply called “entropy”):

$$p = \frac{\rho k T}{\mu m_p} \quad (1.2)$$

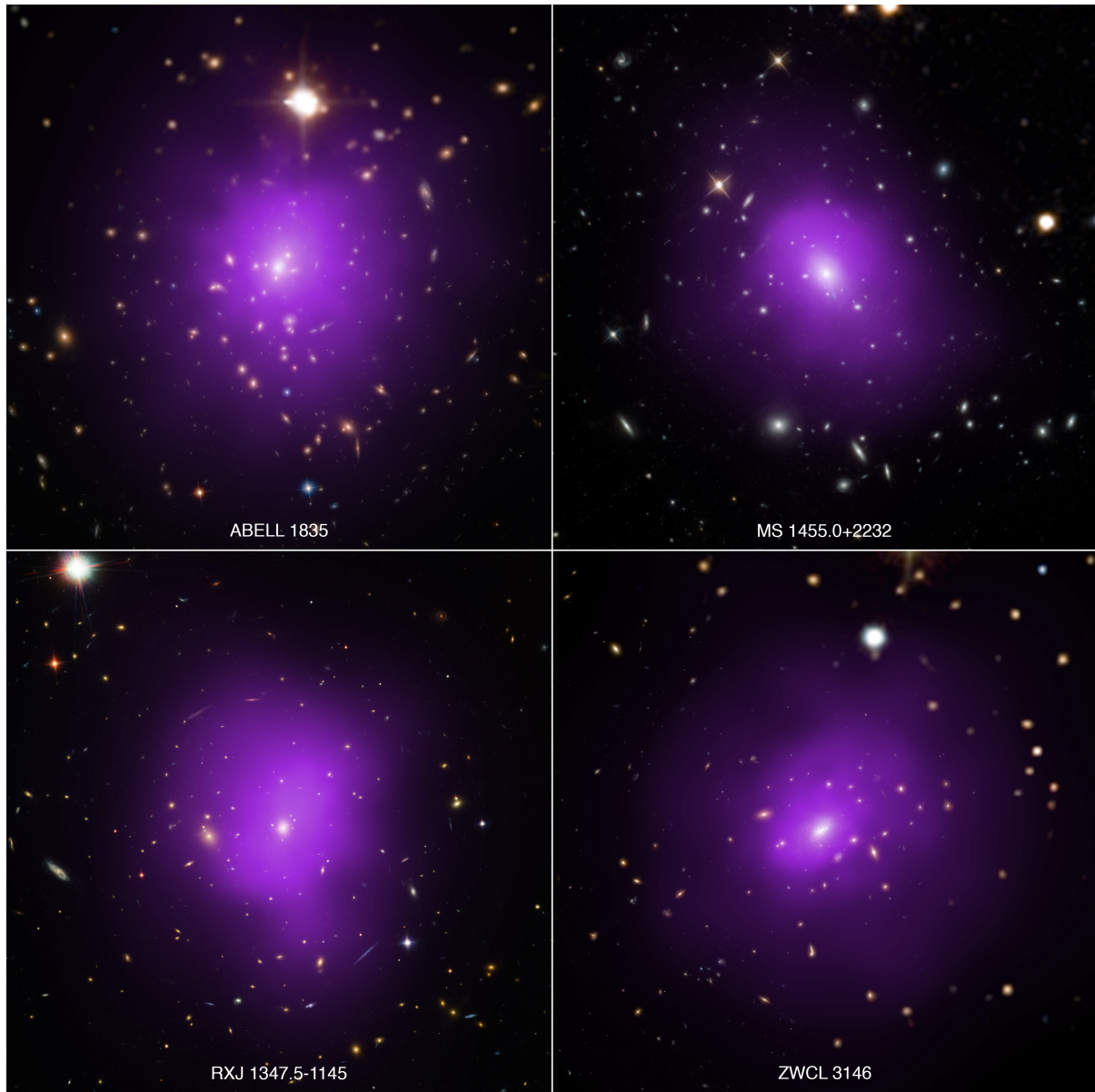


FIGURE 1.1: Composite X-ray (*Chandra*) and optical (Sloan Digital Sky Survey, SDSS) images of four relaxed galaxy clusters. The ICM emission (in purple) is centered on the BCG. Credits: Morandi and Sun (2016).

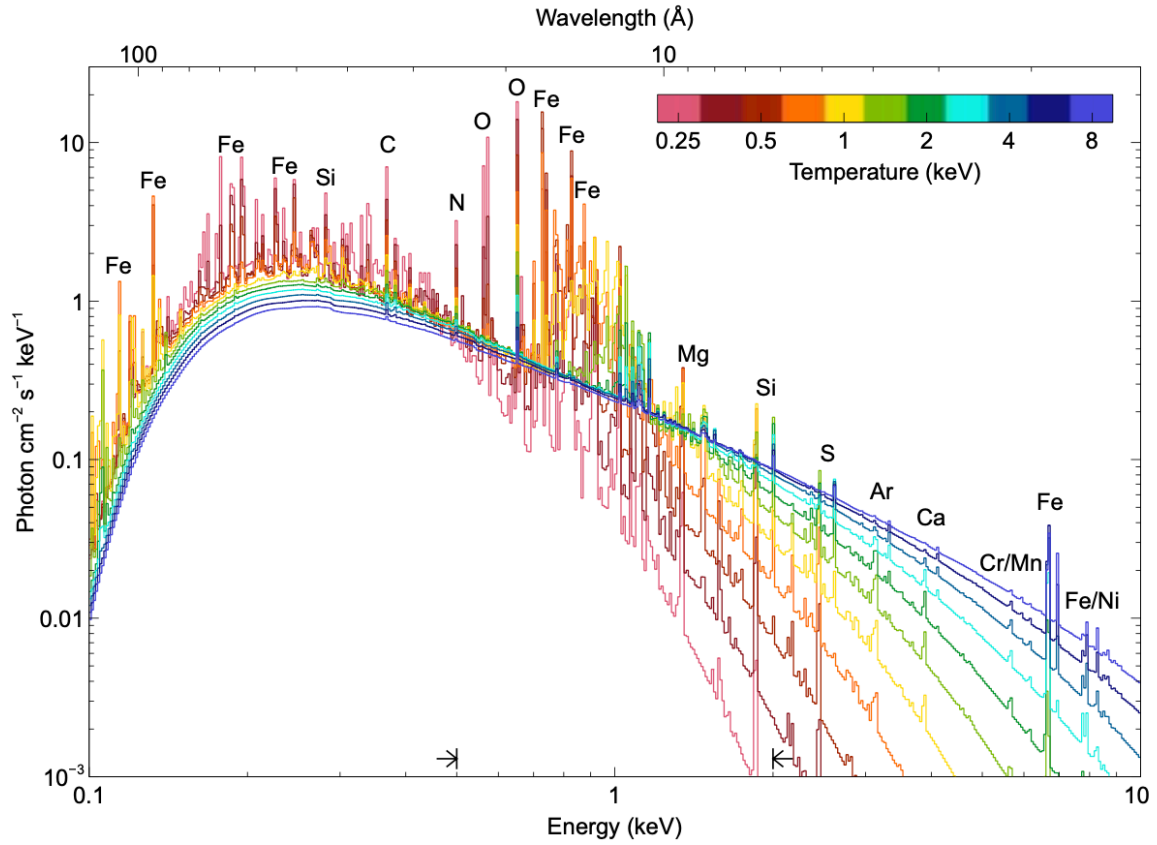


FIGURE 1.2: Spectral models for gas at different temperatures in the typical energy range of X-ray telescopes (0.1 – 10 keV). The spectral line emission is shown on top of the bremsstrahlung continuum. Reproduced from Sanders (2023).

$$S \text{ (or K)} = \frac{kT}{n_e^{2/3}}, \quad (1.3)$$

where $\mu \approx 0.6$ is the molecular weight, and $m_p = 1.67 \times 10^{-24}$ g is the proton mass.

Since the ICM is highly ionized, Coulomb collisions are the dominant forms of interaction in the plasma; neglecting the magnetic field, this yields a mean free path for particles in the ICM of:

$$\lambda_e \sim \lambda_i \sim 23 \text{ kpc} \left(\frac{n_p}{10^{-3} \text{ cm}^{-3}} \right)^{-1} \left(\frac{T}{10^8 \text{ K}} \right)^2 \quad (1.4)$$

where n_p is the particles number density.

For typical values of density and temperature, the mean free path is smaller than the size of the cluster structure (around 1 Mpc). Thus, the ICM can be treated as a fluid.

Furthermore, the sound speed of a wave moving through the ICM is:

$$c_s = \sqrt{\frac{\gamma kT}{\mu m_p}}, \quad (1.5)$$

where $\gamma = 5/3$ is the adiabatic index.

Thus, a sound wave crosses the cluster over a time-scale t_{sc} given by:

$$t_{\text{sc}} \sim 6.6 \times 10^8 \text{ yr} \left(\frac{D}{\text{Mpc}} \right) \left(\frac{T}{10^8 \text{ K}} \right)^2 \quad (1.6)$$

where D is the cluster size.

The sound crossing time-scale is smaller than clusters typical age (a few Gyr), therefore the ICM can be described as in hydrostatic equilibrium (e.g., Molendi 2004). The assumptions above are particularly useful to define relatively simple models for the radial distribution of the ICM. The most common among such models is the ‘‘hot ICM model’’ proposed by Cavaliere and Fusco-Femiano (1976). The main assumption of this model is that gas and galaxies are in hydrostatic equilibrium in the same gravitational potential, with hydrostatic equilibrium defined as:

$$\nabla p(r) = -\rho \nabla \phi(r), \quad (1.7)$$

where $P(r)$ is the pressure, ρ is the density, and $\phi(r)$ is the gravitational potential.

Then, the galaxy and gas distribution (ρ_{gal} and n_{gas} , respectively) can be directly related through:

$$\frac{1}{n_{\text{gas}}} \frac{d}{dr} \left(\frac{n_{\text{gas}} k T}{\mu m_{\text{p}}} \right) = -\frac{d\phi}{dr} = \frac{1}{\rho_{\text{gal}}} \frac{d(\sigma_r^2 \rho_{\text{gal}})}{dr} \quad (1.8)$$

where σ_r is the galaxy velocity dispersion.

Assuming for simplicity that the gas has an isothermal equation of state and that the galaxy velocity dispersion is constant, Eq. 1.8 reduces to:

$$\frac{n_{\text{gas}}(r)}{n_{\text{gas}}(0)} = \left[\frac{\rho_{\text{gal}}(r)}{\rho_{\text{gal}}(0)} \right]^\beta, \quad \text{with} \quad \beta = \frac{\mu m_{\text{p}} \sigma_r^2}{k T} \quad (1.9)$$

By adopting the empirical King model (King, 1966) to describe the distribution of galaxies, the radial model for the gas density is described by:

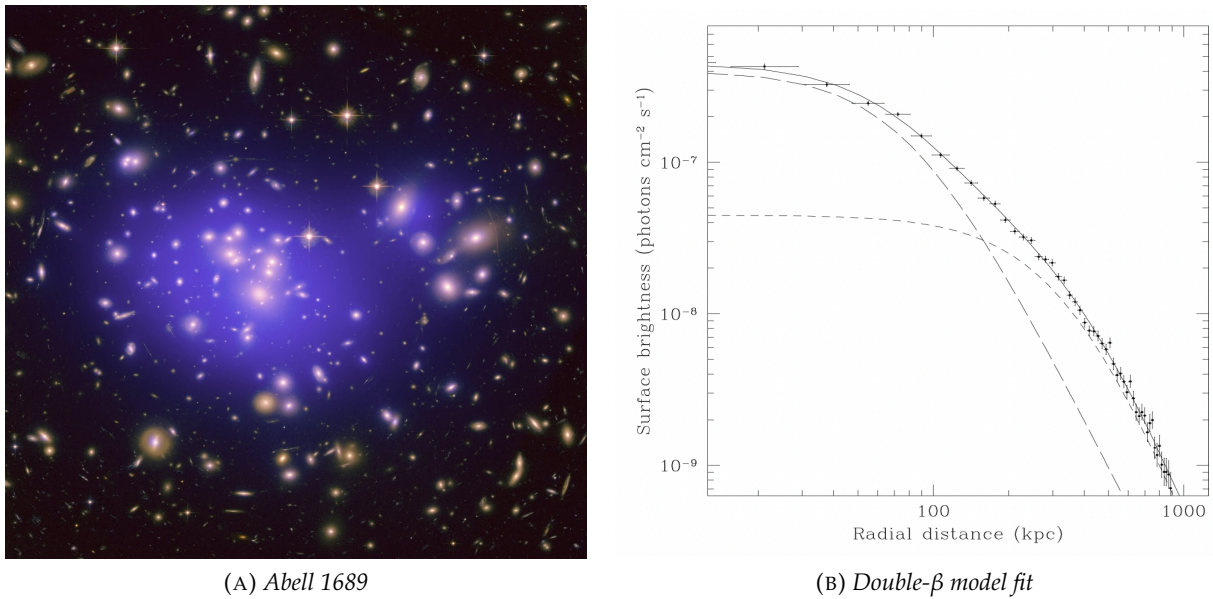
$$n_{\text{gas}}(r) = n_{\text{gas}}(0) \left[1 + \left(\frac{r}{r_c} \right)^2 \right]^{-3\beta/2}, \quad (1.10)$$

where r_c is the core radius of the profile

The solution obtained in Eq. 1.10 is referred to as β -model, and yields the advantage of having a small number of parameters and a simple form. In terms of X-ray surface brightness, which is the direct observable in X-rays, the β -model is a function of r^2 with a slope of $-3\beta + 1/2$ (Bahcall and Lubin, 1994).

With the launch of modern, high resolution X-ray space telescopes, it became clear that clusters do not follow completely the isothermal β -model: typically, the ICM temperature decreases towards the outskirts and, in relaxed systems, towards the cluster center (e.g., Mohr et al. 1993; Xue and Wu 2000; Arnaud 2009). In fact, as anticipated in the first paragraph of this Chapter, clusters are found in two variants (from an X-ray perspective): those with a centrally-symmetric morphology and a cool and dense core (central density of $\sim 10^{-2} \text{ cm}^{-3}$), and those lacking such features. Cool core clusters are actually better described by a double β model, with two different slopes describing the inner and the outer parts (see Fig. 1.3 for an example).

Apart from the continuum emission, the X-ray spectra of galaxy clusters show emission lines from the ionized gas, composed by H, He and heavy elements (or ‘‘metals’’; e.g., for reviews Böhringer and Werner 2010; Sanders 2023). Between 0.1 and 10 keV there are several spectral lines which are suited for abundance measurements (e.g., Bykov et al. 2015; Sanders 2023): below ~ 2 keV the Fe



(A) Abell 1689

(B) Double- β model fit

FIGURE 1.3: Image and surface brightness profile of Abell 1689. *Left panel*: composite X-ray (*Chandra*) and optical (Hubble Space Telescope, HST) image of the cluster Abell 1689 (Credits: Peng et al. 2009). *Right panel*: surface brightness profile of Abell 1689, obtained from *Chandra* observations and fitted with a double β -model; the dashed lines represent the two components. Reproduced from Xue and Wu (2002).

L-shell lines around 1 keV are dominant, while at higher temperatures the Fe K-shell line at 6.7 keV is the clearest spectral feature. Other lines which are important contributors to the X-ray spectrum include those from C, N, O, Ne, Mg, Si, S, Ar, Ca and Ni.

The typical average abundance of iron in the ICM is around $Z \sim 0.3Z_{\odot}$ (e.g., Bahcall 1999; Tozzi et al. 2003, in Anders and Grevesse 1989 solar values), and the abundance ratios between the different elements are nearly solar (e.g., Mernier et al. 2017; Sanders 2023). However, metals are not uniformly distributed in clusters. The abundance radial profiles of galaxy clusters are generally centrally peaked, with the abundance of metals decreasing with radius (see Fig. 1.4). This is because the galaxies that enrich the ICM are concentrated at the center of the cluster (e.g., De Grandi and Molendi 2001; De Grandi et al. 2004; Leccardi and Molendi 2008; Cora et al. 2008; Mernier et al. 2017; Lovisari and Reiprich 2019; Liu et al. 2019a; Liu et al. 2020a). The detection of metals in the ICM is primarily driven by the observation of the iron line at 6.7 keV, as it is the spectral feature with the highest signal to noise ratio, whereas the detection of other elements such as C, N, Si, Mg is limited to deep observations with a high spectral sensitivity in the soft (0.5 - 2 keV) band (e.g., De Grandi and Molendi 2001; Leccardi and Molendi 2008; Mernier et al. 2017).

1.1.2 Cooling of hot atmospheres: from cooling flows to cool cores

A fundamental topic regarding galaxy clusters and the ICM is the *cooling flow problem*, which has arisen since the gas has been observed to be cooling at rates smaller than predicted. In this subsection the standard cooling flow model is presented, and then the main issues of this model are listed. In the next section, we describe the observational evidences *self-regulated feeding and feedback loop*, that has established as the favored scenario to solve the cooling flow problem.

The standard cooling flow model

The bremsstrahlung and line emission of the ICM represent a continuous mechanism through which the gas radiates a fraction of its energy away. The time over which the ICM radiates away a

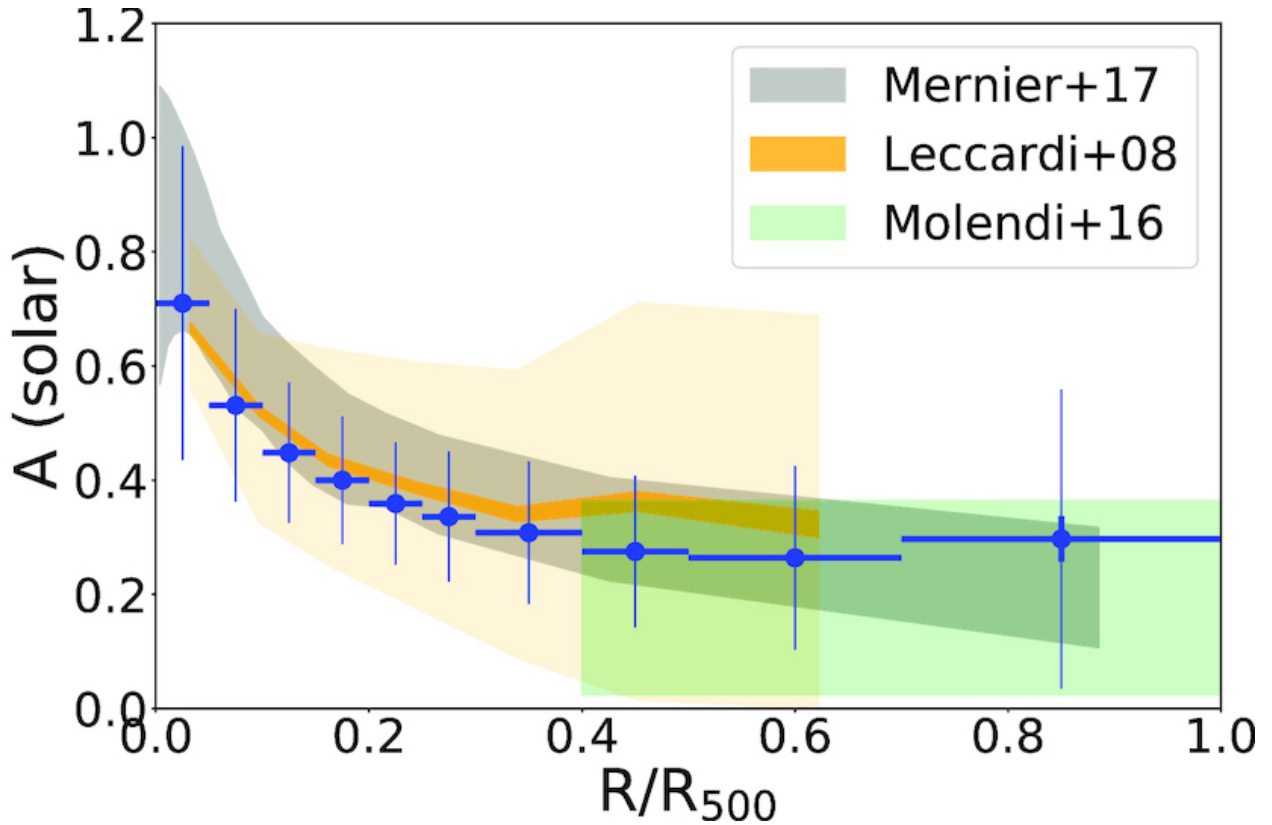


FIGURE 1.4: Median abundance profile from the sample of galaxy clusters presented in Lovisari and Reiprich (2019), in units of R_{500} . The profile shows the increasing abundance trend towards the central regions of galaxy clusters. The colored areas, shown for comparison, represents the average profiles from different literature references.

significant fraction of its energy, defined *cooling time*, can be computed as:

$$t_{\text{cool}} \approx \frac{H_v}{n_e n_H \Lambda(T)} = \frac{\gamma}{\gamma - 1} \frac{kT}{\mu X n_e \Lambda(T)} \quad (1.11)$$

where H_v is the enthalpy per unit volume, n_e is the electron number density, n_H is the hydrogen number density, $\gamma = 5/3$ is the adiabatic index, $\mu \approx 0.6$ is the molecular weight, $X \approx 0.7$ is the hydrogen mass fraction and $\Lambda(T)$ is the cooling function (e.g., Sarazin 1986; Peterson and Fabian 2006; Böhringer and Werner 2010; Fabian 2012; Gitti et al. 2012). This relation can be approximated as $t_{\text{cool}} \propto T^\alpha / n_e$ (where $-1/2 < \alpha < 1/2$ depending on the gas temperature), showing how denser and cooler regions of the ICM are expected to radiate away their energy faster (Fabian, 1994). In this context, the center of relaxed clusters are brighter in X-rays than the outskirts, which means that the gas density increases in the central regions. Specifically, the ICM can reach electron number densities of $n_e \approx 10^{-2} - 10^{-3} \text{ cm}^{-3}$ in the central regions ($\leq 100 \text{ kpc}$), decreasing to 10^{-4} cm^{-3} in the outer parts.

Early works on X-ray observations of clusters showed that, especially in the central regions of relaxed galaxy clusters, the cooling time is close to or shorter than the Hubble time (e.g., Lea et al. 1973; Stewart et al. 1984). This suggested the idea that “cooling flows” could arise within a region where t_{cool} is less than the time for which the system has been relaxed, usually assumed to be the look-back time at $z = 1$ (that is approximately 7.7 Gyr) (Fabian, 1994). Such region is bounded by the so-called *cooling radius*, r_{cool} , at which $t_{\text{cool}} = 7.7 \text{ Gyr}$.

The standard model of cooling flows describes such process as pressure driven. Following Cowie et al. (1983), Mathews and Bregman (1978), and Fabian (1994), the gas pressure at r_{cool} is the result

of the weight of the layers of gas outside this radius (for which cooling is not efficient). Within r_{cool} , the X-ray emitting gas is radiating away its energy and reducing its temperature. To maintain pressure equilibrium at r_{cool} , the gas density must rise, thus establishing an inflow of the gas to the central regions. This description holds, in particular, for an idealized, spherically symmetric, and homogeneous ICM. Although this is not representative of the real cluster atmospheres, this model represents a good description of the *mean* flow. The gas can be assumed to remain in hydrostatic equilibrium while it cools, as the observed cooling times (between a few 10^8 and a few 10^9 yr) are significantly longer than free-fall times (around $10^6 - 10^7$ yr). According to the original cooling flow model, only in the very central regions of the cluster (around kpc scales) cooling is so fast that gas becomes thermally unstable and cools rapidly to lower temperatures (below $10^6 - 10^7$ K).

In the standard model, it is possible to quantify how strongly cooling is occurring by determining the amount of matter which crosses r_{cool} and flows towards the center, that is the mass inflow rate \dot{M} (Fabian 1994 and references therein). This quantity can be inferred through the measurement of the X-ray luminosity associated with the cooling region L_{cool} , by assuming that this represents the sum of the total thermal energy of the gas plus the work pdV done on the gas as it crosses r_{cool} , radiated in dt (e.g., Gitti et al. 2012):

$$L_{\text{cool}} = \frac{dE}{dt} = \frac{(dE_{\text{th}} + pdV)}{dt} \quad (1.12)$$

With the assumption of constant pressure, and considering that $pdV = (\rho kT / \mu m_p) dV = (dMkT) / (\mu m_p)$, the final definition of L_{cool} is:

$$L_{\text{cool}} = \frac{5}{2} \frac{kT}{\mu m_p} \dot{M} \quad (1.13)$$

where T is the gas temperature at r_{cool} (Fabian, 1994).

Usually, L_{cool} ranges between $10^{42} - 10^{45}$ erg s $^{-1}$, accounting for the 10% of the total cluster luminosity. Values of $\dot{M} = 50 - 100 M_{\odot} \text{yr}^{-1}$ deduced from Eq. 1.13 are typical for relaxed galaxy clusters, with some systems showing $\dot{M} > 500 M_{\odot} \text{yr}^{-1}$ (such as A478, A2029 and Hydra A).

Another prediction of the cooling flow model was the presence of low temperature components and strong emission lines (e.g. FeXVII) in the X-ray spectrum (e.g., Peterson and Fabian 2006). The emission from a cooling flow at a frequency ν is obtained by integrating the plasma emissivity at that frequency, inversely weighted by the cooling function:

$$L_{\text{cool}}(\nu) = \frac{5}{2} \frac{\dot{M}}{\mu m_p} \int_0^{T_{\text{max}}} \frac{\epsilon_{\nu}(T) dT}{\Lambda(T)} \quad (1.14)$$

where $\epsilon_{\nu}(T)$ is the spectral emissivity of the gas (Fabian, 1994; Peterson and Fabian, 2006; Sanders, 2023).

Emergence of the cooling flow problem

The properties of relaxed clusters derived from early X-ray observations were fairly consistent with the cooling flow model. In several systems, the ICM in the cluster core was found to have short cooling times, central X-ray surface brightness peaks, high central density, and low central temperature, suggesting that the gas was indeed cooling (e.g., Mushotzky and Szymkowiak 1988; Edge et al. 1992). As reported by Fabian (1994), observations performed with the Solid State Spectrometer (SSS) on the Einstein Observatory revealed low temperature components in the Perseus and Virgo clusters, with the gas in the Perseus cluster losing at least 90% of its thermal energy due to radiative losses. Furthermore, signatures of cooling had been found at other wavelength: filaments of $H\alpha$ emission from ionized gas (Heckman, 1981), and clumps of cold atomic and molecular gas (Edge, 2001).

Nevertheless, several issues remained unresolved: the X-ray surface brightness profiles were not

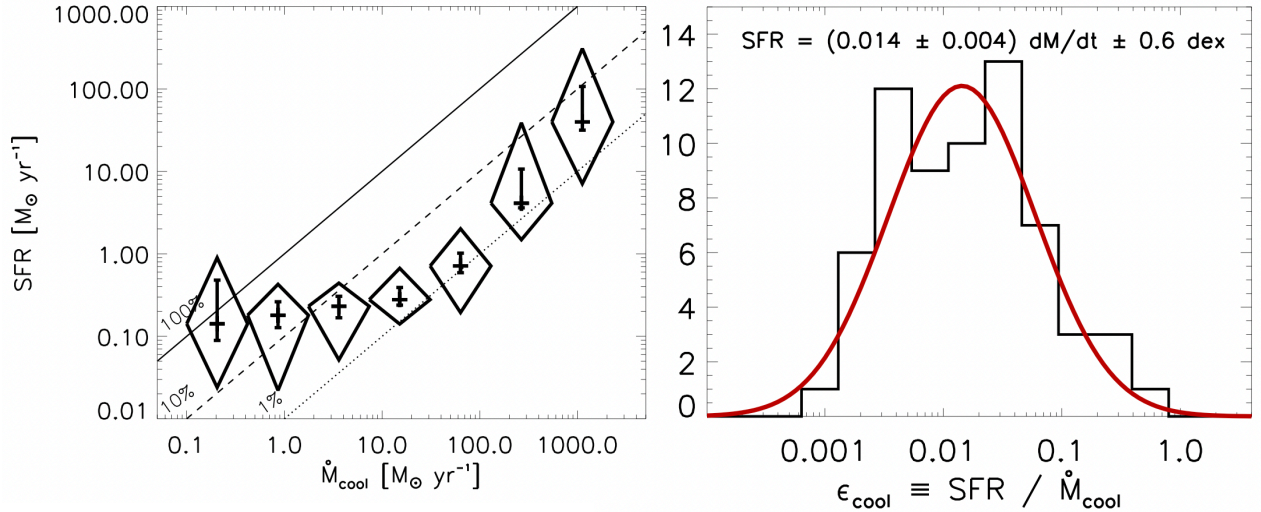


FIGURE 1.5: Efficiency of star formation versus cooling rate, from McDonald et al. (2018). *Left panel*: log-binned star formation rate of the central galaxy as a function of the predicted ICM cooling rate for 107 systems. Diagonal lines show the 1%, 10%, and 100% lines. These data support a picture in which cooling is suppressed by, on average, a factor of ~ 50 in massive systems. *Right panel*: Ratio of the star formation rate in the central BCG to the predicted ICM cooling rate for systems with $\dot{M} > 30 M_{\odot}/\text{yr}$. The distribution of measured cooling efficiencies peaks at $1.4 \pm 0.4\%$. Reproduced from McDonald et al. (2018).

as peaked as expected from a homogeneous flow (Fabian, 1994; Peterson and Fabian, 2006), and the shape of soft X-ray spectra were inconsistent with a simple cooling flow. Moreover, there were some inconsistencies regarding the fate of the cooled gas: at the rate of 100s M_{\odot}/yr^{-1} , the central galaxy should be very bright and blue if all the cooled gas formed stars. In many cases BCGs do have excess blue light indicative of an on-going star formation, but at rates which are a factor of 10 to 100 times lower than the X-ray deduced mass cooling rate (Fabian, 2002). If only ~ 1 –10% of the cooling ICM eventually forms stars, then the efficiency of gas cooling is highly suppressed. Recently, McDonald et al. (2018) used a sample of 107 systems to constrain the star formation efficiency of hot gas cooling, measuring an average ratio of star formation rate (SFR) to cooling rate of $\text{SFR}/\dot{M}_{\text{cool}} = 1.4\% \pm 0.4\%$ for systems with $\dot{M} > 30 M_{\odot}/\text{yr}$ (see Fig. 1.5).

The early inconsistencies were later supported by observations performed with new X-ray space telescopes, and as a consequence this subject has begun to be referred to as *cooling flow problem*. In this respect, the high spatial resolution imaging of *Chandra* and the high spectral resolution of the *XMM-Newton* Reflection Grating Spectrometer (RGS) proved particularly challenging for the cooling flow model (e.g., Peterson et al. 2003; Peterson and Fabian 2006). Spectral data revealed the absence or weakness of the soft X-ray line of Fe XVII and a lack of gas cooling below 1-2 keV, indicating that the amount of ICM radiatively cooling below about one-third of its original temperature is about ten times less than expected. For example, in Peterson et al. (2001), the spectrum of the cluster Abell 1835 (obtained with RGS on *XMM-Newton*) is first fit with a model as the one described in equation 1.14: the data and the model are inconsistent, notably in the prediction of Fe XVII emission line blends at 15 and 17 Å (see Fig. 1.6). A good agreement with data has been found by implementing the same cooling flow model with the subtraction of all the emission coming from temperatures below 2.7 keV.

From cooling flows to cool cores

The discovery that ICM cooling is a mechanism of smaller entity and impact than previously believed led to abandon the terminology “cooling-flow cluster” in favor of “cool core cluster” (first proposed by Molendi and Pizzolato 2001). The latter expression is more representative of the ICM

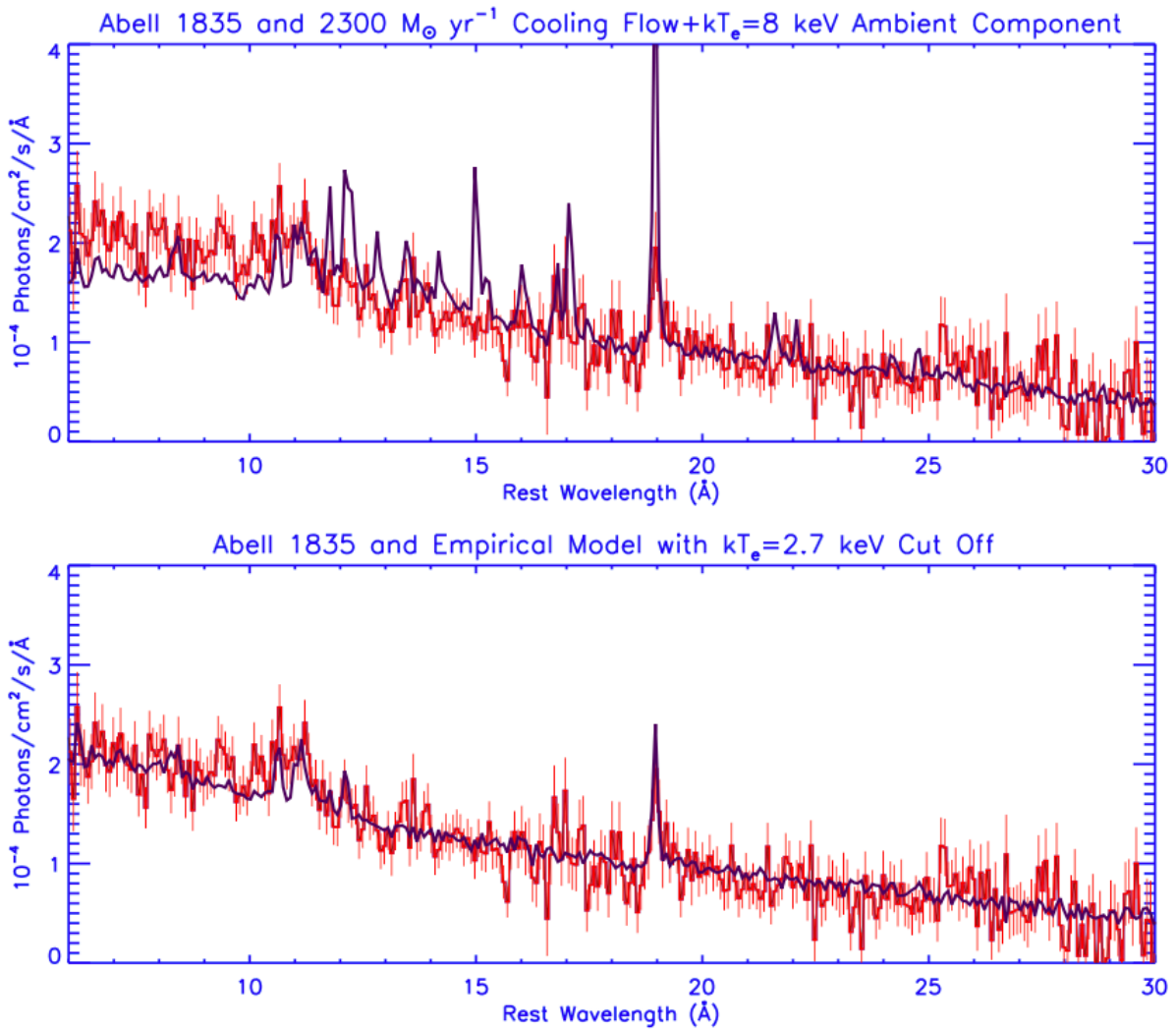


FIGURE 1.6: *Upper panel*: standard cooling flow model (blue) and data obtained from *XMM-Newton*/RGS observations of Abell 1835 (red). *Lower panel*: cooling flow model without emission from $T < 2.7\text{keV}$ (blue) and data (red). Reproduced from Peterson et al. (2001).

temperature drop at the center of relaxed clusters, and does not necessarily imply a copious inflow of cooling gas. Initial estimates of the fraction of clusters presenting a cool core indicated that about 90% of clusters with total mass $M_{\text{tot}} \geq 10^{14} M_{\odot}$, and about 50% of clusters with total mass $M_{\text{tot}} \leq 10^{14} M_{\odot}$ were cool cores (Chen et al., 2007). Those fractions, however, were measured from X-ray selected samples, introducing a bias: cool cores are more easily detected in X-rays due to their prominent surface brightness peak (Eckert et al., 2011) and their higher X-ray luminosity at a fixed mass (Hudson et al., 2010). Instead, by selecting systems from e.g., the Planck Sunyaev–Zeldovich catalogue of clusters, the fraction of cool core clusters is $\sim 29\%$ (Rossetti et al., 2017).

It is important to note that the division between cool core and non-cool core clusters is not sharp. While violent post-merger clusters are easily distinguishable from centrally symmetric clusters with a dense and cool core, some mixed categories exist, such as weak cool cores (with cooling times longer than 1 Gyr and evidence for relatively recent minor mergers, e.g., Hudson et al. 2010), “mini-cool cores” or “coronae” (low temperature, kpc-scale halos associated with the BCG and surrounded by a non-cool core cluster, e.g., Sun 2009), or rapidly cooling merging clusters (e.g., Somboonpanyakul et al. 2021). It is also important to note that recent evidence suggests that cool core and non-cool core clusters do not evolve independently, but rather represent different stages

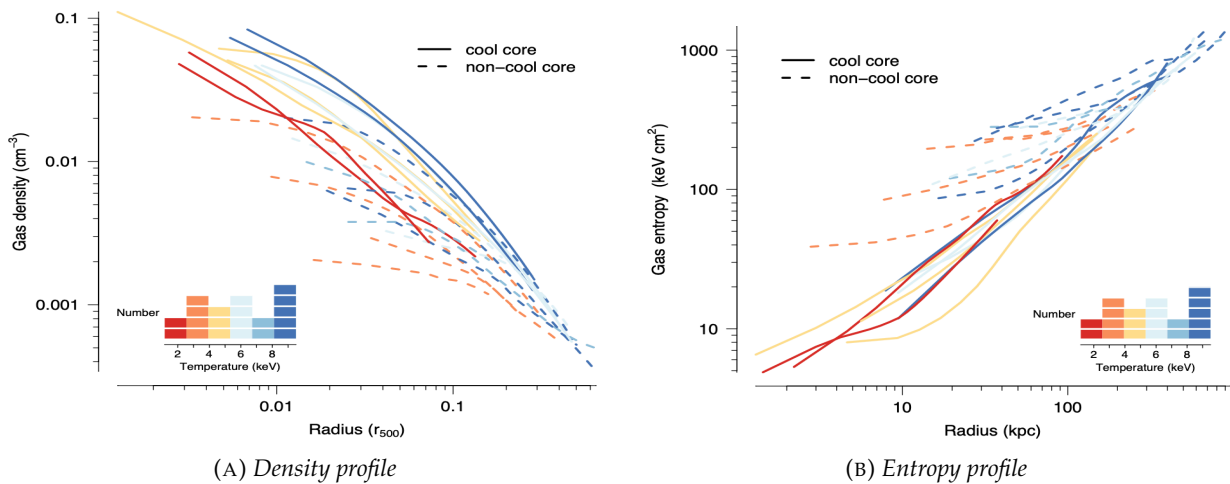


FIGURE 1.7: Density and entropy profiles of the clusters in the sample of Sanderson et al. (2009). *Left panel:* Gas density profile for each cluster, colored according to the mean gas temperature. *Right:* gas entropy profiles as a function of radius.

in the evolution of comparable structures (Molendi et al., 2023).

Nevertheless, there are a few physical properties which allow for a relatively simple (yet not precisely sharp, as reminded above) classification of clusters in the cool core or non-cool core categories. Regarding average cluster properties, Hudson et al. (2010) showed how a central cooling time lower than 1 Gyr easily identifies cool core systems in low redshift cluster samples, while cuspliness (the slope of the density profile at $0.04r_{500}$) is the best parameter for high redshift clusters. Regarding resolved cluster properties, e.g., Sanderson et al. (2009) investigated the thermodynamic radial profiles of the ICM across a sample of 20 galaxy clusters observed with *Chandra* (see Fig. 1.7). These confirmed that denser and more cuspy cores are typical of cool core clusters. A similar dichotomy emerges from the radial entropy profiles: non-cool core clusters have significantly higher entropy in the core and the divergence between the two types occurs within ~ 40 kpc (see also Cavagnolo et al. 2008; Cavagnolo et al. 2009; Hudson et al. 2010). Subsequent works using morphological and spectral parameters found consistent results (e.g., Zhang et al. 2016; Campitiello et al. 2022).

Dynamical perturbations of cool core clusters: sloshing of the ICM

As noted above, the distinction between non-cool core and cool core clusters can be subtle. Although cool core clusters are generally considered to be “relaxed” systems, X-ray observations of several clusters revealed azimuthal asymmetries in the ICM distribution, which are evidence for minor gravitational perturbations of the potential well. Specifically, the high angular resolution of the current generation of X-ray telescopes ($0.5''$ for *Chandra* and $5''$ for *XMM – Newton*) enabled the discovery of sharp contact discontinuities between regions of gas with different temperature and density, which appear as edges in surface brightness in the ICM. These structures, which were discovered around the central density peaks in cool core clusters, were named “cold fronts” (e.g., for reviews Markevitch and Vikhlinin 2007; Zuhone and Roediger 2016).

First examples of cold fronts were found in A2142 (Markevitch et al., 2000) and A3667 (Vikhlinin et al., 2001), and since then in several systems (e.g., Owers et al. 2009; Laganá et al. 2010; Ghizzardi et al. 2010). In X-ray maps, these edges appear as sharp discontinuities in surface brightness. In terms of thermodynamic properties, the gradient in surface brightness corresponds to a jump in the ICM temperature, with the denser, downstream region being cooler than the upstream, rarefied region (see the example of Abell 3526 in Fig. 1.8). Gas pressure profiles revealed approximate pressure

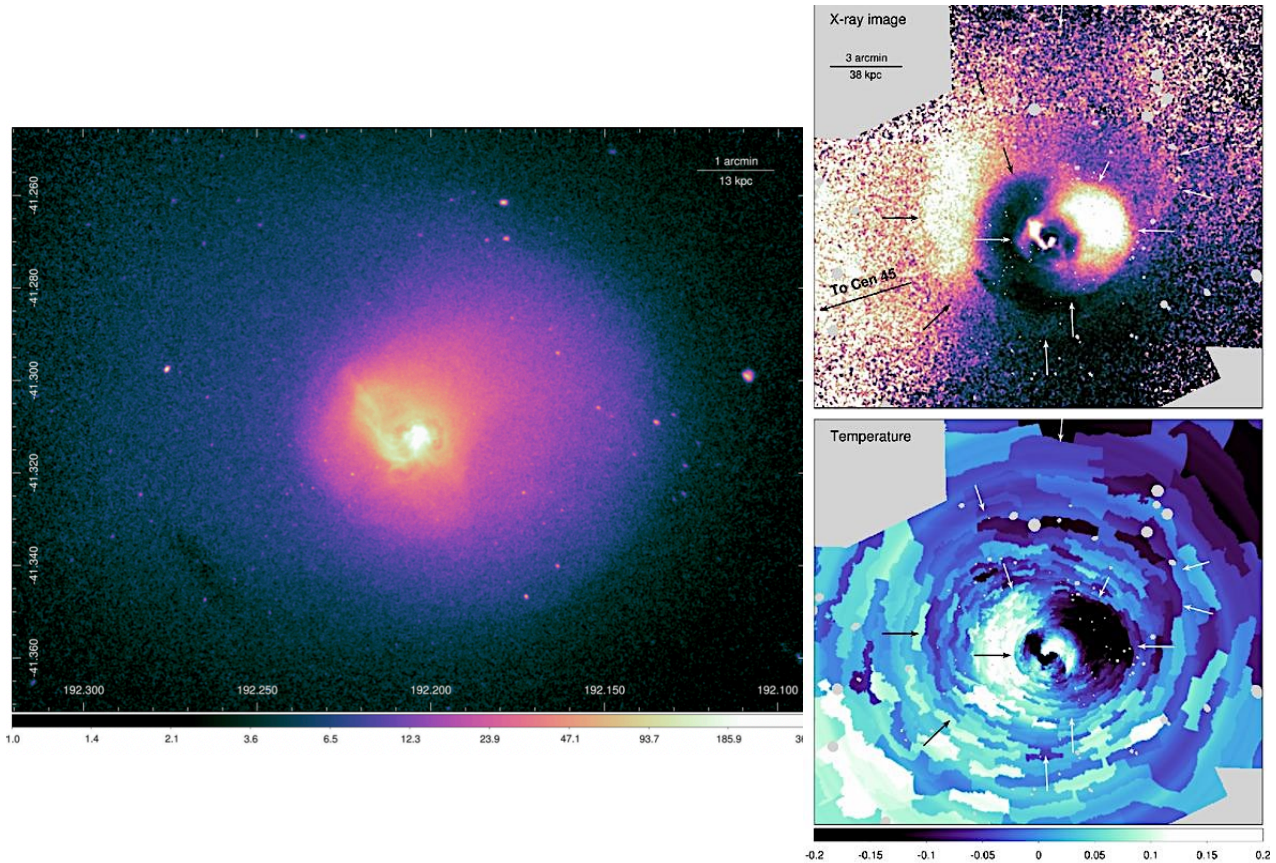


FIGURE 1.8: Sloshing in the Centaurus galaxy cluster. *Left panel:* X-ray (*Chandra*) image of the central 130×100 kpc of the cluster. *Top right panel:* Fractional difference from the average at each radius of the X-ray surface brightness. *Bottom right panel:* Fractional difference from the average at each radius of the X-ray temperature. Note that bright areas in the top right panel correspond to cool (dark blue) areas (relative to the average at that radius) in the bottom right panel. Adapted from Sanders et al. (2016a).

equilibrium between the two sides of the discontinuity. Thus, these edges are contact discontinuities generated at the boundaries of gas clouds moving subsonically through a hotter and less dense surrounding gas (Ascasibar and Markevitch, 2006; Markevitch and Vikhlinin, 2007; Zuhone and Roediger, 2016).

Numerical simulations tailored to reproduce cold fronts were essential in understanding the process that leads to the formation of these fronts in relaxed systems (Zuhone and Roediger 2016 and references therein). Specifically, while relaxed clusters typically show little or no signs of recent merging activity, minor merger or off-center passages of small sub-structures (galaxy groups or massive galaxies) could still offset the bulk of the gas from the center of the potential well while leaving the cool core intact. Such perturbations would set in a “sloshing” motion of the gas in the potential well, that over a few Gyrs creates multiple cold fronts wrapped around the cluster core in a one-armed spiral-like pattern. The idea that sloshing is a long-lasting process is consistent with the observations of numerous clusters showing cold fronts around the core: sloshing may exist in the cores of $\geq 2/3$ of relaxed galaxy clusters (Ghizzardi et al., 2010).

The arrangement of sloshing cold fronts in clear spiral or opposed arcs (with respect to the cluster core) is determined by the composite action of angular momentum injection and viewing angle (with opposed arcs more likely associated to sloshing occurring close to the line of sight; e.g., Zuhone and Roediger 2016). When the sloshing plane is close to the plane of the sky, the movement produces a characteristic spiral pattern of low temperature and high density gas that is relatively

easier to identify (e.g., Kolokythas et al. 2020). On the contrary, the alternating bright arc-like structures caused by sloshing along the line of sight may be more difficult to identify, and thus only a few examples of sloshing along the line of sight are known (e.g. Abell 907, Ueda et al. 2020, and NGC 1550, Kolokythas et al. 2020).

1.2 AGN feeding & feedback in galaxy clusters

So far, the idea that cluster-central active galaxies can inject energy into the gas and reduce cooling to match observed rates has emerged as the most promising candidate to solve the cooling flow problem. At the beginning of the 90s, it was known that BCGs in cool core clusters typically show signs of strong radio activity, but the importance of the active galactic nuclei responsible for the radio emission was underestimated due to their poor optical luminosity (Tabor and Binney, 1993). The understanding changed since X-ray images of the Perseus and Cygnus A clusters taken with the *ROSAT* observatory showed signs of interaction between the radio AGN and the hot atmosphere surrounding them (Boehringer et al., 1993; Carilli et al., 1994). These data revealed deficits in the X-ray emission, spatially coincident with regions of enhanced synchrotron emission.

With the improvement in angular resolution ($\sim 0.5''$) provided by the *Chandra* X-ray observatory, it became clear that the cases of Perseus and Cygnus A are not isolated: in fact, the central regions of many cool core clusters are not relaxed, and their ICM is highly dynamic and not uniformly distributed, as there are signs of bubbles (or “cavities”) on scales often approximately coincident with lobes of extended radio emission; in addition to that, new observations reveal highly disturbed structures in the cores of many clusters, such as shocks, ripples and sharp discontinuities (e.g., for reviews McNamara and Nulsen 2007; McNamara and Nulsen 2012; Fabian 2012; Gitti et al. 2012; Gaspari et al. 2020; Eckert et al. 2021; Donahue and Voit 2022).

These perturbations appeared to be caused by the effect of powerful radio jets from the central AGN, which inflate bubbles of radio emitting plasma and create depressions in the hot, thermal gas surrounding them. Measurements of these cavities’ properties, along with studies of the energetic of the radio jets have led to the understanding that cooling of gas in clusters is probably counteracted by the activity of the AGN (see §1.2.1).

A large number of numerical and observational works has so far shown in great details how bipolar, relativistic outflows emanating from the BCG can inflate large bubbles while driving weak shocks, inducing a circulation of gas and a deposition of energy on scales of several 100s kpc (e.g., for reviews McNamara and Nulsen 2007; McNamara and Nulsen 2012; Fabian 2012; Gitti et al. 2012; Eckert et al. 2021; Hlavacek-Larrondo et al. 2022; Donahue and Voit 2022). At the same time, there has been growing evidence of filamentary warm and cold gas surrounding the BCG, potentially reaching the innermost parsecs and fuelling the central galactic engine (e.g., Edge 2001; McDonald et al. 2010; Olivares et al. 2019; Rose et al. 2019a).

Piecing together the various clues (see Fig. 1.9 for an example), it is nowadays widely accepted that cluster-central AGN can prompt a deposition of energy in the ICM, preventing an over-cooling of the same gas that fuels their SMBHs. This finely tuned balance is usually referred to as the “AGN feeding and feedback cycle”.

Independent evidence for the AGN/ICM coupling

Besides the cooling flow problem, independent evidence for the AGN/ICM coupling emerged from the study of (a) entropy profiles, and (b) metallicity profiles of the hot gas.

First, the observations of the radial entropy profiles of several systems showed that energy is being injected in cluster cores by some heating process. Specifically, at large distances from the center (beyond $0.1r_{200}$), the entropy profiles of galaxy clusters follow the cosmological predictions the virialization process ($K(r) \propto r^{1.1}$) (see e.g., Kaiser 1986; Kaiser 1991; Tozzi and Norman 2001; Voit et al.

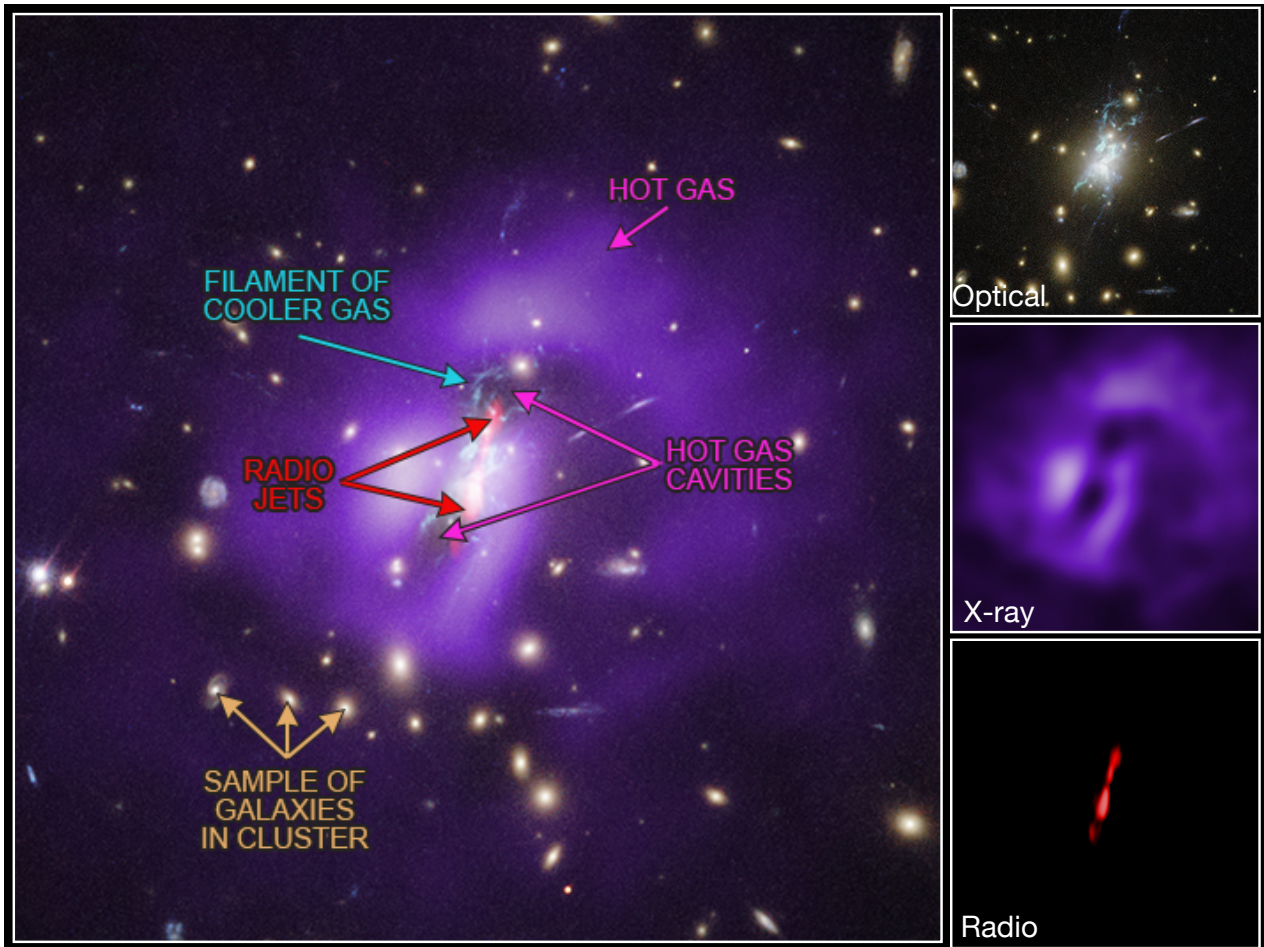


FIGURE 1.9: Composite X-ray, optical, and radio image of the Phoenix cluster, from McDonald et al. (2019). The *left panel* shows the composite X-ray (*Chandra*), radio (JVLA) and optical (HST) image. Highlighted are the radio jets (red) that inflated the X-ray cavities in the hot gas (purple), the galaxies in the cluster, and the central nebular emission of warm gas. The *right panels* show the single images. Credits: X-ray: McDonald et al. (2019); Radio: NRAO/VLA; Optical: NASA/STScI.

2002; Voit and Ponman 2003; Voit 2005; Reiss and Keshet 2015; Babyk 2016; Babyk et al. 2018). Instead, numerous works have shown that in the core of cool core galaxy clusters there is an excess of entropy with respect to the cosmological prediction (see Fig. 1.10). The exact shape of the entropy profile at radii of up to a few tens of kpc has been a matter of debate: early works favored a flat profile with an entropy floor (Donahue et al., 2005; Donahue et al., 2006; Cavagnolo et al., 2009), while subsequent studies found that the entropy profiles in the inner regions of relaxed clusters follow $K(r) \propto r^{2/3}$ (e.g., Panagoulia et al. 2014).

In any case, the excess entropy with respect to the gravitational baseline requires a mechanism that can inject energy in the gas. In this context, the radial range where $K(r)$ is flatter than 1.1 is co-spatial with the region where relativistic jets from cluster-central AGN are observed. This strongly suggests that the excess entropy can be explained as a consequence of the energy injected by AGN feedback (e.g., Donahue and Voit 2022).

Second, metallicity profiles were known to be less centrally peaked than expected from a simple model of enrichment from the clusters' central galaxies. De Grandi et al. (2004) observed that the metal mass profiles are less peaked than the optical light profiles, which implies that the metals get mixed and transported out. The most likely cause is the interaction of the central AGN with the surrounding ICM: bubbles of radio emitting relativistic plasma uplift the metal rich gas from the central parts of the galaxy cluster (e.g., Rebusco et al. 2005; Kirkpatrick and McNamara 2015). This

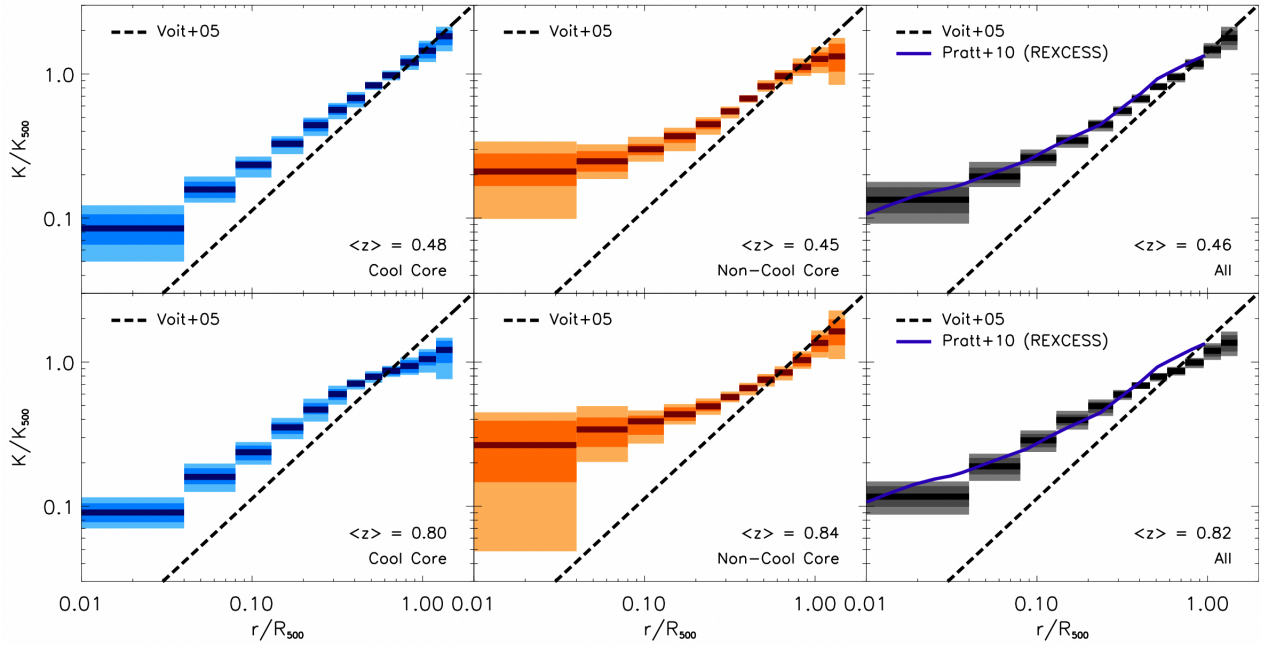


FIGURE 1.10: Deviation of the entropy profiles from the cosmological prediction, from McDonald et al. (2014). The panels show the average entropy profiles of cool core clusters (left), non-cool core clusters (center) and the whole sample (right), divided in two redshift bins (top and bottom rows). The black dashed line shows the baseline gravity-only entropy profile from Voigt (2005), from which the entropy profiles deviate in the central regions of clusters. Reproduced from McDonald et al. (2014).

has also been later observed by Lovisari and Reiprich (2019): using a sample of 207 galaxy groups and clusters, they found that systems with a central active SMBH have a flatter radial profile, indicating that central AGN are efficient at redistributing metals in the ICM.

In the following subsection, we will first summarize the current understanding of how X-ray cavities and weak shock can balance the radiative losses of the hot atmosphere in which they expand, raising its entropy and offsetting precipitous cooling. Then, we will turn to the evidence for the presence of multiphase gas in cluster’s cores, from warm ionized gas to cold molecular gas, and how these phases are linked to both star formation and AGN activity in the BCG.

1.2.1 Evidence of AGN feedback: X-ray cavities and shock fronts

Properties and formation of X-ray cavities

Several models and numerical simulations describe how a relativistic jet piercing the surrounding ambient medium can push the hot gas aside and create depressions in the X-ray images of clusters (see Hardcastle and Croston 2020; Bourne and Yang 2023; Turner and Shabala 2023 for recent reviews). Following Bourne and Yang (2023), a general description of jet propagation in cluster atmospheres can be seen in Fig. 1.11: initially, the relativistic radio jet advances supersonically into the ambient medium, forming a bow shock and inflating a hot lobe that expands into the ICM. The expanding shock wave creates a cocoon of shocked ICM surrounding the jet lobe. Over time the lobe expansion slows, the shock driven into the ICM broadens into a sound wave and the mechanism powering the jet progressively switches off (or reduces its efficiency in driving a relativistic outflow). Once the jet has ceased, the radio lobe/X-ray cavity buoyantly rises through the ICM, potentially entraining dense material in its wake. The evolution at later times is more uncertain, but several numerical simulations predict that mixing will dilute the lobe material into the hot gas until the lobe/cavity becomes undetectable (e.g., Martizzi et al. 2019).

Several observations of cavities in X-ray images of clusters are in good agreement with the first

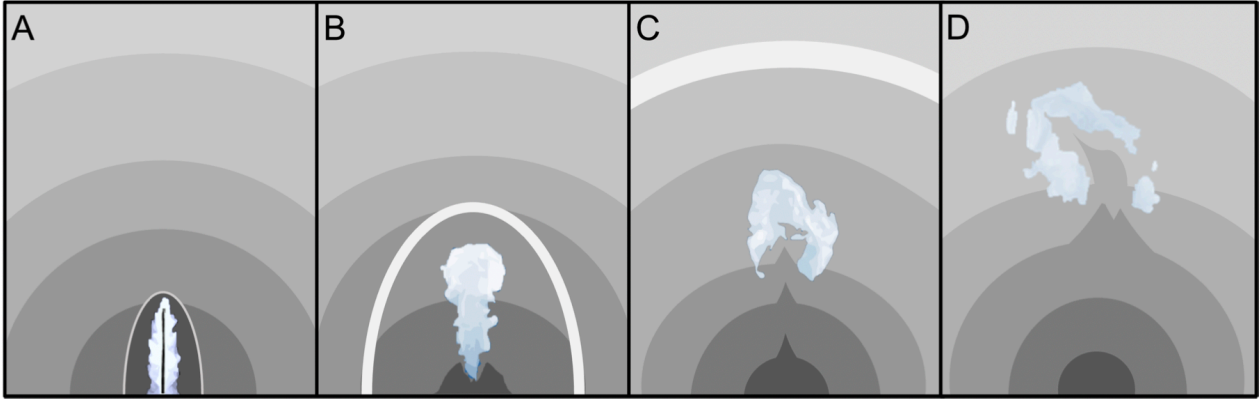


FIGURE 1.11: Schematic representation of a jet inflating an X-ray cavity, from Bourne and Yang (2023). The gray-scale background represents the gas temperature, while the white arc shows the location of the shock front. *Panel A*: the jet drives a bow shock and inflates a lobe/cavity in the ICM. The shock wave results in a layer of shocked ICM surrounding the radio lobe. *Panel B*: The lobe expansion slows, the shock driven into the ICM broadens into a sound wave. *Panel C*: The jet has ceased pushing the cavity, which starts its buoyant rise in the ICM. Instabilities can mix of the cavity and ICM material. *Panel D*: At late times, the cavity is more and more diluted into the ambient medium. Reproduced from Bourne and Yang (2023).

phases of jet evolution of the above description. Systems of cavities in the X-ray images of clusters are usually found in opposite pairs, and they consist in approximately elliptical X-ray surface brightness depressions, 20% to 40% below the brightness level of the surrounding gas. Cavity diameters range from less than 1 kpc to approximately 200 kpc, with typical values around 20-30 kpc. Rims or shells surrounding cavities are observed in several cases. Such rims are typically cooler and denser than the ambient gas, which suggests that they are composed of displaced gas dragged outward from the center by the rising cavities, or gas that has been compressed by the expanding bubble (e.g., Blanton et al. 2010 and references therein).

Radio lobes are also typically spatially coincident with X-ray cavities (e.g., for reviews McNamara and Nulsen 2007; McNamara and Nulsen 2012; Fabian 2012; Gitti et al. 2012; Gaspari et al. 2020; Eckert et al. 2021; Donahue and Voit 2022). However, an exact spatial match between a cavity and the corresponding lobe is not always clear, due to the limits imposed by the sensitivity and resolution of both X-ray and radio observations (e.g., Bîrzan et al. 2020; Timmerman et al. 2022).

From the analysis of X-ray cavities it is possible to infer the time that has passed since the start of the jet activity, assumed to be equal to the age of the cavity (e.g., Bîrzan et al. 2004). This assumption can be justified by considering that the initial phase of relativistic jet propagation (before the cavity is excavated) is relatively short compared to the time taken by the bubble to form, expand, and rise (e.g., Heinz and Enßlin 2004). Traditionally, three methods have been proposed to infer the age of an X-ray cavity from X-ray observations (Bîrzan et al., 2004):

- Assuming that a cavity at distance r from the cluster center rises through the ICM (from $r = 0$) with a speed equal to the local sound speed c_s (Eq. 1.5), then the age of the cavity is the sound crossing time:

$$t_{cs} = r/c_s \quad (1.15)$$

- The buoyant rise of a cavity is governed by the buoyant force $F_g = Vg(\rho_a - \rho_b)$, where V is its volume, g is the local gravitational acceleration, ρ_a and ρ_b are, respectively, the ambient gas and the cavity densities. Its terminal speed, determined by balancing the buoyant force against the drag force, is then $v_t \approx (4v_k/3)\sqrt{2R/r}$, where $v_k = \sqrt{g\bar{r}}$ is the Kepler speed, for a spherical cavity of radius R at a distance r from the cluster center. In this case, the cavity age is the buoyancy-time:

$$t_{buo} = 3r/(4v_k\sqrt{2R/r}) \quad (1.16)$$

- If the time required for the gas to refill the displaced volume of the cavity is considered as representative of the timescale of cavity formation and expansion, then the cavity age can be computed as:

$$t_{\text{ref}} = 2\sqrt{R/g} \quad (1.17)$$

Typically, the age estimates agree to within a factor of 2–3, and values for the cavity age are usually of a few 10^7 yr (e.g., McNamara and Nulsen 2007; McNamara and Nulsen 2012). Different works have adopted different methods to measure cavity ages. The sound speed method may be more suited for small X-ray cavities close to the cluster core and attached to a straight jet. Since such cavities would be in an early stage of evolution, the corresponding radio jet would likely be still mildly relativistic (e.g., Dunn and Fabian 2006; Shurkin et al. 2008). On the contrary, large cavities filled by radio plasma no longer replenished by active jets may be assumed to be in the buoyant rise stage of evolution (e.g., Hlavacek-Larrondo et al. 2012).

Radio observations of lobes can also be used to constrain the age of the outburst. Since the radio lobes are thought to have excavated the cavities, a comparison between the dynamical ages derived from the X-ray analysis and the radiative age of the synchrotron-emitting plasma should return consistent results (e.g., Bîrzan et al. 2007). By considering synchrotron and inverse Compton losses of relativistic electrons, the shape of the radio spectrum can be analyzed to derive radiative ages of the radio emitting plasma (e.g., Harwood et al. 2013). In the few cases in which this method was compared with X-ray estimates (Kolokythas et al., 2020; Biava et al., 2021), an overall agreement was found, especially with sound speed and buoyancy estimates (while refill timescales appear to overestimate the age of the outburst). More studies are nonetheless needed to robustly confirm these results.

Late evolution of X-ray cavities

The late evolution of X-ray cavities is highly uncertain from the observational point of view. As reported by Enßlin and Heinz (2002), McNamara and Nulsen (2007), Diehl et al. (2008), and Bîrzan et al. (2009), cavities are easiest to detect when they are large and are located in the bright central regions of the clusters; at large distances from the core (≥ 100 kpc) a cavity contrast with respect to its environment is generally too low to be detectable. Indeed, only a few cases of large cavities at more than 100 kpc from the center are known (Giacintucci et al., 2020).

An important issue regards cavity disruption, which may happen when Rayleigh-Taylor and shear instabilities are efficient: these effects can disrupt cavities, mixing their contents with the surrounding gas (e.g., Reynolds et al. 2005; Sijacki and Springel 2006; Brighenti et al. 2015). Observational studies of samples of X-ray cavities showed that the distribution of the ratio of projected nuclear distance (r) to radius (R) peaks at $r/R \approx 2$ and falls off rapidly beyond; this may indicate that cavities travel roughly their own diameters before they disintegrate or become too difficult to detect (Diehl et al., 2008). However, there are some evidence that cavities can be fragmented without being destroyed: the numerous small cavities in M87 suggest that some processes (such as magnetic draping, see Lyutikov 2006) may stabilize these structures (McNamara and Nulsen, 2007). The detection in the galaxy group Nest200047 by Brienza et al. (2021) of remnant radio lobes at a distance of 200 kpc from the center, with a long radiative age (around 350 Myr) and a filamentary, threaded morphology may further suggest that radio lobes (and possibly the corresponding X-ray cavities) are long lived (see also the cases of NGC 507, Brienza et al. 2022, and NGC 6068, Candini et al. 2023).

Further advances of this topic will likely come up when future X-ray telescopes (such as *Athena*, Barret et al. 2020, or the *Advanced X-ray Imaging Satellite*, AXIS, Mushotzky and AXIS Team 2019, or the Survey and Time-domain Astrophysical Research Explorer, STAR-X, Zhang et al. 2022b) with a larger collecting area and field of view than the existing facilities will be launched, possibly allowing the detection of X-ray cavities at large (≥ 100 kpc) distances from the center. Further, the availability of X-ray Integral Field Unit Spectroscopy in the future would be key to investigate the

dynamics of X-ray cavities from the kinematics of X-ray emission lines (e.g., Brüggén et al. 2005; Zhang et al. 2022a).

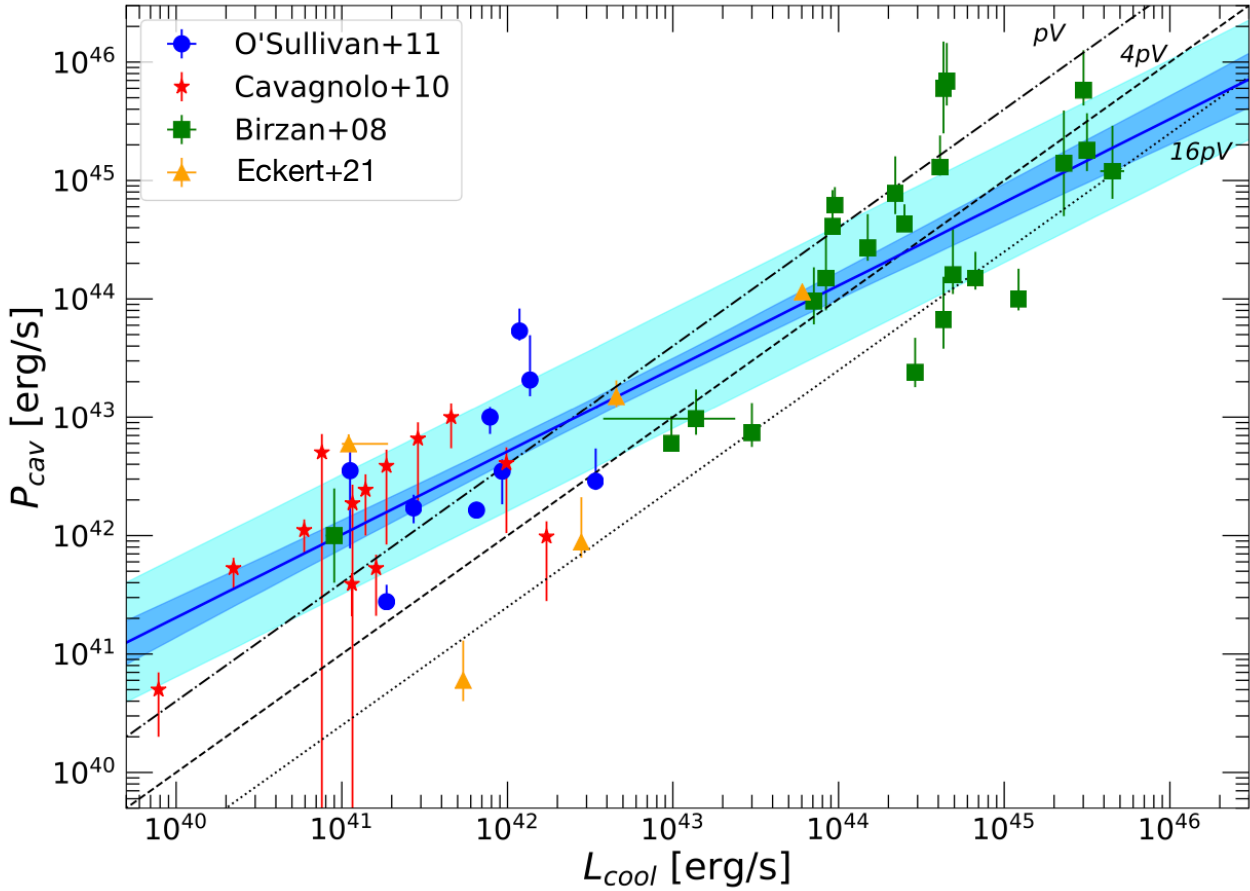


FIGURE 1.12: Cavity power versus cooling luminosity for groups and clusters, from Eckert et al. (2021). Relation between the luminosity within the cooling radius (L_{cool}) and the power injected by the cavities (P_{cav}) for several literature samples. The blue line shows a fit to the data using a power law with intrinsic scatter. The uncertainty on the fitted relation is indicated by the blue shaded area, whereas the cyan range indicates the intrinsic scatter around the relation. The slope of the blue line is lower than unity, indicating that feedback efficiency is higher in groups than in clusters (see text for details). Adapted from Eckert et al. (2021).

Energetics of X-ray cavities

Since the earliest works on AGN-inflated bubbles, there has been growing interest in deriving the energy associated with the X-ray cavity. This is expected to be a proxy for the mechanical energy budget of the AGN, and is thus of great importance to understand the thermal balance of heating and cooling in clusters (e.g., McNamara and Nulsen 2007; McNamara and Nulsen 2012) and, more generally, the energy budget of radio galaxies (e.g., Birzan et al. 2008; O'Sullivan et al. 2011). The energy and power of X-ray cavities can be derived from the total enthalpy of a cavity, H (Churazov et al., 2000; Birzan et al., 2004; Nulsen et al., 2007). This is given by the sum of the pV work done to displace the X-ray emitting gas while the radio bubble is inflated, and the internal energy that provides the pressure supporting the cavities:

$$H = \frac{\gamma}{\gamma - 1} pV = 2.5pV, \quad \text{for } \gamma = 5/3 \quad (1.18)$$

$$4pV, \quad \text{for } \gamma = 4/3 \quad (1.19)$$

where γ is the ratio of specific heats of the cavity plasma; the choice for γ depends on whether the pressure support within cavities is supplied primarily by relativistic plasma ($\gamma = 4/3$) or non-relativistic plasma ($\gamma = 5/3$) (McNamara and Nulsen, 2007; McNamara and Nulsen, 2012; Gitti et al., 2012).

Given the spatial association with radio lobes, it is typically assumed that the internal composition of the cavity is dominated by relativistic plasma, therefore $\gamma = 4/3$ and $H = 4pV$ (Bîrzan et al., 2004).

Eq. 1.19 also assumes that the cavity and the ambient medium are in pressure equilibrium, that is $p_{\text{cavity}} = p_{\text{ICM}}$. The pressure of the ICM can be estimated through measurements of the temperature and density of the surrounding ICM, while the volume is computed from the cavity size (under the assumption of spherical or elliptical symmetry of the cavity 3D geometry).

Several studies of samples of X-ray cavities showed that their enthalpies - measured with Eq. 1.19 - lie between $\sim 10^{55}$ erg and $\sim 10^{61}$ erg (see for example Diehl et al. 2008). When divided by the cavity age t_{cav} (which can be computed following the three methods discussed above), the observational measurements give an estimate of the cavity power P_{cav} .

Heating by AGN feedback is thought to develop through the dissipation of the cavity enthalpy and through shocks driven by the AGN outburst (McNamara and Nulsen, 2007; McNamara and Nulsen, 2012; Gitti et al., 2012). The missing information regards weak shocks created by the motion of the jet through the ambient, which is expected to give a contribution to the total power. The problem with this component is that shocks are quite difficult to detect, and shock detections have been confirmed only for a sub-sample of clusters for which cavities are found (see more in the dedicated subsection below); therefore, studies of AGN feedback in samples of clusters usually include only the cavity power (e.g., Bîrzan et al. 2004; Rafferty et al. 2006; Rafferty et al. 2008), which is a lower limit to the true total mechanical power of the AGN.

The role of X-ray cavities in the regulation of ICM cooling

Once the cavity power is measured, it is possible to compare it with the gas bolometric X-ray luminosity inside the cooling radius L_{cool} , which represents the radiative losses that must be compensated for by any heating mechanism. Over the last 20 years, *Chandra* observations consistently revealed that the mechanical power of AGN (i.e. the cavity power P_{cav}) is comparable to or exceeds the X-ray luminosities of their cooling atmospheres (e.g., for reviews McNamara and Nulsen 2007; McNamara and Nulsen 2012; Fabian 2012; Gitti et al. 2012; Gaspari et al. 2020; Eckert et al. 2021; Donahue and Voit 2022), which means that jets are able to offset radiative cooling of the ICM. Fig. 1.12 shows the average cavity power plotted against the X-ray cooling luminosity for different samples of systems: over six orders of magnitude, the cavity power scales in proportion to the cooling X-ray luminosity, although with a large scatter (which is also due to the fact that cavity sizes and location are subject to uncertainties related to irregular shapes). These results, first obtained in the early 2000s based on non-complete samples of mainly massive systems in the very local Universe ($z \leq 0.3$; see Bîrzan et al. 2004), were later confirmed also with complete samples of galaxy clusters (Bîrzan et al., 2012; Olivares et al., 2022a), extended to lower jet power and halo luminosity regimes (e.g., Macconi et al. 2022), and tested at higher redshift (e.g., Hlavacek-Larrondo et al. 2015).

Besides actually heating the gas by raising its entropy, there is evidence that jets can also mechanically push the cool and enriched central gas to higher altitudes, effectively removing the fuel source for further SMBH accretion and, possibly, star formation (e.g., McNamara and Nulsen 2007; McNamara and Nulsen 2012). Early works on the dynamics of cavities showed that the motions of jet-created bubbles in the gravitationally stratified ICM can uplift a fraction of gas in their wakes (Churazov et al., 2001; Saxton et al., 2001; Brüggen, 2003; Roediger et al., 2007; Revaz et al., 2008). Evidence of such mechanical dredge-up of gas is now clear in many systems from the observation of the molecular and warm gas phases (e.g., McDonald et al. 2010; Russell et al. 2017; Olivares et al. 2019; see more in §1.2.2), but it was already noticed from the analysis of the hot gas itself.

As reported in §1.1.1, the radial abundance of metals is not uniform in cool cores. AGN feedback

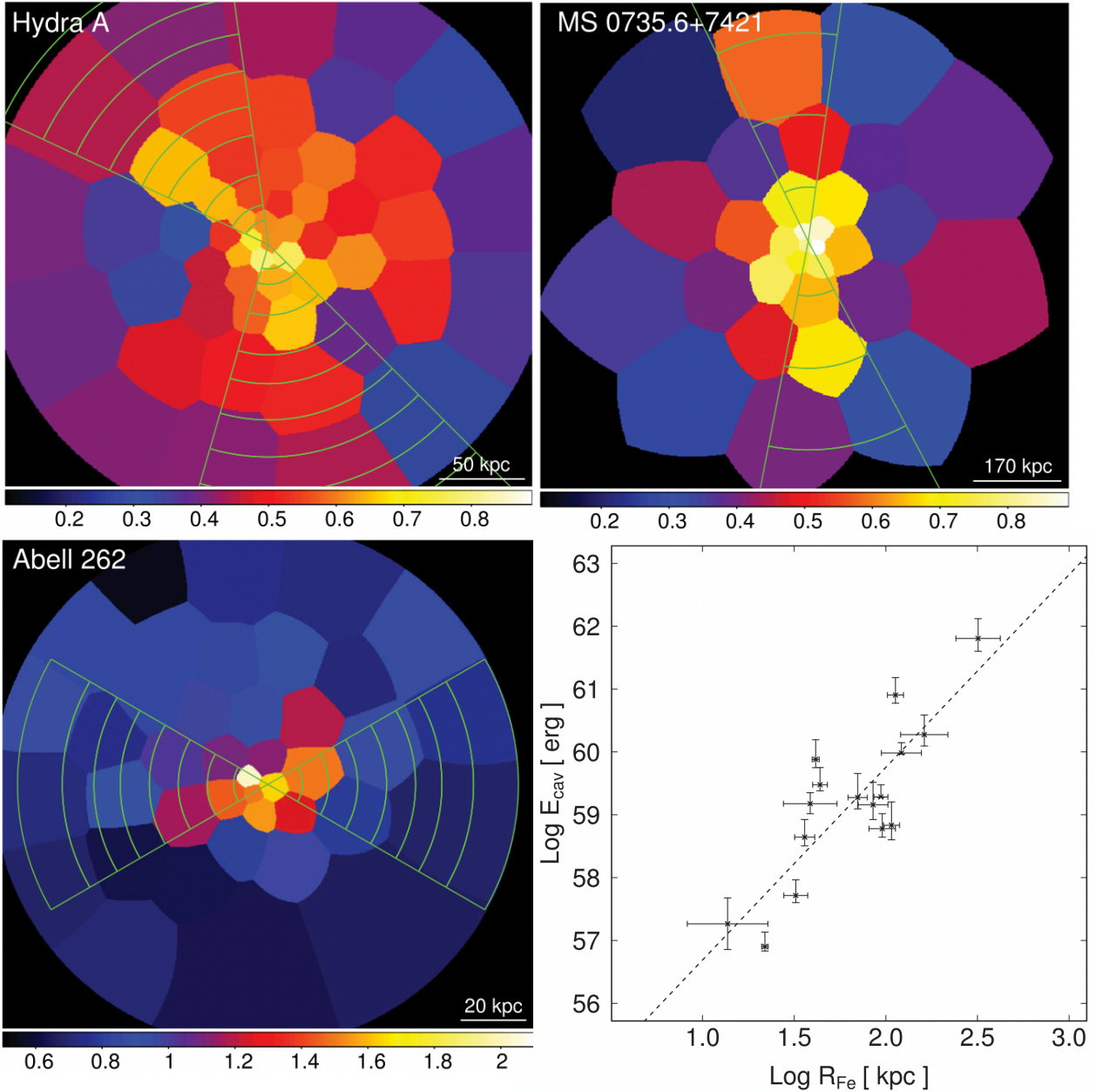


FIGURE 1.13: Uplift of metal-rich gas from cluster-central AGN jets, from Kirkpatrick and McNamara (2015). The top panels and the bottom left panel show three examples of abundance maps (in Z_{\odot}) of galaxy clusters. The overlaid green sectors are along the axis of the X-ray cavities, and correspond to relatively higher-metallicity regions. Bottom right panel: Energy of the cavities versus the largest projected radius to which metal-enriched gas is observed (defined as “iron radius”). Adapted from Kirkpatrick and McNamara (2015).

can additionally introduce azimuthal asymmetries (see Fig. 1.13, top and bottom-left panels). In Hydra A and M 87, cool and metal enriched X-ray filaments are draped along the radio jets, indicating that the filaments were pushed out by the jets (Simionescu et al., 2008; Gitti et al., 2011). From the study of ten galaxy clusters, Kirkpatrick et al. (2011) revealed that the metal-rich plasma can be lifted out by rising X-ray cavities to altitudes between twenty and several hundred kpc, and that the jet power and the cavity energy scale with the largest projected radius to which metal-enriched gas is observed (the so-called “iron radius”, R_{Fe}). The following study of Kirkpatrick and McNamara

(2015) confirmed these results, finding a relation:

$$R_{Fe} [\text{kpc}] = (57 \pm 30) \times \frac{E_{cav}^{0.33 \pm 0.08}}{10^{59} \text{ erg}}, \quad (1.20)$$

which is shown in Fig. 1.13, *bottom right panel*). Numerical simulations (e.g., Gaspari et al. 2012b; Duan and Guo 2018) successfully reproduced the azimuthal asymmetries in metal abundance, confirming that another route to AGN feedback is through outflows of central gas.

The effect of AGN feedback in galaxy groups

While this Thesis is focused on galaxy clusters, it is worth noting that, in the regimes of galaxy groups, the mechanical power of the central AGN appears to largely exceed the radiative losses of the hot gas in the halo (Cavagnolo et al., 2010; O’Sullivan et al., 2011). The best-fit relation shown in Fig. 1.12 has a slope of 0.41 ± 0.09 , which is significantly lower than unity. This result suggests that the feedback efficiency depends on the halo mass, specifically it is higher in groups than in clusters (Eckert et al., 2021).

Moreover, a comparison of the cumulative energy of AGN in groups with the binding energy of the hot gas suggests that groups should progressively be depleted of their halos (Giodini et al., 2010). In particular, the cumulative energy of group-central AGN, E_{SMBH} , is defined as:

$$E_{SMBH} = \epsilon_M \times M_{SMBH} \times c^2, \quad (1.21)$$

where M_{SMBH} is the black hole mass and ϵ_M is the mechanical efficiency. The latter expresses the efficiency of the coupling between the AGN energy output and the energy lost by the hot gas through cooling, and is defined as $\epsilon_M = P / (\dot{M}c^2)$, where P is the AGN power and \dot{M} is the cooling rate (Gaspari and Sądowski, 2017b).

The binding energy of the hot gas, E_{bind} , can be expressed as:

$$E_{bind} \propto M_{gas} \times kT, \quad (1.22)$$

where M_{gas} is the gas mass of the group halo.

The result that $E_{SMBH} \geq E_{bin}$ is obtained by assuming that the duty cycle (that is, the fraction of time that a radio galaxy is “on”) of AGN in groups equals that of AGN in clusters (Eckert et al., 2021). The duty cycle of AGN in clusters, estimated from the fraction of cool core clusters with X-ray cavities, is larger than 70% (Dunn and Fabian, 2006).

The fraction of gas in the halos of groups, around 0.08, is lower than that of clusters, around 0.15, suggesting that some depletion has taken place (Eckert et al., 2021). However, since hot gas is observed in galaxy groups, a complete depletion is likely not occurring. This may be explained by arguing (a) that the coupling of jet activity with the thermodynamics of the halo is weaker than in clusters (e.g., Gaspari and Sądowski 2017b), or (b) that radio galaxies in groups are more frequently active than inactive, compared to AGN in clusters (O’Sullivan et al., 2017), that is, they have a higher duty cycle. For a recent review on AGN feedback in galaxy groups, see Eckert et al. (2021).

Properties of weak shocks driven by AGN activity

Besides carving out cavities in the hot gas, the jet propagation and lobe inflation are expected to drive shock waves in the surrounding medium. While initially expanding at supersonic speed, the shock fronts progressively slow down and broaden into sound waves (e.g. Bourne and Yang 2023). Numerical simulations of jet expansion in the ICM indicate that both low-power and high-power jets can drive shocks waves that become mildly supersonic at kpc scales, and are thus referred to as “weak” shocks; these fronts typically assume the shape of cocoons surrounding the X-ray cavities (e.g., Heinz and Churazov 2005; Brighenti and Mathews 2006; Brügggen et al. 2007; Cielo et al. 2018;

Martizzi et al. 2019; Wittor and Gaspari 2020). However, direct observational evidence of weak shocks is rare. Weak shocks driven by central AGN have been discovered in roughly a dozen systems (Liu et al., 2019b), all targeted with deep *Chandra* exposures, which is lower than the number of known X-ray cavities by more than an order of magnitude (e.g., Shin et al. 2016).

Given the paucity of detected shocks, little is known about their role in the feedback cycle. Nevertheless, the propagation of shock and sound waves is expected to contribute to the total energy released in the ICM by the AGN outburst. Moreover, these waves provide a relatively simple solution as to how the ICM may be isotropically heated, considering that jets (and X-ray cavities) are instead intrinsically directional (e.g., Yang and Reynolds 2016). Besides the power required to inflate X-ray cavities, considering also the mechanical power of weak shocks is necessary to truly test the efficiency of AGN in effectively keeping the ambient gas from rapid cooling.

In the following, we summarize the main equation that describe the propagation and energetics of shock fronts in the ICM, and we briefly review the available observational results. The strength of

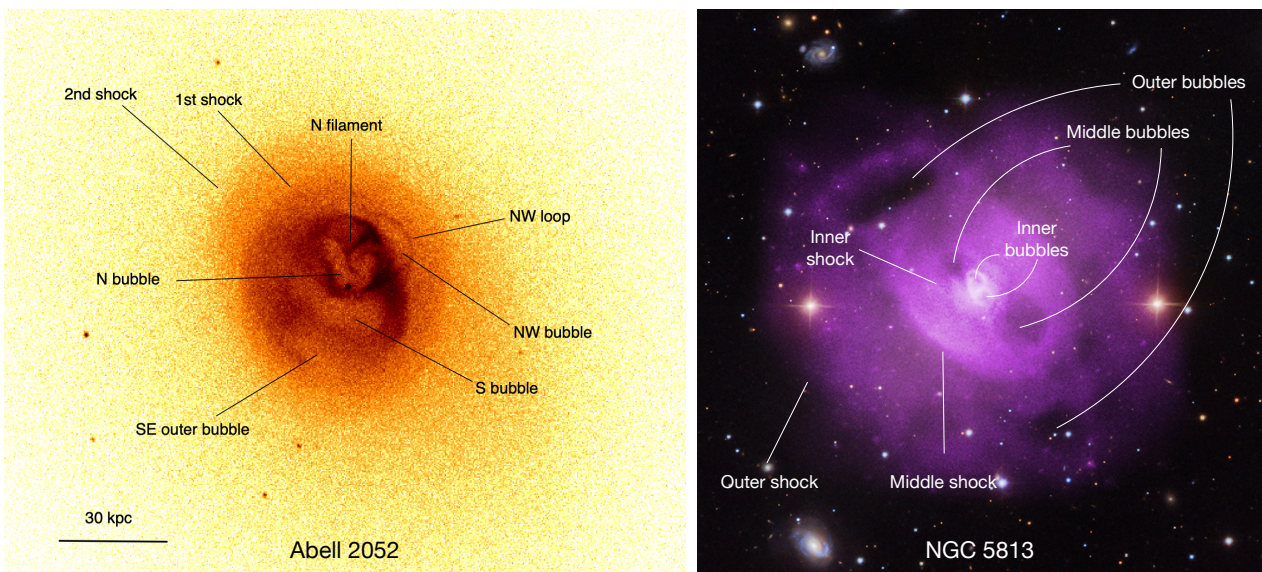


FIGURE 1.14: Example of shock fronts in galaxy clusters. *Left panel:* X-ray (*Chandra*) image of the galaxy cluster Abell 2052, observed for 650 ks. The shock and cavity features are labeled. Reproduced from Blanton et al. (2011). *Right panel:* Composite X-ray (*Chandra*) and optical (SDSS) image of the galaxy group NGC 5813, observed for 650 ks in the X-rays. The shock and cavity features are labeled. Credits: X-ray: Randall et al. (2015), optical: SDSS.

a shock is usually described by the Mach number of the front $\mathcal{M} \equiv v_{sh}/c_s$, where c_s is the sound velocity in the pre-shock gas (*upstream* medium), and v_{sh} is the velocity of the gas with respect to the shock surface. In the following, ρ_1 , T_1 and p_1 are the pre-shock (*upstream*) gas density, temperature, and pressure, while ρ_2 , T_2 and p_2 are the corresponding quantities in the post-shock gas (*downstream*). Using the Rankine-Hugoniot shock jump conditions, it is possible to link the Mach number \mathcal{M} with the density jumps J :

$$J = \frac{\rho_1}{\rho_2} \quad (1.23)$$

$$M = \left[\frac{2J}{\gamma + 1 - J(\gamma - 1)} \right]^{1/2}, \quad (1.24)$$

where $\gamma = 5/3$ is the adiabatic index. As noted above, shock fronts in galaxy groups and galaxy clusters are typically weak (with the exception of the $\mathcal{M} \sim 8$ shock front in Centaurus A, Kraft et al. 2003), with Mach numbers in the range $1.1 \lesssim \mathcal{M} \lesssim 1.7$ (e.g., McNamara and Nulsen 2007; McNamara and Nulsen 2012; Liu et al. 2019b). From the Rankine-Hugoniot relation it is also possible to

link the Mach number of the shock front and the associated temperature and pressure jumps:

$$T_{\text{jump}} = T_1/T_2 = \frac{5\mathcal{M}^4 + 14\mathcal{M}^2 - 3}{16\mathcal{M}^2} \quad (1.25)$$

$$p_{\text{jump}} = p_1/p_2 = \frac{5\mathcal{M}^2 - 1}{4} \quad (1.26)$$

Observationally, detecting shocks from X-ray observations requires (i) to identify an edge in surface brightness in the X-ray image, (ii) to confirm the presence of a density jump by studying the surface brightness profile, and then (iii) to spectroscopically measure temperature and pressure gradients. It is not straightforward to classify a discontinuity as a shock front based on morphological evidence alone. For instance, an X-ray-bright rim of gas surrounding a cavity may be interpreted either as a shock front driven by the outburst, or as cool material pushed aside and compressed by the expansion of the bubble. Measuring a negative or positive temperature gradient is essential to discriminate between the two (see e.g., Cavagnolo et al. 2011). From the analysis of the few shock fronts in galaxy clusters, galaxy groups and elliptical galaxies it was confirmed that AGN-driven shocks are typically mildly supersonic and typically encase the X-ray cavities (e.g., McNamara and Nulsen 2007; McNamara and Nulsen 2012; Gitti et al. 2012; Fabian 2012; see the examples in Fig. 1.14), in agreement with theoretical predictions and numerical simulations. While the majority of the known shock fronts lies at a few tens of kpc from the center (e.g., Machacek et al. 2006; Blanton et al. 2011; Randall et al. 2015), giant shock fronts have also been detected in large cavity systems (shock radius of 250 kpc in MS 0735+7421, e.g., Vantyghem et al. 2014, and shock radius of 200 kpc in Hydra A, e.g., Gitti et al. 2011).

Energetics of weak shock fronts

Once a shock has been identified, it is possible to measure the energy associated with the corresponding outburst. Historically, two methods have been used to estimate the energetic of shocks from observations (e.g., Randall et al. 2015 and references therein). A first approach considers adopting a spherically symmetric model of a point explosion at the center of an initially isothermal, hydrostatic atmosphere, whose conditions are tailored to those of the specific case study. This approach has been used to derive the energy and age of the large-scale shock front in Hydra A (Nulsen et al., 2005), indicating a total energy of $E = 9 \times 10^{60}$ erg. An alternative approach considers the volume of shocked gas and the difference in energy density at the interface (e.g. David et al. 2001; Randall et al. 2015):

$$E_{\text{sh}} = \frac{3}{2} V \times \Delta p = \frac{3}{2} V \times (p_2 - p_1), \quad (1.27)$$

that can be measured from observations. The difference between the two above methods has been estimated to be within a factor of 2 (e.g., Birzan et al. 2004; Randall et al. 2011; Randall et al. 2015; Liu et al. 2019b). The analysis of the few systems where shock fronts have been detected revealed that shock fronts carry a non-negligible amount of energy in the ICM, comparable to the pdV work required to inflate the corresponding X-ray cavities (see Liu et al. 2019b); this is evident from Fig. 1.15, where the comparison between cavity and shock energies for 13 galaxy clusters and groups is shown. The shock energies range between $\sim 10^{55}$ erg for NGC 4552 and $\sim 4 \times 10^{61}$ erg for MS 0735+7421, and the ratio to the cavity energy varies between 0.1 – 10.

Besides estimating the total energy associated with shock fronts, there has been interest in measuring the *effectiveness* of heat transfer to the ICM by the passage of a shock front. Nulsen et al. (2007) proposed to estimate the effectiveness of shocks at heating the surrounding gas by computing the equivalent heat input per unit mass provided by a shock:

$$\Delta Q \sim T \Delta S = e_{th} \Delta \ln \frac{p}{\rho^\gamma}, \quad (1.28)$$

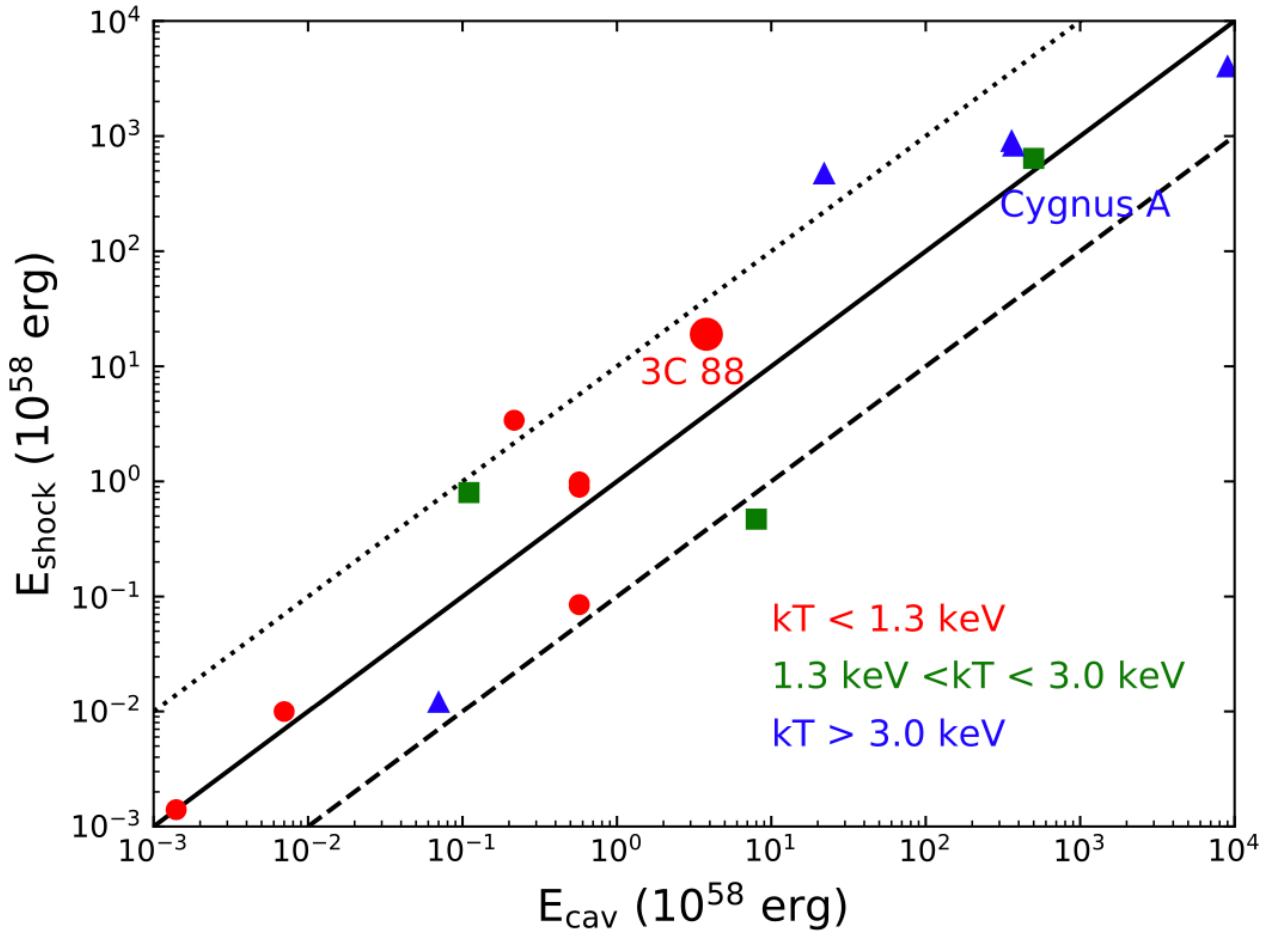


FIGURE 1.15: Shock energy versus cavity energy for 13 galaxy clusters and groups, color-coded by the temperature of the host halo. The dotted, solid, and dashed lines represent $E_{\text{shock}}/E_{\text{cav}} = 10$, 1, and 0.1, respectively. Reproduced from Liu et al. (2019b).

where e_{th} is the specific thermal energy, p is the pressure and ρ is the density of the gas.

The above equation links the fractional heat input, $\Delta Q/e_{th}$, with the observed jump of $\ln p/\rho^\gamma$ in the shock. The quantity $\ln p/\rho^\gamma$ primarily depends on the Mach number of the front, meaning that the fractional heat input of a single, weak shock ($1.1 \leq \mathcal{M} \leq 1.5$) is expected to be relatively small. Indeed, the heat input ΔQ produced by the innermost shock front in M87 (Forman et al., 2005) is around $\sim 2\%$ of the gas specific thermal energy. Similarly, the heat input ΔQ produced by the innermost shock front in the galaxy group NGC5813 (Randall et al., 2011; Randall et al., 2015) is around $\sim 10\%$ of the gas specific thermal energy.

Based on these fractions, it may appear that weak shocks are not very efficient at heating the ICM. However, the timescales of cooling and heating should be taken into account. In NGC 5813 three nested shock fronts are visible (see Fig. 1.14, right panel), with a time difference between the fronts of 10 Myr (Randall et al., 2011; Randall et al., 2015). The thermal energy lost by gas cooling has to be replenished on a timescale given by the ICM cooling time, which is around a few 100s of Myr within the region where the shocks are located. Assuming that the outburst repetition rate above remains constant, there is time for 10 – 20 shocks per cooling time. If each of them accounts for $\sim 10\%$ of the gas thermal energy, then the combined heat input of the shocks is more than sufficient to balance the gas radiative losses.

This comparison, first performed for M 87 and then for the group NGC 5813, showed that repetitive shock heating can – under a few assumptions – provide enough energy to offset and delay gas cooling. However, these calculations were performed (a) for only two systems, as only a couple

of clusters or groups with multiple shock fronts have been discovered, and (b) for shock fronts within 15 kpc (in M 87, Forman et al. 2005) and 30 kpc (in NGC 5813, Randall et al. 2015) from the center. This limits the understanding of how effective shocks are at heating the ICM at larger radii, potentially even outside the cool core of the system. Additionally, so far NGC 5813 is the only known system with multiple shock fronts, each associated with a separate AGN outburst (the shocks in the cluster of M 87 may have been driven by a single outburst, see Brügggen et al. 2007). While the study of this galaxy group was paramount in addressing the whole AGN mechanical output (X-ray cavities *and* shock fronts), these low-mass systems also have shallower gravitational potentials compared to galaxy clusters (e.g., Giodini et al. 2010; McCarthy et al. 2010), thus the effect of AGN-driven shocks on the gas may be more pronounced. As such, the conclusions based on observations of groups may not be applicable to galaxy clusters. The detection of multiple shock fronts driven by successive AGN outbursts in a galaxy cluster would allow one to address the question of how much heating by weak shocks contributes to the feedback cycle in clusters of galaxies.

1.2.2 Evidence of AGN feeding: the multiphase atmospheres of BCGs

In the previous subsection, we explored the main evidence for the AGN *feedback* response to the radiative losses of its hot atmosphere. Still, the idea of a *loop* regulating the AGN – ICM interplay is grounded on a *feeding mechanism* to close the circle. The basic understanding of ICM cooling being able to sustain AGN activity is that the transition of the gas from the hot (10^{6-7} K) through the warm (10^4 K) and to the cold (10 – 100 K) phases can produce a cascade of gas clouds that (provided that they lose angular momentum) may flow to the center and feed the SMBH. In this subsection, we present the main results in support of this picture.

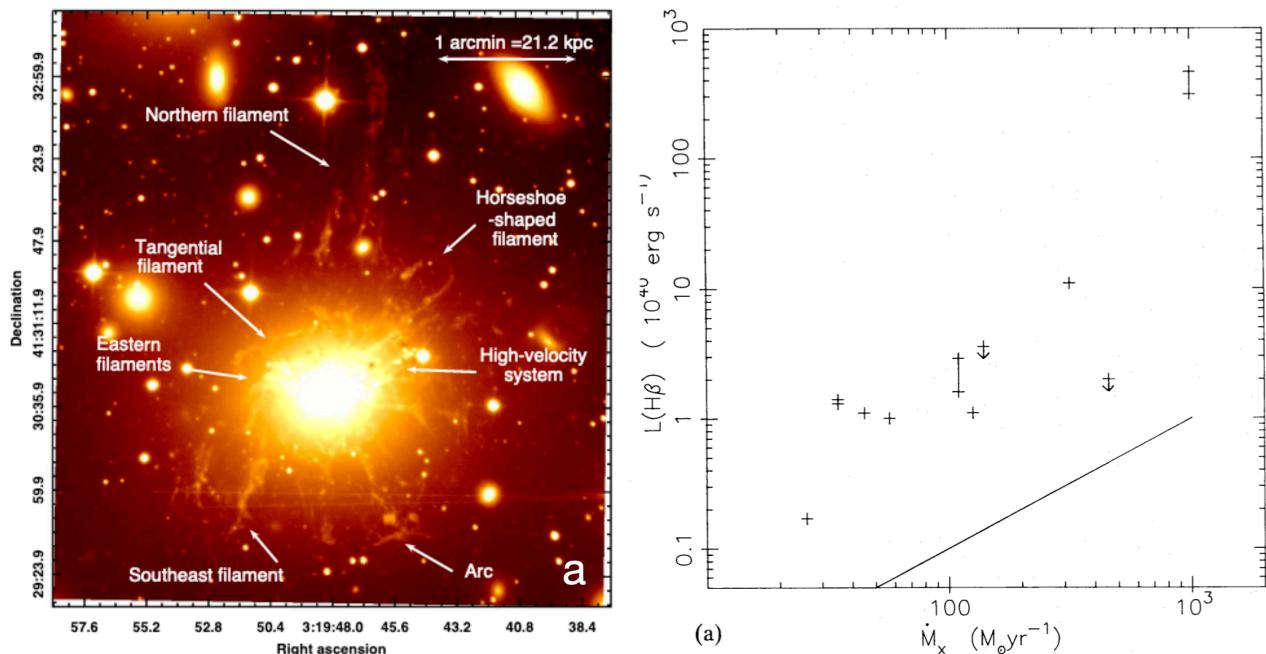


FIGURE 1.16: *Left panel:* Optical image of NGC 1275 (the BCG of the Perseus cluster) including the $H\alpha$ emission line, with major morphological features labeled. Reproduced from Gendron-Marsolais et al. (2018). *Right panel:* Comparison between the luminosity of the $H\beta$ emission line and the classical cooling rate of 12 galaxy clusters. The $H\beta$ luminosity is in excess with respect to the prediction from radiative cooling (represented by the solid line). Reproduced from Johnstone et al. (1987).

Observations of warm and molecular gas filaments in cool cores

Optical emission line nebulae, tracing gas at 10^4 K, were known to be present around the central galaxies of massive clusters from the earliest studies of relaxed clusters. Due to its proximity to us, the spectacular nebula around NGC 1275 (the BCG of the Perseus cluster) was among the first to be discovered (Seyfert, 1943; Burbidge and Burbidge, 1965). So far, nebular emission from BCGs has been observed in several systems, mainly through the observation of the $H\alpha$ emission line (e.g., Crawford et al. 1999; McDonald et al. 2010; Hamer et al. 2016). The nebular emission is usually centered on the BCG (see however the dynamically perturbed cases of e.g., Hamer et al. 2012), and it shows a filamentary morphology that can extend from a few kpc to ~ 50 – 60 kpc (see Fig. 1.16, left panel; e.g., McDonald et al. 2010; Hamer et al. 2016; Gendron-Marsolais et al. 2018; Olivares et al. 2019). Besides $H\alpha$ emission, classic BCG nebulae emit through low-ionization forbidden lines (e.g., [OII], [NII], [OI], [SII]; Ciocan et al. 2021).

Compared to the ionization nebulae energized by UV photons from young stars, the BCG nebulae have relatively stronger luminosity (Donahue and Voit, 2022). Several possibilities have been explored to account for such excess ionization: thermal conduction, X-ray photons emitted by the hot gas (Johnstone et al., 1987; Voit and Donahue, 1990), extreme UV radiation from intermediate temperature mixing layers surrounding the filaments (Begelman and Fabian, 1990), thermal conduction and cosmic rays (Ferland et al., 2009; Ruszkowski et al., 2018), shocks or turbulence (e.g., McDonald et al. 2012). However, which of the above is most likely to power the optical line emission from BCGs is yet poorly understood (Donahue and Voit, 2022).

When high spatial resolution X-ray observations became available (i.e. with *Chandra*), it became clear that not only the optical line emission is present at the cluster center, but it is also usually co-spatial with the densest and cooler phase of the ICM (e.g., McDonald et al. 2010; McDonald et al. 2012). This supports the idea that there exist some physical connections between the optical line luminosity and cooling of the hot gas. It had long been clear that even strong cooling flows (i.e. $100 - 1000 M_{\odot}/\text{yr}$) could not power alone the prodigiously luminous nebulae (e.g., for reviews Hlavacek-Larrondo et al. 2022; Donahue and Voit 2022). Specifically, in the cooling flow model, a scaling between the the gas cooling rate and the emission line luminosities is expected, because as gas cools from 10^7 keV to 10^4 keV it recombines and produces emission lines of the Balmer series. For example, a cooling rate of $100 M_{\odot} \text{ yr}^{-1}$ would produce an $H\beta$ luminosity of around $10^{39} \text{ erg s}^{-1}$ (e.g., Johnstone et al. 1987). However, the right panel of Fig. 1.16 shows that the observed $H\beta$ -line luminosities in 12 cool core clusters exceed by more than an order of magnitude the prediction based on the observed cooling rates (Johnstone et al., 1987). Explaining these luminosities would require the gas to remain ionized 1000 times longer than what is predicted by simple photoionization. As a result, it is likely that shocks, conduction, cosmic rays and AGN photoionization contribute to the observed emission line luminosities (e.g., for reviews Hlavacek-Larrondo et al. 2022; Donahue and Voit 2022; see also the previous paragraph).

As reviewed by Donahue and Voit (2022), the amount of neutral and molecular gas observed in several BCGs is another indication that a simple cooling of hot gas through the range of temperatures $10^7 - 10$ K cannot completely explain the multiphase central gas. The molecular phase, in particular, would not form without dust particles that catalyze the formation of molecules. Dust is probably injected in the surroundings of the BCG by aging stars, rather than directly condensing out of the hot gas, producing a mixture of dusty gas of stellar origin with dust-poor gas of cooling origin.

Molecular gas is of great interest in the context of the AGN feeding and feedback loop, as it represents the coldest and densest gas phase that can condense out of the hot atmosphere. The best tracer for the molecular gas (dominated by H_2 , which is however not detectable in its coldest transitions) is the CO molecule. The earliest detection of CO emission lines in cool core clusters were obtained with the IRAM 30 m telescope, the James Clerk Maxwell Telescope (JCMT) and the Caltech Submillimeter Observatory (CSO) (Edge 2001; Salomé and Combes 2003). These works showed that the mass of molecular gas around a BCG can be as large as $10^{10} - 10^{11} M_{\odot}$ in the most massive systems.

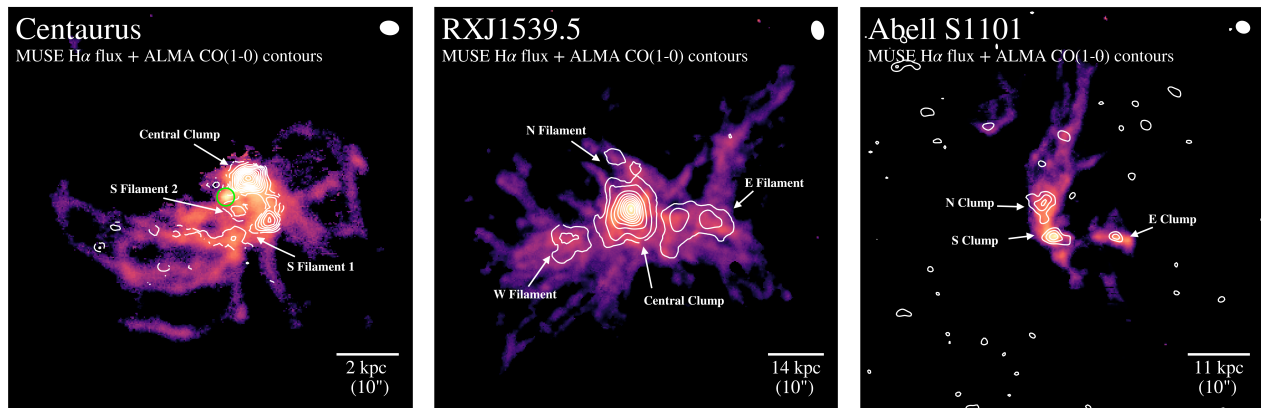


FIGURE 1.17: Connection between cold molecular filaments and warm filaments in cool core clusters. For the three clusters, the CO(1-0) contours are overlaid on the H α flux map. The co-spatial and morphological correlation between the warm ionized and cold molecular nebulae is clear in these maps. Reproduced from Olivares et al. (2019).

Moreover, such molecular gas mass is strongly correlated with the total H α luminosity of the BCG, as shown by Edge (2001) and Pulido et al. (2018). Only with the Atacama Large Millimeter Array (ALMA) it became possible to map the distribution of molecular gas in cool core clusters. Several observations (e.g., Russell et al. 2016; Russell et al. 2017; Russell et al. 2019; Olivares et al. 2019) have revealed that the molecular gas is almost always organized in filaments (an exception is the edge-on molecular disk found in Hydra A, Rose et al. 2020). The molecular filaments at 10 – 100 K are co-spatial with the warm filaments at 10^4 K (see Fig. 1.17; e.g., Salomé et al. 2006; Olivares et al. 2019). The molecular and warm gas phases are also usually co-moving, in the sense that they show matching kinematics in the overlapping filaments and a similar velocity dispersion (e.g., Ciochan et al. 2021). These evidence further support the idea that optical nebulae represent the warm envelopes of molecular clouds.

It is thus clear that the warm and molecular gas phases are connected. In the next two paragraphs, we first address how the two phases are linked with the thermodynamics of the hot gas, and then what evidences do we have from the coldest gas phases that cooling fuels the central AGN activity.

The connection with ICM cooling: thermal instabilities, condensation and uplift

The link between the thermodynamics of the hot gas and the nebular emission was noted early in the study of relaxed clusters, with various works showing how optical line emission from the BCG was detected only in systems with a cooling time shorter than the age of the Universe (e.g., Heckman 1981; Heckman et al. 1989; Cowie et al. 1983; Hu et al. 1985). These findings were refined with the advent of the *Chandra* and *XMM-Newton* telescopes, and more sensitive thresholds for the presence of multiphase gas started to appear. For example, Cavagnolo et al. (2008) showed that nebular H α emission was present only in cool core clusters with a central entropy of $K \leq 30$ keV cm 2 , or $t_{\text{cool}} \leq 1$ Gyr (see Fig. 1.18, top left panel). Later, Pulido et al. (2018) extended the analysis to the molecular gas, revealing how molecular gas is again present only if $t_{\text{cool}} \leq 1$ Gyr (see Fig. 1.18, top right panel). Then, Babyk et al. (2019) found that the molecular gas mass is correlated with the mass and density of the hot gas in the central 10 kpc.

The above works are examples of the existing evidence that hot gas cools to lower temperature, higher density gas phases. Models of how this transition may occur have highlighted the role of thermal instabilities, regulated by how the gas cooling time compares with dynamical times.

A proposed diagnostic of rapid cooling is the ratio of the cooling time, t_{cool} , to the free fall time, t_{ff}

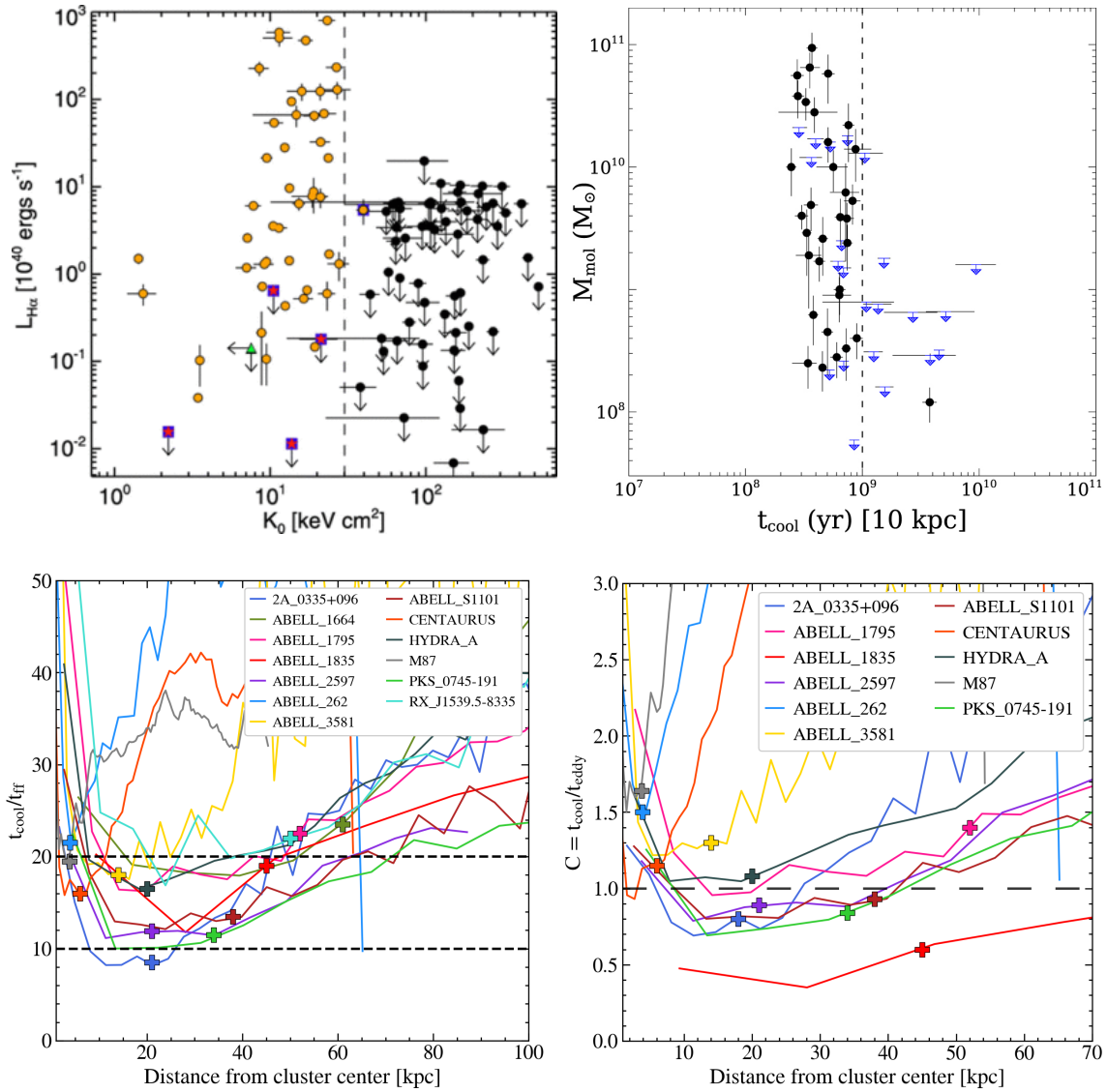


FIGURE 1.18: Different diagnostics of efficient ICM condensation. *Top left panel*: Central entropy versus H α luminosity. Orange circles represent H α detections, black circles are non-detection or upper limits. Note the presence of a sharp H α detection dichotomy beginning at $K \leq 30$ keV cm². Reproduced from Cavagnolo et al. (2008). *Top right panel*: Molecular gas mass versus cooling time measured at 10 kpc. Circular symbols denote systems observed with CO emission while arrow symbols denote upper limits. Note the presence of a sharp H α detection dichotomy beginning at $t_{\text{cool}} \leq 1$ Gyr. Reproduced from Pulido et al. (2018). *Bottom left panel*: ratio of the cooling time to free-fall time as a function of radius. The lines of $t_{\text{cool}}/t_{\text{ff}} = 10$ and 20 are shown with a horizontal dashed line, which are the approximate thresholds for the onset of thermal instabilities. Reproduced from Olivares et al. (2019). *Bottom right panel*: ratio of the cooling time to the eddy time as a function of radius. The line $t_{\text{cool}}/t_{\text{eddy}} = 1$ is shown with a horizontal dashed line, which shows the extent of the condensation region. Colored crosses show the maximum radial extent of the warm filaments. Reproduced from Olivares et al. (2019).

(Nulsen, 1986). The free-fall time is defined as:

$$t_{\text{ff}} = \sqrt{\frac{2r^3}{GM(r)}}, \quad (1.29)$$

where r is the distance from the center, G is the gravitational constant, and $M(r)$ is the total mass within r .

When this ratio falls below unity, or in more realistic atmospheres, below a few 10s (e.g., McCourt et al. 2012; Voit and Donahue 2015; Valentini and Brighenti 2015), the hot gas precipitates in a cascade of warm and, eventually, of cold gas clouds. Indeed, observations of cool core clusters with warm and cold gas phases have found that these condensed phases are present within the radius where $t_{\text{cool}}/t_{\text{ff}} \leq 10 - 20$ (see Fig. 1.18, bottom left panel; e.g., Voit and Donahue 2015; Hogan et al. 2017; Pulido et al. 2018). In this context, McNamara et al. (2016) have shown that the central free-fall times of different clusters span a narrow range of values relative to cooling times. Therefore, t_{cool} alone may be the most sensitive predictor to ICM condensation (see also Hogan et al. 2017).

An alternative diagnostic is the ratio between the cooling time and a turbulent timescale. When cooling is induced by local perturbations of the gas that have a turbulent origin, a condensation of localized hot gas blobs into warm and cold gas is triggered (Gaspari et al. 2012a; Gaspari et al. 2013; Gaspari and Sądowski 2017b; Gaspari et al. 2018; Gaspari et al. 2020; Wittor and Gaspari 2020). In the “chaotic cold-accretion” (CCA) scenario, the collision between the different cold clouds will cancel angular momentum, driving the clouds inwards where they can feed the central SMBH (Gaspari and Sądowski, 2017b). In this approach, the condition for cooling to occur is that the ratio between the cooling time and the turbulent “eddy time” falls below unity (e.g., Gaspari et al. 2018; Wang et al. 2023). The eddy timescale represents the time a vortex requires to gyrate, and is defined as:

$$t_{\text{eddy}} = 2\pi \times \frac{r^{2/3} L^{1/3}}{\sigma_{3D}}, \quad (1.30)$$

where r is the distance from the center, L is the injection scale of turbulence, and σ_{3D} is the velocity dispersion of the gas.

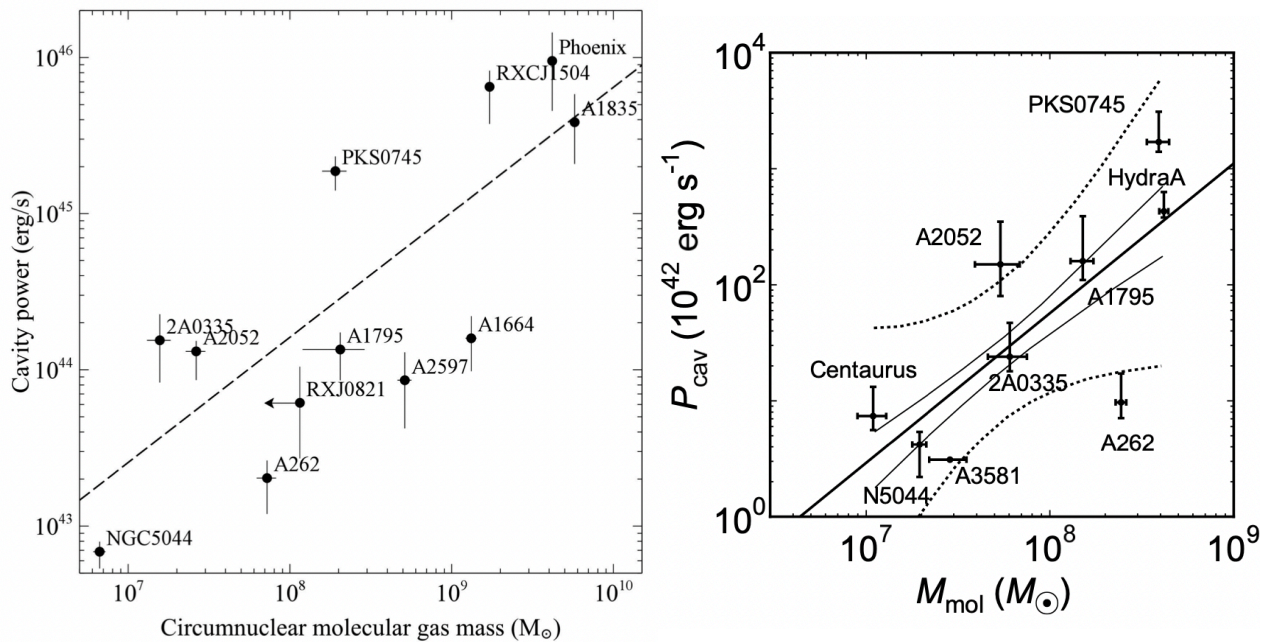


FIGURE 1.19: Comparisons between cavity power and central molecular gas mass. *Left panel*: cavity power versus molecular gas mass within a single ALMA beam centered on the BCG in 12 galaxy clusters, from Russell et al. (2019). *Right panel*: cavity power versus molecular gas mass within 500 pc from the SMBH, from Fujita et al. (2023).

Again, it has been shown that warm and cold filaments observed in several cool core clusters extend to a radius where $t_{\text{cool}}/t_{\text{eddy}} \sim 1$ (see Fig. 1.18, bottom right panel; e.g., Olivares et al. 2019).

An interesting possibility is that AGN feedback may also be *positive*, i.e. jet activity may induce

further ICM condensation. The “stimulated cooling” model (e.g., Brighenti et al. 2015; McNamara et al. 2016) predicts that thermally unstable cooling happens in the wake of X-ray cavities. As these structure rise out of the central cluster potential, they may (a) push hot gas to altitudes where $t_{\text{cool}}/t_{\text{ff}} \leq 10 - 20$, or (b) inject turbulence in the local medium, favoring the condition $t_{\text{cool}}/t_{\text{eddy}} \sim 1$. Either ways, the hot gas condenses into warm and cold filaments encasing the bubbles. The idea that cavities can entrain gas is supported by the metal-rich outflows observed in several systems (that we discussed in §1.2.1). Indeed, a number of cool core clusters were observed to possess warm and cold gas projected behind or draped around the location of X-ray cavities (see the example of Phoenix in Fig. 1.9; see e.g., McNamara et al. 2014; Russell et al. 2017; Russell et al. 2019; Ciocan et al. 2021). A nice example is the cluster Abell 2597, where the condensed cool phases show a mixture of inflow towards the BCG, outflow along the jets and draping around the buoyant X-ray cavities (Tremblay et al., 2018).

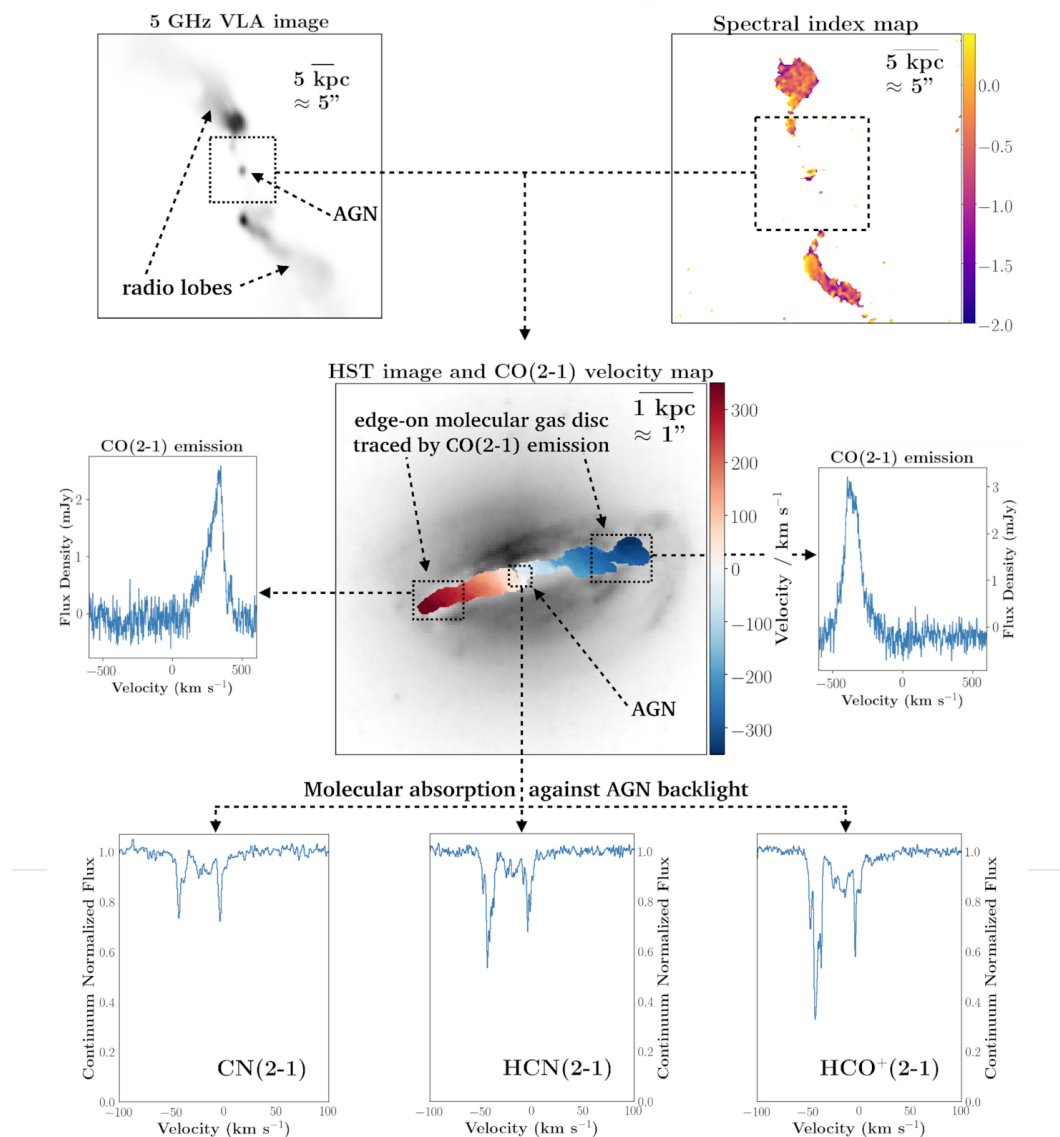


FIGURE 1.20: Molecular emission and absorption in Hydra A. *Top left*: VLA image showing the radio lobes. *Top right*: A spectral index map of the radio galaxy. *Center*: HST near-infrared image. Overlaid is a velocity map that traces the galaxy’s edge-on disc of cold molecular gas. *Center left and right*: Spectra of CO(2–1) emission from the red and blueshifted sides of the edge-on disc. *Bottom*: Some absorption lines seen against the continuum source at the galaxy center. The absorption is produced by the cold molecular gas within the disc that lies along the line of sight to the bright radio core. Reproduced from Rose et al. (2020).

Which of the above parameters (t_{cool} , $t_{\text{cool}}/t_{\text{ff}}$, or $t_{\text{cool}}/t_{\text{eddy}}$) provides the best diagnostic of thermally unstable cooling is still an open question. It is also worth noting that several systems show cold/warm gas embedded in the hot halo even without a direct correlation with X-ray cavities (e.g., Temi et al. 2018; Olivares et al. 2019; North et al. 2021; McKinley et al. 2022). In these systems, the turbulence or uplift required for condensation may have been provided by other mechanisms, such as sloshing (e.g., Vantyghem et al. 2019).

Closing the loop: observational evidences of feeding

So far, we discussed the presence of warm and cold gas in the cooling atmospheres of BCGs, but not the evidence that this multiphase gas fuels SMBH activity. Supporting this argument can be done through indirect and direct studies.

The scaling between the X-ray cavity power and the radiative losses of the hot gas is among the first indirect evidence of the ICM/AGN interplay, as it shows how larger radiative losses are accounted for, on average, by stronger outbursts. However, it is clear that a SMBH cannot “feel” its environment on tens of kpc scales (e.g., Hlavacek-Larrondo et al. 2022; Donahue and Voit 2022). Moreover, several works showed that classical Bondi accretion (a steady-state, spherically symmetric gas flow onto a black hole in a homogeneous medium; see e.g., Edgar 2004 for a review) of hot gas, while likely supplying a fraction of the accreted matter (especially in low mass systems), cannot explain alone how the most powerful AGN outbursts in galaxy clusters are fueled (Rafferty et al., 2006; Hardcastle et al., 2006; Hardcastle et al., 2007b; McNamara et al., 2011; Russell et al., 2013). In this context, recent observations of M 84 resolving the Bondi radius of this system showed that the assumptions of Bondi accretion are not verified (Bambic et al., 2023).

In fact, SMBHs probably “feel” the amount of gas that can be accreted in their immediate surroundings, which is more likely cold and condensed rather than hot (at least for systems showing powerful AGN outbursts); if the cold phase is an end-product of hot gas cooling, then the link between the central engine and the large scale atmosphere is established (e.g., Gaspari et al. 2020). Babyk et al. (2019) found a weak scaling between the cavity power and the total molecular gas mass over six orders of magnitude. However, the total molecular gas mass may be dominated by filaments on kpc scales that do not probe (yet) ongoing accretion. Russell et al. (2019) measured cavity power and molecular gas mass within a single ALMA beam centered on the BCG in 12 galaxy clusters, finding a clear scaling over four orders of magnitude in both quantities (see Fig. 1.19, left panel). This analysis was further refined by Fujita et al. (2023), where the cavity power was compared with the molecular gas mass within a fixed radius of 500 pc, to probe gas as close as possible to the SMBH (see Fig. 1.19, right panel). Again, a scaling over four orders of magnitude between jet power and cold gas mass was found, indicating that the activity of the SMBH is sensitive to the average density of the circumnuclear molecular gas.

In the last years, direct evidence of black hole feeding have started to appear. These are mainly based on the observations of cold gas clouds (in the neutral or molecular phase) close to the SMBH, and with a kinematics that is suggestive of ongoing infall and, eventually, accretion. In particular, a promising technique to study gas accretion is through the observations of gas absorption lines in front of the radio galaxy continuum (David et al., 2014; Tremblay et al., 2016; Rose et al., 2019b; Rose et al., 2019a). A nice example was given by the brightest cluster galaxy of Hydra-A, where individual clouds in motion towards the central engine have been found (see Fig. 1.20; Rose et al. 2020). These results were later confirmed with the observations of other systems (Rose et al., 2019b; Rose et al., 2019a; Rose et al., 2020; Rose et al., 2023).

Another recent study targeted neutral gas in Perseus: Morganti et al. (2023) used JVLA and VLBA observations to target the HI in the central region of the central galaxy NGC 1275 of Perseus. They detected HI absorption centered at the systemic velocity of NGC 1275 against the bright radio continuum, suggesting that the gas is very close to the AGN. They also found evidence that the HI absorption arises from a fast-rotating cold neutral disk around the central engine, at distances as close as 20 pc from the SMBH.

There is thus growing evidence that SMBHs of central galaxies are fueled by cold gas cooling from to hotter phases and eventually flowing to the center. As these studies are relatively recent and extended to a few objects only, it is likely that further insights will come from resolved, multiphase observations in the near future.

1.3 Properties and life-cycle of jetted AGN

In the previous sections, and in particular in §1.2.1, we discussed how AGN activity in clusters is a key mechanism to regulate the thermodynamics of the hot gas halo and the star formation in the BCG. In this section, we summarize the general properties of the different classes of radio galaxies (§1.3.1). This is relevant for this Thesis, as different jet power regimes can lead to different feedback output. Moreover, since the recurrent activity of radio galaxies in clusters is linked to the balance of gas cooling and heating over time, we find useful to outline the current knowledge of the life-cycle of radio galaxies (§1.3.2).

1.3.1 Different classes of radio galaxies: FR I, FR II and FR 0

Nowadays, it is known that SMBH are present in every massive galaxy; the mass of SMBHs - in the range $M_{\text{SMBH}} \sim 10^6 - 10^9 M_{\odot}$ - correlates tightly with the velocity dispersions σ_* of their host bulges (Tremaine et al., 2002), through the relation:

$$\log(M_{\text{SMBH}}[M_{\odot}]) = (8.13 \pm 0.06) + (4.02 \pm 0.32) \log\left(\frac{\sigma_*}{200 \text{ km/s}}\right), \quad (1.31)$$

indicating that the galaxy evolution is strongly related to the SMBH properties. The fraction of SMBHs showing signs of activity ($\approx 1\%$, Urry and Padovani 1995) defines the category of *Active Galactic Nuclei* (AGN). Here we narrow our interest to *jetted* AGN, and in particular to the main differences between Fanaroff-Riley Type I, II, and Type 0 radio galaxies.

Jetted AGN (see Urry and Padovani 1995; Padovani et al. 2017 for classification schemes) display jets composed of relativistic plasma that inflate radio lobes on kpc scales. They can be sub-classified as *blazars* and *radio galaxies* depending on the jet inclination with respect to the observer's line of sight. The jet of a blazar points towards the observer, therefore the emission is amplified (due to relativistic beaming) and the radio spectra are generally flat; on the other hand, the jets of radio galaxies mainly lie in the plane of the sky, so their emission is less affected by relativistic effects. Radio galaxies have been historically classified by Fanaroff and Riley (1974) on the basis of their radio morphology into Fanaroff-Riley Type I (FR I) and Fanaroff-Riley Type II (FR II): the former are *edge-darkened*, presenting bright jets and faint lobes, while the latter are *edge-brightened*, showing bright lobes and collimated jets terminating in hot spots (bright compact knots of emission). The hotspots arise from the impact between the jets and the interstellar medium (ISM), which produces shock waves that re-accelerate the electrons responsible for the synchrotron emission. We present examples of these sources in Fig. 1.21 (*insets*).

The origin of the FR I/FR II dichotomy is not completely understood yet: several hypothesis have been issued, from external agents - such as the interaction between the jets and the environment (e.g., Bicknell 1994), the host galaxy properties, or merging events - to intrinsic factors, namely a different accretion mechanism (Ghisellini and Celotti, 2001). The rate of accretion of matter around a SMBH can be estimated by dividing the luminosity released by the accreting black hole (L_{acc}) and the luminosity at which the gravitational force felt by the infalling material is balanced by the

pressure of the out-coming radiation (*Eddington Luminosity* L_{Edd}):

$$L_{\text{acc}} = \eta \dot{M} c^2 \quad (1.32)$$

$$L_{\text{Edd}} = \frac{4\pi G m_p c}{\sigma_T} M_{\text{SMBH}} \sim 1.3 \times 10^{38} M_{\text{SMBH}} / M_{\odot} \text{ erg/s} \quad (1.33)$$

where η is the efficiency at which the accreted mass is converted into energy, \dot{M} is the rate at which mass is accreted, c is the speed of light, G is the gravitational constant, σ_T is the Thomson cross section and M_{SMBH} is the black hole mass (for a review on accretion processes, see e.g., Czerny and You 2016).

The ratio between the two quantities defined above provides an estimate of the accretion rate of the AGN:

- For $L_{\text{acc}}/L_{\text{Edd}} \approx 10^{-1} - 10^{-2}$ (high accretion) the accretion mechanism efficiently converts gravitational energy into radiation (*quasar mode*): the AGN is thought to be sustained by a geometrically thin, optically thick disk (Shakura and Sunyaev, 1973), in which each element of the disk radiates as a black body. At high masses of the host galaxy (above $\sim 10^{11.5} M_{\odot}$), the fraction of highly accreting AGN showing radio-emitting jets is $\sim 0.1\%$ (e.g., Janssen et al. 2012).
- For $L_{\text{acc}}/L_{\text{Edd}} \leq 10^{-3}$ (low accretion) the disk is unable to radiate the viscosity-generated energy, leading to a geometrically thick and optically thin structure known as Advection-Dominated Accretion Flow (ADAF, Narayan and Yi 1994). In this case, the jet represents the bulk of the AGN energetic output (*jet- or mechanical- mode*). At high masses of the host galaxy (above $\sim 10^{11.5} M_{\odot}$), the fraction of inefficiently accreting AGN showing radio-emitting jets is $\sim 100\%$ (e.g., Janssen et al. 2012).

A classification of radio galaxies that takes into account the accretion mode of the SMBH was proposed by Laing et al. (1994) based on optical emission lines. This classification is grounded on the fact that different excitation modes of the gas reflect different accretion regimes in the central engine of the AGN. For this reason, radio galaxies were divided into high-excitation (HERG) and low-excitation (LERG) radio galaxies, corresponding to highly-accreting and slowly-accreting AGN, respectively. Another definition was proposed by Buttiglione et al. (2010), based on the excitation index parameter (EI):

$$EI = \log \left(\frac{[OIII]}{H\beta} \right) - \frac{1}{3} \left[\left(\frac{[NII]}{H\alpha} \right) + \log \left(\frac{[SII]}{H\alpha} \right) + \log \left(\frac{[OI]}{H\alpha} \right) \right] \quad (1.34)$$

Sources with $EI < 0.95$ are classified as LERGs, while sources with $EI > 0.95$ are classified as HERGs. The vast majority of HERGs resides in FR II radio galaxies, while LERGs display both behaviors.

Considering the environment of these sources, nearby redshift ($z < 0.5$) FR Is are typically located in dense environments (galaxy groups and clusters), while FR IIs generally reside in isolated field galaxy (e.g., Hill and Lilly 1991). Jetted AGN are typically hosted in elliptical galaxies, but the hosts of FR IIs tend to be bluer than those of FR Is, and usually show signatures of recent mergers - irregular morphology and/or relatively high star formation rates (see e.g., Baldi and Capetti 2008). These findings can be related to the accretion mode: for example, Hardcastle et al. (2007b) proposed a scenario for the different radiative efficiency of FR I/LERGs and FR II/HERGs which takes into account the difference source for the gas to be accreted. They proposed that a steady inflow of hot gas from the ambient medium of LERGs (i.e. the ICM of the host galaxy cluster or group) might power an inefficient engine, and lead to the formation of an ADAF disk. On the contrary, cold gas (possibly provided by a wet merger) might both explain the enhanced star formation rate of the host of HERGs, and produce a radiatively efficient AGN with a geometrically-thin accretion disk.

More recently, Macconi et al. (2020) found a correlation between the Eddington scaled X-ray luminosity (considered as a proxy of the accretion efficiency) and the cluster richness of the ambient medium of different classes of radio galaxies (i.e. FR I-LERG, FR II-HERG and FR II-LERG). They found that the more efficient is the accretion, the less dense is the environment, suggesting that the latter would have a strong impact on the accretion regime.

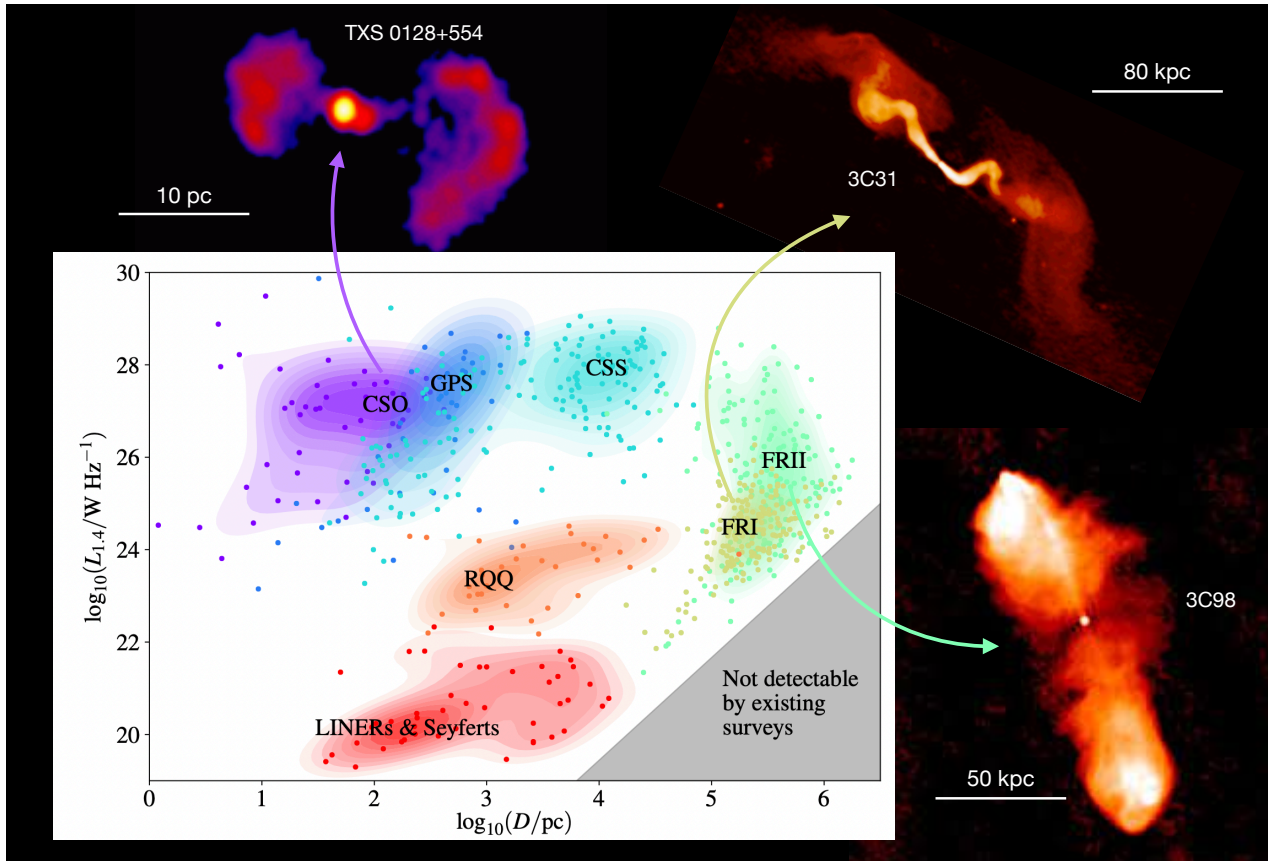


FIGURE 1.21: Categories and evolution of AGN. *Main panel*: plot of 1.4 GHz radio power versus linear-size for different types of AGN. The different classes of sources are color-coded. The filled contours show the space in the plot occupied by the different classes. In Section §1.3.2, we focus on GPS (Gigahertz Peaked Spectrum) and CSS (Compact Steep Spectrum), FR I and FR II radio galaxies. The “CSO” (Compact Symmetric Objects) class is composed of young radio sources with symmetric bipolar jets. The “LINER” (Low-Ionization Nuclear Emission-line Region) sources are star forming galaxies hosting inefficiently accreting AGN. FR 0s are not shown, but they occupy the space between RQQ (Radio Quiet Quasars) and FR Is (Baldi, 2023). Reproduced from Hardcastle and Croston (2020). *Top left inset*: VLBA image of the young radio galaxy TXS 0128+554 (Lister et al., 2020). *Top right inset*: VLA image of the FR I radio galaxy 3C31 (Credits: NRAO/AUI Archives). *Bottom right inset*: LOFAR image of the FR II radio galaxy 3C98 (Hardcastle and Croston, 2020).

The understanding of the different “flavors” of radio galaxies has changed over the decades, since the improvement in the sensitivity of radio observations has revealed the full complexity of jet activity. The advent of wide-field surveys in the optical and radio bands (SDSS¹, FIRST², NVSS³) allowed to investigate the population of radio galaxies in the mJy regime (e.g., Best and Heckman 2012): these observing programs have detected $\sim 18,000$ radio galaxies with radio fluxes at 1.4 GHz higher than 5 mJy.

¹Sloan Digital Sky Survey, e.g., Fukugita et al. (1996).

²Faint Images of the Radio Sky at Twenty centimetres survey, Becker et al. (1995).

³National Radio Astronomy Observatory Very Large Array (VLA) Sky Survey, Condon et al. (1998).

Surprisingly, the bulk of radio galaxies in the Local Universe ($z < 0.05$) is dominated by low-luminosity, compact objects characterized by a paucity of extended radio emission (unresolved at the 5" FIRST resolution); for this reason, they were named Fanaroff-Riley Type 0 radio galaxies (FR 0s, Baldi et al. 2015). These radio galaxies are associated with red massive elliptical galaxy, with a high mass black hole ($M_{\text{SMBH}} \geq 10^8 M_{\odot}$), and spectroscopically classified as low excitation radio galaxy. The similarities with FR Is extend also to the accretion rate of these sources, which suggest that a radiatively inefficient accretion flow is at work in FR 0s. The essential ingredient to distinguish FR 0s from typical extended FR I radio sources is that FR 0s lack extended radio emission (at the 5" resolution of the FIRST radio survey). In fact, VLA observations with a resolution of $\approx 0.2''$ at GHz frequencies have revealed that the majority ($\sim 80\%$) of FR 0s remains compact below ~ 1 kpc (Baldi et al. 2019a). At lower frequencies, the search for extended emission has been performed by Capetti et al. 2020, who observed a sample of 104 FR 0s with LOFAR⁴ and reached analogous conclusions.

Several works showed that FR 0s are not young radio galaxies (Capetti et al., 2019), are not beamed objects (Torresi et al., 2018), and are not simply fading FR Is (Capetti et al., 2020). It has been proposed by Baldi et al. (2015) that the external medium of FR 0s could possess peculiar features (density, clumpiness) capable of decelerate and eventually disrupt the relativistic jets. However, the optical host magnitudes of FR 0s (which give an indication of the density) are similar to those of FR Is, suggesting that the galaxy-scale ISM environment might not be the answer. The hot halo of the galaxy ($10^6 - 10^7$ K) corona could also be responsible for the jet disruption, but the analysis of the hot halo of an FR 0-hosting galaxy has not been undertaken yet (Torresi et al., 2018). Alternatively, FR 0 radio galaxies may be compact due to an intrinsic jet weakness: slow jets, possibly originating from slowly spinning black holes, could fade at progressively larger distances from the core, thus leading to the small size (Baldi et al. 2019b and references therein). Indeed, VLBI observation of FR 0s revealed quickly decelerating jets (Cheng and An, 2018; Cheng et al., 2021), while FR I jets can be relativistic up to tens of kpc from the core (e.g., Bridle and Perley 1984). Up to now a final answer to the nature of FR 0s has not yet been found; it is possible that many mechanisms are at play, with a possible strong connection between black hole properties and ambient density: slowly spinning SMBH could produce quickly decelerating jets, which in turn might be easily disrupted by the environment (Baldi et al., 2019b).

1.3.2 The life-cycle of radio galaxies: transitory, repetitive, and directional activity

The investigation of AGN footprints in clusters and groups (i.e., X-ray cavities and shock fronts) highlights several properties of SMBH activity. Namely, the observation of multiple bubbles in many systems reflects the *transitory* and *repetitive* nature of radio activity in central galaxies. Many systems have several pairs of cavities at increasing distance from the center (from a few kpc to $\sim 10^2$ kpc), with each pair related to an outburst that lasted around 10^7 yr (e.g., Birzan et al. 2004; Fabian et al. 2005; Dunn et al. 2005; Wise et al. 2007; Babul et al. 2013; Hlavacek-Larrondo et al. 2015; Randall et al. 2015; Biava et al. 2021). Second, the AGN activity is *directional*, since bipolar jets are driven in specific and opposite directions by the SMBH. In this context, older and younger pairs of X-ray cavities can be either aligned or misaligned, supporting the idea that the jet can change their orientation over time (e.g., Falceta-Gonçalves et al. 2010; Chon et al. 2012; Babul et al. 2013; Schellenberger et al. 2021). In this subsection, we outline the current knowledge on the transitory, repetitive, and directional nature of AGN activity from the point of view of radio observations.

⁴Low Frequency ARray, van Haarlem et al. (2013).

How radio galaxies evolve over time: newly-born, fading, and restarting sources

Radio galaxies can be observed at different stages of their evolution over time. We refer to the evolutionary scheme reported in Fig. 1.21 (from Hardcastle and Croston 2020), where we also show examples of different classes of radio galaxies. After the SMBH is triggered, radio jets start expanding in the host galaxy and reach sizes that can vary between a few pc and a few kpc. Sources observed at these stages form the class of “young radio sources” (O’Dea, 1998; Orienti, 2016), and are often thought to be the earliest stages of full-fledged, extended radio galaxies (e.g., Fanti et al. 1995). The radio spectrum of these small radio galaxies has a curved shape, with a peak frequency that inversely scales with the source size (e.g., Dallacasa et al. 1995; Dallacasa et al. 2000; Orienti 2016). Depending on the position in the spectrum of the peak frequency, ν_p , young radio galaxies are subclassified as Gigahertz Peaked Spectrum (GPS) and Compact Steep Spectrum (CSS) sources. If the peak is found at frequencies ≤ 100 MHz, the source is classified as a CSS radio galaxy (extended for a few kiloparsecs and typically $\leq 10^5$ yr old); a peak around GHz frequencies identifies a GPS source, with a largest linear size of less than 1 kpc and an age of $\leq 10^3$ yr (see e.g., O’Dea 1998; Orienti 2016; Sadler 2016; O’Dea and Saikia 2021).

If the SMBH activity lasts long enough, or the jets have enough stability so that the young radio galaxy can continue to grow (see the case of FR 0s in §1.3.1), then the jets start expanding outside the host galaxy and reach the surrounding medium (e.g., Morganti 2017; Hardcastle and Croston 2020). Depending on the time at which the source is observed, the properties of the ambient medium, and the collimation of the jets, the radio galaxy can reach sizes that vary between a few tens - hundreds of kpc (classical FR I and FR II sources) and a few Mpc in the most extreme cases (“giant radio galaxies”, see e.g., Dabhade et al. 2023 for a recent review). The integrated radio spectrum of full-fledged radio galaxies is generally steep, with $1 \lesssim \alpha \lesssim 1.5$ (e.g., Konar et al. 2006; McKean et al. 2016). If the lobes are resolved, then spectral gradients may appear: in FR II radio galaxies, for example, the hotspots (sites of the most recent acceleration of particles) have a flatter spectral index, close to the “injection” (i.e. initial, Γ) value $\alpha \approx \Gamma = 0.5 - 0.8$ (e.g., Harwood et al. 2015). Typically, the farthest from the site of acceleration (hotspots in the case of FR II sources, jets in the case of FR I sources), the steeper is the local spectral index (e.g., O’Dea et al. 2009). This can be explained by considering that relativistic particles start to age and to emit at lower frequencies. The spectrum of ageing radio lobes has thus the form of a broken power-law, with spectral index close to the injection value below the break frequency, ν_b , and steeper than Γ at $\nu > \nu_b$.

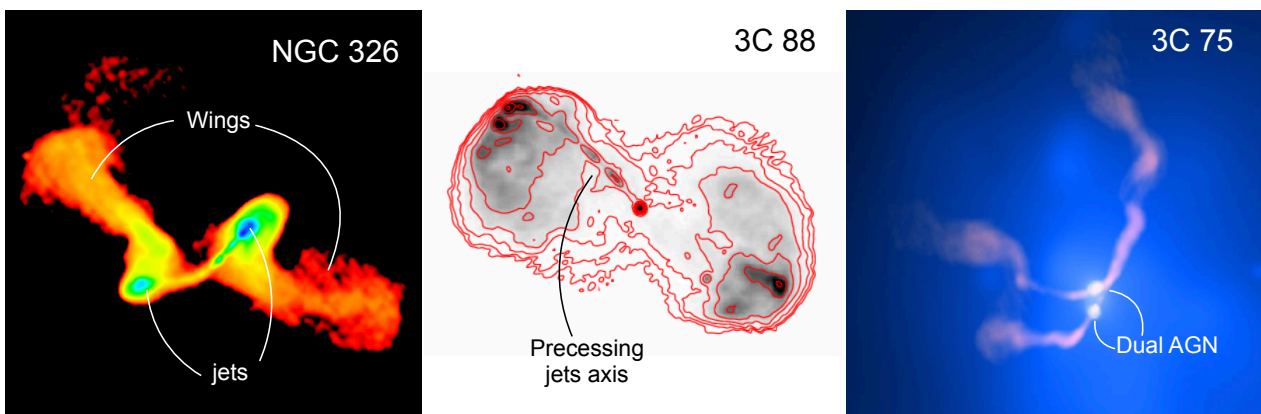


FIGURE 1.22: Examples of changes in the orientation of the jet axis, with labels for the different features. *Left panel:* the X-shaped radio galaxy NGC 326 (Murgia et al., 2001). *Middle panel:* the precessing jets of the radio galaxy 3C 88 (Liu et al., 2019b). *Right panel:* the dual AGN (separation of ~ 7 kpc) in the radio galaxy 3C 75 (Hudson et al., 2006).

The source powering the radio lobe expansion, that is the central engine, can turn off (or greatly reduce its ability to collimate relativistic jets) after a few tens of Myr (Shabala et al., 2008; Turner and Shabala, 2015). Sources in this phase (referred to as dying radio galaxies, Murgia et al. 2011)

show steeper spectra as they fade into the ambient medium, becoming almost invisible at high frequencies and usually assuming an amorphous shape. However, there are cases in which the SMBH goes through a new cycle of jet activity before the previous outbursts fades (Saikia and Jamrozny 2009 for a review). Observationally, this can result in multiple pairs of radio lobes, with the oldest, most distant pairs having a steeper radio spectrum (e.g., Shabala et al. 2020). Restarted radio sources are useful probes to understand the mechanisms responsible for jet triggering, and inferring the efficiency at which SMBHs accrete material and drive relativistic, collimated outflows (e.g., Hardcastle and Croston 2020; Turner and Shabala 2023). In the context of feedback, investigating the so-called “duty-cycle” (the fraction of time that a radio source is *on*) can reveal which environmental condition need to be balanced by a repetitive jet activity (e.g., Shabala et al. 2020).

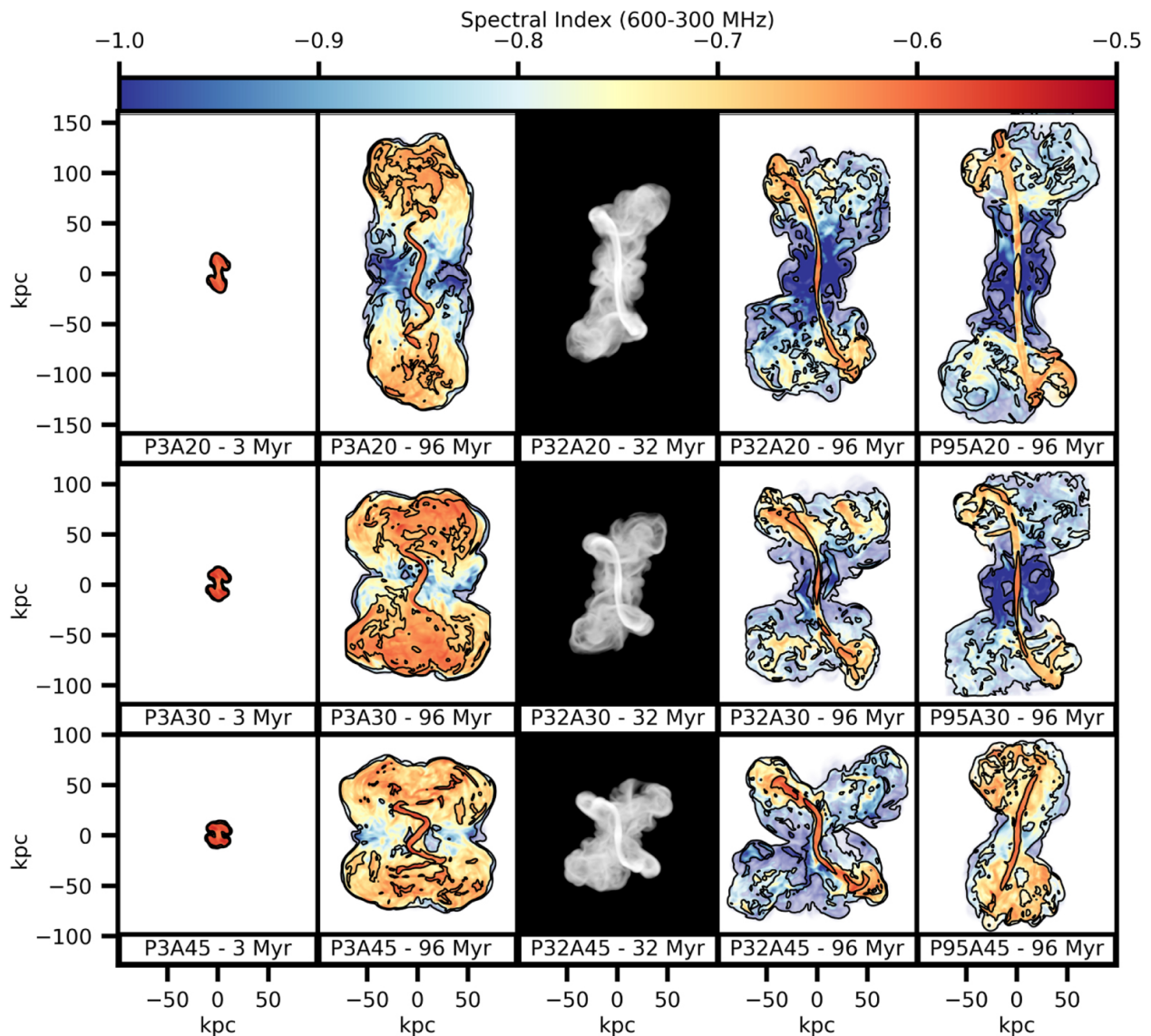


FIGURE 1.23: Simulations of jet precession. Columns 1, 2, 4, and 5: radio spectral index with 300 MHz radio brightness contours (from the image shown in column 3). Each row shows simulations with different precession angles (row 1: 20°, 3: 30°, and 4: 45°). The columns show simulations with differing precession periods, or the same simulations at different times (see Nolting et al. (2023) for details). Note how different precession angles produce an S-shaped or X-shaped morphology, and that the wings have steeper spectral indices with respect to the jet. Adapted from Nolting et al. (2023).

Jet reorientation in the most massive radio galaxies

A clear feature of AGN activity traced by restarted radio galaxies is the directionality of the successive outbursts. In several cases, older and younger radio lobes and jets are aligned along a common axis, suggesting that the jet has been pointing in a similar direction through the successive repetition of jet propagation. Radio galaxies of this kind were defined as “double-double” sources, to convey the observational evidence of concentric and aligned double pairs of lobes (e.g., Lara et al. 1999; Shabala et al. 2008; Orrù et al. 2015; Mahatma et al. 2019).

In other cases, evidence that the jet direction can also change over time was found. Indications of such changes were already found in early works, by testing the alignment of large scale lobes and parsec-scale jets (e.g., Pearson and Readhead 1988; Wehrle et al. 1996). These studies found that $\sim 40\%$ of the sources showed a $\sim 90^\circ$ misalignment between the kpc and pc scale signatures of jet activity. The first investigations of changes in jet orientation were undertaken by studying the so-called “X-shaped” radio galaxies, where two pairs of misaligned lobes are observed (Leahy and Williams, 1984; Leahy and Parma, 1992; Bruno et al., 2019). Usually, these objects exhibit a pair of bright, primary jets (with a relatively flat spectral index), and a pair of fainter, secondary wings (with a relatively steep spectral index; see the example in Fig. 1.22, *left panel*, and the simulations shown in Fig. 1.23). Besides these peculiar sources, a variety of others have so far questioned the idea that SMBH-driven jets are stable, straight, linear outflows. For instance, high-resolution radio observations revealed that even single pairs of jets can show signatures of wobbling of the jet axis (see Fig. 1.22, *middle panel*). An S-shaped or Z-shaped morphology describes the curvature or sharp bending of the jet axis (e.g., Lister et al. 2003; Giroletti et al. 2005; Rubinur et al. 2017). In other cases, multiple *active* jets have been observed propagating from a galaxy’s core (see Fig. 1.22, *right panel*; e.g., Hudson et al. 2006; Gitti et al. 2006; Gitti et al. 2013).

Multiple scenarios have been invoked to explain these different cases. In the case of X-shaped radio galaxies, it has been proposed that wings represent an older episode of AGN activity in a different direction (Dennett-Thorpe et al., 2002; Liu, 2004). Alternatively, backflow of the primary lobe plasma may be diverted depending on the pressure structure of the ambient gas, thus producing misaligned wings (e.g., Kraft et al. 2005; Hodges-Kluck and Reynolds 2011). A third possibility is that the lobes and wings are formed independently by two active binary SMBHs (Lal and Rao, 2007; Lal et al., 2019). This latter scenario can also explain the – so far extremely rare – observations of multiple pairs of jets ejected from a compact region (see e.g., the case of 3C 75, Hudson et al. 2006). Ultimately, jets can experience geodetic precession over time (e.g., Fendt and Yardimci 2022). This mechanism is thought to be occurring in a large number of radio galaxies (see e.g., Krause et al. 2019, who found a fraction of $\sim 70\%$ of precessing jets in a complete sample of 3C radio galaxies). Under favorite combination of jet precession angle and inclination of the jet axis to the line of sight, an X-shaped or S-shaped morphology may appear (see Fig. 1.23 for an example of numerical simulations of precession; see also the modeling of Giri et al. 2022; Lalakos et al. 2022; Nolting et al. 2023). Precession may also naturally explain the S-shaped morphology of jets (see the cases of e.g., Hydra A Taylor et al. 1990, Cygnus A, Steenbrugge and Blundell 2008; Horton et al. 2020).

Overall, it is yet unclear if one of the above scenarios can univocally explain the radio signatures of the changes in jet axis. Combination of different mechanisms may be invoked. For instance, binary SMBHs are predicted to cause jet precession in the active SMBH due to the gravitational interaction of the binary (e.g., Begelman et al. 1980). Following Krause et al. (2019), the geodetic precession of the black hole spins in a binary system can cause precession of the jets ejected along the spin axis of one of the black holes. Assuming that the binary is in a circular orbit, then the jet precession period, P (in units of Myr), for binary SMBHs with total mass M_9 (in units of $10^9 M_\odot$), mass ratio r_M , and separation d_{pc} (in units of parsecs) is given by (e.g., Barker and O’Connell 1975; Stairs 2003; Krause et al. 2019):

$$P = 124 \frac{(1 + r_M)^2}{3r_M^2 + 4r_M} d_{pc}^{5/2} M_9^{-3/2} \text{ [Myr]}. \quad (1.35)$$

The above equation indicates that binary separations ranging between 0.1 pc and 1 kpc will produce jet precession with a period of $10^6 - 10^8$ yr, for typical SMBH masses and mass ratios (see e.g., Krause et al. 2019; Horton et al. 2020; Horton et al. 2023). In addition, a merger of binary SMBHs may lead to a *spin flip* of the merged, more massive SMBH, which would drive jets in a perpendicular direction with respect to the previous outburst (e.g., Merritt and Ekers 2002). The latter case would explain the jet reorientation events characterized by $\sim 90^\circ$ misalignment between the successive outbursts.

In the absence of binary SMBHs, explaining precession or extreme jet-reorientation can be non-trivial (e.g., Schellenberger et al. 2021). Several works have invoked the role of the AGN feeding in influencing the jet direction. For instance, the accretion disk may produce instabilities that precession (e.g., the Lense-Thirring or Bardeen-Petterson effects, Bardeen and Petterson 1975). In this case, if the angular momenta of the disk and of the SMBH are misaligned, then the momentum misalignment would induce a precession of the jet axis. Alternatively, if the disk is re-formed before each outburst, its new orientation may influence the direction of the next pair of jets (e.g., Babul et al. 2013; Gaspari et al. 2018; Soker 2022). However, the above scenario would require the disk to partially contribute to the jet collimation (thus its axis), which is a topic of debate (e.g., Komissarov 2012; Globus and Levinson 2016; Boccardi et al. 2021a). Further observational, numerical, and theoretical investigation is required to address the question of how jets change their orientation over time. Not only the involved spatial scales are extremely difficult to be resolved by observations; there is also a lack of general consensus on physics of accretion, collimation and ejection (e.g., Boccardi et al. 2017; Blandford et al. 2019; Boccardi et al. 2021b; Perucho and López-Miralles 2023).

Chapter 2

How AGN feedback is onset: young radio galaxies in cool core clusters

Abstract

¹The investigation of the feedback cycle in galaxy clusters has historically been performed for systems where feedback is ongoing (“mature-feedback” clusters), that is where the central radio galaxy has pushed aside the ICM. In this Chapter, we present our pilot investigation of “pre-feedback” clusters, defined as objects where the central newly active radio galaxies (age $< 10^3$ yr) may not yet have had time to alter the thermodynamic state of the ICM. We analyze *Chandra* and MUSE observations of two such systems, evaluating the hot gas entropy and cooling time profiles, and characterizing the morphology and kinematics of the warm gas. Based on our exploratory study of these two sources, we find that the hot gas meets the expectations for an as-yet unheated ICM. Specifically, the entropy and cooling time of pre-feedback clusters within 20 kpc from the center fall below those of mature-feedback clusters by a factor ~ 2 . We speculate that with an estimated mechanical power of $\sim 10^{44} - 10^{45}$ erg s^{-1} , the two young radio galaxies may restore the entropy levels in a few tens of Myr, which are typical values of power outbursts and lifetimes for radio galaxies in clusters. Conversely, the properties of the gas at $\sim 10^4$ K seem to remain invariant between the two feedback stages, possibly suggesting that the warm gas reservoir accumulates over long periods ($\sim 10^7$ yr) during the growth of the radio galaxy.

2.1 Motivation

The heating and cooling balance in galaxy clusters has historically been investigated in systems where feedback from AGN is currently regulating the thermodynamics of the ICM (e.g., Bîrzan et al. 2004; O’Sullivan et al. 2011; Eckert et al. 2021; Donahue and Voit 2022). In particular, the well-established feedback cycle paradigm predicts that AGN prompt a deposition of energy in their surroundings, preventing an over-cooling of the gas that fuels their engine; when the AGN shuts down, the ICM starts cooling again.

A potential conundrum is that the above picture was drawn from systems where feedback is already ongoing, whereas the conditions that lead to its *onset* are unknown. A natural solution would be to investigate systems that are right around the point of triggering feedback, as soon after the AGN jets start up as possible. The class of young radio galaxies (GPS and CSS, see e.g., O’Dea 1998; Orienti 2016; Sadler 2016; O’Dea and Saikia 2021; see also §1.3.2) meets this requirement, but only a handful of studies on these sources in clusters exists. Specifically, given the short duration of the young AGN phase, and the fact that studies of feedback in clusters typically target extended radio galaxies, there is a paucity of BCGs in cool core clusters with known central GPS or CSS sources.

¹This Chapter is based on Ubertosi et al. (2023c).

An example is given by the CSS source 1321+045, recently studied by O’Sullivan et al. (2021). The authors found that despite having low central entropy and cooling time (9 keV cm^2 and 390 Myr within 8 kpc), the overall properties of the host cluster are similar to those of other objects with extended central AGN. However, the CSS source 1321+045, having a size of 16 kpc , might have already influenced the surrounding ICM. This Chapter presents our investigation of the onset of feedback in even younger, smaller sources, the GPS radio galaxies.

2.2 Selection of objects and data reduction

2.2.1 A list of “pre-feedback” galaxy clusters

We select targets from the sample of 760 cluster central radio galaxies by Hogan et al. (2015a) and Hogan et al. (2015b) by choosing objects with a peaked radio spectrum, typical of GPS sources. Furthermore, we exclude sources with additional power-law components at MHz frequencies to avoid restarted sources (i.e. young AGN embedded in large-scale radio emission from a previous outburst, see e.g., Morganti et al. 2021). This selection returns a list of five systems, listed in Tab. 2.1. Such a small fraction of young AGN in clusters with respect to the parent sample ($5/760$ objects, $\sim 0.6\%$) is not surprising: as the GPS stage is short ($\sim 10^4 \text{ yr}$) compared to the typical age of radio galaxies ($\sim 10^7 \text{ yr}$), then the relative duration of the GPS stage is expected to be only 0.1% . As such, the selected five radio galaxies provide the current best chance to maximize our knowledge on the ICM properties of galaxy clusters whose dominant galaxies have just turned on their central engine.

Out of the objects listed in Tab. 2.1, here we focus on RX J1350+0940 and CIG J0242-2132, which are the only ones with deep enough X-ray (*Chandra*) and optical (MUSE) data to assess the hot and warm gas properties in the inner 20 kpc , where cooling and feedback are typically at play.

The AGN in the two clusters have the typical radio spectrum of GPS sources, peaking at a rest-frame frequency of $\nu_p = 3.9 \text{ GHz}$ and of $\nu_p = 0.8 \text{ GHz}$, respectively (Hogan et al., 2015b). Both radio galaxies in RX J1350+0940 and CIG J0242-2132 are unresolved on arcsecond (kpc) scales (Kozieł-Wierzbowska et al. 2020 and Hogan et al. 2015b, respectively), and reveal small extension only on milli-arcsecond (pc) scales (Hogan et al., 2015b). Assuming a typical magnetic field of a few μG (e.g., Govoni and Feretti 2004), the non-detection of extended emission at MHz frequencies implies a timescale of at least 10^8 yr since the last radio activity (e.g., Shulevski et al. 2017). Information on the pc-scale properties of both sources are available from the VLBA Calibrator List Tool²: at 2.3 GHz , the AGN in RX J1350+0940 has a largest linear size (LLS) of 90 pc , while that in CIG J0242-2132 has a LLS of 200 pc . Assuming an expansion speed of $0.2 c$ (e.g., Giroletti and Polatidis 2009), the implied kinematic ages are $t_{kin} \sim 700 \text{ yr}$ and $t_{kin} \sim 1600 \text{ yr}$, respectively (see Tab. 2.1).

To identify any peculiarity of these “pre-feedback” clusters, we need to compare our results with the general population of “mature-feedback” clusters. We use the “pre-feedback” term to describe the systems where the central radio galaxy extends on sub-kiloparsec scales and is young enough that no cavities or shocks can have impacted the ICM, while we use the “mature-feedback” term to describe systems where the kpc-scale lobes of the central AGN extend into the ICM, pushing aside the gas. We adopt the ACCEPT sample of Cavagnolo et al. (2009) as representative of the average properties of mature-feedback systems. To restrict the comparison to systems that are comparable to RX J1350+0940 and CIG J0242-2132 in terms of mass and dynamical state, we select the ACCEPT systems with an average temperature $\geq 2 \text{ keV}$ (thus avoiding galaxy groups and elliptical galaxies, e.g., Lovisari et al. 2021) and a central entropy $\leq 30 \text{ keV cm}^2$ (to consider only objects with a cool core).

²<https://obs.vlba.nrao.edu/cst/>; Charlot et al. 2020.

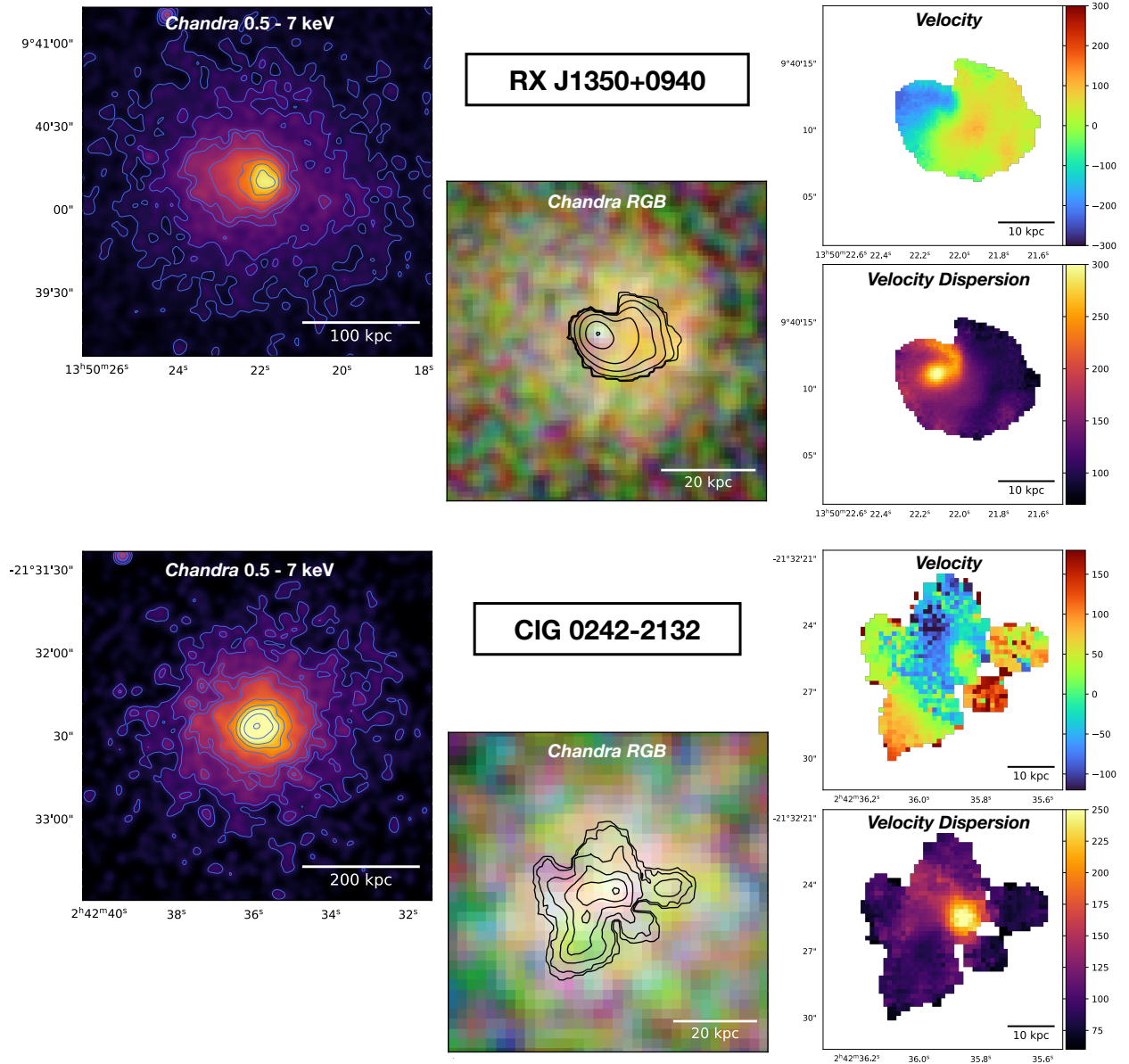


FIGURE 2.1: *Chandra* and MUSE images of the pre-feedback clusters analyzed in this Chapter. For each object, we show in the *left panel* a *Chandra* image (background-subtracted and exposure-corrected) in the 0.5–7 keV band of the large-scale ICM emission. Contours start from the peak of the X-ray emission and decrease in steps of factor two. The images have been smoothed with a Gaussian of $\sigma = 3$ pixels. The *middle panel* shows a RGB *Chandra* image of the central region of each cluster, with the bands 0.3–1.2, 1.2–2.5 and 2.5–7.0 keV shown in red (R), green (G) and blue (B), respectively. Overlaid in black are the total intensity $H\alpha$ contours from the MUSE data. In the *right panels* we show the warm gas kinematics (top) and velocity dispersion (bottom).

2.2.2 Data reduction

The cluster RX J1350+0940 has been observed with *Chandra* for 20 ks (ObsID 14021), while the cluster CIG J0242-2132 has been observed with *Chandra* for 12 ks (ObsID 3266). The data have been reprocessed with CIAO-4.14 and CALDB-4.9.7, using standard data reduction techniques³. Point sources were masked during the analysis. Periods of background flaring were excluded from the data, and scaled blank-sky event files were used to create background spectra. Exposure-corrected,

³See <https://cxc.cfa.harvard.edu/ciao/threads/>.

TABLE 2.1: List of galaxy clusters hosting a young central radio galaxy. The two objects in the gray rows are the focus of this analysis. (1) Object name; (2) Right Ascension; (3) Declination; (4) redshift; (5) conversion between physical and angular scales at the object’s redshift; (6) rest-frame peak frequency (from Hogan et al. 2015b); (7) largest linear size from VLBA data (see Charlot et al. 2020); (8) kinematic age of the source ($LLS/2v$) assuming an expansion speed of $v = 0.2c$.

Object	RA	DEC	z	kpc/''	ν_p [GHz]	LLS [pc]	t_{kin} [yr]
Abell 1885	14:13:43.73	+43:39:45.0	0.088	1.6	2.5	22	170
RX J1350+0940	13:50:22.1	+09:40:10.6	0.133	2.4	3.9	90	700
RX J0132-0804	01:32:41.1	-08:04:06	0.148	2.6	0.1	37	290
RX J2341+0018	23:41:6.8	+00:18:34.1	0.277	4.2	0.4	270	2100
CIG J0242-2132	02:42:35.9	-21:32:26	0.314	4.6	0.8	200	1600

background-subtracted X-ray images of the two clusters were extracted in different energy bands: a broad band image (0.5 – 7 keV) is shown in Fig. 2.1 (left panels); a soft band (0.3 – 1.2 keV), an intermediate band (1.2 – 2.5 keV), and a hard band (2.5 – 7 keV) image were combined to obtain an X-ray RGB map of the central regions (Fig. 2.1, middle panels).

To test the efficiency of ICM cooling from the *Chandra* data, we derived radial profiles of entropy, K , and cooling time, t_{cool} , through Eq. 1.3 and Eq. 1.11, respectively. To be consistent with the ACCEPT sample (Cavagnolo et al., 2009), the electron density was measured from a radial surface brightness profile. The temperature was determined by fitting a `projct*tbabs*apec` model to the spectrum of concentric annuli (centered on the AGN coordinates, see Tab. 2.1) with at least 1000 counts in each bin. The central 1.5'' were excised to avoid contamination from the nuclear X-ray point source found in both clusters. The temperature profile was interpolated on the grid of the density profile to obtain the gas entropy and cooling time profiles in 1.5''- wide annular rings. Testing other methods to derive these quantities provided consistent results (see Appendix A).

These two objects have also been observed with the Very Large Telescope using the Multi-Unit Spectroscopic Explorer (MUSE) integral-field spectrograph (IDs 0104.A-0801 and 0100.A-0792, for RX J1350+0940 and CIG J0242-2132, respectively). The MUSE data were reduced using the MUSE pipeline 2.8.5 (Weilbacher et al., 2014) and the EsoRex command-line tool, to obtain information on the warm gas component surrounding the BCG. We fitted the data following the same method described by Olivares et al. (2019). The average seeing is 1.5'' for RX J1350+0940 and 0.6'' for CIG J0242-2132.

2.3 Results

2.3.1 ICM morphology and warm gas kinematics

We show in Fig. 2.1 a multi-scale, multi-wavelength view of the two objects. The *Chandra* image of the cluster RX J1350+0940 reveals an asymmetric ICM distribution, with a surface brightness edge west of the center. The RGB image in the middle panel confirms this asymmetry, showing that the brightest part of the ICM is primarily located west of the central AGN. The MUSE $H\alpha$ total intensity contours display an extended spiral morphology (with a $LLS \sim 20$ kpc), co-spatial with the X-ray brightest region of the ICM. The total luminosity of the $H\alpha$ line is $L_{H\alpha} = 9.6 \times 10^{41}$ erg s $^{-1}$. These asymmetric structures suggest that the hot and warm gas distributions have been subject to sloshing (see e.g., Kokotanekov et al. 2018). The velocity structure of optical emitting gas of RX J1350+0940 reveals a clear gradient from -200 to $+30$ km s $^{-1}$ from NW to NE of the central

galaxy. The velocity dispersion, σ_{gas} , peaks with 300 km s^{-1} at the position of the BCG and decreases from 250 km s^{-1} to 90 km s^{-1} along the sloshing spiral.

The cluster ClG J0242-2132 shows a rather symmetric morphology from the large-scale *Chandra* image and the RGB zoom-in (Fig. 2.1). The 0.3 – 1.2 keV ICM is evenly distributed around the central AGN, and the warm gas phase traced by the $\text{H}\alpha$ contours has a filamentary structure extending roughly equally in all directions. The total luminosity of the $\text{H}\alpha$ line is $L_{\text{H}\alpha} = 1.7 \times 10^{42} \text{ erg s}^{-1}$. The optical data reveal several radial filaments across the whole azimuth, with $\text{LLS} \sim 40 \text{ kpc}$ and a chaotic velocity field. The velocity dispersion is high, $>120 \text{ km s}^{-1}$, on the region to the NW of the central BCG, likely due to several unresolved filaments overlapping along the line of sight. The rest of the filaments show a velocity dispersion that is on the order of 80 km s^{-1} .

Overall, the extent and morphology of the warm gas in the two objects are similar to those of filaments in mature-feedback BCGs (see e.g., Tremblay et al. 2018; Olivares et al. 2019; Ciocan et al. 2021). The similarity is also evident from the warm gas kinematics. In particular, the cluster ClG J0242-2132 has an average σ_v ($\sim 100 \text{ km s}^{-1}$, excluding the inner 2 kpc) that is similar to that of ten BCGs in mature-feedback clusters observed with MUSE, where $\langle \sigma_v \rangle \sim 110 \text{ km s}^{-1}$ (Olivares et al., 2019). The warm gas in RX J1350+0940 has a slightly larger velocity dispersion along the filaments of 130 km s^{-1} , but still close to the average of the ten BCGs.

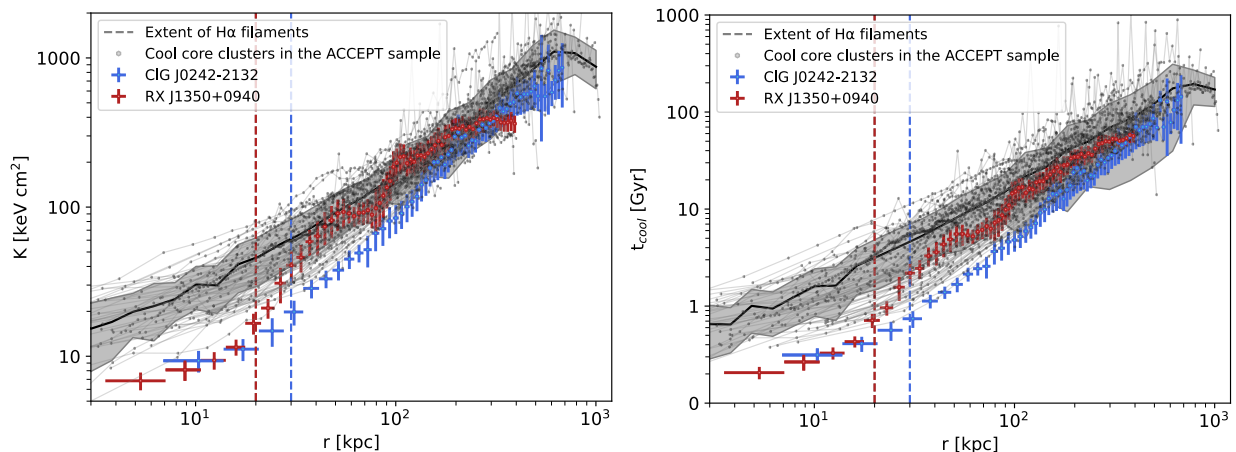


FIGURE 2.2: Profiles of ICM entropy (left) and cooling time (right) for the ACCEP cool core clusters with $kT \geq 2 \text{ keV}$ are plotted in gray, while those of the pre-feedback clusters ClG J0242-2132 and RX J1350+0940 are over-plotted in blue and red, respectively. The black line and the shaded gray area represent the average profile and the scatter of the ACCEP clusters, respectively. See 2.3.2 for details.

2.3.2 ICM entropy and cooling time profiles

We show in Fig. 2.2 the entropy and cooling time radial profiles obtained from the *Chandra* data for the clusters ClG J0242-2132 and RX J1350+0940, and we over-plot the profiles of the ACCEP cool core clusters, the average ACCEP profile and its scatter (see 2.2; Cavagnolo et al. 2009).

We note that at large radii (especially above $\sim 100 \text{ kpc}$), the profiles of both clusters are consistent with those of the clusters in the ACCEP sample. However, in the inner few tens of kpc the profiles deviate from those of mature-feedback clusters, displaying lower entropy and cooling time (see Fig. 2.2). Interestingly, for both clusters, the extent of the $\text{H}\alpha$ filaments approximately traces the region where such deviation occurs (vertical lines in Fig. 2.2). The average entropy of mature-feedback clusters in the inner 20 kpc is $K^{\text{ACC}} = 28.5 \pm 14.0 \text{ keV cm}^2$, while that of the two objects in our sample is $K^{\text{GPS}} = 10.4 \pm 1.9 \text{ keV cm}^2$ (the associated uncertainty is the scatter around the mean). The average cooling time of mature-feedback clusters for $r \leq 20 \text{ kpc}$ is $t_{\text{cool}}^{\text{ACC}} = 1.6 \pm 1.0 \text{ Gyr}$, while that of the two clusters in our sample is $t_{\text{cool}}^{\text{GPS}} = 0.4 \pm 0.2 \text{ Gyr}$. We attribute the radial undulation in the profiles of RX J1350+0940 to sloshing of the ICM (evident from the X-ray morphology of the

cluster, see 2.3.1). The profile of ClG J0242-2132 is smooth between 8 kpc to 500 kpc, and starts to deviate from the ACCEPT clusters at approximately 100 kpc from the center. We also note that RX J1350+0940 and ClG J0242-2132 have central cooling times of approximately 200 – 300 Myr at $r \sim 10$ kpc, which is of the order of the typical time that has passed since the last episode of AGN activity (see 2.2).

We note that there are two ACCEPT clusters with entropy profiles that resemble those of the two pre-feedback clusters in the inner 10s of kpc. The one whose entropy decreases around 10 kpc and crosses the profile of RX J1350+0940 at ~ 4 kpc is Abell 1991, whose central radio galaxy has been classified as a CSS radio source (see Hogan 2014). Thus, this source may potentially be similar to the CSS 1321+045 studied in O’Sullivan et al. (2021), and its decreasing profile may support our results on young radio sources in galaxy clusters. The other galaxy cluster is 2A0335+096 (e.g., Sanders et al. 2009). We observe that its profile is similar to those of the two young sources from large radii to ~ 10 kpc, but it seems constant between 1 – 10 kpc. Additionally, we point out that the cooling time profiles show a more marked difference, with the two pre-feedback clusters having the shortest cooling times within 20 – 30 kpc from the center.

Feedback from cluster central AGN is known to increase the entropy of the ICM gas due to the thermalization of mechanical energy, especially in the central regions of the cluster (e.g., Tozzi 2002; McNamara and Nulsen 2007; Pratt et al. 2010). The lower entropy (and cooling time) of the two pre-feedback clusters is highly suggestive that energy has not (yet) been deposited in the two clusters cores. To investigate this point, we derive the amount of energy required to boost the entropy of the two clusters to the values of the mature-feedback objects. This can be measured as $\Delta E = M_{\text{gas}} \Delta Q$, where M_{gas} is the gas mass within 20 kpc from the center and ΔQ is defined as (see e.g., Chaudhuri et al. 2012):

$$\Delta Q = \frac{kT(< r)}{(\gamma - 1) \mu m_p} \ln \left(\frac{K^{ACC}}{K^{GPS}} \right) \quad (2.1)$$

We derived $M_{\text{gas}} (\leq 20 \text{ kpc})$ by integrating the density profile over the spherical shells (see e.g., Voigt and Fabian 2006), finding $M_{\text{gas}} (\leq 20 \text{ kpc}) \approx 5 \times 10^{10} M_{\odot}$ for RX J1350+0940 and $M_{\text{gas}} (\leq 20 \text{ kpc}) \approx 10^{11} M_{\odot}$ for ClG J0242-2132. With $kT (\leq 20 \text{ kpc})$ of 2.1 keV and 2.6 keV for RX J1350+0940 and ClG J0242-2132, we find that an energy of $\Delta E \sim 6 \times 10^{59}$ erg and $\Delta E \sim 1.4 \times 10^{60}$ erg, respectively, is required to boost the entropy to the values of the mature-feedback sample. These are comparable to the typical outburst energy associated with X-ray cavities and shocks (e.g., Rafferty et al. 2006).

To determine if the AGN could supply these energies, we follow Wójtowicz et al. (2020) to estimate the jet power, P_j , of the two young radio galaxies. Using the linear size, age (see Tab. 2.1), and radio luminosity at 5 GHz of the AGN (9.1×10^{41} erg s⁻¹ for RX J1350+0940 and 1.3×10^{43} erg s⁻¹ for ClG J0242-2132), we find:

$$P_j \sim 2 \times 10^{44} \text{ erg s}^{-1} \text{ (RX J1350+0940)} \text{ and } P_j \sim 10^{45} \text{ erg s}^{-1} \text{ (ClG J0242-2132)}. \quad (2.2)$$

For comparison, using the mechanical power versus 1.4 GHz radio luminosity relation derived by O’Sullivan et al. (2011) (using full-fledged radio galaxies in clusters) we obtain:

$$P_j \sim 3 \times 10^{44} \text{ erg s}^{-1} \text{ (RX J1350+0940)} \text{ and } P_j \sim 2 \times 10^{45} \text{ erg s}^{-1} \text{ (ClG J0242-2132)}, \quad (2.3)$$

respectively, which are in agreement within a factor ≤ 2 from the previous estimate. As a note of caution, we observe that the two young sources, once grown to large sizes, may have a mechanical power that differs from these estimates, as the jet may vary in power depending on the surrounding medium that it crosses (e.g., Holt et al. 2011; Bicknell et al. 2018). We also note that these values were derived under the assumption that the 1.4 GHz radio luminosity of the young radio sources is

comparable to the 1.4 GHz radio luminosity of the galaxies for which the scaling between mechanical and radio power has been derived. While this assumption may not be completely justified, since radio luminosity is expected to change during the growth of a radio galaxy (e.g., Sadler 2016), we observe a relatively good agreement with the results based on Eq. 2.2.

To understand the balance between heating and cooling, we must take into account also the ICM radiative losses over the same volume. Indeed, while enhancing the entropy of the core, the mechanical energy deposited by the jets must also counteract the energy that is simultaneously radiated away by the X-ray emitting ICM (e.g., McNamara and Nulsen 2007). Such losses can be approximated by the bolometric X-ray luminosity of the two clusters within 20 kpc, that is $L_X (< 20 \text{ kpc}) = 1.4 \times 10^{43} \text{ erg s}^{-1}$ for RX J1350+0940 and $L_X (< 20 \text{ kpc}) = 1.5 \times 10^{44} \text{ erg s}^{-1}$ for ClG J0242-2132 from the *Chandra* data. To include this factor, we define a new quantity, the effective jet power P'_j as:

$$P'_j = P_j - L_X. \quad (2.4)$$

Using this quantity, we conclude that the AGN in both clusters could raise the central entropy *and* simultaneously balance the ICM radiative losses by supplying to the gas the ΔE estimated above in 50 - 90 Myr. Interestingly, these are typical timescales of activity for radio galaxies (Morganti et al., 2021).

Ultimately, to offer a possible comparison with simulations of AGN feedback, we observe that the fractional entropy difference within 20 kpc of $\frac{K^{ACC} - K^{GPS}}{K^{GPS}} = 1.7$ is consistent with the results of Gaspari et al. (2012a) that the fractional amplitude of entropy fluctuations through the different stages of AGN feeding and feedback is ~ 2 . We caution that this comparison is speculative, as the two pre-feedback clusters may not be perfectly described by the initial conditions in the simulations of Gaspari et al. (2012a) (set to those of Abell 1795).

2.4 Discussion

The X-ray analysis of the two pre-feedback clusters RX J1350+0940 and ClG J0242-2132 that host central newly active AGN ($\sim 10^3$ yr) revealed that the entropy and cooling time of the ICM within the central 20 kpc are different (by a factor 2–3) from those of mature-feedback ACCEPT clusters (see 2.3). For both the pre-feedback systems, the mechanical power of the young AGN seems tuned to match the magnitude of this difference, thus being able to lift the core entropy by a factor of 2 and counterbalance X-ray radiative losses in a few tens of Myr. Interestingly, such dichotomy in entropy and cooling time profiles was not found in the ≈ 2 Myr old CSS source 1321+04 (O’Sullivan et al., 2021). It is then possible that ICM heating in that cluster may have occurred rapidly, within the few Myr required for the radio galaxy to grow to size $\gtrsim 10$ kpc.

By contrast, we found that the warm gas phase traced by the MUSE data does not show any evolution between different stages of the feedback cycle. The morphological and spectral properties of the ICM in the two clusters considered here suggest that the warm gas is condensing out of the hot phase. According to Gaspari et al. (2018), this occurs when $t_{cool}/t_{eddy} \sim 1$. We computed the eddy timescale from Eq. 1.30. At a distance from the center of $r = 10$ kpc, assuming an injection scale $L = 20$ kpc (that is the extent of H α filaments, see Gaspari et al. 2018; Olivares et al. 2022b) and $\sigma_{3D} \sim \sqrt{3} \langle \sigma_v \rangle$, we measure $t_{cool}/t_{eddy} \sim 1.5$. Such value indicates that the criterion for the formation of multi-phase gas is met, and it is thus plausible that the warm gas originates from condensation of the hotter cluster gas. Therefore, the hot and warm phases seem related, given their similar morphology (see 2.3.1) and the thermodynamic link.

On the other hand, since the hot gas properties differ between pre- and mature-feedback clusters, the warm and hot phases follow different evolutionary paths. This may suggest that the warm gas tank could have been inherited from a previous cycle of cooling and heating (at least 10^8 yr ago, see 2.2). If the filaments were old (the typical survival time may be a few 10^8 yr, e.g., Fujita et al. 2022)

we would expect turbulence to have been partially dissipated, hence a low σ_v ($\leq 50\text{--}100\text{ km s}^{-1}$). This is the contrary of what we measure, suggesting that the filaments have recently condensed out of the hot halo. As a note of caution on this turbulence-based interpretation, we observe that turbulence may be dissipated on longer timescales, and that other mechanisms (besides AGN feedback) can maintain a high level of turbulence in the multi-phase gas (e.g., sloshing in RX J1350+0940). Overall, it is possible that a residual tank of relatively turbulent, centrally-concentrated warm gas is always present, and that new, external filaments condense out of the ICM at each cooling episode. Such scenario is consistent with the simulations of e.g., Li et al. (2015).

Based on our exploratory results on RX J1350+0940 and ClG J0242-2132, we hypothesize that at each feedback cycle the onset of heating may proceed as follows (see for comparison e.g., Gaspari et al. 2011; Li et al. 2015; Weinberger et al. 2022). At the end of the last major episode of AGN activity the ICM starts cooling again, and over a few 10^8 yr the entropy and cooling time of the gas in the inner tens of kpc decrease to roughly half the values measured in mature-feedback clusters, where feedback is ongoing. The low-entropy and short-cooling time ICM condenses into a network of filaments. Multi-phase gas fuels the AGN, that drives jets with high enough mechanical power to increase the central ICM entropy. After $\sim 10^3$ yr (the current state of RX J1350+0940 and ClG J0242-2132) the ICM has still relatively low entropy and cooling time, as the radio galaxy has not yet deposited energy outside $r \sim 1$ kpc, and condensation of the ICM into warm gas proceeds. In a few 10^7 yr (but possibly as low as a few 10^6 yr, as in the CSS source 1321+04, O'Sullivan et al. 2021), the entropy of the core has increased to the values observed in mature-feedback clusters. The warm gas filaments are still observable as the ICM continues to replenish the warm gas tank, with mechanical uplift by radio lobe expansion likely stimulating further ICM condensation (e.g., Revaz et al. 2008; Brighenti et al. 2015). These hypotheses may be confirmed by undertaking a similar analysis of a larger sample of other pre-feedback galaxy clusters.

2.5 Conclusions

In this Chapter we presented an exploratory study on the onset of AGN feedback in galaxy clusters. We used *Chandra* and MUSE observations to investigate the ICM and warm gas properties in two cool core galaxy clusters (ClG J0242-2132 and RX J1350+0940) hosting young central radio galaxies (age $\sim 10^3$ yr) classified as GPS sources. Here we summarize our results:

1. The average ICM entropy and cooling time in the inner 20 kpc of the two pre-feedback clusters ($10.4 \pm 1.9\text{ keV cm}^{-2}$, $0.4 \pm 0.2\text{ Gyr}$) are lower than those measured in mature-feedback systems ($28.5 \pm 14.0\text{ keV cm}^{-2}$, $1.6 \pm 1.0\text{ Gyr}$). The entropy of the former could be boosted to match that of the latter by injecting an energy of $\Delta E \approx 10^{59-60}$ erg. Considering our tentative estimate of the mechanical power of the two young radio galaxies ($10^{44} - 10^{45}\text{ erg s}^{-1}$), such energy injection may be achieved in a few tens of Myr, a reasonable timescales of activity for radio galaxies.
2. The MUSE data reveal warm gas surrounding the BCG and extended for 20 - 30 kpc in radius, likely condensing from the hot ICM. In terms of spatial extent and kinematics, the line-emitting gas in pre-feedback clusters is similar to that observed in mature-feedback objects (the average σ_v is $\sim 100\text{ km s}^{-1}$ in ClG J0242-2132, $\sim 130\text{ km s}^{-1}$ in RX J1350+0940, and $\sim 110\text{ km s}^{-1}$ in 10 mature-feedback clusters, see 2.3.1). The maximum extent of the warm gas filaments approximately traces the radius where the diversification of the entropy and cooling time profiles between pre- and mature-feedback clusters occurs.
3. Altogether, these results point to ClG J0242-2132 and RX J1350+0940 being possible examples of strongly cooling clusters in which the activity of the young central radio galaxy has not

yet affected the ICM and where the multi-phase gas reservoir is accumulated while the radio galaxy grows to larger sizes.

This work is the first observational attempt at characterizing the onset of feedback in galaxy clusters. To confirm our preliminary results it is essential to undertake a similar investigation of a larger number of sources (such as those in Tab. 2.1). In this context, we note that we have been awarded 200 ks of *Chandra* time in Cycle 25 (Proposal ID 25800027, PI: Ubertosi) to observe the three clusters in Tab. 2.1 that still lack high-resolution X-ray observations. Future observations with X-ray telescopes characterized by a high spectral resolution (e.g., *XMM-Newton/RGS*, *XRISM*, or *Athena*) may further shed light on the spectral signature of gas cooling, as well as on the turbulence of the hot, diffuse gas. In addition, we plan to investigate other probes of the multi-phase gas, as well as the source of ionization of the warm phase, to build an evolutionary picture of AGN feedback in galaxy clusters. In this respect, we recently submitted a JWST proposal (PI: Ubertosi) aimed at detecting the intermediate temperature gas (at $\sim 10^{5-6}$ K) in one of the pre-feedback systems.

Chapter 3

AGN feedback at play in the galaxy cluster RBS 797

Abstract

¹This Chapter presents the analysis of a deep *Chandra* observation of the galaxy cluster RBS 797. With the new ~ 427 ks total exposure, we report on the presence of two perpendicular and equidistant pairs of X-ray cavities in the N-S and E-W directions. All the bubbles are associated with the radio lobes of the central AGN, making RBS 797 the first galaxy cluster found to have four equidistant, centrally-symmetric, radio-filled cavities. The two perpendicular outbursts are approximately coeval, with an age difference of $\lesssim 10$ Myr between the E-W and N-S cavities. Additionally, we discover three nested weak shock fronts at roughly 50 kpc, 80 kpc and 130 kpc from the center. The total energy associated with the shocks is $\sim 6 \times 10^{61}$ erg, with the central AGN driving a weak shock every 20-30 Myr with a power $P_{\text{sh}} \approx 10^{46}$ erg s⁻¹. Based on its morphology and age (~ 30 Myr), the inner cocoon shock is associated with the four equidistant X-ray cavities. We discuss how the two cavity systems may be explained either (a) by the presence of binary active SMBHs, or (b) by a fast (< 10 Myr) jet reorientation event. We also report that from the thermodynamic analysis of the inner 30 kpc, there is evidence for ICM condensation into colder gas between and behind the X-ray cavities. Ultimately, we estimate that the total AGN mechanical power (cavities and shocks) of 3.4×10^{46} erg s⁻¹ is enough to balance the ICM radiative losses, estimated as $L_{\text{cool}} = 2.3 \times 10^{45}$ erg s⁻¹.

3.1 Motivation: the cluster RBS 797 and its multi-faceted radio galaxy

The galaxy cluster RBS 797 (RA 09:47:12.76, DEC +76:23:13.74, $z=0.354$) is a perfect case study for investigating the topics of AGN feedback, duty cycle and jet reorientation. The cluster hosts a FR I radio galaxy at its center, showing multiple radio lobe pairs that are misaligned by roughly 90° (see Gitti et al. 2006; Cavagnolo et al. 2011; Gitti et al. 2013), with the largest and brightest lobes extended in the east (E) - west (W) direction (at ~ 30 kpc from the center), radio fainter lobes in the north (N) - south (S) direction (at ~ 27 kpc from the center) and twin jets heading N-S in the inner ~ 10 kpc. At sub-arcsec resolution, a short observation of the radio core with the European VLBI Network (EVN) at 5 GHz uncovered two compact components separated by ~ 77 pc (Gitti et al., 2013). Combining these findings, Gitti et al. (2013) suggested that either the central SMBH has experienced reorientation events, producing subsequent outbursts in perpendicular directions, or the BCG hosts a dual AGN, with the two active SMBHs launching jets in perpendicular directions (coeval outbursts).

The cluster has also been targeted with X-ray observations. Early *Chandra* observations revealed that deep E-W X-ray cavities are associated with the E-W radio lobes (Schindler et al., 2001; Gitti

¹This Chapter is based on Ubertosi et al. (2021b) and Ubertosi et al. (2023b).

et al., 2006; Doria et al., 2012), and that the large mechanical power of the bubbles (Cavagnolo et al. 2011 estimated $\approx 3 - 6 \times 10^{45}$ erg s⁻¹) is of the order of the radiative losses in the ICM, indicating that feedback may be efficient in this galaxy cluster. Moreover, Cavagnolo et al. (2011) noted the presence of two surface brightness edges in the ICM. The first one surrounds the E-W X-ray cavities at ~ 50 kpc from the center, and has been proposed to be a combination of cool gas rims encasing the X-ray cavities, and of a cocoon shock surrounding the bubbles (Cavagnolo et al., 2011). However, due to the insufficient number of counts collected by the previous *Chandra* exposures, no detailed morphological or spectral study of this putative shock could be performed. The second edge was tentatively identified at ~ 80 kpc from the center, but again no classification was possible. Moreover, RBS 797 lacks measurements of the ages and power of the various outbursts (X-ray cavities and putative shocks), which are crucial to understand how the nuclear activity is coupling with the cluster environment.

Overall, the above findings point to RBS 797 being an interesting target to study the history of AGN activity in galaxy clusters and shock heating of the ICM throughout the successive central radio activities.

In this Chapter we present the analysis of the new *Chandra Large Program* observation of RBS 797 (Cycle 21 LP proposal, 420 ks, PI: Gitti), focusing on (i) the detection and analysis of X-ray cavities (§3.3), (ii) the investigation of weak shocks driven in the ICM by the AGN jet activity (§3.4), and (iii) the study of the whole cool core region and the AGN feeding and feedback cycle (§3.5).

With our selected cosmology, at the redshift of RBS 797 ($z = 0.354$), 1'' corresponds to 4.9 kpc. Uncertainties are reported at 1σ .

3.2 Data and Methods

3.2.1 X-ray - Chandra

The new *Chandra* data for RBS 797 have been acquired in VFaint mode during Cycle 21 (ObsIDs: 22636, 22637, 22638, 22931, 22932, 22933, 22934, 22935, 23332, 24631, 24632, 24852, 24865), for a total exposure time of 409 ks. Adding the previous observations (ObsIDs 2202, 7902) the overall uncleaned exposure reaches ~ 458 ks (see the summary of Tab. 3.1). The data have been reprocessed using CIAO-4.13 and CALDB-4.9.6. In our region of interest (within ~ 500 kpc from the center), the available 0.5 - 7 keV total exposure contains $\sim 300,000$ net counts, which allow for a thorough analysis of the cool core region. The removal of background flares reduced the total exposure by $\sim 9\%$ to roughly 427 ks. To correct the astrometry of the 15 ObsIDs, the longest observation (ObsID 22932) was shifted (using the `wcs_match` tool) so that the coordinates of the central X-ray point source match those of the AGN derived from high resolution radio observations (RA: 09 47 12.76, DEC: +76 23 13.74, Gitti et al. 2013). Then, the other ObsIDs were reprojected to match the longest one. Background files were obtained from blank sky event files, normalized to the 9-12 keV count rate of the observations. The `wavdetect` tool was used to obtain a list of point sources, which were masked during the analysis. We produced merged, exposure-corrected, background subtracted *Chandra* images with the `merge_obs` script, that reprojects and combines multiple ObsIDs.

Morphological analysis

Mosaiced exposure-corrected, background subtracted images of RBS 797 have been built using two energy bands (see Fig. 3.1a, 3.1b and 3.1c). A soft band (0.5 - 1.2 keV) image of the cluster core was used to accentuate the cavities and the surrounding rims. Total band (0.5-7 keV) images were used to derive an unsharp masked image, a Gaussian Gradient Magnitude (GGM, see Sanders et al. 2016b) filtered image, and a model-subtracted residual image, to measure the significance of the depressions discussed in §3.3.1 (see Fig. 3.2), and to investigate edges in surface brightness (see §3.4.1).

TABLE 3.1: Summary of the 15 *Chandra* observations of the galaxy cluster RBS 797.

ObsID	Instrument	Raw Exposure (ks)	Clean Exposure (ks)	P.I.
2202	ACIS-I	11.7	9.2	Schindler
7902	ACIS-S	38.3	37.3	McNamara
22636	ACIS-S	44.5	41.4	Gitti
22637	ACIS-S	23.7	22.2	Gitti
22638	ACIS-S	19.8	18.0	Gitti
22931	ACIS-S	24.7	23.5	Gitti
22932	ACIS-S	57.5	55.2	Gitti
22933	ACIS-S	24.7	22.9	Gitti
22934	ACIS-S	25.8	25.0	Gitti
22935	ACIS-S	25.7	23.9	Gitti
23332	ACIS-S	43.5	39.4	Gitti
24631	ACIS-S	24.8	23.3	Gitti
24632	ACIS-S	24.7	23.0	Gitti
24852	ACIS-S	43.5	39.1	Gitti
24865	ACIS-S	25.7	24.4	Gitti
Total		458.8	427.8	

By subtracting two images smoothed on different scales (for example, a and b , with $a < b$), it is possible to obtain an unsharp masked image, where spatial features larger than a but smaller than b are preserved. To produce an unsharp masked image we tested several smoothing scale combinations (between $1''$ - $5''$). The unsharp masked image in Fig. 3.1d has been obtained by subtracting two images, smoothed with a Gaussian of $1''$ and $3''$ kernel size, respectively; this choice best emphasizes structures in the cluster core. Additionally, we applied the GGM filter with a $2''$ smoothing scale to the $0.5 - 7$ keV *Chandra* image of RBS 797.

As an alternative and complementary method to accentuate morphological features, we modeled the emission of the ICM with two elliptical β -models on SHERPA² and then subtracted it off the image (e.g., McDonald et al. 2015; Calzadilla et al. 2019a). The orientation and eccentricity of the two models were left free to vary, while the centers were fixed to the X-ray peak. The resulting residual image is shown in Fig. 3.1e.

Spectral analysis

Spectral fitting (in the $0.5 - 7$ keV band, with a binning of 25 counts per bin) has been performed using Xspec12.10, selecting the table of solar abundances of Asplund et al. (2009). An absorption model (tbabs) was always included to account for Galactic absorption, with the column density fixed at $N_{\text{H}} = 2.28 \times 10^{20} \text{ cm}^{-2}$ (HI4PI Collaboration et al., 2016). For models with redshift as a parameter, we froze it to the value of the cluster ($z = 0.354$).

When analyzing the thermodynamic properties of the ICM, the spectra extracted from the 15 OBSIDs were jointly fitted with a combination of different models:

- The model `tbabs*apec` is composed of a photoelectric absorption model (tbabs), convolved with a thermal model (apec). The column density and redshift were fixed, while the other parameters (temperature kT , abundance and normalization) were left free to vary.
- The model `projct*tbabs*apec` combines the previous model with the component `projct`, that computes the combined spectra of emission from a set of nested shells projected into annular regions. The inclusion of this component allows us to derive the deprojected electron density n_e of the ICM by combining the normalization (*norm*) of the apec component with the volume (V)

²The CIAO modeling and fitting application, see <https://cxc.cfa.harvard.edu/sherpa/>.

of the emitting region. Assuming $n_e = 1.2 n_H$, $n = n_e + n_H = 1.83 n_e$ (where n and n_H are the total density and the proton density, respectively), the electron density can be estimated as:

$$n_e = \sqrt{10^{14} \left(\frac{4\pi \times norm \times [D_A(1+z)]^2}{V/1.2} \right)}, \quad (3.1)$$

where D_A is the angular diameter distance (1026 Mpc for RBS 797). The electron density can then be combined with the deprojected temperature of the apec component to obtain the pressure p , the entropy S and the cooling time t_{cool} of the ICM, using Eq. 1.2, 1.3, and 1.11.

Thermodynamic maps of the ICM

To enable high-resolution 2D mapping of ICM thermodynamic properties we built spectral maps from the *Chandra* data by using the contour binning technique (CONTBIN, Sanders 2006) and setting a minimum signal-to-noise ratio (SNR) of 60. The spectrum extracted from each region was fit with a `tbabs*apec` model, leaving the temperature, metallicity and normalization free to vary. As done for the radial profile described in §3.5.1, we verified whether the inclusion of intrinsic absorption or the fit with a two-temperature model could improve the description of the extracted spectra, but we found that no additional component is required.

Then, by combining the temperature and normalization we derived maps of pseudo-pressure and pseudo-entropy in arbitrary units, using the following method: the apec normalization is proportional to the volume integral of the square of the electron density, i.e. $norm \propto \int n_e^2 dV$. Thus, the average projected electron density can be derived from the square root of the apec normalization scaled by a factor that accounts for the volume. We define this factor as $R \times n_{pix}$, where R is the average distance of the spectral region from the center and n_{pix} is the number of pixels in each spectral region (see also e.g., Rossetti et al. 2007; Blanton et al. 2011; Randall et al. 2015). Therefore, we measure the pseudo-electron density using the following proportion:

$$n_e \propto \left(\frac{norm}{R \times n_{pix}} \right)^{1/2} \quad (3.2)$$

From the pseudo-density it is trivial to measure pseudo-pressure and pseudo-entropy using Eq. 1.2 and Eq. 1.3.

3.2.2 Radio - VLA

To allow a comparison with the X-ray data, we employ the archival radio observations of RBS 797 performed with the VLA at 1.4 GHz (configuration A, B and C, see Gitti et al. 2006; Doria et al. 2012), and at 4.8 GHz (configuration A and B, see Gitti et al. 2013), which best emphasize the structure of the central radio galaxy (inner 50 kpc) and the diffuse radio emission at larger scales (~ 100 kpc). We re-analysed the archival data (using standard reduction procedures in AIPS³-31DEC20). The total intensity maps we produced are consistent with those already published, therefore the radio contours used in this work are from Gitti et al. (2006) and Gitti et al. (2013).

RBS 797 was also observed during the VLASS survey⁴ (Lacy et al., 2020) at 3 GHz. In order to characterize the radio source at this frequency so far unobserved, we generated radio contours from the survey maps (see Fig. 3.1d).

We also show in §3.4.2 the radio contours of our new JVLA observations at 3 GHz, whose detailed analysis is presented in Chapter 4.

³NRAO's Astronomical Image Processing System, see <http://www.aips.nrao.edu/index.shtml>.

⁴<https://science.nrao.edu/vlass>.

3.3 Equidistant and perpendicular pairs of X-ray cavities in the core of RBS 797

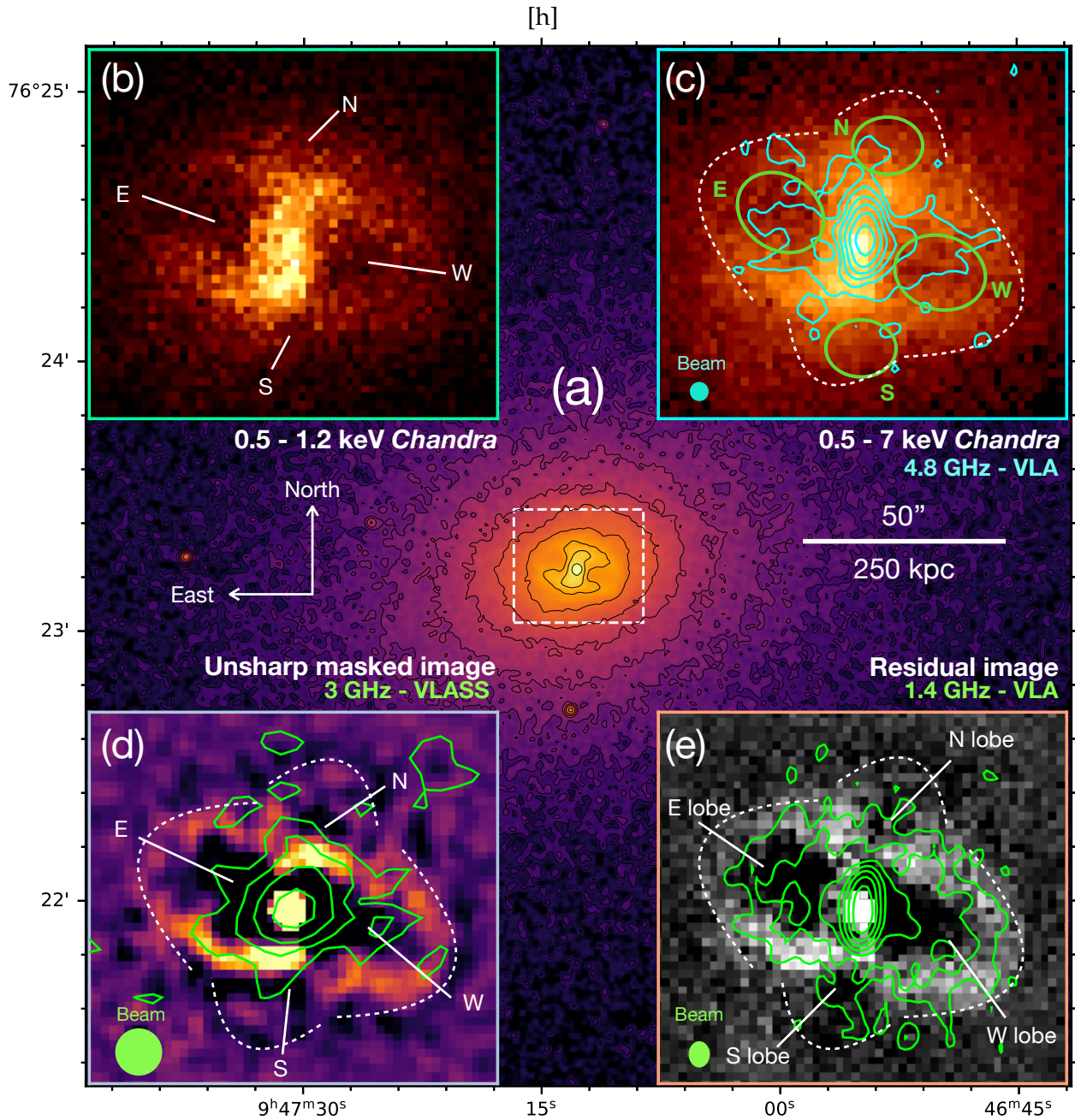


FIGURE 3.1: Exposure-corrected, background-subtracted mosaiced *Chandra* images of RBS 797. (a) 0.5-7 keV image, with a white dashed box indicating the region covered by the zoom-ins. Black contours are spaced by a factor of 2, with the highest being 4×10^{-6} cts s^{-1} cm^{-2} . (b) 0.5-1.2 keV image of the core; white labels indicate the position of the X-ray cavities. (c) 0.5-7 keV image of the core, with ellipses showing the shape of the E-W-N-S cavities, and white dashed arcs encompassing the rims (see text for details). Cyan contours at 4.8 GHz ($\sigma_{\text{rms}}=0.01$ mJy/beam, $\sim 1.3''$ resolution, Gitti et al. 2013) show the morphology of the radio galaxy. (d) Unsharp masked image of RBS 797, obtained by subtracting a $3''$ smoothed image from a $1''$ smoothed one, with white dashed arcs as in panel c. Green contours at 3 GHz are from the VLASS (contours spaced by a factor of 2 starting from $3 \times \sigma_{\text{rms}}=0.1$ mJy/beam, $2.5''$ resolution). (e) Double β -model residual image of RBS 797, with white dashed arcs as in panel c. Green contours at 1.4 GHz ($\sigma_{\text{rms}}=0.02$ mJy/beam, $\sim 1.5''$ resolution) are from Gitti et al. (2006).

3.3.1 Detection of two additional X-ray cavities in the deep *Chandra* data

The mosaiced 0.5 - 1.2 keV *Chandra* image of Fig. 3.1*b* captures the details of the AGN - ICM interaction in RBS 797: the already known E and W X-ray cavities are perfectly visible as deep, elliptical depressions surrounded by bright rims and located at $\sim 5.5''$ (~ 27 kpc) from the BCG. As also noted by Cavagnolo et al. (2011), the rims are not symmetric, being brighter in an S-shaped region starting south of the E cavity and ending north of the W cavity.

The E-W cavities in RBS 797 have previously been associated with the radio lobes of the BCG (Gitti et al., 2006; Cavagnolo et al., 2011; Doria et al., 2012). As mentioned in the introduction, Gitti et al. (2013) discovered N-S extensions of the radio galaxy, in a direction orthogonal to the E-W cavities. Therefore, to investigate the imprints of AGN activity on the ICM also in this direction, we searched for X-ray counterparts to the observed N-S radio lobes. Interestingly, the deeper *Chandra* exposures do indeed unveil two additional depressions north and south of the nucleus. The two depressions are almost perpendicular to the larger E-W cavities, and nearly at the same projected distance from the AGN ($\sim 5.5'' \sim 27$ kpc). The unsharp and residual images (Fig. 3.1*d* and 3.1*e*) emphasize the N-S holes, which appear to be surrounded by faint rims: the northern rim is unambiguous in the residual and unsharp images, and can be identified in the 0.5-7 keV image as a strip of brighter pixels above the N feature. The southern one corresponds to a bright blob in the unsharp masked image below the S depression. We verified that the X-ray cavities are recovered in the unsharp masked image regardless of the specific smoothing choice, therefore we are confident that they are not spurious features. We used ellipses to describe each cavity, the semi-axes

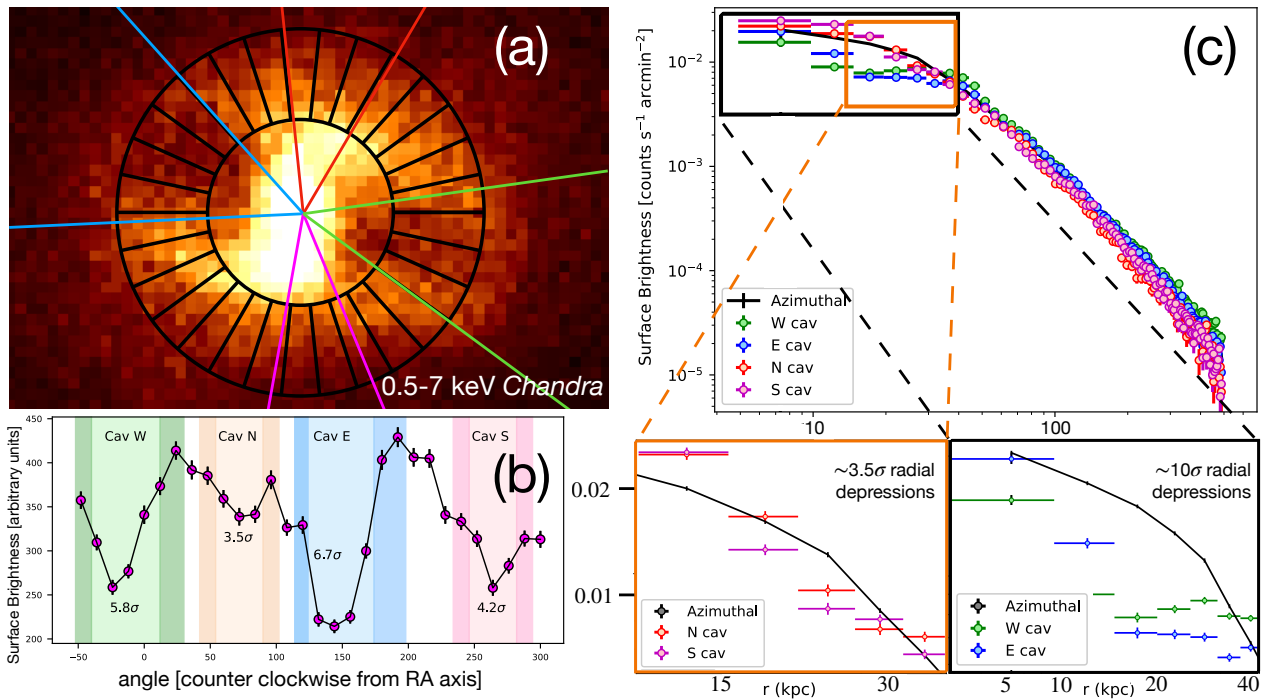


FIGURE 3.2: Significance of the X-ray cavities in RBS 797. (a) 0.5 - 7 keV band *Chandra* image of the core: black sectors used for the azimuthal analysis and colored sectors along each cavity used for the radial analysis are superimposed. (b) Azimuthal variation of surface brightness measured in 30 sectors extending $4''$ - $8''$ from the center. Light colored rectangles correspond to each cavity, while darker strips indicate reference regions used to measure the significance. (c) The upper panel shows the comparison between the background-subtracted, 0.5–7 keV surface brightness profile (black line) of the cluster (cavities excluded) in $1''$ bins, and the four profiles extracted along the E, W, N, and S cavity regions. Zoom-ins of the radial range where the cavities are present are shown in the lower right panel (E and W cavities) and in the lower left panel (N and S cavities).

of which have been chosen by comparing the unsharp, residual and original image (see Tab. 3.2).

Putative depressions N and S of the nucleus were originally identified by Cavagnolo et al. (2011), who also noted the coincidence of radio emission with the X-ray structures. However, a clear detection of these structures was lacking due to the short exposure. Our deep Chandra observation allows us to securely detect the new N-S depressions, thus identifying RBS 797 as the first galaxy cluster for which two symmetric X-ray cavity pairs coincident with resolved radio emission are found at the same projected distance from the center. This peculiar geometry challenges classical methods to estimate the cavity significance (i.e. surface brightness deficits w.r.t. the azimuthal mean, see e.g., Hlavacek-Larrondo et al. 2015). As the whole azimuth is disturbed either by part of the rims or by the cavities themselves, it is nontrivial to define a reference surface brightness. In particular, the already known E-W depressions are deep, thus the shallower N-S depressions would lie above the azimuthal mean. In turn, the significance of the N-S cavities would be based on a surrounding surface brightness which is influenced by the presence of the E-W depressions. To circumvent this obstacle, we considered the annulus from $4''$ to $8''$, divided into 30 equal sectors (Fig. 3.2a) and then relied on the comparison between the surface brightness measured in the sectors covering each cavity, S_c (with uncertainty E_c), and that measured in the immediate surroundings, S_s (with uncertainty E_s). The results are shown in Fig. 3.2b, where the lighter and darker strips correspond to S_c and S_s , respectively. The surface brightness decrement of each structure (D) and the significance at which the decrement is recovered, D over the error in D , were computed as:

$$D = 1 - \frac{S_c}{S_s} \quad (3.3)$$

$$\text{significance} = \frac{D}{(1 - D) \sqrt{\left(\frac{E_c}{S_c}\right)^2 + \left(\frac{E_s}{S_s}\right)^2}} \quad (3.4)$$

The N-S cavities also represent radial deficits w.r.t. the azimuthally averaged radial surface brightness profile (extracted after masking the cavities, e.g., Doria et al. 2012; see Fig 3.2c). Overall, in the E-W cavities the net counts drop by about $D = 30\%$ with a significance ranging from $\sim 6-10\sigma$ depending on the method adopted, while in the N-S structures the net counts drop by about $D = 10\%$ at $3.5 - 4.2\sigma$ (based on the analysis shown in Fig. 3.2b, 3.2c). We made various tests by varying the choice for the sectors, also considering elliptical annuli, and always found consistent results. Additionally, we verified that N-S dips can be recovered by extracting a surface brightness profile from two linear projections (one to the north and one to the south of the center, respectively) along a straight cut parallel to the axis of the E-W cavities (a similar method has been previously used to test the existence of small cavities in MS 0735+7421, see Vantyghem et al. 2014). These alternative methods are shown in Appendix B. For comparison, the other dark structures visible in the unsharp masked image have typically 5% fewer counts at about 1σ confidence only. Additionally, we followed the method outlined in Martz et al. (2020) to measure cavity signal-to-noise ratios (SNR) w.r.t. the double β -model. For each cavity region, the counts in the image of Fig. 3.1c, N_I , were compared with the counts in the double β -model residual image of Fig. 3.1e, N_M . The deficit of the structures is defined as:

$$\text{Deficit} = 1 - \frac{N_I}{N_M}, \quad (3.5)$$

and the SNR for the deficit is (see Eq. 9 in Martz et al. 2020):

$$\text{SNR} = \frac{|N_I - N_M|}{\sqrt{|N_I - N_M| + 2N_M}} \quad (3.6)$$

Using the above equations, the N-S cavities represent deficits of about 10% at a SNR of 5, while the deeper E-W cavities have deficits of about 25% at a SNR of 17. These estimates are consistent with the deficits based on the observed surface brightness, thus strengthening our results.

These tests demonstrate that the N-S depressions represent an additional system of X-ray cavities, created by the central AGN. The suggested presence of rims surrounding the N-S cavities further strengthens this interpretation. The new cavity detection is strongly supported by the morphology of the central radio source: the 1.4 GHz contours overlaid on Fig. 3.1e show radio lobes coincident with the E-W cavities, and reveal significant extensions partly filling the N-S depressions. The 4.8 GHz emission (Fig. 3.1c) extends towards the E-W cavities over the same scales as the 1.4 GHz contours. Furthermore, a third structure extends northward, terminating in a lobe coincident with the N cavity. The 3 GHz VLASS contours (2.5'' resolution) overlaid on Fig. 3.1d confirm the cross-like morphology of the AGN, with four radio extensions headed towards the perpendicular cavity pairs. Thus, the co-spatiality of significant radio emission with the four depressions is key to demonstrating that the N-S holes are real X-ray cavities and not artificial dips produced by the “ ∞ -shaped” morphology of the bright rims.

We note that RBS 797 might resemble e.g., 2A0035+096 (Sanders et al., 2009) or 4C+00.58 (Hodges-Kluck et al., 2010), in which multiple X-ray cavities have been found near the cluster core; in these clusters, however, the association of radio emission from the central AGN with the cavities is not straightforward. Furthermore, we observe the similarity of RBS 797 to Cygnus-A, in which additional cavities filled with radio emission and perpendicular to the main cavity system have been discovered (see Chon et al. 2012). The peculiarity of RBS 797 is that, for the first time, multiple, perpendicular systems of radio-filled X-ray cavities are found at the same projected distance from the BCG.

Cavity ages from X-ray data

Measuring the age of the cavities is crucial to investigate the activity cycle of the central AGN. Bîrzan et al. (2004) originally discussed three methods to measure cavity ages from X-ray data, typically in agreement within a factor of 2. These are the sonic time, the buoyancy time, and the refill time (for the definition and equations see Chapter 1, Eq. 1.15, 1.16, 1.17). We derived the ages of the E, W, N, S cavities in RBS 797 following the above methods, and assuming that the cavities all lie in the plane of the sky. The cavity radius R in the equations of Chapter 1 (Eq. 1.15, 1.16, 1.17) has been defined as $R \equiv r_{\text{eff}} = \sqrt{ab}$, where r_{eff} is the effective radius of an ellipsoid of semi-axes a and b . The cavities were treated as prolate ellipsoids to compute the volume; a systematic uncertainty of 10% was included for distances and semi-axes (e.g., Sun et al. 2003). Since the sound speed depends on the ambient temperature, and g can be derived from the ICM pressure gradient and density by assuming hydrostatic equilibrium⁵ (Voigt and Fabian, 2006), we built radial profiles of thermodynamic quantities by extracting spectra from concentric circular annuli (cavities excluded). The complete description and analysis of the radial profiles is presented in a following section (see §3.5.1). Here we are interested only in the ICM temperature $kT=4.04^{+0.29}_{-0.26}$ keV and electron density $n_e=6.52^{+0.22}_{-0.21} \times 10^{-2} \text{ cm}^{-3}$ measured at the distance of the cavities from the center (in the radial bin encompassing the cavities, between 5''-6''), which are key to derive the sound speed $c_s=1008 \pm 54 \text{ km s}^{-1}$ and acceleration $g=(5.4 \pm 0.6) \times 10^{-8} \text{ cm s}^{-2}$. The above temperature and electron density are consistent with those reported in Cavagnolo et al. (2011) and Doria et al. (2012). We note that measuring local values of c_s in four sectors (one for each cavity) produced negligible differences ($\approx 6\%$) w.r.t. the azimuthally averaged value reported above.

⁵Hydrostatic equilibrium is uncertain in systems with strong AGN feedback signatures (e.g., Gaspari et al. 2011); however, since the cavities are found at the same projected distance from the center, even a difference in g of a factor of e.g. 2 would make the buoyancy and refill ages of the two cavity pairs scale by the same factor ($\sqrt{g} \sim 1.4$). As we are interested in relative ages (see §3.3.2), deviations from hydrostatic equilibrium do not affect the main results.

TABLE 3.2: Properties of the four X-ray cavities in RBS 797. (1) Cavity name; (2) Projected distance from the center of the radio galaxy; (3) semi-major axis; (4) semi-minor axis; (5) effective radius (\sqrt{ab}); (6) sound crossing time; (7) buoyancy time; (8) refill time; (9) expansion time. See §3.3.1 for details.

Cavity	D_{AGN} (kpc ["])	a (kpc ["])	b (kpc ["])	r_{eff} (kpc ["])	t_{cs} (Myr)	t_{buo} (Myr)	t_{ref} (Myr)	$t_{\text{exp,cs}}$ (Myr)
E	27.9 (5.7)	15.7 (3.2)	12.7 (2.6)	14.1 (2.9)	26.5±1.7	26.8±2.4	56.7±4.2	13.4±1.6
W	25.5 (5.2)	15.7 (3.2)	12.7 (2.6)	14.1 (2.9)	23.8±1.5	24.1±2.2	56.7±4.2	13.4±1.6
N	29.4 (6.0)	9.8 (2.0)	7.4 (1.5)	8.5 (1.7)	28.8±1.9	36.1±3.2	43.9±3.3	8.1±1.0
S	27.0 (5.5)	9.8 (2.0)	7.4 (1.5)	8.5 (1.7)	26.0±1.7	32.6±3.4	43.9±3.3	8.1±1.0

Additionally, we propose a further method to constrain the ages: we computed the time required for each cavity to reach its observed size by expanding at the sound speed, $t_{\text{exp}} = r_{\text{eff}}/c_s$. This method assumes either that the cavity has been excavated directly at the position where it is observed, or that it has expanded and risen at the same speed (c_s), reaching a distance from the center comparable to its radius.

For the E-W cavities, both t_{cs} and t_{buo} suggest an average outburst age of 25 ± 2 Myr (consistent with Doria et al. 2012). The refill time and the sound expansion time are a factor of ~ 2 higher and lower, respectively. The N-S cavities have a t_{cs} comparable to that of the E-W cavities (which is expected considering the dependencies on D_{AGN} and c_s). On the other hand, the buoyancy and refill time suggest average ages of ≈ 40 Myr. The sound expansion times set the lowest age estimates of ≈ 5 -8 Myr. The complete results of the four methods are reported in Tab. 3.2.

We caution that the uncertainties on ages reported above and in Tab. 3.2 include only statistical uncertainties (which are small given the depth of the *Chandra* exposure), since systematic uncertainties related to the assumptions of each method are not known. Projection effects represent an additional source of uncertainty for the position and 3D structure of the cavities, as we do not know the inclination of either the E-W or N-S cavities with respect to the plane of the sky. For instance, if the four cavities were buoyantly rising in the cluster atmosphere, from the definition of t_{buo} we should expect coeval outbursts to be found at the same distance from the center and to have similar sizes. In this context, we note that the moderate discrepancy of buoyancy ages between the two cavity pairs (a factor of ≈ 1.5) is mostly related to the different ratio between the observed size and distance from the center. On the one hand, the difference in ratio is likely to be affected by projection effects, so that the observed distance and size of the cavities might be underestimated. On the other hand, the different $D_{\text{AGN}}/r_{\text{eff}}$ could hint at AGN of different jet kinetic power (see e.g., Diehl et al. 2008) which have inflated equidistant holes of varying sizes.

The above considerations indicate that we are unable to place robust constraints to the 3D distance of the cavities from the BCG, which represents a limitation of our work. Further, it is clear that it is not straightforward to draw conclusions on the cavity dynamics based on the age computed with a single method. Therefore, we decided not to prefer any method over the others, and to interpret the range in ages returned by the four estimates as an indication of our uncertainty for the true outburst ages (see also §3.3.2).

3.3.2 Interpretation of the perpendicular X-ray cavities: rapid jet reorientation or binary SMBHs?

As mentioned in §3.1, Gitti et al. (2006) and Gitti et al. (2013) discovered perpendicular radio lobes of the radio galaxy (see Fig. 3.3a), and tentatively identified two compact radio core components.

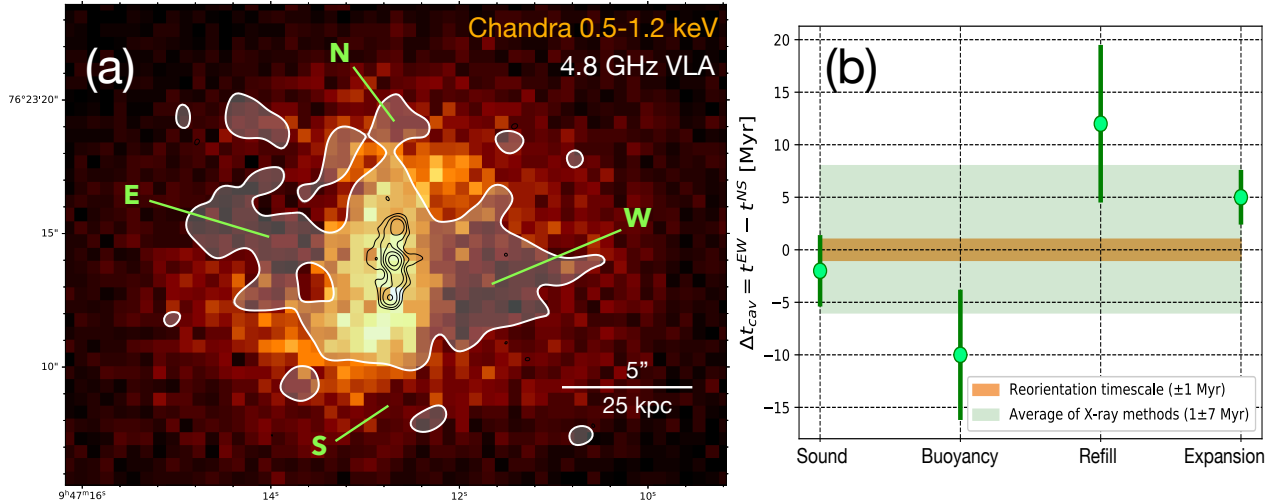


FIGURE 3.3: Outburst interval of the X-ray cavities in RBS 797 from the X-ray *Chandra* data. (a) 0.5-1.2 keV image of the core of RBS 797. Black contours at 4.8 GHz ($\sigma_{\text{rms}}=0.01$ mJy/beam, $\sim 0.5''$ resolution, Gitti et al. 2013) show the morphology of the inner jets of the radio galaxy. The filled white contour at 4.8 GHz is the largest contour (at $3 \times \sigma_{\text{rms}}$) shown in Fig. 3.1c. Green labels indicate the four X-ray cavities. (b) The age difference of the E-W and N-S cavities, $\Delta t_{\text{cav}} = t^{\text{EW}} - t^{\text{NS}}$, for the different methods is shown and compared to the theoretical reorientation timescale (± 1 Myr, orange area; see §3.3.2).

To explain this peculiar radio morphology, Gitti et al. (2013) originally proposed that the perpendicular outbursts were produced either following a reorientation event of the AGN jets (subsequent scenario), or by the contemporaneous activity of two SMBHs in the BCG of RBS 797 (coeval scenario). In the following, we focus on whether the four X-ray cavities we discovered in the follow-up *Chandra* observation can help us in discriminating between the subsequent and coeval cases.

Overall, our X-ray analysis has unveiled that the two perpendicular outbursts have comparable ages, constrained by the different methods to be ~ 10 -50 Myr old. Specifically, Fig. 3.3b shows the age difference between the two outbursts, computed as $\Delta t_{\text{cav}} = t^{\text{EW}} - t^{\text{NS}}$. Here t^{EW} and t^{NS} represent, for each method, the average age of each cavity pair. It is interesting to note that the X-ray methods do not agree on which cavity system is older: the suggested time interval is at most ± 10 Myr, with the average of the X-ray methods lying at $\Delta t_{\text{cav}} \sim 0$ (1 ± 7 Myr, green area in Fig. 3.3b).

Altogether, if the four cavities are the consequence of a reorientation event, the above timescales suggest that the AGN axis changed rather quickly, specifically in $\lesssim 10$ Myr. It is noteworthy that the range of ages in RBS 797 is short when compared to the mean outburst interval of known galaxy clusters with multiple generations of cavities (~ 100 Myr in the sample of Birzan et al. 2004; ~ 20 Myr for Perseus and Virgo, Babul et al. 2013; ~ 50 -60 Myr for MS0735, Vantyghem et al. 2014; Biava et al. 2021). Additionally, a radio spectral index study for the X-shaped radio galaxy A3670 (X-shaped radio galaxies are believed to have experienced reorientation events, see e.g., Liu 2004) found a difference of ~ 20 Myr between the lobes and the wings (Bruno et al., 2019), which is larger than our estimate of $\lesssim 10$ Myr. Therefore, considering the above timescales on which misaligned outbursts are typically observed, it is possible that the two outbursts in RBS 797 might have been inflated during the nearly contemporaneous activity of two SMBHs.

We note that with the available data we cannot definitely exclude that the two outbursts are not coeval on timescales shorter than our uncertainties. In RBS 797, the mean age difference between the E-W and N-S cavities is $\Delta t_{\text{cav}} = 1 \pm 7$ Myr (from the average of the X-ray methods). The timescales for jet reorientation are uncertain, but theoretical works suggest that the reorientation could typically happen in $\Delta t_{\text{reo}} \approx 1$ Myr (orange area in Fig. 3.3b), or longer if the jets are switched off during the event (see e.g., Dennett-Thorpe et al. 2002; Liu 2004; Lal and Rao 2007). A rapid change in the AGN feeding can also cause such a fast jet reorientation; e.g., CCA has been shown to

flicker very rapidly in less than a Myr, with a sudden change in angular momentum (Gaspari et al., 2017a). While it is possible that reorientation happened on timescales shorter than ~ 1 Myr, the reoriented jets would take ≈ 10 Myr to propagate in the ICM (assuming a jet advance speed of $0.01 c$, e.g., Matthews and Taylor 2021) and inflate radio lobes. The derived AGN outburst timescales in RBS 797 thus seem at the boundary between a fast jet reorientation and coeval, binary SMBHs activity; our analysis indicates that the latter might be possible, given that the $\Delta t_{cav} \lesssim 10$ Myr is sensibly smaller than literature values for misaligned cavity systems.

Therefore, our results are still consistent with a coeval scenario, that is the presence of a binary system of *two active* SMBHs in the core of RBS 797, possibly coincident with the two compact components discovered by Gitti et al. (2013). In particular, the detection in the *Chandra* images of RBS 797 of four perpendicular, equidistant X-ray cavities with similar ages is a tantalizing indication for the presence of two AGN.

In the next sections (§3.4 and §3.5) we discuss the effect of the X-ray cavities and of other footprints of AGN activity (i.e. shock fronts in the ICM) on the heating – cooling balance in the cluster RBS 797. Then, in Chapter 4, we leverage the information obtained from a wealth of multi-frequency radio observations of RBS 797, to build a consistent and detailed picture of AGN activity in this cluster. We will show how the combination of X-ray and radio data can put stronger constraints on which scenario (jet reorientation or binary SMBHs) is more viable.

3.4 Multiple AGN-driven shock fronts in the ICM of RBS 797

As noted in §3.1, past works suggested the possible presence of shock fronts in the ICM of the cluster, likely related to the outburst(s) of the central AGN. The deep *Chandra* data allow us to further investigate these claims. In this section we present our search and detection of shock fronts in the cluster core, which enables the investigation of AGN feedback by both X-ray cavities and shocks.

3.4.1 The detection and analysis of shocks

The top panel of Fig. 3.4 shows the background subtracted, exposure corrected *Chandra* image. In the bottom panels we show the original image filtered with a $2''$ GGM filter (Sanders et al., 2016b), and the residual *Chandra* image, obtained by subtracting from the *Chandra* image a 2D double β -model). In the inner ~ 50 kpc there are the four equidistant X-ray cavities previously discussed in §3.3.1, best visible in the residual image (right panel). Beyond the X-ray cavities, the images reveal the presence of three distinct and nested surface brightness edges, at approximate projected distances from the center of ~ 50 kpc, ~ 80 kpc and ~ 130 kpc. In the following, we refer to the three features as *inner*, *middle* and *outer* edges.

The inner edge surrounds the AGN-inflated cavities, and consists of an ellipse with P.A. $\approx 345^\circ$ and ellipticity (ratio between major and minor axis) of ~ 1.2 . The edge is located at a distance along the major axis of $\sim 11''$ (54 kpc), and appears stronger along the E-W direction. Within this shell of bright X-ray emission there are the four cavities (at a distance of $\sim 5.5''$ from the center, see §3.3.1 and Tab. 3.2) and the surrounding rims (at a distance of $\sim 8''$ from the center). The middle edge appears sharper in the N-S direction, and is described by an ellipse with P.A. $\sim 20^\circ$ and ellipticity 1.1. The outer edge is described by an ellipse with P.A. $\sim 100^\circ$ and ellipticity 1.1, and is particularly pronounced in the E-W direction. While the inner and middle edges were already noted by Cavagnolo et al. (2011), the deeper *Chandra* observations allowed us to recover the third outer edge. Most importantly, thanks to the higher number of counts we are able to perform a thorough morphological and spectral analysis of such edges for the first time (see §3.4.1).

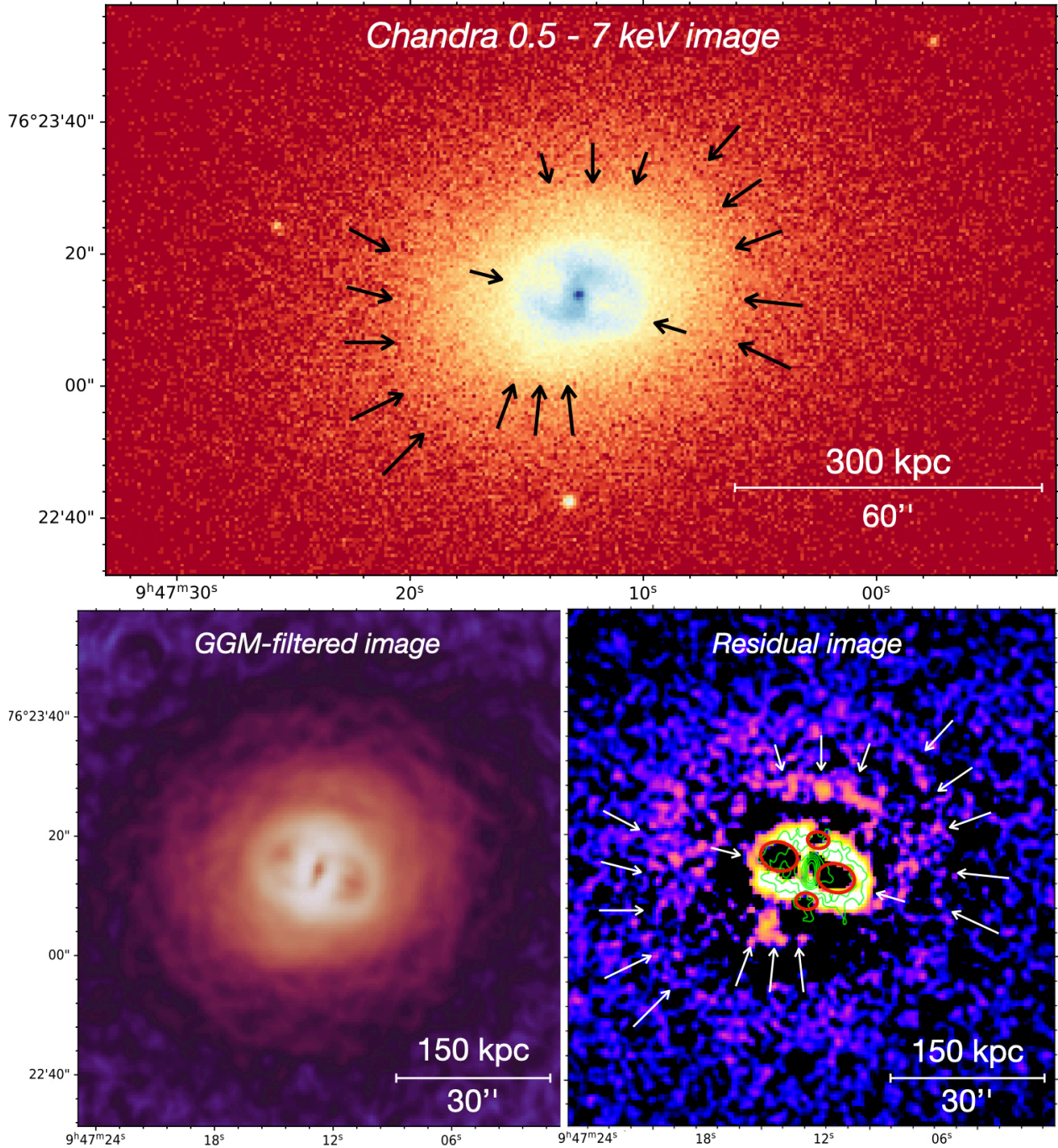


FIGURE 3.4: Original and filtered *Chandra* images of RBS 797 showing the nested shock fronts in the ICM. *Top panel:* Background subtracted, exposure corrected *Chandra* image of RBS 797 in the 0.5 - 7 keV band. *Bottom left panel:* *Chandra* image filtered with the GGM method using $\sigma = 2''$. *Bottom right panel:* Double β -model residual image of RBS 797, highlighting the four X-ray cavities (red ellipses). The green contours at 1.4 GHz (at 3, 5, 10, 20, 40, 75, 150 \times the σ_{rms} of 0.02 mJy/beam, at $\sim 1.5''$ resolution; see Gitti et al. 2006) show the morphology of the central radio galaxy. In the top and bottom right panels, the arrows indicate the position of the surface brightness edges at progressively increasing distances from the center. See §3.4.1 for details.

Detailed properties of the shocks

Our aim is to secure the identification and investigate the properties of the edges visible in Fig. 3.4. In particular, this requires one [i] to identify the exact position and magnitude of each front by

studying the surface brightness profile across the edge and [ii] to measure thermodynamic properties (e.g., temperature and pressure) inside and outside the front to determine its nature. In the following we first describe the procedure we employed to search for and investigate shock fronts, and then we present the results for RBS 797.

We performed a systematic search for edges in the ICM by extracting surface brightness profiles (centered on the X-ray centroid, that coincides with the AGN in the BCG) in circular or elliptical sectors of varying opening angles (between 30° and 90°) and different binning (between $0.7''$ to $2''$). This strategy was adopted to determine the geometry that best describes the fronts. The resulting profiles were visually inspected to identify possible jumps in surface brightness. For each edge, the profile was fit in Proffit with a single power-law model and with a broken power-law model: a surface brightness edge at distance r_J and characterized by a density jump J was considered a detection if an F-test between the single and the broken power-law indicated a significant statistical improvement (more than 99% confidence).

For the detected surface brightness edge, the Mach number \mathcal{M} of the front was derived from the best-fit density jump J using the Rankine - Hugoniot conditions (see e.g., Markevitch and Vikhlinin 2007), and in particular Eq. 1.24. Moreover, the Mach number can be used to predict the expected temperature and pressure jumps, $T_{\text{jump}}^{\text{exp}}$ and $p_{\text{jump}}^{\text{exp}}$, respectively, using Eq. 1.25 and 1.26.

To measure the spectral properties of the detected surface brightness jumps, we extracted the spectra of three concentric regions: the first region is a wedge extending between $0.75r_J - r_J$; the second is a wedge extending between $r_J - 1.5r_J$; the third wedge extends from $1.5r_J$ to the edge of the *Chandra* image, and allows for deprojection. These bin widths were chosen to avoid the inclusion of thermal emission far from the jump: while selecting larger regions would increase the number of counts, it may also lead to smearing thermodynamic gradients. Spectra were fitted with a `projct*tbabs*apec` model to measure the deprojected temperature and density (Eq. 3.1), which were combined to derive the pressure jump across each edge (Eq. 1.2).

Applying the above procedure to RBS 797 allowed us to confirm the shock front nature of the three concentric and nested systems of edges noted in the previous paragraphs. In Fig. 3.5 we show the arc region that best describes each front and the fitted surface brightness profiles, while in Tab. C.1 of Appendix C and Tab. 3.3 we report the surface brightness analysis and thermodynamic properties of the shocks, respectively. The details of the spectral fitting are shown in Tab. C.2 of Appendix C, while below we report the main properties of each detected shock:

Inner edges (S1, S2, S_{in}) - The innermost surface brightness edge in RBS 797 is the bright cocoon surrounding the four X-ray cavities. By extracting the surface brightness profile in elliptical sectors (with ellipticity 1.2 and P.A. 345°) we recovered sharp and significant density jumps between angles 130° - 190° and 310° - 15° , i.e. beyond the E - W cavities (first two rows in Tab. C.1, S1 and S2 panels in Fig. 3.5). The edges are located at roughly $10'' - 11''$ ($\approx 50 - 55$ kpc) from the center. We name these inner east and inner west edges S1 and S2, respectively. By substituting in Eq. 1.24 the fitted density jumps we measured Mach numbers $\mathcal{M}_{S1} = 1.33 \pm 0.05$ and $\mathcal{M}_{S2} = 1.27 \pm 0.04$. The spectral analysis confirms the shock front nature of the edges (first two rows of Tab. 3.3): S1 is characterized by a temperature jump $T_{\text{jump}}^{\text{obs}} = 1.35 \pm 0.18$ and a pressure jump $p_{\text{jump}}^{\text{obs}} = 1.80 \pm 0.24$. The front S2 is less pronounced, being associated with a temperature jump of $T_{\text{jump}}^{\text{obs}} = 1.13 \pm 0.08$ and $p_{\text{jump}}^{\text{obs}} = 1.50 \pm 0.13$. While the lower Mach number of S2 compared to S1 is consistent with a less pronounced shock to the west, it is also possible that this is due to projection effects: low temperature gas in the W cavity rims, projected in front of the S2 front, may be damping the temperature gradient (similarly to what has been found for Hydra A, see Gitti et al. 2011).

As the geometry of the edge is suggestive of a cocoon shock propagating in the ICM, we also analyzed the radial profile extracted from a complete ellipse with ellipticity 1.2 and P.A. 345° . We found a density jump (named S_{in}) at $\sim 10.7''$ (52.4 kpc) from the center with a Mach number $\mathcal{M}_{S_{\text{in}}} = 1.20 \pm 0.03$. With the spectral analysis we found a temperature jump of $T_{\text{jump}}^{\text{obs}} = 1.18 \pm 0.07$

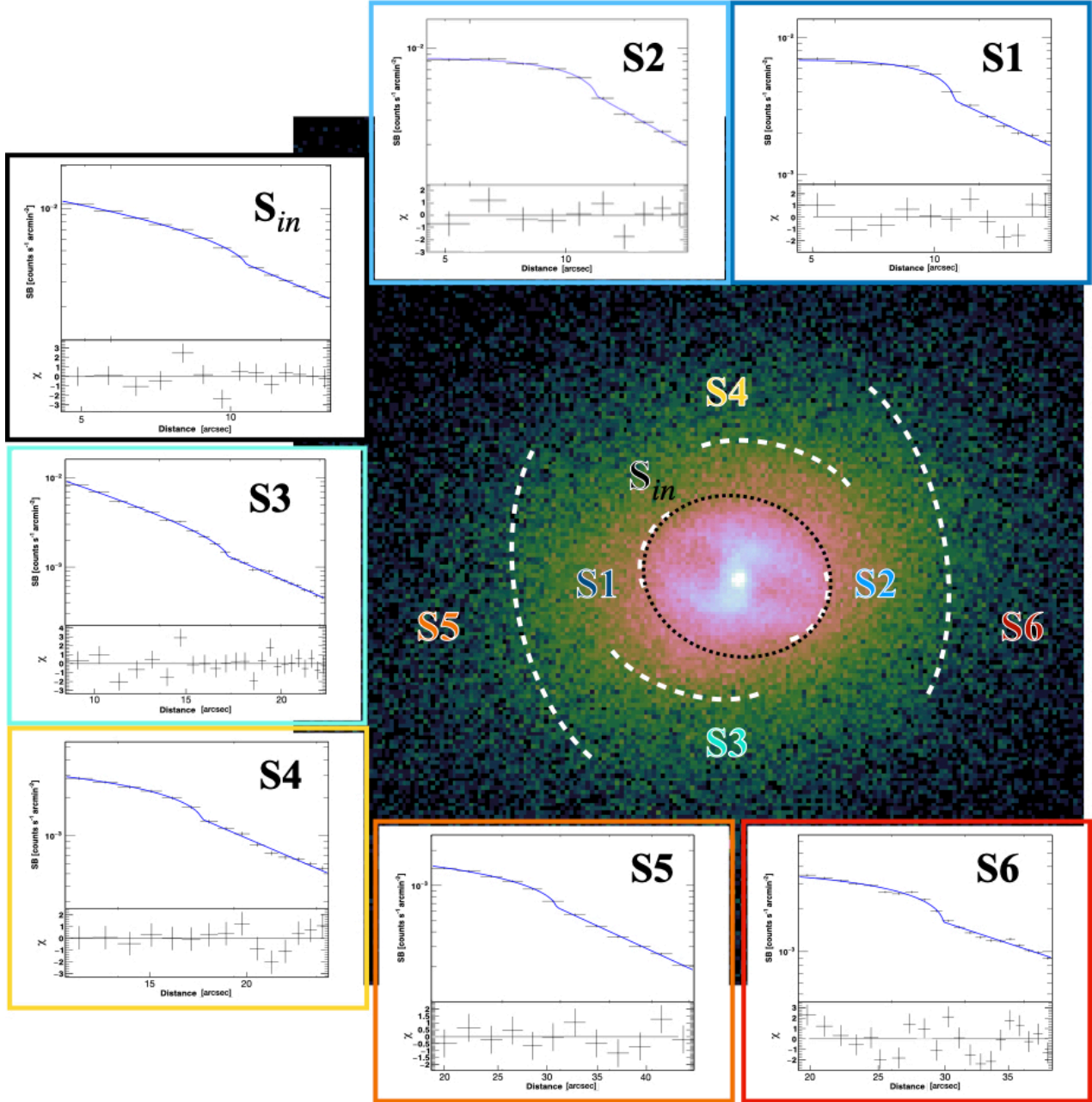


FIGURE 3.5: Surface brightness profiles across the weak shocks in RBS 797. *Central panel*: 0.5 - 7 keV *Chandra* image of RBS 797. The white (black) dashed regions indicate the positions and extents of the arc-like (cocoon-like) edges found on opposed sides of the center, as results from the surface brightness analysis reported in Tab. C.1. Colored labels indicate the name of each edge. *Sub-panels*: Surface brightness profile across each edge fit with the broken power-law model (blue line) described in Tab. C.1. Residuals of the fit are shown in the bottom box of each plot.

and a pressure jump $p_{\text{jump}}^{\text{obs}} = 1.88 \pm 0.16$ (see Fig. 3.5, and third row of Tab. C.1 and Tab. 3.3). Thus, the inner edge is continuous around the azimuth, and consists of a cocoon shock driven by the jets of the central AGN. The lower Mach number of S_{in} with respect to S1 and S2 probably indicates that the shock strength varies with azimuth (as also found e.g., in Hydra A, Gitti et al. 2011), so $\mathcal{M}_{S_{\text{in}}}$ is the result of an average across the azimuth. Thus, we suggest that S1 and S2 are the highest Mach number parts of a single shock (S_{in}). In this respect, the ellipticity of S_{in} (1.2) provides an indication of the ratio of the mean shock speeds along the major and minor axes.

Middle edges (S3, S4) - The second front identified from the images in Fig. 3.4 is located at a distance of $16''$ - $17''$ (≈ 80 kpc) from the center. Extracting surface brightness profiles from elliptical sectors (ellipticity 1.1 and P.A. 20°) revealed two significant jumps south of the center (S3, angles 200° - 270° , Mach number $\mathcal{M}_{S3} = 1.24 \pm 0.03$) and north of the center (S4, angles 45° - 110° , Mach number $\mathcal{M}_{S4} = 1.30 \pm 0.08$). The spectral analysis revealed that the shock front S3 has a temperature jump $T_{\text{jump}}^{\text{obs}} = 1.23 \pm 0.11$ and a pressure jump $p_{\text{jump}}^{\text{obs}} = 1.67 \pm 0.21$, while the shock front S4 has a temperature jump $T_{\text{jump}}^{\text{obs}} = 1.24 \pm 0.12$ and a pressure jump $p_{\text{jump}}^{\text{obs}} = 2.36 \pm 0.29$ (see Fig. 3.5, Tab. C.1 and Tab. 3.3). We tested whether S3 and S4 may be part of a single front over 360° as done for the inner edge, but the surface brightness profile from the complete ellipse did not reveal any significant jump.

Outer edges (S5, S6) - The presence of a third set of fronts at a distance of $\approx 27''$ (or 135 kpc) from the center was not noticed in previous studies of RBS 797. Outer edges in surface brightness to the E-W are visible in the images of Fig. 3.4. Fitting surface brightness profiles to the E-W in elliptical sectors (ellipticity 1.1 and P.A. 102°) returned evidences for prominent density jumps at the location of the edges (between angles 140° - 252° and 304° - 87° ; see Fig. 3.5 and last two rows of Tab. C.1 and Tab. 3.3). In particular, we find that the eastern outer front (S5) has a Mach number $\mathcal{M}_{S5} = 1.19 \pm 0.03$ and coincides with jumps in temperature and pressure of 1.37 ± 0.26 and 1.91 ± 0.41 , respectively. The western outer front is traveling with a Mach number $\mathcal{M}_{S6} = 1.25 \pm 0.04$ and coincides with jumps in temperature and pressure of 1.41 ± 0.24 and 2.34 ± 0.43 , respectively.

Overall, the above results confirm the existence of three sets of nested shock fronts in the ICM of RBS 797. The significance of the measured density jumps J is more than $\sim 6\sigma$ (see Tab. C.1). For the inner edge and the middle edge, the significance of the measured temperature jumps is between 2 - 3σ , while the significance of the pressure jumps is between 3 - 5σ . For the outer edge, the significance of temperature and pressure jumps is between 1.5 - 3σ . Moreover, the predicted and measured temperature and pressure jumps are in agreement within errors (see Tab. 3.3, fourth to seventh columns). With Mach numbers in the range 1.2 - 1.3 the edges can be classified as weak shocks, likely resulting from successive energy injection events by the AGN activity. The Mach number of the shock fronts remains nearly constant within uncertainties from the inner, to the middle, to the outer shock fronts. In an idealized case, we could expect a decreasing trend of Mach number with radius, due to the outward increase of ICM sound speed and the progressive deceleration of the shock waves. However, this trend may be hidden and blurred by several effects, such as (a) projection; (b) different outburst power; (c) non-azimuthally uniform density gradient of the upstream gas; and (d) different duration of jet driving phase between the successive outbursts. It is interesting to note the continual change in position angle of the different shock groups: from E-W (inner shocks) to N-S (middle shocks) and again to E-W (outer shocks). It is likely that the middle and outer opposed shock arcs represent the highest Mach number parts of complete middle and outer cocoon shocks that encompass the whole azimuth, respectively, as we were able to verify for the inner jump. For instance, we might not be able to detect *middle* E-W surface brightness jumps as these would be located in a rather narrow region in between the inner and outer E-W fronts, which would prevent the surface brightness profile at the interface of the shocks from being accurately measured. Besides, it is known that the central AGN in RBS 797 is characterized by multiple changes in position angle of its lobes and jets (Gitti et al., 2006; Gitti et al., 2013; Cavagnolo et al., 2011), up to 90° misalignment. Thus, the nested groups of opposed and misaligned shock fronts might trace older episodes of differently oriented AGN activity cycles. We further investigate this scenario in §3.4.2.

Shock energetics and timescales

Measuring the age and energetics of the shocks provides essential information for probing the

TABLE 3.3: Properties of the AGN-driven, nested shocks in RBS 797. (1) Shock label; (2) distance of the shock from the center (measured from the front mid-aperture); (3) Mach number of the shock, obtained from the density jump reported in Tab. C.1; (4 - 5) temperature and pressure jumps predicted by the Mach number; (6 - 7) observed temperature (deprojected) and pressure jumps, obtained from the fit to the spectrum of the ICM in the downstream and upstream sides of the edge (see Tab. C.2); (8) age of the shock (see Eq. 3.7); (9) energy of the shock (see Eq. 3.8); (10) shock power, defined as $P_{\text{sh}} = E_{\text{sh}}/t_{\text{age}}$. The energy and power of fronts S1, S2, S3, S4, S5 and S6 are referred to the half ellipsoid covered by each front, while for S_{in} the full ellipsoid was considered (see text for details).

Shock	r_{sh} [kpc ($''$)]	\mathcal{M}	$T_{\text{jump}}^{\text{exp}}$	$P_{\text{jump}}^{\text{exp}}$	$T_{\text{jump}}^{\text{obs}}$	$P_{\text{jump}}^{\text{obs}}$	t_{age} [Myr]	E_{sh} [10^{60} erg]	P_{sh} [10^{45} erg s^{-1}]
S1 - Inner East	53.9 (11.0)	1.33 ± 0.05	1.33 ± 0.05	1.98 ± 0.17	1.35 ± 0.18	1.80 ± 0.24	28.5 ± 2.4	8.3 ± 1.7	8.6 ± 1.8
S2 - Inner West	50.5 (10.3)	1.27 ± 0.04	1.26 ± 0.04	1.77 ± 0.08	1.13 ± 0.08	1.50 ± 0.13	32.8 ± 2.8	4.2 ± 0.8	4.1 ± 0.8
S_{in} - Inner Total	52.4 (10.7)	1.20 ± 0.03	1.19 ± 0.02	1.54 ± 0.06	1.18 ± 0.07	1.88 ± 0.16	33.4 ± 1.3	6.6 ± 0.5	6.3 ± 0.6
S3 - Middle South	79.4 (16.2)	1.20 ± 0.03	1.19 ± 0.03	1.54 ± 0.08	1.23 ± 0.11	1.67 ± 0.21	50.9 ± 4.3	8.0 ± 1.9	5.0 ± 1.2
S4 - Middle North	81.8 (16.7)	1.19 ± 0.03	1.18 ± 0.03	1.51 ± 0.10	1.24 ± 0.12	2.36 ± 0.29	54.9 ± 4.5	6.3 ± 1.5	3.7 ± 0.8
S5 - Outer East	136 (27.7)	1.19 ± 0.03	1.18 ± 0.03	1.49 ± 0.08	1.37 ± 0.26	1.91 ± 0.41	84.7 ± 6.4	18.5 ± 5.5	7.0 ± 2.1
S6 - Outer West	129 (26.3)	1.25 ± 0.04	1.24 ± 0.03	1.70 ± 0.10	1.41 ± 0.24	2.34 ± 0.43	82.8 ± 6.9	19.9 ± 3.0	7.7 ± 1.5

impact of these features on the cluster thermodynamic conditions. The age of the shocks t_{age} can be determined by assuming that the shock has traveled from the center to its current position (r_{sh} , the distance to the mid-aperture of the front, reported in Tab. 3.3) with its observed Mach number \mathcal{M} , i.e.:

$$t_{\text{age}} = \frac{r_{\text{sh}}}{\mathcal{M} c_{\text{S}}} \quad (3.7)$$

where $c_{\text{S}} = \sqrt{\gamma kT / (\mu m_{\text{p}})} \approx 5.2 \times 10^2 \sqrt{kT [\text{keV}]} \text{ km s}^{-1}$ is the upstream sound speed (measured from the temperature outside the shock).

We note that this method may slightly overestimate the true shock age (by a relatively modest factor of $\sim 10 - 20\%$, see Randall et al. 2011), given that when the shock was initially launched it likely had a higher Mach number. Using Eq. 3.7 we found an age of 33.4 ± 1.3 Myr for the inner shock S_{in} , 52.9 ± 2.8 Myr for the middle shock (estimated as the average between S3 and S4), and 83.8 ± 1.4 Myr for the outer shock (average between S5 and S6). See Tab. 3.3 for details.

To compute the energy deposited by each shock we considered Eq. 1.27 (e.g. David et al. 2001; Randall et al. 2015). This equation can be rewritten in terms of pre-shock (upstream) pressure p_{out} , shock volume V and Mach number \mathcal{M} as:

$$E_{\text{sh}} = \frac{3}{2} p_{\text{out}} \times V \times \left(\frac{5\mathcal{M}^2 - 5}{4} \right) \quad (3.8)$$

The pressure inside (downstream) and outside (upstream) each front is known from the spectral analysis of the shocks (see Tab. C.2). For each front of each shock pair (S1 and S2, S3 and S4, S5 and S6) we computed the volume as that of one half of a prolate ellipsoid (assuming that the two fronts of each pair are parts of a single cocoon) of major and minor axes set by the annular sector used for the surface brightness and spectral analysis (see Tab C.2; for comparison, see also Randall et al. 2011; Snios et al. 2018). For the cocoon front S_{in} , we considered the full prolate ellipsoid. The shock energies are reported in Tab. 3.3. For the inner edge we have two estimates of the total shock energy, i.e. $E_{\text{S1}} + E_{\text{S2}} = 12.5 \pm 2.5 \times 10^{60}$ erg or $E_{\text{S}_{\text{in}}} = 6.6 \pm 0.3 \times 10^{60}$. The first method likely represents an upper limit to the true shock energy, as it assumes that the whole shock front has the Mach number of its strongest parts. Thus, we consider $E_{\text{S}_{\text{in}}}$ as our best estimate for the shock energy. For the middle and outer shocks we compute the total energy as $E_{\text{sh}}^{\text{m}} = E_{\text{S3}} + E_{\text{S4}}$ and

$E_{\text{sh}}^{\text{o}} = E_{\text{S5}} + E_{\text{S6}}$, respectively, which may overestimate the true shock energy by a factor up to 2 (based on the comparison with the inner edge).

We thus find that the energy rises from the inner shock ($E_{\text{sh}}^{\text{in}} \sim 0.7 \times 10^{61}$ erg), to the middle shock ($E_{\text{sh}}^{\text{m}} \sim 1.4 \times 10^{61}$ erg), to the outer shock ($E_{\text{sh}}^{\text{o}} \sim 3.8 \times 10^{61}$ erg), mostly due to the larger volume occupied by the progressively more distant fronts (see also Randall et al. 2015). These values can be summed up to obtain the total energy injected through shocks in the ICM of RBS 797, that is $E_{\text{sh}}^{\text{tot}} = 5.9 \pm 1.5 \times 10^{61}$ erg.

Ultimately, we computed the shock power as the ratio between the shock energy and the shock age, $P_{\text{sh}} = E_{\text{sh}}/t_{\text{sh}}$. This information is crucial to understand how effective the energy injection by shocks is with respect to other form of energy inputs (e.g. X-ray cavities) or losses (i.e. radiative cooling), a topic we discuss in §3.5.3. On the one hand, the shock energy computed using Eq. 3.8 may be overestimated by up to a factor of ~ 2 (see Randall et al. 2011). On the other hand, as stated above the shock ages may also be slightly overestimated. Thus, in computing the shock power as $E_{\text{sh}}/t_{\text{sh}}$, these two effects partially compensate for one another. We report the shock powers in Tab. 3.3; we estimate total powers of $P_{\text{sh}}^{\text{in}} = 6.3 \pm 0.6 \times 10^{45}$ erg s $^{-1}$, $P_{\text{sh}}^{\text{m}} = 8.7 \pm 1.9 \times 10^{45}$ erg s $^{-1}$ and $P_{\text{sh}}^{\text{o}} = 1.5 \pm 0.4 \times 10^{46}$ erg s $^{-1}$. Since the middle and outer shock powers are based on the highest Mach number parts of the shocks, the true P_{sh}^{m} and P_{sh}^{o} may be slightly lower. It is then possible to conclude that, within errors, the shock power has remained nearly constant, releasing for every outburst roughly $(0.6 - 1.5) \times 10^{46}$ erg s $^{-1}$ in the ICM.

3.4.2 Interpretation: reconstructing the history of feedback in RBS 797

The three weak shocks propagating in the ICM indicate that AGN feedback in RBS 797 has perturbed the environment. The discovery of shocks in ellipticals, groups and clusters has been limited mainly because of the large exposures typically needed to detect such features, and only a few tens of objects with weak shocks due to AGN activity are known. The number of known systems with multiple shock fronts is even lower (M87, Forman et al. 2017, Abell 2052, Blanton et al. 2009, and NGC5813, Randall et al. 2015), making RBS 797 the fourth object known to have more than one AGN-driven shock and the farthest in redshift. Coupled with the presence of multiple X-ray cavities in its cool core (Schindler et al., 2001; Cavagnolo et al., 2011; Doria et al., 2012), this makes RBS 797 one of the rare windows to investigate feedback history and ICM heating in clusters.

Episodic and repetitive AGN activity in RBS 797

The analysis of the weak shocks in RBS 797 (§3.4.1) revealed that the power released by the AGN in shocks has not changed drastically in between outbursts, injecting roughly 10^{61} erg about every 25 Myr. We now aim to perform a similar evaluation for the four X-ray cavities at the center of RBS 797. The analysis of §3.3.1 indicated that the two pairs of cavities on perpendicular axes have similar ages (around ~ 30 Myr). Our new JVLA data (see Chapter 4) further supports the existence of the four cavities, as the 3 GHz radio contours (Fig. 3.6, top panel) are found for the first time to nicely fill also the newly discovered N-S cavities.

To determine the energetics of the four X-ray cavities (whose shape is shown with white ellipses in Fig. 3.6), we consider that $H = [\gamma/(\gamma - 1)]pV = 4pV$ (assuming $\gamma = 4/3$) is the enthalpy of a cavity (where p is the pressure of the surrounding ICM and V is the cavity volume), which is also the minimum total energy required to inflate the cavity (e.g., Bîrzan et al. 2004). From the pressure profile shown in Fig. 3.7 we find an ICM pressure at the average distance of the cavities from the center (~ 27 kpc) of $p = 9.7 \pm 0.8 \times 10^{-10}$ erg cm $^{-3}$. The volumes have been determined from the sizes reported in Tab. 3.2, by assuming that the cavities are prolate ellipsoids and including a 10% relative uncertainty. Results are reported in Tab. 3.4. Then, to compute the cavity power $P_{\text{cav}} = E_{\text{cav}}/t_{\text{age}}$, we considered the age estimates we derived in §3.3.1. To account for the different methods used to determine the age of each cavity (sound speed, buoyancy, refill and expansion timescale, see e.g., McNamara and Nulsen 2012), we computed the mean of the four values for each

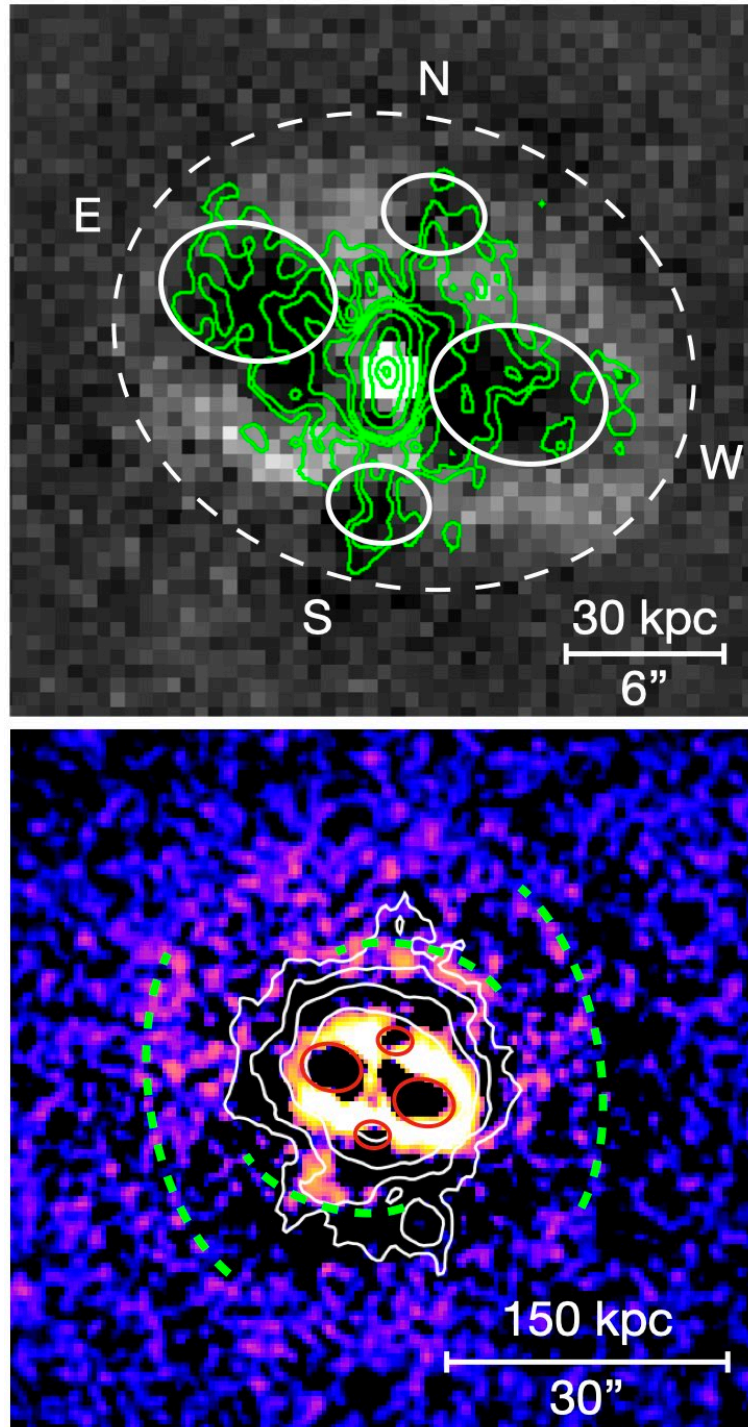


FIGURE 3.6: Combined X-ray and radio data of RBS 797, showing the interaction between the central radio galaxy, the hot ICM, and the diffuse radio emission. Residual *Chandra* images of RBS 797. *Upper panel*: zoom on the inner ~ 60 kpc. The four white ellipses and corresponding labels indicate the shape and name of the X-ray cavities. The dashed white ellipse traces the inner cocoon shock. Green contours at 3 GHz from the new JVLA observations (see §3.2.2; Chapter 4) are overlaid. The resolution is $0.9'' \times 0.8''$, the σ_{rms} noise is $5 \mu\text{Jy}/\text{beam}$, and the contours are drawn at $(6, 8, 10, 12, 16, 48, 96, 256, 360) \times \sigma_{\text{rms}}$. *Lower panel*: residual image of the inner ~ 300 kpc. Green dashed arcs mark the position of the middle and the outer shock fronts. White contours at 1.4 GHz from the VLA ($3''$ resolution, see §3.2.2 for details) show the diffuse radio emission surrounding the AGN (see Doria et al. 2012).

TABLE 3.4: Energetics of the four X-ray cavities in RBS 797. (1) Cavity name; see also Fig. 3.6); (2) Energy of the cavity, computed as $E_{cav} = 4pV$ (see text for details); (3) Age of the X-ray cavity, computed as the average of the sound cross, buoyancy, refill and expansion timescales reported in Tab. 3.2; (4) Cavity power $P_{cav} = E_{cav}/t_{age}$.

	E_{cav} [10^{60} erg]	t_{age} [Myr]	P_{cav} [10^{45} erg s $^{-1}$]
Cavity E	1.4±0.2	30.9±15.6	1.4±0.9
Cavity W	1.4±0.2	29.5±16.2	1.5±0.9
Cavity N	0.29±0.04	29.2±13.3	0.32±0.17
Cavity S	0.29±0.04	27.7±12.9	0.34±0.18

cavity (third column in Tab. 3.4), assuming the scatter as an estimate of our uncertainty (which is larger than statistical errors). The similar ages of the bubbles are compatible with the E-W and N-S X-ray cavities being nearly coeval.

Overall, the difference in power between the E-W ($\sim 3 \times 10^{45}$ erg s $^{-1}$) and the N-S ($\sim 6 \times 10^{44}$ erg s $^{-1}$) cavity pairs reflects the difference in energy (a factor of 5), which in turn is caused by the E-W cavities being larger than the N-S ones. In §3.3.2 we argued that the nearly coeval cavities are consistent with both a rapid reorientation of the AGN jets and the presence of binary AGN in the BCG. Both scenarios may account for the different power: either the AGN has reoriented its jets *and* reduced/increased its mechanical power (see also e.g., MS 0735.6+7421, Vantyghem et al. 2014), or the X-ray cavities might have been excavated by two AGN with different mechanical power.

By summing the values of each cavity (Tab. 3.4, second column for energy and fourth column for power), we deduce that the total energy stored in the four X-ray cavities is $E_{cav}^{tot} = 3.3 \pm 0.5 \times 10^{60}$ erg, while the total power is $P_{cav}^{tot} = 3.6 \pm 2.2 \times 10^{45}$ erg s $^{-1}$. By comparing these values with the total energy carried by shocks, we find that $E_{sh}^{tot}/E_{cav}^{tot} \sim 18$. This value is slightly higher than those of other galaxy clusters and groups with shocks and X-ray cavities, where the E_{sh}/E_{cav} ratio ranges between 0.1 - 10 (Liu et al., 2019b). It is worth mentioning, however, that if we are missing older X-ray cavities associated with the middle and outer shocks, then the ratio obtained for RBS 797 might be overestimated. In any case, while cavities are good *tracers* of jet feedback, the exact mechanism and timescales over which they thermalize their energy into the gas is highly uncertain. On the contrary, the energy associated with shock fronts (which are more difficult to detect) is by definition already deposited in the ICM. Without entering a detailed comparison, which would require a careful modeling of these mechanisms, we note that in RBS 797 the shock power is an order of magnitude larger than the radiative losses of the gas (§3.5.3). This possibly supports the idea that regardless of the energy stored in cavities, shocks alone effectively counterbalance gas cooling.

It is useful to compare RBS 797 with the galaxy group NGC 5813, where Randall et al. (2011) and Randall et al. (2015) found three collinear pairs of X-ray cavities, each associated with an elliptical shock front. First, it is interesting to note that both NGC 5813 and RBS 797 have an outburst repetition rate of 1 shock every $\approx 2 \times 10^7$ yr. Thus, at least for these two examples, we observe that the repetition interval of low mass systems is similar to that of high mass systems. Nonetheless, while in NGC 5813 the alignment of the outbursts enables a clear association of each X-ray cavity system with its shock, the misaligned cycles of AGN activity in RBS 797 determined a complex ICM geometry, which in turn prevents us from clearly linking X-ray cavities and shocks.

In this context, we note the good agreement between the age of the E-W/N-S cavities ($\sim 28 - 31$ Myr) and the age of the inner edge ($t_{age}^{in} = 33.4 \pm 1.3$ Myr). This similarity in timescales further strengthens the association between the X-ray cavities and the inner shock already evident in the

morphology. Furthermore, we may speculate that the inner shock, being stronger in the E-W direction (see §3.4.1), has been driven by the same jet episode that inflated the E-W X-ray cavities. This hypothesis could suggest that the N-S cavities are younger than the E-W ones (by a factor smaller than our uncertainties, that point to the cavities being nearly coeval; see Tab. 3.2 and §3.3.2), since otherwise the inner cocoon shock would have disrupted any previous N-S small bubble (see e.g., the example of M87 in Churazov et al. 2001).

However, we observe that projection effects may hide the true 3D distribution of the cavities within the cocoon shock. Moreover, even though the N-S cavity power indicates a weaker outburst with respect to the E-W one, the N-S jet activity may also have driven weak shock waves that we are unable to detect. Indeed, any AGN jet episode can drive weak shocks, regardless of the jet power (see the simulations of Bourne and Sijacki 2021), with shocks driven by weaker jets quickly broadening into sound waves (which are difficult to detect even in local, deeply observed clusters, see e.g., Graham et al. 2008a). With these notes of caution in mind, we favor the idea that the observed inner shock has been driven by the E-W jet activity, given the available evidence.

Regarding the middle and outer shocks, the detection of other, external X-ray cavities is likely prevented by the increasing difficulty in detecting cavities at large distances from the center (e.g., Birzan et al. 2009) and by the complicated geometry of the cluster. For instance, older cavities produced ~ 80 Myrs ago (when the outer shock was launched) may have been overridden and distorted by the passage of the middle shock ~ 54 Myr ago (see also Bogdán et al. 2014). In this respect, we notice that RBS 797 shows diffuse radio emission within its cool core, with an extent of ≈ 100 kpc and slightly elongated to N-S. The diffuse radio source has been classified as a radio mini-halo (Gitti et al., 2006; Doria et al., 2012).

Without entering a detailed discussion, we may speculate a connection between the AGN activity and the diffuse radio emission. Shocks may (re)-accelerate relativistic seeds from AGN outbursts via several mechanisms including compression and turbulence (generated downstream by shocks themselves), and advect the plasma on 100 kpc scales (e.g., Brunetti and Jones 2014). By overplotting the 1.4 GHz VLA radio contours on the *Chandra* residual image in the lower panel of Fig. 3.6, we notice that the N-S radio protrusions are roughly parallel to the axis of outer shock, while the roundish structure outside the cavities seems to be caged within the middle shock. It may thus be possible that we are observing the remnant of what once were distinct AGN outbursts in several directions: due to the passage of multiple shocks the radio emission may have been distorted until a rather amorphous and nearly circular shape has formed. This scenario has been recently tested by Bonafede et al. (2023), who found that shocks alone cannot account for the observed diffuse radio emission. Instead, the AGN-driven shocks are likely propagating onto an already existing mini-halo, leaving imprints in its spectral properties.

3.5 Global ICM properties and X-ray emission from the AGN in RBS 797

The following subsections are dedicated to the analysis of the global properties of the ICM in RBS 797, and to the X-ray emission of its central AGN. After deriving the radial profiles (§3.5.1) and maps (§3.2.1) of thermodynamic quantities, we study the abundance distribution in the ICM (§3.5.1). Ultimately, we perform a spectral modelling of the central X-ray point source, coincident with the core of the radio galaxy.

3.5.1 Results

Radial profiles of thermodynamic properties

Radial profiles of thermodynamic variables (temperature, density, pressure, entropy and cooling time) are essential tools for investigating cooling, feedback, and the thermodynamic state of clusters. In order to build such profiles, we extracted the spectra of circular annuli centered on the AGN

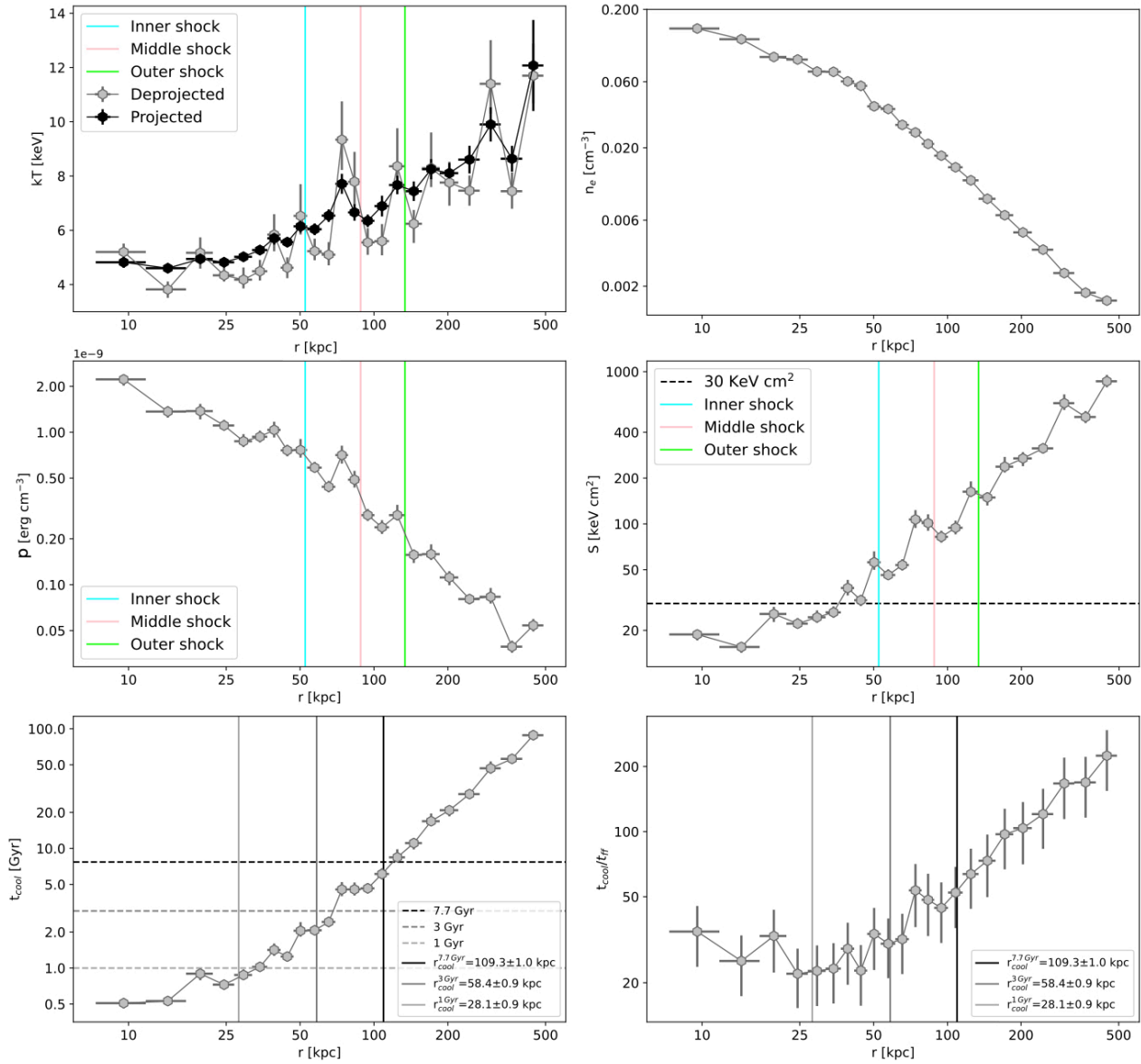


FIGURE 3.7: Radial profiles of ICM thermodynamic quantities in RBS 797. *Upper left*: projected (black dots) and deprojected (grey dots) temperature profiles; *Upper right*: electron density profile; *Middle left*: pressure profile; *Middle right*: entropy profile, with the horizontal dotted line showing the $S \leq 30 \text{ keV cm}^2$ threshold for the condensation of the ICM into multi-phase gas clouds; *Lower left*: cooling time profile, with horizontal lines showing different indicators (1 Gyr, 3 Gyr and 7.7 Gyr) of the cool core region, the extent of which for each indicator is marked by the vertical lines; *Lower right*: radial profile of the ratio between the cooling time and the free-fall time ($t_{\text{cool}}/t_{\text{ff}}$), with the different estimates for the cooling radius overlaid with vertical lines. In the temperature, pressure and entropy profiles the colored vertical lines show the distance from the center of the three nested weak shocks (see §3.4.1). For details on how these profiles were built see §3.5.1.

and extending between $1.5'' - 100''$ (7.5 kpc - 500 kpc). The width of each annulus is designed to obtain more than 8000 counts in the 0.5 - 7 keV band, enabling us to constrain temperatures with an accuracy of 5% (8% when deprojected). The spectra were fit with a projected (`tbabs*apec`) and a deprojected (`projct*tbabs*apec`) thermal model.

We show the resulting radial profiles of temperature (projected in black and deprojected in gray), density, pressure, entropy and cooling time (estimated using Eq. 3.1,1.2,1.3,1.11) in the first five panels of Fig. 3.7. We verified that neither intrinsic absorption (`ztbabs*tbabs*apec`) or an additional thermal component (`tbabs*(apec+apec)`) is required in any of the annuli.

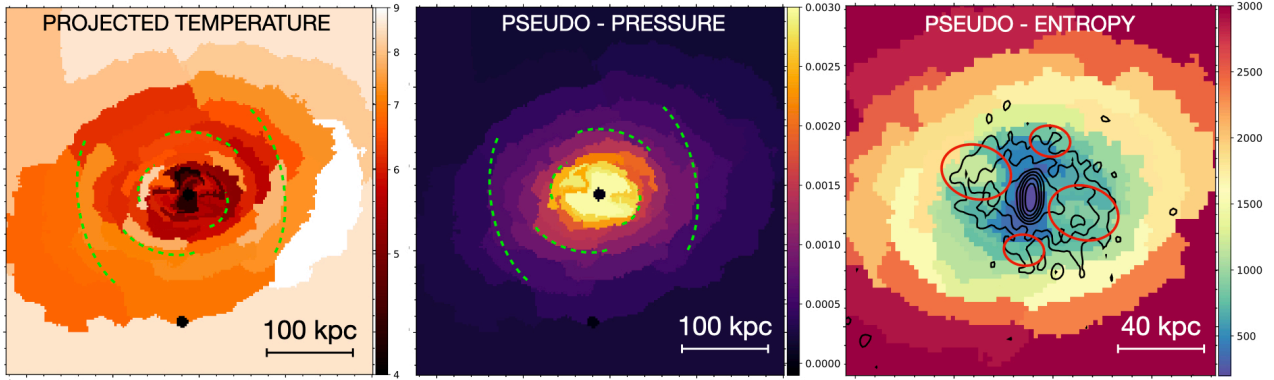


FIGURE 3.8: Maps of projected temperature (in keV, *left panel*), pseudo-pressure (in arbitrary units, *middle panel*) and pseudo-entropy (in arbitrary units, *right panel*). The spectrum extracted from each region has a $\text{SNR} \geq 60$. Relative uncertainties on the mapped values are $\leq 20\%$. In the *left* and *middle* panels, the green dashed arcs indicate the position and extent of the arc-like edges identified in §3.4.1. In the *right panel* the black contours show the radio galaxy at 1.4 GHz (see Gitti et al. 2006), while the red ellipses indicate the X-ray cavities. The central X-ray point source has been excluded from the spectral fitting.

The inwardly increasing density and decreasing temperature, entropy and cooling time confirm that RBS 797 is a cool core cluster (as already noticed by Schindler et al. 2001; Birzan et al. 2004; Gitti et al. 2006; Cavagnolo et al. 2011; Doria et al. 2012). With our deeper exposure, we are now able to resolve localized gradients in thermodynamic properties. We overplot on the temperature, pressure and entropy profiles the distance from the center of the three nested shocks. Both the projected and deprojected temperature profiles reveal an increase in temperature behind the three edges; moreover, the pressure and entropy within the edges are higher than outside.

The radial spectral analysis allows us to characterize the efficiency of ICM cooling in RBS 797. First of all, we aim at determining the extent of the cool core region, usually defined in the literature as the region where the gas has a cooling time less than 7.7 Gyr (corresponding to the look-back time of $z \sim 1$ for the assumed cosmology; Birzan et al. 2004). Other studies instead consider more conservative thresholds, as 3 Gyr or 1 Gyr (typical timescale from the last major merger; e.g. McDonald et al. 2018). Thus, we fitted the cooling time profile with a power-law and located the intersection with $t_{\text{cool}} = 1, 3, 7.7$ Gyr. We find that the cooling radius in RBS 797 (where cooling time is less than 7.7 Gyr⁶) is $r_{\text{cool}}^{7.7 \text{ Gyr}} = 109.3 \pm 1.0$ kpc (or $22.4''$ - consistent with Doria et al. 2012). The cooling time falls below 3 Gyr within 58.4 ± 0.9 kpc and below 1 Gyr within 28.1 ± 0.9 kpc. Second of all, we wish to locate the radial range over which the ICM is not only cooling, but multi-phase gas is also expected to be present. To fulfill this aim, we employed different ICM cooling diagnostics. On the one hand, according to McNamara et al. (2016) the gas should become multi-phase when the entropy is lower than 30 keV cm^2 or the cooling time falls below 1 Gyr. As it can be seen in Fig. 3.7, these conditions are both satisfied within roughly 30 kpc from the center. On the other hand, it has been suggested that cooling of the ICM into warm clouds occurs when the ratio between the cooling time and the free fall time (t_{ff}) is of the order of a few tens (10 - 30, e.g., Voit and Donahue 2015).

To measure the free fall time, we derived the hydrostatic mass (e.g., Voigt and Fabian 2006) of RBS 797 from the deprojected pressure and density profile. Then, from the mass profile $M(r)$ it is possible to obtain the free fall time profile $t_{\text{ff}}(r)$ using Eq. 1.29. We show in Fig. 3.7 the radial profile of $t_{\text{cool}}/t_{\text{ff}}$, which reveals that the ratio approaches ~ 20 -30 below ~ 35 kpc from the center, which is

⁶We are aware that for RBS 797 ($z = 0.354$) the time that has passed since $z = 1$ is not 7.7 Gyr but ~ 4 Gyr. However, a $t_{\text{cool}} \leq 7.7$ Gyr is the typical approach of several studies in the literature (e.g., Birzan et al. 2004; Rafferty et al. 2006), and has also been adopted for studies of clusters at higher redshift than RBS 797, up to $z \sim 1.2$ (e.g., Hlavacek-Larrondo et al. 2012; Hlavacek-Larrondo et al. 2015; Birzan et al. 2017). Thus, using this threshold - while possibly non-physical - enables us to draw comparison with the literature.

also the extent of gas with $S \leq 30 \text{ keV cm}^2$ and $t_{\text{cool}} \leq 1 \text{ Gyr}$. Therefore, in RBS 797 we find that the conditions for the presence of multi-phase gas are met within a few tens of kpc from the center. We note that the azimuthally averaged radial analysis can predict the extent of the region where condensation should occur, but does not provide information on the azimuthal geometry of cold and dense gas. Thus, in the following subsection we show different methods for building maps of ICM thermodynamic quantities, that can provide valuable information on the radial and azimuthal variations of thermodynamic quantities and cooling efficiency.

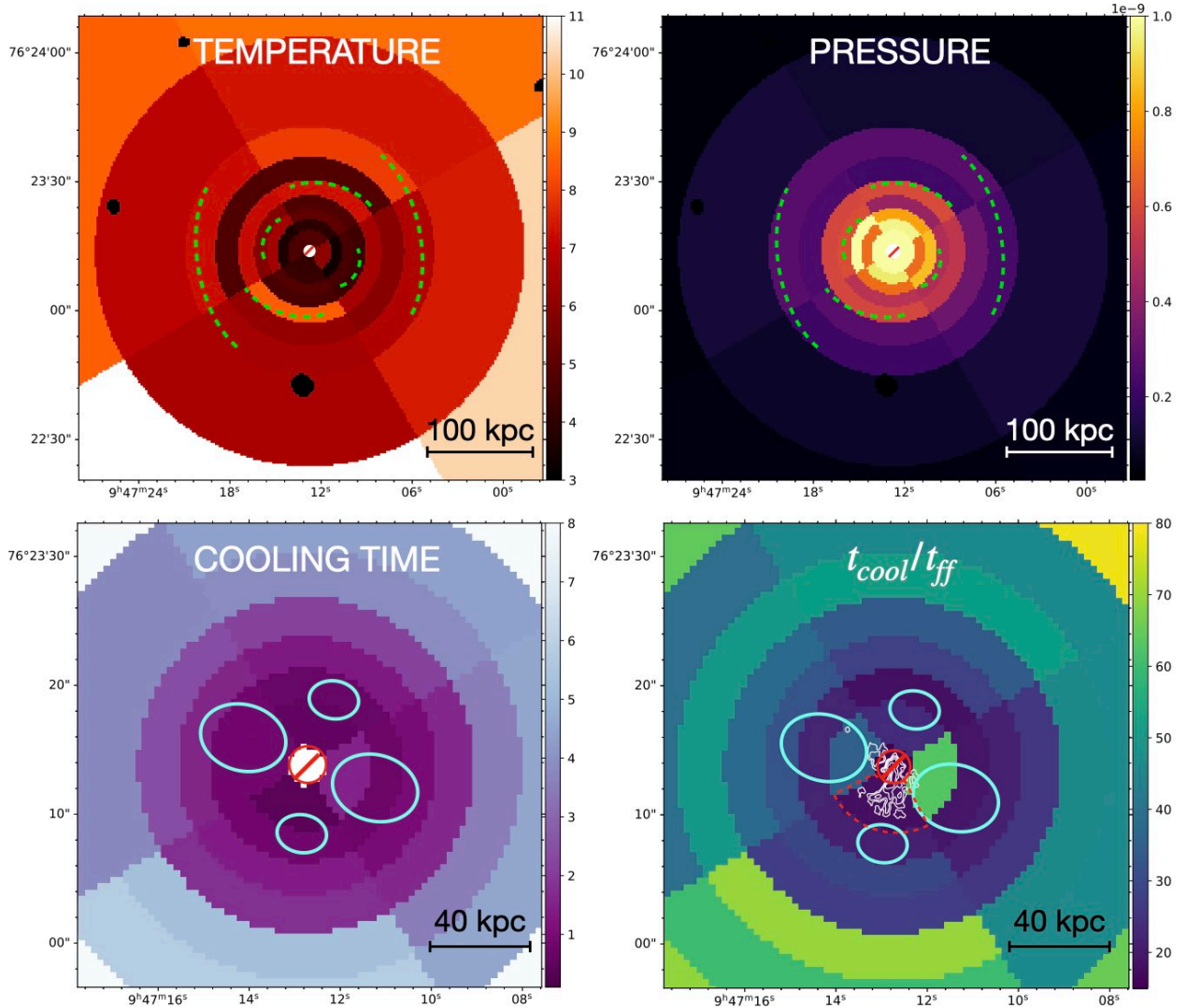


FIGURE 3.9: Maps of deprojected temperature (*upper left*, in keV), pressure (*upper right*, in erg cm^{-3}), cooling time (*lower left*, in Gyr) and $t_{\text{cool}}/t_{\text{ff}}$ ratio (*lower right*) of the ICM, built by dividing the azimuth in four sectors and nine annuli (see text for details). In the *upper* panels, the green dashed arcs indicate the position and extent of the arc-like edges identified in §3.4.1. In the *lower* panels, cyan ellipses show the position of the X-ray cavities. In the *lower right* panel, white contours from Calzadilla et al. (2022) trace the morphology of the central [OII] emitting nebulae, and the red dashed wedge shows the region where the minimum in $t_{\text{cool}}/t_{\text{ff}}$ is found. Relative uncertainties in temperature, pressure and cooling time are on the order of $\sim 10\%$, while those in $t_{\text{cool}}/t_{\text{ff}}$ are on the order of $\sim 20\%$. The central X-ray point source has been excluded from the spectral fitting.

Spectral maps of the ICM

We show in Fig. 3.8 the maps of projected temperature, pseudo-pressure, and pseudo-entropy of

the ICM in RBS 797, obtained with the method outlined in §3.2.1. These images show that the cooler and lower entropy gas is preferentially found in the bright central bar oriented north-south, and in the rims of the four X-ray cavities. These low entropy structures are likely the results of the combined expansion of the four X-ray cavities in the ICM, that may have uplifted the surrounding low entropy medium and/or triggered its condensation. By overlaying on the thermodynamic maps the arcs representing the shock fronts discussed in §3.4.1, it is possible to appreciate the presence of high temperature and high pressure regions behind the arcs. Additionally, the entropy map shows that the low entropy gas encasing the X-ray cavities is more extended to the west. This supports the idea that low temperature gas projected in front of S2 may be damping the temperature gradient, as hypothesized in §3.4.1.

Overall, the radial and thermodynamic maps analysis revealed that the ICM of RBS797 presents several radial and azimuthal gradients in spectral properties. In order to further investigate these features with improved statistics, and with the aim of measuring *deprojected* thermodynamic quantities at different radii and orientations, we performed a spectral mapping in annular sectors. In particular, we divided the azimuth in four sectors with angular aperture of 90° , starting in the west, with a center line at P.A. 345° for the first sector (to match the approximate symmetry of the central region). Then, each sector was divided in 9 annular regions, so that each annular sector contained at least the same number of counts (8000 in the 0.5 - 7 keV band) as the annuli used to construct the radial profiles in Fig. 3.7. By fitting the spectra with a `projct*tbabs*apec` model we are thus able to probe *radial and azimuthal* variations of deprojected thermodynamic properties (see also Gitti et al. 2010). To derive useful information on the distribution of cooling gas we also mapped the cooling time and the $t_{\text{cool}}/t_{\text{ff}}$ ratio, by measuring the free fall time at the radial distance of each annulus from the center (Eq. 1.29).

The resulting deprojected temperature and pressure maps (see Fig. 3.9) highlight the concentric, nested and misaligned weak shocks (as found in the projected thermodynamic maps of Fig. 3.8). We note that due to the choice of circular symmetry, and the fact that the wedges do not exactly follow the shock fronts, the outer jump is less well defined.

The cooling time and $t_{\text{cool}}/t_{\text{ff}}$ maps (lower panels in Fig. 3.9) confirm that short cooling time (≤ 1 Gyr) gas is filling the space between and around the perpendicular radio lobes and cavities, supporting a strong connection between the AGN outbursts and ICM cooling. We note that the innermost southern wedge (red dashed region in Fig. 3.9) represents the locus where cooling should be most effective: we measure a local cooling time of $t_{\text{cool}} = 438 \pm 51$ Myr and $t_{\text{cool}}/t_{\text{ff}} = 17.9 \pm 2.0$ (and an entropy $S = 15.4 \pm 1.2$ keV cm², not shown here). We thus expect that filamentary multi-phase warm gas arising from condensation of the ICM should preferentially be found in this region. In this context, Cavagnolo et al. (2011) noted filamentary structures in the residual optical image of the BCG extending 8 - 10 kpc southward. These structures were recently confirmed by Calzadilla et al. (2022), who produced continuum-subtracted [O II] maps of nebular emission using the *Hubble Space Telescope*. The overlay of [O II] contours on the $t_{\text{cool}}/t_{\text{ff}}$ map (see lower right panel in Fig. 3.9) reveals that cool gas at $\sim 10^4$ K is coincident with the region where the minimum in $t_{\text{cool}}/t_{\text{ff}}$ is found (within ~ 20 kpc south from the center). These results may indicate that the local ICM is actually condensing into cool gas.

Metallicity of the ICM

A previous study of the metallicity distribution based on the analysis of the ~ 50 ks exposure found tentative indications of higher abundances in the direction of the E-W cavities compared to the surrounding medium (Doria et al., 2012), possibly suggesting that the thrust associated with the cavities' expansion was uplifting enriched gas from the center, as seen in a number of other systems (e.g. Kirkpatrick et al. 2011; Kirkpatrick and McNamara 2015). Our aim is to follow-up on this argument with the deeper *Chandra* exposure, by analyzing the radial and azimuthal distribution of metals in RBS 797.

Constraining the abundances of the ICM with *Chandra* typically requires spectra with a high SNR

($\gtrsim 100$). Therefore, to map the ICM abundances we built another set of maps requiring for each spectral extraction region a minimum SNR of 100 in the 0.5 - 7 keV band. Fitting the spectra with a `tbabs*apec` model allowed us to map abundances with relative uncertainties of ≤ 10 -15%. The metallicity map obtained with this choice of SNR is shown in Fig. 3.10. We note that within the inner ~ 50 -70 kpc the abundance is higher than outside ~ 80 kpc from the center, which is expected in a cool core cluster. A peculiar feature in the metallicity map is the presence of a ring of enhanced metallicity at ~ 50 kpc from the center. By overlaying 1.4 GHz radio contours on the map it is possible to see that this ring surrounds the lobes of the central radio galaxy to the east, north, west and south-west of the center. On the one hand, this feature is consistent with the scenario proposed by Doria et al. (2012) that the AGN is responsible for mechanical uplift of enriched gas from the center. On the other hand, the deep *Chandra* exposure seems to rule out a bipolar uplift, as the ring covers almost the whole azimuth. In fact, the discovery of four equidistant cavities excavated by the AGN in perpendicular directions is consistent with an azimuthally-symmetric enhancement. This has been also predicted by high-resolution hydrodynamical simulations of AGN jet feedback (e.g., Gaspari et al. 2011).

We note that both the analysis of Doria et al. (2012) and the metallicity map shown in Fig. 3.10 do not take into account projection effects. Measuring accurate deprojected abundances requires an even larger SNR. Thus, to build a high-fidelity radial profile of abundances we extracted the spectrum from nine concentric circular annuli (extending between $1.5''$ - $100''$ from the center) centered on the AGN, requiring ~ 30000 counts per bin (or $\text{SNR} \sim 200$). By fitting again the spectra with a `tbabs*apec` model we verified that relative uncertainties on projected and deprojected abundances are of $\sim 6\%$ and $\sim 10 - 15\%$, respectively. The projected and deprojected profiles shown in Fig. 3.10 confirm the general decreasing trends of abundances with radius; there is a clear gradient at roughly 80 kpc from the center, with average (deprojected) abundances of $\langle Z(r \leq 80 \text{ kpc}) \rangle = 0.62 \pm 0.04 Z_{\odot}$ and of $\langle Z(r \geq 80 \text{ kpc}) \rangle = 0.41 \pm 0.05 Z_{\odot}$. Furthermore, the projected and deprojected profiles hint at a slightly lower central abundance (by approximately 15%) than in the region where the X-ray cavities are located (20 - 50 kpc, overplotted in green). As a sanity check, we tested whether our results could be affected by the iron bias (see e.g., Buote 1999) by fitting a two-temperature model to spectra of the 9 radial bins, finding that the plasma is well described by a single temperature model; thus, we conclude that the abundances are not being underestimated. We also exclude that the inverse iron bias (see e.g., Gastaldello et al. 2010) is responsible for the higher abundance at the cavities edges, as this effect is typical of clusters with temperatures of 2 - 4 keV - while RBS 797 has temperatures that do not fall below 4 keV (see §3.5.1). We thus conclude that the *Chandra* data hint at a slight excess in metallicity between 20 - 50 kpc with respect to the central gas, which may be due to the AGN pushing enriched gas outwards while inflating its radio lobes.

3.5.2 The central X-ray point source

At the center of the *Chandra* image of RBS 797 there is a bright X-ray point source that coincides with the radio core of the AGN. Given its location, this point source likely represent the non-thermal X-ray emission from the nucleus of the radio galaxy. Indeed, the study of the previous *Chandra* exposures found that the X-ray source is well described by an absorbed power-law (Cavagnolo et al., 2011). To measure its properties with our deeper X-ray observations, we extracted the spectrum of a circle with radius $1.5''$ (~ 7 kpc, which encloses 90% of the encircled energy fraction) centered on the source. The background spectrum was extracted from an annulus extending between $2''$ to $6''$ from the center. The resulting source spectrum has roughly 5000 net counts in the 0.5 - 7 keV band.

As also observed by Cavagnolo et al. (2011), we found that the spectrum has the typical appearance of a slightly absorbed power-law. There are no indications for the presence of residual thermal components possibly related to the central ICM, suggesting that the plasma properties between

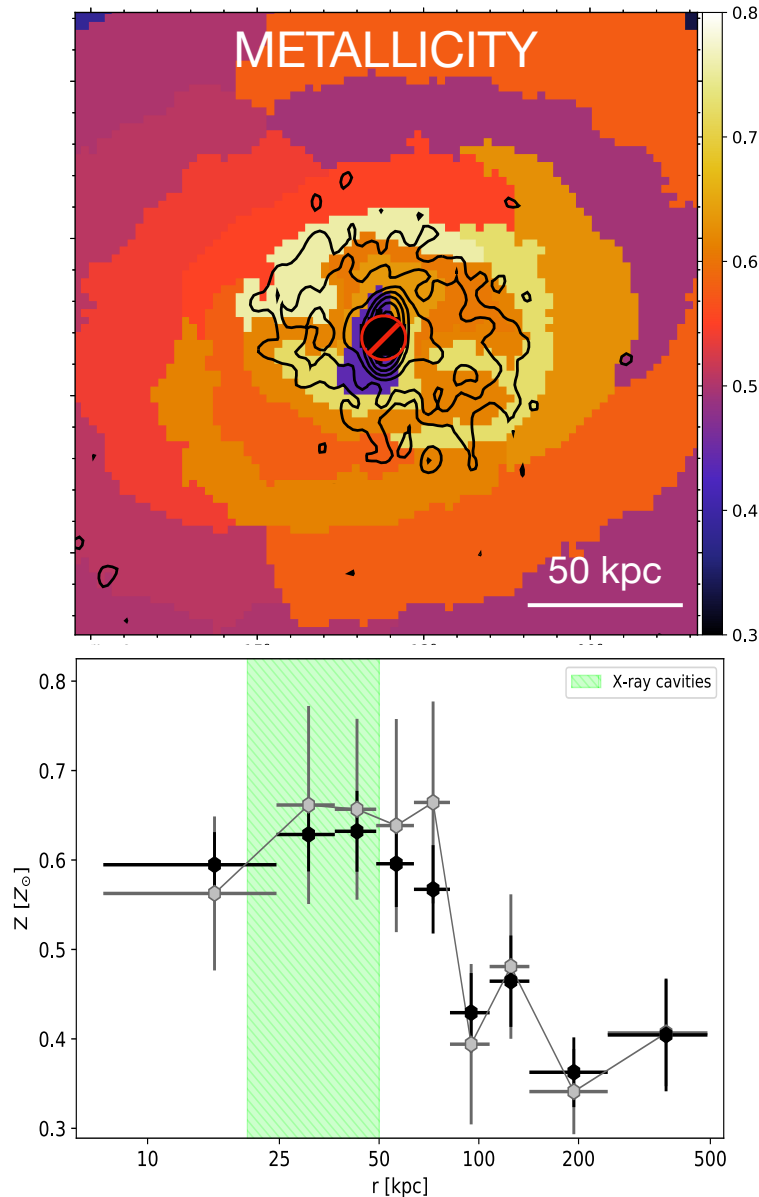


FIGURE 3.10: *Upper panel*: metallicity map of the ICM in Z_{\odot} . The spectrum extracted from each region has a $\text{SNR} \sim 100$. Relative uncertainties on the mapped values are $\leq 10\text{-}15\%$. Overlaid in black are the contours of the radio galaxy at 1.4 GHz (same as in Fig. 3.4; Gitti et al. 2006). The central X-ray point source has been excluded from the spectral fitting. *Lower panel*: projected (black dots) and deprojected (grey dots) metallicity radial profile, with the green region showing the radial range where the X-ray cavities are located.

$2'' - 6''$ (the local background extraction region) and those within $1.5''$ from the center are similar (see also the rather flat temperature and metallicity profiles of Perseus in this radial range, e.g., Schmidt et al. 2002; Fabian et al. 2006). Using a Galactic-absorbed power-law model (tbabs*po, without intrinsic absorption) to describe the spectrum results in a rather poor fit: the unphysically flat power-law index ($\Gamma = 0.31 \pm 0.04$) and the $\chi^2/D.o.f. = 548.6/373 = 1.47$ indicate that an additional component is likely required. Indeed, adding an intrinsic absorber (ztbabs) at the cluster redshift of 0.354 resulted in a good fit: we find a modest intrinsic column density of $N_H^{int} = (7.49 \pm 0.82) \times 10^{22} \text{ cm}^{-2}$ and power-law index $\Gamma = 1.70 \pm 0.12$, for a $\chi^2/D.o.f. = 385.9/372 = 1.03$. The improvement is thus statistically significant (F-test value of 156.8 and null-hypothesis probability 2×10^{-30}).

The value of N_H^{int} is consistent with previous estimates (Cavagnolo et al., 2011), and suggests that

the AGN is not heavily obscured. The steep power-law index is typical of radio galaxies in BCGs; converting the power-law index to spectral index ($\alpha_X = \Gamma - 1 = 0.7$) we find a good agreement with the spectral index measured at GHz radio frequencies ($\alpha_R \sim 0.9$, Gitti et al. 2006). The 2 - 10 keV power-law luminosity is $L_{2-10\text{keV}} = (1.37 \pm 0.04) \times 10^{44} \text{ erg s}^{-1}$, while the bolometric power-law luminosity is $L_{\text{bol}}^X = (4.18 \pm 0.02) \times 10^{44} \text{ erg s}^{-1}$.

The 2 - 10 keV luminosity and the 5 GHz luminosity of the unresolved radio core of the AGN ($5.4 \times 10^{40} \text{ erg s}^{-1}$, Gitti et al. 2006) can be combined to estimate the mass of the supermassive black hole in RBS 797 using the fundamental black hole plane (Gültekin et al., 2019), obtaining $M_{\text{SMBH}} \sim 1.4 \times 10^9 M_{\odot}$. This value is in good agreement with the estimate of $M_{\text{SMBH}} \sim 1.5 \times 10^9 M_{\odot}$ based on the central velocity dispersion (Cavagnolo et al., 2011).

3.5.3 Discussion

Are heating and cooling balanced in RBS 797?

To test the ICM-AGN feedback cycle paradigm, we aim at comparing the shock and cavity powers with the amount of radiative losses in the X-ray band. Several studies in the literature have considered that the gas bolometric X-ray luminosity within the cooling radius of cool core clusters can be considered as a proxy for the magnitude of ICM cooling and flowing to the center (e.g., Fabian et al. 1984; Bîrzan et al. 2004; Rafferty et al. 2006).

We determined that RBS 797 has a cool core (where $t_{\text{cool}} \leq 7.7 \text{ Gyr}$) with a cooling radius of 109 kpc (see §3.5.1). We thus extracted the spectrum of the gas within the cooling radius (excluding the inner 1.5'') and of the region between 109 kpc - 500 kpc to allow for deprojection. The spectra were fitted with a deprojected thermal model (`projct*tbabs*apec`), obtaining the following results:

- For $r \leq r_{\text{cool}}$ the ICM has a temperature $kT = 5.55_{-0.05}^{+0.03} \text{ keV}$, an abundance $Z = 0.56 \pm 0.02 Z_{\odot}$ and radiates a bolometric luminosity of $L_{\text{bol}}^X \equiv L_{\text{cool}} = (2.34 \pm 0.01) \times 10^{45} \text{ erg s}^{-1}$.
- For $r > r_{\text{cool}}$ we measure a temperature $kT = 8.28 \pm 0.12 \text{ keV}$, an abundance $Z = 0.40 \pm 0.03 Z_{\odot}$ and a bolometric luminosity of $L_{\text{bol}}^X = (1.45 \pm 0.02) \times 10^{45} \text{ erg s}^{-1}$. The $\chi^2/D.o.f.$ is 5896/6012 (= 0.98).

We also tested the inclusion of an isobaric cooling component (`mkcflow`) to constrain the spectroscopic mass deposition rate, i.e. the rate at which gas is actually cooling to lower temperatures, by fitting a `tbabs*(apec+mkcflow)` model to the spectrum of the ICM for $r \leq r_{\text{cool}}$. The high temperature and abundance of the `mkcflow` component were tied to the values of the `apec`, while the low temperature was fixed at 0.1 keV. We found that we can only place an upper limit on the mass deposition rate of $\dot{M}_{\text{cool}} \leq 37 M_{\odot} \text{ yr}^{-1}$ (at 99% confidence). By reducing the size of the extraction region to $r \leq 30 \text{ kpc}$ (where the entropy is smaller than 30 keV cm^{-2} , see §3.5.1), we still measure an upper limit on the mass deposition rate of $\dot{M}_{\text{cool}} \leq 40 M_{\odot} \text{ yr}^{-1}$. We note that Doria et al. (2012) obtained a $\dot{M}_{\text{cool}} = 231_{-227}^{+316} M_{\odot} \text{ yr}^{-1}$ from the previous *Chandra* observations. While this estimate would suggest a much higher mass deposition rate, the associated large uncertainties are fully consistent with our more stringent upper limit.

Altogether, we find that cavity power alone ($P_{\text{cav}}^{\text{tot}} = 3.6 \times 10^{45} \text{ erg s}^{-1}$) can balance radiative losses within the cool core of RBS 797. Including the energy injected in shocks, the total heating power of the AGN in RBS 797 is of roughly $3.4 \times 10^{46} \text{ erg s}^{-1}$, which exceeds the cooling luminosity, $L_{\text{cool}} = (2.34 \pm 0.01) \times 10^{45} \text{ erg s}^{-1}$ by a factor ~ 14 . Additionally, we note that the outer shock, which is located at $\sim 130 \text{ kpc}$ from the center, lies outside the cool core ($r_{\text{cool}} \sim 109 \text{ kpc}$). Thus, the AGN in RBS 797 may not only be able to match radiative losses within the cool core, but also to heat the gas at larger distances from the center. Similar results were obtained in the cases of Hydra A (e.g. Nulsen et al. 2005; Wise et al. 2007), and of MS 0735.6+7421 (e.g., McNamara et al. 2005; Gitti et al. 2007), where however giant cavities (with radius exceeding 100 kpc) and large-scale shock fronts (at distances of more than 200 kpc from the center) were found. The fact that in RBS 797 smaller shock fronts (and the possibly associated undetected cavities) lie outside r_{cool} may

imply that heating beyond the cool core is more common than previously thought (i.e. there may be undetectable cavities and shock fronts or sound waves at $r \geq r_{\text{cool}}$ in many other systems).

We can also test the local balance of shock heating and radiative cooling. Following the strategy applied by Randall et al. (2011) and Randall et al. (2015) to NGC 5813, we consider that the fractional effective heat input from one shock is $\Delta \ln(p/\rho^\gamma)$ (see Eq. 1.28). Considering the Mach numbers of the shock fronts (see Tab. 3.3), we find that the change in $\ln(p/\rho^\gamma)$ across the inner, middle, and outer shocks is $\sim 1\%$, $\sim 0.4\%$ and $\sim 0.5\%$, respectively. Taking the reciprocal of these values, we find that ~ 100 , ~ 250 , and ~ 200 outbursts are needed per local cooling time to completely offset cooling with shock heating at the location of the inner, middle and outer shock edges, respectively. The cooling time outside the edges is 2 Gyr (inner shock), 5 Gyr (middle shock) and 9 Gyr (outer shock). Assuming an outburst interval of 25 Myr (see §3.4.2) gives 80 shocks (inner shock), 200 shocks (medium shock) and 360 shocks (outer shock) per local cooling time. Thus, we find that in RBS 797 there is agreement between the number of shocks required to offset radiative cooling and those expected per local cooling time (as found by Randall et al. 2011; Randall et al. 2015 for the galaxy group NGC 5813).

3.6 Summary and Conclusions

Overall, the new, deep Chandra data revealed that RBS 797 is a beautiful example of how strongly the AGN activity can impact the ICM conditions. Our results can be summarized as follows:

1. With the deepest to date *Chandra* observation of RBS 797 (427 ks) we unveiled the existence of two additional X-ray cavities (in the N-S direction) at the same distance from the center as the previously known E-W cavities (~ 27 kpc). Using archival, multi-frequency VLA data, we highlighted the co-spatiality of the four cavities with the radio lobes of the central radio galaxy. Thus, we find RBS 797 to be the first system in which four equidistant, radio filled X-ray cavities are symmetrically found in perpendicular directions.
2. We computed the ages of the cavities by means of the X-ray data: the four cavities have similar ages, being approximately 10-50 Myr old, and with an age difference between the two outbursts of at most ~ 10 Myr. Considering the geometry and timescales of the four symmetrical X-ray cavities, we argue that the scenario in which a binary AGN is powering the two perpendicular outbursts might be preferred, although a rapid jet reorientation of a single AGN cannot be excluded.
3. We discovered that AGN activity in RBS 797 has driven three nested shock fronts, found at projected distances of 50 kpc, 80 kpc and 130 kpc from the center, with Mach numbers in the range 1.2 - 1.3. We find that the total energy required to drive the shocks in RBS 797 is roughly 6×10^{61} erg. The mechanical power does not change drastically in between the successive activity cycles, with the AGN driving every 20-30 Myr a weak shock with power $P_{\text{sh}} \approx 10^{46}$ erg s^{-1} . Based on the morphology and timescales of the inner cocoon shock and the E-W X-ray cavities, we suggest that the bubbles and the shock likely originate from the same outburst.
4. The inflation of X-ray cavities has left footprints in the ICM: we found hints for a ring of enhanced metallicity surrounding the bubbles between ~ 30 - 50 kpc from the center, likely explained in the context of mechanical uplift of central enriched gas. The low entropy (≤ 30 keV cm^2) and short cooling time ($t_{\text{cool}} \leq 1$ Gyr) ICM is preferentially found between and behind the X-ray cavities, which may indicate that the bubbles are stimulating cooling. In this context, the region with the shortest cooling time (~ 440 Myr) and minimum $t_{\text{cool}}/t_{\text{ff}}$ ratio (~ 18) is located within 20 kpc south of the center, where filamentary patches of [O II] nebular emission tracing star-forming gas were recently detected (Calzadilla et al., 2022).
5. We estimated that within the cooling radius of RBS 797 ($r_{\text{cool}}^{7.7 \text{ Gyr}} = 109.3 \pm 1.0$ kpc), the X-ray emitting gas is radiating its energy at the remarkable rate of $L_{\text{cool}} = (2.34 \pm 0.01) \times 10^{45}$ erg s^{-1} . Such radiative losses are overcome by the total mechanical power in RBS 797 (by shocks and

X-ray cavities), i.e. 3.4×10^{46} erg s⁻¹. Moreover, the distance from the center to the outer shock (135 kpc) is larger than the cooling radius, suggesting that the gas outside $r = r_{\text{cool}}$ is also being heated.

These results are of particular relevance in the context of AGN feedback in galaxy clusters. First, RBS 797 is the first high-mass system where multiple AGN-driven shocks are found, enabling the discussion of shock heating over time (so far probed only in the galaxy group NGC 5813, Randall et al. 2015). Second, this cluster is a fortunate laboratory where to study the energy partition between shocks and cavities, and the stability of jet kinetic power over time.

Besides offering new perspectives on these topics, the results presented in this Chapter also stimulate follow-up questions. *Are there binary supermassive black holes at the heart of RBS 797? Is it possible to solve the puzzle of the perpendicular X-ray cavities and the multiple outbursts?* Using deep and multi-frequency radio data (part of which have been requested, awarded and analyzed within the duration of the PhD), in [Chapter 4](#) we complete the picture of AGN activity in this cluster.

Moreover, placing RBS 797 in the context of how feedback generally operates is required to draw broader conclusions. *How does this cluster compare to other systems where both X-ray cavities and shocks have been detected? Is the ICM of RBS 797 overpowered by the central AGN?* Using a sample of 15 elliptical galaxies, galaxy groups and galaxy clusters where both shocks and X-ray cavities have been discovered, in [Chapter 5](#) we address the questions of how much shock heating contributes to the feedback cycle, and if extreme episodes of energy injection can “overheat” the ICM. *Ultimately, how rare are misaligned radio morphologies, such as those observed in RBS 797? What is the most likely cause of such misalignments in cluster- and group- central galaxies?* In [Chapter 6](#) we construct a sample of 16 cool core galaxy clusters and galaxy groups to investigate the frequency and causes of such misalignments, focusing on the physics of SMBH ejection and on the possible role of the environment.

Chapter 4

A JVLA, LOFAR, e-Merlin, VLBA and EVN study of RBS 797: can binary SMBHs explain the outburst history of the central radio galaxy?

Abstract

¹ In this Chapter, we present a radio multi-frequency (144 MHz – 9 GHz) and multi-scale (50 kpc – 5 pc) investigation of the central radio galaxy in RBS 797, by means of dedicated JVLA, LOFAR (with international stations), e-Merlin, VLBA and EVN data. We confirm the co-spatiality of the four radio lobes with the two perpendicular sets of X-ray cavities discovered by *Chandra* (Chapter 3). The radiative age of the E-W lobes (31.4 ± 6.6 Myr) and of the N-S lobes (32.1 ± 9.9 Myr) supports a coeval origin of the perpendicular outbursts, that also have similar *active phase* duration (~ 12 Myr). Based on the analysis of the inner N-S jets (on scales of ≤ 10 kpc), we (a) confirm the S-shaped jet morphology; (b) show the presence of two hotspots per jet with a similar spectral index; (c) estimate the age of the twisting N-S jets to be less than ~ 8 Myr. Based on these results, we determine that jet precession (with period ~ 9 Myr and jet advance speed $\sim 0.01c$) can explain the properties of the N-S jets. We also find that the synchrotron injection index has steepened between the large, older outburst ($\Gamma \sim 0.5$) and the younger S-shaped jets ($\Gamma \sim 0.9$), possibly indicating the transition from a FR I-like activity to a FR II-like one in the last 10 Myr. The e-Merlin, VLBA and EVN data reveal a single, compact core at the heart of RBS 797 surrounded by extended radio emission whose orientation depends on the spatial scale sampled by the data. We explore several engine-based scenarios to explain these results. Piecing together the available evidence, we argue that RBS 797 likely hosts (or hosted) binary active SMBHs. The detection of a single component in the VLBI data is still consistent with this interpretation, since the predicted separation of the binary SMBHs (≤ 0.6 pc) is an order of magnitude smaller than the resolution of the available radio data (5 pc).

4.1 Context: the variations in jet orientation over time

As noted in Chapter 1, several radio galaxies display evidence for changes in the jet propagation axis over time. This evidence manifests through e.g., a twisted (S-shaped) jet morphology, larger and older lobes misaligned from the current radio jets or a sharp bending in the jet path. The dynamics of jets showing such complex morphologies can involve a progressive precession of the

¹This Chapter is based on Ubertosi et al. (submitted to A&A in December 2023).

material ejected from the AGN (e.g., Begelman et al. 1980; Steenbrugge and Blundell 2008; Krause et al. 2019; Horton et al. 2020; Fendt and Yardimci 2022; Giri et al. 2022; Lalakos et al. 2022), or an abrupt change of the direction of the jet stream (e.g., Merritt and Ekers 2002; Dennett-Thorpe et al. 2002; Liu 2004). In turn, these mechanisms reflect engine-based phenomena. For instance, tidal interactions between the accretion disk and the SMBH may cause either a long-lasting precession of the jet axis or a complete realignment of the jets (e.g., Bardeen and Petterson 1975; Babul et al. 2013; Gaspari et al. 2018; Soker 2022). Alternatively, binary SMBHs could (a) cause jet precession in the active SMBH in case they are orbiting each other (e.g., Begelman et al. 1980), or (b) simultaneously drive jets in different directions, if they are both active (e.g., Hudson et al. 2006), or (c) cause an orthogonal change of the jet axis following the merger of the binary (e.g., Merritt and Ekers 2002). As evidenced in the previous Chapter, the central radio galaxy of the galaxy cluster RBS 797 represents an exemplary case of multiple and misaligned jet activities. In this Chapter we thoroughly investigate how the above scenarios may apply to RBS 797, exploiting a large collection of radio data spanning orders of magnitude in frequency, spatial scales sampled, and angular resolution.

4.2 Radio observations of RBS 797: data reduction

4.2.1 VLBA, EVN and e-Merlin data reduction

The observations of the BCG in RBS 797 comprise new data from the Very Long Baseline Array (VLBA) using bands L, C and X; the European VLBI Network (EVN) using bands L and C; and the Multi-Element Radio-Linked Interferometer Network (eMerlin) using bands L and C. In the following subsections we describe the observations and the data reduction procedure for the different arrays and frequencies considered. A summary of the observations presented in this article is provided in Tab. 4.1.

VLBA and EVN data

The radio core of RBS 797 has been observed by the VLBA in L band (1.6 GHz), C band (5 GHz) and X band (8.4 GHz) on February 4, 2014 (project code: BG224, PI: Gitti) in phase-referencing mode, with 8 IFs (each with a bandwidth of 32 MHz and 128 channels). For all the observing frequencies, the source J0954+7435 has been used as phase calibrator, while the source J2005+7752 has been used as fringe finder. The target has been observed in 4 min scans bracketed by 60 s scans of the phase calibrator, for a total time-on-source of 4 h in L band (60 scans on the target), 40 min in C band (10 scans on the target), and 1 h 20 min in X band (20 scans on the target).

The BCG of RBS 797 has been targeted with the EVN in phase-referencing mode (with 8 IFs, each with a bandwidth of 16 MHz and 32 channels). On February 26, 2014 and March 9, 2014 the BCG was observed at 1.6 GHz (project code: EG080-A, PI: Gitti) and at 5 GHz (project code: EG080-B, PI: Gitti), respectively. At both frequencies, J0954+7435 has been used as phase calibrator (observed in scans of 60 s), while 3C345 was observed as fringe finder. The target has been observed in 3m 30s scans for a total time-on-source of ~ 5 h at each frequency.

The strategy adopted to process the data in AIPS (Greisen, 2003) is similar for the VLBA and EVN observations. We followed standard reduction techniques, namely:

- Correction of Earth orientation parameters and ionospheric delays (tasks VLBAEOPS, VLBAEOCR). Removal of bad data from system temperatures of the EVN data.
- Correction of delays and amplitudes; we applied digital sampling corrections and removed instrumental delays on phases (VLBACCOR VLBAMPCL for the VLBA, FRING for the EVN). Then,

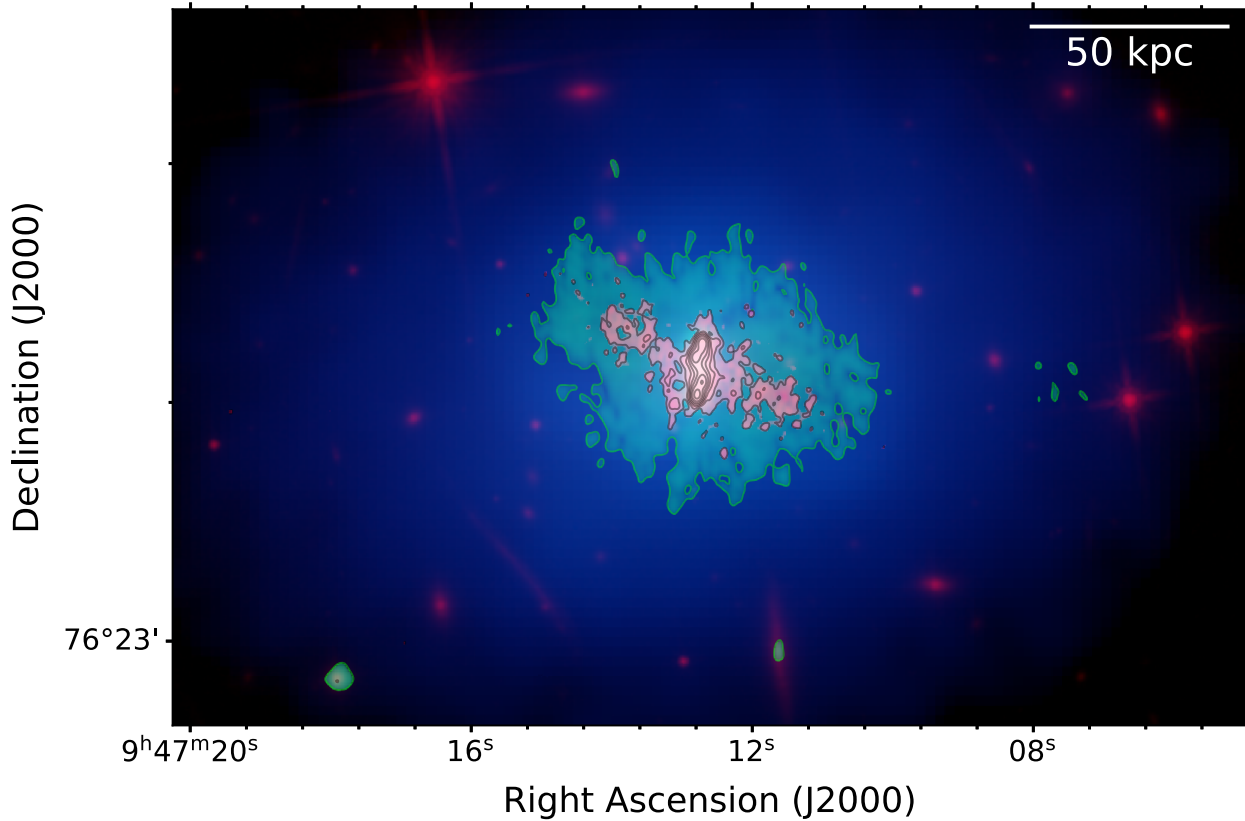


FIGURE 4.1: Composite optical (HST, red), *Chandra* (X-ray, blue), 3 GHz (JVLA, green), 144 MHz (LOFAR-International, pink) image of RBS 797. Black contours (described in Fig. 4.2) outline the 144 MHz emission of the radio galaxy.

we calibrated the bandpass (BPASS). At this point, we removed bad data from system temperatures and gain curves of the VLBA observations. To complete the amplitude calibration, we applied the corrections with the task VLBAAMP.

- The time-dependent delays in phases were corrected by fringe-fitting the data of the calibrator (FRING). To properly correct the delays we used an image of the calibrator as a model for fringe-fitting.
- Ultimately, we applied the calibration to the data and averaged the different IFs. After editing the final visibilities, self-calibration was attempted only for the L-band data (due to the low flux density of the target), finding however no significant improvement in dynamical range or sensitivity.

We found that supplying an image model during fringe-fitting is crucial when J0954+7435 is used as a calibrator: since the calibrator itself is resolved into a double component, assuming a point source as a model for fringe-fitting results in a bad description of rate and delays (see Appendix D). When using the software DIFMAP (Shepherd, 1997) to fit visibilities with gaussian-like or point-like components, the uncertainties on flux densities were computed as:

$$\delta S_\nu = \sqrt{N_{beam}\sigma_{rms}^2 + (f_\%S_\nu)^2 + \delta_{difmap}^2} \quad (4.1)$$

where N_{beam} is the ratio between the area within which the flux density is computed and the beam area, σ_{rms} is the local r.m.s. noise, $f_\%$ is the relative uncertainty on the flux density scale (here

we assume $f_{\%} = 10\%$), S_v is the flux density indicated by the fit and δ_{difmap} is the statistical fit uncertainty (at 1σ confidence level, typically around $5\%S_v$) returned by the fit in DIFMAP.

e-Merlin data

The e-Merlin observations of RBS 797 (project code EG080, PI: Gitti) have been performed at L band (1.6 GHz) and C band (5 GHz) on March 28, 2014 and March 10, 2014, respectively. At both frequencies, the source J0954+7435 has been used as phase calibrator. The fringe finders were 0319+415 for the L band data and 1331+305 for the C band data. After being passed through the e-MERLIN pipeline (Argo, 2015), any problematic data such as spurious signals or data from faulty antennas were identified and flagged.

Images were made in AIPS with the task IMAGR. We found that the best results are achieved by setting the robust parameter to $R = 0$ for the C band data and by selecting a natural weighting for the L band data. We tested the combination of the e-Merlin and EVN data at matching frequencies, finding no improvement in image quality as either the e-Merlin or the EVN data dominate for different weighting schemes.

Peak and total flux densities (above the $5 \times \sigma_{\text{rms}}$ contour) of the radio emission were measured in AIPS at the different frequencies, with the uncertainties being computed as:

$$\delta S_v = \sqrt{N_{\text{beam}} \sigma_{\text{rms}}^2 + (f_{\%} S_v)^2}, \quad (4.2)$$

where we assume the typical flux density scale uncertainty of $f_{\%} = 5\%$. By inspecting the radio images, we noticed that there is a shift in the astrometry of the e-Merlin observations, by -38 milliarcseconds in RA and $+3$ milliarcseconds in DEC. In order to properly compare the e-Merlin results with those obtained from other facilities, we corrected the data for this astrometric offset by shifting the images in AIPS.

4.2.2 JVLA observations and data reduction

We analyze new Karl Jansky Very Large Array (JVLA) observations of RBS 797 (Project code 22A-301, PI: Ubertyosi) performed with the A array at S band (2 – 4 GHz), C band (4.5 – 6.5 GHz) and X band (8 – 10 GHz). In all observations the source 3C 286 (J0137+3309) was used as the primary flux density calibrator, while J0713+4349 and J1044+8054 were used as polarization and phase calibrator, respectively. The data were calibrated in CASA v.6.4.1 using standard data reduction techniques for continuum and polarization calibration². Self-calibration was attempted, but without success given the relatively low flux density of the target (peak flux density of a few mJy at GHz frequencies). Nonetheless, the noise in our images is close to the thermal expected one.

The data were imaged in CASA using the task `tclean`, and testing different weighting combinations. For the S band (3.0 GHz) data, we find that an image made with `robust = 0` highlights the jet structure in the inner 15 kpc, while an image made with `robust = 2` recovers extended emission on larger scales, reaching the lobe of the radio galaxy. For the data at C and X bands, the images that best capture the radio morphology are obtained by setting `robust = 0`. These images are shown in Fig. 4.2. We measured the peak and total flux density (above the $5 \times \sigma_{\text{rms}}$ contour) of the radio emission at the different frequencies. The uncertainties were computed as in Eq. 4.2, assuming the typical flux density scale uncertainty of 5%.

4.2.3 LOFAR long-baseline observations

RBS 797 has been observed by the LOw Frequency ARray (LOFAR, van Haarlem et al. 2013) in 2018 (Project code: LC 10_010, PI: Bonafede). The observations used the HBA antennas and the same

²See <https://casaguides.nrao.edu/>.

TABLE 4.1: Summary of the EVN, VLBA, e-Merlin, JVLA and LOFAR data presented in this work. We separate the primary, sensitive data (that we use to derive the main results) from the shorter-observing time complementary data (that we use to verify the results based on primary data). (1) Name of the radio telescope; (2) project code; (3) date of the observations; (4) time spent on the target source RBS 797; (5) observing frequency; (6) Name of the calibrators; (7) principal investigator.

PRIMARY DATA						
Telescope	Project Code	Obs. Date	Time on source	Frequency	Calibrators	PI
JVLA	22A-301	May 2022	1h 30m	3.0 GHz	3C286, J0713+4349, J1044+8054	Ubertosi
			40m	5.5 GHz		
			2h	9.0 GHz		
LOFAR	LC 10_010	June 2018	8h	144 MHz	3C295, L619462	Bonafede
eMerlin	EG080	March 28, 2014	6h	1.6 GHz	0319+415, J0954+7435	Gitti
		March 10, 2014	6h	5.0 GHz	1331+305, J0954+7435	
VLBA	BG 224	February 4, 2014	4h	1.6 GHz	J2005+7752, J0954+7435	Gitti
			40m	5.0 GHz		
			1h 20m	8.4 GHz		
EVN	EG080	February 26, 2014	5h	1.6 GHz	3C345, J0954+7435	Gitti
		March 9, 2014	5h	5.0 GHz		
COMPLEMENTARY DATA						
Telescope	Project Code	Date	Time on source	Frequency	Calibrators	PI
EVN	RSG05	May 3, 2013	1h	5.0 GHz	0133+476, J0954+7435	Gitti
	RSG07	December 1, 2015	1h 30m	1.6 GHz	J0958+6533, J1027+7428, J0954+7435	Giroletti
VLBA	BE 056	July 8, 2014	20m	5.0 GHz	4C 39.25, J1044+8054	Edge

setup of the LOFAR Two Meter Sky Survey (LoTSS, e.g., Shimwell et al. 2022). The source has been observed between 120 MHz and 168 MHz (central frequency 144 MHz) for 8h, using the calibrator 3C295.

To calibrate the data (including the international stations) we followed the prescriptions detailed in Morabito et al. (2022) (see also <https://lofar-vlbi.readthedocs.io>) using the HOTCAT High Performance Computing cluster at INAF Trieste (Taffoni et al., 2020; Bertocco et al., 2020). The data were first passed through the Pre-factor3 software package (van Weeren et al., 2016; Williams et al., 2016; de Gasperin et al., 2019), which uses the calibrator source to derive the corrections for polarization alignment, Faraday rotation, bandpass, and clock offsets. Then, a first set of phase calibration solutions for the core and remote stations (derived using a sky model of the field from the TGSS survey, Intema et al. 2017) are added to the calibrator solutions.

The LOFAR-VLBI pipeline is subsequently used to calibrate the international stations. This requires to select a bright and compact source separated by less than 1 degree from the target from the Long-Baseline Calibrator Survey (LBCS, Jackson et al. 2022). We derived the solutions for the international stations using L619462, which is located at 0.56° from the target RBS 797. After splitting out the target visibilities, the solutions from the delay calibrator were applied to the target.

To improve the image quality, self-calibration was performed on the target using the Default Pre-processing Pipeline DPPP (van Diepen et al., 2018) to find the solutions, and WSClean v3.2 (Offringa et al., 2014) to obtain images. We performed three cycles of self-calibration solving for total electron content (TEC) and phase, and a final cycle of amplitude corrections. The angular resolution of the final image is of $0.36'' \times 0.25''$ (see Fig. 4.1). To correct for possible offset in the absolute flux density scale (see Shimwell et al. 2022), we compared the flux density of the unresolved delay

TABLE 4.2: Image parameters of the EVN, VLBA, e-Merlin, JVLA and LOFAR data used in this work. We note that the weighting obtained with a specific absolute value of the robust parameter depends on the processing software: the parameter refers to the CASA task `tclean` for the JVLA data, to the WSClean software for the LOFAR data, and to the AIPS task `IMAGR` for the e-Merlin, VLBA and EVN data. (1) Name of the radio telescope; (2) project code; (3) observing frequency; (4) robust parameter used during imaging; (5) beam major and minor axes; (6) beam position angle; (7) r.m.s. noise; (8) peak flux of the image; (9) total flux density within $5\sigma_{\text{rms}}$; (10) corresponding figure.

Telescope	Project Code	Frequency	Robust	Beam [mas]	P.A.	σ_{rms}	Peak	S_{ν} ($5\sigma_{\text{rms}}$)	Figure
JVLA	22A-301	3.0 GHz	2	900×900	0°	$5.0 \mu\text{Jy}/\text{beam}$	$2.07 \text{ mJy}/\text{beam}$	$10.09 \pm 0.50 \text{ mJy}$	Fig. 4.2
			0	590×400	5.7°	$6.0 \mu\text{Jy}/\text{beam}$	$1.69 \text{ mJy}/\text{beam}$	$4.89 \pm 0.24 \text{ mJy}$	
		5.5 GHz	0	388×250	15.4°	$5.5 \mu\text{Jy}/\text{beam}$	$1.57 \text{ mJy}/\text{beam}$	$2.97 \pm 0.15 \text{ mJy}$	
		9.0 GHz	0	230×200	-4.5°	$3.0 \mu\text{Jy}/\text{beam}$	$1.36 \text{ mJy}/\text{beam}$	$2.07 \pm 0.10 \text{ mJy}$	
LOFAR	LC 10-010	144 MHz	0	360×250	170.4°	$40 \mu\text{Jy}/\text{beam}$	$13.0 \text{ mJy}/\text{beam}$	$134.4 \pm 26.9 \text{ mJy}$	Fig. 4.2
eMerlin	EG080	1.6 GHz	5	150×150	0°	$14 \mu\text{Jy}/\text{beam}$	$1.51 \text{ mJy}/\text{beam}$	$3.44 \pm 0.20 \text{ mJy}$	Fig. 4.6
		5.0 GHz	0	35×35	0°	$20 \mu\text{Jy}/\text{beam}$	$0.50 \text{ mJy}/\text{beam}$	$0.94 \pm 0.08 \text{ mJy}$	
VLBA	BG 224	1.6 GHz	0	6.3×4.6	82.3°	$25 \mu\text{Jy}/\text{beam}$	$0.61 \text{ mJy}/\text{beam}$	$0.94 \pm 0.09 \text{ mJy}$	Fig. 4.7
		5.0 GHz	0	2.2×1.4	-80.9°	$30 \mu\text{Jy}/\text{beam}$	$0.38 \text{ mJy}/\text{beam}$	$0.47 \pm 0.05 \text{ mJy}$	
		8.4 GHz	0	1.3×0.9	-86.4°	$30 \mu\text{Jy}/\text{beam}$	$0.39 \text{ mJy}/\text{beam}$	$0.40 \pm 0.05 \text{ mJy}$	
	BE 056	5.0 GHz	3	5.6×4.6	7.17°	$25 \mu\text{Jy}/\text{beam}$	$0.35 \text{ mJy}/\text{beam}$	$0.47 \pm 0.06 \text{ mJy}$	–
EVN	EG080	1.6 GHz	0	9.1×6.7	-46.9°	$30 \mu\text{Jy}/\text{beam}$	$1.37 \text{ mJy}/\text{beam}$	$1.65 \pm 0.17 \text{ mJy}$	Fig. 4.7
		5.0 GHz	0	2.6×1.6	-62.6°	$15 \mu\text{Jy}/\text{beam}$	$0.51 \text{ mJy}/\text{beam}$	$0.70 \pm 0.07 \text{ mJy}$	
	RSG05	5.0 GHz	0	7.2×5.2	-13.9°	$20 \mu\text{Jy}/\text{beam}$	$0.68 \text{ mJy}/\text{beam}$	$0.84 \pm 0.09 \text{ mJy}$	–
	RSG07	1.6 GHz	0	29.1×23.9	-36.4°	$64 \mu\text{Jy}/\text{beam}$	$1.50 \text{ mJy}/\text{beam}$	$1.91 \pm 0.22 \text{ mJy}$	–

calibrator between the LOFAR-VLBI image and the $6''$ LOFAR survey image, finding a correction factor of 1.61 that was applied to the images. We computed the uncertainties on the flux densities using Eq. 4.2 and assuming a 20% uncertainty on the absolute flux density scale to account for uncertainties in the above correction factor of LOFAR-VLBI data. This conservative choice is higher than the typical 10% assumed for LOFAR data (Shimwell et al., 2022). The angular resolution of the final image is of $0.36'' \times 0.25''$, and the r.m.s. noise is $\sigma_{\text{rms}} = 40 \mu\text{Jy}/\text{beam}$.

4.2.4 Complementary archival data

To complement the analysis of the targeted, deep observations presented above we consider additional archival data from different facilities. We use two EVN snapshot observations, one at 1.6 GHz (project RSG07), and the other at 5 GHz (project RSG05, published in Gitti et al. 2013). We also use a snapshot VLBA observation at 5 GHz to understand if time variability is present in RBS 797 (project BE056, see §4.3.3). We reduced the data with the same approach presented in §4.2.1. A summary of the observations is reported in Tab. 4.1 and 4.2.

Additionally, we relied on archival VLA data at 1.4 GHz (arrays A, B, and C; see Gitti et al. 2006; Doria et al. 2012), and at 4.8 GHz (arrays A and B, see Gitti et al. 2013). These data were used in combination with our new JVLA and LOFAR observations to measure the spectral properties of the radio galaxy (see §4.3.1).

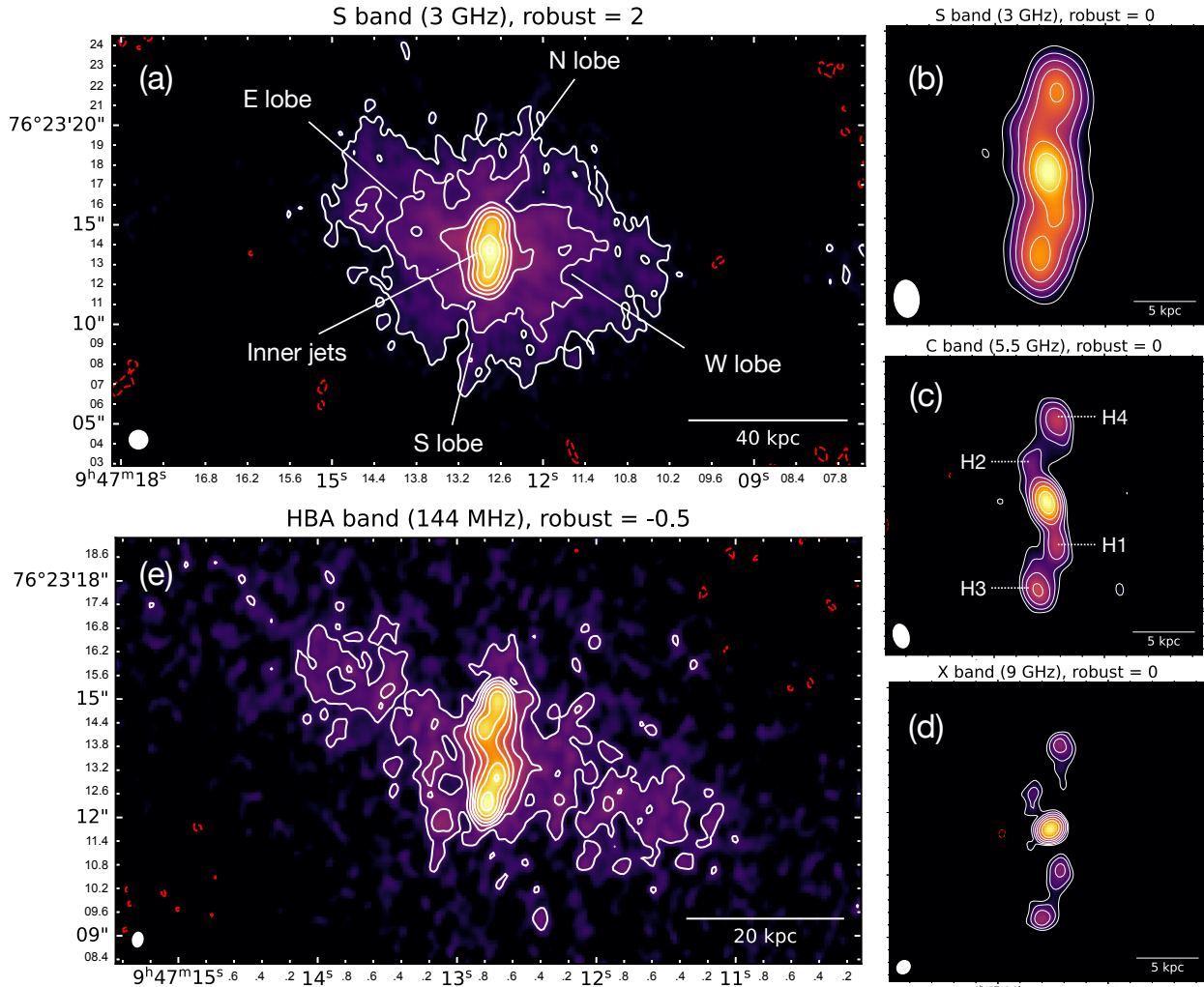


FIGURE 4.2: Final JVLA and LOFAR maps of RBS 797. (a) 3 GHz JVLA image at $0.9''$ resolution, obtained by setting the robust parameter to 2. (b), (c), (d) 3 GHz, 5.5 GHz, and 9 GHz JVLA images obtained by setting robust = 0. The beam sizes are $0.59'' \times 0.40''$ at 3 GHz, $0.39'' \times 0.25''$ at 5.5 GHz, and $0.23'' \times 0.20''$ at 9 GHz. (e) 144 MHz LOFAR image with the International Stations at $0.36'' \times 0.25''$ resolution, obtained by setting robust = -0.5. In each panel, the beam is shown with a white circle in the bottom left corner. In panels (a) and (e), contours start at $3\sigma_{\text{rms}}$ and increase by a factor of 2; in panels (b), (c), and (d), contours start at $5\sigma_{\text{rms}}$ and increase by a factor of 2. The first negative contour ($-3\sigma_{\text{rms}}$ or $-5\sigma_{\text{rms}}$) is plotted in dashed red. See Tab. 4.2 for the σ_{rms} noise levels of the images. Structures discussed in this work are labelled.

4.3 Results: multi-scale morphological and spectral properties of the radio galaxy

Given the large difference in physical scales to which the employed data are sensitive (from tens of kpc down to tens of pc), in this section we present our results by progressively zooming into the radio core of RBS 797. Starting from the kpc scales, we present the new observations performed with the JVLA and LOFAR telescopes. Then, we probe the connection between the kpc and pc scales using the e-Merlin observations. Ultimately, we present the images obtained from the EVN and VLBA data, that allow us to peer into the pc scales.

4.3.1 The kpc scale

Radio galaxy morphology

We show in Fig. 4.2 the images obtained from the JVLA data at 3 GHz, 5.5 GHz, and 9 GHz and the image obtained from the LOFAR-VLBI data at 144 MHz. The 3 GHz JVLA image obtained with $\text{robust} = 2$ unveils the full morphology of the radio galaxy at a resolution of $0.9''$ (a preliminary image was presented in Ubertosi et al. 2023b; see Chapter 3). This image allows one to appreciate the multi-faceted morphology of the radio galaxy in RBS 797, with its perpendicular pairs of radio lobes that fill all the four X-ray cavities in the ICM (see also Ubertosi et al. 2021b; see Chapter 3) and the inner north-south jets of the AGN.

Such north-south jets, with a distinctive S-shape, are better visible in the maps at 3.0 GHz ($\sim 0.5''$ resolution), 5.5 GHz ($\sim 0.3''$ resolution), and 9 GHz ($\sim 0.2''$ resolution) shown in the right panels. The jets extend for $1.8''$ (~ 9 kpc) on each side of the core. We identify a total of four bright hotspots, two on each sides of the nucleus and symmetric with respect to the core. The connection between the inner jets and the larger, diffuse radio emission is clearer in the LOFAR image with international stations ($\sim 0.3''$ resolution). At 144 MHz the central emission is dominated by the S-shaped jets, while the core is not visible. The brightest, innermost part of the extended east-west lobes is also visible at $\sim 3 - 6 \sigma_{\text{rms}}$. The emission is nearly perpendicular to the north-south jets, and it is detected up to a distance of $\sim 6''$ (~ 29 kpc) on each side of the core.

The symmetric morphology of the inner north – south jets strongly suggests that the whole structure mainly lies in the plane of the sky, i.e. the angle between the jet axis and the line of sight is nearly 90° . We note that the two southern hotspots are brighter by a factor $\sim 1.2 - 1.7$ than the northern ones (from 144 MHz to 9 GHz). If this is caused by relativistic effects (e.g. Pearson 1996), then the southern jet would be the approaching jet and the northern jet the receding one. From the jet/counter-jet ratio, we estimate an upper limit to the inclination angle of $i \leq 84^\circ$. This supports the above argument of the jets mainly lying in the plane of the sky.

We note the absence in the 5.5 GHz JVLA map of the faint E-W jets detected at $\sim 4 - 5 \sigma_{\text{rms}}$ in the narrow-band 4.8 GHz VLA images of Gitti et al. (2006) and Gitti et al. (2013). The small E-W jet-like features in Gitti et al. (2013) may represent the brightest patch of the diffuse, large lobe emission that is visible in the 3 GHz ($\text{robust} = 2$) and in the LOFAR maps. Given the lower sensitivity to extended emission of the $\text{robust} = 0$ JVLA maps, such diffuse components are likely resolved out. Alternatively, it is possible that the features in the old VLA maps (Gitti et al., 2006; Gitti et al., 2013) were caused by serendipitous noise structures near the core.

Spectral properties of the inner jets

The spectral properties of the radio emission can provide useful information on the history of the AGN outbursts. The available JVLA and LOFAR data with similar resolution and uv-coverage enable a spatially-resolved spectral study of the north – south jets over nearly two orders of magnitude in frequency (144 MHz – 9 GHz). To this end, we produced images at the four frequencies by matching the uv-range of the data ($15.2 \text{ k}\lambda - 481.9 \text{ k}\lambda$), selecting a uniform weighting scheme and imposing a common restoring beam. The resulting maps in Fig. 4.3 (top panels) have a resolution of $0.4''$.

We show in the bottom panels of Fig. 4.3 the maps of spectral index between 144 MHz – 3 GHz, 3 GHz – 5.5 GHz and 5.5 GHz – 9 GHz, with overlaid the contours from the 3 GHz data. Across the four frequencies, the core spectral index remains fairly flat. Using a beam-sized region, and treating the LOFAR flux density as a limit (the core is undetected in the 144 MHz image), we fitted the core measurements with a power-law, finding $\langle \alpha_{\text{core}} \rangle = 0.19 \pm 0.02$.

The spectral index along the jets is steeper than in the core, and across the four frequencies ranges between $0.9 \leq \alpha \leq 2$. The spectral index distribution is not uniform, but we note a flatter α at

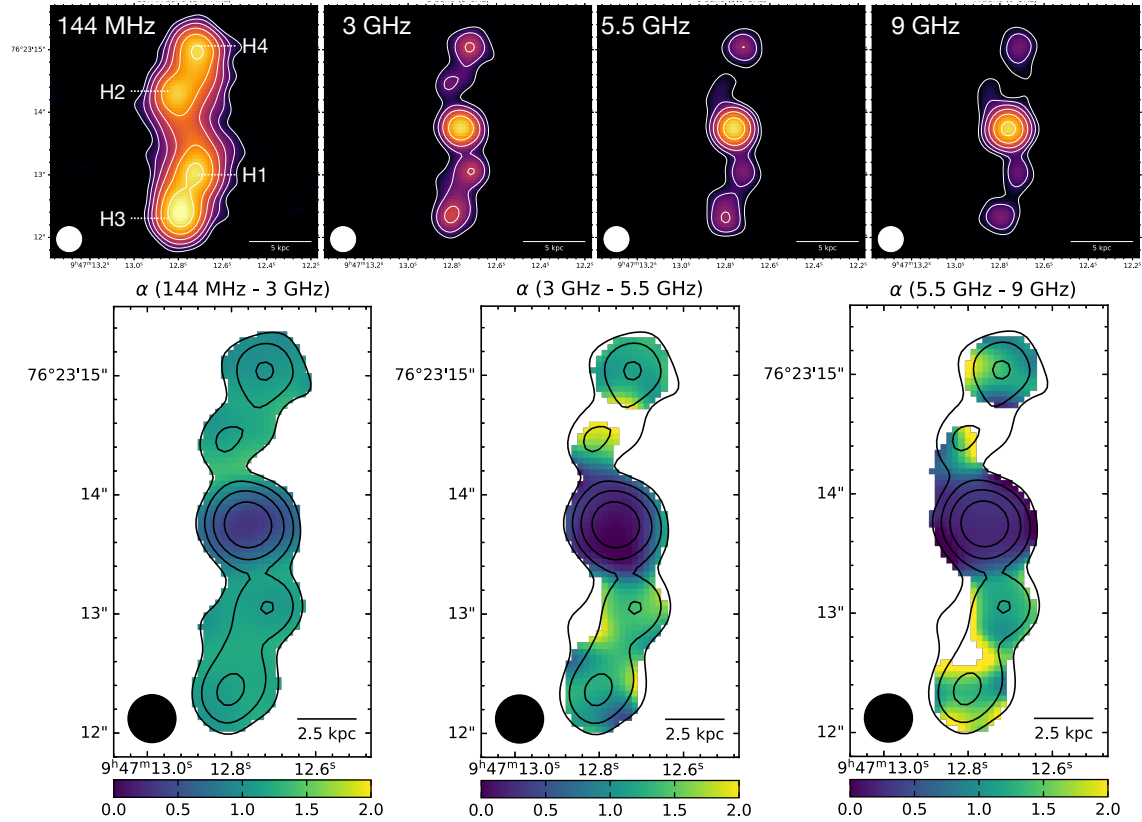


FIGURE 4.3: *Top panels*: LOFAR and JVLA maps used to compute the spectral index maps, at a resolution of $0.4''$. The beam is shown in the bottom left corner. Contours start at $5\sigma_{\text{rms}}$ and increase by a factor of 2, with the σ_{rms} of the maps being $43 \mu\text{Jy}/\text{beam}$ (144 MHz), $22 \mu\text{Jy}/\text{beam}$ (3 GHz), $12 \mu\text{Jy}/\text{beam}$ (5.5 GHz), $7 \mu\text{Jy}/\text{beam}$ (9 GHz). *Bottom panels*: spectral index maps between 144 MHz and 3 GHz (left), 3 GHz and 5.5 GHz (center), 5.5 and 9 GHz (right). The maps are displayed with a matching colorscale of $0 \leq \alpha \leq 2$. Contours from the 3 GHz map in the top panel are overlaid on the images. The relative uncertainty on the spectral index range between 2.5% - 15% (144 MHz - 3 GHz), 6% - 15% (3 GHz - 5.5 GHz), 7% - 30% (5.5 - 9 GHz). Structures discussed in this work are labelled.

the center of the hotspots, and a progressive steepening behind them. This is consistent with particles being accelerated at the hotspots of jets, which have a spectral index at lower frequencies that is close to the injection index (e.g., O’Dea et al. 2009). The flatter hotspot spectrum is evident from Fig. 4.4 (left panel), where we compare the radio spectrum of the core, of the hotspots (from beam-sized regions), and of the trailing plasma in the remaining area. The difference between the hotspots and the trailing plasma becomes more evident at increasing frequencies. Such spectral steepening at GHz-frequencies is likely caused by radiative losses from particle ageing.

To investigate the spectral ageing of the relativistic particles, we derived a radiative age map of the inner jets by combining the images at the different frequencies (144 MHz, 3 GHz, 5.5 GHz and 9 GHz). We used the Broadband Radio Astronomy Tools software (BRATS, Harwood et al. 2013), that can fit ageing models to 2D maps of radio emission. We tested two radiative age models that consider synchrotron and inverse-Compton losses, where the electron population has a continuously isotropized pitch angle distribution. The JP model (Jaffe and Perola, 1973) uses a constant magnetic field, while the Tribble model (Tribble, 1993) assumes a Gaussian distribution for the magnetic field. We did not consider the KP model (Kardashev, 1962; Pacholczyk, 1970) because it is less physically realistic compared to the JP and Tribble models (e.g., Brienza et al. 2020).

The input parameters of the JP and Tribble models are the magnetic field B and the injection index Γ . The magnetic field has been estimated from the 3 GHz map adopting equipartition assumptions. We measured a k-corrected radio power of $(1.79 \pm 0.09) \times 10^{24} \text{ W/Hz}$ from a prolate ellipsoid of

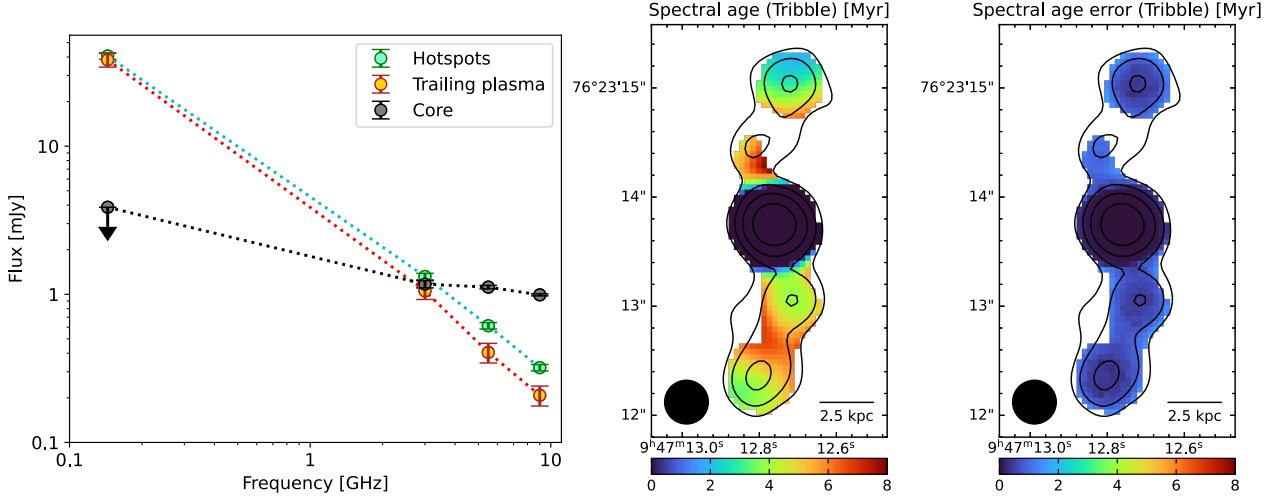


FIGURE 4.4: *Left panel:* Radio spectrum of the different components (core, hotspots, and trailing regions) of the north - south radio emission on kpc scales. The 144 MHz flux density of the core is interpreted as an upper limit, since the core is not detected at low frequency (see §4.3.1 for details). Note that the dotted lines connecting the points do not represent fits to the spectrum. *Right panel:* Spectral age map (assuming a Tribble model) and associated uncertainty map. Contours from the 3 GHz map of Fig. 4.3 are displayed on top of the image. The beam is shown in the bottom left corner. See §4.3.1 for details.

major semi-axis $1.83''$, minor semi-axis $0.66''$, and position angle 90° from the west axis (volume of 3.34 arcsec^3 , or 392.3 kpc^3). Using these parameters and assuming an energy ratio of protons to electrons of 1, we derived an equipartition magnetic field of $B_{eq} = 16 \pm 2 \mu\text{G}$ along the $\sim 8 \text{ kpc}$ - long jets, and we fixed $B = B_{eq}$. Using the `findinject` task of BRATS, we found an injection index $\Gamma = 0.9$. Typical values can range between $0.5 - 0.8$ (e.g., Carilli et al. 1991), with steeper indices (up to 1.2) found for cluster - central powerful radio sources (e.g., Harwood et al. 2015).

Fitting the two models to the data resulted in the Tribble model having a lower reduced- $\chi^2 = 1.12$ than the JP model ($\chi^2 = 1.31$). Moreover, the two models give consistent best-fit radiative ages. As a note of caution, we also report that fixing the magnetic field to the minimum energy loss field (e.g., de Gasperin et al. 2017) value of $B = 3.4 \mu\text{G}$ (Ubertosi et al. 2021b; see Chapter 3) returns radiative ages that are larger than those obtained by adopting $B = B_{eq}$ by $\sim 30\%$, but consistent within $\sim 2\sigma$. Considering this, and the fact that the Tribble model describes a more general case, we adopt this one as the best fit to the radio image. We show in Fig. 4.4 (*right panel*) the radiative age map and the associated uncertainty map.

The radiative ages are determined with high accuracy (relative uncertainties are between 5% - 25%), likely due to the availability of radio data over six octaves in frequencies. The core has a radiative age consistent with zero, which is in agreement with its spectral index being below the injection index. The jets have radiative ages that range between 2 - 7 Myr, with the hotspots being relatively younger than the trailing radio plasma behind and around them. In particular, the average age of the hotspots is $t_{\text{rad,H}^*} = 4.4 \pm 0.5 \text{ Myr}$, compared to the average (hotspot-removed) jet age of $t_{\text{rad,jet}} = 5.8 \pm 0.3 \text{ Myr}$.

The typical model of an ageing radio galaxy would predict the lower ages to be found in the hotspot of each lobe (or in the proximity of the jet termination point), with the surrounding plasma displaying larger radiative ages (e.g., Carilli et al. 1991). In the case of RBS 797 we instead see two bright spots for each jet, and a similar radiative age across the four hotspots. This supports the presence of multiple acceleration sites along the jets, not only the terminal ones. We further discuss this finding in §4.4.

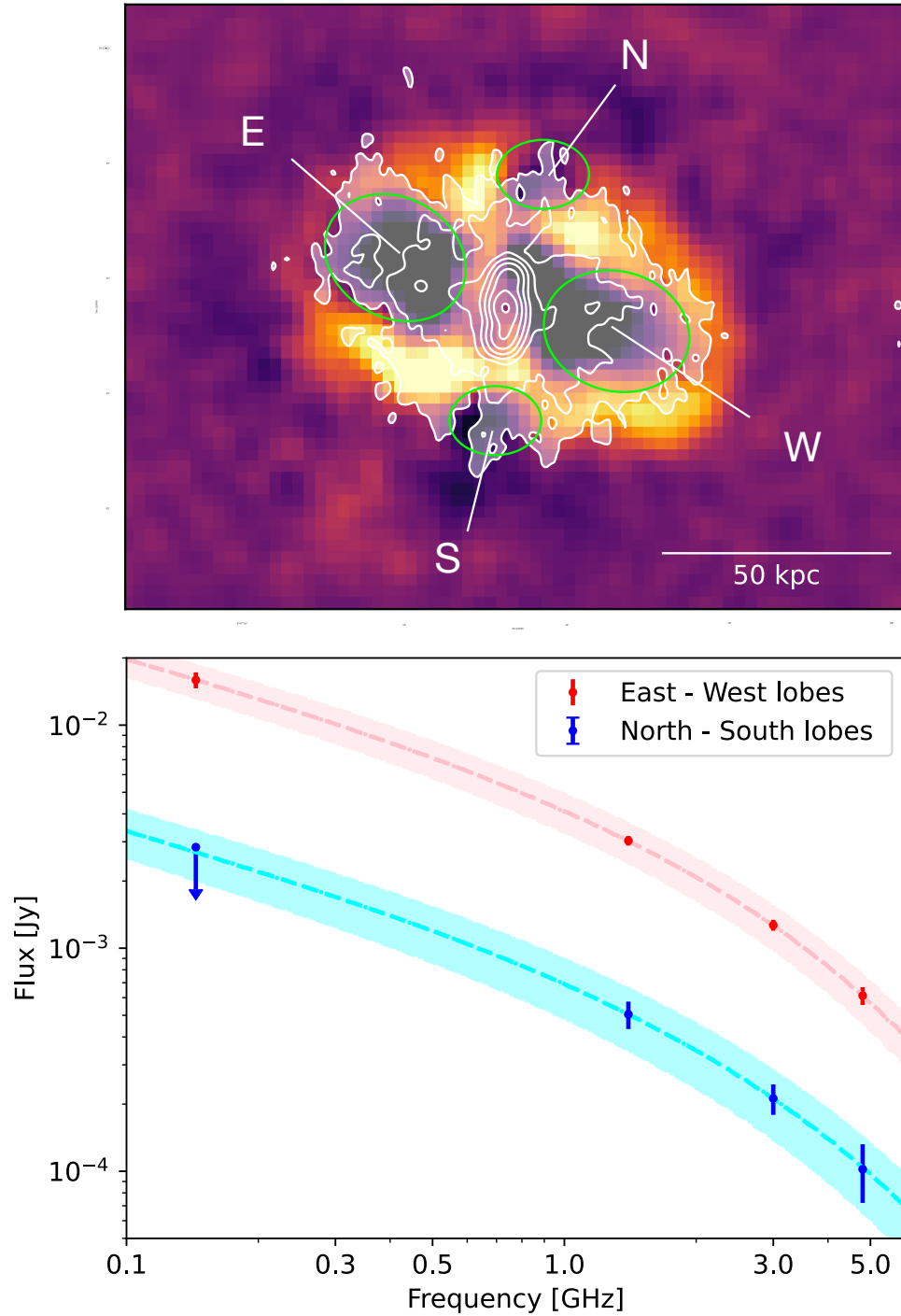


FIGURE 4.5: Top: Residual *Chandra* image of RBS 797, with overlaid white contours from the JVLA 3 GHz image of Fig. 4.2. The X-ray cavities described in Ubertosi et al. (2021b) (see Chapter 3) are shown with green ellipses and labelled. Bottom: Spectrum of the radio emission from the E-W and N-S cavities (see regions in top panel) in RBS 797, fitted with a CI-off model (see §4.3.1 for details). Colored areas show the 1σ uncertainties on the best-fit model.

Spectral properties of the perpendicular lobes

An open question on RBS 797 is which pair of the perpendicular radio lobes and corresponding X-ray cavities is older. Based on deep X-ray observations, we determined in Chapter 3 (Ubertosi et al., 2021b) that the two pairs of X-ray cavities are ≈ 30 Myr old, and they put an upper limit on

TABLE 4.3: Best fit parameters for the CI-off model fitted to the radio spectrum of the E-W and N-S lobes of RBS 797 (see Fig. 4.5 and §4.3.1). (1) Pair of radio lobes; (2) break frequency; (3) injection index; (4) total age of the radio emission; (5) active phase duration; (6) remnant phase duration.

	ν_b [GHz]	Γ	t_{age} [Myr]	t_{on} [Myr]	t_{off} [Myr]
E-W	3.1 ± 0.2	0.54 ± 0.03	31.4 ± 6.6	11.4 ± 2.4	20.1 ± 4.2
N-S	3.0 ± 0.3	0.54 ± 0.04	32.1 ± 9.9	12.8 ± 4.0	19.3 ± 6.0

the age difference between the two outbursts of ≤ 10 Myr. Ubertosi et al. (2021b) also attempted a spectral modeling of the lobes radio spectra, finding a tentative upper limit on the radiative age of $t_{EW} \leq 37$ Myr and $t_{NS} \leq 38$ Myr. However, given the availability at the time of two frequencies only (1.4 GHz and 4.8 GHz old VLA data), no conclusive result could be obtained.

With the new LOFAR and JVLA data at 144 MHz and 3 GHz, respectively, in combination with the old VLA data published in Gitti et al. (2006) and Gitti et al. (2013), we can now perform a detailed spectral modeling of the radio lobes between 144 MHz, 1.4 GHz, 3 GHz and 4.8 GHz. Flux densities have been measured from maps obtained by setting a common uv-coverage (4.2 k λ – 175.4 k λ), using uniform weighting, and forcing a restoring beam of 1.5''.

We note that the missing uv-coverage in the LOFAR data between baselines of roughly 50k λ – 75k λ limits the sensitivity to extended emission between scales of 2'' – 4'' (Morabito et al., 2022). For this reason, for the fainter N-S lobes we only have upper limits on the extended emission from the LOFAR data. Similarly, the 4.8 GHz VLA data detects the lobes only at $\sim 3\sigma_{rms}$. As the signal-to-noise would be too low, we cannot derive spatially-resolved spectral measurements, but we can obtain integrated values for each component. To this aim, we measured the flux densities within the regions defining the X-ray cavities (see Fig. 4.5, top panel). The resulting spectrum of the E-W lobes and the N-S lobes is shown in Fig. 4.5, bottom panel.

We note that the spectra of the two lobe pairs follow a similar steepening trend towards higher frequencies, with the N-S lobes being a factor of approximately 5 fainter than the E-W lobes. Interestingly, the E-W cavities are also roughly five times more powerful than the N-S cavities, in agreement the already known scaling between radio and mechanical powers (e.g. Bîrzan et al. 2008; Cavagnolo et al. 2010; O’Sullivan et al. 2011).

Using the software SYNCHROFIT (Quici et al., 2022) we fitted the two spectra using a continuous injection with a remnant phase model (CI-off, Komissarov and Gubanov 1994). With respect to the JP or Tribble models (that are based on a single injection event), the CI-off model describes an electron population that is injected at a constant rate for a duration t_{on} (the active phase), then the nuclear activity shuts down and the electrons age for a time t_{off} (the remnant phase). The choice of the CI-off for the lobes of RBS 797 is physically motivated by the fact that the diffuse lobe emission is not currently powered by active jets, as the most recent activity is in the north - south direction and on smaller scales (see §4.3.1).

The model requires the redshift ($z = 0.354$) and the magnetic field to be fixed, and returns the injection index Γ , the break frequency ν_b (which is related to the total age of the source, $t_{off} + t_{on}$), and the remnant fraction ($t_{off}/(t_{off} + t_{on})$). In the region of the lobes, we measure an equipartition magnetic field that ranges between 3.2 μ G to 4.2 μ G depending on the selected region. For comparison, the minimum energy loss field is $B_{min} = 3.4 \mu$ G. Given the similarity between these values, we adopted a common magnetic field $B = B_{min}$ during fitting.

As it is possible to see from Fig. 4.5, the CI-off model provides a good description of the integrated radio spectrum of the E-W and N-S lobes. The best fit parameters for the E-W and N-S lobes are reported in Tab. 4.3. We find that the spectra of the two pairs of lobes are described by similar parameters. First, we note that the total age of the radio lobes (~ 30 Myr) is in good agreement

with the age of the X-ray cavities and of the corresponding weak shock in the ICM (see [Chapter 3](#)). Second, the similar total age, active phase duration, and remnant phase duration of the E-W and N-S lobes suggest that it is difficult to determine which outburst is younger. Rather, these results support a coeval origin of the two pairs of radio lobes, as suggested before from the X-ray data. We discuss these results in the framework of radio activity in RBS 797 in [§4.4](#).

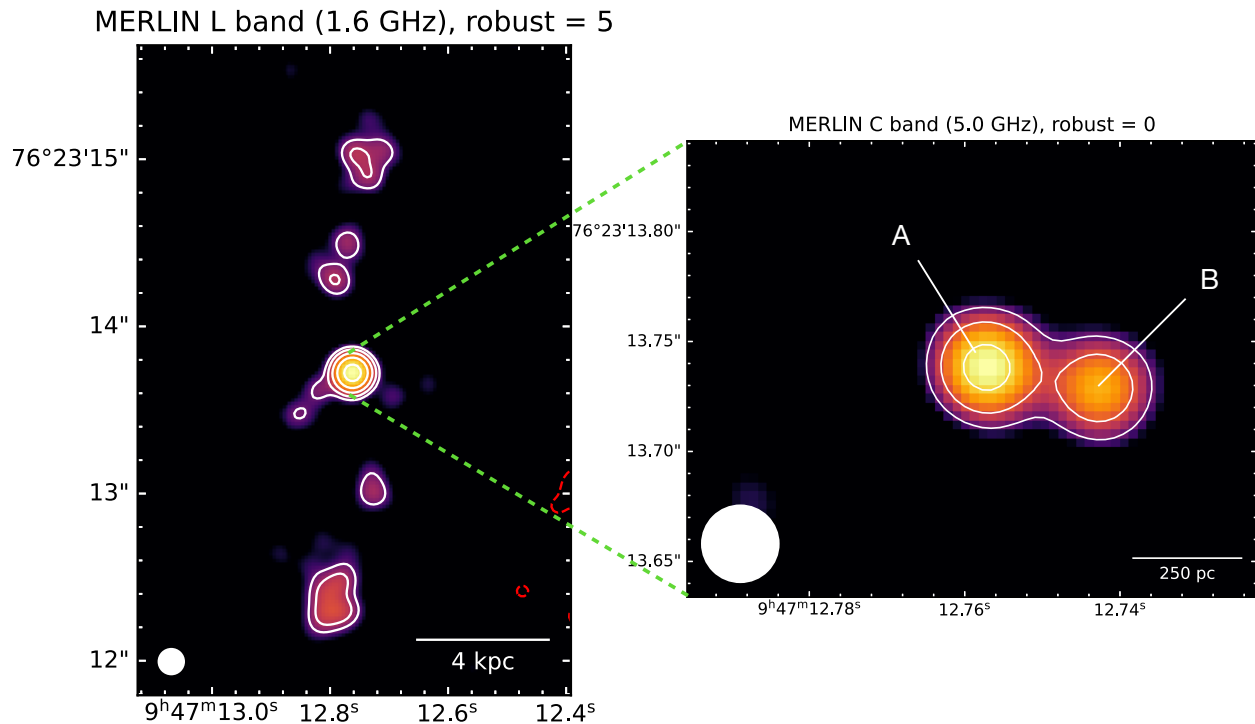


FIGURE 4.6: e-Merlin images at 1.6 GHz (left) and 5 GHz (right) of RBS 797. In both panels, contours are drawn at $5\sigma_{\text{rms}}$, and increase by a factor of 2; the first negative contour (at $-5\sigma_{\text{rms}}$) is drawn in dashed red. The beam is shown in the bottom left corner ($0.15'' \times 0.15''$ at 1.6 GHz and $0.035'' \times 0.035''$ at 5 GHz). See [Tab. 4.2](#) for details on the resolution and noise level of the images. Structures discussed in this work are labelled.

4.3.2 From the kpc to the pc scale

We present in [Fig. 4.6](#) the images obtained from the e-Merlin observations of RBS 797 at L band (1.6 GHz) and C band (5 GHz). [Tab 4.2](#) reports the parameters used during imaging and the corresponding image properties.

The 1.6 GHz image shows the inner jet structure with a resolution of $0.15''$ (~ 0.7 kpc). The core is visible at the center of the image (with an unresolved flux density of 1.51 mJy), and the jet emission mainly coming from the four hotspots is recovered on larger scales (total flux density 3.4 mJy). This image represents the highest resolution view of the ~ 8 kpc long jets of RBS 797, and confirms the S-shaped morphology revealed by the JVLA and LOFAR images of [Fig. 4.2](#).

The 5 GHz image has a resolution of $0.035''$ (~ 170 pc). The emission is resolved into two components, with the brighter one (labelled A) centered on the position of the radio core (RA, DEC = 09:24:12.76, +76:23:13.74) and the fainter one (labelled B) located at a distance of $0.05''$ (~ 250 pc) westward. Although the dynamic range of the 5 GHz e-Merlin image is relatively small (around 25), the two components are detected at more than $5\sigma_{\text{rms}}$, up to $\sim 28\sigma_{\text{rms}}$ for the brighter component and $\sim 20\sigma_{\text{rms}}$ for the fainter one. Using the software DIFMAP we fitted the combination of two Gaussian components to the uv data. We found that A is described by a Gaussian with flux density $S_A = 0.55 \pm 0.04$ mJy and a nominal deconvolved major axis of 1.1 ± 0.1 mas (5.4 ± 0.5 pc). This is a factor of ~ 32 smaller than the beam size, strongly suggesting that the component is unresolved.

The second component is described by a Gaussian with flux density $S_B = 0.38 \pm 0.04$ mJy and a deconvolved major axis of 10.2 ± 1.4 mas (51 ± 7 pc). This is a factor ~ 3 smaller than the beam size, possibly suggesting that the component may be extended.

Given its position, compactness, and flux density, we identify the brighter component, A, with the central engine of RBS 797. The second component is more difficult to interpret. This fainter component, B, could arise from a second SMBH in the BCG of RBS 797, which has been argued as a possible explanation for the multiple and misaligned outbursts in this cluster (Gitti et al. 2006; Gitti et al. 2013; see Chapter 3). Alternatively, it could represent remnant extended emission from the large scale outburst (see §4.3.1), since its relative position with respect to the core matches the orientation of the large east – west lobes of the radio galaxy (see Fig. 4.2). This alternative interpretation would be in agreement with its possible classification as an extended component from the DIFMAP fitting procedure. We also considered the possibility that this feature would be part of the southern approaching jet, however this seems hard to reconcile with the position angle of the component S1 detected with VLBA (see next section). We exploit the information from the VLBA and EVN data presented in the next section to discuss which of the two scenarios is more plausible.

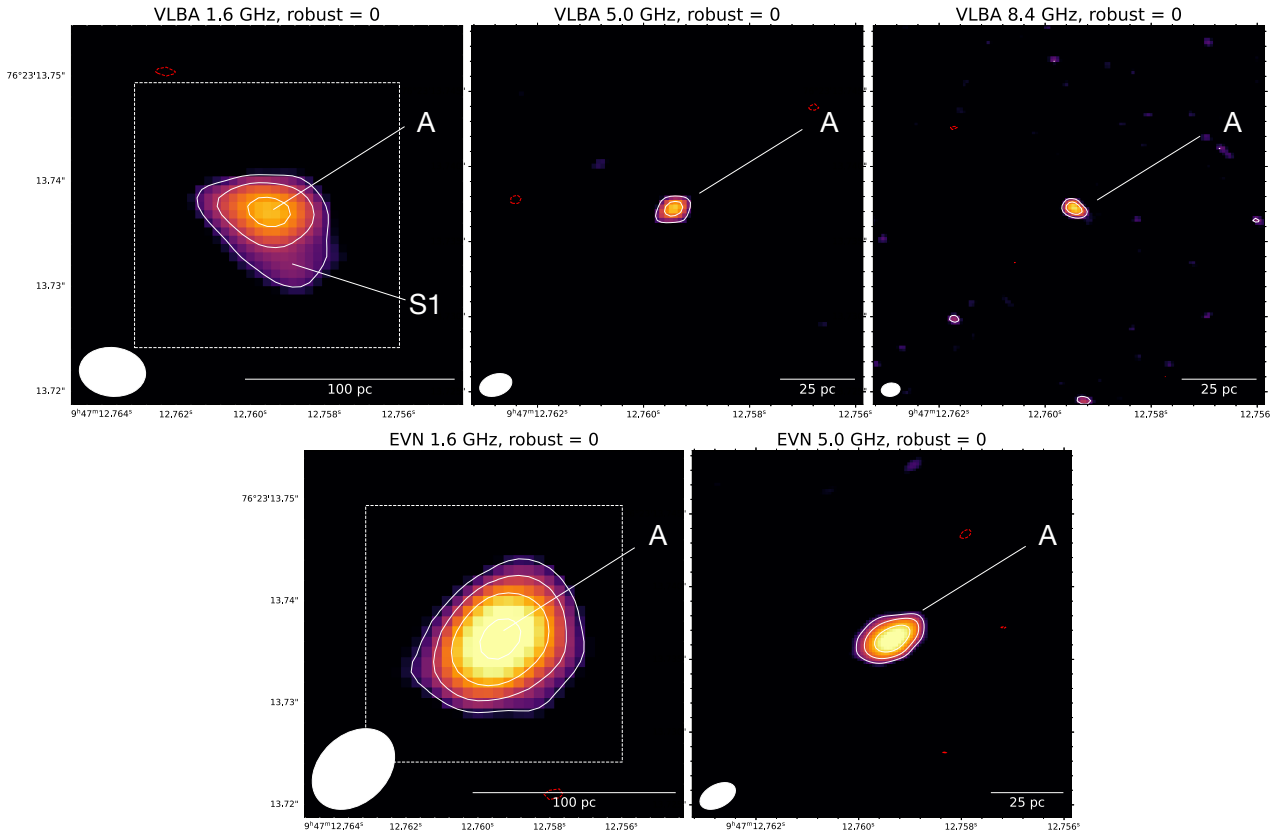


FIGURE 4.7: VLBA and EVN maps of RBS 797 at different frequencies. *Top panels:* VLBA images at 1.6 GHz, 5 GHz, and 8.4 GHz. The beam sizes are 6.3×4.6 mas at 1.6 GHz, 2.2×1.4 mas at 5 GHz, and 1.3×0.9 mas at 8.4 GHz. *Bottom panels:* EVN images at 1.6 GHz and 5 GHz. The beam sizes are 9.1×6.7 mas at 1.6 GHz, and 2.6×1.6 mas at 5 GHz. In each panel, the beam is shown in the bottom left corner, and contours start at $5\sigma_{\text{rms}}$ and increase by a factor of 2; the first negative contour at $-3\sigma_{\text{rms}}$ is drawn in dashed red (see Tab. 4.2 for the resolution and noise levels of the images). The 1.6 GHz VLBA and EVN images have a matched field of view. The white dashed square shows the extent of the images at 5 GHz (EVN and VLBA) and at 8.4 GHz (VLBA). Structures discussed in this work are labelled.

TABLE 4.4: Results of `modelfit` in DIFMAP applied to EVN and VLBA data of RBS 797. See §4.2.1 for details. (1) Name of the radio telescope; (2) project code; (3) observing frequency; (4) date of the observations; (5) robust parameter used during imaging; (6) $\chi^2/\text{degrees of freedom}$; (7) label of the component; (8) major axis of the component, in mas; (9) ratio between minor and major axis of the component; (10) position angle of the ellipse describing the component, in degrees; (11) flux density of the component.

Telescope	Project Code	Frequency	Obs. Date	Robust	$\chi^2/D.o.f.$	Component	a	b/a	Φ	S	
VLBA	BG 224	1.6 GHz	Feb. 4, 2014	0	1.13 (229130)	A	2.5	1.0	0	0.75 ± 0.09 mJy	
						S1	5.8	0.7	-16.1	0.27 ± 0.04 mJy	
		5.0 GHz	Feb. 4, 2014	0	1.14 (54424)	A	0.6	1.0	0	0.47 ± 0.05 mJy	
		8.4 GHz	Feb. 4, 2014	0	1.19 (109548)	A	0.05	1.0	0	0.40 ± 0.05 mJy	
	BE 056	5.0 GHz	Jul. 4, 2014	3	1.21 (13831)	A	2.5	1.0	0	0.47 ± 0.06 mJy	
EVN	EG080	1.6 GHz	Feb. 26, 2014	0	1.16 (236740)	A	3.0	1.0	0	1.65 ± 0.17 mJy	
			5.0 GHz	Mar. 9, 2014	0	1.07 (314572)	A	0.9	1.0	0	0.70 ± 0.07 mJy
		RSG05	5.0 GHz	May 3, 2013	0	1.12 (9068)	A	3.4	1.0	0	0.84 ± 0.09 mJy
		RSG07	1.6 GHz	Dec. 1, 2015	0	1.06 (12092)	A	7.0	1.0	0	1.91 ± 0.22 mJy

4.3.3 The pc scale

We show in Fig. 4.7 the VLBA images at 1.6 GHz, 5 GHz and 8.4 GHz (top panel), and the EVN images at 1.6 GHz and 5 GHz (bottom panel). The parameters of the images are reported in Tab. 4.2. From these images we identify a single source at the phase center; the emission appears unresolved, with the exception of the VLBA 1.6 GHz image, where a faint extension is visible south of the peak.

We used DIFMAP to identify components from the uv-data and measure their flux densities. Based on this analysis, we find that the VLBA data at 1.6 GHz are well described by the combination of two components: a bright one (A, 0.75 ± 0.09 mJy) coincident with the radio peak, and a fainter one (S1, 0.27 ± 0.04 mJy) at a distance of 12 mas (~ 60 pc) south of A. We observe that the position angle of the jet-like component S1 matches the jet orientation on JVLA and LOFAR scales (see Fig. 4.2). Additionally, the one-sidedness of the jet is consistent with the possible interpretation presented in §4.3.1 of the southern jet being the approaching one. The VLBA data at higher frequencies are described by a single, unresolved component (coincident with A), with a flux density of 0.47 ± 0.05 mJy (at 5 GHz) and 0.40 ± 0.05 mJy (at 8.4 GHz).

The EVN data at 1.6 GHz is fitted with a single component with a flux density of 1.65 ± 0.17 mJy, that we identify as A from the VLBA maps. Similarly, the 5 GHz data are fitted with a single component with flux density 0.70 ± 0.07 mJy. Component S1 is not visible in the 1.6 GHz EVN map, although there are hints of a south-west extension in the map shown in Fig. 4.7 (bottom left). Additionally, the total flux density within the $5\sigma_{\text{rms}}$ contour at 1.6 GHz is higher than the peak flux by $\sim 20\%$ (see Tab. 4.2), further supporting the presence of extended flux in the EVN map. Therefore, A+S1 are likely unresolved into a single component (the EVN beam area is twice as large as the VLBA beam area). However, forcing a smaller beam to the EVN data and using a uniform weighting to improve the resolution results in a worse image sensitivity, which prevents us from fitting other components to the data in DIFMAP.

The simultaneous VLBA observations at the different frequencies (all performed on February 4, 2014) allow us to obtain a reliable measurement of the source spectral index. We measured the flux density of the core component (A) from maps obtained by matching the uv-range between the observing frequencies ($5 \text{ M}\lambda - 50 \text{ M}\lambda$), and we fitted a power-law to the flux densities at 1.6 GHz, 5 GHz, and 8.4 GHz. This returned a spectral index of $\alpha_A = 0.25 \pm 0.04$. Such rather flat value is consistent with the core spectral index on the kpc scale from LOFAR and JVLA data of 0.19 ± 0.02

(see §4.3.1). We also deduce that the spectral index of component S1 is steeper than 0.65 at 3σ confidence, based on the sensitivity of the 5 GHz and 8.4 GHz observations (which do not detect this component).

Comparing our results with those presented in Gitti et al. (2013), we find the absence in our maps of the second component detected in the snapshot EVN observation at 5 GHz (performed on May 3, 2013) at a distance of 77 pc south-west from the radio core. The non-detection at all frequencies and between the different instruments suggests that it was, most likely, a spurious detection. A re-analysis of the data indicates that the component was in fact an artifact caused by the phase calibrator being resolved into a double itself, as described in Appendix D.

Ultimately, we note that from the VLBA and EVN data we find no evidence of the second component B visible in the e-Merlin image at 5 GHz of Fig. 4.6. This supports our interpretation of B as extended radio emission, likely resolved out in the VLBI data due to the different uv-coverage.

Does the radio core of RBS 797 show time variability?

We note that there is an inconsistency in the flux density of RBS 797 between the different observations. At 1.6 GHz, the EVN total flux density is larger than the VLBA total flux density by a factor of ~ 1.75 , while at 5 GHz the EVN total flux density is larger than the VLBA total flux density by a factor of ~ 1.5 . This is inconsistent with the typical flux density scale error associated with the EVN and VLBA telescopes (around 10%).

To gain more insights on this difference, we retrieved other EVN and VLBA snapshot observations of RBS 797 (see §4.2.4 and Tab. 4.1) and we measured the (unresolved) flux densities in DIFMAP. Based on the flux densities reported in Tab. 4.4, we find that the 5 GHz emission oscillated between ~ 0.7 mJy and ~ 0.5 mJy between May 2013 and July 2014. The 1.6 GHz flux density increased from ~ 1 mJy to ~ 1.7 mJy between the 4th and the 26th of February 2014, and the following observation on December 1, 2015 measured a flux density of ~ 1.9 mJy (consistent with the previous measurement). A clear trend is that the EVN flux densities are always higher than the corresponding VLBA flux densities at the same frequency. The 5 GHz EVN flux density (0.7 mJy) is also higher than the nearly contemporaneous 5 GHz eMerlin flux density (0.55 mJy). This may indicate a technical origin, or a different sensitivity to the structures of the source. However, we verified that matching the uv-coverage and image parameters does not solve such inconsistency. Excluding the Jodrell Bank and Westerbork stations from the EVN data (which provide the shortest spacings and therefore the highest sensitivity) still does not change these results. Additionally, the mismatch is not caused by transferring solution from a strongly variable phase calibrator (J0954+7435), which does not show significant flux density variations.

Interstellar scintillation may cause flux density variations in compact radio sources such as flat spectrum AGN, which typically occur on timescales of a few hours or days, at most (e.g., Koay et al. 2018). Yet, the variations measured in RBS 797 are on weeks and month timescales, and we do not find evidence of significant variability within the duration of each observation.

One possibility is that the variability is intrinsic to the source itself, which is not uncommon for the radio cores of BCGs (e.g., Hogan et al. 2015b; Hogan et al. 2015a). Interestingly, we find evidence of time variability also on VLA scales. We compared the 4.8 GHz VLA observations published in Gitti et al. (2006) (performed in 2004) and our JVLA data at 5.5 GHz (4.5 – 6.5 GHz bandwidth), obtained in 2022. We built comparable maps by matching the uv-range, frequency, and bandwidth (4.8 GHz, 128 MHz) of the data. Using circles with radius of $1''$ centered on the radio core, we measured flux densities of $S_{4.8}^{2004} = 1.07 \pm 0.06$ mJy and $S_{4.8}^{2022} = 1.54 \pm 0.14$ mJy. The two measurements are different by a factor 1.44 at a significance of 2.9σ . Thus, we have independent indications of variability from the radio core of RBS 797, besides the evidence from VLBI data. Nevertheless, given the suspicious systematic difference between the EVN and VLBA observations, and the poor sampling of the light curve, we cannot draw strong conclusions on the origin and amplitude of such variability,

which currently remains unexplained. Future ad-hoc monitoring of this source may shed lights on this issue.

4.4 Discussion: which mechanism caused the complex radio morphology of the central AGN?

4.4.1 Deciphering the morphology of the radio galaxy in RBS 797

The new radio images shown in the previous sections confirm the earlier claims that the central AGN of RBS 797 has been going through several episodes of activity, the directionality of which has changed over time. Combining our results with the previous works of Gitti et al. (2006), Gitti et al. (2013), Ubertosi et al. (2021b), and Ubertosi et al. (2023b) (see Chapter 3), we can summarize what is currently known on the outburst history of RBS 797 as follows. On 50 – 100 kpc scale the presence of three shock fronts and of diffuse radio emission (see also Bonafede et al. 2023) supports an interaction between the AGN and its environment that dates back to ≈ 80 Myr ago. On scales of 10 – 50 kpc, the quickly varying orientation of the jet axis is demonstrated by the perpendicular pairs of radio lobes and corresponding X-ray cavities that have similar ages (~ 30 Myr) down to a few Myr of accuracy (§4.3.1). Zooming into the inner 10 kpc, north-south curved jets are visible, with multiple sites of relativistic particle acceleration. The S-shaped structure is recent, with an age of a few Myr (§4.3.1 & §4.3.2). Ultimately, going down to hundreds and tens of pc an active core connected to a southward jet feature is visible, with possible evidence of time variability on months timescales (§4.3.3 & §4.3.3).

To understand the history of the multiple misaligned outbursts we need to identify the mechanism that drives such changes in orientation. A clear dynamical feature is the S-shaped jet morphology. These shapes have long been associated with precession over time of the jet axis (e.g., Rubinur et al. 2017; Horton et al. 2020; Nolting et al. 2023 and references therein), which is likely to be occurring in RBS 797. Indeed, we have independent evidence that the north – south jets are precessing. First, we noticed the presence of multiple hotspots in the radio maps, which is one of the expected signatures of precession (e.g., Mahatma et al. 2023). Second, the hotspots have similar spectral indices and radiative ages, indicating that particle are simultaneously being accelerated at each of these locations (see also Hardcastle et al. 2007a), which can be a consequence of the swirling jet path (Horton et al., 2023). Considering the above information, in the next paragraphs we use the observed jet morphology in RBS 797 to constrain the main parameters of the precession motion.

Modelling jet precession

The distinct S-shape of the kpc – scale jets in RBS 797 visible in Fig. 4.2 may be explained with a precession motion around the jet axis. Such morphologies have been observed in several radio galaxies, from pc to hundreds of kpc scales (e.g., Machalski et al. 2016; Bruni et al. 2021; Nandi et al. 2021). The observable signatures of precession (jet curved structures in radio maps) can be linked to the dynamical parameters that regulate such motion. These are, mainly, the precession period P , the half-opening angle of the jet precession cone ψ , the inclination of the jet along the line of sight i , and the jet advance speed v . The exact mapping between the radio morphology and these quantities depends on the model assumed for the physics of jet propagation and precession. Here we consider the kinematic precession model of Hjellming and Johnston (1981), which includes relativistic effects³. The model parameters are the distance to the source (d), the position angle of the jet precession axis in the plane of the sky (χ), the precession period (P), the half-opening angle of

³While it was built to fit the jet morphology of the microquasar SS433, it does not assume any a-priori condition related to microquasars, and it is relatively simple. Thus, it can be generalized to describe jets from radio galaxies. Indeed, it has been used before to model extragalactic AGN jets (see e.g., Rubinur et al. 2017; Kharb et al. 2019).

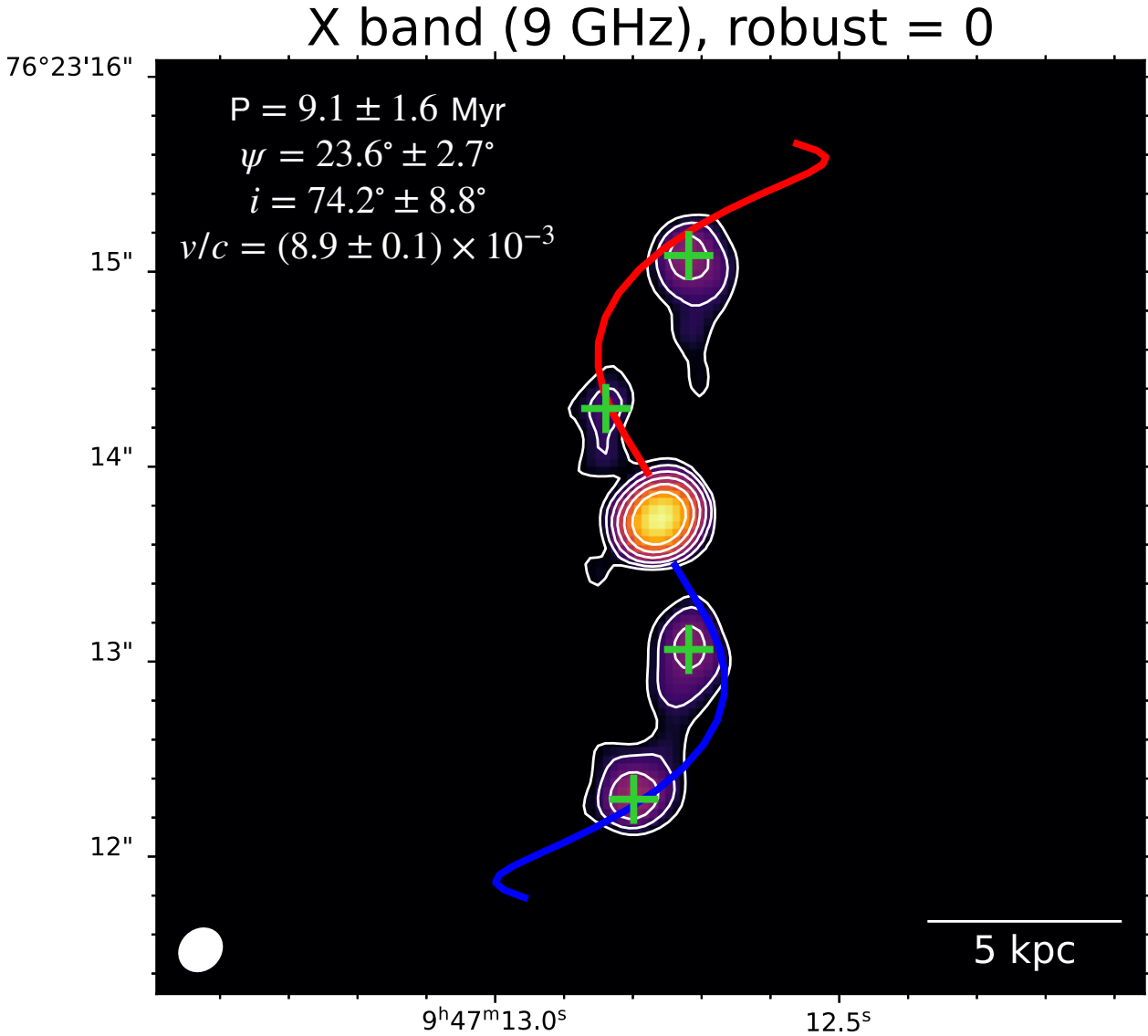


FIGURE 4.8: Jet precession model of Hjellming and Johnston (1981) fitted to the radio images of the kpc-scale jets in RBS 797. Contours are the same as those shown in Fig. 4.2. The red line represents the receding jet path and the blue line represents the approaching jet path. The location of the green crosses corresponds to the position of the observed hotspots, while their extent represents the resolution of the radio observation (the beam is shown in the bottom left corner). Best fit parameters are reported in the top left corner. We note that the uncertainties on the best fit parameters represent the combination of statistical and systematic uncertainties (see §4.4.1 for details).

the jet precession cone (ψ), the precession axis inclination to the line of sight (i), and the jet advance speed (v/c). From the equations detailed in Hjellming and Johnston (1981), the model predicts the position at a time $t_{eject} + \Delta t$ of two opposite jet blobs launched from the SMBH at a time t_{eject} . The position is expressed in the form of offsets from the core position δRA and δDEC . Evolving the model from the initial time t_{eject} (for example, 20 Myr ago) to t_{obs} (i.e. the present time) produces the predicted model jet path projected onto the plane of the sky over 20 Myr of jet activity. Such model can be readily compared to the real jet path observed from radio maps.

In order to derive the parameters of the jet precession motion in RBS 797, we followed a similar approach to that of Coriat et al. (2019). We used the `scipy.optimize` package to minimize the difference between (a) the observed offsets of each hotspot (H1, H2, H3 and H4) with respect to

the core, δRA_{obs} and δDEC_{obs} , and (b) the jet path predicted by the model in the form δRA_{mod} and δDEC_{mod} . The observed hotspot offsets have been weighted by the beam width (resolution of radio observations) during the minimization process.

The model parameters that we fixed before evolving the model are the distance to the source $d = 1881.7$ Mpc (the luminosity distance), and the position angle of the jet precession axis in the plane of the sky, $\chi = 90^\circ$ (that is the position angle of the whole S-shaped jet structure, measured from the west axis). We set constraints in input to the model parameters as follows:

- P : the precession period was bound to vary between 2 Myr (the smaller radiative age we measure from the spectral modelling of the jets, see Fig. 4.4, right panel) and 20 Myr (twice the maximum radiative age we measured). We verified that for $P > 20$ Myr the model predicts a jet bending on scales of tens of kpc, which would be in disagreement with the observed bending on a few kpc scale.
- ψ : the half-opening angle of the jet precession cone was bound to vary between 10° and 30° to approximately match the observed morphology of the S-shaped jets.
- i : the jet precession axis inclination with respect to the line of sight was bound between 60° and 90° . As noted in §4.3.1, the symmetry of the jets suggests that the whole structure is not strongly oriented towards the observer.
- v/c : the jet advance speed in units of the speed of light c was bound between $10^{-3}c$ and $10^{-1}c$, in comparison with typical speed of kpc – scale jets (e.g., Meyer et al. 2017; Kappes et al. 2019; Perucho et al. 2019).

The minimization procedure consists in `scipy.optimize` exploring the parameter space of the above quantities and computing every time the predicted jet path. The optimized model is the one for which the distance between the predicted and observed jet paths is the smallest. The minimization was realized 1000 times, and we assumed the dispersion of the derived parameters around the mean as a good estimate of the statistical error σ_{stat} . Additionally, the minimization was performed not only at one frequency, but using all the available radio maps that detect the hotspots: LOFAR at 144 MHz, JVLA at 3 GHz, 5.5 GHz, 9 GHz (Fig. 4.2), and e-Merlin at 1.4 GHz (Fig. 4.6). The dispersion around the mean of the precession parameters at different frequencies was assumed as a good indicator of the systematic error σ_{syst} . The final uncertainty on each best fit parameter is given by $\sqrt{\sigma_{stat}^2 + \sigma_{syst}^2}$.

We show in Fig. 4.8 an overlay of the best-fit precession model on the 9 GHz JVLA image of RBS 797, where we also report the best-fit parameters. The predicted jet path is color coded according to the approaching (blue) and the receding (red) jet. We obtain a precession model with period $P \sim 9$ Myr, rotating with a half-opening precession cone angle of $\psi \sim 24^\circ$ and inclined by $i \sim 74^\circ$ degrees with respect to the line of sight. The jet advances with a speed of $v \sim 10^{-2}c$. We observe that within the uncertainties on the hotspots position (given by the resolution of radio observations), the model provides a nice representation of the jets morphology. The predicted inclination along the line of sight is in line with the jets mainly lying in the plane of the sky. The best-fit jet advance speed agrees with the order-of-magnitude dynamical speed of the jets: based on the radiative age of the jet structures ($\sim 2 - 7$ Myr) and the jet length of ~ 8 kpc, we would expect a dynamical velocity ranging between $0.004c \lesssim v_{dyn} \lesssim 0.01c$. We additionally note that the comparison between the estimated jet radiative ages (§4.3.1) and the predicted precession period indicates that the jet are currently half way through a full precession round.

The connection between the inner jets and the outer lobes: single or multiple precession modes?

The precession model detailed above provides a good description of the north – south jet motion. However, it is not straightforward to fit the older outbursts into this scenario. The perpendicular

pairs of radio lobes on ~ 50 kpc scales have been inflated over similar timescales, and do not lie on the jet path predicted by the precession model (see Fig. 4.8). Here we discuss whether the morphological evidence support a single dynamical effect, or if the combination of multiple mechanisms is required to explain all the outbursts.

Can a single precession mode explain the multi-faceted morphology visible in Fig. 4.2? In this context, numerical simulations are instructive. It has been found that a prolonged wobbling outflow coupled with jet self-interactions can cause very complex morphologies to appear (e.g., Horton et al. 2020; Horton et al. 2023; Lalakos et al. 2022; Nolting et al. 2023). Synthetic radio maps presented in these works show a plethora of structures in multiple directions (even orthogonal ones). Nolting et al. (2023) stressed that the viewing angle of the observer (i in this work, θ in their work) may generate very different apparent radio shapes. The case of RBS 797 may be akin to those of the above simulations. However, we note that the most “misaligned morphologies” (as those observed in RBS 797) occur either when the half-opening angle of the precession cone is large (up to $\sim 45^\circ$) or when the precession axis is nearly aligned with the line of sight ($i \leq 45^\circ$). On the contrary, we found in §4.4.1 that the precession cone is relatively narrow ($\psi \sim 24^\circ$) and that the source is not strongly oriented towards us ($i \sim 74^\circ$). Thus, the above scenarios may apply to RBS 797 only if the parameters that regulate the precession motion are time dependent (e.g., Martí et al. 1997; Laing and Bridle 2014; Giri et al. 2022). For example, if the half-opening angle of the precession cone ψ was larger in the past, and possibly as high as 45° , then it would be possible to find radio emission in the direction perpendicular to that of the current jet axis. Thus, we argue that a simple and stationary precession model cannot explain the whole history of AGN activity.

We can only be speculative about mechanisms that are more elaborate than a single precession mode. A first possibility is that precession was already in place ~ 30 Myr ago, during the large lobe formation. A short precession period (a few Myr) and a large precession cone half-opening angle ($\psi \approx 45^\circ$) would explain how the N – S and E – W lobes (and cavities) have very similar radiative and dynamical ages. The end of the activity around 20 Myr ago (see §4.3.1) could have been followed by a jet axis flip by a large angle (nearly 90°). As a consequence, the following (and present) jet activity, started within the last ~ 10 Myr, is oriented in a different direction.

A second idea involves the superposition of two wobbling modes of the jet – SMBH. Besides precession, the nutation motion of jets has also been predicted in the context of jet dynamics (Gangardt et al., 2021) and observationally confirmed on pc scales (Britzen et al., 2018; Dominik et al., 2021; von Fellenberg et al., 2023). We can hypothesize that the jets in RBS 797 experience a long period nutation of the jet axis modulated by a shorter time precession motion. A long period nutation ($P_{nut} \sim 10$ s of Myr) with a wide nutation angle would explain how the large E-W lobes are orthogonal to the current N-S jets, and a small period precession ($P_{pre} \sim$ a few Myr) would account for the nearly coeval lobes on 50 kpc scales and the S-shaped jets on 10 kpc scales.

Interestingly, all the above processes are usually associated with the presence of binary SMBHs in the central engine (e.g., Merritt and Ekers 2002; Britzen et al. 2018). Below we discuss how the spectral properties of the radio plasma can provide further insights on this topic.

The connection between the inner jets and the outer lobes: injection index and jet power

The injection index of the radio plasma has changed between the previous activity that produced the large E-W and N-S radio lobes ($\Gamma \sim 0.54$, see §4.3.1 and Tab. 4.3) and the current activity of the north – south jets ($\Gamma \sim 0.9$, see §4.3.1). This indicates that the initial energy distribution of the electrons powering the current north – south jets was characterized by a relatively higher number of particles at low energies. We noted in §4.3.1 that the steep injection index of the jets is consistent with those found in powerful FR IIs. Conversely, the injection index of the radio lobes is consistent with the range of $0.5 \leq \Gamma \leq 0.7$ expected for radio galaxies (including FR Is, e.g., Laing and Bridle

2013). It has been argued that the injection index positively scales with the jet mechanical power (Blundell et al., 1999; Konar and Hardcastle, 2013). This scaling would agree with powerful FR IIs having steeper injection indices. Interestingly, Konar and Hardcastle (2013) also reported that, in sources that show multiple episodes of activity, a difference in the injection index is expected if the jets change their direction from one outburst to the other.

These arguments are particularly relevant in the case of RBS 797. Specifically, the steeper Γ of the youngest AGN activity supports an increase in mechanical power of the jets, and a possible transition from an FR I radio galaxy (the older, large lobe phase on 50 kpc scales that carved out the E-W and N-S cavities) to a more powerful FR II (the current north – south twisted jets on ~ 5 -10 kpc scales). The morphology of the radio emission is also in agreement with this interpretation (see Fig. 4.2): the diffuse morphology of the large radio lobes and the presence of hotspots in the north – south jets favours a FR I interpretation of the former activity and a FR II interpretation of the latter (Fanaroff and Riley, 1974).

This transition may have been driven by a mechanism that could either be extrinsic or intrinsic to the central engine. In the first case, a change in the accretion rate of the SMBH may have determined an increase of the mechanical power. RBS 797 is a strongly cooling galaxy cluster, and the rate at which gas cools out of the ICM and ultimately feeds the AGN is expected to flicker over time (e.g., Gaspari et al. 2012a; Li et al. 2015). In the second scenario, the conditions of the central engine may have changed between the outbursts. It has been previously claimed that RBS 797 may host (or may have hosted in the past) binary SMBH (Gitti et al., 2006; Gitti et al., 2013). If the binary SMBHs merged between the older and the younger outbursts, this may have caused a flip of the new SMBH spin (Merritt and Ekers, 2002), which would explain the different direction of the new jet activity. The sudden increase in black hole mass may also be linked to higher – power jets (Blandford and Znajek, 1977). Alternatively, the older and younger outbursts may not have been driven by the same SMBH: if the binary has not coalesced, it is possible that after one SMBH switched off (the one producing the lobe emission) the second SMBH turned on in a different direction. If so, it would be unsurprising to observe different jet powers in successive outbursts.

4.4.2 Is the central AGN powered by binary SMBHs?

Over time, the AGN activity in RBS 797 has been characterized by different processes, including a clear jet precession and possibly a reorientation event between the older and the most recent outbursts. Leveraging the morphological and spectral information on this radio galaxy, we found strong independent evidence for claiming the existence of binary SMBHs in the core of RBS 797. These include:

- The clear twisted morphology of the jets on kpc scale and the existence of multiple, coeval hotspots along these structures. These features are strongly indicative of a precession motion, which in turn is usually attributed to the presence of massive binary SMBHs orbiting each other (e.g., Nandi et al. 2021; Horton et al. 2023).
- The existence of the perpendicular and equidistant E – W and N – S lobes (and corresponding X-ray cavities) on larger scales (~ 50 kpc). The dynamical estimates (from X-ray data; see Chapter 3) and the radiative estimates (this work, §4.3.1) nicely agree on the fact that both pairs of lobes/cavities were formed around 30 Myr ago and are coeval (with a ~ 10 Myr uncertainty). The analysis of the radio spectrum further revealed that the jet activities that powered these outbursts had a very similar duration of the active phase (~ 10 Myr) and of the fading phase (~ 20 Myr).

Additionally, we note the tentatively identified radio variability from the core of the radio galaxy would be expected from binary SMBHs models (e.g., Kun et al. 2014; Komossa et al. 2023; Gutiérrez et al. 2023). However, given the unconfirmed nature of such variability we do not further address

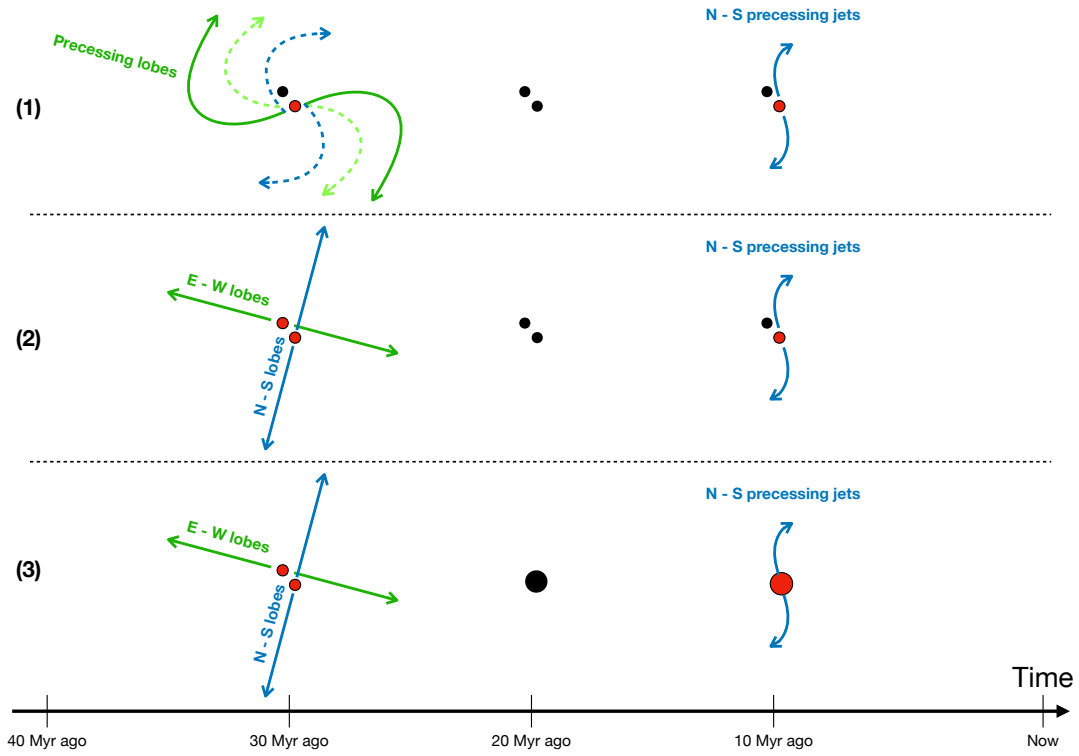


FIGURE 4.9: Schematic representation of the three scenarios involving binary SMBHs at the center of the radio galaxy in RBS 797, detailed in §4.4.2. Arrows represent jets, while circles represent SMBHs (red indicates an active one, black indicates a quiescent one).

this topic.

We are aware that interactions between a single SMBH and its accretion disc can also induce jet precession (Bardeen and Petterson, 1975), due to a forced alignment of the SMBH spin and the disk spin. The precession rate is expected to be slow, and the change in the jet orientation is a single event. This model would be hard to apply to RBS 797: not only we have evidence for multiple changes in jet orientation over time (see also Ubertosi et al. 2021b; Ubertosi et al. 2023b; see Chapter 3), but most importantly the Baarden - Petterson effect would not be able to account for the perpendicular, equidistant and coeval outer lobes (see also Krause et al. 2019 for similar arguments).

Therefore, in the following we assume that the presence of binary SMBHs in RBS 797 is the most likely explanation for the morphological and spectral radio properties. Based on this assumption, we can envisage three possible scenarios to explain the outburst history of the central radio galaxy. These are presented below (see also the schematic view of Fig. 4.9):

1. *Binary SMBHs with one of them active and an evolving precession.* If precession was already in place 30 Myr ago with a wide opening angle ($\geq 45^\circ$, to explain the perpendicular position of the outer lobes) and a small precession period (< 10 Myr, to explain the similar age of the structures), then the formation of a multi-lobed morphology on tens of kpc scales would be expected (Nolting et al., 2023; Horton et al., 2023). Following this scenario (upper row in Fig. 4.9), after a period of inactivity one of the SMBH in the binary system started again its activity in the N – S direction (producing the N-S twisted jets on ~ 10 kpc scales, see Fig. 4.2), with the gravitational perturbation of the secondary component still causing the jets to precess. Assuming that a single jet episode created both the N – S and E – W outer lobes would be consistent with the very similar injection spectral index $\Gamma \sim 0.54$ of the perpendicular structures on 50 kpc scales (see §4.4.1). The change in jet precession axis from the older (on

50 kpc scales) to the younger (on 10 kpc scales) activity may have been induced either by a sudden change of the SMBH spin axis, or by a long-term nutation motion of the jet direction (see §4.4.1).

2. *Binary SMBHs, both of them active 30 Myr ago and only one active now.* Another possibility to explain the coeval origin of the perpendicular outer lobes is to hypothesize that both SMBHs were active ~ 30 Myr ago (middle row in Fig. 4.9). This scenario would not require jet re-orientation to occur between the older and the younger outbursts: one of the SMBHs would simply renew its jets in the N – S direction, and the other would remain silent.
3. *Binary SMBHs, both of them active 30 Myr ago, then a merger around 10 Myr ago and the resulting single SMBH active now.* This case assumes a coeval activity around 30 Myr ago of both SMBHs (as the second scenario), but includes a merging event in between the older and younger outbursts (last row in Fig. 4.9), that brought the two SMBHs to coalesce and led to the formation of a single SMBH with a higher mass. On the one hand, it would be unlikely to serendipitously catch a post-merger SMBH that went through AGN activity before and after the event. On the other hand, this scenario would also explain (contrarily to the first two) other results that we presented. A merger between SMBHs is the key mechanism behind the “spin-flip” of the central engine (Merritt and Ekers, 2002), that is the sudden and large change in jet pointing direction (as observed in RBS 797 between the older and younger outbursts). Additionally, a change in the intrinsic properties of the AGN (in this case, the increased SMBH mass) would be compatible with the observed change of synchrotron injection index (Konar and Hardcastle, 2013) and the likely increase of the jet power (Blandford and Znajek, 1977), as we discussed in §4.4.1.

The above scenarios are all based on indirect evidences of binary SMBHs in RBS 797. *Do we have direct evidence for the presence of two compact radio cores in the available data?* The VLBI observations presented in §4.3.3 clearly detect a single, compact component at the center of the radio galaxy, suggesting that if there is a second SMBH on tens of pc scales, either it is not active now or it is non-detected owing to a low level of activity. Based on the sensitivity at 1.4 GHz of the VLBA data, we estimate a 3σ upper limit on the radio power of the second SMBH of $P_{1.4\text{GHz}} \leq 3.2 \times 10^{22}$ W/Hz. Therefore, we tend to exclude that a secondary active SMBH is present on tens to hundreds of pc scales. In this context, it is interesting to note that the precession period caused by the geodetic perturbation of the SMBH spin can be linked to the binary separation. Following Krause et al. (2019) and Horton et al. (2020) we can place an upper limit on the binary separation with the following expression:

$$d_{pc} < 0.18 P_{Myr}^{2/5} M_9^{3/5} \quad (4.3)$$

where d_{pc} is the binary separation in parsec, P_{Myr} is the precession period in Myr and M_9 is the active black hole mass in units of $10^9 M_\odot$. The assumptions behind the above equation (which is a simplification of Eq. 1.35) are that the binary SMBHs are orbiting each other in a circular orbit, and that the observed precessing jets are launched by the more massive black hole. We measured in §4.4.1 a precession period of $P = 9.1 \pm 1.6$ Myr. The mass of the SMBH in RBS 797 has been estimated to be around $1.5 \times 10^9 M_\odot$ (Cavagnolo et al. 2010; Ubertosi et al. 2023b; see §3.5.2 in Chapter 3). We obtain an upper limit on any binary separation of $d_{pc} < 0.6$ pc. This is an order of magnitude smaller than the highest resolution that can be achieved with the available VLBI data (5 pc \sim 1 mas in the 8.4 GHz VLBA observations). Overall, even if both SMBHs are active (i.e. potentially visible through their radio emission), they would be hard to resolve at the redshift of RBS 797 ($z = 0.354$). An alternative method to investigate this point would be to search for double-peaked broad and narrow optical lines (e.g., [OIII]) in the core of the BCG, potentially caused by the orbiting binary SMBHs (see e.g., Smith et al. 2010).

4.5 Summary and Conclusions

The multi-scale and multi-frequency radio data presented in this Chapter represent a crucial complement to the X-ray analysis presented in Chapter 3. While the X-ray observations gave clear insights into the *footprints* of feedback on the ICM, the radio observations revealed the direct details of jet evolution in the cluster RBS 797. Here we summarize our results.

1. The LOFAR (144 MHz, with international stations) and JVLA (3 GHz, 5.5 GHz, 9 GHz) data allowed us to unveil the morphological and spectral properties of the radio galaxy between 10 – 50 kpc (the scale of the perpendicular pairs of radio lobes) and between 2 – 10 kpc (the scale of the inner jets). We presented the first images of the large scale lobes at sub-arcsecond resolution at 144 MHz (0.3'' resolution) and 3 GHz (0.9'' resolution). These images confirm the co-spatiality of the radio lobes with the perpendicular X-ray cavities. By fitting a CI-off model to the observed spectra, we found that the radiative age of the E-W lobes (31.4 ± 6.6 Myr) and of the N-S lobes (32.1 ± 9.9 Myr) supports a coeval origin of the perpendicular outbursts, that also have similar *active phase* duration (~ 12 Myr) and *passive phase* duration (~ 19 Myr). These ages are in good agreement with the X-ray estimates of the cavities and shock ages (see Chapter 3). Based on the 144 MHz – 9 GHz emission from the inner N-S jets (on scales of ≤ 10 kpc), we (a) confirmed the S-shaped jet morphology; (b) showed the presence of two hotspots per jet with a similar radiative age; (c) estimated the age of the twisting N-S jets to be less than ~ 8 Myr. Based on these results, we determined that jet precession (with period ~ 9 Myr and jet advance speed $\sim 0.01c$) can explain the morphological and spectral properties of the N-S twisted jets. We also found that the injection index of the synchrotron emission has steepened between the large scale, older outburst ($\Gamma \sim 0.5$) and the younger S-shaped jets ($\Gamma \sim 0.9$). This evolution in injection index may suggest that the central radio galaxy has transitioned from an FR I-like activity to an FR II-like one around ~ 10 Myr ago, when the N-S jet activity started.
2. The e-Merlin observations at 1.6 GHz show the precessing N-S jets at the highest resolution currently available (0.15''). With the e-Merlin 5 GHz observations (0.035'' resolution), the core emission is resolved into two components (separated by 250 pc), that we interpreted as the radio core (component A, $S = 0.55 \pm 0.04$ mJy) and diffuse, remnant emission from the previous outbursts (component B, $S = 0.38 \pm 0.04$ mJy).
3. The EVN data at 1.6 GHz and 5 GHz reveal the presence of a single, compact core at the heart of RBS 797 (component A). The VLBA data are in agreement with the EVN detection of a single component, but we also found evidence in the 1.6 GHz VLBA data of a faint jet-like feature headed south (component S1, $S = 0.27 \pm 0.04$ mJy at 1.6 GHz). We also showed that there is evidence for monthly-scale time variability of the core radio emission. There is a suspicious (but possibly serendipitous) systematic flux density difference between the EVN and VLBA observations, which may indicate that the variability is not physical. However, we found that the flux measured with the VLA between 2004 and 2022 has also varied (with a significance of 2.9σ). Future ad-hoc monitoring is required to confirm the radio core variability.
4. Piecing together these results, we argued that RBS 797 likely hosts (or hosted) binary active SMBHs in the past. The idea of binary black holes is in agreement with (a) the coeval origin of the large, perpendicular radio lobes (and corresponding X-ray cavities); (b) the very similar active and inactive phase duration of the perpendicular radio lobes; (c) the clear jet precession of the N-S jets; (d) the sudden transition in energy budget, jet power, and synchrotron injection index between the successive outbursts. Radio variability (if confirmed) would be an additional clue. We stress that the detection of a single component in the VLBI data is consistent with the binary black hole interpretation: the predicted separation of the binary

SMBHs (0.6 pc) is an order of magnitude smaller than the resolution of the available radio data (5 pc).

Overall, our study highlights how the combination of radio data over a wide range of frequencies can discriminate between different scenarios. It also underlines the critical need for high resolution observations that are also sensitive to large scale, diffuse radio emission (such as the LOFAR data with international stations, or the 3 GHz JVLA data). This is required to connect the fine structure of the jets in radio galaxies with the complex geometry of their large expanding lobes.

Our work adds up to the handful comparisons between radiative ages and X-ray dynamical timescales of radio lobes and corresponding X-ray cavities (see Biava et al. 2021; Kolokythas et al. 2020). Our work is also the first one in which the radio lobes, the X-ray cavities, and the corresponding weak shock front have consistent ages down to only a few Myr of uncertainties, thus being a critical test for the AGN – ICM connection.

While detailed and insightful on RBS 797, this study is by no means a general investigation of the jet reorientation scenario. Besides, the complex structure of RBS 797 is striking, but it is uncommon in many other systems. For these reasons, we present in Chapter 6 an X-ray/radio investigation of the frequency and causes that characterize jet misalignment episodes in a sample of representative, active radio galaxies in clusters and groups.

Chapter 5

Feedback from FR 0, FR I, and FR II radio galaxies in galaxy clusters and groups

Abstract

¹ When jetted AGN live in dense environments, it is possible to obtain insights on their properties from the imprints they leave on the surrounding environment. In this Chapter we focus on how different classes of radio galaxies may have varying effects on the host cluster or group atmosphere. First, we address how the feedback balance (mechanical power versus ICM radiative losses) varies between FR Is and FR IIs. Using a sample of 15 galaxy clusters and groups where both cavities and shocks are detected, we verify that the most powerful outbursts are found in the strongest cooling systems. Additionally, we observe that the mechanical power of the AGN exceeds the gas radiative losses by a factor that is different for FR I and FR II radio galaxies, being below 1 – a few 10s for FR Is and more than ~ 100 for FR IIs. Interestingly, the central ICM entropy between the different classes does not reflect such dichotomy, suggesting that over-powered outbursts are not related to an over-heating of the gas. Then, we focus on the recently discovered class of radio-compact FR 0 radio galaxies. We analyze a *Chandra* observation of Abell 795, that hosts a FR 0 in its central galaxy. We find that the ICM is likely not responsible for the limited growth of this radio galaxy. Additionally, we discover two possible X-ray cavities in the proximities of the FR 0. Their mechanical power ($\sim 2.2 \times 10^{43} \text{ erg s}^{-1}$) is not too far from the ICM radiative losses ($\sim 10^{44} \text{ erg s}^{-1}$), suggesting that even these small-sized AGN can maintain an effective feedback cycle.

5.1 Motivation

Among the open questions on the feedback cycle in dense environments, the issues of how different jet powers heat the ICM, and what is the role of shock heating are essential. Specifically, numerous feedback simulations predict that different jet powers can lead to variations in the extent and strength of heating throughout the cluster atmosphere (see Bourne and Yang 2023 for a recent review). Investigating the effects of jets on the hot gas is key because (a) it sheds lights on the thermodynamics of the ICM, and (b) it provides insights into the SMBH-environment interplay (e.g., O’Sullivan et al. 2011). When the distinction between low-power (FR I like) or high-power (FR II like) jets is considered, then information on the central engine can also be derived. Thus, it is important to consider distinct feedback regimes and how their efficiency couples to the environment (Bourne and Yang, 2023).

Observationally, the latter traditionally translated into measuring cavity power from X-ray observations and comparing it with the radiative losses of the surrounding gas (e.g., Bîrzan et al. 2012). However, we highlighted in Chapter 3 that, at least in RBS 797, neglecting the mechanical power

¹This Chapter is based on Ubertosi et al. (2021a) and Ubertosi et al. (2023b).

associated with weak shocks results in underestimating the energy output by more than one order of magnitude. We thus aim to explore the feedback mechanism and its dependence on jet power by focusing on the energy input due to the combined effect of cavities *and* weak shocks. This investigation is presented in §5.2 of this Chapter.

Ultimately, we extend our investigation to the low-end of the jet-power distribution by searching for evidence of feedback from the recently discovered FR 0 radio galaxies (see Baldi 2023 for a recent review). Showing jetted emission limited to the kpc scale and being numerically dominant over FR Is in the local Universe, FR 0s could play a critical role in the radio-mode feedback mechanism in galaxies. These small radio galaxies may inject energy on smaller scales than those affected by the jets of FR I/IIs, but could still be able to regulate star formation and gas cooling. Nevertheless, the role of FR 0s in the context of feedback has yet to be explored, and an estimate of their mechanical power is still missing. In §5.3 we address this topic by analyzing the properties of a galaxy cluster that hosts a FR 0 in its central galaxy.

5.2 Shock and cavity heating of hot atmospheres: differences between FR I and FR II radio galaxies

In this Section we focus on the dependence of the feedback efficiency on jet power when both X-ray cavities and shocks are included in the total energy budget. As noted in Chapter 3, the total AGN mechanical power in RBS 797 (which is larger than L_{cool} by a factor ~ 14) may seem extreme with respect to systems in typical samples of galaxy clusters, galaxy groups and elliptical galaxies, where the average ratio between mechanical power and cooling luminosity is close to unity (but with a large scatter; e.g., Bîrzan et al. 2004; Rafferty et al. 2006). However, such samples are mostly composed of systems where only X-ray cavities have been found, whereas in RBS 797 we also consider the energy injected by shocks, that dominates the AGN power. Indeed, by considering only the X-ray cavities, we find a ratio $P_{\text{cav}}/L_{\text{cool}} \sim 1$. Thus, a more consistent comparison should be made with other systems with detections of both X-ray cavities and weak shocks.

5.2.1 The sample

Liu et al. (2019b) assembled a compilation of 13 galaxy clusters, groups and elliptical galaxies in which both X-ray cavities and shocks have been detected, and for which Mach number, shock energy and cavity energies are available. We are interested in the comparison between the cooling luminosity and the shock power (P_{sh}), the X-ray cavity power (P_{cav}), and the total (= shock + cavity) heating power (P_{tot}). Thus, first we verified that these 13 systems also have available measurements of all these quantities. Additionally, we checked whether new shock detections had been claimed in literature after the work of Liu et al. (2019b), finding no new results. Surface brightness edges have been identified in 3C 220.1 by Liu et al. (2020b) and in 3C 320 by Vagshette et al. (2019), however due to the insufficient number of counts a spectral confirmation of their shock front nature was not performed. We also consider here the Perseus cluster due to the weak shock surrounding its inner X-ray cavities (Graham et al., 2008b). We report in Tab. 5.1 the properties of the 15 systems (i.e., 13 from Liu et al. 2019b + Perseus + RBS 797) with corresponding literature references. We find that RBS 797 has the largest cooling luminosity and largest total power among the 15 objects.

5.2.2 Results

The relation between mechanical power and radiative losses

In the three panels of Fig. 5.1 we plot the comparison of P_{cav} vs. L_{cool} , P_{sh} vs. L_{cool} and P_{tot} vs. L_{cool} for the objects we selected. The first panel reveals the trend already well tested (e.g., Bîrzan et al.

TABLE 5.1: Systems with detection of both X-ray cavities and weak shocks, ordered by decreasing X-ray cooling luminosity. (1) Name; (2) cooling luminosity (3) total shock power; (4) total cavity power; (5) total heating power, defined as $P_{\text{tot}} = P_{\text{cav}} + P_{\text{sh}}$; (6) FR class of the central radio galaxy (based on radio morphology and/or radio power, see literature references in column 8); (7) central entropy from Cavagnolo et al. (2009), defined as the excess entropy above the best-fitting power law found at larger radii (see §5.2.2 for details); (8) Literature references for the values reported in columns 2 - 6: [1] Bîrzan et al. (2004), [2] Graham et al. (2008b), [3] Vantyghem et al. (2014), [4] Biava et al. (2021), [5] Nulsen et al. (2005), [6] Wise et al. (2007), [7] Bîrzan et al. (2012), [8] Snios et al. (2018), [9] Blanton et al. (2009), [10] Croston et al. (2011), [11] Vagshette et al. (2017), [12] Rafferty et al. (2006), [13] Croston et al. (2009), [14] Kraft et al. (2012), [15] Churazov et al. (2001), [16] Forman et al. (2005), [17] Forman et al. (2007), [18] Forman et al. (2017), [19] Gitti et al. (2010), [20] Randall et al. (2011), [21] Randall et al. (2015), [22] Liu et al. (2019b), [23] Jones et al. (2002), [24] O’Sullivan et al. (2005), [25] Baldi et al. (2009), [26] Machacek et al. (2006).

(*): The value is taken from Liu et al. (2019b).

Name	L_{cool} [10^{43} erg s $^{-1}$]	P_{sh} [10^{43} erg s $^{-1}$]	P_{cav} [10^{43} erg s $^{-1}$]	P_{tot} [10^{43} erg s $^{-1}$]	FR-class	K_0 [keV cm 2]	Reference
RBS 797	234	2900	360	3360	FR I	20.0±2.4	This work
Perseus	67	120	32	152	FR I	19.4±0.3	[1,2]
MS0735.6+7421	26	1100	1700	2800	FR II	16.0±3.2	[3,4]
Hydra A	25	200	210	410	FR I	13.3±0.7	[1,5,6]
Cygnus A	29	1000	210	1210	FR II	23.6±0.9	[1,7,8]
A 2052	8.4	1.0	3.2	4.2	FR I	9.5±0.7	[1,9]
3C 444	8.0	2900	61	2961	FR II	-	[10,11]
Centaurus A	3.0	1.2	0.74	1.94	FR I	2.3±0.1	[1,12,13]
3C 310	1.7	190	130	320	FR II	-	[14]
M 87	0.98	2.4	1.0	3.4	FR I	3.5±0.1	[1,15,16,17,18]
HCG 62	0.15	4.0	0.38	4.4	FR I	3.4±0.1	[19]
NGC 5813	0.055	3.5	0.18	3.7	FR I	1.4±0.2	[20,21]
3C 88	0.055	10	2.0	12	FR II	7.3±1.7(*)	[22]
NGC 4636	0.030	0.16	0.11	0.27	FR I	1.4±0.1	[23,24,25]
NGC 4552	0.0025	0.33	0.015	0.35	FR I	-	[26]

2004; Rafferty et al. 2006; Bîrzan et al. 2012) between the mechanical power of X-ray cavities and the cooling luminosity of the ambient gas. With a span in P_{cav} and L_{cool} of about five orders of magnitude, these 15 systems confirm that larger ICM radiative losses are accounted for by more powerful outbursts. In the second panel we show that also the shock power scales with the X-ray cooling luminosity, suggesting that the whole AGN mechanical output is set in response to the amount of available fuel. We emphasize that this is the first time that the scaling between mechanical power *probed by shocks* and cooling luminosity is verified. This is important because while X-ray cavities are easier to detect, shocks provide a more natural mechanism to heat the surrounding gas. These plots reveal that the SMBH-ICM interplay manifests itself also through shocks, thus confirming the early results of Bîrzan et al. (2004) based on cavities only.

Comparing the shock power and the cavity power would provide useful insights into whether the outburst energy is equally divided between the two signatures of feedback. However, as already noted in Chapter 3 for the case of RBS 797, a detailed comparison between P_{cav} and P_{sh} would require to have a clear association between a shock front and the corresponding X-ray cavities for each system. Restricting the comparison to the objects in Tab. 5.1 with a single shock front and a corresponding single pair of X-ray cavities, we would select only 3C 444, 3C 310, HCG 62, 3C 88, and NGC 4552. For these systems, the ratio of P_{sh} to P_{cav} ranges between 1.5 (3C 310) and 48 (3C 444). Based on these 5 systems alone, it would appear that the shock power is typically larger than the cavity power. However, the exact factor is poorly constrained. A larger number of objects, and a uniform derivation of shock and cavity powers (see more in the last paragraph of §5.2.2) would be necessary to draw definitive conclusions on this topic. We refer the reader to Liu et al. (2019b) for a similar comparison between shock energy and cavity energy.

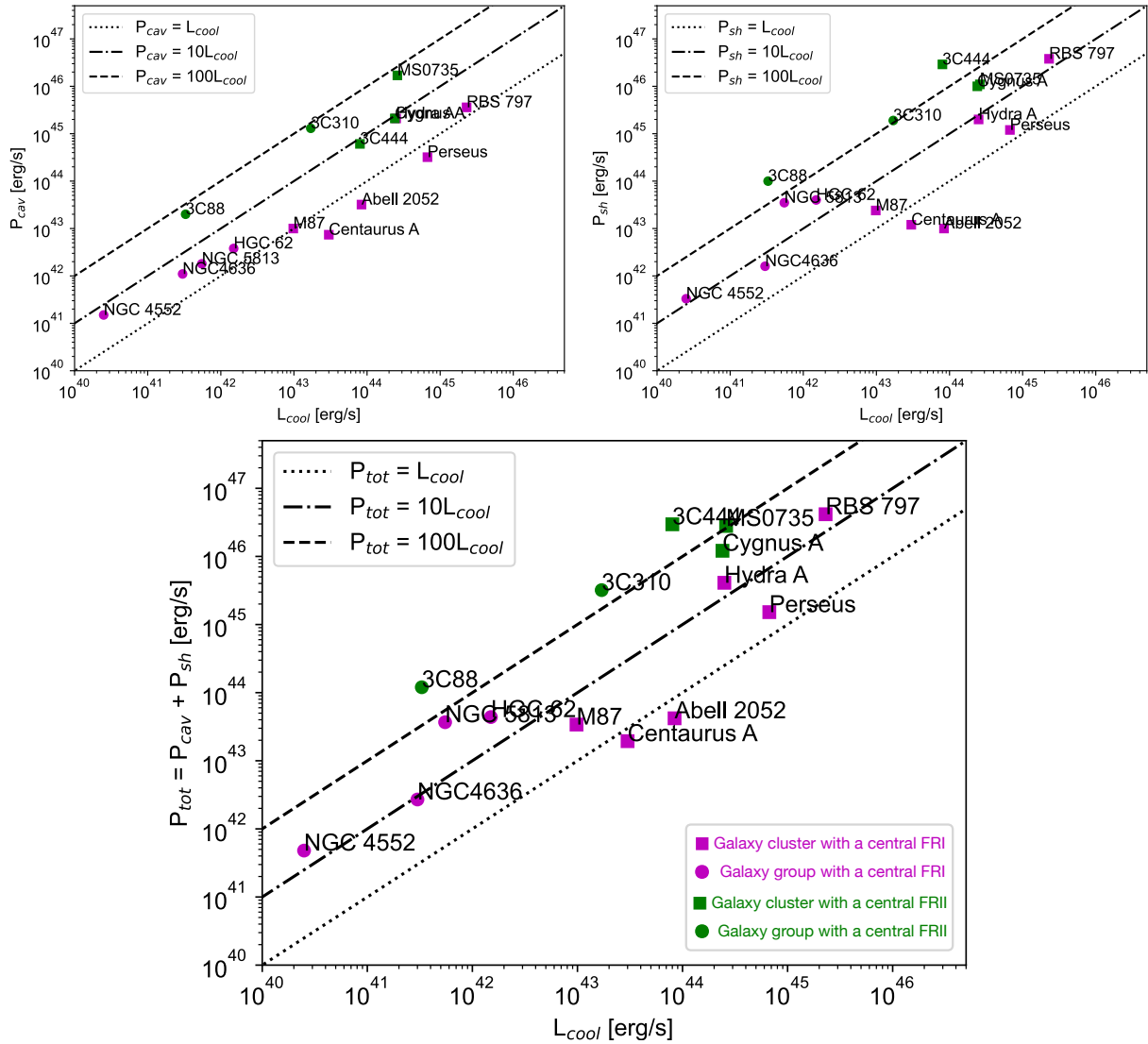


FIGURE 5.1: Mechanical cavity power (*top left panel*), shock power (*top right panel*) and total heating power (*lower panel*) versus cooling luminosity for the 15 systems listed in Tab. 5.1. Overplotted are lines of $P/L_{cool} = 1, 10, 100$. Dots are for elliptical galaxies and galaxy groups, while squares are for galaxy clusters. The color of the points indicates the FR type of central radio galaxy: FR Is are in magenta, while FR IIs are in green.

We note that the majority of the systems have $P_{cav}/L_{cool} \geq 1$ and $P_{sh}/L_{cool} \geq 1$ (dotted lines in the first two panels of Fig. 5.1). Given that shocks are more likely associated with powerful radio galaxies, it is unsurprising that our selection criteria identify systems where cooling is largely balanced by mechanical feedback. These trends are consistent with the plot in the third panel, which shows the scaling between the total average heating power $P_{tot} = P_{cav} + P_{sh}$ and the cooling luminosity.

A distinction between FR-classes

As mentioned above, while RBS 797 has a high total mechanical power, it may not be in a relative sense an extremely heated object. Indeed, when dividing the total AGN power by its high cooling luminosity, we estimate a ratio $P_{tot}/L_{cool} \sim 14$, whereas there are systems in the third plot of Fig. 5.1 (P_{tot} vs. L_{cool}) that are able to provide total mechanical power that exceeds by two orders of magnitude the radiative losses of their gaseous halos. In particular, we note that the upper area of the P_{tot}/L_{cool} space is populated by the 3C sources 3C 88, 3C 310 and 3C 444, by Cygnus A and by

MS 0735.6+7421, which have $P_{\text{tot}}/L_{\text{cool}}$ ratios ranging between 50 (Cygnus A) to 370 (3C 444). By considering the Fanaroff-Riley class of the radio galaxies in our compilation (see Tab. 5.1), we find that the sources named above are all FR II radio galaxies, while the other systems host FR I AGN at their center, characterized by $0.5 \leq P_{\text{tot}}/L_{\text{cool}} \leq 60$. We note that this distinction holds also for the $P_{\text{cav}}/L_{\text{cool}}$ and $P_{\text{sh}}/L_{\text{cool}}$ comparison (upper and middle panel of Fig. 5.1). The two classes seem to overlap at $P_{\text{tot}}/L_{\text{cool}} \sim 50 - 60$, where we find that NGC 5813, a low luminosity FR I radio galaxy, has a larger ratio than Cygnus A, the archetypal FR II radio galaxy. However, the different environments have to be taken into consideration: NGC 5813 is a galaxy group (Randall et al., 2011), while Cygnus A is at the center of a galaxy cluster (e.g., Steenbrugge et al. 2014). In this context, previous studies noted that the relative ratio of X-ray cavity heating power to cooling luminosity appears to be 5 times higher in low mass systems than in rich clusters (e.g., Gitti et al. 2012). By separating the systems in our compilation between galaxy clusters (squares in Fig. 5.1) and galaxy groups and elliptical galaxies (circles in Fig. 5.1), we find that FR IIs have $P_{\text{tot}}/L_{\text{cool}} \geq 180$ while FR Is have $9 \leq P_{\text{tot}}/L_{\text{cool}} \leq 66$ in galaxy groups and elliptical galaxies. In galaxy clusters, FR IIs have $P_{\text{tot}}/L_{\text{cool}} \geq 50$ while FR Is have $0.5 \leq P_{\text{tot}}/L_{\text{cool}} \leq 16$. These values are consistent with AGN in galaxy groups and elliptical galaxies having relatively more power to counter cooling than sources in galaxy clusters - with FR IIs always providing a more violent feedback.

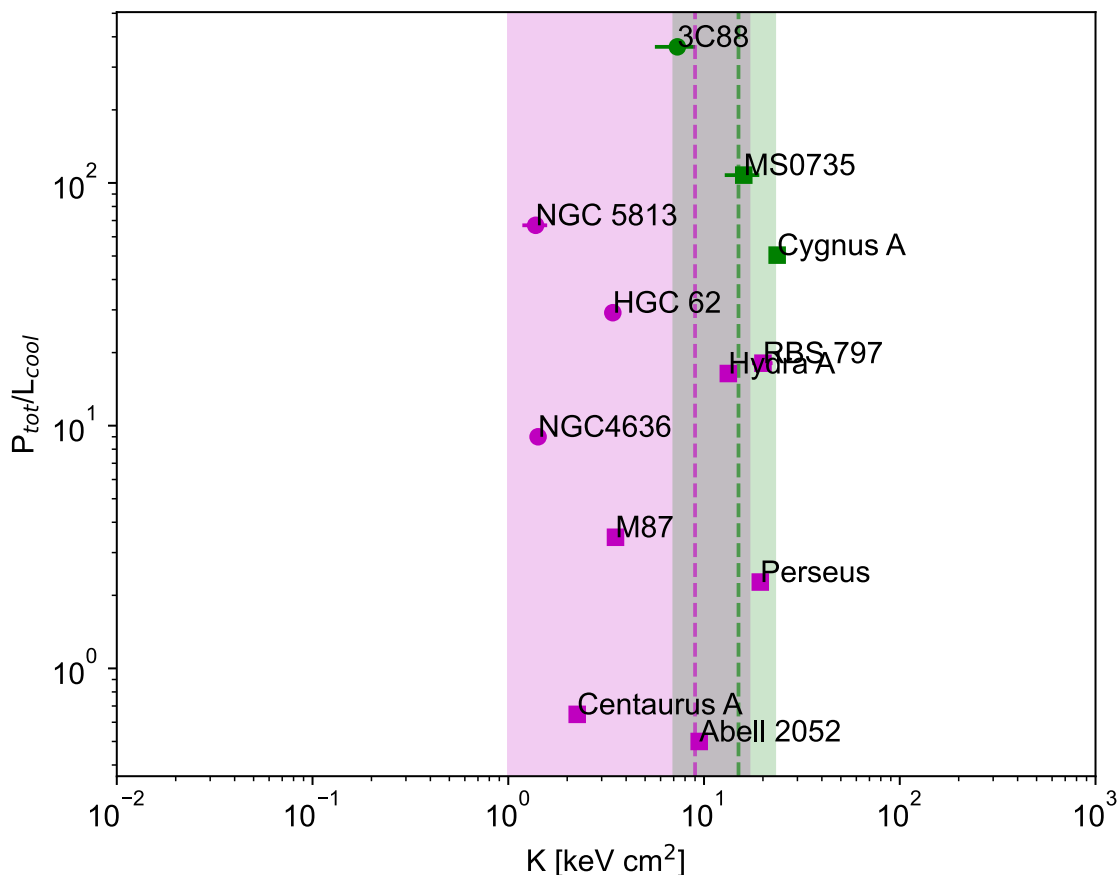


FIGURE 5.2: Feedback ratio versus central entropy excess (from Cavagnolo et al. 2009). Dots are for elliptical galaxies and galaxy groups, while squares are for galaxy clusters. The color of the points indicates the FR type of central radio galaxy: FR Is are in magenta, while FR IIs are in green. Using the same color-coding, the dashed vertical line and the shaded area represent the average central entropy and scatter, respectively, of the two sub-samples.

The effect of extreme feedback

Overall, it appears that both classes of radio galaxies have mechanical power that correlates with the cooling luminosity of their hot atmospheres, suggesting that FR Is and FR IIs can achieve a self-regulated equilibrium between input fuel and output energy. However, FR IIs seem to be able to sustain a more extreme feedback. In this respect, sources populating the upper space of the P_{tot} vs. L_{cool} plot may be expected to have more efficiently heated the ambient gas and quenched any residual cooling. We can test this scenario by considering that the entropy of the ICM is a good proxy for the cooling efficiency of the gas. Cavagnolo et al. (2009) analyzed the entropy profiles of 239 systems (the ACCEPT sample) and measured the central entropy K_0 , that quantifies the typical excess of core entropy above the best-fitting power law found at larger radii. Specifically, Cavagnolo et al. (2009) fitted the entropy profiles of the clusters in their sample with the following model:

$$K(r) = K_0 + K_{100} \times \left(\frac{r}{100 \text{ kpc}} \right)^\alpha, \quad (5.1)$$

where K_0 is the aforementioned central entropy, K_{100} is a normalization for entropy at 100 kpc, and α is the power-law index. As underlined by Cavagnolo et al. (2009), K_0 represents the typical excess of core entropy above the best-fitting power law at larger radii, and not the minimum entropy or the entropy at $r = 0$.

By cross matching the list of Tab. 5.1 with the ACCEPT sample, we find that 11 out of 15 objects have tabulated values of K_0 (missing sources are 3C 444, 3C 310, 3C 88 and NGC 4552). We additionally include 3C 88 since Liu et al. (2019b) determined the core entropy of this group in a similar fashion to that of Cavagnolo et al. (2009).

Based on the core entropy values for systems in our list (see Tab. 5.1 and Fig. 5.2), we find that the hot atmospheres of FR I radio galaxies have K_0 in the range 1 - 20 keV cm², with an average of 9 ± 8 keV cm² (where the uncertainty is the dispersion around the mean). For the three FR IIs matching our criteria, the central entropy is in the range 7 - 24 keV cm² (with an average of 15 ± 8 keV cm²). The clear overlap between the two classes indicates that differences of orders of magnitude in feedback output do not cause any over-heating of the central gas. Therefore, we find that the FR IIs in the plots of Fig. 5.1, while providing a stronger feedback, are not dramatically quenching cooling of the surrounding environment. Since the central cooling time of these systems ranges between hundreds of Myr and ~ 1 Gyr, the above finding may suggest that the thermodynamic regulation of the ICM on long timescales is resilient to episodic, excessively-powerful outbursts (for numerical simulations supporting this picture, see e.g., Gaspari et al. 2011; Le Brun et al. 2014; Prasad et al. 2015; Duan and Guo 2020; Bourne and Sijacki 2021). Indeed, as noted by McNamara and Nulsen (2012), the process through which AGN heat the surrounding gas is “gentle”, and relies on frequent, successive outbursts rather than single, overpowered ones.

We note that these results are speculative and should be treated with caution. In particular, the values reported in Tab. 5.1 are subject to different assumptions made in the literature. For instance, cavity power depends on cavity age, which can be estimated with several methods. Moreover, the shock energy and power may be estimated as done in this work (and in e.g. Randall et al. 2015; Liu et al. 2019b), or by adopting a point explosion model tailored to the specific object (Nulsen et al., 2005). In any case, the difference between these varying assumptions is typically within a factor of a few (e.g., Birzan et al. 2004; Randall et al. 2011; Randall et al. 2015; Liu et al. 2019b), while the trends we noticed in Fig. 5.1 refer to differences of at least one order of magnitude. Thus, we argue that the effect of non-uniform assumptions is not dominant. On the other hand, the systems we considered are probably not representative of the population of galaxy clusters, galaxy groups and elliptical galaxies. More likely, they represent the tip of the iceberg of an underlying larger population of objects with X-ray cavities *and* weak shocks launched by the central AGN which have not been detected due to limited statistics. As such, we do not provide correlations of P_{cav} vs. L_{cool} , P_{sh} vs. L_{cool} or P_{tot} vs. L_{cool} , limiting ourselves to discussing general trends. Enlarging the sample to

allow a deeper, statistically consistent comparison is a future perspective of this work.

5.3 A first look at feedback from FR 0 radio galaxies: the case of Abell 795

After having explored how the “classical” FR I and FR II radio galaxies show different behaviours in cool core cluster environments, we now turn to a newly discovered population of radio galaxies, namely those of the FR 0 class. As noted in the Introduction (§1.3.1), FR 0s are characterized by a lack of extended jets on kpc scales. Such compact morphology has been suggested to derive either from an intrinsic jet weakness, or from an hostile environment limiting the growth of the radio galaxy. While the first explanation is favoured by studies of jet bulk speed in these sources (e.g., Giovannini et al. 2023), the effect of the environment is still under investigation. Additionally, the galactic-scale jets of FR 0s are expected to contribute to quenching star formation in their host galaxies (Baldi, 2023); however, the feedback properties of FR 0 radio galaxies are virtually unexplored.

In this section we focus on a *Chandra* observation of the galaxy cluster Abell 795 (hereafter A795), whose central galaxy J092405.30+14 is a FR 0 radio galaxy (Torresi et al., 2018). Thus, this system offers the opportunity to investigate the possible link between the compact radio morphology of a FR 0 and the thermodynamics of its environment.

Radio observations of the BCG J092405.30+14 in the GHz band disclosed its compact radio morphology: it is unresolved in the FIRST images, thus implying an upper limit on its size at 1.4 GHz of 5'' (~ 12 kpc); Hogan et al. (2015a) did not resolve the source at 4.8 GHz with the VLA in configuration C (resolution of 3.4'' ~ 8.3 kpc), but resolved it at 8.4 GHz with the VLA in configuration A (resolution of 0.2'' ~ 0.48 kpc). This source has also been observed with MERLIN at 5 GHz (sub-arcsec resolution), which revealed an elongation in the north-east direction with a largest linear size of 0.30'' (~ 0.73 kpc), suggesting a core-jet morphology (Kunert-Bajraszewska et al., 2010). On the contrary, few information are available in the literature on the host cluster A795, located at a redshift of $z = 0.1374$. Rines et al. (2013) investigated the spectroscopic redshifts of the cluster’s galaxies, and classified this system as morphologically disturbed; also, A795 is included in the clusters samples of Mantz et al. (2015) and Zhang et al. (2016), who confirmed the globally unrelaxed state of the ICM. However, no specific information on this cluster cooling properties and ICM detailed conditions are available.

5.3.1 *Chandra* observation and data reduction

A795 was observed in 2010 by the *Chandra* X-ray telescope (ObsID 11734) for a total exposure time of 30 ks. Data reprocessing has been performed with CIAO 4.12 and CALDB 4.9.0: with the `chandra_repro` script we performed the bad pixel removal and the instrumental error correction, and with the `deflare` scripts we removed the background flares. The final exposure time is 29.7 ks. The CIAO tool `wavdetect` has been used to identify point sources in the event file, which we compared to optical reference objects (catalogue USNO-A2.0) to verify that the astrometry of the data is accurate. At last, the `blanksky` background file corresponding to ObsID 11734 was reprojected to match the observation, and scaled by the hard energy (9 – 12 keV) count rate of the image.

Spectral fitting was performed in the energy range 0.5 – 7 keV with `Xspec - v. 12.10`; background spectra were extracted from the `blanksky` event file in the region of interest, and subtracted before the fitting procedure. For every thermal model and photoelectric absorption model employed in this work, we used the table of abundances of Asplund et al. (2009). Redshift has always been fixed to the value of the cluster ($z = 0.1374$, Rines et al. 2013), and the galactic absorption was fixed at $N_{\text{H}} = 2.89 \times 10^{20} \text{ cm}^{-2}$ (HI4PI Collaboration et al., 2016).

5.3.2 X-ray morphology and spectral properties of the ICM in A795

Large scale properties of the ICM

Fig. 5.3 (panel *a*) shows a background-subtracted, exposure-corrected 0.5 – 2 keV *Chandra* image of A795, smoothed with a Gaussian of kernel size 3". An inspection of the central regions reveals the presence of an offset of 7.3" (~ 17.7 kpc) between the peak of the X-ray ICM emission (RA, DEC = 09:24:05.8, +14:10:23.3) and the position of the central AGN (RA, DEC = 09:24:05.3, +14:10:21.5). We also note that the ICM is arranged in a spiral-like shape, with surface brightness edges visible on the east side and west side of the core. We extracted a surface brightness profile from concentric circular annuli of bin size of 2", centered on the X-ray peak and extending to 168" (~ 405 kpc) from the center. The single β -model (Cavaliere and Fusco-Femiano, 1976) provides the best descriptions of the resulting profile (fitted in Proffit; see Fig. 5.3, panel *b*, with best-fit parameters of slope $\beta = 0.47 \pm 0.01$, core radius $r_c = 33.5 \pm 1.5$ kpc, and normalization of $1.28^{+0.08}_{-0.07} \times 10^{-3}$ cts s $^{-1}$ arcmin $^{-2}$). We found the addition of a second β -model not to be statistically significant.

We note that the observed offset between the X-ray peak and the BCG hints at the presence of dynamical disturbances in the ICM. Indeed, the prevalence of a single β -model for the surface brightness profile suggests that A795 might not be a strong cool core cluster, which typically need a second β -model component to fit the surface brightness (e.g., Mohr et al. 1999). Moreover, the undulating pattern of the residuals from the β -model fit (Fig. 5.3) might be the outcome of azimuthally averaging surface brightness discontinuities in the ICM. To better highlight possible substructures, we produced a residual image (shown in Fig. 5.3, panel *c*) by subtracting the best-fit surface brightness model from the data. This image unveils the presence of a large scale spiral in the ICM: starting from the cluster's center it bends to south-east following the surface brightness edges, then proceeds to north-west reaching a distance of ≈ 180 kpc from the X-ray peak.

Spiral geometries of the X-ray emission are common in sloshing galaxy clusters, and are usually associated with cold fronts. The visual inspection of the residual image highlights the two opposite surface brightness edges, east and west of the center, already noted in the original *Chandra* image. The temperature distribution of the ICM can help in classifying the observed edges in surface brightness: cold fronts are expected to show lower temperature and higher density in the downstream region of the discontinuity. We produced a temperature map of the ICM in A795 by binning the *Chandra* image with the CONTBIN algorithm (Sanders, 2006) in order to reach a signal-to-noise ratio of 30. The ICM spectrum of each region was fitted with an absorbed thermal model (tbabs*apec). The resulting temperature map (Fig. 5.3, panel *c*) shows that the coolest gas in A795 nicely follows the spiral shape of the ICM, suggesting that the two edges could be cold fronts.

To measure the thermodynamical properties of each jump and confirm their cold front nature, we extracted spectra from three sectors: the first following the discontinuity, the second enclosing the region outside the edge, and the third extended to the edge of the chip (to account for the ICM along the line of sight). The resulting spectra were fitted with a deprojected, absorbed thermal model (project*tbabs*apec). We found that the inner side of each front has a lower temperature and a higher density than the outer side, specifically:

- For the East front, we measured a temperature gradient $T^{\text{out}}/T^{\text{in}} = 2.07 \pm 0.53$, a density jump $n_e^{\text{in}}/n_e^{\text{out}} = 2.67 \pm 0.10$, and a pressure ratio $p^{\text{in}}/p^{\text{out}} = 1.29 \pm 0.41$ ($\chi^2/\text{D.o.f.} = 344.8/388$).
- For the West front, we measured a temperature gradient $T^{\text{out}}/T^{\text{in}} = 1.61 \pm 0.46$, a density jump $n_e^{\text{in}}/n_e^{\text{out}} = 2.66 \pm 0.13$, and a pressure ratio $p^{\text{in}}/p^{\text{out}} = 1.63 \pm 0.65$ ($\chi^2/\text{D.o.f.} = 364.1/377$).

These results confirm that the discontinuities are cold fronts. Thus, our analysis unveiled that A795 is a disturbed cluster, in which the coldest gas phase has been displaced from the center and is now oscillating over the cluster scale.

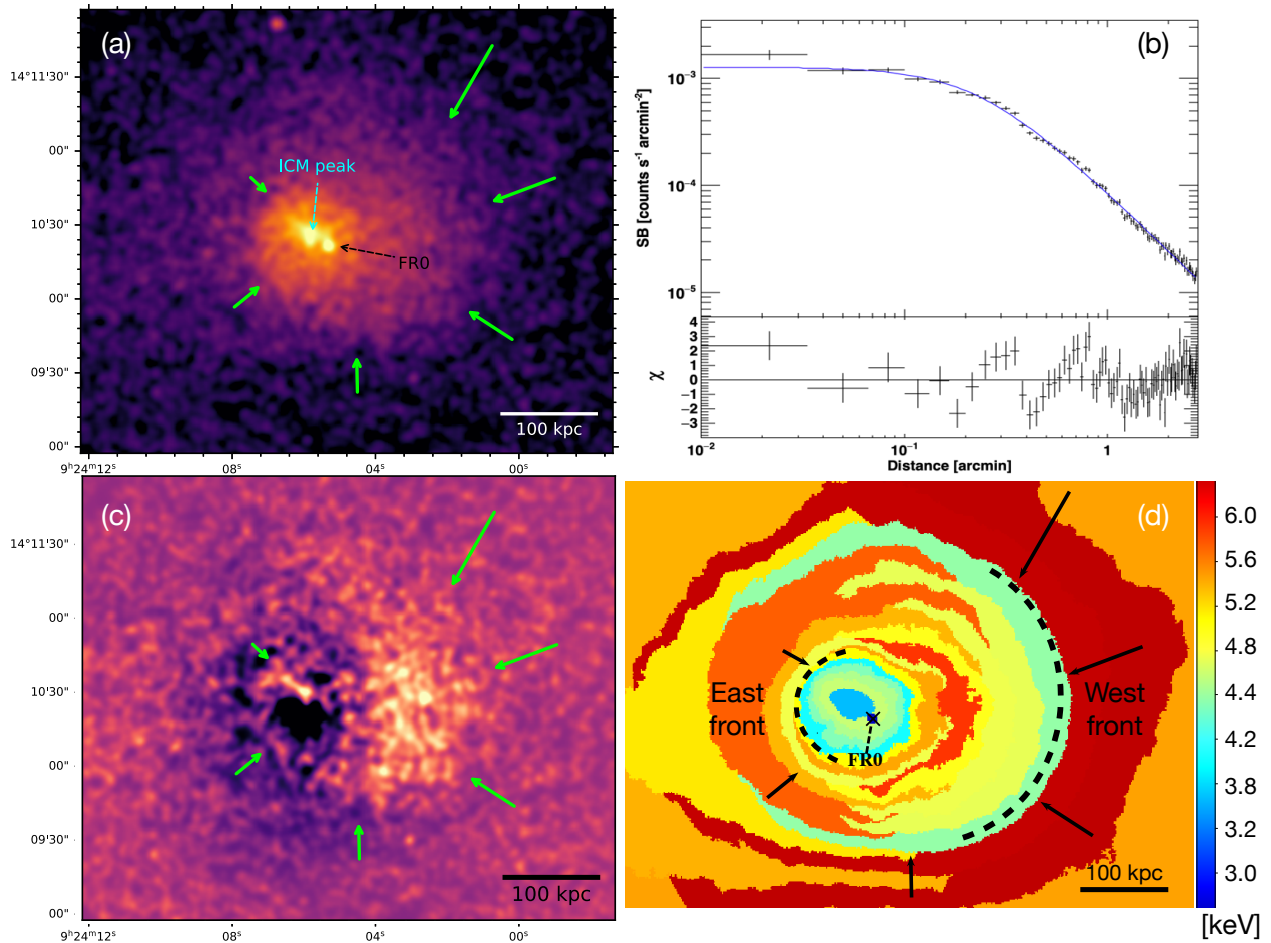


FIGURE 5.3: *Panel a*: *Chandra* image (0.5 – 2 keV) of A795, Gaussian-smoothed with kernel radius of 3". The ICM peak and the position of the FR 0 in the BCG are indicated. *Panel b*: 0.5 – 2 keV surface brightness profile (black points) of A795, fitted with a β -model (blue line). The lower panel shows the residuals from the best-fit model. *Panel c*: 2D β -model subtracted *Chandra* image over the same region of panel *a*. *Panel d*: Temperature map of A795; relative errors on temperature are of $\approx 25\%$. In the panels, the arrows (green in *a* and *c*, black in *d*) highlight the spiral geometry of the ICM.

The efficiency of ICM cooling in A795

To investigate the properties of the ICM at different distances from the center, we produced radial profiles of thermodynamic variables by extracting the spectra of six concentric regions which contained at least 4000 net counts centered on the X-ray peak and extending to ≈ 380 kpc from the cluster center. We fitted the spectra with a `projct*tbabs*apec` model, where the first component performs a 3-D to 2-D projection of ellipsoidal shells onto elliptical annuli. Radial plots of the best-fit temperature and electron density are shown in Fig. 5.4 (panels *a* and *b*). To obtain a higher-resolution density profile, the surface brightness radial profile shown in Fig. 5.3 was deprojected in Proffit (Eckert et al., 2012). As visible in Fig. 5.4 (panel *b*), the two methods of deriving the electron density give consistent results. Then, the best-fit spectral temperature profile was interpolated on the grid of the density profile. The combination of temperature and density is necessary to obtain the cooling time of the ICM, using Eq. 1.11.

The cooling time profile for A795 is presented in Fig. 5.4. The generally decreasing t_{cool} towards the central regions of the cluster is indicative of a cool core system. Hudson et al. (2010) argued that strong cool core clusters display $t_{\text{cool}}[\text{Gyr}] < 1$ in the inner tens of kpc. The cooling time of A795 remains higher than 1 Gyr, which provides a evidence to classify A795 as a weak cool core cluster. However, we note that the central radial bin ($0 \leq r[\text{kpc}] \leq 5$) has a cooling time of $1.06^{+0.28}_{-0.26}$ Gyr,

and its surface brightness is not consistent with the global single β -model profile of Fig. 5.3; within errors only the X-ray peak might be at the boundary between strong and weak cool core systems.

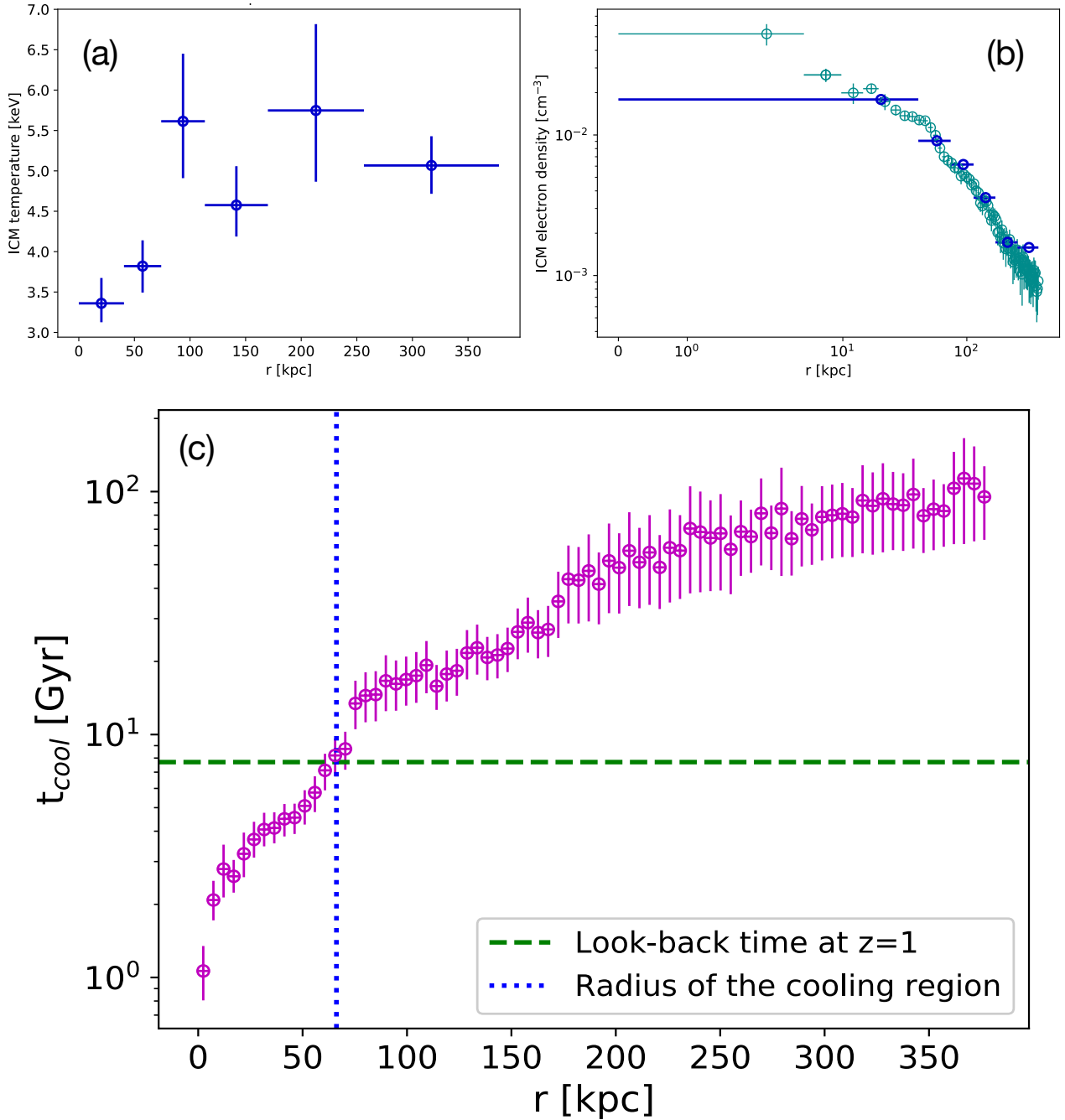


FIGURE 5.4: Radial profiles of temperature (panel *a*), electron density (panel *b*), and cooling time (panel *c*) for A795. The turquoise points in panel *b* represent the density profile obtained by deprojecting the surface brightness profile, while the blue points show the comparison with the spectroscopically-derived density. The cooling time profile of A795 in panel *c* has been obtained by interpolating the temperature profile on the grid of the high-resolution density profile, and then combining the two quantities. The green, dashed horizontal line corresponds to $t_{\text{cool}} = 7.7$ Gyr; the blue, dotted vertical line at $r = 66.2$ kpc indicates the cooling radius. The cooling time profile is consistent with the central t_{cool} reported in Zhang et al. (2016).

Our aim is to evaluate the strength of radiative losses due to ICM cooling in A795. To this end, we derived the cooling radius of A795, r_{cool} , and the enclosed bolometric X-ray luminosity, L_{cool} .

TABLE 5.2: Spectral analysis of the ICM around J092405.30+14: (1) considered region (see Fig. 5.5); (2) temperature; (3) metallicity; (4) normalization of the spectrum; (5) $\chi^2/\text{degrees of freedom}$.

Region	kT keV	Z Z_{\odot}	$norm$	$\chi^2/\text{D.o.f.}$
Annulus	$3.81^{+0.23}_{-0.23}$	$0.75^{+0.20}_{-0.18}$	$5.26^{+0.26}_{-0.26}$	77.1/70
NE-sector	$3.54^{+0.41}_{-0.33}$	$0.97^{+0.51}_{-0.38}$	$1.74^{+0.19}_{-0.19}$	30.0/26
SW-sector	$4.30^{+0.30}_{-0.29}$	$0.86^{+0.30}_{-0.26}$	$3.34^{+0.21}_{-0.21}$	45.7/49

We used the typical definition of cooling radius, that is the distance from the center at which t_{cool} is less than 7.7 Gyr (e.g., Birzan et al. 2004). For A795 we measured a cooling radius of $r_{\text{cool}} = 27.3 \pm 1.3 \text{ arcsec} = 66.2 \pm 3.2 \text{ kpc}$ (see Fig. 5.4).

To estimate the radiative losses of the ICM in the region where cooling is efficient, we performed a spectral analysis of the emission inside the cooling region. We measured the deprojected bolometric luminosity of the cooling region by extracting the spectrum of two concentric annuli, the first being the cooling region and the second extending from r_{cool} to the edge of the *Chandra* field of view. Assuming that the emission from the cooling region can be described by a single thermal model, we fitted the spectra with a `projct*tbabs*apec` model and computed the 0.1-100 keV luminosity of the `apec` component within r_{cool} . We measure a cooling luminosity of $L_{\text{cool}} = (1.07 \pm 0.06) \times 10^{44} \text{ erg s}^{-1}$. We note that the addition of a cooling model component (`mkcflow`) did not improve the results of the fitting procedure.

Properties of the ICM around the central FR 0

The analysis shown in the previous paragraphs revealed that the hot gas of A795 is dynamically unrelaxed. *What is the impact of these perturbations on the central radio galaxy? Is the cluster environment “hostile” for the growth of this FR 0?* To investigate the properties of the ambient gas around the FR 0, an annulus of inner radius 2" and outer radius 12", centered on the BCG has been used to extract the spectrum of the ICM surrounding J092405.30+14 (see Fig. 5.5, left panel). We extracted the background spectrum from the blanksky event file using the same region, and fitted the data in the 0.5 - 7 keV with a `tbabs*apec` model. Results are presented in Tab. 5.2.

Considering the sloshing motion of the ICM and the geometry of the cold gas spiral, we expected that the north-east side of the AGN, in the proximity of the X-ray peak, could consist of lower temperature gas w.r.t. the south-west side. We splitted the annulus in two sectors, the first one including the X-ray peak, and the second one the remaining portion of the region (NE and SW sectors in Fig. 5.5). By fitting the spectra of the two regions with a thermal model (Tab. 5.2 second and third row), we verified that the ICM around the FR 0 is subject to the temperature gradients induced by sloshing. Indeed, the north-east sector has a temperature that is significantly lower than that of the south-west sector (within 1σ uncertainties), and lower than the average temperature (but consistent within 1σ uncertainties).

As proposed by Baldi et al. (2015), a high density gas might be capable of decelerating and disrupting the radio jets. Here we discuss both the density of the surrounding medium, and the effects of sloshing-induced turbulence on the jet stability. If the cluster’s gas exhibited extreme thermodynamical conditions (i.e. peculiar with respect to those of the ICM surrounding extended FR Is in BCGs) we could infer that the environment of J092405.30+14 is interfering with the jet propagation.

1. **The density of the ICM:** The electron density of the ICM around J092405.30+14 is $2.14 \times 10^{-2} \text{ cm}^{-3}$ (from the radial spectral analysis of §5.3.2). This value is in line with typical ICM densities around FR Is at the center of galaxy clusters ($\approx 10^{-3} - 10^{-1} \text{ cm}^{-3}$, e.g., Haarsma et al. 2010; McDonald et al. 2017): this suggests that if FR 0s’ compactness is due to the frustration and disruption of the jet on small scales ($\approx 1 - 15 \text{ kpc}$), the local density of the ICM is not responsible for it, at least in A795.

2. **The effect of sloshing:** We found that there is a multi-temperature medium around J092405.30+14 with an asymmetrical distribution, suggesting that even the central regions ($r \lesssim 30$ kpc) are affected by the large scale oscillation. Therefore, we consider the possibility that the ICM turbulence is affecting the stability of radio jets. In clusters and groups displaying sloshing motions of the gas there are FR Is whose jets have not been disrupted (e.g., the FR I at the center of the galaxy group 3C449, Lal et al. 2013; the radio galaxy in the NGC 1550 group, Kolokythas et al. 2020). Thus, we argue that unless there are intrinsic differences between the jets of FR 0s and FR Is, sloshing alone is not capable of preventing their propagation: only if the jet presents a low Lorentz factor and is launched by a slowly spinning black hole, then turbulence induced by the gas motion might quench the weak jet as soon as it enters the ICM (e.g., Baldi et al. 2019a).
3. **Warm ionized gas:** The ICM is not the only turbulent gas phase found in the proximity of J092405.30+14: Hamer et al. (2016) studied the warm ionized gas dynamics in the cores of 73 galaxy clusters, among which A795 is present. They found that a roughly spherical cloud of H α -emitting gas with an extent of ~ 11 kpc surrounds the BCG of A795; the high FWHM of the H α line (400 – 800 km/s) might suggest that we are seeing a system of H α clouds along the line of sight, with high-velocity random motions. It is possible that the warm gas around J092405.30+14 might be slowing the jet expansion in the outer medium. To verify this hypothesis would require to model the clumpiness of these gas clouds, so that the jet frustration could also be compatible with the lack of X-ray absorbing cold gas (Torresini et al., 2018) in the central engine of the BCG. If future observations of A795 will detect molecular gas clouds, co-spatial with the warm phase, it might become possible to put stronger constraints on the jet frustration. Once again, however, it should be noted that H α -emitting clouds have also been detected by Hamer et al. (2016) around FR Is at the center of galaxy clusters: this suggests that the jet has to be intrinsically weak to get easily disrupted by the warm and/or cold gas.
As a note of caution, we point out that the H α line broadening might be caused by non-gravitational kinematics, for example outflow motions (see e.g., Kang et al. 2017): the warm gas velocity dispersion is a factor of $\gtrsim 2$ greater than the stellar velocity dispersion ($\sigma_* = 261 \pm 9$ km s $^{-1}$, Alam et al. 2015), implying that the hydrogen gas might not only be tracing the gravitational potential of the host galaxy, but could also be influenced by an additional non-virial component.
4. **The combined effect of sloshing and warm gas:** We argue that even the co-existence of sloshing and of the H α nebula is likely not able to explain the compactness of the radio source. Indeed, it is possible to find examples of galaxy clusters displaying sloshing motions with H α clouds in their cores which still host extended FR Is at their center (e.g., A3581, Canning et al. 2013; A2495, Pasini et al. 2019; A1668, Pasini et al. 2021).

The overall considerations point to the conclusion that the reason(s) behind FR 0s' radio compactness has to be searched primarily in the intrinsic properties of the jet and/or BH spin. The environment can still play a role, although not the major one. In fact, our X-ray study of the environment of J092405.30+14 has revealed a complex, multi-phase and possibly turbulent ambient, but in line with typical properties of the ICM surrounding extended radio galaxies. This might highlight the critical role of the jet stability, and – in turn – of the black hole spin: unless the central engine of this FR 0 has peculiar parameters that lead to the formation of unstable jets, the environment alone cannot explain the radio compactness.

Evidences of AGN feedback from the FR 0: X-ray cavities in the ICM

The clearest imprints of feedback in clusters are, as noted in the Introduction (§1.2.1), shocks and X-ray cavities. These are however historically associated with the extended lobes of FR Is and

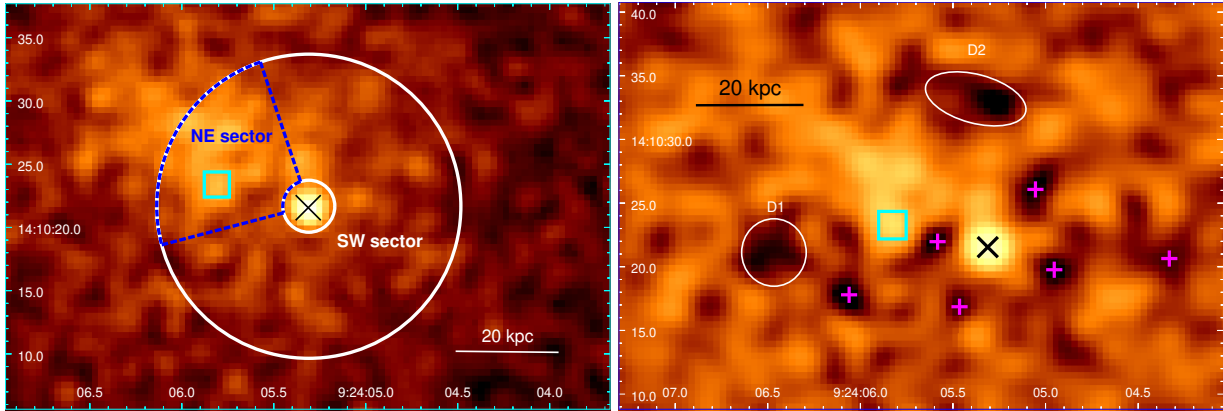


FIGURE 5.5: Zoom-in in the central regions of A795. *Left panel*: 0.5-7 keV image of A795, Gaussian-smoothed with a kernel radius of $1.5''$; the regions used to study the multi-phase gas around J092405.30+14 are over-plotted: the white annulus is the extraction region for the ambient gas spectrum; the blue dashed sector shows the NE sector, while the SW sector is composed by the remaining portion of the annulus. The cyan box and the black cross denote the positions of the X-ray peak and the BCG, respectively. *Right panel*: 0.5 – 2 keV unsharp mask image of A795, obtained by subtracting two images smoothed with a Gaussian of $1''$ and $5''$ axes, respectively; the positions of the AGN (black cross), of the X-ray peak (cyan box), and of the two depressions (white ellipses) are marked. The pink plus signs are examples of the depressions with a negligible deviations (2-8%) w.r.t. the best β -model.

FR IIs. The presence of an FR 0 at the center of this cluster offers the opportunity to investigate the following question: *Are FR 0 radio galaxies able to excavate X-ray cavities in the ICM?*

To address this topic, we inspected the 0.5 – 2 keV *Chandra* image searching for depressions in surface brightness, and we also used the unsharp masking technique to enhance substructures in the X-ray image. After testing several smoothing combinations, by subtracting two images of the cluster (smoothed with a Gaussian of $1''$ and $5''$ axes, respectively) we obtain the unsharp mask image that better emphasizes substructures in the ICM (Fig. 5.5, right panel). By inspecting the result, we identify two depressions (named D1 and D2) close to the BCG and symmetric with respect to the X-ray peak.

We note that the other depressions visible in Fig. 5.5 (marked with pink plus signs) do not represent a significant deviation w.r.t. the best β -model fit (between 2% – 8%, with a significance of 1.04σ) so we do not include them in our analysis. On the contrary, D1 and D2 show a deficit of $\approx 34\%$ and $\approx 21\%$ respectively, which is typical of X-ray cavities (e.g., McNamara and Nulsen 2007), at a significance of $\sim 2.4\sigma$. Following the classification of Hlavacek-Larrondo et al. (2015), we refer to D1 and D2 as *putative* cavities, given their $< 3\sigma$ significance.

Our aim is to measure the cavity power $P_{\text{cav}} = 4pV/t_{\text{age}}$, where p is the pressure of the ICM around each cavity (estimated from the radial spectral analysis, §5.3.2), V is the cavity volume and t_{age} is the age of the cavity system. We assume that the 3D shape of each cavity is that of a prolate ellipsoid and compute their volume as $V = (4\pi/3)R_m^2 R_M$.

The ages of the two cavities have been derived following two approaches:

1. Assuming that D1 and D2 are moving at the sound speed c_s of the ICM (with $c_s = 938 \text{ km s}^{-1}$ at the distance of the cavities from the center, from Eq. 1.5), we obtain cavity ages of 42.4 ± 2.0 Myr for D1 and 28.8 ± 1.3 Myr for D2.
2. Alternatively, if the cavities are rising buoyantly in the cluster's atmosphere, their age can be computed using Eq. 1.16. We obtain $t_{\text{age,D1}} = 83.2 \pm 12.5$ Myr and $t_{\text{age,D2}} = 53.7 \pm 8.1$ Myr.

The difference between the two methods reflects the uncertainty related to the ages of the depressions; therefore, for the following computation we use the average between the two estimate as our best guess for t_{age} , that is 62.8 ± 20.4 Myr for D1 and 41.3 ± 12.5 Myr for D2. Thus, we measure a

TABLE 5.3: Properties of the putative cavities D1 and D2 in A795: (1) name of the depression; (2) semi-major axis; (3) semi-minor axis; (4) distance from the BCG; (5) work done to create the cavity; (6) ages computed with the sound speed (first entry) and the buoyant time (second entry); (7) cavity power $P_{\text{cav}} = pV / \langle t_{\text{age}} \rangle$.

	R_M	R_m	D	pV	t_{age}	P_{cav}
	kpc	kpc	kpc	10^{58}erg	Myr	10^{43}erg s^{-1}
D1	6.4	6.2	40.6	2.0 ± 0.5	42.4 ± 2.0 83.2 ± 12.5	1.0 ± 0.6
D2	9.9	4.6	27.7	1.4 ± 0.2	28.8 ± 1.3 53.7 ± 8.1	1.2 ± 0.5

cavity power of $(1.0 \pm 0.6) \times 10^{43}\text{erg s}^{-1}$ for D1 and $(1.2 \pm 0.5) \times 10^{43}\text{erg s}^{-1}$ for D2. We summarize the properties of the two depressions in Tab. 5.3.

We point out that D1 and D2 are not symmetric with respect to the AGN, but they are offset toward north-east; the radio lobes inflated by bipolar jets are expected to be approximately on opposite sides of the nucleus. As AGN-inflated radio bubbles can be subject to gas motions and turbulence in the central regions of galaxy clusters (e.g., Morsony et al. 2010), we could speculate (similarly to Pasini et al. 2019 for the older generation of cavities in A2495) that sloshing motions of the ICM have influenced the cavity system's direction of motion, leading to the observed asymmetry. Indeed, the position of D1 and D2 agrees with the direction of motion of the ICM nearby the center (towards north-east, see Fig. 5.5). Additionally, the distance of the two cavities from J092405.30+14 is compatible with sloshing motions: we assume that the ICM sloshes with a Mach number in the range $\mathcal{M}^2 = v_{\text{slosh}}^2 / c_s^2 = 0.3\text{-}0.5$ (e.g., Ascasibar and Markevitch 2006), and proceed to compute the expected distance of D1 and D2 from the AGN as $v_{\text{slosh}} \times t_{\text{age}}$; we obtain $\sim 33 - 43$ kpc for D1 and $\sim 22 - 28$ kpc for D2, to compare with a measured distance of 40.6 kpc for D1 and 27.7 kpc for D2. Far from establishing a causal link between the position of the depressions and the turbulence of the ICM, our result might at least suggest that a sloshing-influenced motion of the cavities is not ruled out. Therefore, we may speculate that the cavities have been inflated in the past in the proximity of the FR 0 ($\sim 1 - 10$ kpc from the core). Later, the gas turbulent motion could have dragged the cavities away toward northeast (~ 30 kpc from the core).

5.3.3 The heating cooling balance in a galaxy cluster with a central FR 0

As noted in the Introduction (§1.2.1) and as shown in §5.2, a strong evidence for the self-regulated feedback loop is that comparisons between the mechanical jet power and the radiative losses of the ICM show a scaling between the two quantities (e.g., McNamara and Nulsen 2007; McNamara and Nulsen 2012). The total mechanical power of the cavities in A795 is $P_{\text{cav}} = 2.2 \pm 0.8 \times 10^{43}\text{erg s}^{-1}$, while the X-ray luminosity of the cooling region is $L_{\text{cool}} = 1.07 \pm 0.06 \times 10^{44}\text{erg s}^{-1}$. By comparing the measurements for A795 with those of other clusters (we consider the samples of Rafferty et al. 2006; Hlavacek-Larrondo et al. 2015) we can verify if A795 follows the typical distribution of P_{cav} versus L_{cool} . As shown in Fig. 5.6, the putative system of cavities in A795 follows the distribution of the other galaxy cluster samples, with the cavities being slightly under-powered with respect to the ICM radiative losses. This indicates that if the two depressions are real cavities, their power is almost enough to counterbalance radiative cooling. It is also possible that FR 0s need, on average, $16pV$ of enthalpy to offset cooling; a large sample of FR 0s at the center of clusters would be needed to test this idea.

We note that it is unclear whether the jets of FR 0s are able to expand into the external medium and excavate cavities in the ICM. The FIRST observation of J092405.30+14 did not detect 1.4 GHz radio emission corresponding to the two depressions. The flux difference between the NVSS (114 ± 3.4 mJy, with a resolution of $45'' \sim 110$ kpc) and the FIRST (108.25 ± 0.15 mJy, with a resolution of $5'' \sim 12$ kpc) observations at 1.4 GHz of A795 is 5.7 ± 3.4 mJy: this could be indicative of the presence of

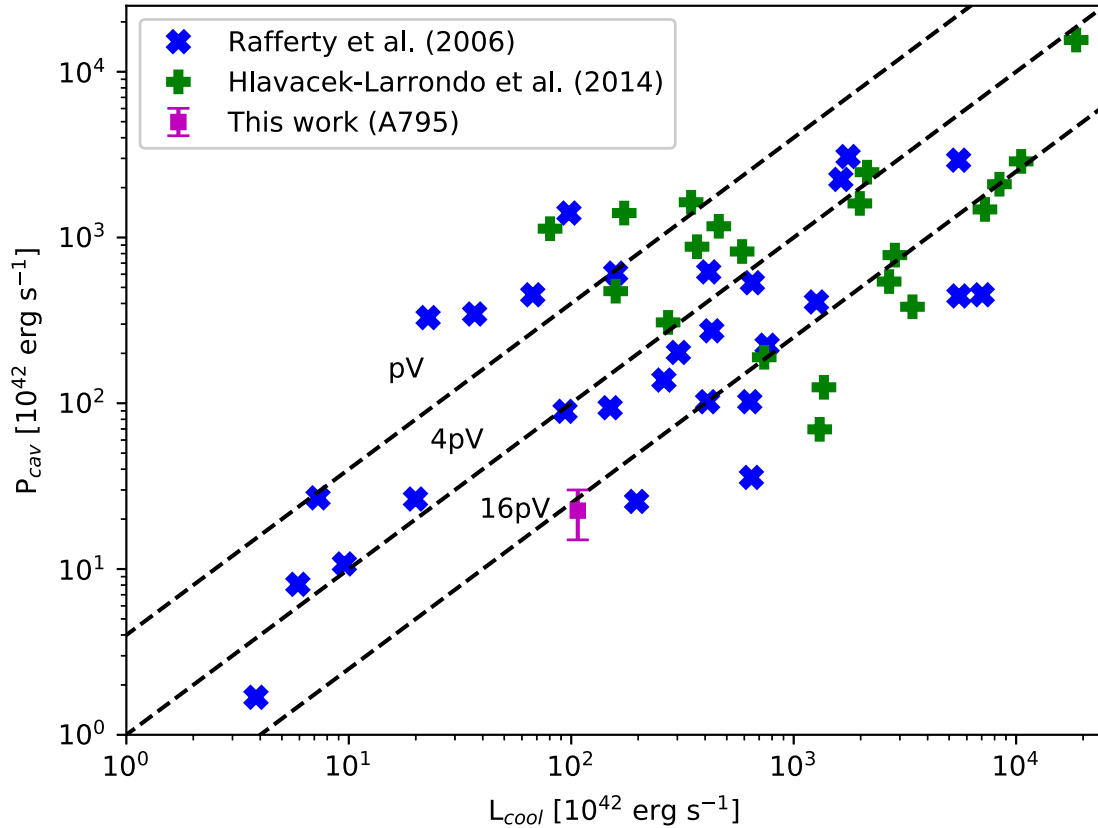


FIGURE 5.6: Cavity power versus X-ray cooling luminosity of the ICM. Different symbols denote systems in different samples; the magenta square represents the cavity system of A795, with the error bars expressing the uncertainty in cavity power due to the different age estimates.

extended components, but given the low angular resolution of the NVSS we do not have any information on their morphology.

It is also possible that the structures are filled with an aged electron population, emitting at lower frequencies. In fact, Capetti et al. (2020) observed three FR 0s at 150 MHz which show a head-tail structure extending for ~ 50 kpc, although none of these sources was classified as extended in the FIRST images at 1.4 GHz. Therefore, at MHz frequencies FR 0s could reach sizes comparable to the distance between J092405.30+14 and the two depressions we detected (the average distance of D1 and D2 from the AGN is ~ 34 kpc). At present, no low frequency, arcsecond-resolution radio observations of A795 are present.

As a sanity check, we verify whether the 5 GHz luminosity of J092405.30+14 ($L_{5\text{GHz}} = 4.52 \pm 0.05 \times 10^{40} \text{ erg s}^{-1}$, Kunert-Bajraszewska et al. 2010) could be compatible with the measured cavity power. By studying a sample of sub-Eddington AGN, Merloni and Heinz (2007) derived the following relations:

$$\log P_{\text{cav}} = (0.54 \pm 0.09) \log L_{0,5\text{GHz}} + 22.1^{+3.5}_{-3.5} \quad (5.2)$$

$$\log P_{\text{cav}} = (0.81 \pm 0.11) \log L_{i,5\text{GHz}} + 11.9^{+4.1}_{-4.4} \quad (5.3)$$

where P_{cav} has been estimated from the enthalpy of the X-ray cavities and by modelling the radio emission of jets, while $L_{0,5\text{GHz}}$ and $L_{i,5\text{GHz}}$ are the *observed* (not corrected for beaming) and *intrinsic* 5 GHz luminosities, respectively. As we have no information on the beaming factor of J092405.30+14,

we used both equations to compute P_{cav} ; from Eq. 5.2 we find $P_{\text{cav}} = (1.1 \pm 0.5) \times 10^{44} \text{ erg s}^{-1}$. We derived the intrinsic 5 GHz luminosity with the *fundamental plane of black hole activity* (Merloni et al., 2003), by combining the X-ray luminosity of the FR 0 with the mass of the central SMBH (from Torresi et al. 2018). We obtained $L_{i,5\text{GHz}} = (1.6 \pm 0.8) \times 10^{39} \text{ erg s}^{-1}$; Eq. 5.3 gives $P_{\text{cav}} = (4.5 \pm 2.3) \times 10^{43} \text{ erg s}^{-1}$. Both estimates are consistent with the measured power $P_{\text{cav}} = 2.2 \pm 0.8 \times 10^{43} \text{ erg s}^{-1}$ of D1 and D2. This confirms that the radio emission of the FR 0 is compatible with our estimate of the cavity power based on *Chandra* data.

Finally, we check whether the cavity system of A795 follows the trends $P_{\text{cav}} - L_{\text{radio}}$ (total radio power between 10 MHz - 10 GHz) and $P_{\text{cav}} - P_{1.4\text{GHz}}$ (monochromatic radio power at 1.4 GHz) reported in O’Sullivan et al. (2011). We use the NVSS observation of A795 ($114 \pm 3.4 \text{ mJy}$ at 1.4 GHz) to estimate the monochromatic and total radio power associated to the AGN: assuming a spectral index $\alpha = 1$ we obtain $L_{\text{radio}} = 1.1 \pm 0.1 \times 10^{41} \text{ erg s}^{-1}$ and $P_{1.4\text{GHz}} = 5.7 \pm 0.2 \times 10^{24} \text{ W Hz}^{-1}$. With a cavity power $P_{\text{cav}} = 2.2 \pm 0.8 \times 10^{43} \text{ erg s}^{-1}$ we find that the cavity system of A795 lies within the distributions of cavity systems of O’Sullivan et al. (2011). Given these results, we conclude that the scenario where J092405.30+14 has a sufficient power to inflate the two depressions is energetically consistent.

5.4 Summary and conclusions

In this Chapter we explored the different feedback output of radio galaxies. We first considered a sample of galaxy groups, galaxy clusters and elliptical galaxies where both shocks and X-ray cavities were detected. By comparing the shock and cavity power of classical FR Is and FR IIs sources within these systems with the radiative losses of their hot atmospheres, we investigated the different response to cooling provided by the two classes of radio galaxies. Here are our main conclusions:

- By evaluating shocks and cavity power (P_{sh} and P_{cav}) versus cooling (L_{cool}) for the 15 systems in our sample, we verified the already known scaling of P_{cav} vs. L_{cool} . Additionally, we demonstrated for the first time that such scaling exists also for P_{sh} vs. L_{cool} . This indicates that the whole feedback output of cluster-central AGN ($P_{\text{tot}} [= P_{\text{sh}} + P_{\text{cav}}]$) is set in response to the strength of ICM cooling.
- We noticed that while RBS 797 has the largest mechanical power and cooling luminosity of the sample, it is not the object with the most “extreme” feedback. In particular, we observed that systems with FR I radio galaxies at their center (as RBS 797) have feedback ratios $P_{\text{tot}}/L_{\text{cool}}$ within a few tens, while systems with central FR II AGN have total mechanical power that can exceed by more than two orders of magnitude the cooling luminosity of the surrounding atmosphere. This difference becomes more evident when massive systems (clusters) are distinguished from smaller systems (groups and elliptical galaxies).
- Interestingly, we found that the average central entropy of systems hosting FR Is ($9 \pm 8 \text{ keV cm}^2$) is consistent with that of systems hosting FR IIs ($15 \pm 8 \text{ keV cm}^2$). This result suggests that differences of orders of magnitude in feedback output do not over-heat the central gas. In turn, this supports the idea that the thermodynamic properties of the ICM are resilient to episodic and powerful outbursts.

Then, we focused on providing a first view at feedback from radio-compact FR 0 radio galaxies. We analyzed *Chandra* observations of the galaxy cluster A795, that hosts a FR 0 in its BCG. Here we summarize our results.

- From the spatially-resolved spectral analysis of the ICM we deduced that A795 is a weakly CC cluster, with a cooling time $< 7.7 \text{ Gyr}$ inside $r_{\text{cool}} = 66 \pm 3 \text{ kpc}$. The gas in this cluster

is sloshing, as evidenced from the spiral shape of the ICM, the two opposite cold fronts, and explains the offset of ~ 17 kpc between the X-ray peak and the BCG.

- By comparing the temperature, density, and dynamics of the ICM surrounding the FR 0 with those of ICM around typical FR Is in BCGs, we concluded that the environment alone cannot explain the observed radio size of this class of sources, and that an intrinsic jet weakness is likely necessary.
- We identified two putative cavities at an average distance of ~ 34 kpc from the central AGN: by measuring their power ($P_{\text{cav}} = 2.2 \pm 0.8 \times 10^{43} \text{ erg s}^{-1}$) and comparing it to the bolometric luminosity within the cooling region ($L_{\text{cool}} = (1.07 \pm 0.06) \times 10^{44} \text{ erg s}^{-1}$), we found that these cavities might be able to offset and reduce the cooling efficiency in A795. If confirmed by future studies, this could be the first evidence that FR 0s can contribute to the thermodynamic regulation of their surroundings.

In the future, we plan to enlarge the sample of ellipticals, galaxy groups, and galaxy clusters with known shocks and X-ray cavities to allow a deeper comparison between gas cooling and feedback response. We also plan to test the dichotomy in feedback ratio between FR Is and FR IIs (and possibly intermediate classes) using X-ray cavity power only, which will allow us to consider a larger number of systems.

Ultimately, we note that, besides A795, other clusters of galaxies are expected to host FR 0-like radio galaxies in their BCGs. Therefore, a comparison with the environmental properties of other FR 0s in clusters, and between cluster- and field- FR 0s will be useful to confirm our results and to better characterize the behavior of this peculiar class of radio sources. Assembling a sample of cluster-central FR 0s with *Chandra* observations is a natural continuation of this project. Moreover, deeper *Chandra* data of A795 would be critical to confirm the detection of the X-ray cavities. In the future we will also present new radio observations at different frequencies and resolution (a total 8h of JVLA time, PI: Ubertyosi, awarded and observed) to better map the radio morphology of the FR 0 in A795.

Chapter 6

Jet reorientation in the central galaxies of clusters and groups

Abstract

¹ Recent observations of galaxy clusters and groups with misalignments between their central AGN jets and X-ray cavities, or with multiple misaligned cavities, have raised concerns about the jet – bubble connection in cooling cores, and the processes responsible for jet realignment. To investigate the frequency and causes of such misalignments, we construct a sample of 16 cool core galaxy clusters and groups with cavities in the X-ray images and jets in VLBI radio maps. Using VLBA radio data we measure the parsec-scale position angle of the jets, and compare it with the position angle of the X-ray cavities detected in *Chandra* data. Using the overall sample and selected subsets, we consistently find that there is a 30% – 38% chance to find a misalignment larger than $\Delta\Psi = 45^\circ$ when observing a cluster/group with a detected jet and at least one cavity. We determine that projection may account for an apparently large $\Delta\Psi$ only in a fraction of objects ($\sim 35\%$), and given that gas dynamical disturbances (as sloshing) are found in both aligned and misaligned systems, we exclude environmental perturbation as the main driver of cavity-jet misalignment. Moreover, we find that large misalignments (up to $\sim 90^\circ$) are favored over smaller ones ($45^\circ \leq \Delta\Psi \leq 70^\circ$), and that the change in jet direction can occur on timescales between one and a few tens of Myr. We conclude that misalignments are more likely related to actual reorientation of the jet axis, and we discuss several engine-based mechanisms that may cause these dramatic changes.

6.1 Motivation

In [Chapter 3](#) and [Chapter 4](#) we inquired into the radio and X-ray morphology of the radio galaxy and associated cavities in RBS 797, revealing a complex superposition of numerous, misaligned outbursts of the central AGN. This is not an isolated case, as other cluster- or group-central AGN are known to have ejected material in different directions over time (see e.g., [Falceta-Gonçalves et al. 2010](#); [Chon et al. 2012](#); [Babul et al. 2013](#); [Schellenberger et al. 2021](#); [Schellenberger et al. 2023](#)). These dedicated works shed many lights on some well-studied individual objects, but without providing a unique answer as to why the direct evidence (the jets) and the smoking gun (the X-ray cavities) of feedback seem disconnected in these cases. It is unknown which of the proposed mechanisms – actual changes in the jet axis, projection effects, or environmental-driven perturbations – is the dominant driver of jet-cavity misalignments in central galaxies. Besides, focusing on individual objects prevents one from understanding *how frequently successive outbursts are rotated with respect to one another*. It is thus essential to analyze a larger sample of clusters and groups to provide a broader picture.

¹This Chapter is based on [Ubertosi et al. \(2023d\)](#).

In this Chapter we present the investigation of jets and X-ray cavity alignment using a tailored sample of galaxy clusters and groups to assess the relative importance of projection and environmental effects, to evaluate how rare these misalignments are, and to gain new insights on the mechanism through which AGN jets change direction over time. Combining *Chandra* and Very Long Baseline Array (VLBA) data, we observationally investigate the alignment of X-ray cavities (on kpc scales) and radio jets (on pc scales).

This Chapter is organized as follows. Section 6.2 presents the criteria for the sample selection; Section 6.3 and 6.4 describe the data and the methods use to measure position angles of jets and X-ray cavities, and Section 6.5 shows the results. We discuss our findings in Section 6.6, while Section 6.7 summarizes our work.

6.2 Sample selection

We select groups and clusters from the parent catalog presented in Hogan (2014), Hogan et al. (2015b), and Hogan et al. (2015a), where 59 central cluster and group galaxies have been classified by their radio morphology on parsec scales. The fairly uniform VLBA observations at 5 GHz are suited to determine the presence and direction of jets in the central dominant galaxies. Since we are driven by the aim of a *Chandra* – VLBA comparison, we include only the sources that have more than 10ks of observations in the *Chandra* archive (45 out of 59 objects). By excluding the objects that do not show evidence for extended radio jets in VLBA data and of X-ray cavities in the *Chandra* data (see the analysis performed in §6.3 and 6.4), we obtain a final sample of 16 systems (see Tab. 6.1). We note that all these systems host ionized gas nebulae at their centers (as probed by optical line emission, such as H α ; see Hogan 2014 and references therein), strongly indicating the presence of a cooling core in the host cluster or group.

The 59 radio-bright BCGs in the sample of Hogan et al. (2015b) and Hogan et al. (2015a) do not form a complete sample, but were treated as representative of their parent, complete catalog of over 700 clusters. Our further selection (as detailed above and in §6.3) is mainly based on the presence of at least one jet in the radio images. Compact radio sources may either be pointing directly towards us (meaning that any jet would be projected on the core), or may be in a fading phase (they were driving jets in the past that are no longer visible). Thus, the sources in our sub-sample constitute the BCGs with the most active AGN at their centers, and with a small jet inclination angle to the plane of the sky. Far from being complete, the clusters and groups in our sample (Tab. 6.1) are representative of systems where AGN feedback activity is ongoing and vigorous. Studying such systems matches our aim to understand how frequently and why the pc-scale and kpc-scale evidence of feedback are misaligned.

6.3 Data and Methods

In the following, we describe the procedure used to calibrate and analyze the VLBA and *Chandra* data, and to obtain the final sample shown in Tab. 6.1.

6.3.1 VLBA radio data

Data reduction

The 5 GHz VLBA observations presented in Hogan (2014), Hogan et al. (2015b), and Hogan et al. (2015a) were performed in phase referencing mode (project codes BE056A, BE056B, BE056C, BE063B, BE063C, BE063E, BE063F, BE063H, BE063I, BE063J, BE063K). The average time spent on

TABLE 6.1: Final sample of galaxy clusters and groups we selected to investigate jet-cavity misalignment, ordered by decreasing M_{500} . The mass is taken from the MCXC catalogue, which is based on the ROSAT X-ray luminosity (Piffaretti et al., 2011). For 4C+55.16 (not present in MCXC) the mass is taken from Zou et al. (2021).

Name	redshift	kpc/''	M_{500} [$10^{14}M_{\odot}$]
Abell 2390	0.230	3.67	8.95
ClG J1532+3021	0.362	5.04	8.16
4C+55.16	0.242	3.82	7.40
Abell 478	0.088	1.65	6.42
RX J1447.4+0827	0.376	5.16	4.60
Abell 1664	0.128	2.28	4.06
RXC J1558.3-1410	0.097	1.79	3.87
ZwCl 8276	0.076	1.44	3.24
Abell 496	0.033	0.65	2.91
ZwCl 235	0.083	1.56	2.80
Abell 2052	0.035	0.69	2.49
Abell 3581	0.022	0.44	1.08
NGC 6338	0.027	0.55	0.87
IC 1262	0.033	0.65	0.86
NGC 5098	0.036	0.72	0.52
NGC 5044	0.009	0.18	0.51

each target source was 20 minutes. The strategy we adopted to process the data is based on standard reduction techniques in AIPS. We first performed a correction of Earth orientation parameters and ionospheric delays (tasks VLBAEOPS, VLBATECR). Then, we solved for delays and amplitudes, by applying digital sampling corrections (VLBACCOR), removing instrumental delays on phases (VLBAMPCL), calibrating the bandpass (BPASS), and applying the corrections (VLBAAMP). To correct the time-dependent delays in phases, we fringe-fitted the data (FRING). Sources with a flux density larger than 20 mJy – 30 mJy were self-fringed, while the others were referenced to the phase calibrator. Ultimately, we applied the calibration to the data and averaged the different IFs. Between two and ten cycles of self-calibration were attempted, and we found a significant improvement in sensitivity only for sources with a flux density larger than ~ 50 mJy.

Morphological classification of the sources

Hogan (2014) classified their radio sources as extended or unresolved based on the morphology of the detected emission or as undetected. We re-analyzed the calibrated data using the software DIFMAP, which can be used to image, characterize the morphology, and measure the flux density of a source by fitting its calibrated visibilities with different functions (an unresolved δ -function, a circular gaussian, an elliptical gaussian, or a combination of these). Based on our analysis, we

classified as undetected the targets for which no component with a flux density above $3 \times \sigma_{\text{rms}}$ could be fit to the visibilities; as unresolved the targets described with a single component smaller than the beam area; and as extended the targets described by least two components.

We verified the presence of extensions in all of the sources classified as extended in the parent catalogue of Hogan (2014). Out of the sources classified as unresolved in Hogan (2014), we found evidence for extended jet-like emission in NGC 5098, ZwCl 8276, and RX J1447.4+0828. Specifically, Hogan (2014) reported the possible presence of extended emission in NGC 5098 (based on a visual inspection), which we confirm to be detected by fitting the visibilities in DIFMAP with an unresolved δ -function (the core) and a gaussian (the extended jet). The extended components we detected in ZwCl 8276 and RXJ 1447+0828 are located along the beam major axis and, on the basis of a by-eye inspection of the images, the sources would be classified as unresolved; however, the best fit with DIFMAP is a combination of a central bright component and two more components on each side of the core in both clusters.

Of the sources classified as undetected in the parent sample of Hogan (2014), our analysis revealed that Abell 795 is in fact detected (but unresolved) at $20\sigma_{\text{rms}}$ (with $\sigma_{\text{rms}} = 50 \mu\text{Jy}/\text{beam}$), having a flux density of 1 mJy. The location of the detected radio emission matches the optical center of the BCG (RA, DEC = 9:24:05.3017, +14:10:21.524), while the phase center of the observation is offset by $\sim 5''$ north-west, which may explain why it was missed in the analysis of Hogan (2014).

Overall, the fitting procedure in DIFMAP allowed us to confirm the presence of jets (at more than $5\sigma_{\text{rms}}$ significance) in 23 sources (out of the starting 45 BCGs, see §6.2).

6.3.2 Chandra X-ray data

Data reduction

We retrieved the data from the *Chandra* archive (cda.harvard.edu/chaser) and reprocessed the observations using CIAO-4.14. Point sources were identified using the tool `wavdetect`, and masked during the analysis. For each target, we verified if the astrometry of the *Chandra* observation needed further corrections beyond its nominal pointing accuracy ($0.4''$), and proceeded to update the coordinates using the `wcs_match` and `wcs_update` tools. We filtered the data from periods contaminated by background flares. The blank-sky event files have been selected as background file, and normalized by the 9-12 keV count-rate of the observation.

To investigate, in detail, the morphology of the ICM, we produced images and corresponding background and exposure maps in the 0.5 – 2 keV energy band. We also used the software SHERPA to fit the images with two-dimensional, elliptical double β models and produce residual images, that can emphasize substructures in the ICM/IGrM (see Fig. 6.3).

6.4 Measurement of position angles

In the following, we describe the methods we employed to measure the position angle of jets (on the parsec scale) and of X-ray cavities (on the kpc scale). A schematic representation is shown in Fig. 6.1.

Measuring the jet position angle in the plane of the sky

The DIFMAP analysis returned the integrated flux (F) and position relative to phase center in polar coordinates (r, θ) of each component (see Appendix H). To measure the position angle of the jet in the reference frame centered on the core, we adopted the following approach. We identified the core as the component with the highest radio flux density in the image (see Fig. 6.2). The position angle $\Phi_{\perp\text{LOS}}$ in the plane of the sky of the extended jet-like component at (r_2, θ_2) in the reference

TABLE 6.2: Position and inclination angles of the radio jets from the VLBA data and position angle of the X-ray cavities from the *Chandra* data. (1) Cluster name. (2) Position angle in the plane perpendicular to the line of sight. (3) Jet/counter-jet ratio. (4) Inclination angle in the plane parallel to the line of sight. (5) Name of the cavity (I stands for inner, O stands for outer). (6) Cavity position angle. (7) Literature reference for the X-ray cavities. (8) Degree of misalignment between the jet direction and the X-ray cavity direction (measured as the difference between columns 2 and 6). References: [1] Lima Neto and Ulmer, 2011; [2] Sonkamble et al., 2015; [3] Bîrzan et al., 2020; [4] Hlavacek-Larrondo et al., 2013a; [5] Hlavacek-Larrondo et al., 2011; [6] Sun et al., 2003; [7] Giacintucci et al., 2014; [8] Prasow-Émond et al., 2020; [9] Calzadilla et al., 2019b; [10] Ettori et al., 2013; [11] Giacintucci, 2016; [12] Dupke and White, 2002; [13] Ubertosì et al., 2023a; [14] Blanton et al., 2011; [15] Johnstone et al., 2005; [16] Canning et al., 2013; [17] O’Sullivan et al., 2019; [18] Schellenberger et al., 2023; [19] Pandge et al., 2019; [20] Randall et al., 2009; [21] O’Sullivan et al., 2014; [22] Schellenberger et al., 2021.

*: the X-ray cavity was identified in this work (see Appendix G for RXC J1558.3-1410 and Appendix I for the outer cavity in ZwCl 8276).

Cluster	$\Phi_{\perp\text{LOS}} [^\circ]$	R	$\Phi_{\parallel\text{LOS}}$	Cavity	$\Theta_{\text{cav}} [^\circ]$	Ref.	$\Delta\Psi$
Abell 2390	100.9 ± 28.5	2.1	20.3 ± 7.2	I1	5.2 ± 20.1	1, 2, 3	84.3
				O1	152.4 ± 21.8		51.5
				O2	-7.7 ± 22.4		71.4
CIG J1532+3021	353.2 ± 16.0	3.6	35.4 ± 11.3	I1	203.6 ± 26.9	4	30.4
				I2	23.6 ± 26.9		30.4
4C+55.16	16.2 ± 67.2	16.4	57.5 ± 9.3	I1	268.1 ± 29.7	5	71.9
				I2	36.7 ± 21.7		20.5
Abell 478	241.3 ± 25.4	5.8	49.5 ± 16.7	I1	99.0 ± 21.1	6, 7	37.7
				I2	206.5 ± 28.6		34.8
RX J1447.4+0827	68.1 ± 15.5	1.1	3.6 ± 5.1	I1	80.4 ± 33.1	8	12.3
				I2	265.6 ± 17.9		17.5
Abell 1664	280.9 ± 8.3	6.0	49.9 ± 16.3	I1	4.9 ± 24.5	9	84.0
				I2	184.9 ± 24.5		84.0
				O1	46.4 ± 30.6		54.5
				O2	226.4 ± 30.6		54.5
RXC J1558.3-1410	153.4 ± 9.6	4.2	39.8 ± 12.8	I1*	215.1 ± 19.7	This work	61.7
ZwCl 8276	265.8 ± 60.3	1.0	0.3 ± 5.0	I1	77.9 ± 30.2	10, This work	7.9
				I2	257.9 ± 30.2		7.9
				O1*	114.9 ± 23.9		29.1
Abell 496	136.9 ± 15.6	1.1	2.4 ± 5.0	I1	126.6 ± 17.8	11, 12	10.3
				I2	322.0 ± 33.1		5.1
				O1	128.9 ± 20.5		8.0
ZwCl 235	153.4 ± 38.9	1.3	7.2 ± 5.3	I1	141.7 ± 17.3	13	11.7
				I2	291.3 ± 13.1		42.1
Abell 2052	253.3 ± 17.5	1.1	3.6 ± 5.1	I1	84.3 ± 49.5	14	11.0
				I2	271.6 ± 56.8		18.3
				O1	37.1 ± 20.8		36.2
				O2	248.2 ± 25.4		5.1
Abell 3581	189.7 ± 59.8	10.2	54.1 ± 12.4	I1	163.3 ± 27.4	15, 16	26.4
				I2	325.9 ± 26.8		43.8
				O1	338.8 ± 21.2		30.9
NGC 6338	293.7 ± 21.2	3.3	32.9 ± 10.9	I1	137.9 ± 44.2	17, 18	24.2
				I2	317.9 ± 44.2		24.2
				O1	210.0 ± 20.2		83.7
IC 1262	284.2 ± 15.6	7.0	51.2 ± 15.1	I1	85.3 ± 24.1	19	18.9
				I2	265.3 ± 24.1		18.9
				O1	286.9 ± 25.1		2.7
NGC 5098	244.7 ± 21.2	6.7	50.8 ± 15.4	I1	72.1 ± 32.5	20	7.4
				I2	221.1 ± 30.3		23.6
NGC 5044	140.3 ± 19.4	1.2	4.4 ± 5.3	I1	68.7 ± 40.5	21, 22	71.6
				I2	209.4 ± 35.9		69.1
				O1	64.5 ± 16.1		75.8
				O2	250.3 ± 21.9		70.0

frame centered on the core at (r_1, θ_1) is defined as:

$$\Phi_{\perp\text{LOS}} = \arctan \left(\frac{r_2 \sin \theta_2 - r_1 \sin \theta_1}{r_2 \cos \theta_2 - r_1 \cos \theta_1} \right), \quad (6.1)$$

that is the angle between the line connecting (r_2, θ_2) to (r_1, θ_1) and the horizontal (right ascension) axis. If more than one jet is present (i.e. two sided sources), we considered the average between the angles of the two jets as the best estimate of the overall position angle.

We note that the statistical errors on the parameters obtained from the DIFMAP fit may underestimate the real uncertainties (see e.g., Deller et al. 2018). As a more robust estimate of the position

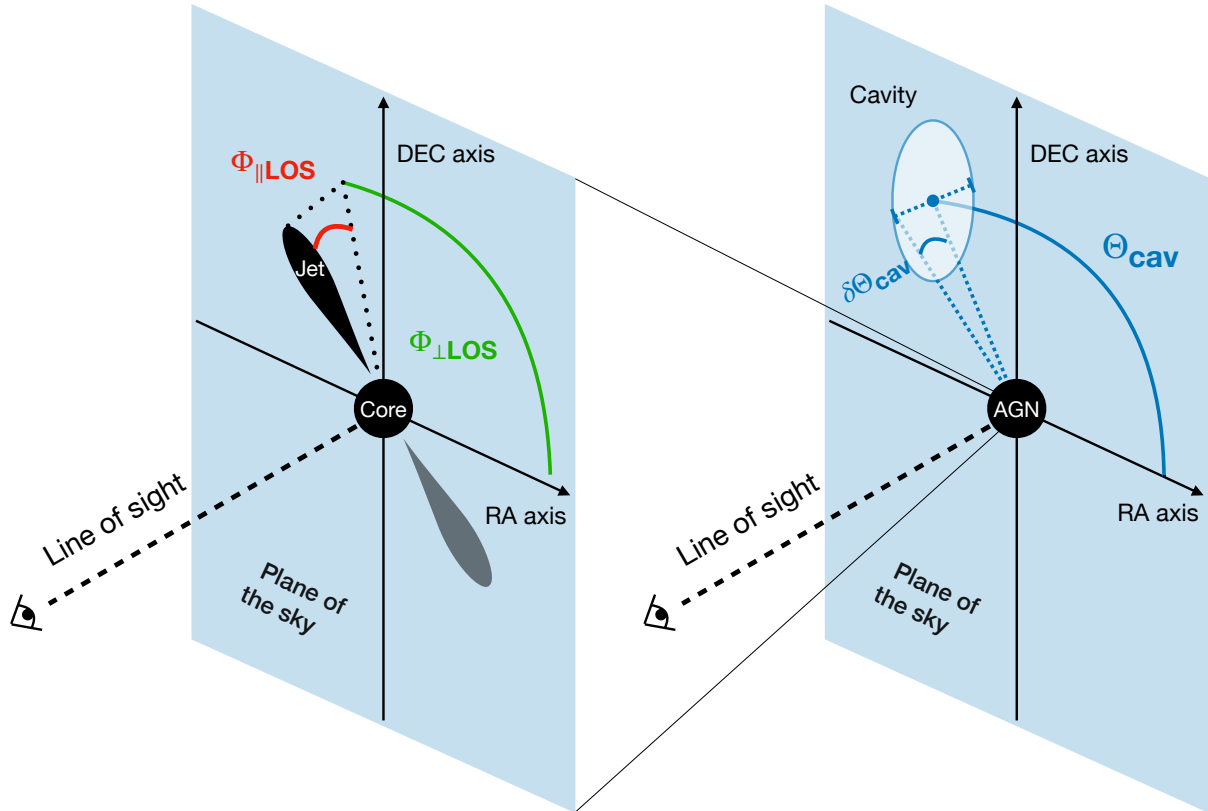


FIGURE 6.1: *Left*: schematic representation of a core+jet system, showing the jet position angle $\Phi_{\perp\text{LOS}}$ and the jet inclination angle $\Phi_{\parallel\text{LOS}}$. *Right*: schematic representation of an AGN + cavity system, showing the bubble position angle in the plane of the sky, Θ_{cav} , and the associated uncertainty, $\delta\Theta_{\text{cav}}$.

angle uncertainty, $\delta\Phi_{\perp\text{LOS}}$, we used the deconvolved angular width of the component (circle or ellipse) describing the jet emission at its distance from the core. In cases where the jet emission was unresolved by the DIFMAP fitting procedure (i.e. the component is a δ -function), we considered the angular width of the beam at the distance of the jet from the core. In practice, given a jet-like component described by an ellipse with major semi-axis a and minor semi-axis b , and located at a distance R from the core, the uncertainty (in degrees) was determined as:

$$\delta\Phi_{\perp\text{LOS}} = \left(\frac{\sqrt{ab}}{R} \right) \times \frac{180}{\pi}, \quad (6.2)$$

where a and b , in the case of an unresolved component, are the beam major semi-axis and minor semi-axis, respectively. We list in Tab. 6.2 our measurements of the jet position angle perpendicular to the line of sight for the systems in our sample. In Appendix E we show the comparison with two alternative methods that provided consistent results with those presented here. Furthermore, we show in Appendix F that using archival VLBA data at different frequencies returns position angle measurements that are in good agreement with those derived here from the 5 GHz radio maps.

Measuring the jet inclination angle along the line-of-sight

As we are interested in the 3D geometry of the jets, we used the jet/counter-jet flux ratio to constrain the inclination angle of the jets with respect to the line of sight, which allows us to weight the

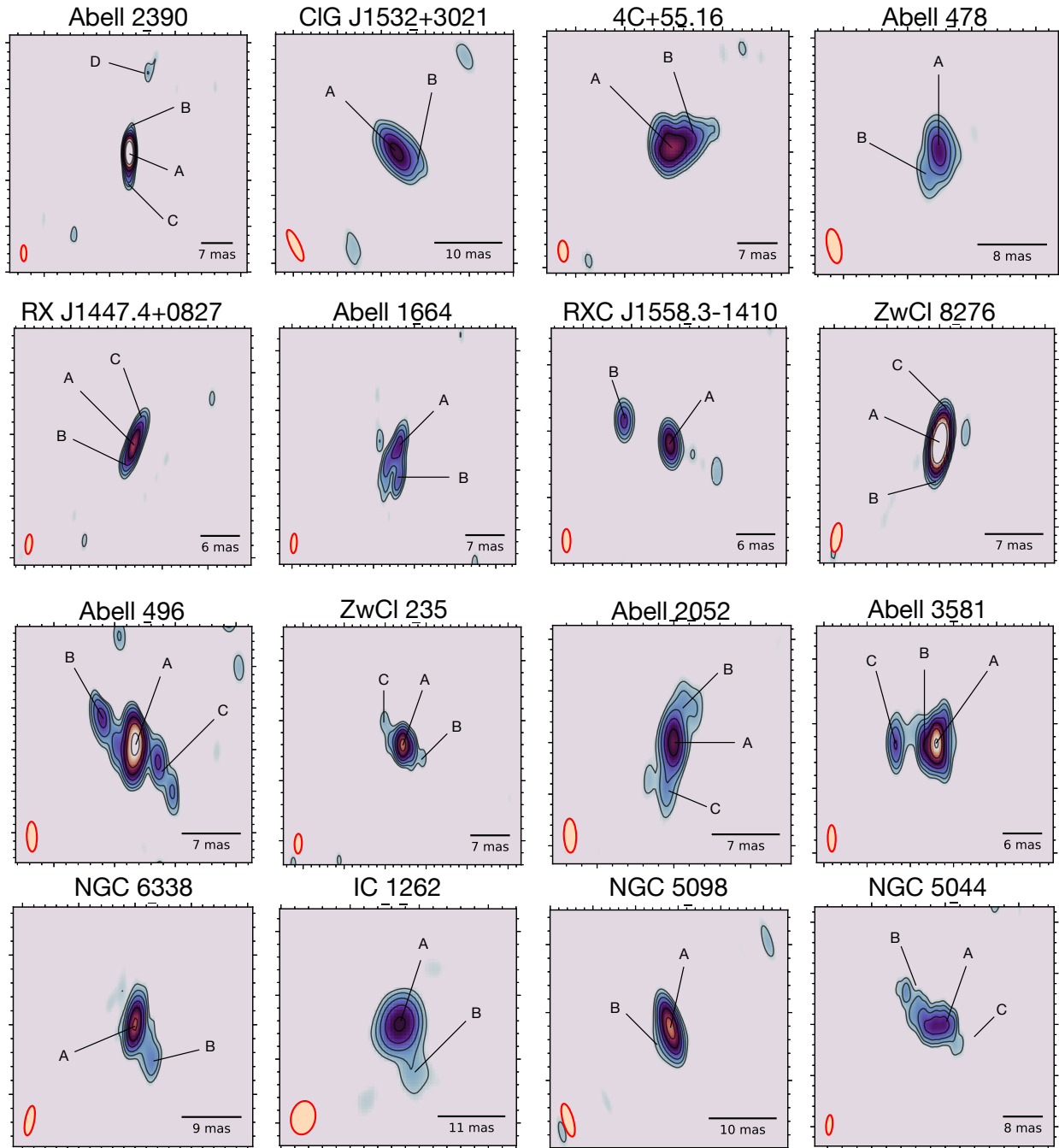


FIGURE 6.2: VLBA images at 5 GHz of the systems in our sample. Labels indicate the position of the components identified using DIFMAP (see Tab. H.1). The contours overlaid in black start from $5 \times \sigma_{\text{rms}}$ (see the values in Tab. H.1) and increase by a factor of 2. The beam is overlaid with an orange ellipse in the bottom left corner. See §6.3.1 for details.

importance of projection. The jet/counter-jet flux ratio, R_j , is defined as:

$$R_j = \frac{F_{\text{jet}}}{F_{\text{c-jet}}} \quad (6.3)$$

where F_{jet} and $F_{\text{c-jet}}$ are the integrated fluxes of the jet and of the counter-jet, respectively, measured in regions placed over each feature. For one-sided objects, the counter-jet flux was assumed to be lower than $5 \times \sigma_{\text{rms}}$. The inclination angle of the jet in a plane parallel to the line of sight, $\Phi_{\parallel\text{LOS}}$,

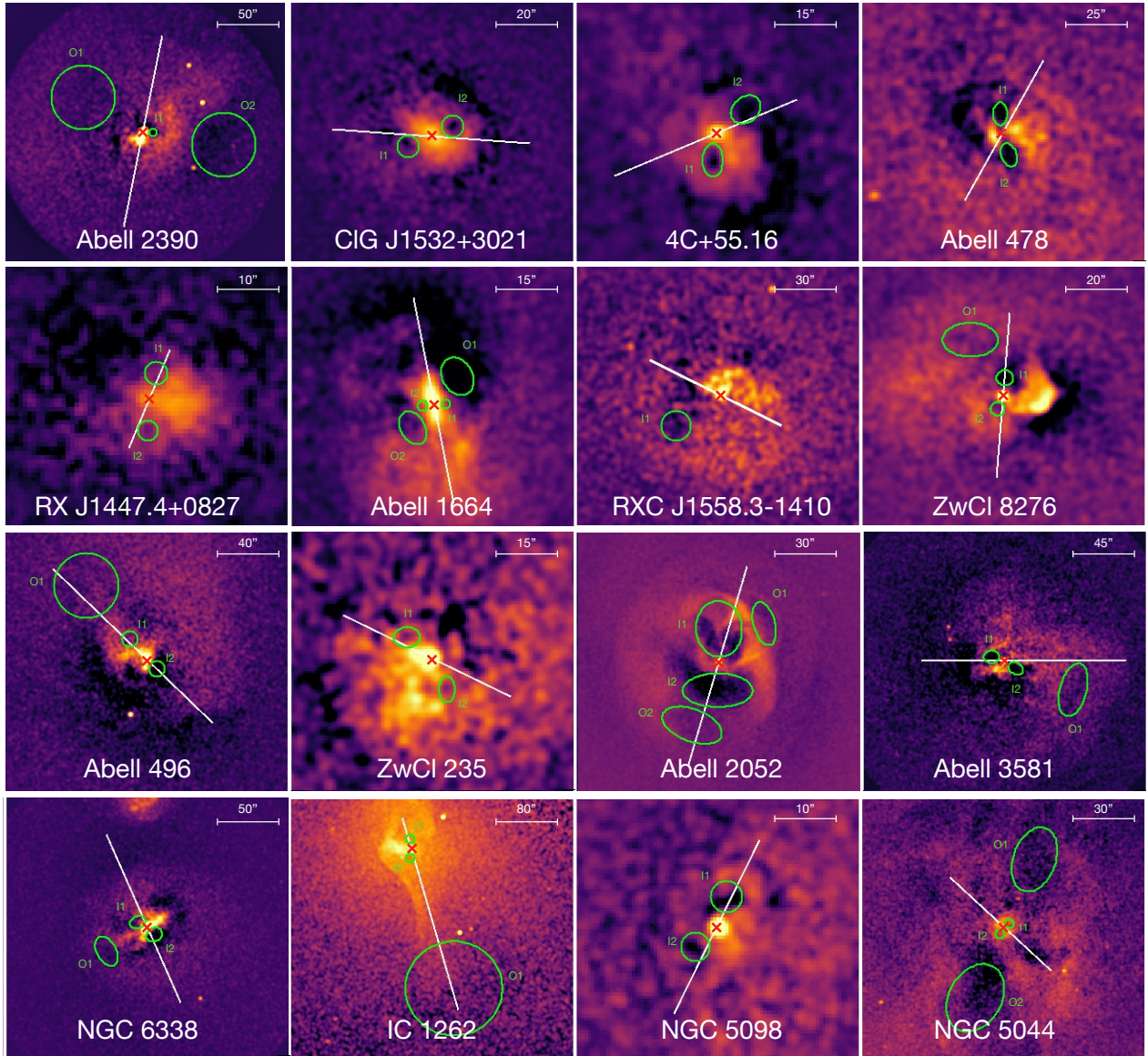


FIGURE 6.3: Residual *Chandra* images of the systems in our sample. Overlaid in green are the X-ray cavities (see Tab. 6.2 for details and literature references), while the white line shows the orientation of the radio jet in the plane of the sky, $\Phi_{\perp\text{LOS}}$. The red cross shows the position of the central AGN. See §6.6.2 for details.

can be computed using (e.g., Scheuer and Readhead 1979):

$$\cos \Phi_{\parallel\text{LOS}} = \frac{1}{\beta} \times \left(\frac{R_j^{\frac{1}{2+\alpha}} - 1}{R_j^{\frac{1}{2+\alpha}} + 1} \right), \quad (6.4)$$

where α is the radio spectral index of the jets, assumed to be $\alpha = -0.6$. As the VLBA data probe the parsec scales, where the jets are still mildly relativistic, we assumed a Lorentz factor $0.6 \leq \beta \leq 1$ (see e.g., Giroletti et al. 2004; Giovannini et al. 2011). This returned a possible range of inclination angles along the line of sight. Thus, we used the median angle as our estimate of $\Phi_{\parallel\text{LOS}}$, and the range width as the statistical uncertainty. We also added in quadrature a systematic uncertainty of 5° (that is $R_j = 1.2$, which could be intrinsic; see e.g., McCarthy et al. 1991).

Measuring the X-ray cavities position angle

Out of the 23 objects where we could detect one or two sided jets from the VLBA data, there are literature indications for X-ray cavities in 15 objects. We inspected the counts and residual images of the other 8 objects, searching for $\sim 20\% - 30\%$ decrements in surface brightness at a signal-to-noise ratio greater than 3. We found one object where a clear cavity was visible, that is RXC J1558.3-1410 (see Appendix G). Hlavacek-Larrondo et al. (2013b) noted the presence of cavities in this cluster, but without detailing its/their position(s). Thus, we are unable to confirm that the structure we detect is coincident with the cavities they identified. We also found evidence of an external cavity in ZwCl 8276, besides the two inner bubbles noticed by Ettori et al. (2013). The existence of this external cavity, (shown in Fig. 6.3), is supported by the LOFAR detection of lobe-like radio emission matching the position of this outer bubble (Bîrzan et al., 2020).

Overall, there are 16 systems in which the *Chandra* data allows us to measure the position angle of at least one X-ray cavity. The following method was systematically adopted to measure the position angle of the cavities in the *Chandra* images of the 16 systems. For each cluster or group, we measured the angle Θ_{cav} between the center of the ellipse describing a cavity and the RA axis with respect to the core of the central AGN, whose precise location is known from the VLBA data. The uncertainty in the position angle of the cavity, $\delta\Theta_{\text{cav}}$, is given by the width of the cavity in the direction perpendicular to the line connecting the AGN and the center of the cavity (for a schematic representation see Fig. 6.1, right panel).

We point out that we are unable to measure the inclination angle of cavities to the line of sight, as done for the radio jets. Relativistic arguments can constrain projection effects of radio jets on the pc-scale (see Eq. 6.4 and Scheuer and Readhead 1979), whereas it is non-trivial to directly estimate the depth of cavities in a cluster or group atmosphere from X-ray observations. Very few works have attempted to constrain cavity inclination angles, only in systems with remarkably deep cavities (as in e.g., RBS 797, Cavagnolo et al. 2011) and with several assumptions. Besides, the detectability of X-ray cavities is hampered when the structures lie at large angles (greater than 45°) from the plane of the sky (see Enßlin and Heinz 2002; Mroczkowski et al. 2022), so that the majority of detected X-ray cavities in groups and clusters lie at less than 45° from the plane of the sky (Brüggen et al., 2009). Thus, we assume that the X-ray cavities in our sample are not far from the plane of the sky. While this represents a limitation of this work, we are confident that any tentative cavity inclination angle would likely be smaller than the associated uncertainty.

Out of the 45/59 objects of Hogan et al. (2015a) and Hogan et al. (2015b) with more than 10 ks of *Chandra* data, the above procedures led us to consider only the 23/45 with one- or two-sided jets, and then the 16/23 with at least one X-ray cavity. Our final sample, thus comprising 16 objects, is listed in Tab. 6.1. The sample covers a mass range of $5 \times 10^{13} M_\odot \leq M_{500} \leq 9 \times 10^{14} M_\odot$, and is composed of 11 galaxy clusters and 5 galaxy groups. For each object we were able to measure the position and inclination angles of the jets ($\Phi_{\perp\text{LOS}}$, $\Phi_{\parallel\text{LOS}}$) and the position angle of the cavities (Θ_{cav}). These values are reported in Tab. 6.2.

6.5 Results

6.5.1 Jet-cavity misalignments in the plane of the sky

Focusing on the position angles in the plane of the sky of jets and X-ray cavities, we defined the quantity $\Delta\Psi = |\Phi_{\perp\text{LOS}} - \Theta_{\text{cav}}|$, which represents the degree of misalignment between the jet direction (measured on parsec scales) and the X-ray cavity direction (measured on kiloparsec scales). The values that $\Delta\Psi$ can assume range between $0^\circ - 90^\circ$, with $\Delta\Psi = 0^\circ$ indicating a perfect alignment and $\Delta\Psi = 90^\circ$ indicating an orthogonal misalignment. For the sake of clarity, we note that for a cluster or a group with a number N of X-ray cavities, there are N pairs of $(\Phi_{\perp\text{LOS}}, \Theta_{\text{cav}})$ for which an estimate of $\Delta\Psi$ can be obtained.

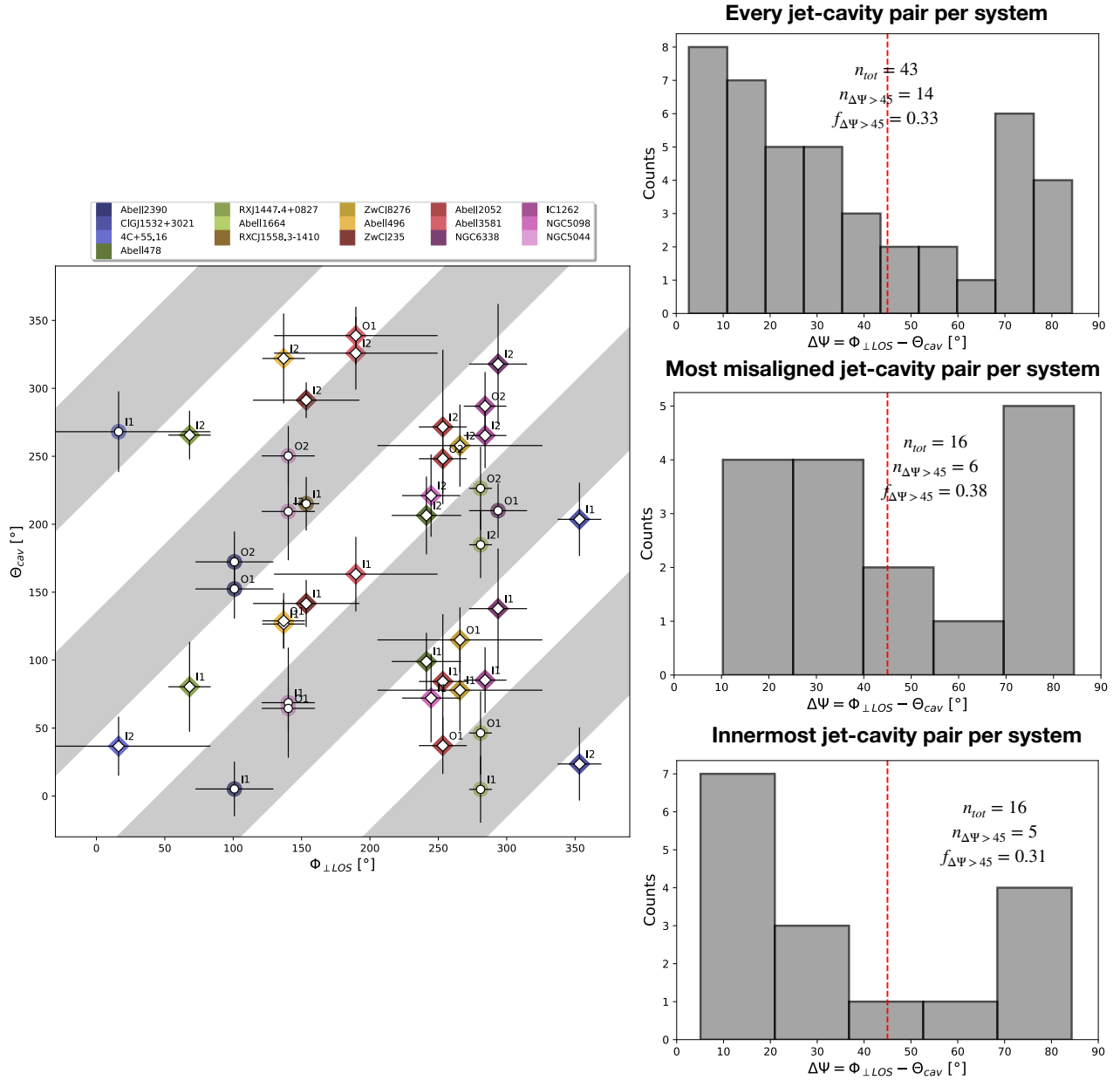


FIGURE 6.4: *Left*: Plot of jet position angle in the plane of the sky versus cavity position angle for the 16 systems in our sample. Each point is a jet-cavity pair, meaning that systems with more than one X-ray cavity are represented by more than one point on the plot. The gray shaded areas represent spaces of the plot where the difference $\Delta\Psi = \Phi_{\perp LOS} - \Theta_{cav}$ is greater than 45° . jet-cavity pairs falling inside these areas are represented with circles, while those falling outside these areas are represented with squares. The points are color-coded according to the cluster or group they belong to (see the top legend). Labels on the right of each point indicate the corresponding cavity (see Tab. 6.2). *Top right*: histogram of $\Delta\Psi$ for the 43 jet-cavity pairs of the systems in our sample. *Center right*: histogram of the jet-cavity pairs with the largest $\Delta\Psi$ for each systems. *Bottom right*: histogram of the jet – innermost cavity pair for each system. In each panel, the red dashed line shows the threshold of 45° between aligned and misaligned jet-cavity pairs.

From now on, we arbitrarily classify as *aligned* the jet-cavity pairs for which $\Delta\Psi < 45^\circ$, and as *misaligned* the jet-cavity pairs for which $\Delta\Psi > 45^\circ$. In the last column of Tab. 6.2 we list the values of $\Delta\Psi$ for the cavities of each cluster or group in our sample. Additionally, we show in Fig. 6.4 a plot of Θ_{cav} versus $\Phi_{\perp LOS}$ for the jet-cavity pairs in our sample. Given that the 180° ambiguity in the definition of the position angle does not allow one to immediately evaluate $\Delta\Psi$ from this figure, we

overplot as gray shaded areas the regions where $\Delta\Psi > 45^\circ$.

Among the 16 systems in our sample, there are 10 systems in which all the detected X-ray cavities are aligned with the radio jet seen at 5 GHz; these are CIG J1532+3021, Abell 478, RX J1447.4+0827, ZwCl 8276, Abell 496, ZwCl 235, Abell 2052, Abell 3581, IC 1262 and NGC 5098. An additional 2/16 objects, 4C+55.16 and NGC 6338, have at least one X-ray cavity that is aligned with the radio jet. In the remaining 4/16 objects, Abell 2390, Abell 1664, RXC J1558.3-1410 and NGC 5044, all the detected X-ray cavities are found at more than 45° from the axis of the radio jet. We provide a short summary of the properties of each system in [Appendix I](#).

To further investigate the fraction of misaligned systems/X-ray cavities, we show in Fig. 6.4 (top right) the histogram of $\Delta\Psi$ for the 43 jet-cavity pairs of our sample. As expected from models of cavity formation, the majority of the X-ray cavities are aligned with the radio jet. However, as noted in the Introduction (§1.3.2) and in §6.1, cases of spatial misalignment are known. Indeed, taking 45° as a threshold for a misaligned cavity-pair, there are 14/43 misaligned jet-cavity pairs, which corresponds to a fraction of 33%. A similar argument can be made by considering, for each cluster or group, only the jet-cavity pair with the largest $\Delta\Psi$. The corresponding histogram in Fig. 6.4 (center right) shows that in 6/16 systems there is a cavity-jet pair with $\Delta\Psi > 45^\circ$, corresponding to a fraction of 38%. Moreover, restricting the histogram to the jet – innermost cavity pair for each system (Fig. 6.4, bottom right), we find a fraction of $5/16 = 31\%$ of systems with $\Delta\Psi > 45^\circ$. These results suggest that there is a 30% – 40% chance to find a misalignment larger than $\Delta\Psi = 45^\circ$ when observing a cluster/group with a detected jet and at least one X-ray cavity.

We note that in the histograms of Fig. 6.4 there is a peak at $\Delta\Psi \approx 70^\circ - 80^\circ$, which comprises the cases where the jet and the cavity are nearly orthogonal. We discuss this feature and its interpretation in §6.6.3.

6.5.2 Jet inclination angle with respect to the line of sight

As reported in §6.4, we constrained the jet inclination in a plane parallel to the line of sight using the jet – counterjet flux density ratio (see Tab. 6.2). The angle $\Phi_{\parallel\text{LOS}}$ ranges between 0° (jets lying in the plane of the sky) to $\sim 60^\circ$. There are 6/16 systems with $0^\circ \leq \Phi_{\parallel\text{LOS}} \leq 10^\circ$ (RX J1447.4+0827, ZwCl 8276, Abell 496, ZwCl 235, Abell 2052, and NGC 5044), 4/16 systems with $10^\circ \leq \Phi_{\parallel\text{LOS}} \leq 45^\circ$ (Abell 2390, CIG J1532+3021, RXC J1558.3-1410, and NGC 6338), and 6/16 systems with $\Phi_{\parallel\text{LOS}} \geq 45^\circ$ (4C+55.16, Abell 478, Abell 1664, Abell 3581, IC 1262, and NGC 5098).

We notice that the lack of systems with jets nearly aligned along the line of sight is set by the combination (1) of our criterion of having at least one jet in the radio images (we are avoiding objects with $\Phi_{\parallel\text{LOS}} \approx 90^\circ$); (2) of the assumptions on β and α in Eq. 6.4 (that is, we do not consider superluminal motion, $\beta > 1$, or jets with an inverted spectrum, $\alpha \geq 0$); (3) of the limited dynamic range of the VLBA snapshot data (~ 20 min of time on source), they may hide faint counterjets in one-sided sources; (4) of spherical geometry arguments: a given polar angle interval $\Delta\Phi$ covers more area on the sphere near the equator than near the poles, thus we expect only a small fraction of randomly pointed vectors to be pointed at us.

6.6 Discussion

In the following, we test different scenarios to explain the alignments and misalignments between jets and X-ray cavities in our sample. After assessing the relative importance of external factors, such as projection effects and environmental disturbances, we turn to the discussion of effects related to the central engine. Specifically, we show how the distribution of $\Delta\Psi$ for the clusters and groups in our sample can provide insights on the likelihood of jet reorientation, and we consider the timescales of such mechanisms.

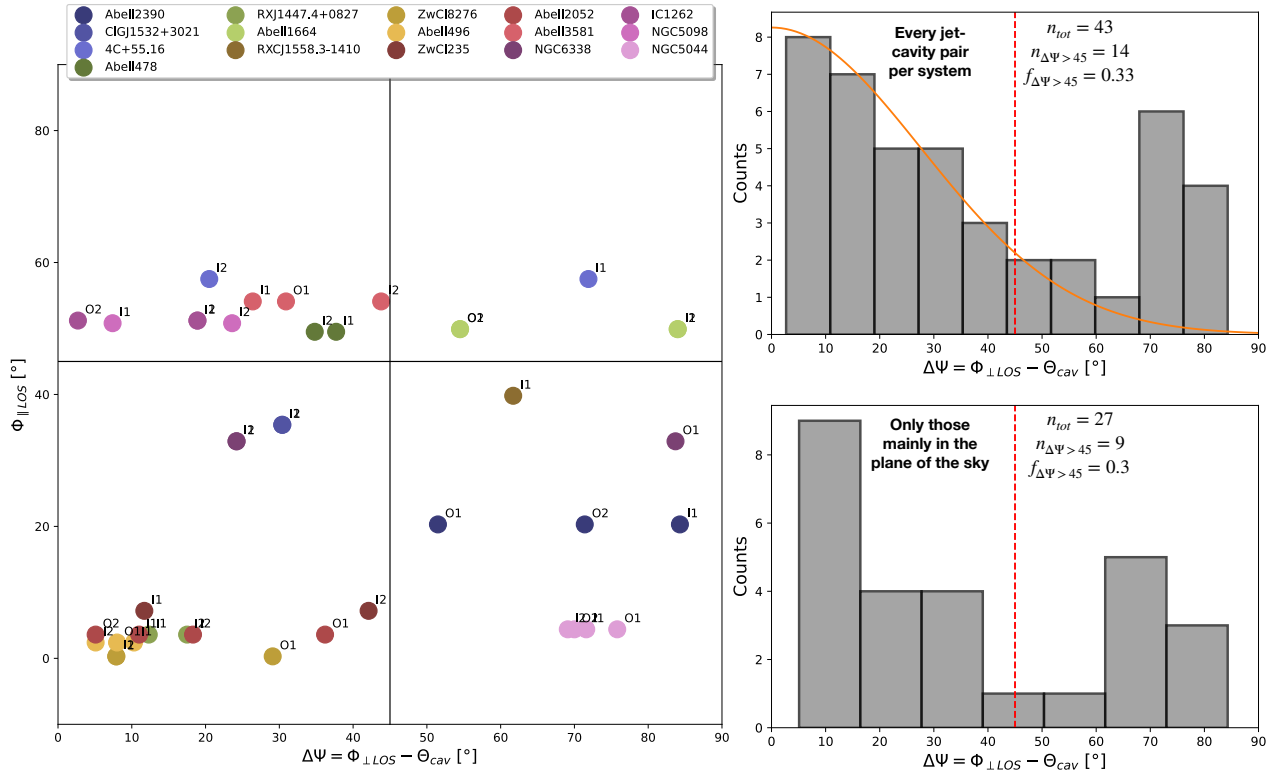


FIGURE 6.5: *Left*: Diagnostic plot of misaligned jets and X-ray cavities. The jet inclination angle along the line of sight, $\Phi_{\parallel\text{LOS}}$, is plotted against the difference between the jet and the cavities position angles in the plane of the sky, $\Delta\Psi$. Points are color-coded according to the cluster or group they belong to (see the top legend). Labels on the right of each point indicate the corresponding cavity (see Tab. 6.2). *Top right*: same as in Fig. 6.4 (top right panel), but with the addition of the orange line, that is the fit with a Gaussian function to the systems with $\Delta\Psi \leq 45^\circ$ (see §6.6.3 for details). *Bottom right*: same as the top panel but including only the systems for which projection effects are negligible, that is $\Phi_{\parallel\text{LOS}} < 45^\circ$. In both panels, the red dashed line shows the threshold of 45° used to classify jet-cavity pairs as aligned or misaligned.

6.6.1 Projection effects

As noted in §6.5.1, there are systems in our sample where some X-ray cavities are misaligned by more than 45° from the radio jet of the AGN. However, there is the possibility that the misalignment is only apparent. Indeed, projection effects may cause a large apparent offset, even though the actual 3D misalignment between jets and cavity directions is small. Using the information obtained from the analysis of the jet direction with respect to the line of sight (§6.4 and 6.5.2) we can systematically reconstruct the 3D geometry of jets and verify whether projection effects may reconcile the largest misalignments we found.

We show in Fig. 6.5 (left panel) the jet inclination along the line of sight, $\Phi_{\parallel\text{LOS}}$, plotted against the difference between the jet and the cavity position angles in the plane of the sky, $\Delta\Psi$. This figure can be used as a diagnostic plot for the degree of misalignment of each jet-cavity pair in the systems of our sample. As done before, we use $\Phi_{\parallel\text{LOS}} = 45^\circ$ and $\Delta\Psi = 45^\circ$ as thresholds between jets in the plane of the sky or along the line of sight and between aligned or misaligned jet-cavity pairs, respectively. We can thus divide the 43 jet-cavity pairs between the four quadrants of the plot, obtaining the following results:

- *Bottom-left quadrant*: aligned jet-cavity pairs which are mainly lying in the plane of the sky.
- *Upper-left quadrant*: aligned jet-cavity pairs where the jet is primarily oriented towards us.
- *Upper-right quadrant*: misaligned jet-cavity pairs where the jet is primarily oriented towards us.
- *Bottom-right quadrant*: misaligned jet-cavity where the jet is mainly lying in the plane of the sky.

Overall, the (mis)alignments of jet-cavity pairs that are located in the two bottom quadrants, where projection effects are relatively negligible, are robustly confirmed even in 3D. By restricting the analysis to these jet-cavity pairs (a total of 27 pairs), we still find that a fraction of $9/27 = 30\%$ is misaligned by more than 45° , up to nearly orthogonal misalignments. Such fraction of misaligned jets in the plane of the sky is clearly independent of the inclination angle along the line of sight. Therefore, projection effects may account for an apparently large $\Delta\Psi$ only in a fraction ($\sim 35\%$) of the misaligned jet-cavity pairs in our sample (as in Abell 1664 or for the cavity I1 in 4C+55.16).

6.6.2 The environment

In this subsection we consider whether environmental effects may favor misalignments between successive AGN outbursts. First, we note that over the mass range covered by our sample ($5 \times 10^{13} M_\odot \leq M_{500} \leq 9 \times 10^{14} M_\odot$) there is no clear evidence for the degree of misalignment of the different jet-cavity pairs being related to the mass of the host halo. Based on the 16 systems in our sample, dramatic changes in jet direction can be found both in massive galaxy clusters (such as Abell 2390, with $\Delta\Psi_{max} = 84.3^\circ$) and in galaxy groups (such as NGC 6338, with $\Delta\Psi_{max} = 83.7^\circ$, or NGC 5044, with $\Delta\Psi_{max} = 75.8^\circ$).

A potentially important question is whether gravitational perturbances that trigger large scale gas motions could play a major role. Specifically, cavities pointing to a different direction than the jets may have been shifted from their original axis by the gas motions.

If gas bulk motions (such as sloshing) were responsible for the jet-cavity misalignments, we should expect misaligned pairs to be more likely found in disturbed clusters and groups. Typical evidence of sloshing include a spiral morphology of the ICM/IGrM, and/or the presence of one or more cold fronts. We checked in the literature if the objects in our sample are reported to be in a sloshing state. Interestingly, all the systems are dynamically disturbed, with all but one (NGC 6338, which is merging with another group) showing evidence of sloshing. The relevant references are given in Tab. 6.2. Even though no dedicated X-ray studies are available for RXC J1558.3-1410, we remark that the *Chandra* image reveals a bright spiral residual feature in the ICM (see Fig. G.1 in Appendix G), which indicates that sloshing is likely present also in this system.

Nice comparisons are offered by Abell 496, Abell 3581, Abell 1664 and NGC 6338 (see Fig. 6.3), which are all strongly disturbed systems. In Abell 496 and Abell 3581 the different generations of X-ray cavities are nearly aligned with each other and with the radio jet. Conversely, in Abell 1664 and NGC 6338 the different generations of X-ray cavities are largely misaligned by more than 45° from each other and from the radio jet. Even though we cannot exclude that in some systems the present position of the X-ray cavities may have been influenced by the large scale motions, we argue that the environment does not play the major role, as gas dynamical perturbations are present in the whole sample. That is, if sloshing was so effective at dragging X-ray cavities away from their original position, we should expect to find misaligned bubbles in all of the systems of our selection, given their clearly disturbed nature. On the contrary, several systems where dynamical perturbations are present display multiple generations of well-aligned X-ray cavities and jets. Sloshing may become a dominant mechanism for the dynamics of X-ray cavities at later times (as for the oldest, detached radio lobe of NGC 5044, see O’Sullivan et al. 2014), when the age of the X-ray cavities approaches the typical sloshing timescales ($10^8 - 10^9$ yr, e.g., Su et al. 2017). By assembling a larger sample of systems with detections of X-ray cavities and jets, in the future we could investigate more specific trends between misalignments and dynamical perturbations. For instance, comparing $\Delta\Psi$ with the offset between the BCG and the X-ray peak, or with the sloshing timescale at the distance of the cavities from the center, may provide further insights on the relative importance of environmental mechanisms.

6.6.3 The likelihood of jet reorientation

The above results argue against projections or environmental effects, alone, being able to explain the jet-cavity misalignments. All in all, it seems more likely that the large changes in direction are related to actual reorientation of the SMBH-driven jets. We now turn to the questions of how likely it is for jets to experience reorientation, and whether there is a favored angle.

Our analysis of §6.5.1 unveiled that $\sim 30\% - 40\%$ of the jet-cavity pairs in our sample have a $\Delta\Psi$ larger than 45° . Furthermore, when excluding systems that may be biased by projection effects (see §6.6.1), we find that 30% of jet-cavity pairs are misaligned by an angle (in the plane of the sky) ranging between 45° and 90° . This suggests that a change in the jet position angle of AGN may be a relatively common mechanism, as roughly 1/3 of the X-ray cavities in our sample are more than 45° away from the currently driven jets.

A peculiar feature in the distribution of $\Delta\Psi$ is the peak around $\approx 75^\circ$. We note that the peak is resilient to the systems aligned along the line of sight being removed from the histogram (see Fig. 6.5, bottom right panel). If no changes in time of the position angle of the jets occurred, one might expect that cavities and corresponding jets should always be perfectly aligned, i.e. $\Delta\Psi = 0^\circ$. This is clearly an idealized case, as there are several effects that contribute to widening the distribution around zero. These can be both intrinsic to the physics of jets and X-ray cavities (such as slow precession of the jet axis over time, cavities expanding asymmetrically, or buoyant forces governing the motion of bubbles at later times²) and related to observational biases (cavities not being perfect ellipses, resolution of radio and X-ray observations, projection effects). All of these likely result in a broadening of the distribution to a nearly Gaussian shape. This is indeed the case for the jet-cavity pairs with $\Delta\Psi \leq 45^\circ$: fitting a Gaussian function to this side of the distribution we find a mean $\mu = 0.0^\circ \pm 1.2^\circ$ with standard deviation $\sigma = 27.6^\circ \pm 1.6^\circ$ (see Fig. 6.5, top right panel). This scatter of $\sim 30^\circ$ expresses the above widening effects.

The effect of jet reorientation on the histogram depends on whether there is a favored angle by which jets are reoriented. If jet reorientation caused a random change in the position angle of the jets, one would expect a uniform distribution of misaligned jets and X-ray cavities combined with the Gaussian-like distribution at $\Delta\Psi < 45^\circ$. However, the presence of the peak at $\Delta\Psi \sim 75^\circ$ in Fig. 6.5 (right panels) may suggest that when a change in jet orientation between successive AGN outbursts occurs, the change in position angle is more likely to be large, rather than randomly distributed between $0^\circ - 90^\circ$. That is, we may cautiously propose that the mechanism of jet reorientation favors large changes in jet position angle, causing nearly orthogonal misalignments between the successive AGN outbursts.

We note that these conclusions would strongly benefit from increasing the sample size to include a larger number of objects. We can estimate the robustness of the above result for our sample of 16 clusters with a total of 43 X-ray cavities. We performed 10^3 realizations of drawing 43 values between $0^\circ - 90^\circ$ from the combination of a Gaussian (with μ, σ set to those derived above) and a uniform distribution. The relative number of points drawn from the Gaussian was set to 29/43 (the jet-cavity pairs with $\Delta\Psi \leq 45^\circ$), while the remaining 14/43 values (the jet-cavity pairs with $\Delta\Psi \geq 45^\circ$) were drawn from the uniform component. We find that the probability of having $n_{70^\circ-90^\circ} / n_{45^\circ-70^\circ} > 2$ (as observed) is of 1.6%, thus we can reject the uniform distribution at $\sim 2.5\sigma$ confidence.

We also note that this is not the first time that a secondary peak at large angles is found when studying small and large scales misalignments. Earlier works found a secondary peak at around 90° (Pearson and Readhead, 1988; Wehrle et al., 1996; Cao, 2000), more recently confirmed in Kharb

²In case of a non-spherical potential well, a buoyant bubble will preferentially rise in the direction of the shallower potential (that is the minor axis of the dominant galaxy, in case of an elliptical morphology). However, the majority of radio galaxies already have their jets oriented within $\sim 30^\circ$ of the optical minor axis of their host (Palimaka et al., 1979; Battye and Browne, 2009; Vazquez Najar and Andernach, 2019), which limits the magnitude of misalignments induced by an asymmetric potential.

et al. (2010). These works were based on radio data (misalignments were evaluated through VLA and VLBA comparisons), and the sources of those samples were mainly blazars or quasars, for which projection effects are certainly not negligible. In our study we find a very similar result (a peak at $\Delta\Psi \sim 70^\circ - 80^\circ$) using the X-ray counterparts of large scale radio lobes (the cavities), and, most importantly, even when restricting the analysis to sources where projection effects are negligible (see Fig. 6.5, bottom right panel). Therefore, while limited by the statistics of our sample, we confirm the earlier claims of a bimodality in the distribution of misalignments. In turn, this supports the idea that the mechanism behind the changes in jet orientation favors large misalignments over small ones.

6.6.4 The timescales and mechanism of jet reorientation

The observed misalignments raise the question of how quickly jets can change propagation direction over time. To investigate this point, we searched in the literature references listed in Tab. 6.2 which X-ray cavities in our sample had an estimate of their ages (24 out of 43 X-ray cavities). We show in Fig. 6.6 a plot of $\Delta\Psi$ versus the age of each X-ray cavity (obtained through different methods, which typically agree within a factor of two; see Bîrzan et al. 2004). No clear trend is visible in this figure. This may indicate that larger changes in jet axis orientation do not always occur on longer timescales. We also verified that no trends are visible when plotting $\Delta\Psi$ versus the projected distance of the cavities from the center – this is a less physical quantity than the cavity age, but is more independent on dynamical assumptions. By focusing on the systems with $\Delta\Psi > 45^\circ$, we see that the young X-ray cavities in NGC 5044 and in Abell 1664, likely formed only a few Myrs ago, are already misaligned by a large angle from the radio jet currently being driven by the central engine. The case of NGC 5044 is remarkable, with the 1 Myr old inner X-ray cavities being at $\sim 70^\circ$ from the jet seen in VLBA images. Schellenberger et al. (2021) discussed many possibilities for such misalignment, ruling out binary black holes and precession scenarios.

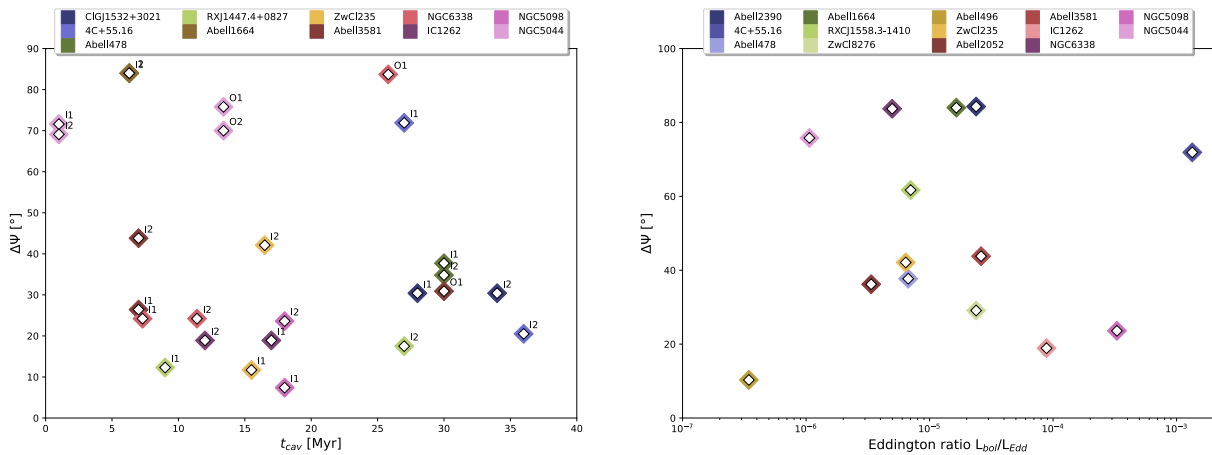


FIGURE 6.6: *Left panel:* Jet – cavity position angle difference $\Delta\Psi$ versus cavity age t_{cav} for the cavities in the systems of Tab. 6.2 with an available estimate of the age from the literature. *Right panel:* Largest jet – cavity position angle difference $\Delta\Psi$ for each system in our sample versus the Eddington ratio of the central AGN (see Sect. 6.6.4 for details). In the right panel, only the 14/16 systems with available measurements of L_{bol} and L_{Edd} are plotted.

In the case that the jet’s direction of propagation is linked to the spin of the rotating SMBH only, dramatically altering the SMBH rotation axis on short timescales is non-trivial. To address this issue, the case has been made that the jet direction could be influenced by the accreting material. We point out that, in the following discussion, we do not assume a one-to-one relation between an accretion episode and a jet episode. Rather, during continuous gas accretion, the variations of the accretion rate, the magnetic field, or the spin of the SMBH may drive the formation of a relativistic

jet (e.g., Blandford and Znajek 1977; Ćemeljić et al. 2022).

Babul et al. (2013) argued that infalling clouds may form a thin accretion disk misaligned from the spin axis of the SMBH. In this case, the orientation of the disk would influence the direction of the emerging jet. Thin accretion disks are usually associated with radiatively efficient AGN with high accretion rates, such as quasars and Seyferts. By contrast, radiatively inefficient radio galaxies, which are common at the center of galaxy groups and clusters, are more likely powered by geometrically thick accretion flows with a low accretion rate (Ghisellini and Celotti, 2001). We also note that our analysis in Sect. 6.6.3 suggests that the change in jet position angle over time is more likely to be nearly orthogonal, rather than completely random between $0^\circ - 90^\circ$. This is reminiscent of X-shaped radio galaxies, where the Bardeen – Petterson mechanism (Bardeen and Petterson, 1975) may cause orthogonal reorientation of the jets (Liu, 2004). However, X-shaped radio galaxies are preferentially high accretion rate AGN (e.g., Garofalo et al. 2020; Giri et al. 2022).

The question thus arises whether the systems with reoriented jets can have larger accretion rates, thus temporarily allowing the disk to influence the spin of the SMBH. To investigate this point, we derived the Eddington ratio of the systems in our sample. The Eddington ratio is defined as:

$$f_{\text{Edd}} = \frac{L_{\text{bol}}}{L_{\text{Edd}}}, \quad (6.5)$$

where L_{bol} is the AGN bolometric luminosity, and L_{Edd} is the Eddington luminosity. The latter is defined as:

$$L_{\text{Edd}} = 1.3 \times 10^{38} M[M_\odot] \text{ erg/s}, \quad (6.6)$$

where M is the mass of the SMBH (see Czerny and You 2016 for a review). The L_{bol} and L_{Edd} for the majority of the systems in our sample were retrieved from Mezcua et al. (2018), who used the 2 – 10 keV X-ray nuclear luminosity and a bolometric correction factor of 20 to estimate L_{bol} . For NGC 6338, NGC 5044, and 4C+55.16 the bolometric and Eddington luminosities were derived from the X-ray nuclear luminosity and black hole mass reported in Russell et al. (2013), respectively, adopting the same bolometric conversion factor of Mezcua et al. (2018). A similar method has been used to derive L_{bol} , L_{Edd} from the literature references of NGC 5098 (Randall et al., 2009; Arzoumanian et al., 2021) and IC 1262 (Bi et al., 2020; Arzoumanian et al., 2021). No useful data is available for CIG J1532+3021 and RX J1447.4+0827.

Fig. 6.6 (right panel) shows the largest degree of misalignment of each cluster or group in our sample versus the Eddington ratio. We find low levels of accretion, $f_{\text{Edd}} \leq 10^{-3}$, for all the AGN, with an average of $\bar{f}_{\text{Edd}} = 1.5 \times 10^{-5}$. For comparison, the isolated X-shaped radio galaxies in Joshi et al. (2019) have $\bar{f}_{\text{Edd}} = 4 \times 10^{-3}$. Additionally, the systems in our sample with and without reoriented jets have similar accretion efficiencies.

Likely, the Eddington ratios we measure represent the *current* accretion efficiencies. Since the accretion rate can flicker over time (e.g., Schawinski et al. 2015; King and Nixon 2015), we may hypothesize that the AGN with reoriented jets have been highly accreting in the past, thus allowing the Bardeen-Petterson effect to trigger the reorientation of the jets. While we cannot verify this hypothesis, the above result suggests that any high-accretion efficiency phase must have been short enough to allow the AGN to quickly transition back to a low-accretion efficiency phase (the one observed at present).

In this context, theoretical and computational works have argued that the radiatively inefficient, geometrically thick disk (ADAF-like, Narayan and Yi 1995) in the core of cluster and group-central galaxies may be fed by individually infalling molecular clouds, whose angular momentum varies over time (e.g., Gaspari et al. 2017a; Soker 2022). These parcels of cold gas may temporarily boost the accretion rate (e.g., Gaspari et al. 2017a).

For completeness, Lalakos et al. (2022) showed that during the first phases of AGN activity the jets can naturally experience intermittency and fast (down to 10^{-2} Myr) changes in orientation. This

may explain the formation of radio galaxies with a complex morphology, where nearly orthogonal outbursts are separated by a relatively small time difference (see e.g., X-shaped radio galaxies, Liu 2004, or the perpendicular, equidistant, and nearly coeval pairs of X-ray cavities in RBS 797, Ubertosi et al. 2021b and Chapter 3). However, the timescales shown in Fig. 6.6 (left panel) do not reflect a rapid flickering of jet direction in the first ~ 1 Myr of AGN activity, before stabilizing to a collimated and stable structure. Indeed, in NGC 5044 there are at least two aligned outbursts (with an age of ~ 13 Myr) that preceded the youngest, misaligned one (the one seen on VLBA scales), which indicates that flickering would have had to last at least an order of magnitude longer than the timescales explored in Lalakos et al. (2022). The same holds e.g., for NGC 6338, and likely for Abell 2390 (note that although there are no estimates of the X-ray cavity ages in this system, the 100 kpc – scale bubbles O1 and O2 are plausibly older by 10 – 100 Myr than the current radio jet - see also Alcorn et al. 2023).

Therefore, if jet reorientation in cluster and group-central galaxies is driven by a temporary phase of high accretion efficiency, this phase must be short lived. Babul et al. (2013) and Garofalo et al. (2020) estimated that the quasar-like phase should last a few Myrs to allow any appreciable changes in the jets direction. This is a reasonable timescale for most of the AGN in our sample, for which the cavity ages shown in Fig. 6.6 (left panel) are larger than $\sim 5 - 10$ Myr.

However, NGC 5044 is an exception. The difference in time between the two most recent outbursts in NGC 5044 is of ≤ 1 Myr, meaning that the thin disk phase in this system should have lasted only a few $10^4 - 10^5$ yr (see also Schellenberger et al. 2021). Thus, it is possible that other scenarios apply to this peculiar system. For example, McKinney et al. (2013) showed that while the innermost region of a thick accretion flow remains aligned with the BH spin axis over time, the outer accretion flow can be tilted by a large angle. This outer thick disk can gradually push away and deflect the jet, which can eventually bend by up to 90° and continue to propagate orthogonal to the SBMH spin axis. Such deflection occurs at 100 gravitational radii (r_g), and by $300 r_g$ the orthogonal deflection is completed. For typical black hole masses of $10^8 - 10^{10} M_\odot$, the above scale of $300 r_g$ corresponds to $0.001 - 0.1$ pc. For the lowest redshift system in our sample, NGC 5044 (black hole mass of $2 \times 10^8 M_\odot$ and $1'' = 150$ pc, see Schellenberger et al. 2021), resolving such scales with radio observations would require a resolution of ≤ 0.5 mas. If any outer thick disk is deflecting the jets in NGC 5044, this can only be confirmed with radio observations that have a resolution of an order of magnitude higher than those currently available.

Besides NGC 5044, this scenario may apply to all of the systems in our sample with misaligned jet-cavity pairs. However, we are unable to pinpoint the mechanism that can exhaustively explain the observed properties of the jet reorientation mechanism: the re-alignment of the jets can be fast (down to ≤ 1 Myr) and nearly orthogonal changes in position angle seem favored. If any temporary highly-efficient accretion phase has driven jet reorientation in the past, it must have been rather short lived (\leq a few Myr). The solution may be provided in the future by models, simulations and observations that can account for the properties of AGN outbursts on scales that span several orders of magnitude (between 10^{-4} pc to 10^4 pc).

6.7 Conclusions

In this Chapter we presented the analysis of VLBA and *Chandra* data of 16 cool core galaxy clusters and galaxy groups, to understand how common jet and cavities misalignments are and which causes may be responsible for such mismatch. Below we report our main findings.

- For each system we measured the jet position angle ($\Phi_{\perp\text{LOS}}$) and the cavity position angle (Θ_{cav}) in the plane of the sky. Using the full sample and selected subsets, we found that between 30% to 38% of the jet-cavity pairs are misaligned by more than $\Delta\Psi = \Phi_{\perp\text{LOS}} - \Theta_{\text{cav}} = 45^\circ$.
- By measuring the jet inclination angle along the line of sight ($\Phi_{\parallel\text{LOS}}$) we determined that projection effects may bias our measurement of $\Delta\Psi$ in around half of the sample. Restricting the

analysis to the AGN whose jets lie in the plane of the sky, we still found a fraction of $\sim 30\%$ of misaligned systems, supporting the above conclusions.

- We retrieved information on the dynamical state of the host clusters and groups, finding that all are examples of disturbed systems. Even though we cannot exclude that gas motions may have perturbed X-ray cavities away from their original trajectory in some systems, the ubiquity of disturbances excludes the possibility that a perturbed environment plays the major role in producing large misalignments.
- The distribution of $\Delta\Psi$ appears to be the combination of a Gaussian centered at 0° with $\sigma = 27.6^\circ \pm 1.6^\circ$ plus a peak around $\Delta\Psi \sim 75^\circ$. We conclude that, at 2.5σ significance, large misalignments are favored over small ones.
- By considering the age of the X-ray cavities, we find that larger misalignments ($\Delta\Psi > 75^\circ$) do not occur on longer timescales, with the shortest time difference being around 1 Myr in NGC 5044. Considering our findings and reviewing previous literature results, we cautiously propose that in addition to the spin axis of the SMBH, the geometry of the accretion flow may influence the direction of jet propagation.

Chapter 7

Thesis Conclusions

Jetted SMBH activity plays a crucial role in shaping the properties of the hot diffuse gas at the heart of galaxy clusters and groups. By inflating X-ray cavities and driving shocks into the medium, radio galaxies can quench cooling of the gaseous halo of their host elliptical galaxies, suppressing star formation and self-regulating their life-cycle. This picture has been developed observationally and numerically over the last thirty years and is now well established. However, it is still affected by a number of uncertainties regarding how the feedback operates in detail. These include: the connection between the pc scales, where the active SMBH resides and relativistic jets are launched, and the kpc scales, where the evidence of mechanical feedback appears; the thermodynamic conditions that onset feedback; the timescales of the ICM/AGN coupling and the mechanism through which mechanical feedback can balance cooling.

In this Thesis, we observationally tackled the different drivers, stages, and outcomes of the feeding and feedback cycle. Our multi-frequency perspective was mainly based on the synergy between high-resolution (sub-arcsecond) X-ray and radio data. The most relevant results presented in this Thesis are outlined below.

Novel insights on the triggering of AGN feedback

For the first time, we investigated the thermodynamic properties of the ICM in galaxy clusters where feedback is just about to start ([Chapter 2](#)). Using *Chandra* and MUSE observations, we probed the hot (10^7 K) and warm (10^4 K) gas phases in two cool core galaxy clusters hosting a newly-born radio galaxy at their center. We found that the average ICM entropy and cooling time in the inner 20 kpc of these “pre-feedback” clusters fall a factor of 2 below those of typical galaxy clusters with full-fledged radio galaxies. *This is a striking result, favoring the idea that gas cools twice more rapidly in the absence of feedback. Moreover, the difference between the entropy of the hot atmospheres of young and mature radio galaxies traces the amount of energy requested to compensate cooling.* In particular, we estimated that the entropy of pre-feedback clusters could be boosted to match that of mature-feedback ones by injecting an energy of $\Delta E \approx 10^{59-60}$ erg. With a mechanical power of the two young radio galaxies of $10^{44} - 10^{45}$ erg s^{-1} , such energy injection may be achieved in a few tens of Myr, a typical timescale for AGN activity in galaxy clusters.

Furthermore, our analysis of the MUSE data provides new constraints on the properties of the warm gas phase in cool core clusters. We detected warm filaments of gas around the BCG of the two pre-feedback clusters. Interestingly, the spatial extent and kinematics of the line-emitting gas in pre-feedback clusters (20 – 40 kpc, $\sigma_v \sim 115$ km s^{-1}) are similar to those observed in mature-feedback objects (10 – 60 kpc, $\sigma_v \sim 110$ km s^{-1}). *Since the properties of the hot gas vary between pre- and mature-feedback clusters but the properties of the warm gas do not, it may be possible that the time evolution of the warm and hot gas phases is different.* Additionally, the warm gas filaments cannot have originated only from local instabilities induced by uplift around or in the wake of X-ray cavities (e.g., McNamara et al. 2016), as feedback is (yet) absent in the two systems. Rather, new filaments condense out of the ICM at each cooling episode. With the upcoming approved *Chandra* program (200 ks) we will test these results in three additional pre-feedback clusters.

The galaxy cluster RBS 797: an exemplary case of the jet feedback paradigm

Using the deepest to date, dedicated *Chandra* observation of RBS 797 (427 ks), we detected a plethora of feedback footprints in the X-ray emission of the ICM (Chapter 3). The cluster hosts two perpendicular and equidistant pairs of X-ray cavities at ~ 30 kpc from the center. Additionally, we discovered three nested shock fronts driven by the AGN activity, found at projected distances of 50 kpc, 80 kpc and 130 kpc from the center, with Mach numbers in the range 1.2 - 1.3. *This discovery makes RBS 797 the first cluster where three concentric shock fronts have been detected. This is remarkable, as it provides a unique window to study repetitive shock heating in massive galaxy clusters.* In this context, we find that the total energy required to drive the shocks in RBS 797 is roughly 6×10^{61} erg. The average mechanical power remains notably stable over 80 Myr of jet activity, with the AGN driving every 20-30 Myr a weak shock with power $P_{\text{sh}} \approx 10^{46}$ erg s $^{-1}$.

Additionally, the *Chandra* data provided a clean view of the central 50 kpc, where the inner cocoon shock surrounds the four perpendicular and equidistant X-ray cavities. These bubbles have uplifted central enriched gas to an altitude of 30 – 50 kpc, as well as likely promoted condensation in their wakes (where the hot gas with the shortest cooling time (~ 440 Myr) and minimum $t_{\text{cool}}/t_{\text{ff}}$ ratio (~ 18) is spatially associated with filamentary patches of [O II] nebular emission). A remarkable result based on the X-ray data was that the four perpendicular and equidistant X-ray cavities have similar dynamical ages (around 30 Myr old), and with an age difference between the two outbursts smaller than ~ 10 Myr. This relatively short outburst interval may be explained either by a coeval activity of active binary SMBHs, or by a rapid reorientation of the jets from a single AGN.

Complementing the deep *Chandra* data, the large collection of radio data at different frequencies allowed us to fulfill a key request of feedback studies, that is bridging the pc and kpc scales of jet activity (Chapter 4). Specifically, the LOFAR and JVLA data confirmed the co-spatiality of the radio lobes with the perpendicular X-ray cavities. Most importantly, we obtained an independent confirmation of the coeval origin of the X-ray cavities from the radiative age of the corresponding radio lobes. Our work adds up to the handful comparisons between radiative ages and X-ray dynamical timescales of radio lobes and corresponding X-ray cavities (see Biava et al. 2021 and Kolokythas et al. 2020), and *for the first time, we found that the radio lobes, the X-ray cavities, and the associated weak shock front all have consistent ages down to only a few Myr of uncertainties. This represents a critical test for the AGN – ICM connection.* We further leveraged the radio data to perform a morphological, spectral and dynamical analysis of jet precession between sub-kpc and a few kpc scales. This allowed us to confirm important theoretical predictions on (a) the dynamics and radiative ageing of electrons in the jet hotspots, and (b) the variation over time of the spectral injection index, possibly linked to a FR I to FR II transition.

Taken together, these results are consistent with the idea that binary active SMBHs powered the perpendicular X-ray cavities in the past, and are responsible for the observed jet precession. We tested this idea by using the VLBI observations of the radio heart of RBS 797, which complete the multi-scale picture. These revealed a single active core at pc scales, with hints of time variability. We stress that the detection of a single component in the VLBI data is still consistent with the above binary interpretation: the separation of the binary SMBHs predicted by the observed jet precession (0.6 pc) is an order of magnitude smaller than the resolution of the available radio data (5 pc).

Therefore, our deep and dedicated analysis of the galaxy cluster RBS 797 has yielded unprecedented insights into shock and X-ray cavity heating, repetitive feedback, jet reorientation and precession, and duty cycle. It also underlined the critical need for deep, high resolution observations, required to connect the fine structure of jets in radio galaxies with the complex structure of their hot atmospheres.

The effect of different jet power regimes on feedback in cool cores

By exploring the diverse regimes of jet power, we evaluated the feedback efficiency of FR I and

FR II radio galaxies, while simultaneously investigating the impact of small-sized jets from the newly unveiled FR 0s on their host gaseous halos (Chapter 5).

We built a sample of 15 galaxy clusters and groups where both shocks and X-ray cavities were detected. *For the first time, we showed that not only the X-ray cavity power, but also the shock power scales with the radiative losses of the hot gas over five orders of magnitude.* Our analysis supports the idea that the whole feedback output of cluster-central AGN is set in response to the strength of ICM cooling. Interestingly, we observed that the cluster-central FR IIs in our sample have a total mechanical power that can exceed by a factor of ~ 100 the radiative losses of the surrounding atmosphere, compared to the factor of 1 – 10 of FR Is. This dichotomy becomes more evident when massive systems (clusters) are distinguished from smaller systems (groups and elliptical galaxies). However, we also find that the central entropy of systems hosting FR Is is consistent with that of systems hosting FR IIs, implying that *differences of orders of magnitude in feedback output do not over-heat the central gas.* *This argument favors the idea that the thermodynamic properties of the ICM are resilient to episodic and overpowered outbursts.*

We also investigated the jet stability and feedback properties of a cluster-central FR 0 radio galaxy in the galaxy cluster Abell 795. We confirmed that the hot gas around this FR 0, which shows typical thermodynamical properties of cool core clusters, cannot have hampered the jet propagation; an intrinsic jet weakness is likely required to explain the inability of the radio galaxy to grow to large sizes. Moreover, our tentative detection of X-ray cavities in the cluster atmosphere – if confirmed – would be the first evidence that FR 0s can regulate the heating and cooling balance of their surroundings through mechanical feedback, similarly to the well known FR I and FR II radio galaxies.

The (mis)alignment between jets and X-ray cavities: clues on jet reorientation

Several past studies focused on individual systems to investigate peculiar mismatches between the position of X-ray cavities in the cluster or group atmosphere (on kpc scales) and the direction of the radio jet (on pc scales). To address this problem with a systematic approach, in Chapter 6 we conducted an investigation of jet – cavity alignment in a sample of 16 relaxed clusters and groups of galaxies, which provided important new results on the occurrence and driving mechanisms of changes in the orientation of relativistic jets.

We consistently found that there is a 30% – 38% chance to find a jet – cavity misalignment larger than 45° when observing a cluster/group with a detected jet and at least one cavity. Importantly, we confirmed that misalignments (a) cannot be explained only by projection effects, and (b) are not strongly favored by a dynamically perturbed cluster atmosphere. Specifically, sloshing (or merging) systems can host both aligned and misaligned jet – cavity pairs, supporting the idea that a perturbed environment does not play the major role in producing large misalignments.

Rather, changes over time of the jet direction are the favored mechanism to explain the observed mismatches. Furthermore, the analysis of the distribution of (mis)alignments revealed that 90° changes are favored, which may provide an important observational constraint on jet reorientation models. Considering our findings and reviewing previous literature results, we cautiously proposed that the effect of the accretion flow may contribute with the spin of the SMBH in setting the direction of the outburst propagation.

Final remarks

The various aspects addressed in this Thesis represent a step forward in the understanding of the AGN feedback loop in massive structures. Based on our results, we emphasize the importance of the *timescales* of the different processes to interpret the drivers, stages, and outcomes of the jet – hot atmosphere coupling. The concept of *feedback loop* is grounded in a succession of numerous intertwined processes, such as gas cooling, multi-phase condensation, SMBH activation, heating regulation, repetitive jet activity. Yet, these processes are regulated by very different timescales.

Within a typical cooling timescale of the central ICM (a few 10^8 yr), there is room for several AGN outbursts (lasting between 10^6 yr and 10^7 yr), with each one potentially stimulating additional gas condensation. The varying directionality and power of successive outbursts, in turn, reflect faster processes occurring on sub-kpc scales, related to the accretion flow and the central engine.

Our study of pre-feedback clusters (Chapter 2) confirmed the long-term predictions of the feedback loop paradigm, that over a few 10^8 yr without feedback the central entropy and cooling time decrease to half the value of systems where feedback is ongoing. But on shorter timescales, the AGN itself can manifest multiple cycles of activity (as in RBS 797, see Chapter 3 and Chapter 4). Between these successive phases, the jet direction may dramatically change (Chapter 6). Rather than “a feedback loop”, we may thus propose the idea of “loops within loops” as a more comprehensive interpretation of the heating/cooling balance in clusters and groups of galaxies.

To conclude, we note that the ability to accurately measure the timescales of feedback processes translates into the need of resolving small spatial scales. In this context, there is great potential for development in the radio band, where sensitive arrays with high spatial resolution will be available in the immediate future (e.g., the next generation VLA, LOFAR2.0, and the Square Kilometer Array). In the X-rays, there will be an unprecedented opportunity for discovery in terms of hot gas kinematics (with *XRISM* and *new Athena*), of X-ray cavity evolution at late times and of feedback at high redshift (with e.g., *AXIS*). However, it is likely that the sharp “eye” of *Chandra* will not be replaced in the near future, thus limiting our ability to spatially resolve the most energetic events of the Universe.

Appendix A

Methods to derive entropy and cooling time profiles of pre-feedback galaxy clusters

The profiles shown in Fig. 2.2 have been obtained by following a similar procedure to that adopted for the ACCEPT clusters, in order to enable a fair comparison. In particular, as reported in §2.3.2, the ICM temperature was directly measured from the spectra of concentric annuli with at least 1000 counts per bin. This requirement results in 11 annular rings for RX J1350+0940 (with a size of 3", 2.5", 2.8", 6", 8", 9", 12", 15", 20", 40", 50") and 5 annular rings for CLG J0242-2132 (with a size of 3.3", 3.6", 7", 25", and 110"). Instead, the density was determined by deprojecting a background-subtracted, exposure-corrected surface brightness profile extracted in the 0.5-2.0 keV band, with a bin size of 1.5" (3.5 kpc for RX J1350+0940 and 7 kpc for CLG J0242-2132). The deprojected profile was then converted to an electron density profile by providing the count rate and normalization of the spectrum in each annulus of the temperature profile (Eckert et al., 2011). The temperature profile was interpolated on the grid of the density profile, and the two quantities were combined to obtain the gas entropy and cooling time.

In the following, we present how different methods of deriving the ICM temperature and density (and, in turn, entropy and cooling time) return consistent result. As reported above, the temperature of the ICM has been measured from fitting the spectra from concentric annuli centered on the BCG with a deprojected thermal model. The electron density of the ICM can be determined not only by converting a deprojected surface brightness radial profile to a radial density profile, but also from the deprojected normalization of the spectra (see Ubertosi et al. 2021a for a comparison between the two methods). For the sake of clarity, we label the electron density derived from spectral fitting as n_e^{sp} and that obtained from surface brightness analysis n_e^{sb} . In the left panels of Fig. A.1 we show the comparison between the two density profiles for CLG J0242-2132 and RX J1350+0940, which are consistent with each other.

To obtain the entropy and cooling time of the ICM it is necessary to combine the temperature and density (Eq. 1.3 and Eq. 1.11). The combination of temperature and n_e^{sp} is straightforward, given that the two quantities have been derived from the same radial bins. The combination of temperature and n_e^{sb} requires to associate a temperature measurement to each of the – more refined – radial bins of the density profile. The temperature can be either (i) interpolated over the bins of the density profile (as reported in §2.3.2), or (ii) assumed to be constant within the radial range covered by the spectral bins. In the middle and right panels of Fig. A.1 we show the comparison between the different methods of deriving the entropy and cooling time radial profiles of the two clusters. The different methods are in good agreement with each other, supporting the results discussed in §2.3.2.

We note that CLG J0242-2132 is included in the ACCEPT sample, and was reported to have a larger central entropy than that we measure in our work. However, in Cavagnolo et al. (2009) the central point source was not excised, which resulted in the likely inclusion of non-thermal emission in the spectrum of the inner ~ 30 kpc, shifting the measured temperature to higher values. Indeed, in

Cavagnolo et al. (2009) the central temperature is reported to be ~ 4 keV, to be compared to our measurement (central source excised) of 2.6 keV.

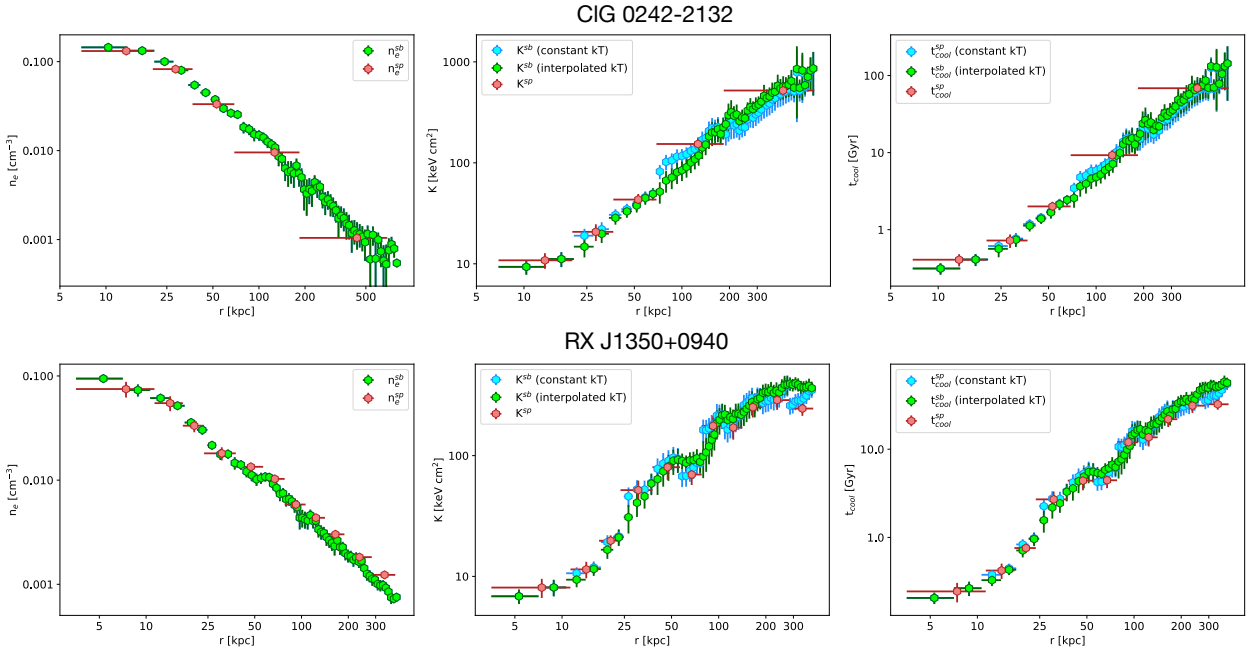


FIGURE A.1: Comparison between the profiles of density, entropy and cooling time obtained with different methods. Green corresponds to the profiles obtained with the method described in §2.3.2 and Appendix A; cyan was obtained by combining the density profile from the surface brightness profile with the temperature profile (without interpolating the temperature profile); red is obtained by combining the density and the temperature derived from spectral fitting.

Appendix B

Alternative methods to detect the N-S cavities in RBS 797

This Appendix shows alternative methods used to confirm the presence of N-S cavities in the ICM.

Elliptical sector

Figure B.1a shows a different choice for the sector used to study azimuthal variations of surface brightness. We used an elliptical region that encompasses the centers of the N-S cavities, crosses the terminal part of the E-W cavities and avoids the bright rims of the E-W cavities. The ellipticity and orientations were chosen to follow the elliptical structure of the cavity region, while the center matches that of Fig. 3.2a. Our starting hypothesis was that the elliptical symmetry could allow to define a proper reference surface brightness, in order to check whether the N-S depressions lie below an azimuthally symmetric *mean* surface brightness. Figure B.1b shows the resulting azimuthal study, with the cavity regions and reference regions coloured as in Fig. 3.2. We note that by using the same method defined in Sect. 3.3.1 to measure significance, thus selecting the immediate surroundings of each cavity as references, we obtain similar results to those that rely on circular symmetry. Moreover, we note that the elliptical sector does not provide azimuthal symmetry for the surface brightness. The surface brightness distribution is asymmetric: the whole N-W side of the cluster is brighter than the S-E side. This supports our hypothesis that the mean, being influenced by the large amount of structures in the ICM around the center (as discussed in Sect. 3.3.1), would not be good choice of reference surface brightness.

Projection regions

Following the method outlined in Vantyghem et al. (2014), we selected linear projections (one to the north and one to the south of the center, respectively) along a straight cut parallel to the axis of the E-W cavities (see Fig. B.1a). The N-S cavities correspond to 10% - 15% deficits w.r.t. the surrounding small rims (see Fig. B.1c). For comparison, Fig. B.1d shows the same method applied to the deeper E-W cavities (20% - 30% deficits w.r.t the surrounding bright rims). These results are consistent with those presented in Fig. 3.2.

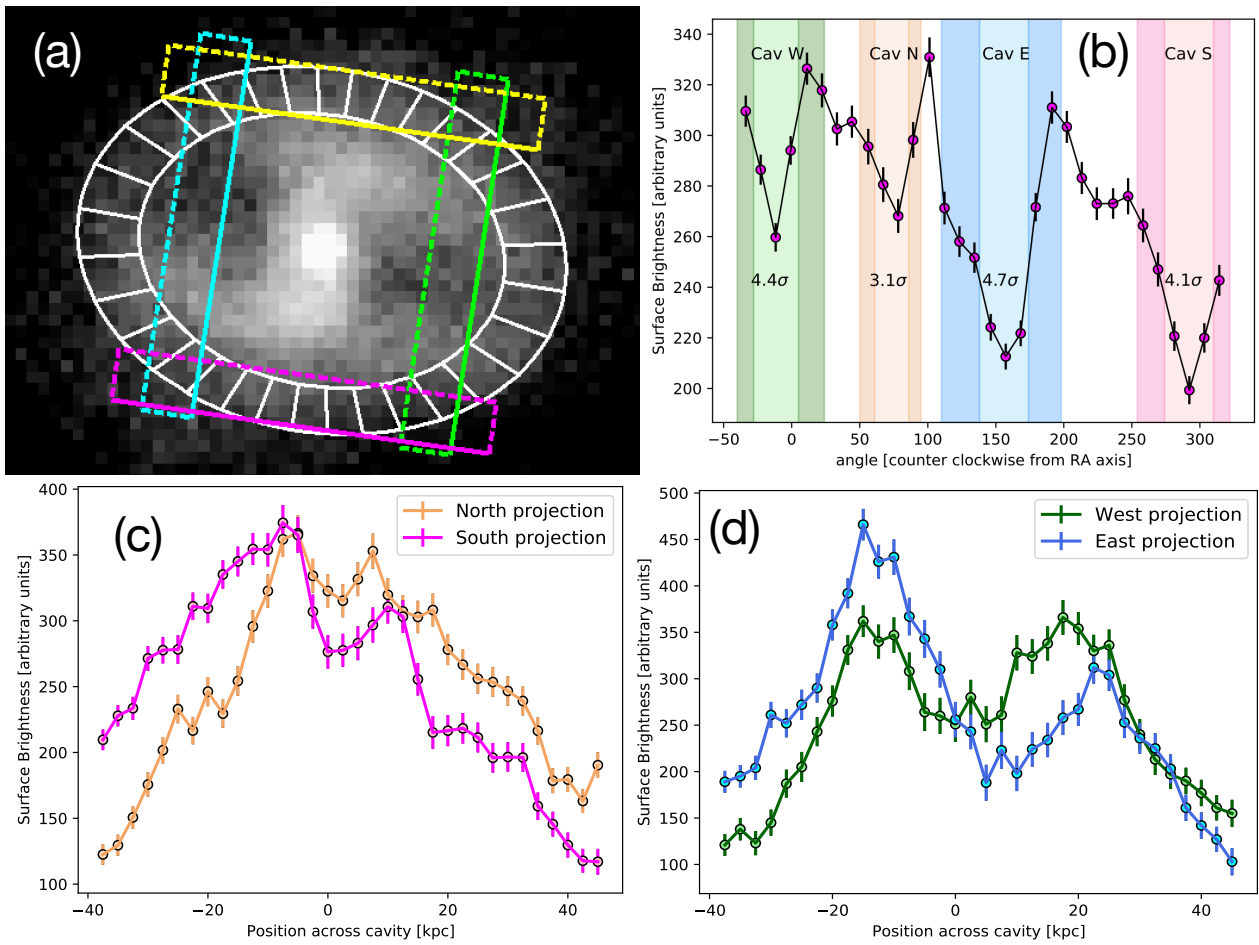


FIGURE B.1: (a) 0.5 - 7 keV band *Chandra* image of the core of RBS 797: white sectors used for the azimuthal analysis of panel *b* and projection regions used for the profiles of panels *c* and *d* are superimposed. (b) Azimuthal variation of surface brightness measured in the sectors of panel *a*. (c) Plot of surface brightness along the linear projections shown in panel *a* for the N-S cavities. (d) Plot of surface brightness along the linear projections shown in panel *a* for the E-W cavities.

Appendix C

Details on the morphological and spectral analysis of shocks fronts in RBS 797

In this Appendix we report the detailed results of the analysis of the shock fronts in RBS 797 (see Chapter 3). We show in Tab. C.1 the results of fitting surface brightness profiles encompassing each shock fronts with a broken power-law model and a power-law model. Furthermore, we summarize in Tab. C.2 the geometry of the sectors we used as spectral extraction regions (first three columns), the $\chi^2/D.o.f.$ (fourth column) and the best-fit parameters within the downstream and upstream side of the shock. The values of temperature and pressure are deprojected.

TABLE C.1: Analysis of the surface brightness profile of the shock fronts in RBS 797. For each edge, we report the best-fit parameters using a broken power-law (columns 2 - 7) and a single power-law (columns 8 - 11). The last two columns show the result of an F-test between the two models. The reported r_f refers to the distance along the major axis of the ellipse used to describe each edge (see Tab. C.2 for the geometric details). The normalizations S_0 are in units of 10^{-2} cts s^{-1} arcmin $^{-2}$. Corresponding surface brightness profiles are shown in Fig. 3.5.

Shock	Broken power-law						Power-law				F-test	
	α_1	α_2	r_f ["]	S_0	J	$\chi^2/d.o.f.$	α	r_s ["]	S_0	$\chi^2/d.o.f.$	F	p
S1	-0.31±0.08	1.35±0.05	11.0±0.1	4.1±0.2	1.49±0.07	13.2/7	2.14±0.02	18.0±1.0	0.14±0.01	195.1/20	59.3	1.2×10 ⁻⁸
S2	-0.23±0.09	1.63±0.07	10.3±0.2	5.1±0.6	1.40±0.06	6.6/4	1.99±0.02	16.8±0.6	0.13±0.01	176.7/19	51.6	6.0×10 ⁻⁸
S_{in}	0.71±0.05	1.36±0.03	10.7±0.1	3.3±0.2	1.29±0.03	14.4/8	1.67±0.01	2.5±0.1	4.8±0.2	353.9/10	94.0	2.8×10 ⁻⁶
S3	1.23±0.03	1.49±0.04	16.2±0.1	0.77±0.3	1.29±0.04	25.6/18	2.14±0.01	18.0±1.0	0.14±0.01	60.6/20	17.1	1.3×10 ⁻⁵
S4	0.26±0.09	1.64±0.05	16.7±0.2	0.94±0.01	1.28±0.05	10.1/10	2.10±0.03	7.2±0.1	0.69±0.07	127.5/12	58.1	3.1×10 ⁻⁶
S5	0.32±0.10	1.95±0.05	30.5±0.4	0.23±0.01	1.27±0.04	6.1/6	2.63±0.02	25.2±0.3	0.16±0.01	269.4/8	130	1.1×10 ⁻⁵
S6	0.01±0.09	1.39±0.04	28.9±0.2	0.69±0.03	1.37±0.04	24.3/15	2.05±0.02	19.2±0.6	0.38±0.02	193.4/17	52.2	1.8×10 ⁻⁷

TABLE C.2: Spectral analysis of three pairs of surface brightness edges in RBS 797. (1) Name of the edge and distance from the center (measured from the front mid-aperture); (2) ellipticity and position angle of the sector used as spectral extraction region; (3) angular range intersecting the position of the edge; (4) $\chi^2/d.o.f.$; (5) side of the edge (within - downstream, outside - upstream); (6-7) inner and outer radius of the annular sector (along the major axis of the ellipse); (8) deprojected ICM temperature; (9) deprojected ICM pressure.

Shock	Ellipticity (P.A.)	$\theta_1 - \theta_2$	$\chi^2/D.o.f.$	Side	R_i [kpc (")]	R_o [kpc (")]	kT [keV]	p_{ICM} [10 ⁻¹⁰ erg cm ⁻³]
S1 (53.9 kpc)	1.2 (345°)	130° - 190°	0.97	downstream	45.6 (9.3)	53.9 (11)	8.9 ^{+0.9} _{-0.8}	12.9 ^{+1.2} _{-1.1}
				upstream	53.9 (11)	63.7 (13)	6.6 ^{+0.7} _{-0.7}	7.1 ^{+0.7} _{-0.7}
S2 (50.5 kpc)	1.2 (345°)	310° - 15°	1.08	downstream	40.2 (8.2)	50.5 (10.3)	5.4 ^{+0.4} _{-0.3}	9.8 ^{+1.0} _{-0.9}
				upstream	50.5 (10.3)	68.6 (14)	4.8 ^{+0.2} _{-0.2}	6.5 ^{+0.6} _{-0.6}
S_{in} (52.4 kpc)	1.2 (345°)	0° - 360°	0.98	downstream	44.1 (9)	52.4 (10.7)	5.9 ^{+0.4} _{-0.4}	10.1 ^{+0.7} _{-0.7}
				upstream	52.4 (10.3)	68.6 (14)	5.0 ^{+0.2} _{-0.2}	5.4 ^{+0.3} _{-0.3}
S3 (79.4 kpc)	1.1 (20°)	200° - 270°	0.97	downstream	63 (12.8)	79.4 (16.2)	7.9 ^{+0.8} _{-0.8}	6.3 ^{+0.7} _{-0.7}
				upstream	79.4 (16.2)	108 (22)	6.4 ^{+0.3} _{-0.4}	3.8 ^{+0.3} _{-0.3}
S4 (81.8 kpc)	1.1 (20°)	45° - 110°	0.91	downstream	63.7 (13)	81.8 (16.7)	6.7 ^{+0.6} _{-0.6}	6.3 ^{+0.6} _{-0.6}
				upstream	81.8 (16.7)	118 (24)	5.4 ^{+0.4} _{-0.4}	2.7 ^{+0.2} _{-0.2}
S5 (136 kpc)	1.1 (102°)	140° - 252°	1.03	downstream	113 (23)	149 (30.5)	9.5 ^{+1.7} _{-1.6}	2.7 ^{+0.4} _{-0.4}
				upstream	149 (30.5)	226 (46.2)	6.9 ^{+0.8} _{-0.8}	1.4 ^{+0.2} _{-0.1}
S6 (132 kpc)	1.1 (102°)	304° - 87°	0.99	downstream	102 (21)	142 (28.9)	8.3 ^{+1.7} _{-1.2}	2.9 ^{+0.8} _{-0.5}
				upstream	142 (28.9)	216 (44)	5.9 ^{+0.7} _{-0.7}	1.3 ^{+0.2} _{-0.2}

Appendix D

VLBI observations of RBS 797: notes on the previous EVN – RSG05 observation

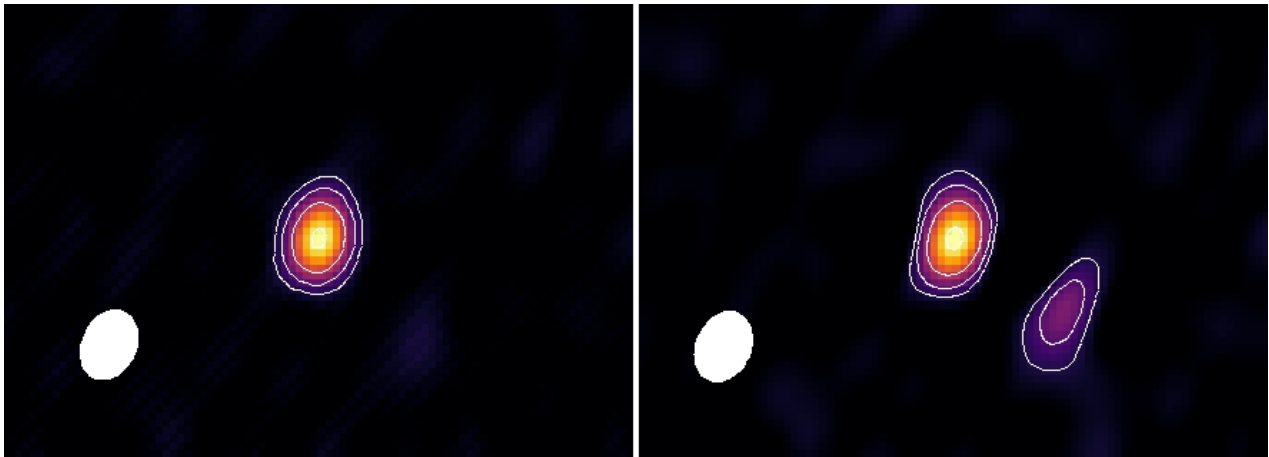


FIGURE D.1: Comparison between the images obtained with (left) or without (right) using an image model for the phase calibrator J0954+7435 during fringe fitting. Contours are drawn at $3\sigma_{\text{rms}}$ and increase by a factor of 2. The beam is shown in the bottom left corner. See Tab. 4.2 for the σ_{rms} noise level and resolution of the image. See text for details.

Gitti et al. (2013) presented the results of a snapshot EVN observation of RBS 797 (Project ID RSG 05). The image at 5 GHz revealed two compact components separated by ~ 77 pc, with the faintest component located south-west of the brightest one. The analysis additionally revealed both components to be unresolved. Two interpretations were proposed: the two components may either be binary SMBHs or a single SMBH and a jet knot.

As reported in §4.2.1 (Chapter 4), we found no evidence of the fainter component in the new deeper VLBA and EVN observations at multiple frequencies. To solve this mismatch, we re-analyzed the RSG 05 EVN data (see §4.2.4 and Tab. 4.1, 4.2). The calibrator J0954+7435 was used as phase calibrator. We found that supplying an image model of the calibrator during fringe-fitting is crucial: since J0954+7435 is resolved into a double component, assuming a point source as a model for fringe-fitting results in a bad description of rate and delays. In support of this, we show in Fig. D.1 a comparison between two images of RBS 797 obtained from the RSG 05 data. The left image was obtained by supplying an image model of J0954+7435 during fringe fitting, while the right image is based on a point source model of the phase calibrator. We note that the right image is fully consistent with the image shown in Gitti et al. (2013), while the left image shows a single component at the phase center, which is in agreement with the results from the deeper VLBA and EVN observations (see Fig. 4.7).

Overall, we conclude that the most likely explanation for the absence in the new VLBI data of the

fainter component identified in Gitti et al. (2013) is that the component was an artifact caused by the unfortunate “double component” nature of the phase calibrator itself.

Appendix E

Alternative methods to measure jets position angles on VLBA scales

In this Appendix we show the two other methods we adopted to measure the position angle of the jets in a plane perpendicular to the line of sight (see [Chapter 6](#)).

- *Largest linear size*: we filtered the VLBA images to exclude all the pixels with a flux density lower than $5\sigma_{\text{rms}}$. Then, we computed the distance of each pixel from all the others. The two most distant pixels set the largest linear size of the radio source. The jet position angle is thus measured as the slope of the line that connects the two most distant pixels. The uncertainty on the position angle is the relative angular width of the beam with respect to the linear size, meaning that larger sources have smaller relative uncertainties. A potential weakness of this method is that in radio images the pixels are usually not independent, as the real resolution element is the beam, not the individual pixel. Local substructures (smaller than the beam) may generate large differences in position angle for small differences in distance between adjacent pixels.
- *Fitting the radio image*: assuming that in the simplest configuration a core+jet morphology can be described as a straight line connecting two points (the core and the jet), we fitted the coordinates of the pixels (above $5\sigma_{\text{rms}}$) in the VLBA images with a straight line, thus treating the image as a scatter plot. Following this analogy, the jet position angle is the slope of the best-fit linear regression. During fitting, the pixels were weighted by their flux densities. Again, a potential weakness is that the pixels are not independent (there is the effect of the beam). Additionally, the assumption of a single line describing a core+jet morphology may not be accurate for highly resolved sources.

In [Fig. E.1](#) we show the comparison between the *Largest linear size*, the *Fitting the radio image*, and the DIFMAP methods. Reassuringly, we find that the three methods provide consistent results. We note that the scatter of the points around the bisector of the plot is smaller than the errorbars: this is likely caused by the relatively large uncertainties that we assigned to the *Largest linear size* and the *Fitting the radio image* methods being conservatively overestimated. We decided to continue the analysis with the DIFMAP results because of its advantages: first, the beam shape is taken into account when fitting components to the visibilities; second, the DIFMAP method does not rely on cleaned images where pixel-scale artifacts may be present, as it works in the uv-domain.

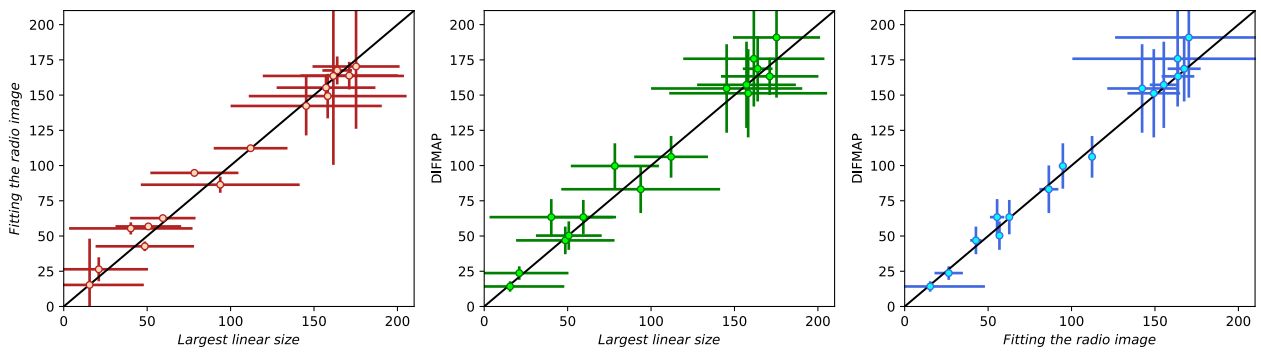


FIGURE E.1: Comparison between the three methods we tested to measure the position angle of the radio jet in the plane of the sky ($\Psi_{\perp\text{LOS}}$). In the three panels, the black line represents the bisector of the plot and not a fit to the points. See [Appendix E](#) for details.

Appendix F

Insights on the jet position and inclination angles from VLBA data at other frequencies

Three sources in the sample presented in Chapter 6 are VLBA calibrators¹, meaning that there are archival snapshot observations at multiple frequencies other than 5 GHz. These are 4C+55.16 (2.3 GHz and 7.6 GHz), RXC J1558.3-1410 (2.3 GHz and 8.7 GHz), and Abell 3581 (8.7 GHz). We used the archival observations of these three systems to validate our method of measuring $\Phi_{\perp\text{LOS}}$ from the 5 GHz maps. In practice, we applied the same fitting procedure in DIFMAP described in Sect. 6.4. The left panel of Fig. F.1 shows the results. It is clear that our measurements of $\Phi_{\perp\text{LOS}}$ are consistent between the different frequencies, thus strengthening our results. Radical changes in jet position angle with frequency are known (e.g., Issaoun et al. 2022), but these are typically found when not only the frequency but also the observed spatial scales change (e.g. from the parsec to the tens of parsecs scales). As the VLBA data at different frequencies probe relatively similar scales, it is likely that the observations used in this work do not suffer from this effect.

It is interesting to discuss the case of RXC J1558.3-1410, which unveils a limitation of our work in terms of angle w.r.t. the line of sight, $\Phi_{\parallel\text{LOS}}$. For this AGN, the data at 8.7 GHz reveal a bright, unresolved component (labeled 'C') that is undetected at 5 GHz (see Fig. F.1, right panel). If this component was a knot of the jet with a relatively steep spectral index ($\alpha \leq -0.5$), it should have been detectable at 5 GHz. Its non-detection suggests that it may be characterized by an inverted spectral index ($\alpha \geq 0$), which is typical of the synchrotron self-absorbed cores of compact radio sources (e.g., Sadler 2016). While from the 5 GHz data alone we identified the core of the AGN as the brightest component, it is likely that the true core is located, in fact, between the two components detected at 5 GHz. While this is not an issue when measuring $\Phi_{\perp\text{LOS}}$, as the whole structure remains aligned, it biases our measurement of $\Phi_{\parallel\text{LOS}}$. Indeed, using the 5 GHz data alone we would misclassify the jet and the counter-jet in this system. Component A in the 5 GHz map, previously classified as the core, has to be considered as the jet, while component B, previously classified as jet, is in fact the counter-jet. Incidentally, for RXC 1558.3-1410, the old and new $\Phi_{\parallel\text{LOS}}$ remain consistent with each other (changing from $39.8^\circ \pm 11.8^\circ$ to $25.1^\circ \pm 6.7^\circ$). However, this system highlights a limitation that may affect our measurements of $\Phi_{\parallel\text{LOS}}$, especially for one-sided sources. We verified the absence of an hidden core in all the other objects of our sample with available archival data at high frequency. For the remaining one-sided sources in our sample (CIG J1532+3021, Abell 478, Abell 1664, NGC 6338, IC 1262, and NGC 5098) no data at other frequencies exist, but we plan to observe them with deeper and multi-frequency VLBA observations in the future.

Ultimately, we note that we are currently unable to measure the spectral index of the different components, which would benefit their classification as jets or core. The available multi-frequency data were not acquired close in time, meaning that flux variability at parsec scales could strongly

¹<https://obs.vlba.nrao.edu/cst/>, Charlot et al. (2020).

bias the results of any spectral index study. Obtaining coeval multifrequency observations of our sample is a future perspective of this work.

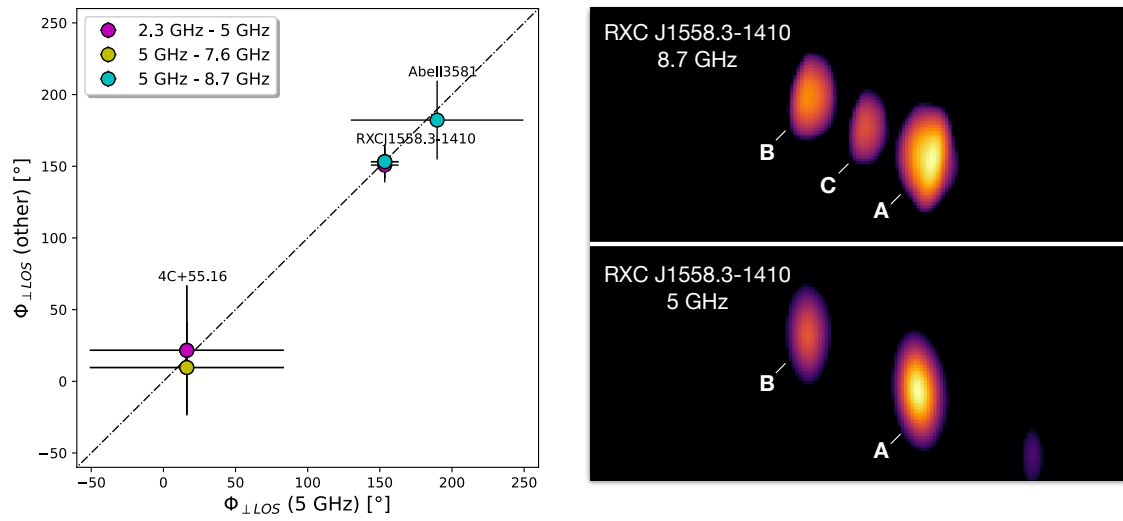


FIGURE F.1: *Left panel*: comparison between $\Phi_{\perp\text{LOS}}$ at 5 GHz and $\Phi_{\perp\text{LOS}}$ measured at other frequencies for the sources in our sample that are VLBA calibrators. The dashed line shows the $y = x$ bisector. *Right panel*: VLBA images of RXC J1558.3-1410 at 8.7 GHz and at 5 GHz. The components identified in DIFMAP are labeled.

Appendix G

RXC J1558.3-1410: X-ray morphological analysis

As reported in [Chapter 6](#), RXC J1558.3-1410 lacks a dedicated X-ray study of the ICM morphology. To verify the existence of X-ray cavities in this system, we inspected both the *Chandra* 0.5 – 2 keV counts image and the residual image. In both of them, a depression in surface brightness is visible east of the center (see [Fig. G.1](#)). The depression is nearly circular, and it is located at $\sim 20'' = 36$ kpc from the center. The signal-to-noise ratio (SNR) of this feature was measured in the *Chandra* counts image by comparing the number of net counts within this region, C_c , with the average number of counts in similar regions with the same size at the same distance from the center, C_s , through the following expression:

$$\text{SNR} = \frac{|C_c - C_s|}{\sqrt{C_c + C_s}} \quad (\text{G.1})$$

For the depression shown in [Fig. G.1](#) (left panel) we measure a $\text{SNR} = 4.8$ (with $C_c = 892$ and $C_s = 1107$), which allows us to identify the feature as a reliable structure. Other depressions that are visible in the residual image do not represent statistically significant drops in the counts image (either they represent small deficits, around 5%, or the SNR is lower than 3). Furthermore, we note that based on archival VLA data at 1.4 GHz (see <http://www.vla.nrao.edu/astro/nvas/>) there is evidence for radio emission extended towards this depression. This supports the classification of the X-ray depression as an AGN-inflated cavity in the ICM.

We also note that on larger scales, the surface brightness distribution has a spiral morphology, with a bright edge west and south-west of the center (see [Fig. G.1](#), right panel). This is typical of clusters experiencing sloshing of the hot gas, which is thus likely present also in RXC J1558.3-1410. The spiral structure is wrapped around the cluster core, and is visible up to a distance of ~ 100 kpc from the center.

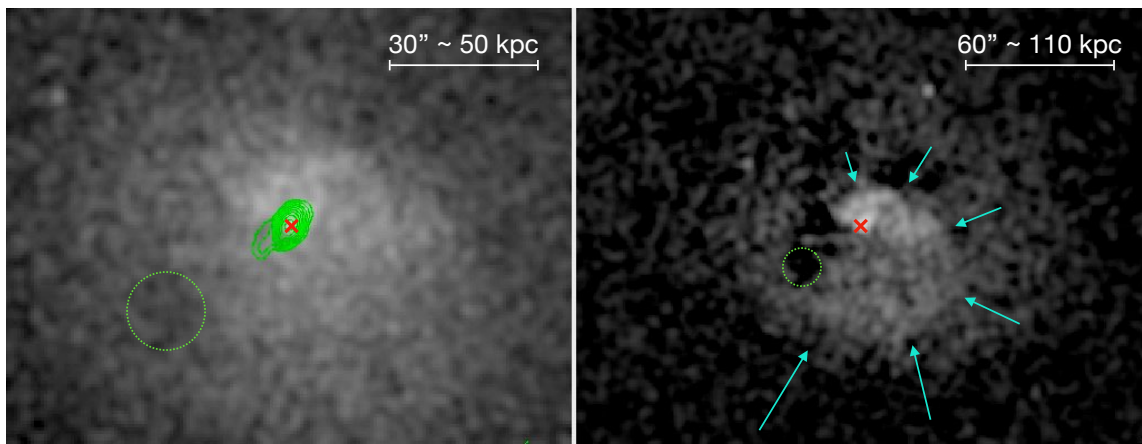


FIGURE G.1: *Chandra* images of RXC J1558.3-1410. *Left panel*: 0.5 – 2 keV counts image, smoothed with a Gaussian of kernel size $3''$. Green contours are the 1.4 GHz radio emission seen in archival VLA data, starting from $3 \times \sigma_{\text{rms}}$ (with $\sigma_{\text{rms}} = 0.4$ mJy/beam, resolution of $2''$) and increasing in steps of 2. *Right panel*: residual *Chandra* image, smoothed with a Gaussian of kernel size $5''$. Cyan arrows show the spiral morphology of the ICM. In both panels, the green dashed circle shows the identified X-ray cavity, while the red cross shows the position of the central AGN.

Appendix H

Results of fitting in DIFMAP the VLBA data of the 16 galaxy groups and clusters

In this Appendix we present the results of fitting the VLBA data for our sample of galaxy clusters and groups (see [Chapter 6](#)) in DIFMAP. [Tab. H.1](#) reports, for each object, the properties of the radio image shown in [Fig. 6.2](#) and the parameters of the components used to fit the visibilities in the uv-domain.

TABLE H.1: Properties of the VLBA images shown in Fig. 6.2 and results of fitting the visibilities in DIFMAP. (1) Name of the system; (2) size and position angle (from the north axis) of the restoring beam; (3) noise of the VLBA image; (4 – 10) DIFMAP results: label of the component, flux density, distance from phase center (polar coordinates), angle from the phase center (polar coordinates, with θ starting from the north axis), major semi-axis, axes ratio, orientation of the component (from the north axis). When $a = 0$ the component is a δ -function. When $b/a = 1$ the component is a circle. When $a \neq 0$ and $b/a \neq 1$ the component is an ellipse with orientation ψ .

* The radio map has been created by applying an uv-taper of $30 M\lambda$ to the visibilities.

Cluster	Beam, PA [mas \times mas, $^\circ$]	σ_{rms} [mJy/beam]	Comp.	Flux [mJy]	r [mas]	θ [deg]	a [mas]	b/a	ψ [deg]
Abell 2390	$3.5 \times 1.2, 0.6$	0.1	A	118	0.002	-160.2	0	1.0	-8.3
			B	7.6	4.68	178.6	1.2	1.0	0
			C	57.5	3.43	-7.0	0	1.0	0
			D	22.8	22.2	-24.1	14.9	1.0	0
ClG J1532+3021	$5.0 \times 1.4, 25.1$	0.05	A	6.2	11.40	108.5	0	1.0	0
			B	1.5	8.59	117.8	1.8	1.0	0
4C+55.16	$3.5 \times 1.7, 4.4$	5.0	A	2136	0.67	83.1	0	1.0	0
			B	1561	1.58	-64.3	8.4	0.37	-51.6
Abell 478	$4.0 \times 1.6, 11.4$	0.05	A	5.4	11.21	106.4	0.8	1.0	0
			B	0.9	14.28	117.6	0	1.0	0
RX J1447.4+0827	$3.2 \times 1.1, -6.0$	0.05	A	8.1	86.69	84.7	0.4	1.0	0
			B	5.6	86.11	83.2	0.6	1.0	0
			C	3.8	87.39	86.0	1.0	1.0	0
Abell 1664	$3.3 \times 1.0, -3.6$	0.05	A	9.5	500.45	144.5	0	1.0	0
			B	2.5	503.46	144.9	1.3	1.0	0
RXC J1558.3-1410	$3.5 \times 1.2, 0.5$	1.5	A	287	0.04	-24.0	1.2	1.0	0
			B	117	7.74	63.9	1.2	1.0	0
ZwCl 8276	$3.5 \times 1.2, -9.0$	0.08	A	72.8	0.11	-11.4	0	1.0	0
			B	5.6	1.67	-3.2	0	1.0	0
			C	15.7	1.09	174.8	0	1.0	0
Abell 496	$3.6 \times 1.2, 1.5$	0.06	A	44.3	69.49	29.3	0.7	1.0	0
			B	7.3	74.79	30.6	0	1.0	0
			C	5.3	62.84	28.5	0	1.0	0
ZwCl 235	$3.3 \times 1.2, -1.9$	0.07	A	16.0	65.54	-145.5	0.7	1.0	0
			B	3.6	64.36	-146.0	1.2	1.0	0
			C	5.3	66.63	-145.0	1.2	1.0	0
Abell 2052	$3.3 \times 1.2, 1.9$	1.7	A	267	0.03	72.6	0.6	1.0	0
			B	64.5	4.56	170.8	1.9	1.0	0
			C	57.5	4.06	-17.2	1.9	1.0	0
Abell 3581	$4.1 \times 1.2, 0.6$	0.3	A	99.2	0.04	-22.5	0.8	1.0	0
			B	128	0.34	58.5	4.8	1.0	0
			C	35.6	7.25	97.9	3.0	1.0	0
NGC 6338	$4.3 \times 1.3, -10.6$	0.1	A	19.9	0.09	1.8	0.8	1.0	0
			B	5.3	4.12	-155.8	3.1	1.0	0
IC 1262*	$5.3 \times 3.8, -11.9$	0.04	A	3.1	395.39	117.8	0.7	1.0	0
			B	0.3	397.27	118.9	4.2	1.0	0
NGC 5098	$5.0 \times 1.6, 15.5$	0.05	A	4.7	34.19	35.6	1.7	1.0	0
			B	1.1	33.12	39.2	0.7	1.0	0
NGC 5044	$3.9 \times 1.3, -4.4$	0.03	A	16.5	147.03	-67.8	1.9	1.0	0
			B	4.8	150.99	-70.5	6.6	1.0	0
			C	0.8	149.64	-64.5	0	1.0	0

Appendix I

Comments on individual galaxy clusters from the aligned/misaligned sample

In this Appendix we detail the individual properties of the galaxy clusters and galaxy groups in the sample presented in [Chapter 6](#).

Abell 2390: galaxy cluster at $z = 0.23$. The VLBA image shows a two-sided jet structure in the north-south direction, predominantly in the plane of the sky (consistent with Augusto et al. 2006). From the X-ray point of view, no unique view on the presence of cavities in this system is present in the literature. From a heavily smoothed and filtered image, Sonkamble et al. (2015) identified a total of 4 X-ray cavities surrounding the central AGN. From our re-analysis of the X-ray data (using all the three available ObsIDs) we find compelling evidence for the existence of one of the X-ray cavities identified by Sonkamble et al. (2015), west of the radio core. Additionally, there are large X-ray cavities east – west of the core, at a distance from the center of ~ 200 kpc (see Lima Neto and Ulmer 2011). These structures are filled by radio emission in the form of large lobes in LOFAR images (see Birzan et al. 2020). Between the two generations of X-ray cavities and the inner jets we find a misalignment of almost 90° , with projection effects playing at most a minor role.

CIG J1532+3021: galaxy cluster at $z = 0.362$ studied by Hlavacek-Larrondo et al. (2013a), who revealed the presence of sloshing motions and X-ray cavities. Two X-ray cavities are clearly visible east – west of the radio core in the *Chandra* image. The VLBA observations reveal a relatively faint source with a small one-sided jet west of the core, nearly aligned with the X-ray cavities.

4C+55.16: galaxy cluster at $z=0.242$. Hlavacek-Larrondo et al. (2011) discovered two X-ray cavities on opposite sides of the radio core. The authors noted a surface brightness edge, interpreted as a cold front, south of the cluster’s center. Whyborn et al. (1985) revealed a pair of radio lobes in the southeast – northwest direction, that coincide with the X-ray cavities. On VLBA scales we find resolved extended emission that is well fitted in DIFMAP by two components, that we identify as the core and a jet. Such interpretation is consistent with the EVN images at 5 GHz published by Whyborn et al. (1985). The northwest cavity is aligned with the radio jet, while the southeast one is misaligned. It is important to note that projection effects may be relatively important in this system, where $\Psi_{\parallel\text{LOS}} \sim 60^\circ$.

Abell 478: galaxy cluster at $z = 0.088$. Sun et al. (2003) and Giacintucci et al. (2014) reported the presence of small X-ray cavities in the north – south direction, and the disturbed state of the cluster. From the VLBA data we recover a one-sided source, misaligned by $\sim 35^\circ$ from the X-ray cavities. The source has a jet-counterjet ratio of roughly 6. Thus, projection effects may be important in this system. Overall, given the mild difference in P.A. between jet and X-ray cavities, and projection effects, it is unclear whether this system can be classified as aligned or misaligned.

RX J1447.4+0827: galaxy cluster at $z = 0.376$. The presence of small X-ray cavities and sloshing signatures in this object has been reported by Prasow-Émond et al. (2020). On VLBA scales, the source is clearly resolved in a two-sided structure oriented northwest – southeast. The jets are aligned with the cavities on larger scales, and the low jet – counterjet ratio (1.1) indicates that projection effects are likely negligible.

Abell 1664: galaxy cluster at $z = 0.128$. Calzadilla et al. (2019b), revealed the presence of two pairs of

X-ray cavities (the inner pair in the east – west direction, the outer pair in the southeast – northwest direction), and of a disturbed ICM. The VLBA data are difficult to interpret: there is extended, diffuse emission south of the brightest component, however its morphology is not straightforwardly reminiscent of a jet. By interpreting the radio source as a core + jet system, the position angle of the AGN jet is misaligned w.r.t. the cavities. The source is also apparently one-sided, with an angle w.r.t. the line of sight of $\sim 50^\circ$.

RXC J1558.3-1410: galaxy cluster at $z=0.097$. As no dedicated studies of the *Chandra* observations of this object exist in the literature, we analyzed the data (see [Appendix G](#)). We identify a cavity southeast of the AGN (the depression is significant at a signal-to-noise ratio of $\text{SNR}=6$). We also identify a positive residual spiral from the residual *Chandra* image, that we attribute to sloshing of the ICM. Archival VLA observations at 1.4 GHz reveal a jet feature headed towards the depression, supporting its cavity classification. Being a VLBA calibrator, this radio galaxy has multi-frequency coverage in the archive. An inspection of the 8.7 GHz observations reveals a two-sided source. Based on the 5 GHz observations only, the brightest component (A) may be misinterpreted as the radio core. However, the 8.7 GHz map reveals a third component left of the brightest one. This third component is likely the true core, self-absorbed (thus invisible) at lower frequencies (see [Appendix F](#) for details).

ZwCl 8276: galaxy cluster at $z = 0.076$. Several structures in the ICM support the idea that the cluster is experiencing sloshing (see [Ettori et al. 2013](#)); X-ray cavities (in the north – south direction) have been identified by [Ettori et al. \(2013\)](#). From our *Chandra* images, and guided by the recent LOFAR observations of this cluster ([Bîrzan et al., 2020](#)), we identify a third, outer and larger X-ray cavity northeast of the AGN. In the VLBA images there are compelling evidence for barely resolved north – south extensions, aligned with the inner X-ray cavities.

Abell 496: galaxy cluster at $z = 0.033$. Several studies have focused on the dynamical status of the ICM in this object, given the clear sloshing spiral visible in X-ray observations (e.g., [Roediger et al. 2012](#); [Ghizzardi et al. 2014](#)). However, no dedicated studies on AGN feedback in this system are available, despite the clear presence of multiple, aligned X-ray cavities in the northeast – southwest direction, coincident with extended radio emission from the central AGN (see [Giacintucci 2016](#); [Giacintucci et al. in prep.](#)). The VLBA data reveal a two-sided structure in the same direction, suggesting that over three cycles of radio activity the AGN’s jet axis has remained nearly constant. From the jet-counterjet ratio we exclude that projection effects play a major role.

ZwCl 235: galaxy cluster at $z = 0.083$. [Ubertosi et al. \(2023a\)](#) revealed two radio-filled cavities in the core of the cluster oriented in the northeast – southwest direction, and of a sloshing spiral wrapped around the core. The VLBA data unveil a two-sided radio source nearly aligned with the X-ray cavities, mainly in the plane of the sky.

Abell 2052: well-studied galaxy cluster at $z = 0.035$. The ICM in this object shows multiple X-ray cavities and shock fronts around the central AGN, signals of multiple outbursts of the radio galaxy (see [Blanton et al. \(2011\)](#) and references therein). The two pairs of X-ray cavities are roughly oriented in the north-south direction. The VLBA reveal a two-sided source extended in the north-south direction. The position angle of the jets is consistent with the results obtained from multifrequency imaging by [Venturi et al. \(2004\)](#). Overall, the jets and the cavities are roughly aligned in this system, where projection effects are likely negligible.

Abell 3581: galaxy group at $z=0.022$. [Johnstone et al. \(2005\)](#) and [Canning et al. \(2013\)](#) reported the presence of a sloshing ICM spiral wrapped around the core and two clear cavities east – west of the central AGN, filled by the radio lobes of the radio galaxy. A third X-ray cavity is found beyond the west cavity and roughly aligned with the inner pair. From the VLBA data (5 GHz and 8.7 GHz) we observe a strongly one-sided source, with a core-jet morphology in the east-west direction, in good agreement with the position of the X-ray cavities.

NGC 6338: merging galaxy group at $z=0.027$. The multifrequency study of this object has been carried out by [O’Sullivan et al. \(2019\)](#), who found radio-filled X-ray cavities in both groups. For our analysis we focus on the southern, larger subgroup, that has two inner X-ray cavities oriented

northeast – southwest, and at least one X-ray cavity on larger scales, west of the core (see also Bîrzan et al. 2020; Schellenberger et al. 2023). The VLBA data reveal a core + jet morphology. The source appears one-sided, although at a level of $3\sigma_{\text{rms}}$ (~ 0.4 mJy/beam) there are indications for a counterjet. The radio source is oriented northeast – southwest, thus being aligned with the inner X-ray cavities but misaligned w.r.t. the older, outer outburst.

IC 1262: galaxy group at $z = 0.033$. The hot gas in this object shows several substructures (ripples, edges and depressions). There are two inner X-ray cavities (oriented north – south) and an outer, larger X-ray cavity south of the center (see Pandge et al. 2019). The VLBA data reveal an extended feature south of the core, that is recovered only by tapering the visibilities during imaging. The position angle of the jet is in relatively good agreement with that of the inner and outer X-ray cavities.

NGC 5098: galaxy group at $z=0.036$. Randall et al. (2009) reported the presence of two X-ray cavities filled by radio emission and mainly oriented in the north – south direction. The group also shows signs of minor merger with a galaxy, that is causing sloshing of the IGrM. On VLBA scales we find a core dominated source with a small jet southeast of the core, nearly aligned with the X-ray cavities.

NGC 5044: well-studied galaxy group at $z=0.009$. Several works reported the presence of multiple X-ray cavities in the intragroup medium of this object, with the different pairs approximately aligned along the southeast – northwest direction (see Schellenberger et al. 2021 and references therein). The VLBA data reveal a two-sided core-jet structure rotated by $\sim 90^\circ$ with respect to the successive cavity pairs (see also Schellenberger et al. 2021). Based on the jet-counterjet ratio the inner jets, the difference in position angle of the jets and the cavities is real and not strongly influenced by projection effects.

Acknowledgements

As written in the quote at the beginning of this Thesis, when people come into our lives, they bring something we must learn, and we are led to those who help us most to grow. With these words, I would like to acknowledge the people who have helped me grow the most during these three years.

I sincerely thank my supervisor, Prof. M. Gitti, for her unwavering dedication to my training. I hope to have learned even a fraction of her invaluable attention to details. I am very grateful to my co-supervisor, Prof. F. Brighenti, for being a critical resource for astrophysical questions, and for always reminding me that not all questions have answers – perhaps not even many.

I am sincerely grateful to Dr. O’Sullivan, Dr. Schellenberger, Dr. Giacintucci, Dr. Vrtilek, Dr. David and all the people I had the pleasure of working with while visiting the Center for Astrophysics in Cambridge. Special mentions go to Dr. O’Sullivan and Dr. Schellenberger for the kind support and guidance that they continue to provide me in our collaboration.

Several other people deserve to be acknowledged for these three years of PhD studies. I want to thank Dr. M. Giroletti and Prof. A. Bonafede for their essential support with radio data analysis. I am grateful to G. V. Pignataro, for the numerous – and useful! – discussions on units of measurement in radio astronomy; to G. Campitiello, for teaching me how to be patient; and to Dr. A. Pensabene, for reminding me to hold on to what I believe to be important.

In the end, if I have changed the most, it is thanks to Villiam. For good.

Bibliography

- Abell, George O. (May 1958). "The Distribution of Rich Clusters of Galaxies." In: *The Astrophysical Journal Supplement* 3, p. 211. DOI: [10.1086/190036](https://doi.org/10.1086/190036).
- Alam, Shadab et al. (July 2015). "The Eleventh and Twelfth Data Releases of the Sloan Digital Sky Survey: Final Data from SDSS-III". In: *The Astrophysical Journals* 219.1, 12, p. 12. DOI: [10.1088/0067-0049/219/1/12](https://doi.org/10.1088/0067-0049/219/1/12). arXiv: [1501.00963](https://arxiv.org/abs/1501.00963) [astro-ph.IM].
- Alcorn, Leo Y. et al. (June 2023). "Extended line emission in the BCG of Abell 2390". In: *Monthly Notices of the Royal Astronomical Society* 522.1, pp. 1521–1534. DOI: [10.1093/mnras/stad948](https://doi.org/10.1093/mnras/stad948). arXiv: [2303.15557](https://arxiv.org/abs/2303.15557) [astro-ph.GA].
- Anders, E. and N. Grevesse (Jan. 1989). "Abundances of the elements: Meteoritic and solar". In: 53.1, pp. 197–214. DOI: [10.1016/0016-7037\(89\)90286-X](https://doi.org/10.1016/0016-7037(89)90286-X).
- Argo, Megan (Feb. 2015). "The e-MERLIN Data Reduction Pipeline". In: *arXiv e-prints*, arXiv:1502.04936, arXiv:1502.04936. DOI: [10.48550/arXiv.1502.04936](https://doi.org/10.48550/arXiv.1502.04936). arXiv: [1502.04936](https://arxiv.org/abs/1502.04936) [astro-ph.IM].
- Arnaud, M. (June 2009). "The β -model of the intracluster medium. Commentary on: Cavaliere A. and Fusco-Femiano R., 1976, A&A, 49, 137". In: *Astronomy & Astrophysics* 500.1, pp. 103–104. DOI: [10.1051/0004-6361/200912150](https://doi.org/10.1051/0004-6361/200912150).
- Arzoumanian, Zaven et al. (June 2021). "The NANOGrav 11 yr Data Set: Limits on Supermassive Black Hole Binaries in Galaxies within 500 Mpc". In: 914.2, 121, p. 121. DOI: [10.3847/1538-4357/abfcd3](https://doi.org/10.3847/1538-4357/abfcd3). arXiv: [2101.02716](https://arxiv.org/abs/2101.02716) [astro-ph.GA].
- Ascasibar, Yago and Maxim Markevitch (Oct. 2006). "The Origin of Cold Fronts in the Cores of Relaxed Galaxy Clusters". In: *The Astrophysical Journal* 650.1, pp. 102–127. DOI: [10.1086/506508](https://doi.org/10.1086/506508). arXiv: [astro-ph/0603246](https://arxiv.org/abs/astro-ph/0603246) [astro-ph].
- Asplund, Martin et al. (Sept. 2009). "The Chemical Composition of the Sun". In: *Annual Review of Astronomy and Astrophysics* 47.1, pp. 481–522. DOI: [10.1146/annurev.astro.46.060407.145222](https://doi.org/10.1146/annurev.astro.46.060407.145222). arXiv: [0909.0948](https://arxiv.org/abs/0909.0948) [astro-ph.SR].
- Augusto, Pedro et al. (Mar. 2006). "The radio properties of the cD galaxy of Abell 2390". In: *Monthly Notices of the Royal Astronomical Society* 367.1, pp. 366–374. DOI: [10.1111/j.1365-2966.2005.09965.x](https://doi.org/10.1111/j.1365-2966.2005.09965.x). arXiv: [astro-ph/0512250](https://arxiv.org/abs/astro-ph/0512250) [astro-ph].
- Babul, Arif et al. (May 2013). "Isotropic Heating of Galaxy Cluster Cores via Rapidly Reorienting Active Galactic Nucleus Jets". In: *The Astrophysical Journal* 768.1, 11, p. 11. DOI: [10.1088/0004-637X/768/1/11](https://doi.org/10.1088/0004-637X/768/1/11). arXiv: [1209.5748](https://arxiv.org/abs/1209.5748) [astro-ph.CO].
- Babyk, Iu. V. (June 2016). "Detail studies of the physical properties in the outer regions of galaxy clusters using Suzaku observations". In: *Astronomy Reports* 60.6, pp. 542–562. DOI: [10.1134/S1063772916040028](https://doi.org/10.1134/S1063772916040028).
- Babyk, Iu. V. et al. (July 2018). "A Universal Entropy Profile for the Hot Atmospheres of Galaxies and Clusters within R_{2500} ". In: *The Astrophysical Journal* 862.1, 39, p. 39. DOI: [10.3847/1538-4357/aacce5](https://doi.org/10.3847/1538-4357/aacce5). arXiv: [1802.02589](https://arxiv.org/abs/1802.02589) [astro-ph.CO].
- Babyk, Iu. V. et al. (Dec. 2019). "Origins of Molecular Clouds in Early-type Galaxies". In: *The Astrophysical Journal* 887.2, 149, p. 149. DOI: [10.3847/1538-4357/ab54ce](https://doi.org/10.3847/1538-4357/ab54ce). arXiv: [1810.11465](https://arxiv.org/abs/1810.11465) [astro-ph.GA].
- Bahcall, N. A. (Apr. 1999). "Clusters and superclusters of galaxies". In: *Formation of Structure in the Universe*. Ed. by Avishai Dekel and Jeremiah P. Ostriker, p. 135.

- Bahcall, Neta A. and Lori M. Lubin (May 1994). “Resolving the Beta-Discrepancy for Clusters of Galaxies”. In: *The Astrophysical Journal* 426, p. 513. DOI: [10.1086/174087](https://doi.org/10.1086/174087). arXiv: [astro-ph/9311061](https://arxiv.org/abs/astro-ph/9311061) [astro-ph].
- Baldi, A. et al. (Dec. 2009). “The Unusual X-Ray Morphology of NGC 4636 Revealed by Deep Chandra Observations: Cavities and Shocks Created by Past Active Galactic Nucleus Outbursts”. In: *The Astrophysical Journal* 707.2, pp. 1034–1043. DOI: [10.1088/0004-637X/707/2/1034](https://doi.org/10.1088/0004-637X/707/2/1034). arXiv: [0904.2569](https://arxiv.org/abs/0904.2569) [astro-ph.CO].
- Baldi, R. D. and A. Capetti (Oct. 2008). “Recent star formation in nearby 3CR radio-galaxies from UV HST observations”. In: *Astronomy & Astrophysics* 489.3, pp. 989–1002. DOI: [10.1051/0004-6361:20078745](https://doi.org/10.1051/0004-6361:20078745). arXiv: [0808.1555](https://arxiv.org/abs/0808.1555) [astro-ph].
- Baldi, Ranieri D. (Dec. 2023). “The nature of compact radio sources: the case of FR 0 radio galaxies”. In: *The Astronomy & Astrophysics Review* 31.1, 3, p. 3. DOI: [10.1007/s00159-023-00148-3](https://doi.org/10.1007/s00159-023-00148-3). arXiv: [2307.08379](https://arxiv.org/abs/2307.08379) [astro-ph.GA].
- Baldi, Ranieri D. et al. (Apr. 2015). “Pilot study of the radio-emitting AGN population: the emerging new class of FR 0 radio-galaxies”. In: *Astronomy & Astrophysics* 576, A38, A38. DOI: [10.1051/0004-6361/201425426](https://doi.org/10.1051/0004-6361/201425426). arXiv: [1502.00427](https://arxiv.org/abs/1502.00427) [astro-ph.GA].
- (Jan. 2019a). “High-resolution VLA observations of FR0 radio galaxies: the properties and nature of compact radio sources”. In: *Monthly Notices of the Royal Astronomical Society* 482.2, pp. 2294–2304. DOI: [10.1093/mnras/sty2703](https://doi.org/10.1093/mnras/sty2703). arXiv: [1810.01894](https://arxiv.org/abs/1810.01894) [astro-ph.GA].
- Baldi, Ranieri Diego et al. (Sept. 2019b). “The High Energy View of FR0 Radio Galaxies”. In: *Galaxies* 7.3, p. 76. DOI: [10.3390/galaxies7030076](https://doi.org/10.3390/galaxies7030076). arXiv: [1909.04113](https://arxiv.org/abs/1909.04113) [astro-ph.HE].
- Bambic, C. J. et al. (July 2023). “AGN feeding and feedback in M84: from kiloparsec scales to the Bondi radius”. In: *Monthly Notices of the Royal Astronomical Society* 522.3, pp. 4374–4391. DOI: [10.1093/mnras/stad824](https://doi.org/10.1093/mnras/stad824). arXiv: [2301.11937](https://arxiv.org/abs/2301.11937) [astro-ph.HE].
- Bardeen, James M. and Jacobus A. Petterson (Jan. 1975). “The Lense-Thirring Effect and Accretion Disks around Kerr Black Holes”. In: *The Astrophysical Journal* 195, p. L65. DOI: [10.1086/181711](https://doi.org/10.1086/181711).
- Barker, B. M. and R. F. O’Connell (July 1975). “Relativistic effects in the binary pulsar PSR 1913+16.” In: *The Astrophysical Journal Letters* 199, p. L25. DOI: [10.1086/181840](https://doi.org/10.1086/181840).
- Barret, Didier et al. (Feb. 2020). “The Athena space X-ray observatory and the astrophysics of hot plasma†”. In: *Astronomische Nachrichten* 341.2, pp. 224–235. DOI: [10.1002/asna.202023782](https://doi.org/10.1002/asna.202023782). arXiv: [1912.04615](https://arxiv.org/abs/1912.04615) [astro-ph.IM].
- Battye, R. A. and I. W. A. Browne (Nov. 2009). “Radio and optical orientations of galaxies”. In: *Monthly Notices of the Royal Astronomical Society* 399.4, pp. 1888–1900. DOI: [10.1111/j.1365-2966.2009.15429.x](https://doi.org/10.1111/j.1365-2966.2009.15429.x). arXiv: [0902.1631](https://arxiv.org/abs/0902.1631) [astro-ph.CO].
- Becker, Robert H. et al. (Sept. 1995). “The FIRST Survey: Faint Images of the Radio Sky at Twenty Centimeters”. In: *The Astrophysical Journal* 450, p. 559. DOI: [10.1086/176166](https://doi.org/10.1086/176166).
- Begelman, M. C. et al. (Sept. 1980). “Massive black hole binaries in active galactic nuclei”. In: *Nature* 287.5780, pp. 307–309. DOI: [10.1038/287307a0](https://doi.org/10.1038/287307a0).
- Begelman, Mitchell C. and A. C. Fabian (May 1990). “Turbulent mixing layers in the interstellar and intracluster medium.” In: *Monthly Notices of the Royal Astronomical Society* 244, 26P–29.
- Bertocco, S. et al. (Jan. 2020). “INAF Trieste Astronomical Observatory Information Technology Framework”. In: *Astronomical Data Analysis Software and Systems XXIX*. Ed. by R. Pizzo et al. Vol. 527. Astronomical Society of the Pacific Conference Series, p. 303.
- Best, P. N. and T. M. Heckman (Apr. 2012). “On the fundamental dichotomy in the local radio-AGN population: accretion, evolution and host galaxy properties”. In: *Monthly Notices of the Royal Astronomical Society* 421.2, pp. 1569–1582. DOI: [10.1111/j.1365-2966.2012.20414.x](https://doi.org/10.1111/j.1365-2966.2012.20414.x). arXiv: [1201.2397](https://arxiv.org/abs/1201.2397) [astro-ph.CO].
- Bi, Sheng et al. (Sept. 2020). “Chandra Survey of Nearby Galaxies: An Extended Catalog”. In: 900.2, 124, p. 124. DOI: [10.3847/1538-4357/aba761](https://doi.org/10.3847/1538-4357/aba761). arXiv: [2007.06026](https://arxiv.org/abs/2007.06026) [astro-ph.GA].

- Biava, Nadia et al. (June 2021). "Constraining the AGN duty cycle in the cool-core cluster MS 0735.6+7421 with LOFAR data". In: *Astronomy & Astrophysics* 650, A170, A170. DOI: [10.1051/0004-6361/202040063](https://doi.org/10.1051/0004-6361/202040063). arXiv: [2104.08294](https://arxiv.org/abs/2104.08294) [astro-ph.HE].
- Bicknell, Geoffrey V. (Feb. 1994). "On the Relationship between BL Lacertae Objects and Fanaroff-Riley I Radio Galaxies". In: *The Astrophysical Journal* 422, p. 542. DOI: [10.1086/173748](https://doi.org/10.1086/173748). arXiv: [astro-ph/9308033](https://arxiv.org/abs/astro-ph/9308033) [astro-ph].
- Bicknell, Geoffrey V. et al. (Apr. 2018). "Relativistic jet feedback - II. Relationship to gigahertz peak spectrum and compact steep spectrum radio galaxies". In: *Monthly Notices of the Royal Astronomical Society* 475.3, pp. 3493–3501. DOI: [10.1093/mnras/sty070](https://doi.org/10.1093/mnras/sty070). arXiv: [1801.06518](https://arxiv.org/abs/1801.06518) [astro-ph.GA].
- Bîrzan, L. et al. (June 2004). "A Systematic Study of Radio-induced X-Ray Cavities in Clusters, Groups, and Galaxies". In: *The Astrophysical Journal* 607.2, pp. 800–809. DOI: [10.1086/383519](https://doi.org/10.1086/383519). arXiv: [astro-ph/0402348](https://arxiv.org/abs/astro-ph/0402348) [astro-ph].
- Bîrzan, L. et al. (Jan. 2007). "Radio Properties of Cavities in the ICM: Imprints of AGN Activity". In: *Heating versus Cooling in Galaxies and Clusters of Galaxies*. Ed. by H. Böhringer et al., p. 115. DOI: [10.1007/978-3-540-73484-0_22](https://doi.org/10.1007/978-3-540-73484-0_22). arXiv: [astro-ph/0612393](https://arxiv.org/abs/astro-ph/0612393) [astro-ph].
- Bîrzan, L. et al. (Oct. 2008). "Radiative Efficiency and Content of Extragalactic Radio Sources: Toward a Universal Scaling Relation between Jet Power and Radio Power". In: *The Astrophysical Journal* 686.2, pp. 859–880. DOI: [10.1086/591416](https://doi.org/10.1086/591416). arXiv: [0806.1929](https://arxiv.org/abs/0806.1929) [astro-ph].
- Bîrzan, L. et al. (Dec. 2009). "The Detectability of AGN Cavities in Cooling-Flow Clusters". In: *The Monster's Fiery Breath: Feedback in Galaxies, Groups, and Clusters*. Ed. by Sebastian Heinz and Eric Wilcots. Vol. 1201. American Institute of Physics Conference Series, pp. 301–304. DOI: [10.1063/1.3293061](https://doi.org/10.1063/1.3293061). arXiv: [0909.0397](https://arxiv.org/abs/0909.0397) [astro-ph.CO].
- Bîrzan, L. et al. (Dec. 2012). "The duty cycle of radio-mode feedback in complete samples of clusters". In: *Monthly Notices of the Royal Astronomical Society* 427.4, pp. 3468–3488. DOI: [10.1111/j.1365-2966.2012.22083.x](https://doi.org/10.1111/j.1365-2966.2012.22083.x). arXiv: [1210.7100](https://arxiv.org/abs/1210.7100) [astro-ph.CO].
- Bîrzan, L. et al. (Oct. 2017). "A study of high-redshift AGN feedback in SZ cluster samples". In: *Monthly Notices of the Royal Astronomical Society* 471.2, pp. 1766–1787. DOI: [10.1093/mnras/stx1505](https://doi.org/10.1093/mnras/stx1505). arXiv: [1706.04775](https://arxiv.org/abs/1706.04775) [astro-ph.GA].
- Bîrzan, L. et al. (Aug. 2020). "LOFAR observations of X-ray cavity systems". In: *Monthly Notices of the Royal Astronomical Society* 496.3, pp. 2613–2635. DOI: [10.1093/mnras/staa1594](https://doi.org/10.1093/mnras/staa1594). arXiv: [2006.09708](https://arxiv.org/abs/2006.09708) [astro-ph.GA].
- Biviano, Andrea (Jan. 2000). "From Messier to Abell: 200 Years of Science with Galaxy Clusters". In: *Constructing the Universe with Clusters of Galaxies*. Ed. by Florence Durret and Daniel Gerbal, 1, p. 1. DOI: [10.48550/arXiv.astro-ph/0010409](https://doi.org/10.48550/arXiv.astro-ph/0010409). arXiv: [astro-ph/0010409](https://arxiv.org/abs/astro-ph/0010409) [astro-ph].
- Blandford, R. D. and R. L. Znajek (May 1977). "Electromagnetic extraction of energy from Kerr black holes." In: *Monthly Notices of the Royal Astronomical Society* 179, pp. 433–456. DOI: [10.1093/mnras/179.3.433](https://doi.org/10.1093/mnras/179.3.433).
- Blandford, Roger et al. (Aug. 2019). "Relativistic Jets from Active Galactic Nuclei". In: *Annual Review of Astronomy and Astrophysics* 57, pp. 467–509. DOI: [10.1146/annurev-astro-081817-051948](https://doi.org/10.1146/annurev-astro-081817-051948). arXiv: [1812.06025](https://arxiv.org/abs/1812.06025) [astro-ph.HE].
- Blanton, E. L. et al. (May 2009). "SHOCKS AND BUBBLES IN A DEEP CHANDRA OBSERVATION OF THE COOLING FLOW CLUSTER ABELL 2052". In: *The Astrophysical Journal* 697.2, pp. L95–L98. DOI: [10.1088/0004-637x/697/2/195](https://doi.org/10.1088/0004-637x/697/2/195). URL: <https://doi.org/10.1088/0004-637x/697/2/195>.
- Blanton, E. L. et al. (Aug. 2011). "A Very Deep Chandra Observation of A2052: Bubbles, Shocks, and Slushing". In: *The Astrophysical Journal* 737.2, 99, p. 99. DOI: [10.1088/0004-637x/737/2/99](https://doi.org/10.1088/0004-637x/737/2/99). arXiv: [1105.4572](https://arxiv.org/abs/1105.4572) [astro-ph.CO].
- Blanton, Elizabeth L. et al. (Apr. 2010). "Active galactic nucleus feedback in clusters of galaxies". In: *Proceedings of the National Academy of Science* 107.16, pp. 7174–7178. DOI: [10.1073/pnas.0913904107](https://doi.org/10.1073/pnas.0913904107). arXiv: [1004.0671](https://arxiv.org/abs/1004.0671) [astro-ph.CO].

- Blundell, Katherine M. et al. (Feb. 1999). "The Nature and Evolution of Classical Double Radio Sources from Complete Samples". In: *The Astronomical Journal* 117.2, pp. 677–706. DOI: [10.1086/300721](https://doi.org/10.1086/300721). arXiv: [astro-ph/9810197](https://arxiv.org/abs/astro-ph/9810197) [astro-ph].
- Boccardi, B. et al. (Nov. 2017). "Radio observations of active galactic nuclei with mm-VLBI". In: *Astronomy and Astrophysics Reviews* 25.1, 4, p. 4. DOI: [10.1007/s00159-017-0105-6](https://doi.org/10.1007/s00159-017-0105-6). arXiv: [1711.07548](https://arxiv.org/abs/1711.07548) [astro-ph.HE].
- Boccardi, B. et al. (Mar. 2021a). "Jet collimation in NGC 315 and other nearby AGN". In: *Astronomy & Astrophysics* 647, A67, A67. DOI: [10.1051/0004-6361/202039612](https://doi.org/10.1051/0004-6361/202039612). arXiv: [2012.14831](https://arxiv.org/abs/2012.14831) [astro-ph.HE].
- Boccardi, Bia et al. (Nov. 2021b). "Accretion mode and jet collimation in active galactic nuclei". In: *Astronomische Nachrichten* 342.1071, pp. 1071–1076. DOI: [10.1002/asna.20210085](https://doi.org/10.1002/asna.20210085).
- Boehringer, H. et al. (Oct. 1993). "A ROSAT HRI study of the interaction of the X-ray emitting gas and radio lobes of NGC 1275." In: *Monthly Notices of the Royal Astronomical Society* 264, pp. L25–L28. DOI: [10.1093/mnras/264.1.L25](https://doi.org/10.1093/mnras/264.1.L25).
- Bogdán, Ákos et al. (Feb. 2014). "Young AGN Outburst Running over Older X-Ray Cavities". In: *The Astrophysical Journal* 782.2, L19, p. L19. DOI: [10.1088/2041-8205/782/2/L19](https://doi.org/10.1088/2041-8205/782/2/L19). arXiv: [1401.6176](https://arxiv.org/abs/1401.6176) [astro-ph.GA].
- Böhringer, Hans and Norbert Werner (Feb. 2010). "X-ray spectroscopy of galaxy clusters: studying astrophysical processes in the largest celestial laboratories". In: *The Astronomy and Astrophysics Review* 18.1-2, pp. 127–196. DOI: [10.1007/s00159-009-0023-3](https://doi.org/10.1007/s00159-009-0023-3).
- Bonafede, A. et al. (Oct. 2023). "Shock imprints on the radio mini halo in RBS797". In: *arXiv e-prints*, arXiv:2310.07773, arXiv:2310.07773. DOI: [10.48550/arXiv.2310.07773](https://doi.org/10.48550/arXiv.2310.07773). arXiv: [2310.07773](https://arxiv.org/abs/2310.07773) [astro-ph.CO].
- Bourne, Martin A. and Debora Sijacki (Sept. 2021). "AGN jet feedback on a moving mesh: gentle cluster heating by weak shocks and lobe disruption". In: *Monthly Notices of the Royal Astronomical Society* 506.1, pp. 488–513. DOI: [10.1093/mnras/stab1662](https://doi.org/10.1093/mnras/stab1662). arXiv: [2008.12784](https://arxiv.org/abs/2008.12784) [astro-ph.HE].
- Bourne, Martin A. and Hsiang-Yi Karen Yang (June 2023). "Recent Progress in Modeling the Macro- and Micro-Physics of Radio Jet Feedback in Galaxy Clusters". In: *Galaxies* 11.3, p. 73. DOI: [10.3390/galaxies11030073](https://doi.org/10.3390/galaxies11030073). arXiv: [2305.00019](https://arxiv.org/abs/2305.00019) [astro-ph.HE].
- Bridle, Alan H. and Richard A. Perley (Jan. 1984). "Extragalactic Radio Jets". In: *Annual Review of Astron and Astrophysics* 22, pp. 319–358. DOI: [10.1146/annurev.aa.22.090184.001535](https://doi.org/10.1146/annurev.aa.22.090184.001535).
- Brienza, M. et al. (June 2020). "Radio spectral properties and jet duty cycle in the restarted radio galaxy 3C388". In: *Astronomy & Astrophysics* 638, A29, A29. DOI: [10.1051/0004-6361/202037457](https://doi.org/10.1051/0004-6361/202037457). arXiv: [2003.13476](https://arxiv.org/abs/2003.13476) [astro-ph.GA].
- Brienza, M. et al. (Dec. 2021). "A snapshot of the oldest active galactic nuclei feedback phases". In: *Nature Astronomy* 5, pp. 1261–1267. DOI: [10.1038/s41550-021-01491-0](https://doi.org/10.1038/s41550-021-01491-0). arXiv: [2110.09189](https://arxiv.org/abs/2110.09189) [astro-ph.HE].
- Brienza, M. et al. (May 2022). "The galaxy group NGC 507: Newly detected AGN remnant plasma transported by sloshing". In: *Astronomy & Astrophysics* 661, A92, A92. DOI: [10.1051/0004-6361/202142579](https://doi.org/10.1051/0004-6361/202142579). arXiv: [2201.04591](https://arxiv.org/abs/2201.04591) [astro-ph.GA].
- Brighenti, Fabrizio and William G. Mathews (May 2006). "Stopping Cooling Flows with Jets". In: *The Astrophysical Journal* 643.1, pp. 120–127. DOI: [10.1086/502645](https://doi.org/10.1086/502645). arXiv: [astro-ph/0601555](https://arxiv.org/abs/astro-ph/0601555) [astro-ph].
- Brighenti, Fabrizio et al. (Apr. 2015). "Hot Gaseous Atmospheres in Galaxy Groups and Clusters Are Both Heated and Cooled by X-Ray Cavities". In: *The Astrophysical Journal* 802.2, 118, p. 118. DOI: [10.1088/0004-637X/802/2/118](https://doi.org/10.1088/0004-637X/802/2/118). arXiv: [1501.07647](https://arxiv.org/abs/1501.07647) [astro-ph.GA].
- Britzen, S. et al. (Aug. 2018). "OJ287: deciphering the 'Rosetta stone of blazars'". In: *Monthly Notices of the Royal Astronomical Society* 478.3, pp. 3199–3219. DOI: [10.1093/mnras/sty1026](https://doi.org/10.1093/mnras/sty1026).
- Brüggen, M. (Aug. 2003). "Simulations of Buoyant Bubbles in Galaxy Clusters". In: *The Astrophysical Journal* 592.2, pp. 839–845. DOI: [10.1086/375731](https://doi.org/10.1086/375731). arXiv: [astro-ph/0301352](https://arxiv.org/abs/astro-ph/0301352) [astro-ph].

- Brüggen, M. et al. (July 2005). "X-Ray Line Tomography of AGN-induced Motion in Clusters of Galaxies". In: *The Astrophysical Journal* 628.1, pp. 153–159. DOI: [10.1086/430732](https://doi.org/10.1086/430732). arXiv: [astro-ph/0503656](https://arxiv.org/abs/astro-ph/0503656) [astro-ph].
- Brüggen, M. et al. (Sept. 2007). "Shock heating by Fanaroff-Riley type I radio sources in galaxy clusters". In: *Monthly Notices of the Royal Astronomical Society* 380.1, pp. L67–L70. DOI: [10.1111/j.1745-3933.2007.00351.x](https://doi.org/10.1111/j.1745-3933.2007.00351.x). arXiv: [0706.1869](https://arxiv.org/abs/0706.1869) [astro-ph].
- Brüggen, Marcus et al. (June 2009). "Evolution of X-ray cavities". In: *Monthly Notices of the Royal Astronomical Society* 395.4, pp. 2210–2220. DOI: [10.1111/j.1365-2966.2009.14684.x](https://doi.org/10.1111/j.1365-2966.2009.14684.x). arXiv: [0902.4242](https://arxiv.org/abs/0902.4242) [astro-ph.GA].
- Brunetti, Gianfranco and Thomas W. Jones (Mar. 2014). "Cosmic Rays in Galaxy Clusters and Their Nonthermal Emission". In: *International Journal of Modern Physics D* 23.4, 1430007–98, pp. 1430007–98. DOI: [10.1142/S0218271814300079](https://doi.org/10.1142/S0218271814300079). arXiv: [1401.7519](https://arxiv.org/abs/1401.7519) [astro-ph.CO].
- Bruni, G. et al. (June 2021). "Hard X-ray selected giant radio galaxies - III. The LOFAR view". In: *Monthly Notices of the Royal Astronomical Society* 503.4, pp. 4681–4699. DOI: [10.1093/mnras/stab623](https://doi.org/10.1093/mnras/stab623). arXiv: [2103.00999](https://arxiv.org/abs/2103.00999) [astro-ph.HE].
- Bruno, L. et al. (Nov. 2019). "Multifrequency JVLA observations of the X-shaped radio galaxy in Abell 3670". In: *Astronomy & Astrophysics* 631, A173, A173. DOI: [10.1051/0004-6361/201936240](https://doi.org/10.1051/0004-6361/201936240). arXiv: [1910.06568](https://arxiv.org/abs/1910.06568) [astro-ph.GA].
- Buote, David A. (Nov. 1999). "X-ray evidence for multiphase hot gas with solar abundances in the brightest elliptical galaxies". In: *Monthly Notices of the Royal Astronomical Society* 309.3, pp. 685–714. DOI: [10.1046/j.1365-8711.1999.02886.x](https://doi.org/10.1046/j.1365-8711.1999.02886.x). arXiv: [astro-ph/9811080](https://arxiv.org/abs/astro-ph/9811080) [astro-ph].
- Burbidge, E. Margaret and G. R. Burbidge (Nov. 1965). "Optical Evidence Suggesting the Occurrence of a Violent Outburst in NGC 1275." In: *The Astrophysical Journal* 142, p. 1351. DOI: [10.1086/148421](https://doi.org/10.1086/148421).
- Buttiglione, S. et al. (Jan. 2010). "An optical spectroscopic survey of the 3CR sample of radio galaxies with $z < 0.3$. II. Spectroscopic classes and accretion modes in radio-loud AGN". In: *Astronomy & Astrophysics* 509, A6, A6. DOI: [10.1051/0004-6361/200913290](https://doi.org/10.1051/0004-6361/200913290). arXiv: [0911.0536](https://arxiv.org/abs/0911.0536) [astro-ph.CO].
- Bykov, A. M. et al. (May 2015). "Structures and Components in Galaxy Clusters: Observations and Models". In: *Space Science Review* 188.1–4, pp. 141–185. DOI: [10.1007/s11214-014-0129-4](https://doi.org/10.1007/s11214-014-0129-4). arXiv: [1512.01456](https://arxiv.org/abs/1512.01456) [astro-ph.CO].
- Calzadilla, Michael S. et al. (Dec. 2019a). "Discovery of a Powerful $>10^{61}$ erg AGN Outburst in the Distant Galaxy Cluster SPT-CLJ0528-5300". In: *The Astrophysical Journal* 887.1, L17, p. L17. DOI: [10.3847/2041-8213/ab5b07](https://doi.org/10.3847/2041-8213/ab5b07). arXiv: [1911.12828](https://arxiv.org/abs/1911.12828) [astro-ph.GA].
- Calzadilla, Michael S. et al. (Apr. 2019b). "Revealing a Highly Dynamic Cluster Core in Abell 1664 with Chandra". In: *The Astrophysical Journal* 875.1, 65, p. 65. DOI: [10.3847/1538-4357/ab09f6](https://doi.org/10.3847/1538-4357/ab09f6). arXiv: [1810.00881](https://arxiv.org/abs/1810.00881) [astro-ph.CO].
- Calzadilla, Michael S. et al. (Dec. 2022). "Testing the Limits of AGN Feedback and the Onset of Thermal Instability in the Most Rapidly Star-forming Brightest Cluster Galaxies". In: *The Astrophysical Journal* 940.2, 140, p. 140. DOI: [10.3847/1538-4357/ac9790](https://doi.org/10.3847/1538-4357/ac9790). arXiv: [2207.01624](https://arxiv.org/abs/2207.01624) [astro-ph.GA].
- Campitiello, M. G. et al. (Sept. 2022). "CHEX-MATE: Morphological analysis of the sample". In: *Astronomy & Astrophysics* 665, A117, A117. DOI: [10.1051/0004-6361/202243470](https://doi.org/10.1051/0004-6361/202243470). arXiv: [2205.11326](https://arxiv.org/abs/2205.11326) [astro-ph.CO].
- Candini, S. et al. (Sept. 2023). "New filamentary remnant radio emission and duty cycle constraints in the radio galaxy NGC 6086". In: *Astronomy & Astrophysics* 677, A4, A4. DOI: [10.1051/0004-6361/202347036](https://doi.org/10.1051/0004-6361/202347036). arXiv: [2305.18077](https://arxiv.org/abs/2305.18077) [astro-ph.GA].
- Canning, R. E. A. et al. (Oct. 2013). "A multiwavelength view of cooling versus AGN heating in the X-ray luminous cool-core of Abell 3581". In: *Monthly Notices of the Royal Astronomical Society* 435.2, pp. 1108–1125. DOI: [10.1093/mnras/stt1345](https://doi.org/10.1093/mnras/stt1345). arXiv: [1305.0050](https://arxiv.org/abs/1305.0050) [astro-ph.CO].

- Cao, X. (Mar. 2000). "Clues to the origin of parsec to kilo-parsec jet misalignments in EGRET sources". In: *Astronomy & Astrophysics* 355, pp. 44–50. DOI: [10.48550/arXiv.astro-ph/0001168](https://doi.org/10.48550/arXiv.astro-ph/0001168). arXiv: [astro-ph/0001168](https://arxiv.org/abs/astro-ph/0001168) [astro-ph].
- Capak, Peter L. et al. (Feb. 2011). "A massive protocluster of galaxies at a redshift of $z \sim 5.3$ ". In: *Nature* 470.7333, pp. 233–235. DOI: [10.1038/nature09681](https://doi.org/10.1038/nature09681). arXiv: [1101.3586](https://arxiv.org/abs/1101.3586) [astro-ph.CO].
- Capetti, A. et al. (Nov. 2019). "The low-frequency properties of FR 0 radio galaxies". In: *Astronomy & Astrophysics* 631, A176, A176. DOI: [10.1051/0004-6361/201936254](https://doi.org/10.1051/0004-6361/201936254). arXiv: [1910.06618](https://arxiv.org/abs/1910.06618) [astro-ph.GA].
- Capetti, A. et al. (Oct. 2020). "The LOFAR view of FR 0 radio galaxies". In: *Astronomy & Astrophysics* 642, A107, A107. DOI: [10.1051/0004-6361/202038671](https://doi.org/10.1051/0004-6361/202038671). arXiv: [2008.08099](https://arxiv.org/abs/2008.08099) [astro-ph.GA].
- Carilli, C. L. et al. (Dec. 1991). "Multifrequency Radio Observations of Cygnus A: Spectral Aging in Powerful Radio Galaxies". In: *The Astrophysical Journal* 383, p. 554. DOI: [10.1086/170813](https://doi.org/10.1086/170813).
- Carilli, C. L. et al. (Sept. 1994). "Observations of interaction between cluster gas and the radio lobes of Cygnus A." In: *Monthly Notices of the Royal Astronomical Society* 270, pp. 173–177. DOI: [10.1093/mnras/270.1.173](https://doi.org/10.1093/mnras/270.1.173).
- Cavagnolo, K. W. et al. (Sept. 2010). "A Relationship Between AGN Jet Power and Radio Power". In: *The Astrophysical Journal* 720.2, pp. 1066–1072. DOI: [10.1088/0004-637X/720/2/1066](https://doi.org/10.1088/0004-637X/720/2/1066). arXiv: [1006.5699](https://arxiv.org/abs/1006.5699) [astro-ph.CO].
- Cavagnolo, K. W. et al. (May 2011). "A Powerful AGN Outburst in RBS 797". In: *The Astrophysical Journal* 732.2, 71, p. 71. DOI: [10.1088/0004-637X/732/2/71](https://doi.org/10.1088/0004-637X/732/2/71). arXiv: [1103.0630](https://arxiv.org/abs/1103.0630) [astro-ph.CO].
- Cavagnolo, Kenneth W. et al. (Aug. 2008). "An Entropy Threshold for Strong H α and Radio Emission in the Cores of Galaxy Clusters". In: *The Astrophysical Journal* 683.2, p. L107. DOI: [10.1086/591665](https://doi.org/10.1086/591665). arXiv: [0806.0382](https://arxiv.org/abs/0806.0382) [astro-ph].
- (May 2009). "Intracluster Medium Entropy Profiles for a Chandra Archival Sample of Galaxy Clusters". In: *The Astrophysical Journals* 182.1, pp. 12–32. DOI: [10.1088/0067-0049/182/1/12](https://doi.org/10.1088/0067-0049/182/1/12). arXiv: [0902.1802](https://arxiv.org/abs/0902.1802) [astro-ph.CO].
- Cavaliere, A. and R. Fusco-Femiano (May 1976). "Reprint of 1976A&A...49..137C. X-rays from hot plasma in clusters of galaxies." In: *Astronomy & Astrophysics* 500, pp. 95–102.
- Charlot, P. et al. (Dec. 2020). "The third realization of the International Celestial Reference Frame by very long baseline interferometry". In: *Astronomy & Astrophysics* 644, A159, A159. DOI: [10.1051/0004-6361/202038368](https://doi.org/10.1051/0004-6361/202038368). arXiv: [2010.13625](https://arxiv.org/abs/2010.13625) [astro-ph.GA].
- Chaudhuri, Anya et al. (Nov. 2012). "Energy Deposition Profiles and Entropy in Galaxy Clusters". In: *The Astrophysical Journal* 759.2, 87, p. 87. DOI: [10.1088/0004-637X/759/2/87](https://doi.org/10.1088/0004-637X/759/2/87). arXiv: [1203.6535](https://arxiv.org/abs/1203.6535) [astro-ph.CO].
- Chen, Y. et al. (May 2007). "Statistics of X-ray observables for the cooling-core and non-cooling core galaxy clusters". In: *Astronomy & Astrophysics* 466.3, pp. 805–812. DOI: [10.1051/0004-6361:20066471](https://doi.org/10.1051/0004-6361:20066471). arXiv: [astro-ph/0702482](https://arxiv.org/abs/astro-ph/0702482) [astro-ph].
- Cheng, X. P. and T. An (Aug. 2018). "Parsec-scale Radio Structure of 14 Fanaroff-Riley Type 0 Radio Galaxies". In: *The Astrophysical Journal* 863.2, 155, p. 155. DOI: [10.3847/1538-4357/aad22c](https://doi.org/10.3847/1538-4357/aad22c). arXiv: [1807.02505](https://arxiv.org/abs/1807.02505) [astro-ph.HE].
- Cheng, Xiaopeng et al. (Sept. 2021). "Parsec-scale properties of eight Fanaroff-Riley type 0 radio galaxies". In: *Monthly Notices of the Royal Astronomical Society* 506.2, pp. 1609–1622. DOI: [10.1093/mnras/stab1388](https://doi.org/10.1093/mnras/stab1388). arXiv: [2105.05396](https://arxiv.org/abs/2105.05396) [astro-ph.HE].
- Chiang, Yi-Kuan et al. (Dec. 2013). "Ancient Light from Young Cosmic Cities: Physical and Observational Signatures of Galaxy Proto-clusters". In: *The Astrophysical Journal* 779.2, 127, p. 127. DOI: [10.1088/0004-637X/779/2/127](https://doi.org/10.1088/0004-637X/779/2/127). arXiv: [1310.2938](https://arxiv.org/abs/1310.2938) [astro-ph.CO].
- Chon, Gayoung et al. (Sept. 2012). "Discovery of an X-ray cavity near the radio lobes of Cygnus A indicating previous AGN activity". In: *Astronomy & Astrophysics* 545, L3, p. L3. DOI: [10.1051/0004-6361/201219538](https://doi.org/10.1051/0004-6361/201219538). arXiv: [1207.0699](https://arxiv.org/abs/1207.0699) [astro-ph.HE].
- Churazov, E. et al. (Apr. 2000). "Asymmetric, arc minute scale structures around NGC 1275". In: *Astronomy & Astrophysics* 356, pp. 788–794. arXiv: [astro-ph/0002375](https://arxiv.org/abs/astro-ph/0002375) [astro-ph].

- Churazov, E. et al. (June 2001). "Evolution of Buoyant Bubbles in M87". In: *The Astrophysical Journal* 554.1, pp. 261–273. DOI: [10.1086/321357](https://doi.org/10.1086/321357). arXiv: [astro-ph/0008215](https://arxiv.org/abs/astro-ph/0008215) [astro-ph].
- Cielo, S. et al. (Sept. 2018). "Feedback from reorienting AGN jets. I. Jet-ICM coupling, cavity properties and global energetics". In: *Astronomy & Astrophysics* 617, A58, A58. DOI: [10.1051/0004-6361/201832582](https://doi.org/10.1051/0004-6361/201832582).
- Ciocan, B. I. et al. (May 2021). "The VLT-MUSE and ALMA view of the MACS 1931.8-2635 brightest cluster galaxy". In: *Astronomy & Astrophysics* 649, A23, A23. DOI: [10.1051/0004-6361/202040010](https://doi.org/10.1051/0004-6361/202040010). arXiv: [2101.10718](https://arxiv.org/abs/2101.10718) [astro-ph.GA].
- Condon, J. J. et al. (May 1998). "The NRAO VLA Sky Survey". In: *The Astronomical Journal* 115.5, pp. 1693–1716. DOI: [10.1086/300337](https://doi.org/10.1086/300337).
- Cora, Sofia A. et al. (May 2008). "On the dynamical origin of the ICM metallicity evolution". In: *Monthly Notices of the Royal Astronomical Society* 386.1, pp. 96–104. DOI: [10.1111/j.1365-2966.2008.13068.x](https://doi.org/10.1111/j.1365-2966.2008.13068.x). arXiv: [0802.0975](https://arxiv.org/abs/0802.0975) [astro-ph].
- Coriat, M. et al. (Apr. 2019). "The twisted jets of Circinus X-1". In: *Monthly Notices of the Royal Astronomical Society* 484.2, pp. 1672–1686. DOI: [10.1093/mnras/stz099](https://doi.org/10.1093/mnras/stz099). arXiv: [1901.02631](https://arxiv.org/abs/1901.02631) [astro-ph.HE].
- Cowie, L. L. et al. (Sept. 1983). "Two-dimensional spectrophotometry of the cores of X-ray luminous clusters." In: *The Astrophysical Journal* 272, pp. 29–47. DOI: [10.1086/161259](https://doi.org/10.1086/161259).
- Crawford, C. S. et al. (July 1999). "The ROSAT Brightest Cluster Sample - III. Optical spectra of the central cluster galaxies". In: *Monthly Notices of the Royal Astronomical Society* 306.4, pp. 857–896. DOI: [10.1046/j.1365-8711.1999.02583.x](https://doi.org/10.1046/j.1365-8711.1999.02583.x). arXiv: [astro-ph/9903057](https://arxiv.org/abs/astro-ph/9903057) [astro-ph].
- Croston, J. H. et al. (May 2009). "High-energy particle acceleration at the radio-lobe shock of Centaurus A". In: *Monthly Notices of the Royal Astronomical Society* 395.4, pp. 1999–2012. ISSN: 0035-8711. DOI: [10.1111/j.1365-2966.2009.14715.x](https://doi.org/10.1111/j.1365-2966.2009.14715.x). eprint: <https://academic.oup.com/mnras/article-pdf/395/4/1999/2925229/mnras0395-1999.pdf>. URL: <https://doi.org/10.1111/j.1365-2966.2009.14715.x>.
- Croston, J. H. et al. (May 2011). "A LARGE-SCALE SHOCK SURROUNDING A POWERFUL RADIO GALAXY?" In: *The Astrophysical Journal* 734.2, p. L28. DOI: [10.1088/2041-8205/734/2/L28](https://doi.org/10.1088/2041-8205/734/2/L28). URL: <https://doi.org/10.1088/2041-8205/734/2/L28>.
- Cucciati, O. et al. (Nov. 2018). "The progeny of a cosmic titan: a massive multi-component proto-supercluster in formation at $z = 2.45$ in VUDS". In: *Astronomy & Astrophysics* 619, A49, A49. DOI: [10.1051/0004-6361/201833655](https://doi.org/10.1051/0004-6361/201833655). arXiv: [1806.06073](https://arxiv.org/abs/1806.06073) [astro-ph.CO].
- Czerny, B. and B. You (Feb. 2016). "Accretion in active galactic nuclei and disk-jet coupling". In: *Astronomische Nachrichten* 337.1-2, p. 73. DOI: [10.1002/asna.201512268](https://doi.org/10.1002/asna.201512268). arXiv: [1507.05852](https://arxiv.org/abs/1507.05852) [astro-ph.HE].
- Dabhade, Pratik et al. (June 2023). "Decoding the giant extragalactic radio sources". In: *Journal of Astrophysics and Astronomy* 44.1, 13, p. 13. DOI: [10.1007/s12036-022-09898-5](https://doi.org/10.1007/s12036-022-09898-5). arXiv: [2208.02130](https://arxiv.org/abs/2208.02130) [astro-ph.GA].
- Daddi, E. et al. (Apr. 2009). "Two Bright Submillimeter Galaxies in a $z = 4.05$ Protocluster in Good-North, and Accurate Radio-Infrared Photometric Redshifts". In: *The Astrophysical Journal* 694.2, pp. 1517–1538. DOI: [10.1088/0004-637X/694/2/1517](https://doi.org/10.1088/0004-637X/694/2/1517). arXiv: [0810.3108](https://arxiv.org/abs/0810.3108) [astro-ph].
- Dallacasa, D. et al. (Mar. 1995). "A sample of small size compact steep-spectrum radio sources. I. VLBI images at 18 cm." In: *Astronomy & Astrophysics* 295, pp. 27–42.
- Dallacasa, D. et al. (Nov. 2000). "High frequency peakers. I. The bright sample". In: *Astronomy & Astrophysics* 363, pp. 887–900. DOI: [10.48550/arXiv.astro-ph/0012428](https://doi.org/10.48550/arXiv.astro-ph/0012428). arXiv: [astro-ph/0012428](https://arxiv.org/abs/astro-ph/0012428) [astro-ph].
- Dannerbauer, H. et al. (Dec. 2017). "The implications of the surprising existence of a large, massive CO disk in a distant protocluster". In: *Astronomy & Astrophysics* 608, A48, A48. DOI: [10.1051/0004-6361/201730449](https://doi.org/10.1051/0004-6361/201730449). arXiv: [1701.05250](https://arxiv.org/abs/1701.05250) [astro-ph.GA].

- David, L. P. et al. (Aug. 2001). “A High-Resolution Study of the Hydra A Cluster with Chandra: Comparison of the Core Mass Distribution with Theoretical Predictions and Evidence for Feedback in the Cooling Flow”. In: *The Astrophysical Journal* 557.2, pp. 546–559. DOI: [10.1086/322250](https://doi.org/10.1086/322250). arXiv: [astro-ph/0010224](https://arxiv.org/abs/astro-ph/0010224) [astro-ph].
- David, Laurence P. et al. (Sept. 2014). “Molecular Gas in the X-Ray Bright Group NGC 5044 as Revealed by ALMA”. In: *The Astrophysical Journal* 792.2, 94, p. 94. DOI: [10.1088/0004-637X/792/2/94](https://doi.org/10.1088/0004-637X/792/2/94). arXiv: [1407.3235](https://arxiv.org/abs/1407.3235) [astro-ph.GA].
- de Gasperin, F. et al. (Feb. 2019). “Systematic effects in LOFAR data: A unified calibration strategy”. In: *Astronomy & Astrophysics* 622, A5, A5. DOI: [10.1051/0004-6361/201833867](https://doi.org/10.1051/0004-6361/201833867). arXiv: [1811.07954](https://arxiv.org/abs/1811.07954) [astro-ph.IM].
- de Gasperin, Francesco et al. (Oct. 2017). “Gentle reenergization of electrons in merging galaxy clusters”. In: *Science Advances* 3.10, e1701634. DOI: [10.1126/sciadv.1701634](https://doi.org/10.1126/sciadv.1701634). arXiv: [1710.06796](https://arxiv.org/abs/1710.06796) [astro-ph.HE].
- De Grandi, S. et al. (May 2004). “On the iron content in rich nearby clusters of galaxies”. In: *Astronomy & Astrophysics* 419, pp. 7–18. DOI: [10.1051/0004-6361:20034228](https://doi.org/10.1051/0004-6361:20034228). arXiv: [astro-ph/0310828](https://arxiv.org/abs/astro-ph/0310828) [astro-ph].
- De Grandi, Sabrina and Silvano Molendi (Apr. 2001). “Metallicity Gradients in X-Ray Clusters of Galaxies”. In: *The Astrophysical Journal* 551.1, pp. 153–159. DOI: [10.1086/320098](https://doi.org/10.1086/320098). arXiv: [astro-ph/0012232](https://arxiv.org/abs/astro-ph/0012232) [astro-ph].
- Deller, A. T. et al. (Aug. 2018). “A VLBI Distance and Transverse Velocity for PSR B1913+16”. In: *The Astrophysical Journal* 862.2, 139, p. 139. DOI: [10.3847/1538-4357/aacf95](https://doi.org/10.3847/1538-4357/aacf95). arXiv: [1806.10265](https://arxiv.org/abs/1806.10265) [astro-ph.SR].
- Dennett-Thorpe, J. et al. (Mar. 2002). “Jet reorientation in active galactic nuclei: two winged radio galaxies”. In: *Monthly Notices of the Royal Astronomical Society* 330.3, pp. 609–620. DOI: [10.1046/j.1365-8711.2002.05106.x](https://doi.org/10.1046/j.1365-8711.2002.05106.x). arXiv: [astro-ph/0110339](https://arxiv.org/abs/astro-ph/0110339) [astro-ph].
- Di Mascolo, Luca et al. (Mar. 2023). “Forming intracluster gas in a galaxy protocluster at a redshift of 2.16”. In: *Nature* 615.7954, pp. 809–812. DOI: [10.1038/s41586-023-05761-x](https://doi.org/10.1038/s41586-023-05761-x). arXiv: [2303.16226](https://arxiv.org/abs/2303.16226) [astro-ph.CO].
- Diehl, Steven et al. (Nov. 2008). “Constraining the Nature of X-Ray Cavities in Clusters and Galaxies”. In: *The Astrophysical Journal* 687.1, pp. 173–192. DOI: [10.1086/591310](https://doi.org/10.1086/591310). arXiv: [0801.1825](https://arxiv.org/abs/0801.1825) [astro-ph].
- Dominik, Rune M. et al. (June 2021). “3C 84: a possibly precessing jet in 43-GHz observations”. In: *Monthly Notices of the Royal Astronomical Society* 503.4, pp. 5448–5454. DOI: [10.1093/mnras/stab799](https://doi.org/10.1093/mnras/stab799).
- Donahue, Megan et al. (Sept. 2005). “Two Clusters of Galaxies with Radio-quiet Cooling Cores”. In: *The Astrophysical Journal Letters* 630.1, pp. L13–L16. DOI: [10.1086/462416](https://doi.org/10.1086/462416). arXiv: [astro-ph/0508587](https://arxiv.org/abs/astro-ph/0508587) [astro-ph].
- Donahue, Megan et al. (June 2006). “Entropy Profiles in the Cores of Cooling Flow Clusters of Galaxies”. In: *The Astrophysical Journal* 643.2, pp. 730–750. DOI: [10.1086/503270](https://doi.org/10.1086/503270). arXiv: [astro-ph/0511401](https://arxiv.org/abs/astro-ph/0511401) [astro-ph].
- Donahue, Megan and G. Mark Voit (Aug. 2022). “Baryon cycles in the biggest galaxies”. In: *Physics Reports* 973, pp. 1–109. DOI: [10.1016/j.physrep.2022.04.005](https://doi.org/10.1016/j.physrep.2022.04.005). arXiv: [2204.08099](https://arxiv.org/abs/2204.08099) [astro-ph.GA].
- Doria, Alberto et al. (July 2012). “A Chandra-VLA Investigation of the X-Ray Cavity System and Radio Mini-Halo in the Galaxy Cluster RBS 797”. In: *The Astrophysical Journal* 753.1, 47, p. 47. DOI: [10.1088/0004-637X/753/1/47](https://doi.org/10.1088/0004-637X/753/1/47). arXiv: [1204.6191](https://arxiv.org/abs/1204.6191) [astro-ph.CO].
- Duan, Xiaodong and Fulai Guo (July 2018). “Metal-rich Trailing Outflows Uplifted by AGN Bubbles in Galaxy Clusters”. In: *The Astrophysical Journal* 861.2, 106, p. 106. DOI: [10.3847/1538-4357/aac9ba](https://doi.org/10.3847/1538-4357/aac9ba). arXiv: [1805.02689](https://arxiv.org/abs/1805.02689) [astro-ph.HE].
- (June 2020). “On the Energy Coupling Efficiency of AGN Outbursts in Galaxy Clusters”. In: *The Astrophysical Journal* 896.2, 114, p. 114. DOI: [10.3847/1538-4357/ab93b3](https://doi.org/10.3847/1538-4357/ab93b3). arXiv: [2004.06841](https://arxiv.org/abs/2004.06841) [astro-ph.HE].

- Dunn, R. J. H. et al. (Dec. 2005). "Radio bubbles in clusters of galaxies". In: *Monthly Notices of the Royal Astronomical Society* 364.4, pp. 1343–1353. DOI: [10.1111/j.1365-2966.2005.09673.x](https://doi.org/10.1111/j.1365-2966.2005.09673.x). arXiv: [astro-ph/0510191](https://arxiv.org/abs/astro-ph/0510191) [astro-ph].
- Dunn, R. J. H. and A. C. Fabian (Dec. 2006). "Investigating AGN heating in a sample of nearby clusters". In: *Monthly Notices of the Royal Astronomical Society* 373.3, pp. 959–971. DOI: [10.1111/j.1365-2966.2006.11080.x](https://doi.org/10.1111/j.1365-2966.2006.11080.x). arXiv: [astro-ph/0609537](https://arxiv.org/abs/astro-ph/0609537) [astro-ph].
- Dupke, R. and III White R. E. (Jan. 2002). "Chandra Analysis of Abell 496". In: *The High Energy Universe at Sharp Focus: Chandra Science*. Ed. by Eric M. Schlegel and Saeqa Dil Vrtilek. Vol. 262. Astronomical Society of the Pacific Conference Series, p. 377. DOI: [10.48550/arXiv.astro-ph/0110070](https://doi.org/10.48550/arXiv.astro-ph/0110070). arXiv: [astro-ph/0110070](https://arxiv.org/abs/astro-ph/0110070) [astro-ph].
- Eckert, D. et al. (Feb. 2011). "The cool-core bias in X-ray galaxy cluster samples. I. Method and application to HIFLUGCS". In: *Astronomy & Astrophysics* 526, A79, A79. DOI: [10.1051/0004-6361/201015856](https://doi.org/10.1051/0004-6361/201015856). arXiv: [1011.3302](https://arxiv.org/abs/1011.3302) [astro-ph.CO].
- Eckert, D. et al. (May 2012). "The gas distribution in the outer regions of galaxy clusters". In: *Astronomy & Astrophysics* 541, A57, A57. DOI: [10.1051/0004-6361/201118281](https://doi.org/10.1051/0004-6361/201118281). arXiv: [1111.0020](https://arxiv.org/abs/1111.0020) [astro-ph.CO].
- Eckert, Dominique et al. (May 2021). "Feedback from Active Galactic Nuclei in Galaxy Groups". In: *Universe* 7.5, p. 142. DOI: [10.3390/universe7050142](https://doi.org/10.3390/universe7050142). arXiv: [2106.13259](https://arxiv.org/abs/2106.13259) [astro-ph.GA].
- Edgar, Richard (Sept. 2004). "A review of Bondi-Hoyle-Lyttleton accretion". In: *New Astronomy Review* 48.10, pp. 843–859. DOI: [10.1016/j.newar.2004.06.001](https://doi.org/10.1016/j.newar.2004.06.001). arXiv: [astro-ph/0406166](https://arxiv.org/abs/astro-ph/0406166) [astro-ph].
- Edge, A. C. (Dec. 2001). "The detection of molecular gas in the central galaxies of cooling flow clusters". In: *Monthly Notices of the Royal Astronomical Society* 328.3, pp. 762–782. DOI: [10.1046/j.1365-8711.2001.04802.x](https://doi.org/10.1046/j.1365-8711.2001.04802.x). arXiv: [astro-ph/0106225](https://arxiv.org/abs/astro-ph/0106225) [astro-ph].
- Edge, A. C. et al. (Sept. 1992). "Properties of cooling flows in a flux-limited sample of clusters of galaxies." In: *Monthly Notices of the Royal Astronomical Society* 258, pp. 177–188. DOI: [10.1093/mnras/258.1.177](https://doi.org/10.1093/mnras/258.1.177).
- Enßlin, T. A. and S. Heinz (Mar. 2002). "Radio and X-ray detectability of buoyant radio plasma bubbles in clusters of galaxies". In: *Astronomy & Astrophysics* 384, pp. L27–L30. DOI: [10.1051/0004-6361:20020207](https://doi.org/10.1051/0004-6361:20020207). arXiv: [astro-ph/0202101](https://arxiv.org/abs/astro-ph/0202101) [astro-ph].
- Ettori, S. et al. (July 2013). "Cold fronts and metal anisotropies in the X-ray cool core of the galaxy cluster Zw 1742+3306". In: *Astronomy & Astrophysics* 555, A93, A93. DOI: [10.1051/0004-6361/201321107](https://doi.org/10.1051/0004-6361/201321107). arXiv: [1305.3926](https://arxiv.org/abs/1305.3926) [astro-ph.CO].
- Fabian, A. C. (Jan. 1994). "Cooling Flows in Clusters of Galaxies". In: *Annual Review of Astronomy and Astrophysics* 32, pp. 277–318. DOI: [10.1146/annurev.aa.32.090194.001425](https://doi.org/10.1146/annurev.aa.32.090194.001425).
- (Sept. 2012). "Observational Evidence of Active Galactic Nuclei Feedback". In: *Annual Review of Astronomy and Astrophysics* 50, pp. 455–489. DOI: [10.1146/annurev-astro-081811-125521](https://doi.org/10.1146/annurev-astro-081811-125521). arXiv: [1204.4114](https://arxiv.org/abs/1204.4114) [astro-ph.CO].
- Fabian, A. C. et al. (Aug. 1984). "Cooling flows in clusters of galaxies". In: *Nature* 310.5980, pp. 733–740. DOI: [10.1038/310733a0](https://doi.org/10.1038/310733a0).
- Fabian, A. C. et al. (Nov. 2005). "On viscosity, conduction and sound waves in the intracluster medium". In: *Monthly Notices of the Royal Astronomical Society* 363.3, pp. 891–896. DOI: [10.1111/j.1365-2966.2005.09484.x](https://doi.org/10.1111/j.1365-2966.2005.09484.x). arXiv: [astro-ph/0501222](https://arxiv.org/abs/astro-ph/0501222) [astro-ph].
- Fabian, A. C. et al. (Feb. 2006). "A very deep Chandra observation of the Perseus cluster: shocks, ripples and conduction". In: *Monthly Notices of the Royal Astronomical Society* 366.2, pp. 417–428. DOI: [10.1111/j.1365-2966.2005.09896.x](https://doi.org/10.1111/j.1365-2966.2005.09896.x). arXiv: [astro-ph/0510476](https://arxiv.org/abs/astro-ph/0510476) [astro-ph].
- Fabian, Andrew C. (Jan. 2002). "Cooling Flows in Clusters of Galaxies". In: *Lighthouses of the Universe: The Most Luminous Celestial Objects and Their Use for Cosmology*. Ed. by Marat Gilfanov et al., p. 24. DOI: [10.1007/10856495_3](https://doi.org/10.1007/10856495_3). arXiv: [astro-ph/0201386](https://arxiv.org/abs/astro-ph/0201386) [astro-ph].
- Falceta-Gonçalves, D. et al. (Apr. 2010). "Precessing Jets and X-ray Bubbles from NGC 1275 (3C 84) in the Perseus Galaxy Cluster: A View from Three-dimensional Numerical Simulations".

- In: *The Astrophysical Journal* 713.1, pp. L74–L78. DOI: [10.1088/2041-8205/713/1/L74](https://doi.org/10.1088/2041-8205/713/1/L74). arXiv: [1003.2406](https://arxiv.org/abs/1003.2406) [astro-ph.CO].
- Fanaroff, B. L. and J. M. Riley (May 1974). “The morphology of extragalactic radio sources of high and low luminosity”. In: *Monthly Notices of the Royal Astronomical Society* 167, 31P–36P. DOI: [10.1093/mnras/167.1.31P](https://doi.org/10.1093/mnras/167.1.31P).
- Fanti, C. et al. (Oct. 1995). “Are compact steep-spectrum sources young?” In: *Astronomy & Astrophysics* 302, p. 317.
- Fendt, Christian and Melis Yardimci (July 2022). “Curved Jet Motion. I. Orbiting and Precessing Jets”. In: *The Astrophysical Journal* 933.1, 71, p. 71. DOI: [10.3847/1538-4357/ac7145](https://doi.org/10.3847/1538-4357/ac7145). arXiv: [2205.08498](https://arxiv.org/abs/2205.08498) [astro-ph.HE].
- Ferland, G. J. et al. (Feb. 2009). “Collisional heating as the origin of filament emission in galaxy clusters”. In: *Monthly Notices of the Royal Astronomical Society* 392.4, pp. 1475–1502. DOI: [10.1111/j.1365-2966.2008.14153.x](https://doi.org/10.1111/j.1365-2966.2008.14153.x). arXiv: [0810.5372](https://arxiv.org/abs/0810.5372) [astro-ph].
- Forman, W. et al. (Dec. 2005). “Reflections of Active Galactic Nucleus Outbursts in the Gaseous Atmosphere of M87”. In: *The Astrophysical Journal* 635.2, pp. 894–906. DOI: [10.1086/429746](https://doi.org/10.1086/429746).
- Forman, W. et al. (Aug. 2007). “Filaments, Bubbles, and Weak Shocks in the Gaseous Atmosphere of M87”. In: *The Astrophysical Journal* 665.2, pp. 1057–1066. DOI: [10.1086/519480](https://doi.org/10.1086/519480). arXiv: [astro-ph/0604583](https://arxiv.org/abs/astro-ph/0604583) [astro-ph].
- Forman, W. et al. (Aug. 2017). “Partitioning the Outburst Energy of a Low Eddington Accretion Rate AGN at the Center of an Elliptical Galaxy: The Recent 12 Myr History of the Supermassive Black Hole in M87”. In: *The Astrophysical Journal* 844.2, 122, p. 122. DOI: [10.3847/1538-4357/aa70e4](https://doi.org/10.3847/1538-4357/aa70e4). arXiv: [1705.01104](https://arxiv.org/abs/1705.01104) [astro-ph.GA].
- Fujita, Yutaka et al. (Jan. 2022). “Massive Molecular Gas as a Fuel Tank for Active Galactic Nuclei Feedback In Central Cluster Galaxies”. In: *The Astrophysical Journal* 924.1, 24, p. 24. DOI: [10.3847/1538-4357/ac31a6](https://doi.org/10.3847/1538-4357/ac31a6). arXiv: [2108.01671](https://arxiv.org/abs/2108.01671) [astro-ph.GA].
- Fujita, Yutaka et al. (Mar. 2023). “The correlation between the 500 pc scale molecular gas masses and AGN powers for massive elliptical galaxies”. In: *arXiv e-prints*, arXiv:2303.16927, arXiv:2303.16927. DOI: [10.48550/arXiv.2303.16927](https://doi.org/10.48550/arXiv.2303.16927). arXiv: [2303.16927](https://arxiv.org/abs/2303.16927) [astro-ph.GA].
- Fukugita, M. et al. (Apr. 1996). “The Sloan Digital Sky Survey Photometric System”. In: *The Astronomical Journal* 111, p. 1748. DOI: [10.1086/117915](https://doi.org/10.1086/117915).
- Gangardt, Daria et al. (June 2021). “A taxonomy of black-hole binary spin precession and nutation”. In: *Physical Review D* 103.12, 124026, p. 124026. DOI: [10.1103/PhysRevD.103.124026](https://doi.org/10.1103/PhysRevD.103.124026). arXiv: [2103.03894](https://arxiv.org/abs/2103.03894) [gr-qc].
- Garofalo, David et al. (Feb. 2020). “A Unified Framework for X-shaped Radio Galaxies”. In: 889.2, 91, p. 91. DOI: [10.3847/1538-4357/ab64e3](https://doi.org/10.3847/1538-4357/ab64e3). arXiv: [1912.10494](https://arxiv.org/abs/1912.10494) [astro-ph.HE].
- Gaspari, M. et al. (Feb. 2011). “The dance of heating and cooling in galaxy clusters: three-dimensional simulations of self-regulated active galactic nuclei outflows”. In: *Monthly Notices of the Royal Astronomical Society* 411.1, pp. 349–372. DOI: [10.1111/j.1365-2966.2010.17688.x](https://doi.org/10.1111/j.1365-2966.2010.17688.x). arXiv: [1007.0674](https://arxiv.org/abs/1007.0674) [astro-ph.CO].
- Gaspari, M. et al. (Feb. 2012a). “Cause and Effect of Feedback: Multiphase Gas in Cluster Cores Heated by AGN Jets”. In: *The Astrophysical Journal* 746.1, 94, p. 94. DOI: [10.1088/0004-637X/746/1/94](https://doi.org/10.1088/0004-637X/746/1/94). arXiv: [1110.6063](https://arxiv.org/abs/1110.6063) [astro-ph.CO].
- Gaspari, M. et al. (July 2012b). “Mechanical AGN feedback: controlling the thermodynamical evolution of elliptical galaxies”. In: *Monthly Notices of the Royal Astronomical Society* 424.1, pp. 190–209. DOI: [10.1111/j.1365-2966.2012.21183.x](https://doi.org/10.1111/j.1365-2966.2012.21183.x). arXiv: [1202.6054](https://arxiv.org/abs/1202.6054) [astro-ph.CO].
- Gaspari, M. et al. (July 2013). “Chaotic cold accretion on to black holes”. In: *Monthly Notices of the Royal Astronomical Society* 432.4, pp. 3401–3422. DOI: [10.1093/mnras/stt692](https://doi.org/10.1093/mnras/stt692). arXiv: [1301.3130](https://arxiv.org/abs/1301.3130) [astro-ph.CO].
- Gaspari, M. et al. (Apr. 2017a). “Raining on black holes and massive galaxies: the top-down multiphase condensation model”. In: *Monthly Notices of the Royal Astronomical Society* 466.1, pp. 677–704. DOI: [10.1093/mnras/stw3108](https://doi.org/10.1093/mnras/stw3108). arXiv: [1608.08216](https://arxiv.org/abs/1608.08216) [astro-ph.GA].

- Gaspari, M. et al. (Feb. 2018). “Shaken Snow Globes: Kinematic Tracers of the Multiphase Condensation Cascade in Massive Galaxies, Groups, and Clusters”. In: *The Astrophysical Journal* 854.2, 167, p. 167. DOI: [10.3847/1538-4357/aaaa1b](https://doi.org/10.3847/1538-4357/aaaa1b). arXiv: [1709.06564](https://arxiv.org/abs/1709.06564) [astro-ph.GA].
- Gaspari, Massimo and Aleksander Sądowski (Mar. 2017b). “Unifying the Micro and Macro Properties of AGN Feeding and Feedback”. In: *The Astrophysical Journal* 837.2, 149, p. 149. DOI: [10.3847/1538-4357/aa61a3](https://doi.org/10.3847/1538-4357/aa61a3). arXiv: [1701.07030](https://arxiv.org/abs/1701.07030) [astro-ph.HE].
- Gaspari, Massimo et al. (Jan. 2020). “Linking macro-, meso- and microscales in multiphase AGN feeding and feedback”. In: *Nature Astronomy* 4, pp. 10–13. DOI: [10.1038/s41550-019-0970-1](https://doi.org/10.1038/s41550-019-0970-1). arXiv: [2001.04985](https://arxiv.org/abs/2001.04985) [astro-ph.GA].
- Gastaldello, Fabio et al. (Feb. 2010). “The inverse iron-bias in action in Abell 2028”. In: *The Energetic Cosmos: from Suzaku to ASTRO-H*, pp. 94–95. arXiv: [0909.4679](https://arxiv.org/abs/0909.4679) [astro-ph.CO].
- Gendron-Marsolais, M. et al. (Sept. 2018). “Revealing the velocity structure of the filamentary nebula in NGC 1275 in its entirety”. In: *Monthly Notices of the Royal Astronomical Society* 479.1, pp. L28–L33. DOI: [10.1093/mnrasl/sly084](https://doi.org/10.1093/mnrasl/sly084). arXiv: [1802.00031](https://arxiv.org/abs/1802.00031) [astro-ph.GA].
- Ghisellini, G. and A. Celotti (Nov. 2001). “The dividing line between FR I and FR II radio-galaxies”. In: *Astronomy & Astrophysics* 379, pp. L1–L4. DOI: [10.1051/0004-6361:20011338](https://doi.org/10.1051/0004-6361:20011338). arXiv: [astro-ph/0106570](https://arxiv.org/abs/astro-ph/0106570) [astro-ph].
- Ghizzardi, S. et al. (June 2010). “Cold fronts in galaxy clusters”. In: *Astronomy & Astrophysics* 516, A32, A32. DOI: [10.1051/0004-6361/200912496](https://doi.org/10.1051/0004-6361/200912496). arXiv: [1003.1051](https://arxiv.org/abs/1003.1051) [astro-ph.CO].
- Ghizzardi, Simona et al. (Oct. 2014). “Metal distribution in sloshing galaxy clusters: the case of A496”. In: *Astronomy & Astrophysics* 570, A117, A117. DOI: [10.1051/0004-6361/201424016](https://doi.org/10.1051/0004-6361/201424016). arXiv: [1407.6814](https://arxiv.org/abs/1407.6814) [astro-ph.CO].
- Giacintucci, S. et al. (Mar. 2020). “Discovery of a Giant Radio Fossil in the Ophiuchus Galaxy Cluster”. In: *The Astrophysical Journal* 891.1, 1, p. 1. DOI: [10.3847/1538-4357/ab6a9d](https://doi.org/10.3847/1538-4357/ab6a9d). arXiv: [2002.01291](https://arxiv.org/abs/2002.01291) [astro-ph.GA].
- Giacintucci, Simona (2016). “Tracing multiple AGN outbursts in the cool core of A496”. In: *Mid-Atlantic Radio-Loud AGN Meeting (MARLAM)*. URL: https://astro.umbc.edu/MARLAM2016/presentations//Giacintucci_Simona_MARLAM4_2016.pdf.
- Giacintucci, Simona et al. (Jan. 2014). “New Detections of Radio Minihalos in Cool Cores of Galaxy Clusters”. In: *The Astrophysical Journal* 781.1, 9, p. 9. DOI: [10.1088/0004-637X/781/1/9](https://doi.org/10.1088/0004-637X/781/1/9). arXiv: [1311.5248](https://arxiv.org/abs/1311.5248) [astro-ph.CO].
- Giodini, S. et al. (May 2010). “Radio Galaxy Feedback in X-ray-selected Groups from COSMOS: The Effect on the Intracluster Medium”. In: *The Astrophysical Journal* 714.1, pp. 218–228. DOI: [10.1088/0004-637X/714/1/218](https://doi.org/10.1088/0004-637X/714/1/218). arXiv: [1002.4212](https://arxiv.org/abs/1002.4212) [astro-ph.CO].
- Giovannini, G. et al. (Feb. 2011). “The jet in M87 from e-EVN observations”. In: *Jets at All Scales*. Ed. by Gustavo E. Romero et al. Vol. 275, pp. 150–154. DOI: [10.1017/S174392131001584X](https://doi.org/10.1017/S174392131001584X). arXiv: [1010.4170](https://arxiv.org/abs/1010.4170) [astro-ph.CO].
- Giovannini, G. et al. (Apr. 2023). “Jets in FR0 radio galaxies”. In: *Astronomy & Astrophysics* 672, A104, A104. DOI: [10.1051/0004-6361/202245395](https://doi.org/10.1051/0004-6361/202245395). arXiv: [2302.12657](https://arxiv.org/abs/2302.12657) [astro-ph.GA].
- Giri, Gourab et al. (Aug. 2022). “Dynamical modelling and emission signatures of a candidate dual AGN with precessing radio jets”. In: *Monthly Notices of the Royal Astronomical Society* 514.4, pp. 5625–5639. DOI: [10.1093/mnras/stac1628](https://doi.org/10.1093/mnras/stac1628). arXiv: [2206.04705](https://arxiv.org/abs/2206.04705) [astro-ph.GA].
- Giroletti, M. et al. (Jan. 2004). “Parsec-Scale Properties of Markarian 501”. In: *The Astrophysical Journal* 600.1, pp. 127–140. DOI: [10.1086/379663](https://doi.org/10.1086/379663). arXiv: [astro-ph/0309285](https://arxiv.org/abs/astro-ph/0309285) [astro-ph].
- Giroletti, M. et al. (Mar. 2005). “The Two-sided Parsec-Scale Structure of the Low-Luminosity Active Galactic Nucleus in NGC 4278”. In: *The Astrophysical Journal* 622.1, pp. 178–186. DOI: [10.1086/427898](https://doi.org/10.1086/427898). arXiv: [astro-ph/0412204](https://arxiv.org/abs/astro-ph/0412204) [astro-ph].
- Giroletti, M. and A. Polatidis (Feb. 2009). “Samples and statistics of CSS and GPS sources”. In: *Astronomische Nachrichten* 330.2, p. 193. DOI: [10.1002/asna.200811154](https://doi.org/10.1002/asna.200811154). arXiv: [0904.1068](https://arxiv.org/abs/0904.1068) [astro-ph.CO].

- Gitti, M. et al. (Mar. 2006). “Multifrequency VLA radio observations of the X-ray cavity cluster of galaxies RBS797: evidence of differently oriented jets”. In: *Astronomy & Astrophysics* 448.3, pp. 853–860. DOI: [10.1051/0004-6361:20053998](https://doi.org/10.1051/0004-6361:20053998). arXiv: [astro-ph/0510613](https://arxiv.org/abs/astro-ph/0510613) [astro-ph].
- Gitti, M. et al. (May 2007). “Cosmological Effects of Powerful AGN Outbursts in Galaxy Clusters: Insights from an XMM-Newton Observation of MS 0735+7421”. In: *The Astrophysical Journal* 660.2, pp. 1118–1136. DOI: [10.1086/512800](https://doi.org/10.1086/512800). arXiv: [astro-ph/0701386](https://arxiv.org/abs/astro-ph/0701386) [astro-ph].
- Gitti, M. et al. (Sept. 2013). “A candidate supermassive binary black hole system in the brightest cluster galaxy of RBS 797”. In: *Astronomy & Astrophysics* 557, L14, p. L14. DOI: [10.1051/0004-6361/201322401](https://doi.org/10.1051/0004-6361/201322401). arXiv: [1308.5851](https://arxiv.org/abs/1308.5851) [astro-ph.CO].
- Gitti, Myriam et al. (May 2010). “Cavities and Shocks in the Galaxy Group HCG 62 as Revealed by Chandra, XMM-Newton, and Giant Metrewave Radio Telescope Data”. In: *The Astrophysical Journal* 714.1, pp. 758–771. DOI: [10.1088/0004-637X/714/1/758](https://doi.org/10.1088/0004-637X/714/1/758). arXiv: [0912.3013](https://arxiv.org/abs/0912.3013) [astro-ph.CO].
- Gitti, Myriam et al. (May 2011). “A Chandra Study of the Large-scale Shock and Cool Filaments in Hydra A: Evidence for Substantial Gas Dredge-up by the Central Outburst”. In: *The Astrophysical Journal* 732.1, 13, p. 13. DOI: [10.1088/0004-637X/732/1/13](https://doi.org/10.1088/0004-637X/732/1/13). arXiv: [1102.5397](https://arxiv.org/abs/1102.5397) [astro-ph.CO].
- Gitti, Myriam et al. (Jan. 2012). “Evidence for AGN Feedback in Galaxy Clusters and Groups”. In: *Advances in Astronomy* 2012, 950641, p. 950641. DOI: [10.1155/2012/950641](https://doi.org/10.1155/2012/950641). arXiv: [1109.3334](https://arxiv.org/abs/1109.3334) [astro-ph.CO].
- Globus, N. and A. Levinson (Sept. 2016). “The collimation of magnetic jets by disc winds”. In: *Monthly Notices of the Royal Astronomical Society* 461.3, pp. 2605–2615. DOI: [10.1093/mnras/stw1474](https://doi.org/10.1093/mnras/stw1474). arXiv: [1604.07408](https://arxiv.org/abs/1604.07408) [astro-ph.HE].
- Govoni, Federica and Luigina Feretti (Jan. 2004). “Magnetic Fields in Clusters of Galaxies”. In: *International Journal of Modern Physics D* 13.8, pp. 1549–1594. DOI: [10.1142/S0218271804005080](https://doi.org/10.1142/S0218271804005080). arXiv: [astro-ph/0410182](https://arxiv.org/abs/astro-ph/0410182) [astro-ph].
- Graham, J. et al. (Dec. 2008a). “Detecting sound-wave-like surface brightness ripples in cluster cores”. In: *Monthly Notices of the Royal Astronomical Society* 391.4, pp. 1749–1757. DOI: [10.1111/j.1365-2966.2008.13861.x](https://doi.org/10.1111/j.1365-2966.2008.13861.x). arXiv: [0808.2408](https://arxiv.org/abs/0808.2408) [astro-ph].
- (May 2008b). “The weak shock in the core of the Perseus cluster”. In: *Monthly Notices of the Royal Astronomical Society* 386.1, pp. 278–288. DOI: [10.1111/j.1365-2966.2008.13027.x](https://doi.org/10.1111/j.1365-2966.2008.13027.x). arXiv: [0801.4253](https://arxiv.org/abs/0801.4253) [astro-ph].
- Greisen, E. W. (Mar. 2003). “AIPS, the VLA, and the VLBA”. In: *Information Handling in Astronomy - Historical Vistas*. Ed. by André Heck. Vol. 285. Astrophysics and Space Science Library, p. 109. DOI: [10.1007/0-306-48080-8_7](https://doi.org/10.1007/0-306-48080-8_7).
- Gültekin, Kayhan et al. (Jan. 2019). “The Fundamental Plane of Black Hole Accretion and Its Use as a Black Hole-Mass Estimator”. In: *The Astrophysical Journal* 871.1, 80, p. 80. DOI: [10.3847/1538-4357/aaf6b9](https://doi.org/10.3847/1538-4357/aaf6b9). arXiv: [1901.02530](https://arxiv.org/abs/1901.02530) [astro-ph.HE].
- Gutiérrez, E. M. et al. (Jan. 2023). “Flares from dual jets in supermassive black hole binaries”. In: *arXiv e-prints*, arXiv:2301.04280, arXiv:2301.04280. DOI: [10.48550/arXiv.2301.04280](https://doi.org/10.48550/arXiv.2301.04280). arXiv: [2301.04280](https://arxiv.org/abs/2301.04280) [astro-ph.HE].
- Haarsma, Deborah B. et al. (Apr. 2010). “Brightest Cluster Galaxies and Core Gas Density in REXCESS Clusters”. In: *The Astrophysical Journal* 713.2, pp. 1037–1047. DOI: [10.1088/0004-637X/713/2/1037](https://doi.org/10.1088/0004-637X/713/2/1037). arXiv: [0911.2798](https://arxiv.org/abs/0911.2798) [astro-ph.CO].
- Hamer, S. L. et al. (Apr. 2012). “The relation between line emission and brightest cluster galaxies in three exceptional clusters: evidence for gas cooling from the intracluster medium”. In: *Monthly Notices of the Royal Astronomical Society* 421.4, pp. 3409–3417. DOI: [10.1111/j.1365-2966.2012.20566.x](https://doi.org/10.1111/j.1365-2966.2012.20566.x). arXiv: [1112.4848](https://arxiv.org/abs/1112.4848) [astro-ph.CO].
- Hamer, S. L. et al. (Aug. 2016). “Optical emission line nebulae in galaxy cluster cores 1: the morphological, kinematic and spectral properties of the sample”. In: *Monthly Notices of the Royal Astronomical Society* 460.2, pp. 1758–1789. DOI: [10.1093/mnras/stw1054](https://doi.org/10.1093/mnras/stw1054). arXiv: [1603.03047](https://arxiv.org/abs/1603.03047) [astro-ph.GA].

- Hardcastle, M. J. et al. (Aug. 2006). "The X-ray nuclei of intermediate-redshift radio sources". In: *Monthly Notices of the Royal Astronomical Society* 370.4, pp. 1893–1904. DOI: [10.1111/j.1365-2966.2006.10615.x](https://doi.org/10.1111/j.1365-2966.2006.10615.x). arXiv: [astro-ph/0603090](https://arxiv.org/abs/astro-ph/0603090) [astro-ph].
- Hardcastle, M. J. et al. (Nov. 2007a). "A Chandra Study of Particle Acceleration in the Multiple Hot Spots of Nearby Radio Galaxies". In: *The Astrophysical Journal* 669.2, pp. 893–904. DOI: [10.1086/521696](https://doi.org/10.1086/521696). arXiv: [0707.2865](https://arxiv.org/abs/0707.2865) [astro-ph].
- Hardcastle, M. J. et al. (Apr. 2007b). "Hot and cold gas accretion and feedback in radio-loud active galaxies". In: *Monthly Notices of the Royal Astronomical Society* 376.4, pp. 1849–1856. DOI: [10.1111/j.1365-2966.2007.11572.x](https://doi.org/10.1111/j.1365-2966.2007.11572.x). arXiv: [astro-ph/0701857](https://arxiv.org/abs/astro-ph/0701857) [astro-ph].
- Hardcastle, M. J. and J. H. Croston (June 2020). "Radio galaxies and feedback from AGN jets". In: *New Astronomy Review* 88, 101539, p. 101539. DOI: [10.1016/j.newar.2020.101539](https://doi.org/10.1016/j.newar.2020.101539). arXiv: [2003.06137](https://arxiv.org/abs/2003.06137) [astro-ph.HE].
- Harwood, Jeremy J. et al. (Nov. 2013). "Spectral ageing in the lobes of FR-II radio galaxies: new methods of analysis for broad-band radio data". In: *Monthly Notices of the Royal Astronomical Society* 435.4, pp. 3353–3375. DOI: [10.1093/mnras/stt1526](https://doi.org/10.1093/mnras/stt1526). arXiv: [1308.4137](https://arxiv.org/abs/1308.4137) [astro-ph.CO].
- Harwood, Jeremy J. et al. (Dec. 2015). "Spectral ageing in the lobes of cluster-centre FR II radio galaxies". In: *Monthly Notices of the Royal Astronomical Society* 454.4, pp. 3403–3422. DOI: [10.1093/mnras/stv2194](https://doi.org/10.1093/mnras/stv2194). arXiv: [1509.06757](https://arxiv.org/abs/1509.06757) [astro-ph.GA].
- Heckman, T. M. (Nov. 1981). "Optical emission-line gas associated with dominant cluster galaxies". In: *The Astrophysical Journal Letters* 250, pp. L59–L63. DOI: [10.1086/183674](https://doi.org/10.1086/183674).
- Heckman, Timothy M. et al. (Mar. 1989). "Dynamical, Physical, and Chemical Properties of Emission-Line Nebulae in Cooling Flows". In: *The Astrophysical Journal* 338, p. 48. DOI: [10.1086/167181](https://doi.org/10.1086/167181).
- Heinz, S. and T. Enßlin (Jan. 2004). "The Interaction of Jets with the Intracluster Medium". In: *The Riddle of Cooling Flows in Galaxies and Clusters of galaxies*. Ed. by T. Reiprich et al., p. 255.
- Heinz, S. and E. Churazov (Dec. 2005). "Heating the Bubbly Gas of Galaxy Clusters with Weak Shocks and Sound Waves". In: *The Astrophysical Journal* 634.2, pp. L141–L144. DOI: [10.1086/498301](https://doi.org/10.1086/498301). arXiv: [astro-ph/0507038](https://arxiv.org/abs/astro-ph/0507038) [astro-ph].
- HI4PI Collaboration et al. (Oct. 2016). "HI4PI: A full-sky H I survey based on EBHIS and GASS". In: *Astronomy & Astrophysics* 594, A116, A116. DOI: [10.1051/0004-6361/201629178](https://doi.org/10.1051/0004-6361/201629178). arXiv: [1610.06175](https://arxiv.org/abs/1610.06175) [astro-ph.GA].
- Hill, Gary J. and Simon J. Lilly (Jan. 1991). "A Change in the Cluster Environments of Radio Galaxies with Cosmic Epoch". In: *The Astrophysical Journal Letters* 367, p. 1. DOI: [10.1086/169597](https://doi.org/10.1086/169597).
- Hjellming, R. M. and K. J. Johnston (June 1981). "An analysis of the proper motions of SS 433 radio jets." In: *The Astrophysical Journal* 246, pp. L141–L145. DOI: [10.1086/183571](https://doi.org/10.1086/183571).
- Hlavacek-Larrondo, J. et al. (Aug. 2011). "AGN feedback and iron enrichment in the powerful radio galaxy, 4C+55.16". In: *Monthly Notices of the Royal Astronomical Society* 415.4, pp. 3520–3530. DOI: [10.1111/j.1365-2966.2011.18960.x](https://doi.org/10.1111/j.1365-2966.2011.18960.x). arXiv: [1103.2585](https://arxiv.org/abs/1103.2585) [astro-ph.CO].
- Hlavacek-Larrondo, J. et al. (Apr. 2012). "Extreme AGN feedback in the MAssive Cluster Survey: a detailed study of X-ray cavities at $z > 0.3$ ". In: *Monthly Notices of the Royal Astronomical Society* 421.2, pp. 1360–1384. DOI: [10.1111/j.1365-2966.2011.20405.x](https://doi.org/10.1111/j.1365-2966.2011.20405.x). arXiv: [1110.0489](https://arxiv.org/abs/1110.0489) [astro-ph.CO].
- Hlavacek-Larrondo, J. et al. (Nov. 2013a). "Probing the Extreme Realm of Active Galactic Nucleus Feedback in the Massive Galaxy Cluster, RX J1532.9+3021". In: *The Astrophysical Journal* 777.2, 163, p. 163. DOI: [10.1088/0004-637X/777/2/163](https://doi.org/10.1088/0004-637X/777/2/163). arXiv: [1306.0907](https://arxiv.org/abs/1306.0907) [astro-ph.CO].
- Hlavacek-Larrondo, J. et al. (May 2013b). "The rapid evolution of AGN feedback in brightest cluster galaxies: switching from quasar-mode to radio-mode feedback". In: *Monthly Notices of the Royal Astronomical Society* 431.2, pp. 1638–1658. DOI: [10.1093/mnras/stt283](https://doi.org/10.1093/mnras/stt283). arXiv: [1211.5606](https://arxiv.org/abs/1211.5606) [astro-ph.CO].
- Hlavacek-Larrondo, J. et al. (May 2015). "X-Ray Cavities in a Sample of 83 SPT-selected Clusters of Galaxies: Tracing the Evolution of AGN Feedback in Clusters of Galaxies out to $z=1.2$ ". In: *The Astrophysical Journal* 805.1, 35, p. 35. arXiv: [1410.0025](https://arxiv.org/abs/1410.0025) [astro-ph.HE].

- Hlavacek-Larrondo, Julie et al. (2022). "AGN Feedback in Groups and Clusters of Galaxies". In: *Handbook of X-ray and Gamma-ray Astrophysics*, 5, p. 5. DOI: [10.1007/978-981-16-4544-0_122-1](https://doi.org/10.1007/978-981-16-4544-0_122-1).
- Hodges-Kluck, Edmund J. et al. (July 2010). "A Deep Chandra Observation of the X-shaped Radio Galaxy 4C +00.58: A Candidate for Merger-induced Reorientation?" In: *The Astrophysical Journal* 717.1, pp. L37–L41. DOI: [10.1088/2041-8205/717/1/L37](https://doi.org/10.1088/2041-8205/717/1/L37). arXiv: [1005.4928](https://arxiv.org/abs/1005.4928) [astro-ph.CO].
- Hodges-Kluck, Edmund J. and Christopher S. Reynolds (May 2011). "Hydrodynamic Models of Radio Galaxy Morphology: Winged and X-shaped Sources". In: *The Astrophysical Journal* 733.1, 58, p. 58. DOI: [10.1088/0004-637X/733/1/58](https://doi.org/10.1088/0004-637X/733/1/58). arXiv: [1103.4863](https://arxiv.org/abs/1103.4863) [astro-ph.CO].
- Hogan, M. T. (Sept. 2014). "The Radio Properties of Brightest Cluster Galaxies". PhD thesis. Durham University, UK.
- Hogan, M. T. et al. (Oct. 2015a). "A comprehensive study of the radio properties of brightest cluster galaxies". In: *Monthly Notices of the Royal Astronomical Society* 453.2, pp. 1201–1222. DOI: [10.1093/mnras/stv1517](https://doi.org/10.1093/mnras/stv1517). arXiv: [1507.03019](https://arxiv.org/abs/1507.03019) [astro-ph.GA].
- Hogan, M. T. et al. (Oct. 2015b). "High radio-frequency properties and variability of brightest cluster galaxies". In: *Monthly Notices of the Royal Astronomical Society* 453.2, pp. 1223–1240. DOI: [10.1093/mnras/stv1518](https://doi.org/10.1093/mnras/stv1518). arXiv: [1507.03022](https://arxiv.org/abs/1507.03022) [astro-ph.GA].
- Hogan, M. T. et al. (Dec. 2017). "The Onset of Thermally Unstable Cooling from the Hot Atmospheres of Giant Galaxies in Clusters: Constraints on Feedback Models". In: *The Astrophysical Journal* 851.1, 66, p. 66. DOI: [10.3847/1538-4357/aa9af3](https://doi.org/10.3847/1538-4357/aa9af3). arXiv: [1704.00011](https://arxiv.org/abs/1704.00011) [astro-ph.GA].
- Holt, J. et al. (Jan. 2011). "The impact of the warm outflow in the young (GPS) radio source and ULIRG PKS 1345+12 (4C 12.50)". In: *Monthly Notices of the Royal Astronomical Society* 410.3, pp. 1527–1536. DOI: [10.1111/j.1365-2966.2010.17535.x](https://doi.org/10.1111/j.1365-2966.2010.17535.x). arXiv: [1008.2846](https://arxiv.org/abs/1008.2846) [astro-ph.CO].
- Horton, Maya A. et al. (Dec. 2020). "3D hydrodynamic simulations of large-scale precessing jets: radio morphology". In: *Monthly Notices of the Royal Astronomical Society* 499.4, pp. 5765–5781. DOI: [10.1093/mnras/staa3020](https://doi.org/10.1093/mnras/staa3020). arXiv: [2010.00480](https://arxiv.org/abs/2010.00480) [astro-ph.GA].
- (May 2023). "New mechanisms for forming multiple hotspots in radio jets". In: *Monthly Notices of the Royal Astronomical Society* 521.2, pp. 2593–2606. DOI: [10.1093/mnras/stad674](https://doi.org/10.1093/mnras/stad674). arXiv: [2302.14023](https://arxiv.org/abs/2302.14023) [astro-ph.HE].
- Hu, E. M. et al. (Dec. 1985). "Long-slit spectroscopy of gas in the cores of X-ray luminous clusters." In: *The Astrophysical Journal Supplement* 59, pp. 447–498. DOI: [10.1086/191081](https://doi.org/10.1086/191081).
- Hudson, D. S. et al. (July 2006). "X-ray detection of the proto supermassive binary black hole at the centre of Abell 400". In: *Astronomy & Astrophysics* 453.2, pp. 433–446. DOI: [10.1051/0004-6361:20064955](https://doi.org/10.1051/0004-6361:20064955). arXiv: [astro-ph/0603272](https://arxiv.org/abs/astro-ph/0603272) [astro-ph].
- Hudson, D. S. et al. (Apr. 2010). "What is a cool-core cluster? a detailed analysis of the cores of the X-ray flux-limited HIFLUGCS cluster sample". In: *Astronomy & Astrophysics* 513, A37, A37. DOI: [10.1051/0004-6361/200912377](https://doi.org/10.1051/0004-6361/200912377). arXiv: [0911.0409](https://arxiv.org/abs/0911.0409) [astro-ph.CO].
- Intema, H. T. et al. (Feb. 2017). "The GMRT 150 MHz all-sky radio survey. First alternative data release TGSS ADR1". In: *Astronomy & Astrophysics* 598, A78, A78. DOI: [10.1051/0004-6361/201628536](https://doi.org/10.1051/0004-6361/201628536). arXiv: [1603.04368](https://arxiv.org/abs/1603.04368) [astro-ph.CO].
- Issaoun, Sara et al. (Aug. 2022). "Resolving the Inner Parsec of the Blazar J1924-2914 with the Event Horizon Telescope". In: *The Astrophysical Journal* 934.2, 145, p. 145. DOI: [10.3847/1538-4357/ac7a40](https://doi.org/10.3847/1538-4357/ac7a40). arXiv: [2208.01662](https://arxiv.org/abs/2208.01662) [astro-ph.HE].
- Jackson, N. et al. (Feb. 2022). "Sub-arcsecond imaging with the International LOFAR Telescope. II. Completion of the LOFAR Long-Baseline Calibrator Survey". In: *Astronomy & Astrophysics* 658, A2, A2. DOI: [10.1051/0004-6361/202140756](https://doi.org/10.1051/0004-6361/202140756). arXiv: [2108.07284](https://arxiv.org/abs/2108.07284) [astro-ph.GA].
- Jaffe, W. J. and G. C. Perola (Aug. 1973). "Dynamical Models of Tailed Radio Sources in Clusters of Galaxies". In: *Astronomy & Astrophysics* 26, p. 423.
- Janssen, R. M. J. et al. (May 2012). "The triggering probability of radio-loud AGN. A comparison of high and low excitation radio galaxies in hosts of different colors". In: *Astronomy & Astrophysics* 541, A62, A62. DOI: [10.1051/0004-6361/201219052](https://doi.org/10.1051/0004-6361/201219052). arXiv: [1206.0578](https://arxiv.org/abs/1206.0578) [astro-ph.CO].

- Johnstone, R. M. et al. (Jan. 1987). "The optical spectra of central galaxies in southern clusters : evidence for star formation." In: *Monthly Notices of the Royal Astronomical Society* 224, pp. 75–91. DOI: [10.1093/mnras/224.1.75](https://doi.org/10.1093/mnras/224.1.75).
- Johnstone, R. M. et al. (Jan. 2005). "The galaxy cluster Abell 3581 as seen by Chandra". In: *Monthly Notices of the Royal Astronomical Society* 356.1, pp. 237–246. DOI: [10.1111/j.1365-2966.2004.08445.x](https://doi.org/10.1111/j.1365-2966.2004.08445.x). arXiv: [astro-ph/0410154](https://arxiv.org/abs/astro-ph/0410154) [astro-ph].
- Jones, C. et al. (Mar. 2002). "Chandra Observations of NGC 4636-an Elliptical Galaxy in Turmoil". In: *The Astrophysical Journal* 567.2, pp. L115–L118. DOI: [10.1086/340114](https://doi.org/10.1086/340114). arXiv: [astro-ph/0108114](https://arxiv.org/abs/astro-ph/0108114) [astro-ph].
- Joshi, Ravi et al. (Dec. 2019). "X-shaped Radio Galaxies: Optical Properties, Large-scale Environment, and Relationship to Radio Structure". In: 887.2, 266, p. 266. DOI: [10.3847/1538-4357/ab536f](https://doi.org/10.3847/1538-4357/ab536f). arXiv: [1911.00016](https://arxiv.org/abs/1911.00016) [astro-ph.GA].
- Kaiser, N. (Sept. 1986). "Evolution and clustering of rich clusters." In: *Monthly Notices of the Royal Astronomical Society* 222, pp. 323–345. DOI: [10.1093/mnras/222.2.323](https://doi.org/10.1093/mnras/222.2.323).
- (Dec. 1991). "Evolution of Clusters of Galaxies". In: *The Astrophysical Journal* 383, p. 104. DOI: [10.1086/170768](https://doi.org/10.1086/170768).
- Kang, Daeun et al. (Aug. 2017). "Outflow Kinematics Manifested by the H α Line: Gas Outflows in Type 2 AGNs. IV." In: *The Astrophysical Journal* 845.2, 131, p. 131. DOI: [10.3847/1538-4357/aa80e8](https://doi.org/10.3847/1538-4357/aa80e8). arXiv: [1707.05895](https://arxiv.org/abs/1707.05895) [astro-ph.GA].
- Kappes, A. et al. (Nov. 2019). "LOFAR measures the hotspot advance speed of the high-redshift blazar S5 0836+710". In: *Astronomy & Astrophysics* 631, A49, A49. DOI: [10.1051/0004-6361/201936164](https://doi.org/10.1051/0004-6361/201936164). arXiv: [1909.02412](https://arxiv.org/abs/1909.02412) [astro-ph.HE].
- Kardashev, N. S. (Dec. 1962). "Nonstationarity of Spectra of Young Sources of Nonthermal Radio Emission". In: *Soviet Astronomy* 6, p. 317.
- Kharb, P. et al. (Feb. 2010). "Extended Radio Emission in MOJAVE Blazars: Challenges to Unification". In: *The Astrophysical Journal* 710.1, pp. 764–782. DOI: [10.1088/0004-637X/710/1/764](https://doi.org/10.1088/0004-637X/710/1/764). arXiv: [1001.0731](https://arxiv.org/abs/1001.0731) [astro-ph.CO].
- Kharb, P. et al. (Feb. 2019). "A Curved 150 pc Long Jet in the Double-peaked Emission-line AGN KISSR 434". In: *The Astrophysical Journal* 871.2, 249, p. 249. DOI: [10.3847/1538-4357/aafad7](https://doi.org/10.3847/1538-4357/aafad7). arXiv: [1812.11074](https://arxiv.org/abs/1812.11074) [astro-ph.GA].
- King, Andrew and Chris Nixon (Oct. 2015). "AGN flickering and chaotic accretion". In: 453.1, pp. L46–L47. DOI: [10.1093/mnrasl/slv098](https://doi.org/10.1093/mnrasl/slv098). arXiv: [1507.05960](https://arxiv.org/abs/1507.05960) [astro-ph.HE].
- King, Ivan R. (Feb. 1966). "The structure of star clusters. III. Some simple dynamical models". In: *Astronomical Journal* 71, p. 64. DOI: [10.1086/109857](https://doi.org/10.1086/109857).
- Kirkpatrick, C. C. et al. (Apr. 2011). "Anisotropic Metal-enriched Outflows Driven by Active Galactic Nuclei in Clusters of Galaxies". In: *The Astrophysical Journal* 731.2, L23, p. L23. DOI: [10.1088/2041-8205/731/2/L23](https://doi.org/10.1088/2041-8205/731/2/L23). arXiv: [1103.0793](https://arxiv.org/abs/1103.0793) [astro-ph.GA].
- Kirkpatrick, C. C. and B. R. McNamara (Oct. 2015). "Hot outflows in galaxy clusters". In: *Monthly Notices of the Royal Astronomical Society* 452.4, pp. 4361–4376. DOI: [10.1093/mnras/stv1574](https://doi.org/10.1093/mnras/stv1574). arXiv: [1507.05973](https://arxiv.org/abs/1507.05973) [astro-ph.GA].
- Koay, J. Y. et al. (Mar. 2018). "The MASIV Survey - IV. Relationship between intra-day scintillation and intrinsic variability of radio AGNs". In: *Monthly Notices of the Royal Astronomical Society* 474.4, pp. 4396–4411. DOI: [10.1093/mnras/stx3076](https://doi.org/10.1093/mnras/stx3076). arXiv: [1711.08140](https://arxiv.org/abs/1711.08140) [astro-ph.GA].
- Kokotanekov, G. et al. (Oct. 2018). "Signatures of multiple episodes of AGN activity in the core of Abell 1795". In: *Astronomy & Astrophysics* 618, A152, A152. DOI: [10.1051/0004-6361/201833222](https://doi.org/10.1051/0004-6361/201833222). arXiv: [1807.11520](https://arxiv.org/abs/1807.11520) [astro-ph.GA].
- Kolokythas, Konstantinos et al. (Aug. 2020). "Evidence of AGN feedback and sloshing in the X-ray luminous NGC 1550 galaxy group". In: *Monthly Notices of the Royal Astronomical Society* 496.2, pp. 1471–1487. DOI: [10.1093/mnras/staa1506](https://doi.org/10.1093/mnras/staa1506). arXiv: [2005.12950](https://arxiv.org/abs/2005.12950) [astro-ph.GA].
- Komissarov, S. S. and A. G. Gubanov (May 1994). "Relic radio galaxies: evolution of synchrotron spectrum". In: *Astronomy & Astrophysics* 285, pp. 27–43.

- Komissarov, Serguei (2012). “Central Engines: Acceleration, Collimation and Confinement of Jets”. In: *Relativistic Jets from Active Galactic Nuclei*, pp. 81–114. DOI: [10.1002/9783527641741.ch4](https://doi.org/10.1002/9783527641741.ch4).
- Komossa, S. et al. (June 2023). “Absence of the predicted 2022 October outburst of OJ 287 and implications for binary SMBH scenarios”. In: *Monthly Notices of the Royal Astronomical Society* 522.1, pp. L84–L88. DOI: [10.1093/mnrasl/slad016](https://doi.org/10.1093/mnrasl/slad016). arXiv: [2302.11646](https://arxiv.org/abs/2302.11646) [astro-ph.HE].
- Konar, C. et al. (Oct. 2006). “Spectral ageing analysis of the double-double radio galaxy J1453+3308”. In: *Monthly Notices of the Royal Astronomical Society* 372.2, pp. 693–702. DOI: [10.1111/j.1365-2966.2006.10874.x](https://doi.org/10.1111/j.1365-2966.2006.10874.x). arXiv: [astro-ph/0607660](https://arxiv.org/abs/astro-ph/0607660) [astro-ph].
- Konar, C. and M. J. Hardcastle (Dec. 2013). “Particle acceleration and dynamics of double-double radio galaxies: theory versus observations”. In: *Monthly Notices of the Royal Astronomical Society* 436.2, pp. 1595–1614. DOI: [10.1093/mnras/stt1676](https://doi.org/10.1093/mnras/stt1676). arXiv: [1309.1401](https://arxiv.org/abs/1309.1401) [astro-ph.CO].
- Kozieł-Wierzbowska, Dorota et al. (Apr. 2020). “Radio Sources Associated with Optical Galaxies and Having Unresolved or Extended Morphologies (ROGUE). I. A Catalog of SDSS Galaxies with FIRST Core Identifications”. In: *The Astrophysical Journals* 247.2, 53, p. 53. DOI: [10.3847/1538-4365/ab63d3](https://doi.org/10.3847/1538-4365/ab63d3). arXiv: [1912.09959](https://arxiv.org/abs/1912.09959) [astro-ph.GA].
- Kraft, R. P. et al. (July 2003). “X-Ray Emission from the Hot Interstellar Medium and Southwest Radio Lobe of the Nearby Radio Galaxy Centaurus A”. In: *The Astrophysical Journal* 592.1, pp. 129–146. DOI: [10.1086/375533](https://doi.org/10.1086/375533). arXiv: [astro-ph/0304363](https://arxiv.org/abs/astro-ph/0304363) [astro-ph].
- Kraft, R. P. et al. (Mar. 2005). “A Chandra Study of the Multicomponent X-Ray Emission from the X-shaped Radio Galaxy 3C 403”. In: *The Astrophysical Journal* 622.1, pp. 149–159. DOI: [10.1086/427822](https://doi.org/10.1086/427822). arXiv: [astro-ph/0501031](https://arxiv.org/abs/astro-ph/0501031) [astro-ph].
- Kraft, R. P. et al. (Mar. 2012). “AN ACTIVE GALACTIC NUCLEUS DRIVEN SHOCK IN THE INTRACLUSTER MEDIUM AROUND THE RADIO GALAXY 3C 310”. In: *The Astrophysical Journal* 749.1, p. 19. DOI: [10.1088/0004-637x/749/1/19](https://doi.org/10.1088/0004-637x/749/1/19). URL: <https://doi.org/10.1088/0004-637x/749/1/19>.
- Krause, Martin G. H. et al. (Jan. 2019). “How frequent are close supermassive binary black holes in powerful jet sources?” In: *Monthly Notices of the Royal Astronomical Society* 482.1, pp. 240–261. DOI: [10.1093/mnras/sty2558](https://doi.org/10.1093/mnras/sty2558). arXiv: [1809.04050](https://arxiv.org/abs/1809.04050) [astro-ph.HE].
- Kravtsov, Andrey V. and Stefano Borgani (Sept. 2012). “Formation of Galaxy Clusters”. In: *Annual Review of Astronomy and Astrophysics* 50, pp. 353–409. DOI: [10.1146/annurev-astro-081811-125502](https://doi.org/10.1146/annurev-astro-081811-125502). arXiv: [1205.5556](https://arxiv.org/abs/1205.5556) [astro-ph.CO].
- Kun, E. et al. (Dec. 2014). “A spinning supermassive black hole binary model consistent with VLBI observations of the S5 1928+738 jet”. In: *Monthly Notices of the Royal Astronomical Society* 445.2, pp. 1370–1382. DOI: [10.1093/mnras/stu1813](https://doi.org/10.1093/mnras/stu1813). arXiv: [1402.2644](https://arxiv.org/abs/1402.2644) [astro-ph.HE].
- Kunert-Bajraszewska, M. et al. (Nov. 2010). “A survey of low-luminosity compact sources and its implication for the evolution of radio-loud active galactic nuclei - I. Radio data”. In: *Monthly Notices of the Royal Astronomical Society* 408.4, pp. 2261–2278. DOI: [10.1111/j.1365-2966.2010.17271.x](https://doi.org/10.1111/j.1365-2966.2010.17271.x). arXiv: [1009.5235](https://arxiv.org/abs/1009.5235) [astro-ph.CO].
- Lacy, M. et al. (Mar. 2020). “The Karl G. Jansky Very Large Array Sky Survey (VLASS). Science Case and Survey Design”. In: *Publications of the Astronomical Society of the Pacific* 132.1009, 035001, p. 035001. DOI: [10.1088/1538-3873/ab63eb](https://doi.org/10.1088/1538-3873/ab63eb). arXiv: [1907.01981](https://arxiv.org/abs/1907.01981) [astro-ph.IM].
- Laganá, T. F. et al. (Feb. 2010). “Spiral-like structure at the centre of nearby clusters of galaxies”. In: *Astronomy & Astrophysics* 511, A15, A15. DOI: [10.1051/0004-6361/200913180](https://doi.org/10.1051/0004-6361/200913180). arXiv: [0911.3785](https://arxiv.org/abs/0911.3785) [astro-ph.CO].
- Laing, R. A. et al. (Jan. 1994). “Spectrophotometry of a Complete Sample of 3CR Radio Sources: Implications for Unified Models”. In: *The Physics of Active Galaxies*. Ed. by Geoffrey V. Bicknell et al. Vol. 54. Astronomical Society of the Pacific Conference Series, p. 201.
- Laing, R. A. and A. H. Bridle (June 2013). “The spectra of jet bases in FR I radio galaxies: implications for particle acceleration”. In: *Monthly Notices of the Royal Astronomical Society* 432.2, pp. 1114–1132. DOI: [10.1093/mnras/stt531](https://doi.org/10.1093/mnras/stt531). arXiv: [1303.6664](https://arxiv.org/abs/1303.6664) [astro-ph.HE].

- (Feb. 2014). “Systematic properties of decelerating relativistic jets in low-luminosity radio galaxies”. In: *Monthly Notices of the Royal Astronomical Society* 437.4, pp. 3405–3441. DOI: [10.1093/mnras/stt2138](https://doi.org/10.1093/mnras/stt2138). arXiv: [1311.1015](https://arxiv.org/abs/1311.1015) [astro-ph.CO].
- Lal, Dharam V. et al. (Feb. 2013). “Gas Sloshing and Radio Galaxy Dynamics in the Core of the 3C 449 Group”. In: *The Astrophysical Journal* 764.1, 83, p. 83. DOI: [10.1088/0004-637X/764/1/83](https://doi.org/10.1088/0004-637X/764/1/83). arXiv: [1210.7563](https://arxiv.org/abs/1210.7563) [astro-ph.CO].
- Lal, Dharam V. et al. (May 2019). “GMRT Low-frequency Imaging of an Extended Sample of X-shaped Radio Galaxies”. In: *The Astronomical Journal* 157.5, 195, p. 195. DOI: [10.3847/1538-3881/ab1419](https://doi.org/10.3847/1538-3881/ab1419). arXiv: [1903.11632](https://arxiv.org/abs/1903.11632) [astro-ph.GA].
- Lal, Dharam Vir and A. Pramesh Rao (Jan. 2007). “Giant Metrewave Radio Telescope observations of X-shaped radio sources”. In: *Monthly Notices of the Royal Astronomical Society* 374.3, pp. 1085–1102. DOI: [10.1111/j.1365-2966.2006.11225.x](https://doi.org/10.1111/j.1365-2966.2006.11225.x). arXiv: [astro-ph/0610678](https://arxiv.org/abs/astro-ph/0610678) [astro-ph].
- Lalakos, Aretaios et al. (Sept. 2022). “Bridging the Bondi and Event Horizon Scales: 3D GRMHD Simulations Reveal X-shaped Radio Galaxy Morphology”. In: *The Astrophysical Journal* 936.1, L5, p. L5. DOI: [10.3847/2041-8213/ac7bed](https://doi.org/10.3847/2041-8213/ac7bed). arXiv: [2202.08281](https://arxiv.org/abs/2202.08281) [astro-ph.HE].
- Lara, L. et al. (Aug. 1999). “Restarting activity in the giant radio galaxy J1835+620”. In: *Astronomy & Astrophysics* 348, pp. 699–704. DOI: [10.48550/arXiv.astro-ph/9906287](https://doi.org/10.48550/arXiv.astro-ph/9906287). arXiv: [astro-ph/9906287](https://arxiv.org/abs/astro-ph/9906287) [astro-ph].
- Le Brun, Amandine M. C. et al. (June 2014). “Towards a realistic population of simulated galaxy groups and clusters”. In: *Monthly Notices of the Royal Astronomical Society* 441.2, pp. 1270–1290. DOI: [10.1093/mnras/stu608](https://doi.org/10.1093/mnras/stu608). arXiv: [1312.5462](https://arxiv.org/abs/1312.5462) [astro-ph.CO].
- Lea, Susan M. et al. (Sept. 1973). “Thermal-Bremsstrahlung Interpretation of Cluster X-Ray Sources”. In: *The Astrophysical Journal Letters* 184, p. L105. DOI: [10.1086/181300](https://doi.org/10.1086/181300).
- Leahy, J. P. and A. G. Williams (Oct. 1984). “The bridges of classical double radio sources.” In: *Monthly Notices of the Royal Astronomical Society* 210, pp. 929–951. DOI: [10.1093/mnras/210.4.929](https://doi.org/10.1093/mnras/210.4.929).
- Leahy, J. P. and P. Parma (Jan. 1992). “Multiple outbursts in radio galaxies.” In: *Extragalactic Radio Sources. From Beams to Jets*. Ed. by Jacques Roland et al., pp. 307–308.
- Leccardi, A. and S. Molendi (Aug. 2008). “Radial metallicity profiles for a large sample of galaxy clusters observed with XMM-Newton”. In: *Astronomy & Astrophysics* 487.2, pp. 461–466. DOI: [10.1051/0004-6361:200810113](https://doi.org/10.1051/0004-6361:200810113). arXiv: [0806.1445](https://arxiv.org/abs/0806.1445) [astro-ph].
- Li, Yuan et al. (Oct. 2015). “Cooling, AGN Feedback, and Star Formation in Simulated Cool-core Galaxy Clusters”. In: *The Astrophysical Journal* 811.2, 73, p. 73. DOI: [10.1088/0004-637X/811/2/73](https://doi.org/10.1088/0004-637X/811/2/73). arXiv: [1503.02660](https://arxiv.org/abs/1503.02660) [astro-ph.GA].
- Lima Neto, Gastão and Melville Ulmer (Aug. 2011). “Abell 2390 revisited: hints of ripples, bubbles and sloshing”. In: *The X-ray Universe 2011*. Ed. by Jan-Uwe Ness and Matthias Ehle, 241, p. 241.
- Lister, M. L. et al. (Feb. 2003). “4C +12.50: A Superluminal Precessing Jet in the Recent Merger System IRAS 13451+1232”. In: *The Astrophysical Journal* 584.1, pp. 135–146. DOI: [10.1086/345666](https://doi.org/10.1086/345666). arXiv: [astro-ph/0210372](https://arxiv.org/abs/astro-ph/0210372) [astro-ph].
- Lister, M. L. et al. (Aug. 2020). “TXS 0128+554: A Young Gamma-Ray-emitting Active Galactic Nucleus with Episodic Jet Activity”. In: *The Astrophysical Journal* 899.2, 141, p. 141. DOI: [10.3847/1538-4357/aba18d](https://doi.org/10.3847/1538-4357/aba18d). arXiv: [2006.16970](https://arxiv.org/abs/2006.16970) [astro-ph.GA].
- Liu, Ang et al. (May 2019a). “On the origin of central abundance drops in the intracluster medium of galaxy groups and clusters”. In: *Monthly Notices of the Royal Astronomical Society* 485.2, pp. 1651–1664. DOI: [10.1093/mnras/stz533](https://doi.org/10.1093/mnras/stz533). arXiv: [1902.07661](https://arxiv.org/abs/1902.07661) [astro-ph.GA].
- Liu, Ang et al. (May 2020a). “The chemical evolution of galaxy clusters: Dissecting the iron mass budget of the intracluster medium”. In: *Astronomy & Astrophysics* 637, A58, A58. DOI: [10.1051/0004-6361/202037506](https://doi.org/10.1051/0004-6361/202037506). arXiv: [2003.12426](https://arxiv.org/abs/2003.12426) [astro-ph.GA].
- Liu, F. K. (Feb. 2004). “X-shaped radio galaxies as observational evidence for the interaction of supermassive binary black holes and accretion disc at parsec scale”. In: *Monthly Notices of the Royal Astronomical Society* 347.4, pp. 1357–1369. ISSN: 0035-8711.

- Liu, Wenhao et al. (Apr. 2019b). “AGN feedback in galaxy group 3C 88: cavities, shock, and jet reorientation”. In: *Monthly Notices of the Royal Astronomical Society* 484.3, pp. 3376–3392. arXiv: 1806.04692 [astro-ph.HE].
- Liu, Wenhao et al. (Mar. 2020b). “AGN feedback in the FR II galaxy 3C 220.1”. In: *Monthly Notices of the Royal Astronomical Society* 492.3, pp. 3156–3168. DOI: 10.1093/mnras/staa005. arXiv: 2001.00506 [astro-ph.HE].
- Lovisari, L. and T. H. Reiprich (Feb. 2019). “The non-uniformity of galaxy cluster metallicity profiles”. In: *Monthly Notices of the Royal Astronomical Society* 483.1, pp. 540–557. DOI: 10.1093/mnras/sty3130. arXiv: 1811.05987 [astro-ph.CO].
- Lovisari, Lorenzo et al. (May 2021). “Scaling Properties of Galaxy Groups”. In: *Universe* 7.5, p. 139. DOI: 10.3390/universe7050139. arXiv: 2106.13256 [astro-ph.CO].
- Lyutikov, M. (Nov. 2006). “Magnetic draping of merging cores and radio bubbles in clusters of galaxies”. In: *Monthly Notices of the Royal Astronomical Society* 373.1, pp. 73–78. DOI: 10.1111/j.1365-2966.2006.10835.x. arXiv: astro-ph/0604178 [astro-ph].
- Macconi, D. et al. (Apr. 2020). “Radio morphology-accretion mode link in Fanaroff-Riley type II low-excitation radio galaxies”. In: *Monthly Notices of the Royal Astronomical Society* 493.3, pp. 4355–4366. DOI: 10.1093/mnras/staa560. arXiv: 2002.09360 [astro-ph.HE].
- Macconi, Duccio et al. (Apr. 2022). “Detection of a radio-filled X-ray cavity within the interstellar medium of NGC 5141”. In: *Astronomy & Astrophysics* 660, A32, A32. DOI: 10.1051/0004-6361/202143024. arXiv: 2202.05857 [astro-ph.GA].
- Machacek, M. et al. (Sept. 2006). “Chandra Observations of Nuclear Outflows in the Elliptical Galaxy NGC 4552 in the Virgo Cluster”. In: *The Astrophysical Journal* 648.2, pp. 947–955. DOI: 10.1086/505963. arXiv: astro-ph/0604406 [astro-ph].
- Machalski, J. et al. (Oct. 2016). “Dynamical analysis of the complex radio structure in 3C 293: clues on a rapid jet realignment in X-shaped radio galaxies”. In: *Astronomy & Astrophysics* 595, A46, A46. DOI: 10.1051/0004-6361/201629249. arXiv: 1608.07057 [astro-ph.GA].
- Mahatma, V. H. et al. (Feb. 2019). “LoTSS DR1: Double-double radio galaxies in the HETDEX field”. In: *Astronomy & Astrophysics* 622, A13, A13. DOI: 10.1051/0004-6361/201833973. arXiv: 1811.08194 [astro-ph.GA].
- Mahatma, V. H. et al. (Apr. 2023). “A low-frequency sub-arcsecond view of powerful radio galaxies in rich-cluster environments: 3C 34 and 3C 320”. In: *Monthly Notices of the Royal Astronomical Society* 520.3, pp. 4427–4442. DOI: 10.1093/mnras/stad395. arXiv: 2302.01357 [astro-ph.GA].
- Mantz, Adam B. et al. (May 2015). “Cosmology and astrophysics from relaxed galaxy clusters - I. Sample selection”. In: *Monthly Notices of the Royal Astronomical Society* 449.1, pp. 199–219. DOI: 10.1093/mnras/stv219. arXiv: 1502.06020 [astro-ph.CO].
- Markevitch, M. et al. (Oct. 2000). “Chandra Observation of Abell 2142: Survival of Dense Subcluster Cores in a Merger”. In: *The Astrophysical Journal* 541.2, pp. 542–549. DOI: 10.1086/309470. arXiv: astro-ph/0001269 [astro-ph].
- Markevitch, Maxim and Alexey Vikhlinin (May 2007). “Shocks and cold fronts in galaxy clusters”. In: *Physics Reports* 443.1, pp. 1–53. DOI: 10.1016/j.physrep.2007.01.001. arXiv: astro-ph/0701821 [astro-ph].
- Martí, J. M. et al. (Apr. 1997). “Morphology and Dynamics of Relativistic Jets”. In: *The Astrophysical Journal* 479.1, pp. 151–163. DOI: 10.1086/303842.
- Martizzi, Davide et al. (Feb. 2019). “Simulations of jet heating in galaxy clusters: successes and challenges”. In: *Monthly Notices of the Royal Astronomical Society* 483.2, pp. 2465–2486. DOI: 10.1093/mnras/sty3273. arXiv: 1805.06461 [astro-ph.GA].
- Martz, C. G. et al. (July 2020). “Thermally Unstable Cooling Stimulated by Uplift: The Spoiler Clusters”. In: *The Astrophysical Journal* 897.1, 57, p. 57. DOI: 10.3847/1538-4357/ab96cd. arXiv: 2003.11104 [astro-ph.GA].
- Mathews, W. G. and J. N. Bregman (Sept. 1978). “Radiative accretion flow onto giant galaxies in clusters.” In: *The Astrophysical Journal* 224, pp. 308–319. DOI: 10.1086/156379.

- Matthews, James H. and Andrew M. Taylor (June 2021). "Particle acceleration in radio galaxies with flickering jets: GeV electrons to ultrahigh energy cosmic rays". In: *Monthly Notices of the Royal Astronomical Society* 503.4, pp. 5948–5964. DOI: [10.1093/mnras/stab758](https://doi.org/10.1093/mnras/stab758). arXiv: [2103.06900](https://arxiv.org/abs/2103.06900) [astro-ph.HE].
- McCarthy, I. G. et al. (Aug. 2010). "The case for AGN feedback in galaxy groups". In: *Monthly Notices of the Royal Astronomical Society* 406.2, pp. 822–839. DOI: [10.1111/j.1365-2966.2010.16750.x](https://doi.org/10.1111/j.1365-2966.2010.16750.x). arXiv: [0911.2641](https://arxiv.org/abs/0911.2641) [astro-ph.CO].
- McCarthy, Patrick J. et al. (Apr. 1991). "Correlated Radio and Optical Asymmetries in Powerful Radio Sources". In: *The Astrophysical Journal* 371, p. 478. DOI: [10.1086/169911](https://doi.org/10.1086/169911).
- McCourt, Michael et al. (Feb. 2012). "Thermal instability in gravitationally stratified plasmas: implications for multiphase structure in clusters and galaxy haloes". In: *Monthly Notices of the Royal Astronomical Society* 419.4, pp. 3319–3337. DOI: [10.1111/j.1365-2966.2011.19972.x](https://doi.org/10.1111/j.1365-2966.2011.19972.x). arXiv: [1105.2563](https://arxiv.org/abs/1105.2563) [astro-ph.CO].
- McDonald, M. et al. (Oct. 2014). "The Redshift Evolution of the Mean Temperature, Pressure, and Entropy Profiles in 80 SPT-Selected Galaxy Clusters". In: *The Astrophysical Journal* 794.1, 67, p. 67. DOI: [10.1088/0004-637X/794/1/67](https://doi.org/10.1088/0004-637X/794/1/67). arXiv: [1404.6250](https://arxiv.org/abs/1404.6250) [astro-ph.HE].
- McDonald, M. et al. (July 2017). "The Remarkable Similarity of Massive Galaxy Clusters from $z \sim 0$ to $z \sim 1.9$ ". In: *The Astrophysical Journal* 843.1, 28, p. 28. DOI: [10.3847/1538-4357/aa7740](https://doi.org/10.3847/1538-4357/aa7740). arXiv: [1702.05094](https://arxiv.org/abs/1702.05094) [astro-ph.CO].
- McDonald, M. et al. (May 2018). "Revisiting the Cooling Flow Problem in Galaxies, Groups, and Clusters of Galaxies". In: *The Astrophysical Journal* 858.1, 45, p. 45. DOI: [10.3847/1538-4357/aabace](https://doi.org/10.3847/1538-4357/aabace). arXiv: [1803.04972](https://arxiv.org/abs/1803.04972) [astro-ph.HE].
- McDonald, M. et al. (Nov. 2019). "Anatomy of a Cooling Flow: The Feedback Response to Pure Cooling in the Core of the Phoenix Cluster". In: *The Astrophysical Journal* 885.1, 63, p. 63. DOI: [10.3847/1538-4357/ab464c](https://doi.org/10.3847/1538-4357/ab464c). arXiv: [1904.08942](https://arxiv.org/abs/1904.08942) [astro-ph.GA].
- McDonald, Michael et al. (Oct. 2010). "On the Origin of the Extended H α Filaments in Cooling Flow Clusters". In: *The Astrophysical Journal* 721.2, pp. 1262–1283. DOI: [10.1088/0004-637X/721/2/1262](https://doi.org/10.1088/0004-637X/721/2/1262). arXiv: [1008.0392](https://arxiv.org/abs/1008.0392) [astro-ph.HE].
- McDonald, Michael et al. (Feb. 2012). "Optical Spectroscopy of H α Filaments in Cool Core Clusters: Kinematics, Reddening, and Sources of Ionization". In: *The Astrophysical Journal* 746.2, 153, p. 153. DOI: [10.1088/0004-637X/746/2/153](https://doi.org/10.1088/0004-637X/746/2/153). arXiv: [1111.0006](https://arxiv.org/abs/1111.0006) [astro-ph.CO].
- McDonald, Michael et al. (Oct. 2015). "Deep Chandra, HST-COS, and Megacam Observations of the Phoenix Cluster: Extreme Star Formation and AGN Feedback on Hundred Kiloparsec Scales". In: *The Astrophysical Journal* 811.2, 111, p. 111. DOI: [10.1088/0004-637X/811/2/111](https://doi.org/10.1088/0004-637X/811/2/111). arXiv: [1508.05941](https://arxiv.org/abs/1508.05941) [astro-ph.GA].
- McKean, J. P. et al. (Dec. 2016). "LOFAR imaging of Cygnus A - direct detection of a turnover in the hotspot radio spectra". In: *Monthly Notices of the Royal Astronomical Society* 463.3, pp. 3143–3150. DOI: [10.1093/mnras/stw2105](https://doi.org/10.1093/mnras/stw2105). arXiv: [2103.16961](https://arxiv.org/abs/2103.16961) [astro-ph.GA].
- McKinley, B. et al. (Jan. 2022). "Multi-scale feedback and feeding in the closest radio galaxy Centaurus A". In: *Nature Astronomy* 6, pp. 109–120. DOI: [10.1038/s41550-021-01553-3](https://doi.org/10.1038/s41550-021-01553-3). arXiv: [2111.02683](https://arxiv.org/abs/2111.02683) [astro-ph.GA].
- McKinney, Jonathan C. et al. (Jan. 2013). "Alignment of Magnetized Accretion Disks and Relativistic Jets with Spinning Black Holes". In: *Science* 339.6115, p. 49. DOI: [10.1126/science.1230811](https://doi.org/10.1126/science.1230811). arXiv: [1211.3651](https://arxiv.org/abs/1211.3651) [astro-ph.CO].
- McNamara, B. R. et al. (Jan. 2005). "The heating of gas in a galaxy cluster by X-ray cavities and large-scale shock fronts". In: *Nature* 433.7021, pp. 45–47. DOI: [10.1038/nature03202](https://doi.org/10.1038/nature03202).
- McNamara, B. R. and P. E. J. Nulsen (Sept. 2007). "Heating Hot Atmospheres with Active Galactic Nuclei". In: *Annual Review of Astronomy and Astrophysics* 45.1, pp. 117–175. DOI: [10.1146/annurev.astro.45.051806.110625](https://doi.org/10.1146/annurev.astro.45.051806.110625). arXiv: [0709.2152](https://arxiv.org/abs/0709.2152) [astro-ph].

- McNamara, B. R. et al. (Jan. 2011). "Are Radio Active Galactic Nuclei Powered by Accretion or Black Hole Spin?" In: *The Astrophysical Journal* 727.1, 39, p. 39. DOI: [10.1088/0004-637X/727/1/39](https://doi.org/10.1088/0004-637X/727/1/39). arXiv: [1007.1227](https://arxiv.org/abs/1007.1227) [astro-ph.CO].
- McNamara, B. R. and P. E. J. Nulsen (May 2012). "Mechanical feedback from active galactic nuclei in galaxies, groups and clusters". In: *New Journal of Physics* 14.5, 055023, p. 055023. DOI: [10.1088/1367-2630/14/5/055023](https://doi.org/10.1088/1367-2630/14/5/055023). arXiv: [1204.0006](https://arxiv.org/abs/1204.0006) [astro-ph.CO].
- McNamara, B. R. et al. (Apr. 2014). "A 10^{10} Solar Mass Flow of Molecular Gas in the A1835 Brightest Cluster Galaxy". In: *The Astrophysical Journal* 785.1, 44, p. 44. DOI: [10.1088/0004-637X/785/1/44](https://doi.org/10.1088/0004-637X/785/1/44). arXiv: [1309.0013](https://arxiv.org/abs/1309.0013) [astro-ph.CO].
- McNamara, B. R. et al. (Oct. 2016). "A Mechanism for Stimulating AGN Feedback by Lifting Gas in Massive Galaxies". In: *The Astrophysical Journal* 830.2, 79, p. 79. DOI: [10.3847/0004-637X/830/2/79](https://doi.org/10.3847/0004-637X/830/2/79). arXiv: [1604.04629](https://arxiv.org/abs/1604.04629) [astro-ph.GA].
- Merloni, Andrea et al. (Nov. 2003). "A Fundamental Plane of black hole activity". In: *Monthly Notices of the Royal Astronomical Society* 345.4, pp. 1057–1076. DOI: [10.1046/j.1365-2966.2003.07017.x](https://doi.org/10.1046/j.1365-2966.2003.07017.x). arXiv: [astro-ph/0305261](https://arxiv.org/abs/astro-ph/0305261) [astro-ph].
- Merloni, Andrea and Sebastian Heinz (Oct. 2007). "Measuring the kinetic power of active galactic nuclei in the radio mode". In: *Monthly Notices of the Royal Astronomical Society* 381.2, pp. 589–601. DOI: [10.1111/j.1365-2966.2007.12253.x](https://doi.org/10.1111/j.1365-2966.2007.12253.x). arXiv: [0707.3356](https://arxiv.org/abs/0707.3356) [astro-ph].
- Mernier, F. et al. (July 2017). "Radial metal abundance profiles in the intra-cluster medium of cool-core galaxy clusters, groups, and ellipticals". In: *Astronomy & Astrophysics* 603, A80, A80. DOI: [10.1051/0004-6361/201630075](https://doi.org/10.1051/0004-6361/201630075). arXiv: [1703.01183](https://arxiv.org/abs/1703.01183) [astro-ph.HE].
- Merritt, David and R. D. Ekers (Aug. 2002). "Tracing Black Hole Mergers Through Radio Lobe Morphology". In: *Science* 297.5585, pp. 1310–1313. DOI: [10.1126/science.1074688](https://doi.org/10.1126/science.1074688). arXiv: [astro-ph/0208001](https://arxiv.org/abs/astro-ph/0208001) [astro-ph].
- Meyer, Eileen et al. (Jan. 2017). "Proper Motions of Jets on the Kiloparsec Scale: New Results with HST". In: *Galaxies* 5.1, p. 8. DOI: [10.3390/galaxies5010008](https://doi.org/10.3390/galaxies5010008). arXiv: [1701.05846](https://arxiv.org/abs/1701.05846) [astro-ph.GA].
- Mezcua, M. et al. (Feb. 2018). "The most massive black holes on the Fundamental Plane of black hole accretion". In: 474.1, pp. 1342–1360. DOI: [10.1093/mnras/stx2812](https://doi.org/10.1093/mnras/stx2812). arXiv: [1710.10268](https://arxiv.org/abs/1710.10268) [astro-ph.GA].
- Mohr, Joseph J. et al. (Aug. 1993). "An X-Ray Method for Detecting Substructure in Galaxy Clusters: Application to Perseus, A2256, Centaurus, Coma, and Sersic 40/6". In: *The Astrophysical Journal* 413, p. 492. DOI: [10.1086/173019](https://doi.org/10.1086/173019).
- Mohr, Joseph J. et al. (June 1999). "Properties of the Intracluster Medium in an Ensemble of Nearby Galaxy Clusters". In: *The Astrophysical Journal* 517.2, pp. 627–649. DOI: [10.1086/307227](https://doi.org/10.1086/307227). arXiv: [astro-ph/9901281](https://arxiv.org/abs/astro-ph/9901281) [astro-ph].
- Molendi, S. et al. (Feb. 2023). "The evolving cluster cores: Putting together the pieces of the puzzle". In: *Astronomy & Astrophysics* 670, A104, A104. DOI: [10.1051/0004-6361/202243421](https://doi.org/10.1051/0004-6361/202243421). arXiv: [2210.14148](https://arxiv.org/abs/2210.14148) [astro-ph.GA].
- Molendi, Silvano (Apr. 2004). "The Intra-Cluster Medium". In: *Plasmas in the Laboratory and in the Universe: New Insights and New Challenges*. Ed. by Giuseppe Bertin et al. Vol. 703. American Institute of Physics Conference Series, pp. 345–354. DOI: [10.1063/1.1718479](https://doi.org/10.1063/1.1718479). arXiv: [astro-ph/0404410](https://arxiv.org/abs/astro-ph/0404410) [astro-ph].
- Molendi, Silvano and Fabio Pizzolato (Oct. 2001). "Is the Gas in Cooling Flows Multiphase?" In: *The Astrophysical Journal* 560.1, pp. 194–200. DOI: [10.1086/322387](https://doi.org/10.1086/322387). arXiv: [astro-ph/0106552](https://arxiv.org/abs/astro-ph/0106552) [astro-ph].
- Morabito, L. K. et al. (Feb. 2022). "Sub-arcsecond imaging with the International LOFAR Telescope. I. Foundational calibration strategy and pipeline". In: *Astronomy & Astrophysics* 658, A1, A1. DOI: [10.1051/0004-6361/202140649](https://doi.org/10.1051/0004-6361/202140649). arXiv: [2108.07283](https://arxiv.org/abs/2108.07283) [astro-ph.IM].
- Morandi, Andrea and Ming Sun (Apr. 2016). "Probing dark energy via galaxy cluster outskirts". In: *Monthly Notices of the Royal Astronomical Society* 457.3, pp. 3266–3284. DOI: [10.1093/mnras/stw143](https://doi.org/10.1093/mnras/stw143). arXiv: [1601.03741](https://arxiv.org/abs/1601.03741) [astro-ph.CO].

- Morganti, Raffaella (Nov. 2017). “The many routes to AGN feedback”. In: *Frontiers in Astronomy and Space Sciences* 4, 42, p. 42. DOI: [10.3389/fspas.2017.00042](https://doi.org/10.3389/fspas.2017.00042). arXiv: [1712.05301](https://arxiv.org/abs/1712.05301) [astro-ph.GA].
- Morganti, Raffaella et al. (Nov. 2021). “Combining LOFAR and Apertif Data for Understanding the Life Cycle of Radio Galaxies”. In: *Galaxies* 9.4, p. 88. DOI: [10.3390/galaxies9040088](https://doi.org/10.3390/galaxies9040088). arXiv: [2111.04776](https://arxiv.org/abs/2111.04776) [astro-ph.GA].
- Morganti, Raffaella et al. (Oct. 2023). “Cold gas in the heart of Perseus A”. In: *Astronomy & Astrophysics* 678, A42, A42. DOI: [10.1051/0004-6361/202347117](https://doi.org/10.1051/0004-6361/202347117).
- Morsony, Brian J. et al. (Sept. 2010). “Swimming against the current: simulations of central AGN evolution in dynamic galaxy clusters”. In: *Monthly Notices of the Royal Astronomical Society* 407.2, pp. 1277–1289. DOI: [10.1111/j.1365-2966.2010.17059.x](https://doi.org/10.1111/j.1365-2966.2010.17059.x). arXiv: [1003.3049](https://arxiv.org/abs/1003.3049) [astro-ph.HE].
- Mroczkowski, Tony et al. (Sept. 2022). “The strongest cool core in REXCESS: Missing X-ray cavities in RXC J2014.8-2430”. In: *Astronomy & Astrophysics* 665, A48, A48. DOI: [10.1051/0004-6361/202243718](https://doi.org/10.1051/0004-6361/202243718). arXiv: [2207.13359](https://arxiv.org/abs/2207.13359) [astro-ph.HE].
- Murgia, M. et al. (Dec. 2001). “A multi-frequency study of the radio galaxy NGC 326. I. The data”. In: *Astronomy & Astrophysics* 380, pp. 102–116. DOI: [10.1051/0004-6361:20011436](https://doi.org/10.1051/0004-6361:20011436). arXiv: [astro-ph/0110252](https://arxiv.org/abs/astro-ph/0110252) [astro-ph].
- Murgia, M. et al. (Feb. 2011). “Dying radio galaxies in clusters”. In: *Astronomy & Astrophysics* 526, A148, A148. DOI: [10.1051/0004-6361/201015302](https://doi.org/10.1051/0004-6361/201015302). arXiv: [1011.0567](https://arxiv.org/abs/1011.0567) [astro-ph.CO].
- Mushotzky, R. and AXIS Team (Apr. 2019). “AXIS a High Spatial Resolution X-Ray Probe Mission Study”. In: *The Space Astrophysics Landscape for the 2020s and Beyond*. Ed. by Moores J. E. et al. Vol. 2135. LPI Contributions, 5025, p. 5025.
- Mushotzky, R. F. and A. E. Szymkowiak (Jan. 1988). “Einstein Observatory Solid State Detector Observations of Cooling Flows in Clusters of Galaxies”. In: *Cooling Flows in Clusters and Galaxies*. Ed. by A. C. Fabian. Vol. 229. NATO Advanced Study Institute (ASI) Series C, p. 53. DOI: [10.1007/978-94-009-2953-1_6](https://doi.org/10.1007/978-94-009-2953-1_6).
- Nandi, S. et al. (Feb. 2021). “Double-peaked Lines, Dual VLBI Components, and Precessing Jets in J1328+2752”. In: *The Astrophysical Journal* 908.2, 178, p. 178. DOI: [10.3847/1538-4357/abd2ba](https://doi.org/10.3847/1538-4357/abd2ba). arXiv: [2012.06290](https://arxiv.org/abs/2012.06290) [astro-ph.HE].
- Narayan, Ramesh and Insu Yi (June 1994). “Advection-dominated Accretion: A Self-similar Solution”. In: *The Astrophysical Journal Letters* 428, p. L13. DOI: [10.1086/187381](https://doi.org/10.1086/187381). arXiv: [astro-ph/9403052](https://arxiv.org/abs/astro-ph/9403052) [astro-ph].
- (Oct. 1995). “Advection-dominated Accretion: Underfed Black Holes and Neutron Stars”. In: *The Astrophysical Journal* 452, p. 710. DOI: [10.1086/176343](https://doi.org/10.1086/176343). arXiv: [astro-ph/9411059](https://arxiv.org/abs/astro-ph/9411059) [astro-ph].
- Nolting, Chris et al. (May 2023). “Simulations of Precessing Jets and the Formation of X-shaped Radio Galaxies”. In: *The Astrophysical Journal* 948.1, 25, p. 25. DOI: [10.3847/1538-4357/acc652](https://doi.org/10.3847/1538-4357/acc652). arXiv: [2301.04343](https://arxiv.org/abs/2301.04343) [astro-ph.HE].
- North, Eve V. et al. (May 2021). “WISDOM project - VIII. Multiscale feedback cycles in the brightest cluster galaxy NGC 0708”. In: *Monthly Notices of the Royal Astronomical Society* 503.4, pp. 5179–5192. DOI: [10.1093/mnras/stab793](https://doi.org/10.1093/mnras/stab793). arXiv: [2103.08988](https://arxiv.org/abs/2103.08988) [astro-ph.GA].
- Nulsen, P. E. J. (July 1986). “Thermal instability in cooling flows.” In: *Monthly Notices of the Royal Astronomical Society* 221, pp. 377–392. DOI: [10.1093/mnras/221.2.377](https://doi.org/10.1093/mnras/221.2.377).
- Nulsen, P. E. J. et al. (Aug. 2005). “The Cluster-Scale AGN Outburst in Hydra A”. In: *The Astrophysical Journal* 628.2, pp. 629–636. DOI: [10.1086/430845](https://doi.org/10.1086/430845). arXiv: [astro-ph/0408315](https://arxiv.org/abs/astro-ph/0408315) [astro-ph].
- Nulsen, P. E. J. et al. (Jan. 2007). “AGN Heating Through Cavities and Shocks”. In: *Heating versus Cooling in Galaxies and Clusters of Galaxies*. Ed. by H. Böhringer et al., p. 210. DOI: [10.1007/978-3-540-73484-0_37](https://doi.org/10.1007/978-3-540-73484-0_37). arXiv: [astro-ph/0611136](https://arxiv.org/abs/astro-ph/0611136) [astro-ph].
- O’Dea, C. P. et al. (Feb. 2009). “Physical properties of very powerful FR II radio galaxies”. In: *Astronomy & Astrophysics* 494.2, pp. 471–488. DOI: [10.1051/0004-6361:200809416](https://doi.org/10.1051/0004-6361:200809416). arXiv: [0810.1213](https://arxiv.org/abs/0810.1213) [astro-ph].

- O'Dea, Christopher P. (May 1998). "The Compact Steep-Spectrum and Gigahertz Peaked-Spectrum Radio Sources". In: *Publications of the Astronomical Society of the Pacific* 110.747, pp. 493–532. DOI: [10.1086/316162](https://doi.org/10.1086/316162).
- O'Dea, Christopher P. and D. J. Saikia (Dec. 2021). "Compact steep-spectrum and peaked-spectrum radio sources". In: *Astronomy & Astrophysics* 29.1, 3, p. 3. DOI: [10.1007/s00159-021-00131-w](https://doi.org/10.1007/s00159-021-00131-w). arXiv: [2009.02750](https://arxiv.org/abs/2009.02750) [astro-ph.GA].
- Offringa, A. R. et al. (Oct. 2014). "WSCLEAN: an implementation of a fast, generic wide-field imager for radio astronomy". In: *Monthly Notices of the Royal Astronomical Society* 444.1, pp. 606–619. DOI: [10.1093/mnras/stu1368](https://doi.org/10.1093/mnras/stu1368). arXiv: [1407.1943](https://arxiv.org/abs/1407.1943) [astro-ph.IM].
- Olivares, V. et al. (Nov. 2019). "Ubiquitous cold and massive filaments in cool core clusters". In: *Astronomy & Astrophysics* 631, A22, A22. DOI: [10.1051/0004-6361/201935350](https://doi.org/10.1051/0004-6361/201935350). arXiv: [1902.09164](https://arxiv.org/abs/1902.09164) [astro-ph.GA].
- Olivares, V. et al. (Oct. 2022a). "AGN feedback duty cycle in Planck SZ selected clusters using Chandra observations". In: *Monthly Notices of the Royal Astronomical Society* 516.1, pp. L101–L106. DOI: [10.1093/mnrasl/slac096](https://doi.org/10.1093/mnrasl/slac096). arXiv: [2208.04888](https://arxiv.org/abs/2208.04888) [astro-ph.GA].
- Olivares, V. et al. (Oct. 2022b). "Gas condensation in brightest group galaxies unveiled with MUSE. Morphology and kinematics of the ionized gas". In: *Astronomy & Astrophysics* 666, A94, A94. DOI: [10.1051/0004-6361/202142475](https://doi.org/10.1051/0004-6361/202142475). arXiv: [2201.07838](https://arxiv.org/abs/2201.07838) [astro-ph.GA].
- Orienti, M. (Feb. 2016). "Radio properties of Compact Steep Spectrum and GHz-Peaked Spectrum radio sources". In: *Astronomische Nachrichten* 337.1-2, p. 9. DOI: [10.1002/asna.201512257](https://doi.org/10.1002/asna.201512257). arXiv: [1511.00436](https://arxiv.org/abs/1511.00436) [astro-ph.GA].
- Orrù, E. et al. (Dec. 2015). "Wide-field LOFAR imaging of the field around the double-double radio galaxy B1834+620. A fresh view on a restarted AGN and doubletjes". In: *Astronomy & Astrophysics* 584, A112, A112. DOI: [10.1051/0004-6361/201526501](https://doi.org/10.1051/0004-6361/201526501). arXiv: [1510.00577](https://arxiv.org/abs/1510.00577) [astro-ph.GA].
- O'Sullivan, E. et al. (May 2005). "Active Galactic Nucleus Feedback and Gas Mixing in the Core of NGC 4636". In: *The Astrophysical Journal* 624.2, pp. L77–L80. DOI: [10.1086/430600](https://doi.org/10.1086/430600). arXiv: [astro-ph/0503563](https://arxiv.org/abs/astro-ph/0503563) [astro-ph].
- O'Sullivan, E. et al. (July 2011). "Heating the Hot Atmospheres of Galaxy Groups and Clusters with Cavities: The Relationship between Jet Power and Low-frequency Radio Emission". In: *The Astrophysical Journal* 735.1, 11, p. 11. DOI: [10.1088/0004-637X/735/1/11](https://doi.org/10.1088/0004-637X/735/1/11). arXiv: [1104.2411](https://arxiv.org/abs/1104.2411) [astro-ph.CO].
- O'Sullivan, Ewan et al. (Jan. 2014). "The impact of sloshing on the intragroup medium and old radio lobe of NGC 5044". In: *Monthly Notices of the Royal Astronomical Society* 437.1, pp. 730–739. DOI: [10.1093/mnras/stt1926](https://doi.org/10.1093/mnras/stt1926). arXiv: [1310.2163](https://arxiv.org/abs/1310.2163) [astro-ph.CO].
- O'Sullivan, Ewan et al. (Dec. 2017). "The Complete Local Volume Groups Sample - I. Sample selection and X-ray properties of the high-richness subsample". In: *Monthly Notices of the Royal Astronomical Society* 472.2, pp. 1482–1505. DOI: [10.1093/mnras/stx2078](https://doi.org/10.1093/mnras/stx2078). arXiv: [1708.03555](https://arxiv.org/abs/1708.03555) [astro-ph.GA].
- O'Sullivan, Ewan et al. (Sept. 2019). "Building a cluster: shocks, cavities, and cooling filaments in the group-group merger NGC 6338". In: *Monthly Notices of the Royal Astronomical Society* 488.2, pp. 2925–2946. DOI: [10.1093/mnras/stz1711](https://doi.org/10.1093/mnras/stz1711). arXiv: [1906.07710](https://arxiv.org/abs/1906.07710) [astro-ph.GA].
- O'Sullivan, Ewan et al. (June 2021). "The Cluster-central Compact Steep-spectrum Radio Galaxy 1321+045". In: *The Astrophysical Journal* 913.2, 105, p. 105. DOI: [10.3847/1538-4357/abf6c6](https://doi.org/10.3847/1538-4357/abf6c6). arXiv: [2104.04548](https://arxiv.org/abs/2104.04548) [astro-ph.CO].
- Overzier, Roderik A. (Nov. 2016). "The realm of the galaxy protoclusters. A review". In: *Astronomy and Astrophysics Reviews* 24.1, 14, p. 14. DOI: [10.1007/s00159-016-0100-3](https://doi.org/10.1007/s00159-016-0100-3). arXiv: [1610.05201](https://arxiv.org/abs/1610.05201) [astro-ph.GA].
- Owers, Matt S. et al. (Oct. 2009). "A High Fidelity Sample of Cold Front Clusters from the Chandra Archive". In: *The Astrophysical Journal* 704.2, pp. 1349–1370. DOI: [10.1088/0004-637X/704/2/1349](https://doi.org/10.1088/0004-637X/704/2/1349). arXiv: [0909.2645](https://arxiv.org/abs/0909.2645) [astro-ph.CO].
- Pacholczyk, A. G. (1970). *Radio astrophysics. Nonthermal processes in galactic and extragalactic sources.*

- Padovani, P. et al. (Aug. 2017). "Active galactic nuclei: what's in a name?" In: *Astronomy and Astrophysics Review* 25.1, 2, p. 2. DOI: [10.1007/s00159-017-0102-9](https://doi.org/10.1007/s00159-017-0102-9). arXiv: [1707.07134](https://arxiv.org/abs/1707.07134) [astro-ph.GA].
- Palimaka, J. J. et al. (July 1979). "A preferred orientation for large radio sources relative to their elliptical galaxies." In: *The Astrophysical Journal Letters* 231, pp. L7–L11. DOI: [10.1086/182995](https://doi.org/10.1086/182995).
- Panagoulia, E. K. et al. (Mar. 2014). "A volume-limited sample of X-ray galaxy groups and clusters - I. Radial entropy and cooling time profiles". In: *Monthly Notices of the Royal Astronomical Society* 438.3, pp. 2341–2354. DOI: [10.1093/mnras/stt2349](https://doi.org/10.1093/mnras/stt2349). arXiv: [1312.0798](https://arxiv.org/abs/1312.0798) [astro-ph.CO].
- Pandge, M. B. et al. (Jan. 2019). "AGN Feedback in Galaxy Groups: A Detailed Study of X-Ray Features and Diffuse Radio Emission in IC 1262". In: *The Astrophysical Journal* 870.2, 62, p. 62. DOI: [10.3847/1538-4357/aaf105](https://doi.org/10.3847/1538-4357/aaf105). arXiv: [1811.05647](https://arxiv.org/abs/1811.05647) [astro-ph.GA].
- Pasini, T. et al. (Nov. 2019). "A BCG with Offset Cooling: Is the AGN Feedback Cycle Broken in A2495?" In: *The Astrophysical Journal* 885.2, 111, p. 111. DOI: [10.3847/1538-4357/ab4808](https://doi.org/10.3847/1538-4357/ab4808). arXiv: [1910.05363](https://arxiv.org/abs/1910.05363) [astro-ph.GA].
- Pasini, T. et al. (Apr. 2021). "A First Chandra View of the Cool Core Cluster A1668: Offset Cooling and AGN Feedback Cycle". In: *The Astrophysical Journal* 911.1, 66, p. 66. DOI: [10.3847/1538-4357/abe85f](https://doi.org/10.3847/1538-4357/abe85f). arXiv: [2102.11299](https://arxiv.org/abs/2102.11299) [astro-ph.GA].
- Pearson, T. J. (Jan. 1996). "Observations of Parsec-Scale Jets". In: *Energy Transport in Radio Galaxies and Quasars*. Ed. by Philip E. Hardee et al. Vol. 100. Astronomical Society of the Pacific Conference Series, p. 97.
- Pearson, T. J. and A. C. S. Readhead (May 1988). "The Millisecond Structure of a Complete Sample of Radio Sources. II. First-EPOCH Maps at 5 GHz". In: *The Astrophysical Journal* 328, p. 114. DOI: [10.1086/166274](https://doi.org/10.1086/166274).
- Peng, E. H. et al. (Aug. 2009). "Discrepant Mass Estimates in the Cluster of Galaxies Abell 1689". In: *The Astrophysical Journal* 701.2, pp. 1283–1299. DOI: [10.1088/0004-637X/701/2/1283](https://doi.org/10.1088/0004-637X/701/2/1283). arXiv: [0906.4153](https://arxiv.org/abs/0906.4153) [astro-ph.CO].
- Perucho, Manel et al. (Jan. 2019). "Long-term FR II jet evolution: clues from three-dimensional simulations". In: *Monthly Notices of the Royal Astronomical Society* 482.3, pp. 3718–3735. DOI: [10.1093/mnras/sty2912](https://doi.org/10.1093/mnras/sty2912). arXiv: [1810.10968](https://arxiv.org/abs/1810.10968) [astro-ph.GA].
- Perucho, Manel and J. López-Mirallas (Sept. 2023). "Numerical simulations of relativistic jets". In: *Journal of Plasma Physics* 89.5, 915890501, p. 915890501. DOI: [10.1017/S0022377823000892](https://doi.org/10.1017/S0022377823000892). arXiv: [2306.05864](https://arxiv.org/abs/2306.05864) [astro-ph.HE].
- Peterson, J. R. et al. (Jan. 2001). "X-ray imaging-spectroscopy of Abell 1835". In: *Astronomy & Astrophysics* 365, pp. L104–L109. DOI: [10.1051/0004-6361:20000021](https://doi.org/10.1051/0004-6361:20000021). arXiv: [astro-ph/0010658](https://arxiv.org/abs/astro-ph/0010658) [astro-ph].
- Peterson, J. R. et al. (June 2003). "High-Resolution X-Ray Spectroscopic Constraints on Cooling-Flow Models for Clusters of Galaxies". In: *The Astrophysical Journal* 590.1, pp. 207–224. DOI: [10.1086/374830](https://doi.org/10.1086/374830). arXiv: [astro-ph/0210662](https://arxiv.org/abs/astro-ph/0210662) [astro-ph].
- Peterson, J. R. and A. C. Fabian (Apr. 2006). "X-ray spectroscopy of cooling clusters". In: *Physics Reports* 427.1, pp. 1–39. DOI: [10.1016/j.physrep.2005.12.007](https://doi.org/10.1016/j.physrep.2005.12.007). arXiv: [astro-ph/0512549](https://arxiv.org/abs/astro-ph/0512549) [astro-ph].
- Piffaretti, R. et al. (Oct. 2011). "The MCXC: a meta-catalogue of x-ray detected clusters of galaxies". In: *Astronomy & Astrophysics* 534, A109, A109. DOI: [10.1051/0004-6361/201015377](https://doi.org/10.1051/0004-6361/201015377). arXiv: [1007.1916](https://arxiv.org/abs/1007.1916) [astro-ph.CO].
- Prasad, Deovrat et al. (Oct. 2015). "Cool Core Cycles: Cold Gas and AGN Jet Feedback in Cluster Cores". In: *The Astrophysical Journal* 811.2, 108, p. 108. DOI: [10.1088/0004-637X/811/2/108](https://doi.org/10.1088/0004-637X/811/2/108). arXiv: [1504.02215](https://arxiv.org/abs/1504.02215) [astro-ph.GA].
- Prasow-Émond, M. et al. (Sept. 2020). "A Multiwavelength Study of the Cool Core Cluster MACS J1447.4+0827". In: *The Astronomical Journal* 160.3, 103, p. 103. DOI: [10.3847/1538-3881/ab9ff3](https://doi.org/10.3847/1538-3881/ab9ff3). arXiv: [2006.04815](https://arxiv.org/abs/2006.04815) [astro-ph.GA].

- Pratt, G. W. et al. (Feb. 2010). "Gas entropy in a representative sample of nearby X-ray galaxy clusters (REXCESS): relationship to gas mass fraction". In: *Astronomy & Astrophysics* 511, A85, A85. DOI: [10.1051/0004-6361/200913309](https://doi.org/10.1051/0004-6361/200913309). arXiv: [0909.3776](https://arxiv.org/abs/0909.3776) [astro-ph.CO].
- Pulido, F. A. et al. (Feb. 2018). "The Origin of Molecular Clouds in Central Galaxies". In: *The Astrophysical Journal* 853.2, 177, p. 177. DOI: [10.3847/1538-4357/aaa54b](https://doi.org/10.3847/1538-4357/aaa54b). arXiv: [1710.04664](https://arxiv.org/abs/1710.04664) [astro-ph.GA].
- Quici, Benjamin et al. (Aug. 2022). "Selecting and modelling remnant AGNs with limited spectral coverage". In: *Monthly Notices of the Royal Astronomical Society* 514.3, pp. 3466–3484. DOI: [10.1093/mnras/stac1328](https://doi.org/10.1093/mnras/stac1328). arXiv: [2205.02423](https://arxiv.org/abs/2205.02423) [astro-ph.GA].
- Rafferty, D. A. et al. (Nov. 2006). "The Feedback-regulated Growth of Black Holes and Bulges through Gas Accretion and Starbursts in Cluster Central Dominant Galaxies". In: *The Astrophysical Journal* 652.1, pp. 216–231. DOI: [10.1086/507672](https://doi.org/10.1086/507672). arXiv: [astro-ph/0605323](https://arxiv.org/abs/astro-ph/0605323) [astro-ph].
- Rafferty, D. A. et al. (Nov. 2008). "The Regulation of Cooling and Star Formation in Luminous Galaxies by Active Galactic Nucleus Feedback and the Cooling-Time/Entropy Threshold for the Onset of Star Formation". In: *The Astrophysical Journal* 687.2, pp. 899–918. DOI: [10.1086/591240](https://doi.org/10.1086/591240). arXiv: [0802.1864](https://arxiv.org/abs/0802.1864) [astro-ph].
- Randall, S. W. et al. (Aug. 2009). "Gas Sloshing and Bubbles in the Galaxy Group NGC 5098". In: *The Astrophysical Journal* 700.2, pp. 1404–1414. DOI: [10.1088/0004-637X/700/2/1404](https://doi.org/10.1088/0004-637X/700/2/1404). arXiv: [0904.0610](https://arxiv.org/abs/0904.0610) [astro-ph.CO].
- Randall, S. W. et al. (Jan. 2011). "Shocks and Cavities from Multiple Outbursts in the Galaxy Group NGC 5813: A Window to Active Galactic Nucleus Feedback". In: *The Astrophysical Journal* 726.2, 86, p. 86. DOI: [10.1088/0004-637X/726/2/86](https://doi.org/10.1088/0004-637X/726/2/86). arXiv: [1006.4379](https://arxiv.org/abs/1006.4379) [astro-ph.CO].
- Randall, S. W. et al. (June 2015). "A Very Deep Chandra Observation of the Galaxy Group NGC 5813: AGN Shocks, Feedback, and Outburst History". In: *The Astrophysical Journal* 805.2, 112, p. 112. DOI: [10.1088/0004-637X/805/2/112](https://doi.org/10.1088/0004-637X/805/2/112). arXiv: [1503.08205](https://arxiv.org/abs/1503.08205) [astro-ph.HE].
- Rebusco, P. et al. (May 2005). "Impact of stochastic gas motions on galaxy cluster abundance profiles". In: *Monthly Notices of the Royal Astronomical Society* 359.3, pp. 1041–1048. DOI: [10.1111/j.1365-2966.2005.08965.x](https://doi.org/10.1111/j.1365-2966.2005.08965.x). arXiv: [astro-ph/0501141](https://arxiv.org/abs/astro-ph/0501141) [astro-ph].
- Reiss, Ido and Uri Keshet (Sept. 2015). "A Dynamically Driven, Universal Thermal Profile of Galaxy Groups and Clusters". In: *The Astrophysical Journal* 810.2, 129, p. 129. DOI: [10.1088/0004-637X/810/2/129](https://doi.org/10.1088/0004-637X/810/2/129). arXiv: [1412.8456](https://arxiv.org/abs/1412.8456) [astro-ph.CO].
- Revaz, Y. et al. (Jan. 2008). "Formation of cold filaments in cooling flow clusters". In: *Astronomy & Astrophysics* 477.3, pp. L33–L36. DOI: [10.1051/0004-6361:20078915](https://doi.org/10.1051/0004-6361:20078915). arXiv: [0711.4051](https://arxiv.org/abs/0711.4051) [astro-ph].
- Reynolds, Christopher S. et al. (Feb. 2005). "Buoyant radio lobes in a viscous intracluster medium". In: *Monthly Notices of the Royal Astronomical Society* 357.1, pp. 242–250. DOI: [10.1111/j.1365-2966.2005.08643.x](https://doi.org/10.1111/j.1365-2966.2005.08643.x). arXiv: [astro-ph/0402632](https://arxiv.org/abs/astro-ph/0402632) [astro-ph].
- Rines, Kenneth et al. (Apr. 2013). "Measuring the Ultimate Halo Mass of Galaxy Clusters: Redshifts and Mass Profiles from the Hectospec Cluster Survey (HeCS)". In: *The Astrophysical Journal* 767.1, 15, p. 15. DOI: [10.1088/0004-637X/767/1/15](https://doi.org/10.1088/0004-637X/767/1/15). arXiv: [1209.3786](https://arxiv.org/abs/1209.3786) [astro-ph.CO].
- Roediger, E. et al. (Feb. 2007). "Metal mixing by buoyant bubbles in galaxy clusters". In: *Monthly Notices of the Royal Astronomical Society* 375.1, pp. 15–28. DOI: [10.1111/j.1365-2966.2006.11300.x](https://doi.org/10.1111/j.1365-2966.2006.11300.x). arXiv: [astro-ph/0611531](https://arxiv.org/abs/astro-ph/0611531) [astro-ph].
- Roediger, E. et al. (Mar. 2012). "Gas sloshing, cold fronts, Kelvin-Helmholtz instabilities and the merger history of the cluster of galaxies Abell 496". In: *Monthly Notices of the Royal Astronomical Society* 420.4, pp. 3632–3648. DOI: [10.1111/j.1365-2966.2011.20287.x](https://doi.org/10.1111/j.1365-2966.2011.20287.x). arXiv: [1112.1407](https://arxiv.org/abs/1112.1407) [astro-ph.CO].
- Rose, Tom et al. (Oct. 2019a). "Constraining cold accretion on to supermassive black holes: molecular gas in the cores of eight brightest cluster galaxies revealed by joint CO and CN absorption". In: *Monthly Notices of the Royal Astronomical Society* 489.1, pp. 349–365. DOI: [10.1093/mnras/stz2138](https://doi.org/10.1093/mnras/stz2138). arXiv: [1907.13526](https://arxiv.org/abs/1907.13526) [astro-ph.GA].

- Rose, Tom et al. (May 2019b). “Deep and narrow CO absorption revealing molecular clouds in the Hydra-A brightest cluster galaxy”. In: *Monthly Notices of the Royal Astronomical Society* 485.1, pp. 229–238. DOI: [10.1093/mnras/stz406](https://doi.org/10.1093/mnras/stz406). arXiv: [1902.01863](https://arxiv.org/abs/1902.01863) [astro-ph.GA].
- Rose, Tom et al. (July 2020). “A molecular absorption line survey towards the AGN of Hydra-A”. In: *Monthly Notices of the Royal Astronomical Society* 496.1, pp. 364–380. DOI: [10.1093/mnras/staa1474](https://doi.org/10.1093/mnras/staa1474). arXiv: [2005.10252](https://arxiv.org/abs/2005.10252) [astro-ph.GA].
- Rose, Tom et al. (Jan. 2023). “Does absorption against AGN reveal supermassive black hole accretion?” In: *Monthly Notices of the Royal Astronomical Society* 518.1, pp. 878–892. DOI: [10.1093/mnras/stac3194](https://doi.org/10.1093/mnras/stac3194). arXiv: [2210.14922](https://arxiv.org/abs/2210.14922) [astro-ph.GA].
- Rossetti, M. et al. (Mar. 2007). “A cluster in a crowded environment: XMM-Newton and Chandra observations of A3558”. In: *Astronomy & Astrophysics* 463.3, pp. 839–851. DOI: [10.1051/0004-6361:20054621](https://doi.org/10.1051/0004-6361:20054621). arXiv: [astro-ph/0611056](https://arxiv.org/abs/astro-ph/0611056) [astro-ph].
- Rossetti, M. et al. (Aug. 2011). “Back and forth from cool core to non-cool core: clues from radio halos”. In: *Astronomy & Astrophysics* 532, A123, A123. DOI: [10.1051/0004-6361/201117306](https://doi.org/10.1051/0004-6361/201117306). arXiv: [1106.4563](https://arxiv.org/abs/1106.4563) [astro-ph.CO].
- Rossetti, M. et al. (June 2017). “The cool-core state of Planck SZ-selected clusters versus X-ray-selected samples: evidence for cool-core bias”. In: *Monthly Notices of the Royal Astronomical Society* 468.2, pp. 1917–1930. DOI: [10.1093/mnras/stx493](https://doi.org/10.1093/mnras/stx493). arXiv: [1702.06961](https://arxiv.org/abs/1702.06961) [astro-ph.CO].
- Rubnur, K. et al. (Mar. 2017). “A candidate dual AGN in a double-peaked emission-line galaxy with precessing radio jets”. In: *Monthly Notices of the Royal Astronomical Society* 465.4, pp. 4772–4782. DOI: [10.1093/mnras/stw2981](https://doi.org/10.1093/mnras/stw2981).
- Russell, H. R. et al. (June 2013). “Radiative efficiency, variability and Bondi accretion on to massive black holes: the transition from radio AGN to quasars in brightest cluster galaxies”. In: *Monthly Notices of the Royal Astronomical Society* 432.1, pp. 530–553. DOI: [10.1093/mnras/stt490](https://doi.org/10.1093/mnras/stt490). arXiv: [1211.5604](https://arxiv.org/abs/1211.5604) [astro-ph.CO].
- Russell, H. R. et al. (May 2016). “ALMA observations of cold molecular gas filaments trailing rising radio bubbles in PKS 0745-191”. In: *Monthly Notices of the Royal Astronomical Society* 458.3, pp. 3134–3149. DOI: [10.1093/mnras/stw409](https://doi.org/10.1093/mnras/stw409). arXiv: [1602.05962](https://arxiv.org/abs/1602.05962) [astro-ph.GA].
- Russell, H. R. et al. (Dec. 2017). “Close entrainment of massive molecular gas flows by radio bubbles in the central galaxy of Abell 1795”. In: *Monthly Notices of the Royal Astronomical Society* 472.4, pp. 4024–4037. DOI: [10.1093/mnras/stx2255](https://doi.org/10.1093/mnras/stx2255). arXiv: [1708.08935](https://arxiv.org/abs/1708.08935) [astro-ph.GA].
- Russell, H. R. et al. (Dec. 2019). “Driving massive molecular gas flows in central cluster galaxies with AGN feedback”. In: *Monthly Notices of the Royal Astronomical Society* 490.3, pp. 3025–3045. DOI: [10.1093/mnras/stz2719](https://doi.org/10.1093/mnras/stz2719). arXiv: [1902.09227](https://arxiv.org/abs/1902.09227) [astro-ph.GA].
- Ruszkowski, Mateusz et al. (May 2018). “Powering of H α Filaments by Cosmic Rays”. In: *The Astrophysical Journal* 858.1, 64, p. 64. DOI: [10.3847/1538-4357/aaba72](https://doi.org/10.3847/1538-4357/aaba72). arXiv: [1802.04298](https://arxiv.org/abs/1802.04298) [astro-ph.HE].
- Sadler, E. M. (Feb. 2016). “GPS/CSS radio sources and their relation to other AGN”. In: *Astronomische Nachrichten* 337.1-2, p. 105. DOI: [10.1002/asna.201512274](https://doi.org/10.1002/asna.201512274). arXiv: [1512.01851](https://arxiv.org/abs/1512.01851) [astro-ph.GA].
- Saikia, D. J. and M. Jamrozy (Sept. 2009). “Recurrent activity in Active Galactic Nuclei”. In: *Bulletin of the Astronomical Society of India* 37, pp. 63–89. DOI: [10.48550/arXiv.1002.1841](https://doi.org/10.48550/arXiv.1002.1841). arXiv: [1002.1841](https://arxiv.org/abs/1002.1841) [astro-ph.CO].
- Salomé, P. and F. Combes (Dec. 2003). “Cold molecular gas in cooling flow clusters of galaxies”. In: *Astronomy & Astrophysics* 412, pp. 657–667. DOI: [10.1051/0004-6361:20031438](https://doi.org/10.1051/0004-6361:20031438). arXiv: [astro-ph/0309304](https://arxiv.org/abs/astro-ph/0309304) [astro-ph].
- Salomé, P. et al. (Aug. 2006). “Cold molecular gas in the Perseus cluster core. Association with X-ray cavity, H α filaments and cooling flow”. In: *Astronomy & Astrophysics* 454.2, pp. 437–445. DOI: [10.1051/0004-6361:20054745](https://doi.org/10.1051/0004-6361:20054745). arXiv: [astro-ph/0603350](https://arxiv.org/abs/astro-ph/0603350) [astro-ph].
- Sanders, J. S. (Sept. 2006). “Contour binning: a new technique for spatially resolved X-ray spectroscopy applied to Cassiopeia A”. In: *Monthly Notices of the Royal Astronomical Society* 371.2, pp. 829–842. DOI: [10.1111/j.1365-2966.2006.10716.x](https://doi.org/10.1111/j.1365-2966.2006.10716.x). arXiv: [astro-ph/0606528](https://arxiv.org/abs/astro-ph/0606528) [astro-ph].

- Sanders, J. S. et al. (July 2009). "Feedback through multiple outbursts in the cluster 2A 0335+096". In: *Monthly Notices of the Royal Astronomical Society* 396.3, pp. 1449–1459. DOI: [10.1111/j.1365-2966.2009.14892.x](https://doi.org/10.1111/j.1365-2966.2009.14892.x). arXiv: [0904.1374](https://arxiv.org/abs/0904.1374) [astro-ph.CO].
- Sanders, J. S. et al. (Mar. 2016a). "A very deep Chandra view of metals, sloshing and feedback in the Centaurus cluster of galaxies". In: *Monthly Notices of the Royal Astronomical Society* 457.1, pp. 82–109. DOI: [10.1093/mnras/stv2972](https://doi.org/10.1093/mnras/stv2972). arXiv: [1601.01489](https://arxiv.org/abs/1601.01489) [astro-ph.GA].
- Sanders, J. S. et al. (Aug. 2016b). "Detecting edges in the X-ray surface brightness of galaxy clusters". In: *Monthly Notices of the Royal Astronomical Society* 460.2, pp. 1898–1911. DOI: [10.1093/mnras/stw1119](https://doi.org/10.1093/mnras/stw1119). arXiv: [1605.02911](https://arxiv.org/abs/1605.02911) [astro-ph.CO].
- Sanders, Jeremy S. (Jan. 2023). "High-resolution X-ray spectroscopy of clusters of galaxies". In: *arXiv e-prints*, arXiv:2301.12791, arXiv:2301.12791. DOI: [10.48550/arXiv.2301.12791](https://doi.org/10.48550/arXiv.2301.12791). arXiv: [2301.12791](https://arxiv.org/abs/2301.12791) [astro-ph.HE].
- Sanderson, Alastair J. R. et al. (May 2009). "A statistically selected Chandra sample of 20 galaxy clusters - II. Gas properties and cool core/non-cool core bimodality". In: *Monthly Notices of the Royal Astronomical Society* 395.2, pp. 764–776. DOI: [10.1111/j.1365-2966.2009.14613.x](https://doi.org/10.1111/j.1365-2966.2009.14613.x). arXiv: [0902.1747](https://arxiv.org/abs/0902.1747) [astro-ph.CO].
- Sarazin, Craig L. (Jan. 1986). "X-ray emission from clusters of galaxies". In: *Reviews of Modern Physics* 58.1, pp. 1–115. DOI: [10.1103/RevModPhys.58.1](https://doi.org/10.1103/RevModPhys.58.1).
- Saxton, Curtis J. et al. (Dec. 2001). "The Centaurus A Northern Middle Lobe as a Buoyant Bubble". In: *The Astrophysical Journal* 563.1, pp. 103–117. DOI: [10.1086/323836](https://doi.org/10.1086/323836). arXiv: [astro-ph/0107558](https://arxiv.org/abs/astro-ph/0107558) [astro-ph].
- Schawinski, Kevin et al. (Aug. 2015). "Active galactic nuclei flicker: an observational estimate of the duration of black hole growth phases of $\sim 10^5$ yr". In: *Monthly Notices of the Royal Astronomical Society* 451.3, pp. 2517–2523. DOI: [10.1093/mnras/stv1136](https://doi.org/10.1093/mnras/stv1136). arXiv: [1505.06733](https://arxiv.org/abs/1505.06733) [astro-ph.GA].
- Schellenberger, Gerrit et al. (Jan. 2021). "A New Feedback Cycle in the Archetypal Cooling Flow Group NGC 5044". In: *The Astrophysical Journal* 906.1, 16, p. 16. DOI: [10.3847/1538-4357/abc488](https://doi.org/10.3847/1538-4357/abc488). arXiv: [2010.13804](https://arxiv.org/abs/2010.13804) [astro-ph.GA].
- Schellenberger, Gerrit et al. (May 2023). "Feedback in the Extremely Violent Group Merger NGC 6338". In: *The Astrophysical Journal* 948.2, 101, p. 101. DOI: [10.3847/1538-4357/acc52e](https://doi.org/10.3847/1538-4357/acc52e). arXiv: [2303.08833](https://arxiv.org/abs/2303.08833) [astro-ph.GA].
- Scheuer, P. A. G. and A. C. S. Readhead (Jan. 1979). "Superluminally expanding radio sources and the radio-quiet QSOs". In: *Nature* 277, pp. 182–185. DOI: [10.1038/277182a0](https://doi.org/10.1038/277182a0).
- Schindler, S. et al. (Sept. 2001). "Discovery of depressions in the X-ray emission of the distant galaxy cluster RBS797 in a CHANDRA observation". In: *Astronomy & Astrophysics* 376, pp. L27–L30. DOI: [10.1051/0004-6361:20010990](https://doi.org/10.1051/0004-6361:20010990). arXiv: [astro-ph/0107504](https://arxiv.org/abs/astro-ph/0107504) [astro-ph].
- Schmidt, R. W. et al. (Nov. 2002). "Chandra temperature and metallicity maps of the Perseus cluster core". In: *Monthly Notices of the Royal Astronomical Society* 337.1, pp. 71–78. DOI: [10.1046/j.1365-8711.2002.05804.x](https://doi.org/10.1046/j.1365-8711.2002.05804.x). arXiv: [astro-ph/0207290](https://arxiv.org/abs/astro-ph/0207290) [astro-ph].
- Seyfert, Carl K. (Jan. 1943). "Nuclear Emission in Spiral Nebulae." In: *The Astrophysical Journal* 97, p. 28. DOI: [10.1086/144488](https://doi.org/10.1086/144488).
- Shabala, S. S. et al. (Aug. 2008). "The duty cycle of local radio galaxies". In: *Monthly Notices of the Royal Astronomical Society* 388.2, pp. 625–637. DOI: [10.1111/j.1365-2966.2008.13459.x](https://doi.org/10.1111/j.1365-2966.2008.13459.x). arXiv: [0805.4152](https://arxiv.org/abs/0805.4152) [astro-ph].
- Shabala, Stanislav S. et al. (Aug. 2020). "The duty cycle of radio galaxies revealed by LOFAR: remnant and restarted radio source populations in the Lockman Hole". In: *Monthly Notices of the Royal Astronomical Society* 496.2, pp. 1706–1717. DOI: [10.1093/mnras/staa1172](https://doi.org/10.1093/mnras/staa1172). arXiv: [2004.08979](https://arxiv.org/abs/2004.08979) [astro-ph.GA].
- Shakura, N. I. and R. A. Sunyaev (Jan. 1973). "Black holes in binary systems. Observational appearance." In: *Astronomy & Astrophysics* 24, pp. 337–355.

- Shepherd, M. C. (Jan. 1997). "Difmap: an Interactive Program for Synthesis Imaging". In: *Astronomical Data Analysis Software and Systems VI*. Ed. by Gareth Hunt and Harry Payne. Vol. 125. Astronomical Society of the Pacific Conference Series, p. 77.
- Shimwell, T. W. et al. (Mar. 2022). "The LOFAR Two-metre Sky Survey. V. Second data release". In: *Astronomy & Astrophysics* 659, A1, A1. DOI: [10.1051/0004-6361/202142484](https://doi.org/10.1051/0004-6361/202142484). arXiv: [2202.11733](https://arxiv.org/abs/2202.11733) [astro-ph.GA].
- Shin, Jaejin et al. (Dec. 2016). "A Systematic Search for X-Ray Cavities in Galaxy Clusters, Groups, and Elliptical Galaxies". In: *The Astrophysical Journals* 227.2, 31, p. 31. DOI: [10.3847/1538-4365/227/2/31](https://doi.org/10.3847/1538-4365/227/2/31). arXiv: [1610.03487](https://arxiv.org/abs/1610.03487) [astro-ph.CO].
- Shulevski, A. et al. (Apr. 2017). "Radiative age mapping of the remnant radio galaxy B2 0924+30: the LOFAR perspective". In: *Astronomy & Astrophysics* 600, A65, A65. DOI: [10.1051/0004-6361/201630008](https://doi.org/10.1051/0004-6361/201630008). arXiv: [1701.06903](https://arxiv.org/abs/1701.06903) [astro-ph.GA].
- Shurkin, K. et al. (Jan. 2008). "Active galactic nuclei-induced cavities in NGC 1399 and NGC 4649". In: *Monthly Notices of the Royal Astronomical Society* 383.3, pp. 923–930. DOI: [10.1111/j.1365-2966.2007.12651.x](https://doi.org/10.1111/j.1365-2966.2007.12651.x). arXiv: [0710.5704](https://arxiv.org/abs/0710.5704) [astro-ph].
- Sijacki, Debora and Volker Springel (Sept. 2006). "Physical viscosity in smoothed particle hydrodynamics simulations of galaxy clusters". In: *Monthly Notices of the Royal Astronomical Society* 371.3, pp. 1025–1046. DOI: [10.1111/j.1365-2966.2006.10752.x](https://doi.org/10.1111/j.1365-2966.2006.10752.x). arXiv: [astro-ph/0605301](https://arxiv.org/abs/astro-ph/0605301) [astro-ph].
- Simionescu, A. et al. (Apr. 2008). "Metal-rich multi-phase gas in M 87. AGN-driven metal transport, magnetic-field supported multi-temperature gas, and constraints on non-thermal emission observed with XMM-Newton". In: *Astronomy & Astrophysics* 482.1, pp. 97–112. DOI: [10.1051/0004-6361:20078749](https://doi.org/10.1051/0004-6361:20078749). arXiv: [0709.4499](https://arxiv.org/abs/0709.4499) [astro-ph].
- Smith, K. L. et al. (June 2010). "A Search for Binary Active Galactic Nuclei: Double-peaked [O III] AGNs in the Sloan Digital Sky Survey". In: *The Astrophysical Journal* 716.1, pp. 866–877. DOI: [10.1088/0004-637X/716/1/866](https://doi.org/10.1088/0004-637X/716/1/866). arXiv: [0908.1998](https://arxiv.org/abs/0908.1998) [astro-ph.CO].
- Snios, Bradford et al. (Mar. 2018). "The Cocoon Shocks of Cygnus A: Pressures and Their Implications for the Jets and Lobes". In: *The Astrophysical Journal* 855.1, 71, p. 71. DOI: [10.3847/1538-4357/aaaf1a](https://doi.org/10.3847/1538-4357/aaaf1a). arXiv: [1802.10106](https://arxiv.org/abs/1802.10106) [astro-ph.HE].
- Soker, Noam (Sept. 2022). "Jittering Jets by Negative Angular Momentum Feedback in Cooling Flows". In: *Universe* 8.9, p. 483. DOI: [10.3390/universe8090483](https://doi.org/10.3390/universe8090483). arXiv: [2111.11906](https://arxiv.org/abs/2111.11906) [astro-ph.GA].
- Somboonpanyakul, Taweewat et al. (Jan. 2021). "The Clusters Hiding in Plain Sight (CHiPS) Survey: CHiPS1911+4455, a Rapidly Cooling Core in a Merging Cluster". In: *The Astrophysical Journal* 907.1, L12, p. L12. DOI: [10.3847/2041-8213/abd540](https://doi.org/10.3847/2041-8213/abd540). arXiv: [2101.01731](https://arxiv.org/abs/2101.01731) [astro-ph.GA].
- Sonkamble, S. S. et al. (Oct. 2015). "X-ray cavities and temperature jumps in the environment of the strong cool core cluster Abell 2390". In: *Astrophysics and Space Science* 359, 21, p. 21. DOI: [10.1007/s10509-015-2508-z](https://doi.org/10.1007/s10509-015-2508-z). arXiv: [1412.8632](https://arxiv.org/abs/1412.8632) [astro-ph.CO].
- Stairs, Ingrid H. (Sept. 2003). "Testing General Relativity with Pulsar Timing". In: *Living Reviews in Relativity* 6.1, 5, p. 5. DOI: [10.12942/lrr-2003-5](https://doi.org/10.12942/lrr-2003-5). arXiv: [astro-ph/0307536](https://arxiv.org/abs/astro-ph/0307536) [astro-ph].
- Steenbrugge, K. C. et al. (Mar. 2014). "Multiwavelength study of Cygnus A. IV. Proper motion and location of the nucleus". In: *Astronomy & Astrophysics* 563, A131, A131. DOI: [10.1051/0004-6361/201322339](https://doi.org/10.1051/0004-6361/201322339). arXiv: [1402.5931](https://arxiv.org/abs/1402.5931) [astro-ph.GA].
- Steenbrugge, Katrien C. and Katherine M. Blundell (Aug. 2008). "Multiwavelength study of Cygnus A - I. Precession and slow jet speeds from radio observations". In: *Monthly Notices of the Royal Astronomical Society* 388.4, pp. 1457–1464. DOI: [10.1111/j.1365-2966.2007.12665.x](https://doi.org/10.1111/j.1365-2966.2007.12665.x). arXiv: [0805.2169](https://arxiv.org/abs/0805.2169) [astro-ph].
- Steidel, Charles C. et al. (Mar. 2000). "Ly α Imaging of a Proto-Cluster Region at $\langle z \rangle = 3.09$ ". In: *The Astrophysical Journal* 532.1, pp. 170–182. DOI: [10.1086/308568](https://doi.org/10.1086/308568). arXiv: [astro-ph/9910144](https://arxiv.org/abs/astro-ph/9910144) [astro-ph].
- Stewart, G. C. et al. (Oct. 1984). "The prevalence of cooling flows in clusters of galaxies." In: *The Astrophysical Journal* 285, pp. 1–6. DOI: [10.1086/162470](https://doi.org/10.1086/162470).

- Su, Yuanyuan et al. (Dec. 2017). "Gas Sloshing Regulates and Records the Evolution of the Fornax Cluster". In: *The Astrophysical Journal* 851.1, 69, p. 69. DOI: [10.3847/1538-4357/aa989e](https://doi.org/10.3847/1538-4357/aa989e). arXiv: [1711.01523](https://arxiv.org/abs/1711.01523) [astro-ph.HE].
- Sun, M. (Oct. 2009). "Every BCG with a Strong Radio Agn has an X-Ray Cool Core: Is the Cool Core-Noncool Core Dichotomy Too Simple?" In: *The Astrophysical Journal* 704.2, pp. 1586–1604. DOI: [10.1088/0004-637X/704/2/1586](https://doi.org/10.1088/0004-637X/704/2/1586). arXiv: [0904.2006](https://arxiv.org/abs/0904.2006) [astro-ph.CO].
- Sun, M. et al. (Apr. 2003). "Chandra Observations of the Galaxy Cluster A478: The Interaction of Hot Gas and Radio Plasma in the Core, and an Improved Determination of the Compton y -Parameter". In: *The Astrophysical Journal* 587.2, pp. 619–624. DOI: [10.1086/368300](https://doi.org/10.1086/368300). arXiv: [astro-ph/0210054](https://arxiv.org/abs/astro-ph/0210054) [astro-ph].
- Tabor, G. and J. Binney (July 1993). "Elliptical galaxy cooling flows without mass drop-out." In: *Monthly Notices of the Royal Astronomical Society* 263, pp. 323–334. DOI: [10.1093/mnras/263.2.323](https://doi.org/10.1093/mnras/263.2.323).
- Taffoni, G. et al. (Jan. 2020). "CHIPP: INAF Pilot Project for HTC, HPC and HPDA". In: *Astronomical Data Analysis Software and Systems XXIX*. Ed. by R. Pizzo et al. Vol. 527. Astronomical Society of the Pacific Conference Series, p. 307.
- Taylor, G. B. et al. (Sept. 1990). "VLA Observations of the Radio Galaxy Hydra A (3C 218)". In: *The Astrophysical Journal* 360, p. 41. DOI: [10.1086/169094](https://doi.org/10.1086/169094).
- Temi, Pasquale et al. (May 2018). "ALMA Observations of Molecular Clouds in Three Group-centered Elliptical Galaxies: NGC 5846, NGC 4636, and NGC 5044". In: *The Astrophysical Journal* 858.1, 17, p. 17. DOI: [10.3847/1538-4357/aab9b0](https://doi.org/10.3847/1538-4357/aab9b0). arXiv: [1711.10630](https://arxiv.org/abs/1711.10630) [astro-ph.GA].
- Timmerman, R. et al. (Dec. 2022). "Measuring cavity powers of active galactic nuclei in clusters using a hybrid X-ray-radio method. A new window on feedback opened by subarcsecond LOFAR-VLBI observations". In: *Astronomy & Astrophysics* 668, A65, A65. DOI: [10.1051/0004-6361/202243936](https://doi.org/10.1051/0004-6361/202243936). arXiv: [2207.05088](https://arxiv.org/abs/2207.05088) [astro-ph.CO].
- Torresi, E. et al. (June 2018). "X-ray study of a sample of FR0 radio galaxies: unveiling the nature of the central engine". In: *Monthly Notices of the Royal Astronomical Society* 476.4, pp. 5535–5547. DOI: [10.1093/mnras/sty520](https://doi.org/10.1093/mnras/sty520). arXiv: [1802.08581](https://arxiv.org/abs/1802.08581) [astro-ph.HE].
- Tozzi, P. (Jan. 2002). "The Heating of the ICM: Energy Crisis and Viable Solutions". In: *Tracing Cosmic Evolution with Galaxy Clusters*. Ed. by Stefano Borgani et al. Vol. 268. Astronomical Society of the Pacific Conference Series, p. 248. DOI: [10.48550/arXiv.astro-ph/0109072](https://doi.org/10.48550/arXiv.astro-ph/0109072). arXiv: [astro-ph/0109072](https://arxiv.org/abs/astro-ph/0109072) [astro-ph].
- Tozzi, P. et al. (Aug. 2003). "Iron Abundance in the Intracluster Medium at High Redshift". In: *The Astrophysical Journal* 593.2, pp. 705–720. DOI: [10.1086/376731](https://doi.org/10.1086/376731). arXiv: [astro-ph/0305223](https://arxiv.org/abs/astro-ph/0305223) [astro-ph].
- Tozzi, P. et al. (June 2022). "The 700 ks Chandra Spiderweb Field. I. Evidence for widespread nuclear activity in the protocluster". In: *Astronomy & Astrophysics* 662, A54, A54. DOI: [10.1051/0004-6361/202142333](https://doi.org/10.1051/0004-6361/202142333). arXiv: [2203.02208](https://arxiv.org/abs/2203.02208) [astro-ph.GA].
- Tozzi, Paolo and Colin Norman (Jan. 2001). "The Evolution of X-Ray Clusters and the Entropy of the Intracluster Medium". In: *The Astrophysical Journal* 546.1, pp. 63–84. DOI: [10.1086/318237](https://doi.org/10.1086/318237). arXiv: [astro-ph/0003289](https://arxiv.org/abs/astro-ph/0003289) [astro-ph].
- Tremaine, Scott et al. (Aug. 2002). "The Slope of the Black Hole Mass versus Velocity Dispersion Correlation". In: *The Astrophysical Journal* 574.2, pp. 740–753. DOI: [10.1086/341002](https://doi.org/10.1086/341002). arXiv: [astro-ph/0203468](https://arxiv.org/abs/astro-ph/0203468) [astro-ph].
- Tremblay, G. R. et al. (Sept. 2018). "A Galaxy-scale Fountain of Cold Molecular Gas Pumped by a Black Hole". In: *The Astrophysical Journal* 865.1, 13, p. 13. DOI: [10.3847/1538-4357/aad6dd](https://doi.org/10.3847/1538-4357/aad6dd). arXiv: [1808.00473](https://arxiv.org/abs/1808.00473) [astro-ph.GA].
- Tremblay, Grant R. et al. (June 2016). "Cold, clumpy accretion onto an active supermassive black hole". In: *Nature Astronomy* 534.7606, pp. 218–221. DOI: [10.1038/nature17969](https://doi.org/10.1038/nature17969). arXiv: [1606.02304](https://arxiv.org/abs/1606.02304) [astro-ph.GA].

- Tribble, Peter C. (Mar. 1993). "Radio spectral ageing in a random magnetic field." In: *Monthly Notices of the Royal Astronomical Society* 261, pp. 57–62. DOI: [10.1093/mnras/261.1.57](https://doi.org/10.1093/mnras/261.1.57).
- Turner, Ross J. and Stanislav S. Shabala (June 2015). "Energetics and Lifetimes of Local Radio Active Galactic Nuclei". In: *The Astrophysical Journal* 806.1, 59, p. 59. DOI: [10.1088/0004-637X/806/1/59](https://doi.org/10.1088/0004-637X/806/1/59). arXiv: [1504.05204](https://arxiv.org/abs/1504.05204) [astro-ph.GA].
- (July 2023). "Dynamics of Powerful Radio Galaxies". In: *Galaxies* 11.4, p. 87. DOI: [10.3390/galaxies11040087](https://doi.org/10.3390/galaxies11040087). arXiv: [2307.08341](https://arxiv.org/abs/2307.08341) [astro-ph.GA].
- Ubertosi, F. et al. (May 2021a). "A Chandra study of Abell 795 - a sloshing cluster with an FR0 radio galaxy at its centre". In: *Monthly Notices of the Royal Astronomical Society* 503.3, pp. 4627–4645. DOI: [10.1093/mnras/stab819](https://doi.org/10.1093/mnras/stab819). arXiv: [2103.08682](https://arxiv.org/abs/2103.08682) [astro-ph.GA].
- Ubertosi, F. et al. (Dec. 2021b). "The Deepest Chandra View of RBS 797: Evidence for Two Pairs of Equidistant X-ray Cavities". In: *The Astrophysical Journal* 923.2, L25, p. L25. DOI: [10.3847/2041-8213/ac374c](https://doi.org/10.3847/2041-8213/ac374c). arXiv: [2111.03679](https://arxiv.org/abs/2111.03679) [astro-ph.GA].
- Ubertosi, F. et al. (Feb. 2023a). "Chasing ICM cooling and AGN feedback from the macro to the meso scales in the galaxy cluster ZwCl 235". In: *Astronomy & Astrophysics* 670, A23, A23. DOI: [10.1051/0004-6361/202244023](https://doi.org/10.1051/0004-6361/202244023). arXiv: [2211.09141](https://arxiv.org/abs/2211.09141) [astro-ph.GA].
- Ubertosi, F. et al. (Feb. 2023b). "Multiple Shock Fronts in RBS 797: The Chandra Window on Shock Heating in Galaxy Clusters". In: *The Astrophysical Journal* 944.2, 216, p. 216. DOI: [10.3847/1538-4357/acacf9](https://doi.org/10.3847/1538-4357/acacf9). arXiv: [2212.10581](https://arxiv.org/abs/2212.10581) [astro-ph.GA].
- Ubertosi, F. et al. (May 2023c). "Waking the monster: The onset of AGN feedback in galaxy clusters hosting young central radio galaxies". In: *Astronomy & Astrophysics* 673, A52, A52. DOI: [10.1051/0004-6361/202345894](https://doi.org/10.1051/0004-6361/202345894). arXiv: [2303.04821](https://arxiv.org/abs/2303.04821) [astro-ph.GA].
- Ubertosi, Francesco et al. (Dec. 2023d). "Jet reorientation in central galaxies of clusters and groups: insights from VLBA and Chandra data". In: *arXiv e-prints*, arXiv:2312.02283, arXiv:2312.02283. DOI: [10.48550/arXiv.2312.02283](https://doi.org/10.48550/arXiv.2312.02283). arXiv: [2312.02283](https://arxiv.org/abs/2312.02283) [astro-ph.GA].
- Ueda, Shutaro et al. (Apr. 2020). "Gas Density Perturbations in the Cool Cores of CLASH Galaxy Clusters". In: *The Astrophysical Journal* 892.2, 100, p. 100. DOI: [10.3847/1538-4357/ab7bdc](https://doi.org/10.3847/1538-4357/ab7bdc). arXiv: [1912.07300](https://arxiv.org/abs/1912.07300) [astro-ph.CO].
- Urry, C. Megan and Paolo Padovani (Sept. 1995). "Unified Schemes for Radio-Loud Active Galactic Nuclei". In: *Publications of the Astronomical Society of the Pacific* 107, p. 803. DOI: [10.1086/133630](https://doi.org/10.1086/133630). arXiv: [astro-ph/9506063](https://arxiv.org/abs/astro-ph/9506063) [astro-ph].
- Vagshette, Nilkanth D. et al. (Apr. 2017). "Detection of a pair of prominent X-ray cavities in Abell 3847". In: *Monthly Notices of the Royal Astronomical Society* 466.2, pp. 2054–2066. DOI: [10.1093/mnras/stw3227](https://doi.org/10.1093/mnras/stw3227). arXiv: [1612.02560](https://arxiv.org/abs/1612.02560) [astro-ph.GA].
- Vagshette, Nilkanth D. et al. (May 2019). "Cavities, shocks and a cold front around 3C 320". In: *Monthly Notices of the Royal Astronomical Society* 485.2, pp. 1981–1989. DOI: [10.1093/mnras/stz476](https://doi.org/10.1093/mnras/stz476). arXiv: [1902.04778](https://arxiv.org/abs/1902.04778) [astro-ph.GA].
- Valentini, Milena and Fabrizio Brighenti (Apr. 2015). "AGN-stimulated cooling of hot gas in elliptical galaxies". In: *Monthly Notices of the Royal Astronomical Society* 448.3, pp. 1979–1998. DOI: [10.1093/mnras/stv090](https://doi.org/10.1093/mnras/stv090). arXiv: [1501.03502](https://arxiv.org/abs/1501.03502) [astro-ph.GA].
- van Diepen, Ger et al. (Apr. 2018). *DPPP: Default Pre-Processing Pipeline*. Astrophysics Source Code Library, record ascl:1804.003. ascl: [1804.003](https://ascl.net/1804.003).
- van Haarlem, M. P. et al. (Aug. 2013). "LOFAR: The LOw-Frequency ARray". In: *Astronomy & Astrophysics* 556, A2, A2. DOI: [10.1051/0004-6361/201220873](https://doi.org/10.1051/0004-6361/201220873). arXiv: [1305.3550](https://arxiv.org/abs/1305.3550) [astro-ph.IM].
- van Weeren, R. J. et al. (Mar. 2016). "LOFAR Facet Calibration". In: *The Astrophysical Journal* 823.1, 2, p. 2. DOI: [10.3847/0067-0049/223/1/2](https://doi.org/10.3847/0067-0049/223/1/2). arXiv: [1601.05422](https://arxiv.org/abs/1601.05422) [astro-ph.IM].
- Vantyghem, A. N. et al. (Aug. 2014). "Cycling of the powerful AGN in MS 0735.6+7421 and the duty cycle of radio AGN in clusters". In: *Monthly Notices of the Royal Astronomical Society* 442.4, pp. 3192–3205. DOI: [10.1093/mnras/stu1030](https://doi.org/10.1093/mnras/stu1030). arXiv: [1405.6208](https://arxiv.org/abs/1405.6208) [astro-ph.GA].

- Vantyghem, A. N. et al. (Jan. 2019). "An Enormous Molecular Gas Flow in the RX J0821+0752 Galaxy Cluster". In: *The Astrophysical Journal* 870.2, 57, p. 57. DOI: [10.3847/1538-4357/aaf1b4](https://doi.org/10.3847/1538-4357/aaf1b4). arXiv: [1811.09653](https://arxiv.org/abs/1811.09653) [astro-ph.GA].
- Vazquez Najar, Lizbeth A. and Heinz Andernach (Aug. 2019). "Radio-Optical Alignment of Radio Galaxies". In: *arXiv e-prints*, arXiv:1908.09989, arXiv:1908.09989. DOI: [10.48550/arXiv.1908.09989](https://doi.org/10.48550/arXiv.1908.09989). arXiv: [1908.09989](https://arxiv.org/abs/1908.09989) [astro-ph.GA].
- Čemeljić, Miljenko et al. (July 2022). "Formation of Episodic Jets and Associated Flares from Black Hole Accretion Systems". In: 933.1, 55, p. 55. DOI: [10.3847/1538-4357/ac70cc](https://doi.org/10.3847/1538-4357/ac70cc). arXiv: [2205.10531](https://arxiv.org/abs/2205.10531) [astro-ph.HE].
- Venemans, B. P. et al. (Jan. 2007). "Protoclusters associated with $z > 2$ radio galaxies . I. Characteristics of high redshift protoclusters". In: *Astronomy & Astrophysics* 461.3, pp. 823–845. DOI: [10.1051/0004-6361:20053941](https://doi.org/10.1051/0004-6361:20053941). arXiv: [astro-ph/0610567](https://arxiv.org/abs/astro-ph/0610567) [astro-ph].
- Venturi, T. et al. (Aug. 2004). "Radio galaxies in cooling core clusters. Renewed activity in the nucleus of 3C 317?". In: *Astronomy & Astrophysics* 422, pp. 515–522. DOI: [10.1051/0004-6361:20040089](https://doi.org/10.1051/0004-6361:20040089). arXiv: [astro-ph/0404571](https://arxiv.org/abs/astro-ph/0404571) [astro-ph].
- Vikhlinin, A. et al. (Apr. 2001). "A Moving Cold Front in the Intergalactic Medium of A3667". In: *The Astrophysical Journal* 551.1, pp. 160–171. DOI: [10.1086/320078](https://doi.org/10.1086/320078). arXiv: [astro-ph/0008496](https://arxiv.org/abs/astro-ph/0008496) [astro-ph].
- Voigt, L. M. and A. C. Fabian (May 2006). "Galaxy cluster mass profiles". In: *Monthly Notices of the Royal Astronomical Society* 368.2, pp. 518–533. DOI: [10.1111/j.1365-2966.2006.10199.x](https://doi.org/10.1111/j.1365-2966.2006.10199.x). arXiv: [astro-ph/0602373](https://arxiv.org/abs/astro-ph/0602373) [astro-ph].
- Voit, G. Mark (Apr. 2005). "Tracing cosmic evolution with clusters of galaxies". In: *Reviews of Modern Physics* 77.1, pp. 207–258. DOI: [10.1103/RevModPhys.77.207](https://doi.org/10.1103/RevModPhys.77.207). arXiv: [astro-ph/0410173](https://arxiv.org/abs/astro-ph/0410173) [astro-ph].
- Voit, G. Mark and Megan Donahue (Sept. 1990). "Self-irradiated Cooling Condensations: The Source of the Optical Line Emission from Cooling Flows". In: *The Astrophysical Journal Letters* 360, p. L15. DOI: [10.1086/185801](https://doi.org/10.1086/185801).
- Voit, G. Mark et al. (Sept. 2002). "Modified Entropy Models for the Intracluster Medium". In: *The Astrophysical Journal* 576.2, pp. 601–624. DOI: [10.1086/341864](https://doi.org/10.1086/341864). arXiv: [astro-ph/0205240](https://arxiv.org/abs/astro-ph/0205240) [astro-ph].
- Voit, G. Mark and Trevor J. Ponman (Sept. 2003). "Signatures of Galaxy Formation in the Intracluster Medium". In: *The Astrophysical Journal Letters* 594.2, pp. L75–L78. DOI: [10.1086/378627](https://doi.org/10.1086/378627). arXiv: [astro-ph/0308475](https://arxiv.org/abs/astro-ph/0308475) [astro-ph].
- Voit, G. Mark and Megan Donahue (Jan. 2015). "Cooling Time, Freefall Time, and Precipitation in the Cores of ACCEPT Galaxy Clusters". In: *The Astrophysical Journal* 799.1, L1, p. L1. DOI: [10.1088/2041-8205/799/1/L1](https://doi.org/10.1088/2041-8205/799/1/L1). arXiv: [1409.1601](https://arxiv.org/abs/1409.1601) [astro-ph.GA].
- von Fellenberg, S. D. et al. (Apr. 2023). "Radio jet precession in M 81*". In: *Astronomy & Astrophysics* 672, L5, p. L5. DOI: [10.1051/0004-6361/202245506](https://doi.org/10.1051/0004-6361/202245506). arXiv: [2303.00603](https://arxiv.org/abs/2303.00603) [astro-ph.HE].
- Wang, Lei et al. (June 2023). "Physical cool-core condensation radius in massive galaxy clusters". In: *Astronomy & Astrophysics* 674, A102, A102. DOI: [10.1051/0004-6361/202244138](https://doi.org/10.1051/0004-6361/202244138). arXiv: [2304.08810](https://arxiv.org/abs/2304.08810) [astro-ph.GA].
- Wehrle, A. E. et al. (Jan. 1996). "Misalignments between the Parsec-scale and Kiloparsec-scale Emission of Radio Sources". In: *Blazar Continuum Variability*. Ed. by H. Richard Miller et al. Vol. 110. Astronomical Society of the Pacific Conference Series, p. 285.
- Weilbacher, P. M. et al. (May 2014). "The MUSE Data Reduction Pipeline: Status after Preliminary Acceptance Europe". In: *Astronomical Data Analysis Software and Systems XXIII*. Ed. by N. Manset and P. Forshay. Vol. 485. Astronomical Society of the Pacific Conference Series, p. 451. arXiv: [1507.00034](https://arxiv.org/abs/1507.00034) [astro-ph.IM].
- Weinberger, Rainer et al. (Nov. 2022). "Active galactic nucleus jet feedback in hydrostatic halos". In: *arXiv e-prints*, arXiv:2211.11771, arXiv:2211.11771. arXiv: [2211.11771](https://arxiv.org/abs/2211.11771) [astro-ph.GA].

- Whyborn, N. D. et al. (May 1985). “Radio and optical observations of the radio galaxy 0831+557.” In: *Monthly Notices of the Royal Astronomical Society* 214, pp. 55–65. DOI: [10.1093/mnras/214.1.55](https://doi.org/10.1093/mnras/214.1.55).
- Williams, W. L. et al. (Aug. 2016). “LOFAR 150-MHz observations of the Boötes field: catalogue and source counts”. In: *Monthly Notices of the Royal Astronomical Society* 460.3, pp. 2385–2412. DOI: [10.1093/mnras/stw1056](https://doi.org/10.1093/mnras/stw1056). arXiv: [1605.01531](https://arxiv.org/abs/1605.01531) [astro-ph.CO].
- Wise, M. W. et al. (Apr. 2007). “X-Ray Supercavities in the Hydra A Cluster and the Outburst History of the Central Galaxy’s Active Nucleus”. In: *The Astrophysical Journal* 659.2, pp. 1153–1158. DOI: [10.1086/512767](https://doi.org/10.1086/512767). arXiv: [astro-ph/0612100](https://arxiv.org/abs/astro-ph/0612100) [astro-ph].
- Wittor, D. and M. Gaspari (Nov. 2020). “Dissecting the turbulent weather driven by mechanical AGN feedback”. In: *Monthly Notices of the Royal Astronomical Society* 498.4, pp. 4983–5002. DOI: [10.1093/mnras/staa2747](https://doi.org/10.1093/mnras/staa2747). arXiv: [2009.03344](https://arxiv.org/abs/2009.03344) [astro-ph.GA].
- Wójtowicz, A. et al. (Apr. 2020). “On the Jet Production Efficiency in a Sample of the Youngest Radio Galaxies”. In: *The Astrophysical Journal* 892.2, 116, p. 116. DOI: [10.3847/1538-4357/ab7930](https://doi.org/10.3847/1538-4357/ab7930). arXiv: [1911.01197](https://arxiv.org/abs/1911.01197) [astro-ph.HE].
- Xue, Sui-Jian and Xiang-Ping Wu (Sept. 2002). “Chandra X-Ray Observatory Observation of A1689: New Determination of Mass Distribution and Comparison to Lensing Measurements”. In: *The Astrophysical Journal* 576.1, pp. 152–158. DOI: [10.1086/341726](https://doi.org/10.1086/341726). arXiv: [astro-ph/0204510](https://arxiv.org/abs/astro-ph/0204510) [astro-ph].
- Xue, Yan-Jie and Xiang-Ping Wu (Nov. 2000). “Properties of the double β model for intracluster gas”. In: *Monthly Notices of the Royal Astronomical Society* 318.3, pp. 715–723. DOI: [10.1046/j.1365-8711.2000.03753.x](https://doi.org/10.1046/j.1365-8711.2000.03753.x). arXiv: [astro-ph/0006131](https://arxiv.org/abs/astro-ph/0006131) [astro-ph].
- Yang, H. Y. Karen and Christopher S. Reynolds (Oct. 2016). “How AGN Jets Heat the Intracluster Medium—Insights from Hydrodynamic Simulations”. In: *The Astrophysical Journal* 829.2, 90, p. 90. DOI: [10.3847/0004-637X/829/2/90](https://doi.org/10.3847/0004-637X/829/2/90). arXiv: [1605.01725](https://arxiv.org/abs/1605.01725) [astro-ph.HE].
- Zhang, Chenhao et al. (June 2016). “A Chandra Study of the Image Power Spectra of 41 Cool Core and Non-cool Core Galaxy Clusters”. In: *The Astrophysical Journal* 823.2, 116, p. 116. DOI: [10.3847/0004-637X/823/2/116](https://doi.org/10.3847/0004-637X/823/2/116). arXiv: [1604.04127](https://arxiv.org/abs/1604.04127) [astro-ph.CO].
- Zhang, Congyao et al. (Nov. 2022a). “Bubble-driven gas uplift in galaxy clusters and its velocity features”. In: *Monthly Notices of the Royal Astronomical Society* 517.1, pp. 616–631. DOI: [10.1093/mnras/stac2282](https://doi.org/10.1093/mnras/stac2282). arXiv: [2203.04259](https://arxiv.org/abs/2203.04259) [astro-ph.HE].
- Zhang, William et al. (Apr. 2022b). “The Survey and Time-domain Astrophysical Research Explorer (STAR-X)”. In: *AAS/High Energy Astrophysics Division*. Vol. 54. AAS/High Energy Astrophysics Division, 108.45, p. 108.45.
- Zou, Hu et al. (Apr. 2021). “Galaxy Clusters from the DESI Legacy Imaging Surveys. I. Cluster Detection”. In: *The Astrophysical Journals* 253.2, 56, p. 56. DOI: [10.3847/1538-4365/abe5b0](https://doi.org/10.3847/1538-4365/abe5b0). arXiv: [2101.12340](https://arxiv.org/abs/2101.12340) [astro-ph.GA].
- Zuhone, John A. and E. Roediger (June 2016). “Cold fronts: probes of plasma astrophysics in galaxy clusters”. In: *Journal of Plasma Physics* 82.3, 535820301, p. 535820301. DOI: [10.1017/S0022377816000544](https://doi.org/10.1017/S0022377816000544). arXiv: [1603.08882](https://arxiv.org/abs/1603.08882) [astro-ph.HE].